JOURNAL OF LIQUID CHROMATOGRAPHY & RELATED TECHNOLOGIES

HPLC
TLC
Capillary Electrophoresis
Supercritical Fluid Techniques
Membrane Technology
Field-Flow Fractionation
Preparative & Analytical Separations

Special Issue on
FIELD-FLOW FRACTIONATION

Edited by

GEORGE KARAISKAKIS
University of Patras
Patras, Greece

JACK CAZES
Florida Atlantic University
Boca Raton, Florida

VOLUME 20 NUMBERS 16 & 17 1997

JOURNAL OF LIQUID CHROMATOGRAPHY & RELATED TECHNOLOGIES

September/October 1997

Aims and Scope. The journal publishes an outstanding selection of critical, peer-reviewed papers dealing with analytical, preparative and process-scale liquid chromatography of all types and related technologies such as TLC; capillary electrophoresis; supercritical fluid extraction and chromatography; membrane separation technology; field-flow techniques; and others. As new separation technologies are introduced, they will also be included in the journal. On a regular basis, special topical issues are devoted to specific technologies and applications. Book reviews, software reviews and a calendar of meetings, symposia and expositions are also included.

Identification Statement. *Journal of Liquid Chromatography & Related Technologies* (ISSN: 1082-6076) is published semimonthly except monthly in May, August, October, and December for the institutional rate of $1,750.00 and the individual rate of $875.00 by Marcel Dekker, Inc., P.O. Box 5005, Monticello, NY 12701-5185. Periodicals postage paid at Monticello, NY. POSTMASTER: Send address changes to *Journal of Liquid Chromatography & Related Technologies*, P.O. Box 5005, Monticello, NY 12701-5185.

Volume	Issues	Institutional Rate	Individual Professionals' and Student Rate	Foreign Postage: Surface	Foreign Postage: Airmail to Europe	Foreign Postage: Airmail to Asia
20	20	$1,750.00	$875.00	$75.00	$110.00	$130.00

Individual professionals' and student orders must be prepaid by personal check or may be charged to MasterCard, VISA, or American Express. Please mail payment with your order to: Marcel Dekker Journals, P.O. Box 5017, Monticello, New York 12701-5176.

CODEN: JLCTFC 20(16&17) i-xx, 2509-2940 (1997)
ISSN: 1082-6076

Printed in the U.S.A.

Subscribe Today!

Use the cards below to subscribe to the *Journal of Liquid Chromatography & Related Technologies* or to recommend the journal to your library for acquisition.

NO POSTAGE
NECESSARY
IF MAILED
IN THE
UNITED STATES

BUSINESS REPLY MAIL
FIRST-CLASS MAIL PERMIT NO. 2863 NEW YORK NY

POSTAGE WILL BE PAID BY ADDRESSEE

PROMOTION DEPT
MARCEL DEKKER INC
270 MADISON AVE
NEW YORK NY 10157-1928

Journal of Liquid Chromatography & Related Technologies

Editor: **JACK CAZES**
Coconut Creek, Florida

The *Journal of Liquid Chromatography & Related Technologies* now publishes an outstanding selection of critical, peer-reviewed papers dealing with analytical, preparative, and process-scale liquid chromatography of all types and related technologies such as TLC; capillary electrophoresis; supercritical fluid extraction and chromatography; membrane separation technology; field-flow techniques; and others. As new separation technologies are introduced, they will also be included in the journal.

On a regular basis, special topical issues will be devoted to specific technologies and applications. Book reviews, software reviews, and schedules of meetings, symposiums, and expositions are also included.

JOURNAL OF LIQUID CHROMATOGRAPHY
& RELATED TECHNOLOGIES

JOURNAL OF LIQUID CHROMATOGRAPHY & RELATED TECHNOLOGIES

Indexing and Abstracting Services. Articles published in *Journal of Liquid Chromatography & Related Technologies* are selectively indexed or abstracted in:

■ Abstracts Journal of the Institute of Scientific and Technical Information of the Russian Academy of Sciences ■ Alerts ■ Aluminium Industry Abstracts ■ Analytical Abstracts ■ ASCA ■ Berichte Pathologie ■ CAB Abstracts ■ Cambridge Scientific Abstracts ■ Chemical Abstracts ■ Chemical Reactions Documentation Service ■ Current Awareness in Biological Sciences ■ Current Contents/Life Sciences ■ Current Contents/Physical and Chemical Sciences ■ Current Opinion ■ Engineered Materials Abstracts ■ Engineering Index ■ Excerpta Medica ■ Metals Abstracts ■ Reference Update ■ Saltykov-Shchedrin State Public Library ■ Science Citation Index ■ Tobacco Abstracts

Manuscript Preparation and Submission. See end of issue.

This journal is also available on CD-ROM through ADONIS™ beginning with the 1991 volume year. For information contact: ADONIS, Marketing Services, P.O. Box 17005, 1001 JA Amsterdam, The Netherlands, Tel: +31-20-626-2629, Fax: +31-20-626-1437.

The journals of Marcel Dekker, Inc., are available in microform from: University Microfilms, Inc., 300 North Zeeb Road, Ann Arbor, Michigan 48106-1346, Telephone: 800-521-0600; Fax: (313) 761-1203.

Contributions to this journal are published free of charge.

Effective with Volume 6, Number 11, this journal is printed on acid-free paper.

FIELD-FLOW FRACTIONATION

Edited by

Dr. George Karaiskakis
University of Patras
Patras, Greece

Dr. Jack Cazes
Florida Atlantic University
Boca Raton, Florida

This is a special issue of
Journal of Liquid Chromatography & Related Technologies,
Volume 20, Numbers 16 & 17, 1997.

MARCEL DEKKER, INC. New York, Basel, Hong Kong

JOURNAL OF LIQUID CHROMATOGRAPHY
& RELATED TECHNOLOGIES

Volume 20, Numbers 16 & 17, 1997

Special Issue on
Field-Flow Fractionation

CONTENTS

J. LIQ. CHROM. & REL. TECHNOL., 20(16 & 17), xi–xiii (1997)

DEDICATION

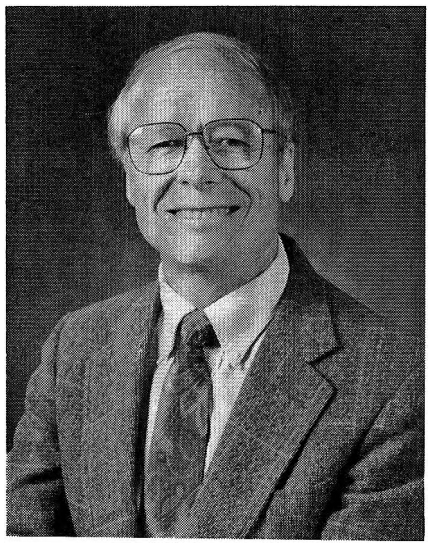

DEDICATED TO THE MEMORY OF
PROFESSOR J. CALVIN GIDDINGS
1930–1996

SCIENTIST, TEACHER, FRIEND, EXPLORER

Albert Einstein once wrote, "If I have been able to look into the future, it is because I stood on the shoulders of giants."

This special issue of the Journal of Liquid Chromatography & Related Technologies is dedicated to Professor J. Calvin Giddings—an intellectual, scientific, and humanitarian giant upon whose shoulders we have stood in our own time. He, his teaching, and his great enthusiasm have inspired so many of

us, too numerous to count, to higher levels of achievement; Cal made research so real, exciting, vibrant, that we wanted to delve into and carry forward that which he so aptly pioneered.

Professor Giddings was born in American Fork, Utah, on September 26, 1930. He received a B.S. degree from Brigham Young University in 1952 and a Ph.D. degree from the University of Utah in 1954 under Henry Eyring. His thesis research dealt with topics in chemical kinetics, quantum chemistry, and chromatography. He did post-doctoral work on the theory of flames with J. S. Hirschfelder at the University of Wisconsin.

In 1957, Dr. Giddings joined the faculty of the University of Utah as Assistant Professor of Chemistry. He became Associate Professor in 1959, Research Professor in 1962, Professor in 1966, and Distinguished Professor in 1989.

A major area of his research has been chromatography in almost all of its fundamental aspects. He has also worked on the unification of separation theory, new separation methodology, macromolecular separations, techniques for diffusion coefficient measurements, theory of diffusion, chemical kinetics, and snow and avalanche physics. He invented and extensively developed the versatile field-flow fractionation method for macromolecular separations. He has been active in research and education dealing with environmental problems.

Dr. Giddings is author or co-author of over 400 publications and Editor of 32 books. He is sole author of "Dynamics of Chromatography" (1965), the textbook, "Chemistry, Man, and Environmental Change" (1973), and the graduate text, "Unified Separation Science" (1991).

Scientific posts he has held include: Advisory Board of Analytical Chemistry (1962-1964); Chemistry Research Evaluation Panel, AFOSR (1964-1969); Exec. Editor of Separation Science & Technology (1966-1996); Exec. Editor of Advances in Chromatography (1965-1991); Advisory Board of Negative Population Growth, Inc.; Editorial Board of Journal of Liquid Chromatography & Related Technologies (1978-1996); Editorial Board of Journal of Microcolumn Separations; Fellow, American Association for the Advancement of Science; Fullbright Grant, Cayetano Heredia University, Lima, Peru.

Dr. Giddings has received many awards, including the ACS Award in Chromatography & Electrophoresis (1967); Utah Award, ACS Local Sections (1970); ROMCOE Award, Outstanding Environmental Achievement in

Education (1973); Tswett Medal in Chromatography (1978); Stephen Dal Nogare Chromatography Award (1979); Distinguished Research Award, University of Utah (1979); ACS Award in Analytical Chemistry (1980); Russian Scientific Council Chromatography Award (1980); Phi Lambda Upsilon Award, University of Nebraska (1983); ACS Award in Separation Science & Technology (1986); Honorary Doctor's Degree, University of Uppsala, Sweden (1987); R&D 100 Award (jointly with M. N. Myers), R&D Magazine (1988); EAS Award for Outstanding Achievements in Fields of Analytical Chemistry (1988); Martin Award, The Chromatography Society, London (1988); Merit Award, Chicago Chromatography Discussion Group (1988); R&D 100 Award (jointly with M. N. Myers), R&D Magazine (1989); National Award in Chromatography, N. E. Regional Chrom. Disc. Group (1990); Nichols Medal, NY Section, ACS (1991); Governor's Medal in Science & Technology (1991); Pittsburgh Analytical Chemistry Award, SACP (1992); Vinci of Excellence Award, Science for Art Competition, LVMH Group, Paris (1993).

Dr. Jack Cazes
Florida Atlantic University
Boca Raton, Florida

J. LIQ. CHROM & REL. TECHNOL., 20(16 & 17), xv–xvi (1997)

PREFACE

Field-Flow Fractionation was developed by Professor J. Calvin Giddings. The expansion of the Field Flow Fractionation technique, all around the world, is a major breakthrough of Professor Giddings, who was one of the true pioneers of chromatography.

Almost all the authors whose papers are presented in this special issue of the Journal of Liquid Chromatography and Related Technologies, which is dedicated to the memory of this eminent scientist and excellent man, belong to the large, world-wide group of pupils and collaborators of Professor Giddings. There are few scientists who have had the impact, both scientifically and educationally, that Professor Giddings has had. His work and his contributions to his collaborators, and this particular field of science, stand as an exceptional achievement.

Professor Giddings didn't only teach his collaborators the FFF method, but he also provided some of them, including me, with basic components of the FFF equipment, so they continued working in the same field under his encouragement and guidance, especially while taking their first steps in scientific research.

I, and evidently all of his pupils and collaborators, feel very fortunate for having had the chance to cooperate with this distinguished scientist and wonderful person—not mentioning the knowledge we gained about this innovative separation technique.

We scientists, from America, Europe, Asia, and Australia, must pledge our honour and continue working with FFF, to spread this important method all around the world. We have the obligation to make the FFF technique well known, in the short-term outlook, to more and more scientists working on biological, pharmaceutical, environmental, and industrial particulate matters and macromolecules.

As can be concluded from the manuscripts in this special issue of the Journal, it is quite evident that the advantages of this method, compared to similar others, are impressive. We must overcome every technical difficulty we may encounter, and impart this important chromatographic technique to as many people as possible.

The remembrance of Professor Giddings will lead our steps to the achievement of our goal, which is to make the FFF technique known to the whole scientific world.

Dr. George Karaiskakis, Guest Editor
Professor of Physical Chemistry
Department of Chemistry
University of Patras
Greece

J. LIQ. CHROM. & REL. TECHNOL., 20(16 & 17), xvii–xix (1997)

FOREWORD

Distinguished Professor J. Calvin Giddings died on October 24, 1997, after a long and courageous battle with cancer. He will be remembered for his many contributions in science, exploration and environment protection.

He received his B.S. degree from Brigham Young University and his Ph.D. from the University of Utah, under Henry Eyring. Professor Eyring suggested that Cal look at the theoretical basis for chromatography, then just beginning to be studied. His insight and careful theoretical development were eventually consolidated in his book Dynamics of Chromatography, which has become a classic in the field.

His interests included the properties of dense gases, and led to the establishment of the foundations for supercritical fluid chromatography and supercritical fluid extraction. This alternative approach to HPLC was studied for several years before others became interested in it for the separation of non-volatile compounds.

Concurrent with the supercritical studies, he began work on thin channel separation methods. The first and most studied was field-flow fractionation (FFF) which was initially conceived while on a vacation trip in the fall of 1965, where he stayed one night in a motel in Evanston, Wyoming, at that time a cowboy town. Between the celebrating cowboys and a noisy heat radiator, he was unable to sleep and began thinking about the effects of fields which led him to the basic idea of FFF. He returned to Salt Lake on the following Monday with the basic theory of FFF well under way. The method has now become a reliable and powerful means for characterization of polymers and particles from a wide variety of fields, ranging from medicine to fabrication to environmental studies.

Another thin channel separation method developed more recently is SPLITT, which allows continuous processing of particles to obtain gram and larger quantities of sized material. He founded FFFractionation, LLC, to develop and market equipment for these techniques.

He was the author of over 400 publications, and the founder of the journal, Separation Science and Technology, continuing as executive editor until shortly before his death. He also served as executive editor for the series Advances in Chromatography for the first 32 volumes.

Professor Giddings was the author of the textbook, "Chemistry, Man, and Environmental Change." The graduate textbook Unified Separation Science grew out of his course on separations.

He received many awards, including the Tswett Medal, the Dal Nogare Award, the Martin Award. In addition, ACS Awards in Chromatography and Electrophoresis, Analytical Chemistry, and Separation Science and Technology were given to him in 1967, 1980, and 1986, respectively, and the Nichols Medal from the New York Section of ACS. He was also awarded an Honorary Doctoral Degree from the University of Uppsala in Sweden.

His interests were varied, writing papers on topics ranging from the properties of snow to world population problems. He was always an explorer with a great passion for the outdoors, which placed him in the forefront on the preservation of the environment. He was a major contributor to the establishment of the Lone Peak Wilderness Area, which is only ~25 miles from downtown Salt Lake City.

In his earlier years, he made several first and early technical rock climbs of mountains in Utah. His kayaking expeditions included a number of first descents of rivers in the western states. He led an expedition on the first successful descent of the Apurímac River in Peru—the source of the Amazon river. This descent involved going through the Andes mountains from west to east. This epic is recounted in his book "Demon River Apurimac," published shortly before his death.

In his later years, he became a mountain bike enthusiast. He always chose the most challenging trails to follow. At the Fifth International Symposium on FFF, held in Park City, Utah, in the summer of 1995, he led a group of the participants down a mountain bike trail—some could not keep up with him, and he had been undergoing chemotherapy for nearly a year.

His enthusiasm extended to those around him in all these areas. His research group was included in several river runs such as the San Juan, Desolation and Grays Canyon in Utah, and weekend excursions to Alpine Canyon near Jackson Hole, Wyoming. Weekend skiing and mountain biking excursions were also frequent.

Professor Giddings will be long remembered for his clear insight and the ability to explain complex ideas in ways that were easy to understand. Those of us who had the opportunity to work closely with him for many years greatly feel the loss of this fine man.

Marcus N. Myers
FFF Research Center
Chemistry Department
University of Utah
Salt Lake City, UT 84112

J. LIQ. CHROM. & REL. TECHNOL., 20(16 & 17), 2509–2524 (1997)

FIELD-FLOW FRACTIONATION IN THE DETERMINATION OF RATES OF SURFACTANT ADSORPTION TO COLLOIDAL SUBSTRATES

Qing Chen, Karin D. Caldwell

Department of Materials Science and Engineering
Center for Biopolymers at Interfaces
University of Utah
Salt Lake City, UT 84112

ABSTRACT

The biomedically interesting process of coating surfaces with poly(ethylene oxide)-containing surfactants has prompted a study of the kinetics of adsorbing Pluronic® F108 on model substrates consisting of polystyrene nanospheres. The sedimentation field-flow fractionation method (sdFFF) is found to offer an accurate and precise way to quantify the mass uptake without the need for potentially perturbing labeling reactions. The pseudo-irreversible adsorption from a 4% solution of the polymeric surfactant is found to be 80% complete within the first hour, with the remaining surface population proceeding to completion during an additional nine hour period. These findings are verified by a more conventional method based on chemical analysis. The potential problems of basing the rate analysis on measured levels of depletion, as opposed to the direct assessment of uptake provided by sdFFF, are discussed.

INTRODUCTION

Non-ionic block copolymeric surfactants of the general composition PEO_m-PPO_n-PEO_m, where PEO and PPO represent poly(ethylene oxide) and poly(propylene oxide), respectively, and m and n represent the number of monomer units in each block, have been used extensively to provide steric stabilization of colloids in suspension.[1-3] Due to their non-toxic nature, these substances have also been employed as emulsifiers and stabilizers in pharmacological preparations intended for intravenous use.[4,5] In recent years, surfactants of this type, commercially available under the trade name of Pluronic®, have been applied as biomaterial surface coatings for the purpose of reducing protein adsorption and bacterial colonization.[6-10] Once coated, the surfaces have proven to retain substantial amounts of their applied protection even under in vivo conditions, i.e., in the presence of high concentrations of electrolytes, proteins and whole cells.[11-13]

Many investigators have found the repulsive effect of these surfactants to be optimal at a molar mass of each block PEO of around 5000 Da. In our own work, the surfactant found to most effectively reduce the adsorption of the clotting protein fibrinogen, a key feature of any biomaterial, is the compound known as Pluronic F108, which is characterized by values for the m and n parameters of 129 and 56, respectively. Thus, polystyrene latex particles pre-coated with this compound have been found to adsorb two orders of magnitude less of fibrinogen per unit area from a solution in physiological saline than do their uncoated counterparts.[11]

The practical importance of these coatings has, therefore, added impetus to investigations of the rate at which surfactants of this type adsorb in a quasi-irreversible manner to hydrophobic surfaces of different chemical composition.

Rates of adsorption to a given substrate can be followed either *indirectly* by quantifying the time course of depletion of solute from a solution in contact with the substrate, or *directly* by determining the actual amounts of solute that adhere to a surface after a given exposure time. While indirect methods, as a rule, are relatively easy to carry out and typically involve the analysis of a solution by spectroscopic or analogous means after removal of the substrate, the direct methods are often more involved, as they require quantitation of the adsorbed solute in the presence of the solid substrate. However, if the substrate is to be used in the absence of its supernatant as is, for example, the case when a coated drug-release vehicle is injected intravenously, the only relevant quantity is that amount of adsorbed solute which remains on the surface after extensive wash with solute-free medium.

In the absence of some easily quantifyable indigenous chromophore, direct determinations of solute uptake are often requiring the introduction of a readable label prior to the adsorption/wash step. Although, many times, this is a viable route, there is always a concern that the labeling reaction may have altered the behavior of the solute molecule and that a determined adsorption rate, therefore, may be an artifact of the system. In order to quantify such uptakes with high accuracy, the substrate must present a large enough surface area to ensure the adsorption of measurable amounts. Whenever possible, it is, therefore, desirable to carry out the adsorption to colloidal substrates, which present a favorable surface-to-volume ratio. In the present communication, we wish to illustrate three ways in which to gain insight into the adsorption of the Pluronic F108 surfactant onto polystyrene latex particles. Two of these are of the direct type, while the third describes the indirect assessment of the amounts associated with the substrate after selected reaction times. Of these, one of the direct methods is based on a sdFFF strategy previously developed in our laboratory.[14] Results from this method, which reports mass uptake on a *per particle* basis, are compared with results from the more conventional quantitations of an introduced chromophor. All three methods are inappropriately slow for an exact analysis of the products of short reaction times, i.e., times of the order of a few seconds. For insight into this domain, the newly developed electrical FFF[15] shows great promise, as will be reported elsewhere.

METHODS

Sedimentation FFF (sdFFF) has long been known to accurately determine the mass, or size, of colloidal particles of uniform composition, while *Flow FFF* (flFFF) determines the diffusion coefficient or hydrodynamic diameter of a retained sample.[16-18] All FFF techniques, operating under "normal mode" in channels of the infinite parallel plate geometry, share a common relationship between the observed retention ratio, R, and the reduced layer thickness λ of the solute cloud that forms when an injected sample is allowed to equilibrate under the influence of an externally applied field:

$$R = V^{\circ}/V_r = 6\lambda[\coth(1/2\lambda) - 2\lambda] \quad (1)$$

Here, V° and V_r represent the channel's void volume and the observed retention volume, respectively. The reduced layer thickness λ is inversely related to both the channel thickness w and the magnitude of the applied field. For sdFFF under a gravitational acceleration G, a particle of mass m, size d,

density ρ_p and a density difference with respect to the suspension medium amounting to $\Delta\rho$, parameter λ_{sd} has the following forms:

$$\lambda_{sd} = kT/\ m(\Delta\rho/\rho_p)Gw \tag{2a}$$

$$\lambda_{sd} = 6kT/d^3\pi\Delta\rho Gw \tag{2b}$$

The latter expression only holds for particles of uniform density. In the case of core-shell particles, or adsorption complexes such as the ones of interest here, the size depends entirely on the surface arrangement of the adsorbed molecule which, in all likelihood, is unknown. Also equation 2a needs to be modified in work with adsorption complexes, to account for the different densities which characterize the core (ρ_c) and the shell (ρ_s), respectively. In a suspension medium of density ρ_m, the expression for the reduced layer thickness is as follows:[14,19]

$$\lambda_{sd} = kT/\{m_c(1-\rho_m/\rho_c) + m_s(1-\rho_m/\rho_s\} \tag{3}$$

with m_c and m_s representing the mass of the core particle and the shell, respectively. The mass of the core, or bare, particle can be determined in a separate analysis. From this analysis, one also arrives at a value for the diameter d, by applying eqs. 1 and 2b. This value, in turn, yields the area per particle, πd^2; by dividing the shell-mass per particle, m_s, with this area one directly determines the surface concentration of adsorbed material. It should be stressed that this determination avoids the otherwise common errors associated with assessing the amount of surface area (particle concentration) in contact with a given aliquot of solute during the adsorption experiment.

In the case of flFFF, the separation chamber has semi-permeable walls which allow the application of a pressure differential across the channel, as well as the one applied along the length dimension of the channel which drives the carrier fluid from injection port to channel exit. This transverse pressure drop results in a cross-flow, V_c, of carrier medium which transports injected particles to the accumulation wall. The resulting diffuse particle cloud has a reduced layer thickness, λ_{fl} whose magnitude depends on the sample's diffusion coefficient, D, in addition to the applied cross-flow:

$$\lambda_{fl} = DV^\circ/V_c w^2 = kTV^\circ/3\pi\eta w^2 V_c d \tag{4}$$

In retention analyses using either method, the zones will become increasingly broader with increasing channel flow rate. However, this broadening will decrease with increased retention of the sample, i.e., with

increased field strength. In FFF, as in other zonal separation methods, the separation efficiency is a function of the zone broadening suffered during the separation process. The customary measure of this broadening is the Plate Height, H, which is defined as the generation of zonal variance per unit distance migrated.[20] In FFF, the plate height is normally considered to be composed of the following terms:[21]

$$H = H_n + H_p + H_i \tag{5}$$

where the polydispersity contribution H_p is kept near zero in work with uniform standard particles, the instrumental band broadening H_i is kept minimal with a careful system design and good operating procedures, while the non-equilibrium contribution H_n dominates the process. The magnitude of this term depends strongly on the level of retention expressed by λ and less so on the linear flow velocity $\langle v \rangle$, the thickness w of the FFF channel, and the diffusion coefficient D of the sample. At high retention, i.e., low values of parameter λ, this plate height contribution is well approximated by:[21]

$$H_n = 24\ \lambda^3 w^2 \langle v \rangle / D \tag{6}$$

The resolution of particles of different mass increases with increasing field strength and decreases with increased flow velocity. An optimal separation program for a kinetics analysis, such as the one of interest here, will seek to accommodate a maximum number of analyses with high mass resolution in a given period of time. In seeking such an optimum, it is important to recall the relationship between resolution (Rs) on the one hand and selectivity (retention difference) and efficiency (plate height) postulated by Giddings:[22]

$$Rs = \Delta t / 4\sigma_t = \frac{1}{4}\ S_d\ (\Delta d/d)\ \sqrt{L / H} \tag{7}$$

Here, an Rs value of unity or above symbolizes complete resolution, implying that the difference Δt in elution time between two components of different diameters exceeds four standard deviations in peak width (time units). The right hand expression in eq. 7 casts Rs in terms of the size selectivity, S_d of the separation (S_d = 3 for sdFFF at high retention), the relative size difference between the two components ($\Delta d/d$), and the square root of the ratio between column length L and plate height H. Inserting the expression for the dominant plate height term of eq. 6, and grouping terms that are constant for a given system and sample pair, makes clear the impact on resolution of the experimental variables field strength (G) and average flow velocity ($\langle v \rangle$):

$$Rs = \text{const.} \sqrt{G^3 / \langle v \rangle} \quad (8)$$

The instrumentation used for the sdFFF analysis has been described in principle elsewhere.[23] The present "column" consists of two highly polished pieces of Hastelloy metal, sandwiched around a stainless steel spacer which specifies the channel dimensions as follows: thickness w = 254 μm, breadth b = 2 cm, and length L = 94 cm. The ends are tapered with 60 degree angles at each apex, and the void volume V^o, determined experimentally from injections of acetone and corrected for dead volume, is 4.83 mL.

The column is coiled to fit inside a rotor basket whose dimensions are such that the channel itself is positioned 15.5 cm from the axis of rotation. Hence, the spin rate of the centrifuge in revolutions per minute (RPM) is converted into channel gravitational acceleration, G, in the following manner:

$$G = [(1/60) \times RPM \times 2\pi]^2 \times 15.5 \text{ cm s}^{-2} \quad (9)$$

Sample injections of 1-4 mL were made directly onto the channel while at stand still. Immediately following injection, the channel flow was stopped and the centrifuge accelerated to its set spin rate where the sample was allowed to relax into its equilibrium distribution (typically 16-25 minutes) before the flow was reinitiated.

The flFFF measurements, in turn, were carried out in a Universal Fractionator from FFFractionation, Inc. (Salt Lake City, UT); the dimensions of its flow channel are: thickness w = 184 μm, breadth b = 2 cm, and length L = 39 cm, for a void volume of 1.30 mL. The actual channel thickness is less than that of the PTFE spacer (254 μm) due to a compression of the YM10 membrane (Amicon) which constitutes the accumulation wall of this channel. The "field," in this case, was a cross-flow of 1 mL/min, while the longitudinal flow was 4 mL/min. As in the case of the sedimentation analog, sample injections were made directly into the channel with a microsyringe. In both cases, effluents were monitored by means of a Linear UV-106 detector.

Photon Correlation Spectroscopy (PCS) was performed on a Brookhaven Model BI-200 instrument with a 72 channel BI-2030 correlator, essentially as described by Weiner.[24] In this manner, the diffusion coefficients of the particulate samples were determined, either by a direct exponential fit of the correlation function or by a polynomial fit whereby the second moment value was collected. In both cases, the diffusion coefficients were converted to the

corresponding hydrodynamic particle diameters by application of the Stokes-Einstein relationship. Each sample was measured 10 times to provide the desired confidence in the measurement.

Adsorption Kinetics by Chemical Assessment was carried out to verify the sdFFF analysis.[14] In this approach, the 261 nm PS latex was allowed to adsorb an end-group labeled Pluronic F108.[25] Previous studies had indicated that the labeled and unlabeled surfactants adsorb to PS latex to the same degree, and that the labeling reaction, therefore, had left the system unperturbed. The label consisted of a pyridyl disulfide group that was easily cleaved off by reduction with 25 mM dithiothreitol (DTT). The released thiopyridone was readily quantified spectrophotometrically from its absorbance at 343 nm. Its extinction coefficient at this wavelength is 8080 $M^{-1}cm^{-1}$.

For the analysis, several 0.4 mL aliquots of 10% PS 261 nm (unwashed) were incubated in solutions of Pluronic F108 in phosphate buffered saline (PBS - pH 7.4, I = 0.15 M). The concentrations at the start of adsorption were: surfactant = 4%, PS latex = 2.5%. These aliquots were rotated end-over-end at room temperature for various lengths of time (5 min, 30 min, 1 h, 2 h, 5 h, 10 h, and 24 h). A Millipore filter was then used to separate the supernatant from the particles. The removed supernatants were examined for their residual concentrations of labeled Pluronic, as described above, while the coated particles were extensively washed on this filter using PBS. After a final suspension in 1 mL of this buffer, reductive cleavage for 30 minutes, and a centrifugation step (14,000 RPM in an Eppendorf Centrifuge for 20 minutes), the released thiopyridone was quantified by a Lambda-6 spectrophotometer from Perkin-Elmer. The remaining PS particles were dried and weighed for estimation of their surface area, and the surface concentration at each time point was finally computed.

MATERIALS

The polystyrene latex particles were supplied by Seradyn, Inc. in suspensions whose concentrations were 10% by weight. They were coated without prior washings. These particles had a density of 1.05 g mL^{-1}.

The bare particles were sized in aqueous solutions of the FL-70 detergent (0.1 %) from Fisher Scientific. For purposes of evaluating particle size and mass by the various analytical techniques, these solutions were assumed to have the same properties as water, i.e., a density of 1.00 g mL^{-1} and a viscosity of 0.89 cp at the ambient temperature of 25 °C.

The Pluronic F108 surfactant (molar mass 14,600 Da) was a generous gift from the BASF Corporation; the density of this (unhydrated) surfactant is 1.16 g mL^{-1}. The pyridyl disulfide activated analog (F108-PDS) was prepared in our laboratory, exactly as described in ref. (25). For each prepared batch, the degree of substitution (average value 86 mole% PDS per mole F108) was determined spectrophotometrically after reductive cleavage with DTT from the Boid Co.

RESULTS

Validation of the Sizing Technique

Our ability to use the protocol described earlier for sdFFF determination of amounts of adsorbed surfactant[14] requires that instrument parameters such as void volume (V^0) and channel thickness (w) are well characterized. Technique validation is therefore essential, and is best carried out as a comparison of sizes determined by several different methods. Table 1 summarizes the sizes determined for five different latex particles (uncoated) using the sdFFF, flFFF, and PCS techniques. The agreement between techniques is seen to be good, and the precision in the data set as a whole is acceptable.

Selection of Optimal Conditions for sdFFF

As discussed in the Methods section, the ability to determine slight shifts in particle size or mass requires careful selection of operating conditions, such that the resolution offered by the system is high. In FFF, a high resolution is usually achieved by operating at high field strength and slow channel flow, as indicated by eq. 8. This, however, implies long analysis times that are particularly impractical for a kinetic study, such as the present one, in which multiple samples need to be processed within a limited time. Somewhat arbitrarily, it was decided to aim for a run time of around 30 minutes. With a 25 minutes' relaxation time, this meant that one sample could be analyzed per hour. In order to build up the rate curve, several consecutive incubations had to be initiated in order to generate the necessary number of points to describe the time evolution of the adsorption process.

The substrate to be used in the adsorption reaction was a PS latex with a nominal diameter of 261 nm. As this particle took up the Pluronic F108 surfactant, its mass did increase to cause a shift in the sdFFF elution pattern in the direction of higher retention, i.e., longer retention times. At maximum

Table 1

Comparison of Particle Sizing Measurements for Polystyrene Particles by Different Methods

Nominal	SdFFF	FlFFF	PCS
212	219.0±1.7	214.0±1.0	216.0±6.0
261	260.0±0.5	257.0±10.0	261.0±3.2
272	269.0±3.5	271.0±8.0	270.0±5.4
314	333.0±1.4	336.0±7.0	335.0±13.3
394	389.0±3.0	394.0±18.0	397.0±18.7

Each sample was injected 3 times in FFF measurement and 10 times in PCS measurement, respectively.

surface coverage, the new mass may well be simulated by a 272 nm latex. Therefore, a series of sample separations was carried out to identify suitable conditions for differentiating PS 261 from PS 272 in a time frame of 30 minutes. The results of this study, compiled as Figures 1a-c, led to the selection of a flow rate of 2.0 mL min^{-1} ($\langle v \rangle$ = 0.656 cm s^{-1}) and a spin rate of 1200 RPM.

Rate Analyses

Under the selected conditions, it was possible to differentiate between different levels of uptake, as seen in Figure 2. Particles subjected to adsorption times ranging from 5 min to 24 h were sampled and analyzed. Since the injected samples were still surrounded by their surfactant-containing supernatant during the stop-flow relaxation, the short reaction times are uncertain. Once the entire data set was collected, the determined surface concentrations G were fitted to an expression of the form:

$$d\Gamma_t/dt = k_s (\Gamma_\infty - \Gamma_t)^q, \qquad (10)$$

where Γ_∞ and Γ_t are the surface concentrations at infinite time and time t, respectively, q is the apparent order of the adsorption reaction, and k_s is the rate constant associated with the reaction, according to the sdFFF experiment. As seen in Figure 3, the latter two parameters are found to be: q = 3.32 and k_s = 0.611.

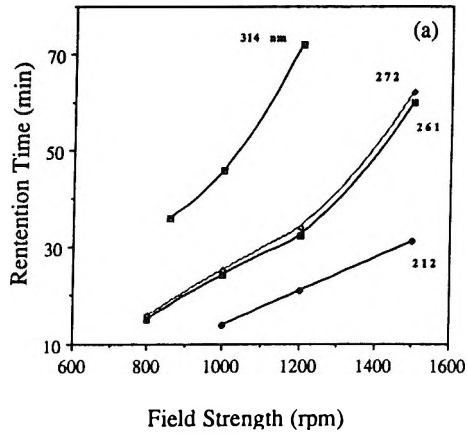
(a)
314 nm
272
261
212
Rentention Time (min)
70
50
30
10
600
800
1000
1200
1400
1600
Field Strength (rpm)

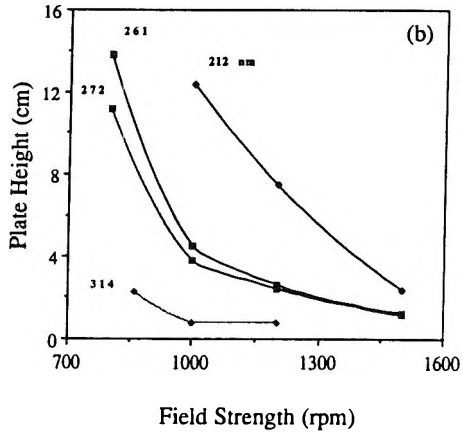
(b)
261
212 nm
272
314
Plate Height (cm)
16
12
8
4
0
700
1000
1300
1600
Field Strength (rpm)

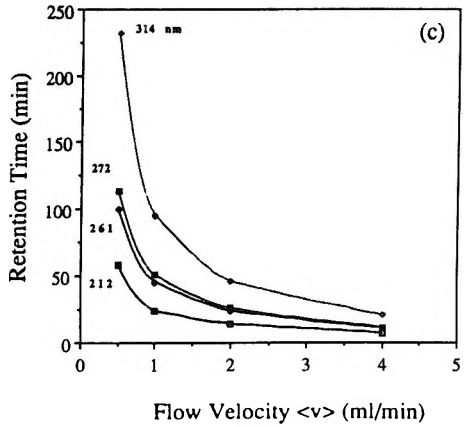
(c)
314 nm
272
261
212
Retention Time (min)
250
200
150
100
50
0
0
1
2
3
4
5
Flow Velocity <v> (ml/min)

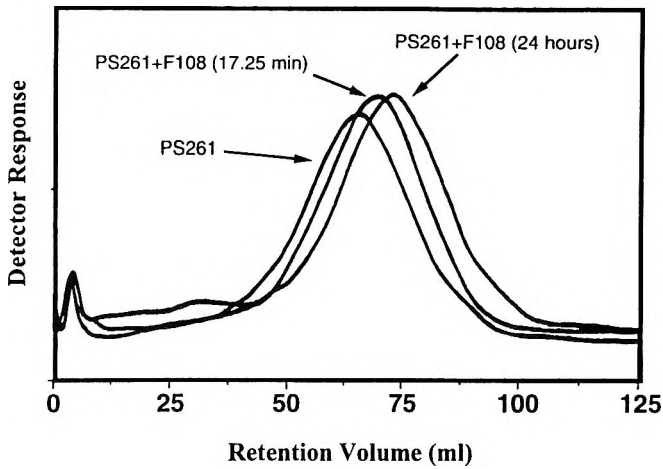

Figure 2. Comparison of fractograms of bare and surfactant coated particles. The shift of the peaks of coated particles to larger retention volumes is due to the increase in mass caused by the surfactant adsorption. Experimental conditions: flow = 2.0 mL/min, field = 1200rpm, relaxation time = 16 minutes.

In order to verify the accuracy of this analysis, the adsorption kinetics was also followed by an alternate direct method, in this case based on quantitation of an introduced, spectroscopically identifiable label, as described in the Methods section above.

The rate curve determined by this approach is likewise included in Figure 3 and is labeled "Chemical." The two parameters q and k_c, identifying order and rate constant, respectively, are for this curve: q = 3.68 and k_c = 0.635, in remarkably good agreement with the characteristics determined by sdFFF.

The labeled Pluronic F108 did also serve as a suitable marker for an indirect analysis of the adsorption kinetics. In this case, the uptake of surfactant by the particles was determined from the reduction in supernatant concentration with time.

Figure 1 (left). Optimization of Resolution in SdFFF: (a) Plot of field strength versus retention time, (b) The effect of field strength on plate height, (c) Plot of velocity versus retention time (1000 rpm). Flow velocity = 2 mL/min in (a) and (b).

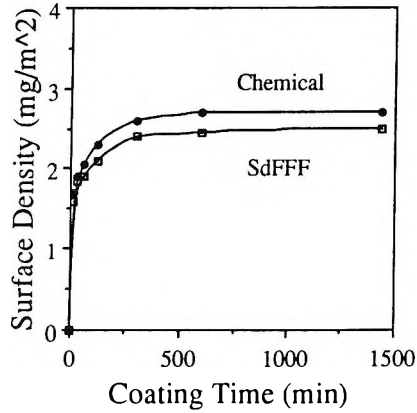

Figure 3. Adsorption rate curves recorded with the SdFFF and Chemical methods.

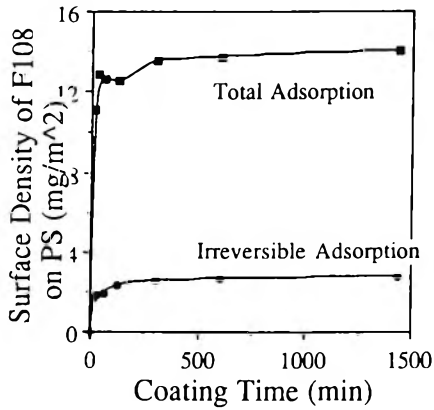

Figure 4. Adsorption kinetics for Pluronic F108 on polystyrene latex, 261 nm, determined by the indirect (depletion) chemical method.

The data show some scatter, as seen from the curve labeled "Total adsorption" in Figure 4. Nevertheless, it appears from this figure that the labeled surfactant formed a multi-layered coat on the particles, since the surface densities determined by depletion far exceeded those determined by direct assessment of the amount of surfactant that was pseudo-irreversibly adsorbed to the particles and remained on the surface even after extensive wash.

DISCUSSION

Adsorption studies, whether of equilibrium uptakes or the rates of attachment, are often done in an indirect manner, i.e., by following the depletion out of a liquid phase of the adsorbing entity. Although the resulting isotherm or rate process may be correctly characterized, the developed adsorption complex may well have little resemblance with a modified surface that is practically useful. This is due to the fact that the modified surface, as a rule, is to serve in an environment free from soluble adsorbate, as is the case when sterically stabilized and drug loaded liposomes are introduced into the human circulatory system, or when antibody coated latex particles are utilized as agglutinating indicators in immunodiagnostic products. For the latter type of complexes, the only relevant parameter is the amount of adsorbate that remains associated with the solid substrate under practical working conditions.

Direct determinations of adsorbed solutes are often difficult to carry out due to a lack of an indigenous label that can be assayed reproducibly, even in the presence of the substrate to which it is adsorbed. However, the deliberate introduction of an extraneous label can, at times, so perturb the behavior of the solute that such physical characteristics as binding and rate constants have little in common with their counterparts which describe the behavior of the unadulterated solute. It is therefore often a desirable goal to be able to perform direct characterizations of adsorption complexes without the need for labeling. The use of sedimentation field-flow fractionation to determine mass uptakes on colloidal substrates may consequently be of significant value.

The adsorption of PEO containing block copolymers to surfaces, for the purpose of suppressing the adhesion of biological macromolecules or particles, has considerable practical appeal. For this reason, as well as for the purpose of gaining basic scientific knowledge, we have set out to investigate the kinetics of forming pseudo-irreversible adsorption complexes between the potent adhesion suppressor Pluronic F108 and surfaces of hydrophobic composition, exemplified by colloidal latex standards of polystyrene.

In this work, the variance in the sdFFF size measurement is significantly less than 1%, implying that the variance in the corresponding mass analysis is well below 3%. Since the problem at hand is to determine subtle differences in particle mass, come about as a result of the adsorption of surfactant, it is relevant to note that the difference in buoyant mass between a bare and a fully Pluronic F108-coated PS particle with a core diameter of 261 nm, as used here, is 16% or in comfortable excess of the random error in the measurement.

Due to the need for relaxation in the sdFFF analysis, and for an exhaustive wash step in case of the "chemical" analog, both of which require around 20 minutes, the early time points are highly uncertain in each case. Yet, from Figure 3 one can unambiguously conclude that around 80% of the surface population takes place during the first hour. The remaining 20% are taken up much more slowly, presumably after extensive rearrangement of the already adsorbed molecules, and the process appears to be complete after about 10 hours.

As noted, the very early phase of the adsorption kinetics occurs much too rapidly for accurate analysis with either of the two methods described here. It has, therefore, been gratifying to discover that the electrical FFF, currently under development in our laboratories, does not require stop-flow relaxation and can, therefore, provide insight into the very early time points. Indeed, highly stable surfactant-particle complexes have shown to form as the result of adsorption times of a mere 10 s.[26] Further examination of the early phase of the adsorption process is under way and will be the subject of a subsequent communication.

ACKNOWLEDGMENT

Partial support for this work from the Center for Biopolymers at Interfaces at the University of Utah is gratefully acknowledged.

REFERENCES

1. T. F. Tadros, B. Vincent, J. Phys. Chem., **84**, 1575-1580 (1980).

2. J. A. Baker, J. C. Berg, Langmuir, **4**, 1055-1061 (1988).

3. B. Kronberg, P. Stenius, Y. Thorssell, Colloids and Surfaces, **12**, 113-123 (1984).

4. S. S. Davis, L. Illum, Biomaterials, 9, 111-117 (1988).

5. R. Jeppson, S. Ljungberg, Acta Pharm. Suecica, **10**, 129-140 (1973).

6. M. Amiji, K. Park, Biomaterials, **13**, 682-692 (1992).

7. J. H. Lee, P. Kopeckova, J. Kopecek, J. D. Andrade, Biomaterials, **11**, 455-463 (1990).

8. R. H. Müller, **Colloidal Carriers for Controlled Drug Delivery and Targeting**, CRC Press, Boston, 1991.

9. T. Blunk, D. F. Hochstrasser, J.-C. Sanchez, B. W. Müller, R. H. Müller, Electrophoresis, **14**, 1382-1387 (1993).

10. M. J. Bridgett, M. C. Davis, S. P. Denyer, Biomaterials, **13**, 411-416 (1992).

11. J.-T. Li, K. D. Caldwell, Colloids and Surfaces B: Biointerfaces, 7, 9-12 (1996).

12. J. S. Tan, D. E. Butterfield, C. L. Voycheck, K. D. Caldwell, J.-T. Li, Biomaterials, **14**, 823-833 (1993).

13. L. Illum, L. O. Jacobsen, E. M. Müller, S. S. Davis, Biomaterials, **8**, 113-117 (1987).

14. J.-T. Li, K. D. Caldwell, Langmuir, 7, 2034-2039 (1991).

15. K. D. Caldwell, Y.-S. Gao, Anal. Chem., **65**, 1764-1772 (1993).

16. J. C. Giddings, Science, **260**, 1456-1465 (1993).

17. J. C. Giddings, F. J. Yang, M. N. Myers, Science, 1244-1245 (1976).

18. J. C. Giddings, G. Karaiskakis, K. D. Caldwell, M. N. Myers, J. Coll. Interface Sci., **92**, 66-80 (1983).

19. R. Beckett, J. Ho, Y. Jiang, J. C. Giddings, Langmuir, 7, 2040-2047 (1991).

20. J. C. Giddings, **Unified Separation Science**, John Wiley & Sons, Inc., New York, 1991.

21. G. Karaiskakis, M. N. Myers, K. D. Caldwell, J. C. Giddings, Anal. Chem., **53**, 1314-1317 (1981).

22. J. C. Giddings, Pure & Appl. Chem., **51**, 1459-1471 (1979).

23. J. C. Giddings, M. N. Myers, K. D. Caldwell, S. R. Fisher, "Analysis of Biological Macromolecules and Particles," in **Methods of Biochemical Analysis**, D. Glick, ed., John Wiley & Son, Inc., New York, 1980, pp. 79-136.

24. B. B. Weiner, in **Modern Methods of Particle Size Analysis**, H. G. Barth, ed., John Wiley & Sons, Inc., New York, 1984, pp. 93-116.

25. J.-T. Li, J. Carlsson, J.-N. Lin, K. D. Caldwell, Bioconjugate Chem., 7, 592-599 (1996).

26. Q. Chen, M. S. Thesis, University of Utah, Salt Lake City, UT, 1996.

Received January 31, 1997
Accepted April 30, 1997
Manuscript 4453

J. LIQ. CHROM. & REL. TECHNOL., 20(16 & 17), 2525–2541 (1997)

COLLOIDAL INTERACTIONS STUDIED BY SEDIMENTATION FIELD-FLOW FRACTIONATION

A. Athanasopoulou,[1] G. Karaiskakis,[1,]* A. Travlos[2]

[1] Department of Chemistry
University of Patras
265 00 Patras, Greece

[2] Institute of Materials Science
N.C.S.R. Demokritos
GR-15310 Agia Paraskevi, Greece

ABSTRACT

Sedimentation Field-Flow Fractionation (SdFFF) is a relatively new technique for the separation and characterization of monodisperse or polydisperse colloidal materials and macromolecules. In the present work, with the aid of SdFFF, the interactions between the polydisperse, irregular Hydroxyapatite (HAP) particles were studied. The stability of HAP, which is of paramount importance in its applications, is dependent upon the total potential energy of interaction between the Hydroxyapatite particles. The latter, which is the sum of the attraction potential energy and that of repulsion, depends on particle size, the Hamaker constant, the surface potential, and the Debye-Hückel reciprocal distance, which is immediately related to the ionic strength of carrier solution.

The larger the repulsion and the lower the attraction caused by increasing the particle's surface potential, and decreasing the effective Hamaker constant, or the ionic strength of the carrier solution, results in a higher stability. Variation of the ionic strength of the carrier solution by adding different amounts of electrolytes led to the size variation of HAP particles and to the determination of their critical aggregation concentration.

From the variation of the number average particle diameter of HAP with time, for different salt concentrations, the rate constants for the bimolecular process of aggregation were determined.

Comparison of the experimental rate constants found by SdFFF with those determined theoretically gives invaluable information about the aggregation mechanism.

INTRODUCTION

A colloidal dispersion is never thermodynamically stable. The total free energy of a dispersed system can always be lowered by reduction of the interfacial area. This reduction can occur by coalescence, or for solid dispersed in liquids, by aggregation, which is a common phenomenon for both natural and industrial colloids.[1] The high degree of stability, which is frequently observed in colloidal systems, is a kinetic phenomenon in that the rate of aggregation of such systems may be practically zero. Thus, in studies of the colloidal state, the kinetics of aggregation are of paramount importance.[2] Although the kinetics of aggregation can be described easily by a bimolecular equation, it is not an easy thing to do experimentally. One technique for doing this is, literally, to count the particles microscopically. In addition to particle size limitations, this is an extraordinarily tedious procedure. Light scattering is particularly well suited to kinetic studies since, in principle, experimental turbidities can be interpreted in terms of the number and size of the scattering particles.[2]

In the present work, sedimentation field-flow fractionation is used for the kinetic study of hydroxyapatite particles' aggregation. Normal SdFFF, which is a subtechnique of field-flow fractionation (FFF), obeys the basic principles originally formulated by Giddings et al.[3] and is capable of analysing particles up to 1 μm diameter. When the effective particle size exceeds ca. 1 μm

(specifically when the particle radius becomes larger than the mean thickness of the steady-state particle layer), the steric limit of FFF (SFFF) is approached.[4] Unlike normal FFF, where smaller particles elute before larger ones, SFFF has an elution order with larger particles eluting first.

In normal SdFFF, where the interactions between the colloidal particles and the channel wall are absent, the diameter of a spherical particle, d_i, (for non-spherical particles d_i is the Stokes diameter, which is the diameter of a sphere of equal diffusivity), is given by the relation:[4]

$$d_i = \left(\frac{36kT}{\pi G w \Delta\rho V^0} \right)^{1/3} V_R^{1/3} \qquad (1)$$

where k is the Boltzmann constant, T is the absolute temperature, G is the centrifugal acceleration, w is the channel thickness, $\Delta\rho$ is the difference in density between the particle and carrier liquid, V^o is the retention volume of non-retained material, equal to the channel void volume, and V_R is the experimental retention volume.

For polydisperse samples, such as that of HAP under study, the number, d_N, and weight, d_w, average particle diameters can be determined from the measured d_i values, by the known procedure described elsewhere.[5]

While, in normal SdFFF, the separation parameter is the particle diameter, in potential barrier SdFFF (PBSdFFF), developed recently in our Laboratory,[6-9] the separation parameter should be the particle diameter or the surface potential, the Hamaker constant, and the ionic strength of the carrier solution. This provides a flexibility in varying the interaction energy between the particles and the FFF channel wall by adjusting one of the above parameters. Experimentally, this should be done by changing the surface tension, which is immediately related to the Hamaker constant (by adding a surfactant to the suspending medium), or the particle's surface potential (by varying the solution pH), and the ionic strength of the carrier solution (by adding an indifferent electrolyte).

Although the interactions between colloidal particles and solid surfaces have been studied in detail by FFF,[6, 7, 10, 11] little work has been performed for the interactions between colloidal particles themselves yielding colloidal aggregates.[12] The purposes of the present investigation were (i) to study the aggregation of hydroxyapatite particles in the presence of various electrolytes

Figure 1. Transmission electron micrograph of hydroxyapatite (HAP) particles (88,000×).

by SdFFF, (ii) to determine the rate constants for the bimolecular process of HAP particles' aggregation, and (iii) to investigate possible aggregation mechanisms describing the experimental data. The selection of HAP as a model sample to study the aggregation process by FFF, is due to the fact that it is often considered a prototype of dental enamel mineral.

While numerous studies have been carried out to investigate the growth and/or dissolution kinetics of HAP, not only to simulate the formation process of bone and tooth but also to create more bioactive materials,[13] as far as we know, there is no work on the aggregation of HAP and, consequently, on its stability.

EXPERIMENTAL

Materials

Polydisperse, irregular colloidal particles of hydroxyapatite (HAP) [$Ca_5(PO_4)_3OH$], provided by Prof. Koutsoukos, with number average diameter

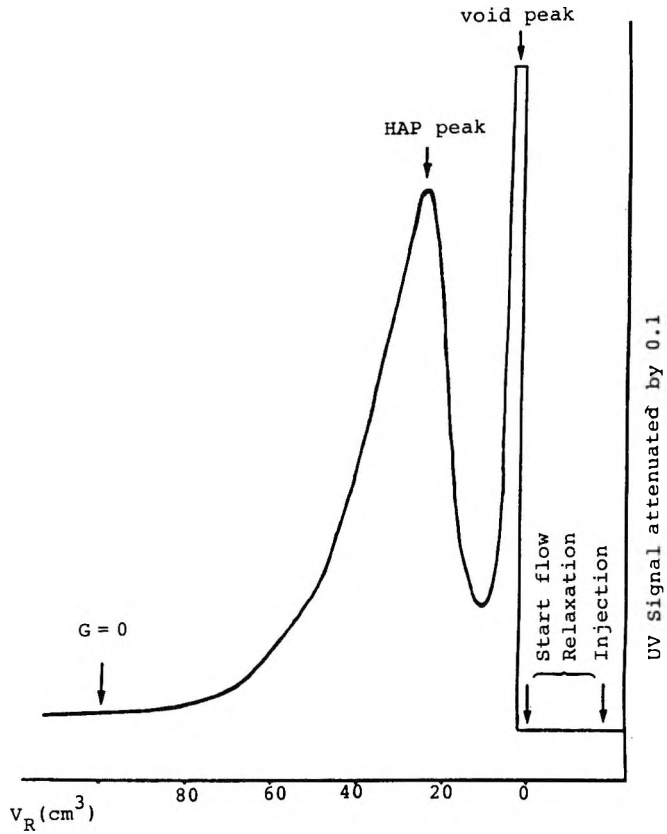

Figure 2. Fractogram of HAP particles obtained by SdFFF. Carrier : 0.5% v/v FL-70 + 0.02% w/w NaN_3; sample = 100 il; flow-rate = 140 $cm^3 h^{-1}$; relaxation time = 10 min.

d_N = (0.261 ± 0.046) μm, were used as sample. The morphology of the HAP particles was studied by means of a Phillips CM-20 transmission electron microscope at 200 kV (cf. Figure 1). The carrier was triply distilled water containing 0.5% (v/v) of a low-foaming, low-alkalinity, phosphate-, chromate-, and silicate-free detergent FL-70 and 0.02% (w/w) sodium azide as bacteriocide.

The electrolytes added to this carrier solution to adjust its ionic strength were: (i) Potassium nitrate from Riedel-De Haen A.G., (ii) Potassium sulphate from Merck A.G., and (iii) Barium nitrate from Riedel-De Haen A.G.

Apparatus and Procedure

The dimensions of the SdFFF system, which has been described in detail elsewhere,[6] were 38.4 cm × 2.35 cm × 0.0197 cm with a channel void volume of 1.68 cm^3, measured by the elution of the non-retained peak of sodium benzoate. The analysis was performed with a Gilson Minipuls 2 peristaltic pump coupled with a Gilson model 111 UV detector operated at 254 nm and a Goerz model RE 541 recorder.

The electrophoretic mobilities of the HAP particles were measured in a microelectrophoresis apparatus (Rank, Mark II) by using a four-electrode capillary cell.

For the kinetic study of the HAP particles' aggregation, 100 μL of 3 mg/cm^3 HAP suspension, which was kept thermostated at 25° C while it was continuously agitated, were injected quickly at various time intervals into the SdFFF column, and then analysed by the known procedure described elsewhere.[5] In order to study the influence of the solution ionic strength on the HAP particle's size, 100 μL of 3 mg/cm^3 sample were injected directly into the SdFFF column using as carrier the detergent FL-70 with various amounts of electrolytes. In both studies, the flow rate (140 $cm^3\ h^{-1}$), the field strength (350 rpm), and the relaxation time (10 min) were kept constant during the analysis time. The obtained fractograms had the form of Figure 2.

RESULTS AND DISCUSSION

Theory

The total potential energy of interaction between two colloidal particles, U_{tot}, is given by the sum of the energy of interaction (repulsion) of the double layers, U_R, and the energy of interaction (attraction) of the particles themselves due to van der Waals forces, U_A. Consequently:

$$U_{tot} = U_R + U_A \tag{2}$$

For identical spherical particles U_R and U_A are defined as follows: [2,14]

$$U_R = \frac{\varepsilon r \psi_o^2}{2} \ln\left[1+\exp(-\kappa H)\right] \quad (\kappa r >> 1) \tag{3}$$

$$U_R = \frac{\varepsilon r^2 \psi_o^2}{R} \exp(-\kappa H) \qquad (\kappa r << 1) \tag{4}$$

$$U_A = -\frac{A_{212} r}{12H} \tag{5}$$

where ε is the dielectric constant of the dispersing liquid, r is the radius of the particle, ψ_0 is the particle's surface potential, κ is the reciprocal double-layer thickness, R is the distance of the centers of the two particles, A_{212} is the effective Hamaker constant of two particles of type 2 separated by the medium of type 1 and H is the nearest distance between the surfaces of the particles (=R-2r). The A_{212} and κ parameters are given by the expressions:[2, 14]

$$A_{212} = \left(A_{11}^{1/2} - A_{22}^{1/2}\right)^2 \tag{6}$$

$$\kappa = \left(\frac{4\pi e^2 N_A}{1000\varepsilon kT} \sum_i c_i z_i^2\right)^{1/2} = \left(\frac{8\pi e^2 N_A I}{1000\varepsilon kT}\right)^{1/2} \tag{7}$$

where A_{11} and A_{22} are the Hamaker constants for the particles and the suspending medium, respectively, *e* is the electronic charge, c_i is the bulk solution concentration of ionic species i, z_i is its charge and I is the ionic strength of the suspending medium.

Equations (2-7) show that the total potential energy of interaction between two colloidal spherical particles depends on the surface potential of the particles, the effective Hamaker constant, and the ionic strength of the suspending medium. Of the various quantities which affect the total interaction potential energy, none is as accessible to empirical adjustment as κ. This quantity depends on both the concentration and valence of the indifferent electrolyte as shown by Equation (7). It has long been known that the addition of an indifferent electrolyte can cause a colloid to undergo aggregation. Furthermore, it is known that for a particular salt a fairly sharply defined concentration is needed to induce aggregation. This concentration may be called the critical aggregation concentration (CAC). The actual concentration of electrolyte at the CAC depends on: (1) the time allowed to elapse before the evaluation is made, (2) the uniformity or,more likely, the polydispersity of the sample, (3) the potential at the surface , (4) the value of Hamaker constant, and (5) the valence of the electrolyte ion of opposite charge to the colloid. The

CAC value for a particular electrolyte is essentially determined by the valence of the counterion, regardless of the nature of the ion with the same charge as the surface (the Schulze-Hardy rule).

The rate of diffusion-controlled aggregation of spherical particles in a disperse system as a result of collisions in the absence of any energy barrier to aggregate, v_r, is given by the von Smoluchowski equation:[2, 14]

$$v_r = -k_r N_o^2 \tag{8}$$

where k_r is effectively a second-order rate constant for diffusion-controlled rapid aggregation, and N_o is the initial number of particles per unit volume.

In the presence of an energy barrier to aggregate, an expression analogous to Equation (8) is applied for the rate v_s:

$$\upsilon_s = -k_s N_o^2 \tag{9}$$

where k_s is the rate constant of slow aggregation in the presence of an energy barrier. The stability ratio, W, of a dispersion is defined as the ratio of the rate constants for aggregation in the absence, k_r, and presence, k_s, of an energy barrier, respectively:

$$W = \frac{k_r}{k_s} \tag{10}$$

Both rapid and slow aggregation, as Equations (8) and (9) show, are described by a bimolecular kinetic equation:[2]

$$\frac{1}{N_i} = \frac{1}{N_o} + k_{app} t_i \tag{11}$$

where N_i is the total number of particles per unit volume at time t_i, N_o is the initial number of the same particles and k_{app} is the apparent rate constant for the aggregation process. Thus, the most reliable way to evaluate a rate constant for aggregation is to measure the number of independent kinetic units per unit volume, N_i, or whichever other parameter which is related to N_i, as a function of time. The time of the experiment is measured from the addition of indifferent electrolyte to the colloid. In the present work, the number average particle diameters were measured by the sedimentation field-flow fractionation technique as a function of time. Therefore, Equation (11) must be converted to

another one in which the particle diameter is immediately related to time. Considering that d_o and d_i are the diameters for spherical particles at times t_o (initial time) and t_i, respectively, the corresponding volumes of the particles V_o and V_i will be given by the relationships:

$$V_o = \frac{4}{3}\pi\left(\frac{d_o}{2}\right)^3 \tag{12}$$

$$V_i = \frac{1}{6}\pi d_i^3 \tag{13}$$

For polydisperse samples, as it is the case here, the d_o and d_i in Equations (12) and (13) are replaced by the d_{N_o} and d_{N_i}, which are the measured number average diameters at times t=0 and t_i, respectively. Taking into consideration that, every time the sample volume is kept constant, the combination of Equations (11), (12) and (13) yields:

$$d_{N_i}^3 = d_{N_o}^3 + d_{N_o}^3 N_o k_{app.} t_i \tag{14}$$

Equation (14) shows that a plot of $d_{N_i}^3$ vs. t_i should be linear with an intercept equal to $d_{N_o}^3$ and a slope equal to $d_{N_o}^3 N_o k_{app.}$, from which the apparent rate constant for aggregation, k_{app}, can be calculated. The N_o value should be determined from the ratio of the total volume of the injected solid HAP sample, V_{tot}, to the volume of the particle, V_o, which can be computed from Equation (12), using as d_o the d_{N_o} value found from the intercept or measured by SdFFF at time t=0 ($N_o = V_{tot.}/V_o$). The V_{tot} value can be computed from the relation:

$$V_{tot} = V_i c_i / \rho_i \tag{15}$$

where V_i is the injected volume of the suspension, c_i is the sample concentration and ρ_i is the density of the solid sample.

Results

The variation of number average diameter, d_N, for the hydroxyapatite particles with the electrolytes' KNO_3, K_2SO_4 and $Ba(NO_3)_2$ concentration, c, is shown in Figures 3, 4 and 5, respectively. In the first two cases, d_N increases

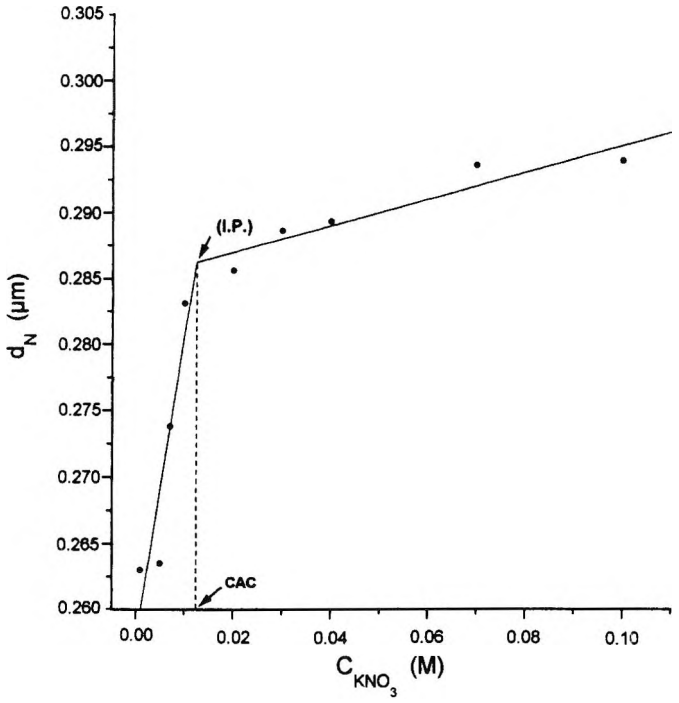

Figure 3. Variation of number average diameter, d_N, for the HAP's particles with the electrolyte KNO_3 concentration, c_{KNO_3}. CAC : Critical aggregation concentration; I.P.: Intersection point of the two straight lines.

with the electrolyte concentration until the critical aggregation concentration is reached, at which point the d_N values remain approximately constant. The starting point of the maximum number average diameter corresponds to the electrolyte concentration called CAC. There is an uncertainty about the exact localization of this starting point and, thus, a relatively large error is introduced in the measurement of the CAC values. The latter can be conveniently and more accurately determined from the intersection points (I.P.) of the two straight lines that can be drawn in Figures 3 and 4.

The obtained CAC values for the electrolytes KNO_3 and K_2SO_4 are 1.27×10^{-2}M and 0.54×10^{-2}M, respectively. These CAC values, according to Schulze-Hardy rule mentioned earlier, had to be about the same, as the HAP sample is a negative colloid at the working pH range. The deviation of the CAC_{KNO_3} and $CAC_{K_2SO_4}$ values, contrary to the theoretical predictions,

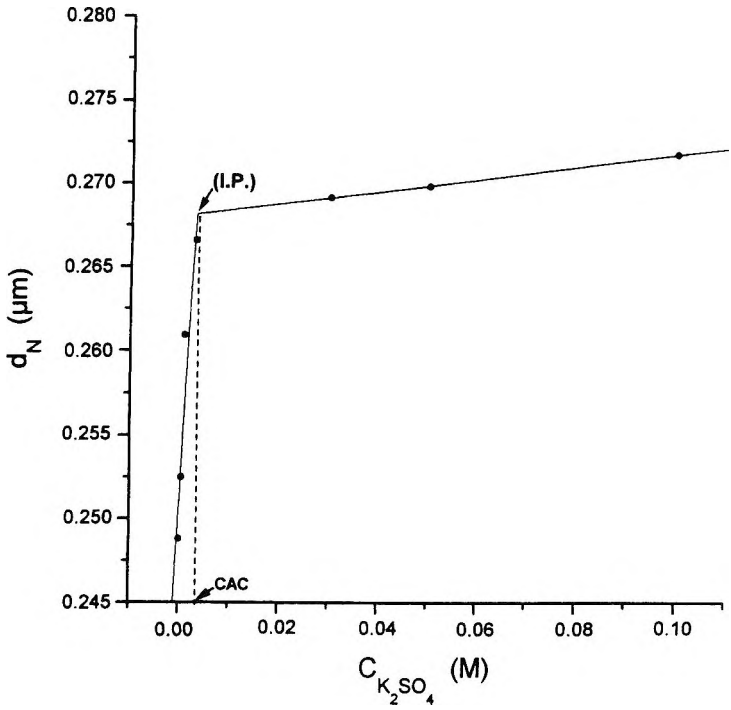

Figure 4. Variation of number average diameter for the HAP's particles with the electrolyte K_2SO_4 concentration.

would be attributed either to the increased polydispersity in K_2SO_4 than in KNO_3, which was verified by TEM pictures or to particle's conformation, although previous work[15] has shown that particle shape has little or no effect on SdFFF retention until the aspect ratio becomes quite large (>50-100). The aspect ratio in the HAP's particles, as the TEM pictures have shown, ranges between 4 and 20, thus making possible the use of this sample for studying the aggregation process by SdFFF. Theory predicts that the CAC value varies inversely with the sixth power of the valence, z, of the counterion (K^+, Ba^{++}) in solution:[2]

$$CAC \propto z^{-6} \qquad (16)$$

From the theoretical ratio of CAC for KNO_3 and $Ba(NO_3)_2$, which is $1^{-6} : 2^{-6} = 64$, one can determine the $CAC_{Ba(NO_3)_2}$ ($\approx 2 \times 10^{-4}$ M) using as CAC_{KNO_3} that found by SdFFF. This explains the fact why the variation of

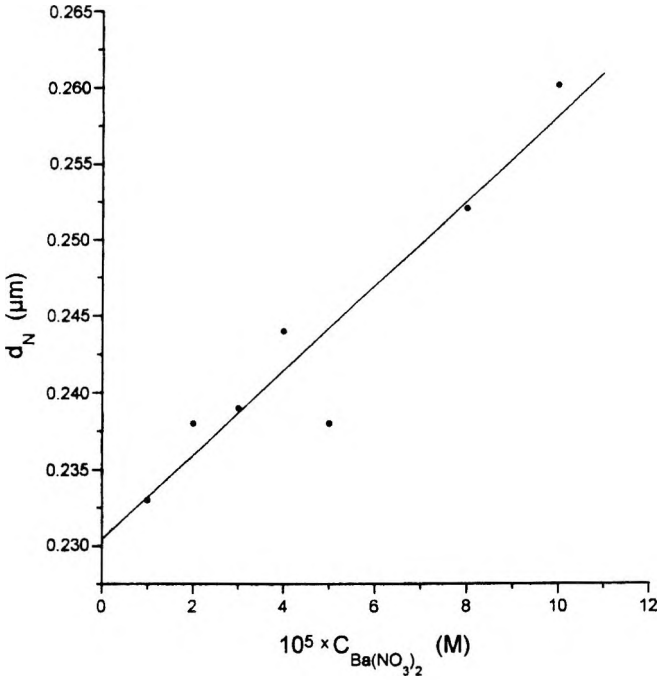

Figure 5. Variation of number average diameter for the HAP's particles with the electrolyte $Ba(NO_3)_2$ concentration.

the d_N values for the HAP particles with the electrolyte $Ba(NO_3)_2$ concentration, shown in Figure 5, is approximately linear in the working concentration range $\left(1x10^{-5}\,M\langle C_{Ba(NO_3)_2}\langle 1x10^{-4}\,M\right)$, as the intersection point of the two straight lines encountered in Figures 3 and 4 corresponds to 2 $\times$ 10^{-4}M $Ba(NO_3)_2$. Thus the plateau of the d_N values is out of the working concentration range, as at concentrations of $Ba(NO_3)_2$ higher than 1 $\times$ 10^{-4}M the detergent FL-70 is no longer soluble in water, therefore making impossible the analysis of HAP particles by SdFFF in that particular concentration range.

For the determination of the apparent rate constant, k_{app}, for the HAP particles' aggregation, as it was mentioned earlier, the plots of $d_{N_i}^3$ vs. t_i at various electrolyte concentrations are necessary [cf. Figures 6 and 7]. The found k_{app} values for the aggregation of the HAP particles in the presence of two electrolytes are compiled in Table 1. It is possible to make a calculation

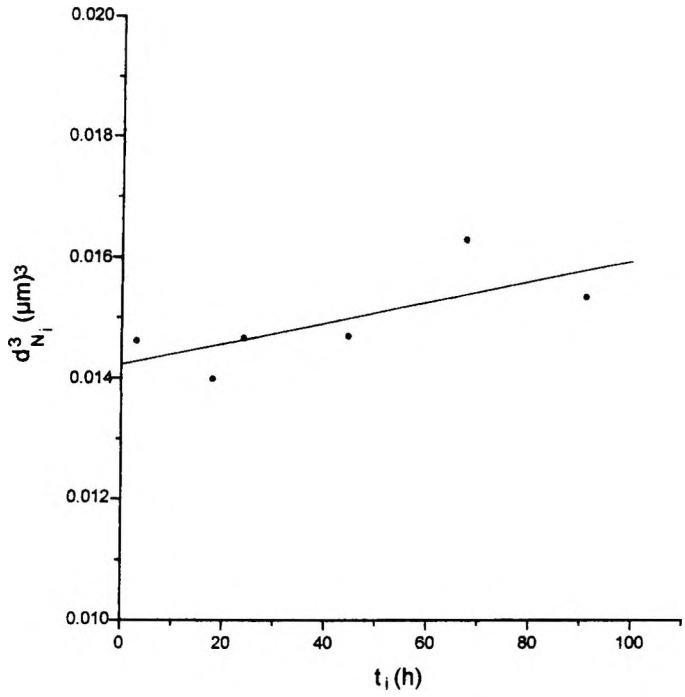

Figure 6. Plot of Equation (14) for the aggregation of HAP particles in the presence of 1×10^{-5}M KNO_3.

which shows whether the values of k_{app} are determined solely by the rate at which two HAP particles can diffuse up to each other (diffusion control), or whether the rate of reaction is limited by other slower processes.

The expected relationship between the rate constant for bimolecular collision (k_1) of HAP's particles and on their diffusion coefficient in the medium, D, was determined many years ago by Smoluchowski[16], whose treatment for spherical particles gives:

$$k_1 = 8\pi rD \tag{17}$$

$$k_{-1} = \frac{6D}{r^2} \tag{18}$$

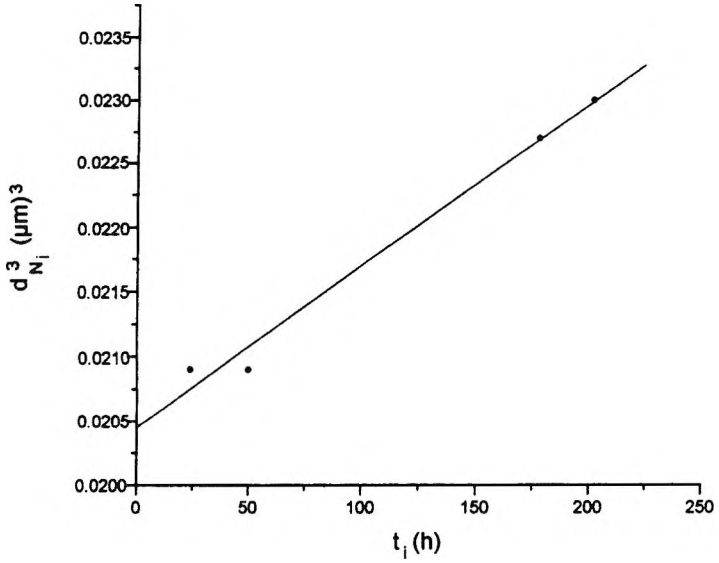

Figure 7. Plot of Equation (14) for the aggregation of HAP particles in the presence of 5×10^{-5}M $Ba(NO_3)_2$.

where k_{-1} is the rate constant for the dissociation of the formed aggregates. Combination of Equations (17) and (18) with the Stokes-Einstein relationship yields:

$$k_1 = \frac{8kT}{3n} \text{ cm}^3 \text{ s}^{-1} \qquad (19)$$

where n is the viscosity of the medium. For water at 25°C, using n = 0.97 cp we calculate from Equation (19) a k_1 value of 1.1×10^{-11} cm^3s^{-1}. This value is about ten orders of magnitude greater than the value of k_{app} actually measured. Thus, aggregation rates are slower than those expected if the process was simply diffusion controlled when electrostatic repulsion is absent. Probably, extra repulsive hydration forces,[17] occuring at close approach of particles, are involved in the observed slow processes. The foregoing discussion indicates that the minimal mechanism for the aggregation reaction of HAP particles would be:

$$\text{Particle 1} + \text{Particle 2} \underset{k_{-1}}{\overset{k_1}{\Leftrightarrow}} \text{Intermediate complex} \xrightarrow{k_2} \text{Stable aggregate} \qquad (20)$$

Table 1

Apparent Rate Constants for Slow Aggregation, k_{app}, Stability Factors, W, and Rate Constants for the Rate-Determining Step, k_2, of HAP Particles' Aggregation, and Fractions of the Total Number of Collisions Which are Effective in Producing Stable HAP's Aggregates, ξ, Determined by SdFFF

Electrolyte:	**1×10^{-3} M KNO_3**	**5×10^{-5} M $Ba(NO_3)_2$**
$k_{app}(cm^3s^{-1})$	2.5×10^{-21}	1.8×10^{-21}
$k_1(cm^3s^{-1})$	1.1×10^{-11}	1.1×10^{-11}
$W=k_1/k_{app}$	4.4×10^{9}	6.1×10^{9}
$k_2(s^{-1})$	2.7×10^{-7}	2.0×10^{-7}
ζ	2.3×10^{-10}	1.7×10^{-10}

Theoretical rate constants for rapid aggregation, k_1, were calculated by Equation (19).

where k_1 and k_{-1} are the rate constants determined by Equations (17) and (18), respectively, and k_2 is the rate constant for the process representing the rate-determining step in the aggregation reaction. Since k_{app}, describing the overall process is smaller than the calculated k_1 value, there must be rapid equilibration of the individual particles and their intermediate complexes followed by the slower step of irreversible aggregation.

Under these conditions, the value of k_{app} is given by:

$$k_{app} = \left(\frac{k_1}{k_{-1}}\right) k_2 \qquad (21)$$

Straightforward calculation, using Equations (17) and (18) gives $k_1 = 1.1\times10^{-11}$ $cm^3\ s^{-1}$ and $k_{-1} = 1.2\times10^{3}\ s^{-1}$ for the HAP's particles having $d_N = 0.261$ μm.

Thus, $k_1/k_{-1} = 9.2\times10^{-15}$ and the k_2 parameter takes the values $2.7\times10^{-7}\ s^{-1}$ (in the presence of 1×10^{-3} M KNO_3), and $2.0\times10^{-7}\ s^{-1}$ [in the presence of 5×10^{-5} M $Ba(NO_3)_2$]. The fraction of the total number of collisions which are effective in producing a stable aggregate is thus only $\zeta=k_2/(k_{-1}+k_2)=2.3\times10^{-10}$ (in the presence of 1×10^{-3}M KNO_3) and $\zeta = 1.7\times10^{-10}$ [in the presence of 5×10^{-5} M $Ba(NO_3)_2$].

A second treatment of the experimental results, taking into consideration that k_{app} and k_1 are identical with k_s and k_r, respectively, defined by Equations (8) and (9), leads to the stability factor, W, of HAP's particles. The found values (cf. Table 1) are too high, indicating that the HAP's particles are very stable, even in the presence of significant quantities of electrolytes.

ACKNOWLEDGMENTS

The authors would like to pay tribute to the services of the late Professor J. Calvin Giddings, who supplied the SdFFF system. They are also grateful to Professor P. Koutsoukos, who supplied the hydroxyapatite sample and to M. Barkoula for typing the manuscript.

REFERENCES

1. F. Family, D. P. Landau, eds., **Kinetics of Aggregation and Gelation**, North Holland, Amsterdam, 1984.

2. P. C. Hiemenz, **Principles of Colloid and Surface Chemistry**, Marcel Dekker, Inc., New York, 1977.

3. J. C. Giddings, F. J. F. Yang, M. N. Myers, Anal. Chem., **46**, 1917-1924 (1974).

4. J. C. Giddings, M. N. Myers, Sepn. Sci. Technol., **13**, 637-645 (1978).

5. E. Dalas, G. Karaiskakis, Colloids Surfaces, **28**, 169-183 (1987).

6. A. Koliadima, G. Karaiskakis, J. Chromatogr., **517**, 345-359 (1990).

7. A. Koliadima, G. Karaiskakis, Chromatographia **39**, 74-78 (1994).

8. A. Athanasopoulou, G. Karaiskakis, Chromatographia, **40**, 734-736 (1995).

9. A. Athanasopoulou, G. Karaiskakis, Chromatographia, **43**, 369-372 (1996).

10. A. Athanasopoulou, A. Koliadima, G. Karaiskakis, Instrum. Sci. Technol., **24(2)**, 79-94 (1996).

11. M. Hansen, J. C. Giddings, Anal.Chem., **61**, 811-819 (1989).

12. H. K. Jones, B. N. Barman, J. C. Giddings, J. Chromatogr., **455**, 1-15 (1988).

13. K. Onuma, A. Ito, T. Tateishi, T. Kameyama, J. Crystal Growth, **154**, 118-125 (1995).

14. M. J. Rosen, **Surfactants and Interfacial Phenomena**, John Wiley & Sons, New York, 1989.

15. J. J. Kirkland, L. E. Schallinger, W. W. Yau, Anal.Chem., **57**, 2271-2275 (1985).

16. J. Lansman, D. H. Haynes, Biochim. Biophys. Acta, **394**, 335-347 (1975).

17. A. M. Carmona-Ribeiro, L. S. Yoshida, H. Chaimovich, J. Phys. Chem., **89**, 2928-2933 (1985).

Received January 10, 1997
Accepted April 9, 1997
Manuscript 4436

J. LIQ. CHROM. & REL. TECHNOL., 20(16 & 17), 2543–2553 (1997)

AGE-DEPENDENT ELUTION OF HUMAN RED BLOOD CELLS IN GRAVITATIONAL FIELD-FLOW FRACTIONATION

Philippe J. P. Cardot,[1] Jean-Marie Launay,[2] Michel Martin[3,*]

[1] Laboratoire de Chimie Analytique et Bromatologie
Université de Limoges
Faculté de Pharmacie
2, rue du Docteur Marcland
87000 Limoges, France

[2] Hôpital Lariboisière
Service de Biochimie et de Biologie Moléculaire
2, rue Ambroise Paré
75475 Paris Cedex 10, France

[3] Ecole Supérieure de Physique et Chimie Industrielles
Laboratoire de Physique et Mécanique des Milieux Hétérogènes
(URA CNRS 857)
10, rue Vauquelin
75231 Paris Cedex 05, France

ABSTRACT

The technique of field-flow fractionation (FFF) which combines the earth gravitational force with a carrier liquid flow in a horizontal, ribbon-like channel is well suited for the separation of micron-sized particulate species such as cells. We investigated the selective elution, in a phosphate buffer, of human red blood cells (RBC) which migrate along the FFF channel more slowly than the carrier.

Fractions of the channel effluent were collected and the activities of various intracellular enzymes, which either reveal the presence of white cells or are known to be related to cell age, were evaluated for each fraction. The hemoglobin sub-fraction composition was also determined.

From analysis of these biochemical determinations, nucleated cells and reticulocytes appeared to be eluted as unretained species while mature RBC form a well defined, retained peak. The steady variation of the activity of age-related enzymes within this peak demonstrates that RBC are separated according to age. These observations, linked to the fact that reticulocytes have a drastically different FFF behavior from RBC, reveal that particle shape and stiffness are, when combined with size and density, key biophysical factors controlling the retention of biological micron-sized particles in FFF.

INTRODUCTION

Field-Flow Fractionation (FFF) is a dynamic separation technique based on the differential elution of the sample constituents by a laminar flow in a flat, ribbon-like, channel according to their sensitivity to an external field applied in a direction perpendicular to that of the flow.[1] FFF applies to a wide variety of macromolecular and particulate species, but the elution mechanism of Brownian, submicron colloidal species differs greatly from that of super-micron particles.[2,3] For the latter, the interplay of steric interactions of the particles with the channel walls and of hydrodynamic lift forces of various origins[4-6] leads to the earlier elution of larger spherical particles.[2,3,7,8] The corresponding elution mechanism is only poorly understood, even for rigid spherical particles. Still, FFF was shown to apply successfully to micron-sized, non rigid particles as evidenced by the increasing number of reports devoted to the separation of cellular materials such as human red blood cells.[9-17]

In the present study, human blood cells were analyzed by the simplest FFF technique, gravitational FFF (GFFF), in which the primary field is the natural earth gravitational field. In order to gain some insight into the separation mechanism of these "soft" particles by FFF, as well as to further evaluate the potential of this technique for blood cell analysis, fractions collected from the channel effluent were subsequently analyzed by means of different erythrocyte and blood markers. They allow a more detailed characterization of the effluent than classical UV photometers generally used in FFF of red blood cells (RBC).

METHODS

The gravitational FFF channel was made from the void space obtained after cutting a 92 cm-long, 2 cm-wide rectangular band with tapered ends in a 175 μm thick Mylar sheet. This sheet was compressed between two horizontal mirror glass plates coated with silicone oil (Silbione, Rhône-Poulenc, Paris, France) to avoid interactions between the cells and the channel walls. The septum injector, as well as connecting tubes from injector to channel and from channel to detector and to fraction collector, were Teflon. The inlet and outlet connecting tubes perforated the upper and lower glass plates, respectively. The overall dead volume from injector to detector was 3.35 mL. The channel effluent was monitored by a Waters 440 (Milford, MA, USA) UV photometer operating at 313 nm. Isotonic (290-320 mOsm/L) phosphate buffer (NaCl 0.1 M, Na_2HPO_4 1.12 M, KH_2PO_4 0.2 M, pH = 7.20) was used for sample dilution and as carrier liquid. A carrier flow of 0.3 mL/min was delivered by an HPLC reciprocating piston pump (Model 110, Beckman, Berkeley, CA, USA).

All human blood samples were collected from the same donor with EDTA as anti-coagulant and diluted in the carrier liquid. 100 μL of an approximately 2-fold dilution of human peripheral red blood cells, containing few residual nucleated cells and platelets, were injected with a syringe through the septum injector.

When fractions of the channel effluent were collected, the detector was removed and replaced by a fraction collector (Model 201, Gilson, Villiers-le-Bel, France). Three consecutive runs were performed under identical experimental conditions. Fractions from each run collected during the same time interval were combined together in a pool. The pools were analyzed by means of the following erythrocytes and blood markers : pyruvate kinase (PK, EC 2.7.1.40) and glucose-6-phosphate-dehydrogenase (G6PD, EC 1.1.1.49) activities,[18-21] foetal hemoglobin (HbF) and glycosylated hemoglobin (HbA1C) composition[22] for RBC; myeloperoxidase (MPO),[23] and alkaline phosphatase (AP, EC 3.1.3.1)[24] activities for leukocytes and platelets.

RESULTS

A typical fractogram of such a blood sample is presented in Figure 1. Three peaks were obtained. The third one corresponds to the RBC, as evidenced by the direct microscopic examination of the cells collected from this peak, which shows an absence of nucleated cells.

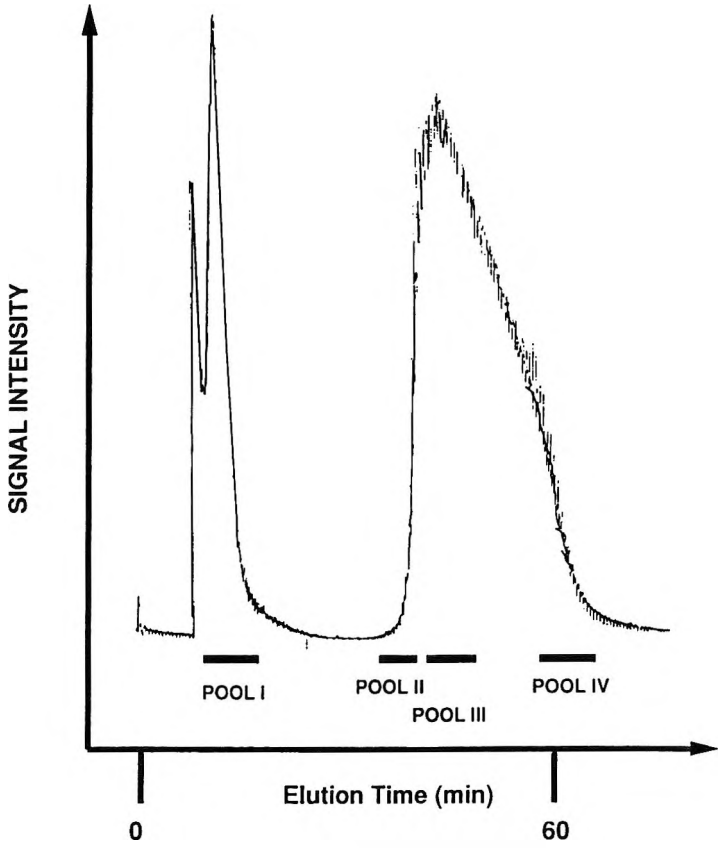

Figure 1. Fractogram of a human blood sample. The positions of the four collected fractions are indicated on the fractogram. Three successive runs were performed in identical experimental conditions. Fractions from each run collected during the same time interval were combined together in a pool. The enzymatic activities and hemoglobin compositions of the four pools so obtained were subsequently evaluated.

The first and second peaks correspond to particles and macromolecules like plasma proteins not affected enough by the external field to be retained. Four pools (see Figure 1) corresponding to the void volume peak (pool I), and to the beginning, the center and the end of the RBC peak (pools II, III and IV, respectively) have been selected for subsequent biochemical analysis. The results of the determinations are reported in Table 1. PK and G6PD activities clearly increase with the elution time, *i.e.*, from pool I to pool IV. MPO and AP activities observed in pool I indicate the presence of leukocytes, which could

Table 1

Biochemical Probes Characterizing the Four Pools Collected From the GFFF Channel Effluent*

Pool	Alkaline Phosphatase Activity	Myeloperoxydase Activity	Hemoglobin F Fract. (%)	Hemoglobin A1C Fraction (%)	Hemoglobin (Quantity Per Pool (mg)	Pyruvate Kinase Activity	Glucose-6-phosphate-dehydrogenase Activity
	0.81	1.43				1.0	0.3
I	0.74	1.35	1	6.2	0.27	0.8	0.1
						1.1	<0.05
II	<0.1	<0.15	0.2	8.5	2.49	6.8	4.3
						5.1	3.7
						12.3	6.5
III	<0.1	<0.15	0.4	8	25.84	13.4	5.6
						12.8	4.9
						21.3	10.3
IV	<0.1	<0.15	0.3	6.3	3.86	19.6	8.7
						18.2	9.4

* All enzyme activities were determined by microfluorometric methods referenced in text and are expressed as μmol/min/g hemoglobin. All assays were performed as recommended by the International Committee for Standardization in Haematology, except the final fluorometric measurements because of their low enzymatic activity levels.

explain the residual PK and G6PD activities in pool I. However, a small, but finite, hemoglobin content, suggesting the presence of a small amount of RBC or RBC lysates, was found in this pool. The subsequent analysis of hemoglobin profile revealed both a high percentage of hemoglobin F, as well as a high HbF/HbA1C ratio. These two values, which are quite larger than in pools II, III or IV, are of the same order of magnitude as that found in patients with hemolytic regenerative anemia and whose reticulocyte percentages number around 8%. This series of informations suggests that the few physiological circulating reticulocytes eluted within the fractions collected in pool I.

The microscopic observation performed on fractions of pools II to IV did not reveal the presence of nucleated cells, a fact corroborated by the undetectable activity of either MPO or PA. The significant increase of PK and G6PD activities observed from pool I to pools II-IV, therefore, indicates the presence of RBC in the latter, which was also checked by microscopy. Furthermore, PK and G6PD activities are seen to steadily increase from pool II

to pool IV, by a factor 2.5 for G6PD and larger than 3 for PK. These observations indicate that young cells, which have larger PK and G6PD enzymatic activities,[25] are retained longer than old cells. The hemoglobin subfraction analysis confirms this effect as the proportion of HbA1C, which is lower in younger cells,[26] decreases from pool II to pool IV.

The observed order of elution of RBC vs. age is in agreement with a previous report on the GFFF separation of transfused and endogenous RBC.[10] Using the quantitative correlation established by Corash, Piomelli et al.,[19] one can associate a RBC age to each value of the PK or G6PD enzymatic activity. Averaging the numbers obtained for each enzyme and each activity determination for a given pool, one gets the following means and standard deviations : 99 ± 19 days for pool II, 59 ± 20 days for pool III and 19 ± 6 days for pool IV. These figures, which have to be compared to the average lifetime of human erythrocytes in the circulation (120 days), reflect the high age selectivity obtained in a GFFF run of RBC. Compared to the classical density gradient centrifugation techniques,[19,25] GFFF offers a number of specific advantages : (i) a simple fractionation instrument, easily home-made, is used; (ii) the separation is more rapid than in density gradient centrifugation methods (in Figure 1, the run duration was about 75 minutes, however it has been demonstrated that the use of stronger driving forces such as a centrifugal force[9] or that force given by a cross-flow[11,14] instead of the earth's gravitational force, allows to obtain much faster separations); (iii) a small sample volume is required (about 0.3 ml of donor's blood have been used in the experiments); (iv) most importantly, the carrier liquid is kept unchanged during the duration of the FFF run, and its composition may be adjusted to physiological conditions (including sterilization) in such a way that the integrity of the cells is maintained, so that viable RBC can be collected at the end of the FFF channel for further use. The physiological constancy of the environmental medium confers a specific advantage to FFF over density gradient techniques for which the change of the osmolarity of the medium associated with the formation of the density gradient has been shown to induce volume and density changes to the RBC.[27]

DISCUSSION

It is tempting to interpret the retention behavior observed for RBC to that known for rigid spherical particles. However, the computation, from fluid mechanics principles, of the transversal lift force acting on particles in flow is not yet completed, even for rigid spheres, when the particles travel in the vicinity of a wall as it is the case in the FFF channel. Therefore, the

interpretation of RBC retention can only be qualitative. According to FFF retention models of micron-sized particles in which hydrodynamic lift forces play a dominant role,[4-6] the retention time of rigid spherical particles increases with decreasing particle volume and increasing particle density (when this density is larger than the carrier liquid density), as experimentally demonstrated.[3,7,8] It has been established that, as the RBC become older, their density increases,[27-29] their volume decreases,[27,28] and they become markedly less biconcave and more spherical.[28] One can, therefore, conclude that, since old RBC elute before young ones, the retention time of RBC increases with increasing cell volume, decreasing density and decreasing sphericity. Thus, as concerns the variation of retention with particle volume and density, the behavior of RBC appears to be opposite to the known behavior of rigid micron-sized spherical particles.

Still, the overall elution order observed between the leukocytes and the erythrocytes is in agreement with that of rigid spheres, since leukocytes are generally less dense and are bigger than RBC. Therefore, one is led to conclude that erythrocytes possess a specific physical characteristic which varies within the RBC elution peak and which influences their retention strongly enough to compensate the opposite combined effects of variations of volume and density. On a physical ground, the major differences between RBC and rigid spheres arise from their shape and the fact that RBC are extremely soft and elastic and may change their shape to a bell-like or paraboloid form when flowing through capillaries.[30] In addition, the orientation of these particles relative to the direction of the flow and the variations of the orientation induced by the velocity gradient may have some influence on the migration of the RBC. Lift forces appear, then, to be quite sensitive to the shape and the deformability of the particles. Because, as they become older, RBC become stiffer and their shape is less biconcave and more spherical, these findings suggest that the lift force increases with increasing sphericity and increasing stiffness of the RBC, if one assumes, in agreement with observations that the mean hemoglobin content per cell remains constant,[21,27,28] that the field force (weight of a RBC) does not change with cell age.

Intriguing is the observation, discussed above, that reticulocytes, which are the youngest RBC and become completely mature within one or two days after entering the circulation, are eluted in pool I, well ahead of the RBC peak, while young adult RBC are the more retained erythrocytes. Such a drastic behavioral difference has to be associated with a significant change in the biophysical characteristics during the maturation process of reticulocytes. It is known that these cells have a larger volume than mature RBC[31] and, from density gradient sedimentation experiments, that their density is smaller than

the average density of the RBC.[27] Although, as mentioned above, these effects can explain, according to known lift force models for rigid spheres, an earlier elution of the reticulocytes, they are unlikely to be the sole and, even, the dominating factors accounting for the retention difference between reticulocytes and normal erythrocytes since they cannot explain the relative retention of young and old RBC. One is led to speculate again on the major role played by shape and stiffness factors in the migration of the reticulocytes in the FFF channel. These factors might be associated with residual organelles[30] or morphological characteristics: reticulocytes appear to be more globular than RBC, although their shape is irregular and polylobulated.[32] Only in the late stage of their maturation process does the biconcave disk shape of the young RBC appear.[30]

The biochemical analysis of fractions collected from the FFF channel effluent has allowed to demonstrate that RBC are separated according to their age. In addition, it has revealed a complex and rich variety of retention behavior which suggests that particle shape and deformability play a dominant role in the flow of RBC. It is hoped that fluid mechanics difficulties involved in the calculation of the lift force on particles moving near a wall will be soon overcome. This would be of great interest for the quantitative interpretation of FFF retention data as well for a better biophysical understanding of blood circulation in capillaries.

ACKNOWLEDGMENTS

Dr. Jean-Louis Laplanche (Service de Biochimie, Hôpital Lariboisière) is kindly ackowledged for performing the hemoglobin analyses. Dr. Martin Czok and Prof. J.-P. Andreux (Université Paris XI) as well as Dr. Robert Parsons (Abbott Laboratories) are gratefully acknowledged for helpful critical discussions. We are grateful to Dr. Francis Vérillon (Gilson, Villiers-le-Bel, France) for the gracious loan of the fraction collector used in the experiments.

REFERENCES

1. J. C. Giddings, Science, **260**, 1456-1465 (1993).

2. J. C. Giddings, M. N. Myers, Sepn. Sci. Technol., **13**, 637-645 (1978).

3. K. D. Caldwell, T. H. Nguyen, M. N. Myers, J. C. Giddings, Sepn. Sci. Technol., **14**, 935-946 (1979).

4. M. Martin, J. Gril, O. Besançon , R. Reynaud, Lecture presented at the 6th International Symposium on Column Liquid Chromatography, Philadelphia, PA, June 7-11, 1982.

5. P. S. Williams, T. Koch, J. C. Giddings, Chem. Eng. Comm., **111**, 121-147 (1992).

6. P. S. Williams, S. Lee, J. C. Giddings, Chem. Eng. Comm., **130** 143-166 (1994).

7. M. Martin, "Particle Sizing by Field-Flow Fractionation," in **Particle Size Analysis 1985**, P. J. Lloyd, ed., John Wiley, Chichester, 1987, pp. 65-85.

8. J. C. Giddings, M. H. Moon, Anal. Chem. **63**, 2869-2877 (1991).

9. K. D. Caldwell, Z.-Q. Cheng, P. Hradecky, J. C. Giddings, Cell Biophys., **6**, 233-251 (1984).

10. P. J. P. Cardot, J. Gerota, M. Martin, J. Chromatogr., Biomed. Appl., **568**, 93-103 (1991).

11. J. C. Giddings, B. N. Barman, M.-K. Liu, "Separation of Cells by Field-Flow Fractionation," in **Cell Separation Science and Technology**, D. S. Kompala, P. Todd, eds., ACS Symp. Ser. 464, American Chemical Society, Washington, DC, 1991, pp. 128-144.

12. E. Urbankova, A. Vacek, N. Novakova, F. Matulik, J. Chmelik, J. Chromatogr., Biomed. Appl., **583**, 27-34 (1992).

13. J. P. Andreux, A. Mérino, M. Renard, F. Forestier, P. Cardot, Exp. Hematol., **21**, 326-330 (1993).

14. B. N. Barman, E. R. Ashwood, J. C. Giddings, Anal. Biochem., **212**, 35-42 (1993).

15. V. Yue, R. Kowal, L. Neargarder, L. Bond, A. Muetterties, R. Parsons, Clin. Chem., **40**, 1810-1814 (1994).

16. X. Tong, K. D. Caldwell, J. Chromatogr. B, **674**, 39-47 (1995).

17. R. Parsons, V. Yue, X. Tong, P. Cardot, A. Bernard, J. P. Andreux, K. Caldwell. J. Chromatogr. B, **686**, 177-188 (1996).

18. M. L. Lowe, A. F. Stella, B. S. Mosher, J. B. Gin, J. A. Demetriou, Clin. Chem., **18**, 440-445 (1972).

18. L. M. Corash, S. Piomelli, H. C. Chen, C. Seaman, E. Gross, J. Lab. Clin. Med., **84**, 147-151 (1974).

20. E. Beutler, K. G. Blume, J. C. Kaplan, G. W. Löhr, B. Ramot, W. N. Valentine, Brit. J. Haematol., **35**, 331-340 (1977).

21. G. Salvo, P. Caprari, P. Samoggia, G. Mariani, A. M. Salvati, Clin. Chim. Acta, **122**, 293-300 (1982).

22. A. Mosca, A. Carpinelli, Clin. Chem., **32**, 202-203 (1986).

23. K. Suzuki, H. Ota, S. Sasagawa, T. Sakatani, T. Fujikura, Anal. Biochem., **132**, 345-352 (1983).

24. D. M. Miller, A. Yang, M. Liepman, Amer. J. Hematol., **18**, 159-169 (1985).

25. S. Piomelli, L. M. Corash, D. D. Davenport, J. Miraglia, E. L. Amorosi, J. Clin. Invest., **17**, 940-948 (1968).

26. J. F. Fitzgibbons, R. D. Koler, R. T. Jones, J. Clin. Invest., **58**, 820-824 (1976).

27. S. Piomelli, G. Lurinsky, L. R. Wassernan, J. Lab. Clin. Med., **69**, 659-674 (1967).

28. R. C. Leif, J. Vinograd, Proc. Nat. Acad. Sci., **51**, 520-528 (1964).

29. D. Danon, Y. Marikovsky, J. Lab. Clin. Med., **64**, 668-674 (1964).

30. M. M. Wintrobe, G. R. Lee, T. C. Bithall, J. Forester, J. W. Athens, J. N. Lukens, **Clinical Hematology**, 9th edition, Vol. 1, Lea & Febiger, Philadelphia, PA, 1993, Chap. 5.

31. S. A. Killmann, Acta Med. Scand., **176**, 529-535 (1964).

32. M. Bessis, **Réinterprétation des Frottis Sanguins**, Masson-Springer, Paris, Berlin, 1976, p. 47.

Received January 21, 1997
Accepted March 21, 1997
Manuscript 4384

J. LIQ. CHROM. & REL. TECHNOL., 20(16 & 17), 2555–2577 (1997)

ISOPERICHORIC FOCUSING FIELD-FLOW FRACTIONATION FOR CHARACTERIZATION OF PARTICLES AND MACROMOLECULES

Josef Janča

Université de La Rochelle
Pôle Sciences et Technologie
Avenue Marillac
17042 La Rochelle Cedex 1, France

ABSTRACT

The discoveries and innovations in science reflect always a symbiosis of the continuity of thought, knowledge, and experience inherited permanently from the predecessors, and of the outstanding capability of imagination and creativity in breakthrough moments. The invention of the field-flow fractionation concept and its impressive growth belong to such a step forward on the evolution spiral and represent a most important contribution to the science of separation of large molecules and particles in the course of the last 30 years. A generic focusing field-flow fractionation principle has developed both in theory and in analytical methodology. Particular methods and techniques were proposed and implemented independently by several laboratories in the world. This review summarizes the progress achieved during the last few years.

INTRODUCTION

Known and exploited from about 5000 years B. C., recognized by Archimedes some 2222 years ago, and reviewed for the first time in 1556 by Georgii Agricolae[1] (a german physician living in Jáchymov, Bohemia), the recovery of the fine gold grains or other metals from the sand, soil, and clay by panning or sluicing is based on different buoyancies of the particles in a gravitational field and perpendicular water stream. This antique craft work, lying somewhere between the art and science, is beautifully represented in Fig. 1, reproduced from Ref. 1. An aerostat, shown in Fig. 2, created by Joseph and Etienne Montgolfier,[2] is a phenomenological predecessor of the generic inventions of the isopycnic[3] and isoelectric[4] focusing methods. Regarding the long pathways of history, the ingenious and sophisticated field-flow fractionation (FFF) principle in its polarization variant was proposed by J. Calvin Giddings very recently.[5]

The idea[6] of the focusing FFF appeared in 1982. This emerging principle was mentioned also in a review on FFF[7] without any reference that could be given at the time of submission of the paper. Giddings[8] preferred the non-generic term hyperlayer FFF attributed to this principle. Later, the focusing FFF[9-11] was clearly identified as a new methodology beside the classical polarization FFF,[5] and the first theoretical and experimental results were cited. In this article, the developments derived from the original idea are described. Several laboratories all over the world contributed independently to this progress. As a result, various focusing mechanisms were subsequently proposed and exploited under conditions of dynamic FFF. The generalized principle of the isoperichoric focusing FFF belongs to the newest achievements in this field. The aim is to report on the new focusing FFF methods and their experimental implementations or potential analytical applications, and to acknowledge their adherence to the family of FFF methodology, a great challenge raised by Giddings in 1966.

Some principles not frequently known are briefly explained to facilitate the understanding of the complementarity, but also of the differences concerning the new focusing and the classical polarization FFF.

FOCUSING AND POLARIZATION FIELD-FLOW FRACTIONATION METHODOLOGIES

FFF is based on a simultaneous action of the effective field forces and of the fluid flow on the fractionated sample inside a separation channel. The mutual orientation of the field forces and of the carrier fluid flow is

Figure 1. Medieval sluicing technology for gold and other metals separation from the sand, soil, and clay particles.

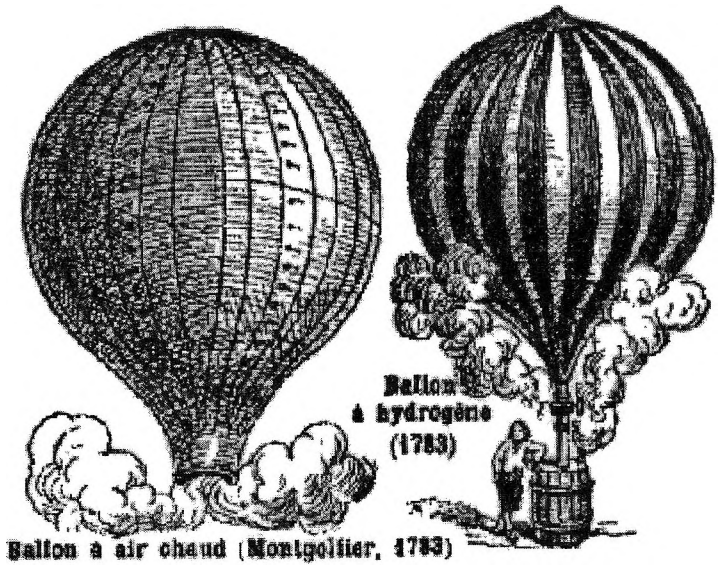

Figure 2. Aerostats of Montgolfier's brothers.

perpendicular, as shown in Fig. 3a. The recent applications of the FFF concern the fractionation of the macromolecules and particles dissolved or suspended in a liquid. The sample to be fractionated is injected into the channel as a short pulse, or as a continuous stream, carried by the liquid flow, as in chromatography. The field interacts with the sample and induces the formation of the concentration gradient of each sample component across the channel. This gradient is balanced by an opposite, dispersive flux. Consequently, a steady-state concentration distribution is established. Simultaneously, a flow velocity profile is formed across the channel due to the viscosity effects that accompany the flow processes. As a result, the sample components are eluted at different velocities, corresponding to their positions within the flow velocity profile and leave the channel at different elution times. This situation is shown schematically in Fig. 3b for the focusing separation mechanism and in Fig. 3c for the polarization mechanism. The resulting zones are either focused at different altitudes or differentially compressed at the accumulation wall of the channel. The substantial difference between the focusing and polarization mechanisms lies in the driving field force whose intensity and direction is dependent on the position across the channel in focusing FFF, while it is position independent in polarization FFF.

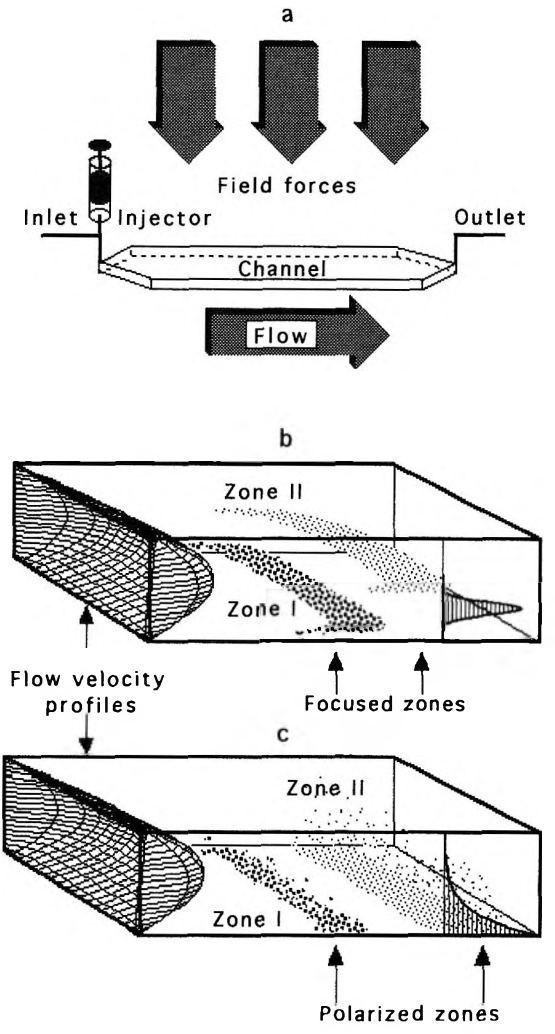

Figure 3. Principle of focusing and polarization field-flow fractionation. a) Mutual orientation of the field forces and of the fluid flow inside the separation channel; b) Section of the channel demonstrating the principle of focusing FFF with two distinct zones focused at different positions, the parabolic flow velocity profile, and the schematic representation of the Gaussian concentration distribution of focused species within a particular zone; c) Section of the channel demonstrating the principle of polarization FFF with two distinct zones concentrated differentially at the accumulation wall, the parabolic flow velocity profile, and the schematic representation of the exponential concentration distribution of one separated species.

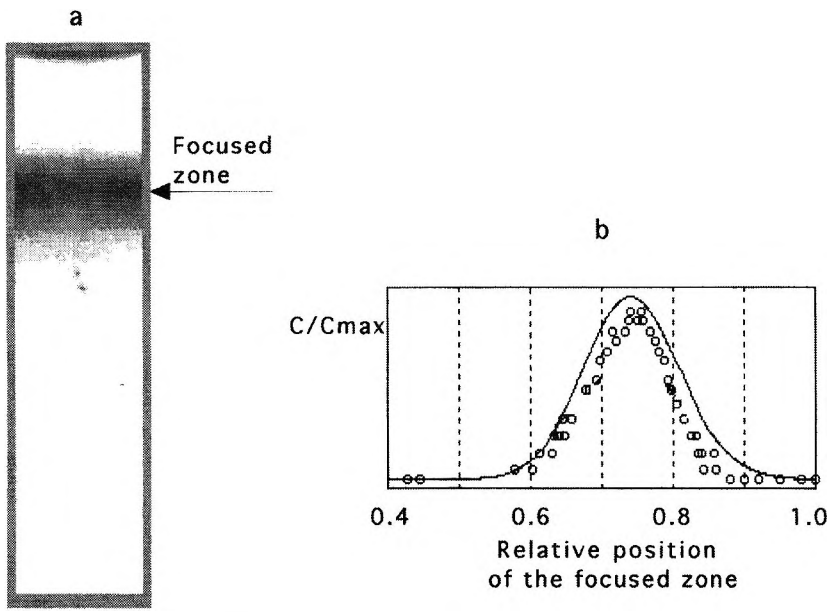

Figure 4. Isoperichoric focusing of the colored nanosize polyaniline particles in a density gradient formed in a suspension of the colloidal silica particles. a) Scanned macrophotograph of the zone of the colored polyaniline particles focused under conditions of static thin-layer isopycnic focusing; b)Theoretical (—) and experimental (o) shapes of the steady-state concentration distribution within a focused zone in a bidisperse suspension of the nanosize polyaniline particles in silica colloidal particles.

ISOPERICHORIC FOCUSING AND FIELD-FLOW FRACTIONATION

The gradient of the effective property of the carrier liquid, combined with the action of a field, can lead to the focusing of the separated species. For example, the particles of a given density focus in the density gradient combined with the gravitational or centrifugal field at their isopycnic positions, the amphoteric species focus in the pH gradient combined with the electrical field at their isoelectric points, etc. All these particular focusing phenomena are referred to by the general term *isoperichoric focusing*, introduced by Kolin in his seminal paper[12] on the genesis of isoelectric focusing and generalization of the idea. This means that the responding quality of the focused species and the corresponding local effective property of the carrier liquid do not induce the displacement of that species at the isoperichoric point, but induce the converging transport outside this point.

The theory predicts the isopycnic focusing in bidisperse suspension of the nanosize particles of different densities without *a priori* imposed large size ratio of the focused to the density gradient forming particles.[13] This prediction was evidenced experimentally by the focusing of the polyaniline particles in a suspension with silica particles of close average diameters, and partly superposed particle size distributions.[14] The image of the focused zone in the isoperichoric focusing experiment, carried out under static conditions, and the comparison of the experimental result with the theoretical prediction is shown in Fig. 4.

Usually, the same primary field forces which produce the density or pH gradient, such as centrifugal forces or electric field forces, etc., are used to generate the isoperichoric focusing effect. An original proposal[15] consists of the use of the secondary field forces of different nature to generate the focusing phenomenon within the corresponding gradient established by the primary field. This new isoperichoric focusing principle, exploiting the combined action of two fields of different nature, applied under static or dynamic FFF conditions, is very promising for high performance analytical and micropreparative separations. The experimental test was performed by using the static thin-layer and the dynamic isoperichoric focusing FFF of model polystyrene latex particles.[16] While separation was not observed under static conditions, focusing FFF resulted in very good resolution as shown in Fig. 5a. An important advantage is that both the static thin-layer focusing cell and the channel for dynamic isoperichoric focusing FFF, applying the combination of the electric and gravitational fields, are very simple, as can be seen in Fig. 5b and c, and are much less expensive compared to the centrifuge. As the distance between the electrodes is short (roughly from 100 μm to a few mm), a low voltage (of the order of 100 mV to a few V) is enough to create the high electric field strength (Vcm^{-1}). Theoretical calculations[13] verified the above mentioned increase of resolution of separation of the dynamic isoperichoric focusing FFF compared with the experiments under static conditions.

The simultaneous use of two fields of different nature represents a challenging alternative of the isoperichoric focusing FFF, but not the only one. Natural gravitation alone was used to separate large particles (100 to 200 μm) of density marker beads in a density gradient under conditions of isopycnic focusing FFF.[17] The scanned macrophotographs of this former experiment in Fig. 6a shows, clearly, the focusing inside the channel under different operational conditions. More powerful centrifugal forces were applied to demonstrate the focusing of the polystyrene and poly(glycidylmethacrylate) latex particles in a density gradient formed by sedimentation of colloidal silica particles in a centrifuge rotor.[18] Unfortunately, the experimental work was

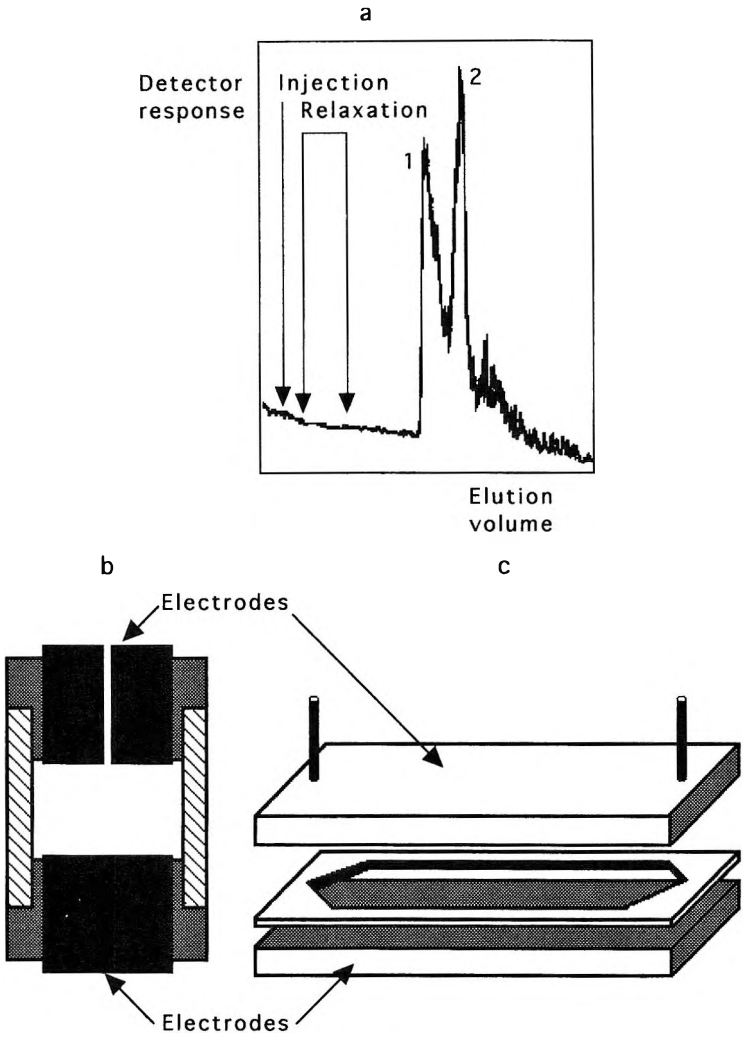

Figure 5. Isoperichoric focusing field-flow fractionation in coupled electric and gravitational fields. a) Fractogram of two samples of polystyrene latex particles. Particle diameters were 9.87 μm (1) and 40.1 μm (2). While this dynamic FFF separation shows a good resolution of the separated samples, no detectable resolution was achieved under static conditions in thin-layer isoperichoric focusing cell; b) Design of the cell for static thin-layer isoperichoric focusing and of the channel for dynamic focusing field-flow fractionation.

suspended before the reproducible results could be obtained. The last version of the apparatus, built up in 1982[19,20] for these applications, is shown in Fig. 6b. In isopycnic focusing FFF experiments, using the natural gravitational field forces alone,[17] some doubts existed as to the possibility to establish the density gradients sufficiently strong to generate the focusing phenomena during the elution time allowed. Another plausible explanation of the observed focusing phenomenon is that the density gradient formed inside the channel is, in fact, stepwise due to the injection of the focused particles in a liquid whose density is different from the density of the bulk carrier liquid at the injection point. A careful experimental investigation of the analytical and preparative focusing FFF in preformed stepwise density gradient[21,22] confirmed that the focusing under such conditions is very rapid. The gradient of the effective property can be preformed, for example, by pumping carrier liquids of various densities through different inlets of the channel. If the layers of different densities flow under conditions hindering their mixing, a step density gradient is formed which can be stabilized by the primary field.[21,22] The preforming of the pseudo-continuous gradient is typical for, but not limited to, the density gradient. The unpublished results obtained by Nováková and Janča within the frame of the work published in Refs. 21, 22 are reproduced in Fig. 7. They show a very rapid focusing of the density marker particles on an in situ preformed stepwise density gradient, as well as an excellent stability of the different density layers, along the separation channel. On the other hand, a recent study of the transient state in the settling of the same colloidal silica[23] as used previously[17] indicates that the kinetics of this transport phenomenon is quite a slow process, even at high centrifugal field forces.

The electrical field alone was applied to establish a pH gradient and to separate the acidic and basic components of horse heart myoglobin by isoelectric focusing FFF.[24] This separation is demonstrated in Fig. 8a. The design of the separation channel, published originally in Ref. 25, is shown in Fig. 8b, which was reproduced in Ref. 26 without the citation of the original source. Another attempt to separate the amphoteric proteins was less successful.[27] A former colleague continued the investigation of the operational variables influencing the formation of the pH gradient under conditions of isoelectric focusing FFF.[26,28] His results generally agree with the known theoretical and experimental findings. The original idea to use the channels with modulated cross-sectional permeability in focusing FFF, elaborated in 1983,[29] was applied[28] without the accurate citation. These channels allow to overcome the problem of the identical longitudinal velocities of two distinct zones focused at the same, but opposite, distances from the central axis of the channel of rectangular cross-section in which the axially symmetrical flow velocity profile is formed (see Fig. 9).

a

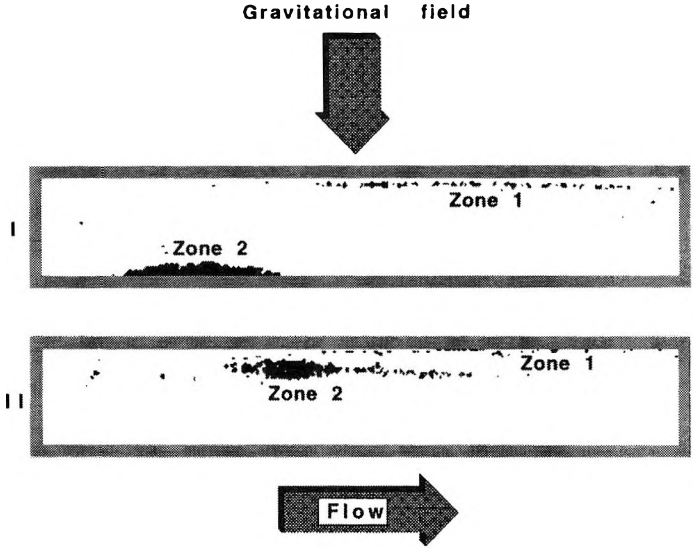

b

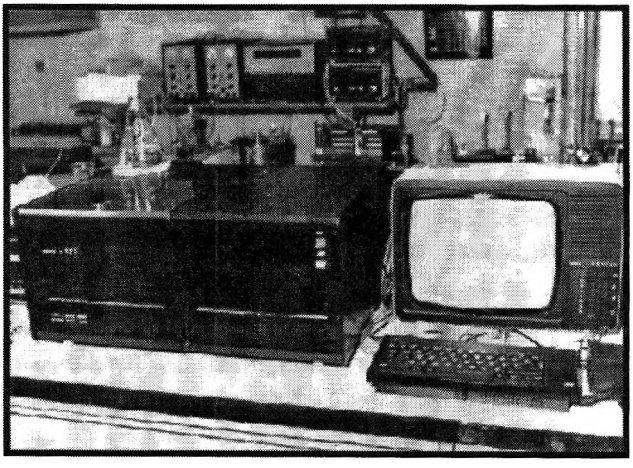

A detailed experimental study[30-32] of the isoelectric focusing FFF in a channel with modulated cross-sectional permeability (trapezoidal cross-section) resulted in the distinct focusing of cytochrome c and in the efficient separation of horse spleen ferritin, equine myoglobin and horse heart cytochrome c. Although the resolution was clearly superior to the former results,[27] it was, nevertheless, largely inferior compared with dynamic capillary isoelectric focusing with electroosmotic flow.

The focusing process is intrinsically related to the gradient of the effective forces. Only if the magnitude of the converging forces is position dependent and only if they vanish at the isoperichoric point, the focusing effect can appear. Various combinations of the fields and gradients determining other focusing FFF methods are described in the following paragraphs.

CROSS-FLOW VELOCITY GRADIENT COMBINED WITH FIELD ACTION

The focusing can be achieved by the action of a velocity gradient of the cross-flow of the carrier liquid opposite to the action of an external field. The longitudinal flow of the carrier liquid is imposed simultaneously.[33,34] This elutriation focusing FFF was used to separate model mixtures of polystyrene latex particles and silica particles in a trapezoidal cross-section channel, shown schematically in Fig. 10 together with the fractogram of a mixture of polystyrene latex particles. Giddings[35] proposed similar focusing FFF principle, but operating in a rectangular cross-section channel with two opposite semipermeable walls. The flow rates through the walls should be different to form the velocity gradient.

Figure 6 (left). Isoperichoric focusing field-flow fractionation using gravitational or centrifugal field forces. a) Scanned macrophotographs of the channel demonstrating the isopycnic focusing FFF of two different densities particles in gravitational field (diameter ca. 200 μm) in two different average densities carrier liquids. Two distinct focused zones are formed and the flow of the carrier liquid causes their longitudinal separation. In low density carrier liquid (I), higher density particles are in contact with the lower wall and the lower density particles are focused in the upper part of the channel. In high density carrier liquid (II), higher density particles are focused in the upper part of the channel and the lower density particles are focused near the upper wall; b) Apparatus for sedimentation FFF which was applied for isopycnic focusing FFF using centrifugal field forces.

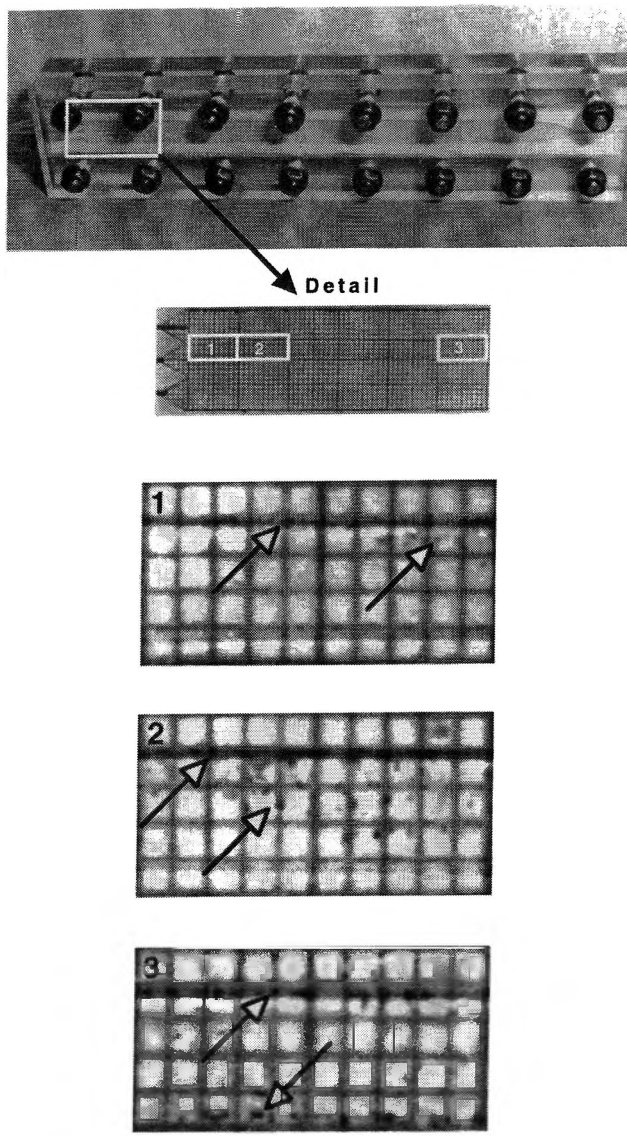

Figure 7. Isopycnic focusing FFF in preformed stepwise density gradient. Separation channel and the scanned photographs showing the evolution of two focused layers of the particles at three different longitudinal positions inside the channel. The detail 1 shows one layer of the particle mixture positioned at the interface between two different densities liquids and the beginning of the separation of the more dense particles, detail 2 shows the separation in progress of different densities particles, detail 3 shows two different densities particles focused at the interfaces of different densities liquids.

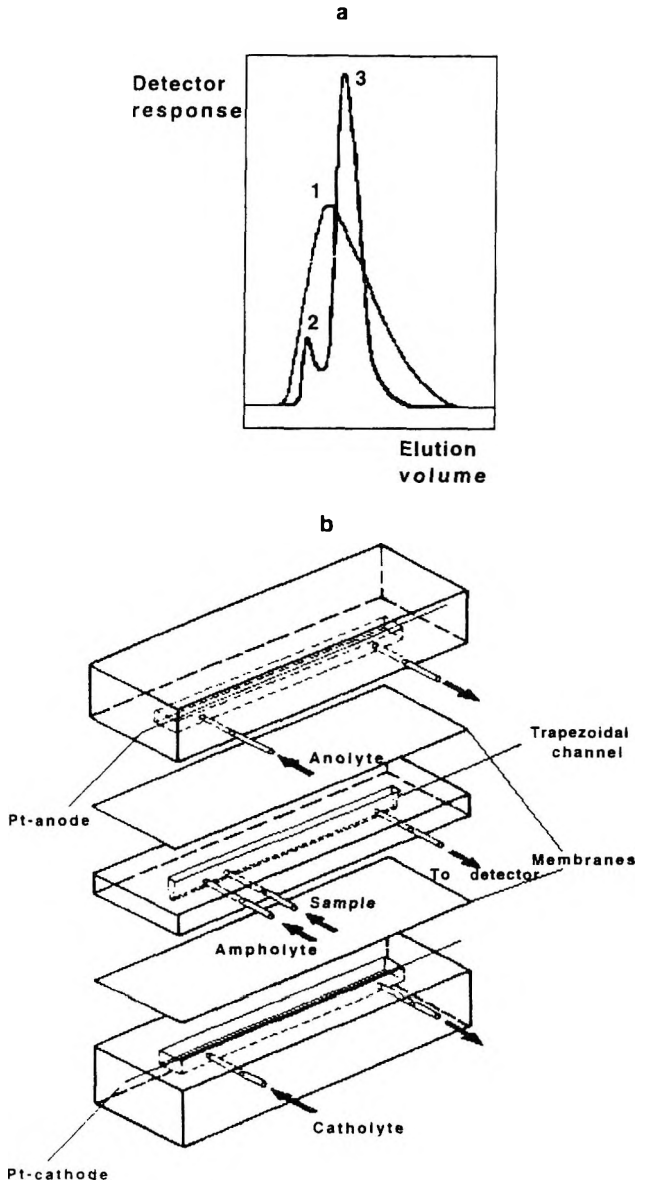

Figure 8. Isoperichoric focusing field-flow fractionation using the electric field. a) Fractograms without the electric field applied (1) and with the active field showing the separation of acidic (2) and basic (3) components of horse heart myoglobin by isoelectric focusing field-flow fractionation; b) Schematic representation of the channel for isoelectric focusing FFF.

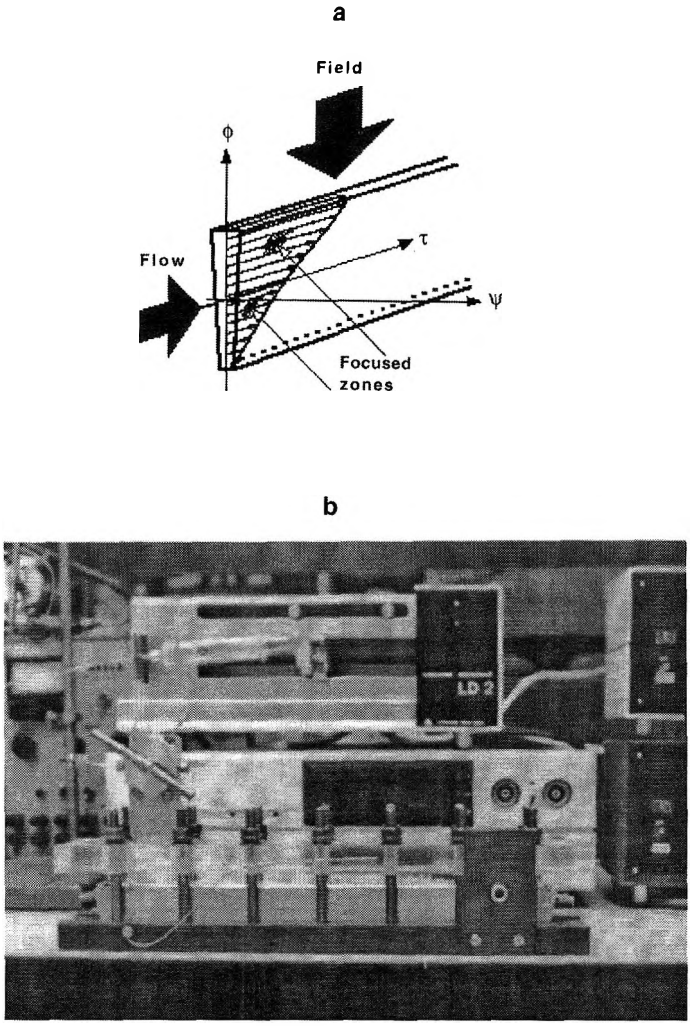

Figure 9. Modulated cross-sectional permeability channel for focusing FFF. a) Schematic representation of the trapezoidal cross-section channel and the corresponding flow velocity profile with two focused zones; b) Apparatus for isoelectric focusing FFF with the trapezoidal cross-section channel which was used for the separation demonstrated in Fig. 8.

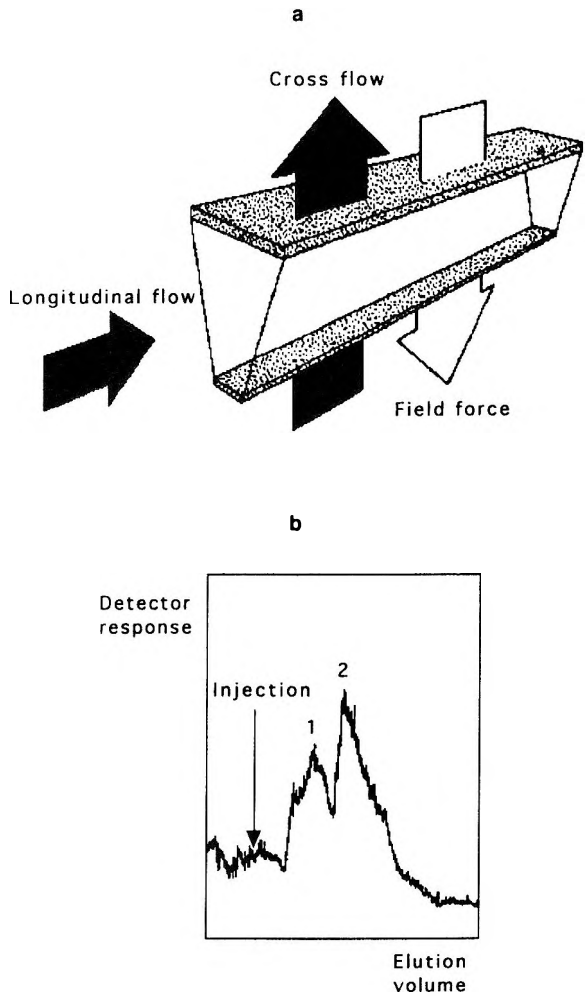

Figure 10. Principle of elutriation focusing field-flow fractionation in trapezoidal cross-section channel and the separation of two different diameter polystyrene latex particles. a) Focused zones are formed due to the field forces and the opposite velocity gradient of the carrier liquid flow across the semipermeable lower and upper walls of the channel. Separation of the focused zones in the direction of the longitudinal flow in trapezoidal cross-section channel is facilitated by the formation of axially asymmetrical flow velocity profile; b) Fractogram showing the separation of two polystyrene latexes of 1.6 μm in diameter (1) and of 5 μm in diameter (2) particles.

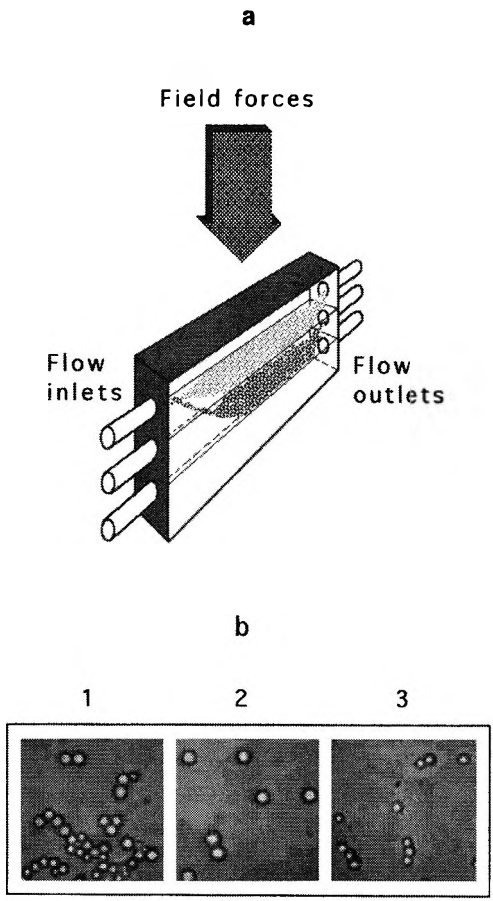

Figure 11. Continuous preparative focusing field-flow fractionation. a) Separation channel for continuous preparative focusing FFF operating in natural gravitational field with three inlet capillaries allowing to preform the step density gradient by pumping three liquids of different densities and with three outlet capillaries to collect the separated fractions; b) Optical microscopy photographs showing the preparative fractionation of the polydisperse silica particles (3 to 5.9 μm in diameter). Original unfractionated sample (1) and the fractions taken from the lower (2) and the upper (3) outlets demonstrate clearly the narrowing of the particle size distributions of the fractions.

LIFT FORCES COMBINED WITH A FIELD ACTION

The hydrodynamic lift forces that appear at high flow rates of the carrier liquid, combined with the field forces, are able to concentrate the suspended particles into the focused layers. The original observation of the lift effect was described by Segré and Silberberg.[36] The particles flowing in capillaries tend to concentrate spontaneously into the layers due to the lift forces, even without other effective field, as demonstrated by Small.[37] Whenever the other field forces are superposed, the focused zones can appear. The retention behavior of the particles under the simultaneous effect of the primary field, and lift forces generated by the high longitudinal flow rate, can vary with the nature of various superposed primary field forces. The strong effect of the lift forces in FFF was described by Caldwell et al.[38] for the separation of human and animal cells and of model latex particles. Wahlund and Litzen[39] observed the interference of the lift forces in classical polarization flow FFF, performed in an asymmetrical channel with one semipermeable wall. The combined effect of the gravitation or the cross-flow with the lift forces resulted in a good separation of polystyrene latex or silica particles.[40,41] The field forces should concentrate the retained particles at the accumulation wall, thus generating the conditions of polarization FFF. However, at high flow rates, the lift forces become operational and pull the particles away from the wall. As a result, the transition from polarization to focusing FFF appears first, followed by the proper focusing effect. Another application of this technique to fractionate the coal and limestone particles was published by Barman et al.[42]

SHEAR STRESS COMBINED WITH A FIELD ACTION

A high shear gradient can lead to the deformation of the macromolecular coils, which results in a decrease of the chain entropy. The entropy gradient generates the driving forces that displace the macromolecules into a low shear zone. The observation by Giddings et al.[43] of the reversed elution order of high molecular weight polystyrenes in thermal FFF at high flow rates can be attributed to this phenomenon. However, a detailed study of the effect of the operational variables indicated another possibility to explain the reversed elution order.[44] More experimental work is needed to draw any conclusions concerning the origin of the observed phenomena.

GRADIENT OF A NONHOMOGENEOUS FIELD ACTION

The use of a high-gradient magnetic field was proposed to separate paramagnetic and diamagnetic species by a mechanism of focusing FFF. In a

series of theoretical papers summarized in Ref. 45, Semyonov et al. treated various aspects of focusing FFF but no experimental results appeared until now. However, the idea is highly interesting and merits experimental verification.

PREPARATIVE FRACTIONATION

No substantial difference distinguishes the analytical and preparative use of FFF. While the main objective of the analytical separation is to determine the required parameters of the examined sample, or to prove the existence of the investigated components, preparative fractionation is performed to obtain a sufficient amount of specific fractions to use for subsequent analysis, or for other experimental work.

Focusing FFF can be used for continuous preparative fractionation.[9,46] If the fractionation channel is equipped with several outlet capillaries at various positions (and occasionally with several inlets to preform a stepwise gradient in the direction of the focusing) and the sample to be fractionated is continuously pumped into the channel, the focused layers eluting through the individual outlets can be collected. This general principle is schematically demonstrated in Fig. 11a. The experimental demonstration of its feasibility was given by the fractionations of various samples of silica particles[34] of which one example is shown in Fig. 11b. In this particular case, the natural gravitation and the counteracting cross-flow gradient produced the focusing effect and the silica particles were separated according to their sizes, similarly as for analytical scale separation shown in Fig. 10b. The particle size of the studied sample was within the range that is interesting, e.g., for the fractionation of blood cells. Although another focusing FFF was not yet implemented under preparative conditions, it is evident that, for example, the isopycnic or isoelectric focusing FFF already performed in analytical scale (see Figs. 5a, 6a, 7, and 8a) can easily be transformed into large scale separations.

OUTLINES AND PERSPECTIVES

All progress passes through the discoveries, inventions, and innovations. The advances in science and technology are due to the understanding and mastering of the laws of nature, as well as due to the prediction and exploration of the phenomena do not appearing spontaneously in the universe. Analytical chemistry follows this process as a particular scientific discipline, but also in context with the whole area of scientific research.

Focusing FFF represents, most recently, a modest contribution to the science and technology of separation and analysis of macromolecules of synthetic or natural origin within a wide range of molar masses, of particles in the submicron and micron ranges, and of organized structures, such as cells and microorganisms. This does not mean that low molar mass species cannot be separated. The molecules not influenced by the field and, thus, not exhibiting the focusing effect can still be separated, providing that an equilibrium between them and the focused species is established. However, this hypothesis has yet to be realized.

The research and technology related to the life sciences and to the macromolecular chemistry and technology, the analytical problems appearing in context with the protection of the environment, and many other scientific and technological activities, have stimulated the development of new analytical separation methods.

The present review of the achievements in focusing FFF clearly indicates that most of the experimental implementations have been obtained with model systems. Some of them represent a clear proof that *"it works"* rather than a practical application elaborated to minutest details.

The advantages of these methods already mentioned above are evident. Some of them are inherently related to the separation principle of focusing FFF, such as the absence of a large surface area within the separation channel that can be of crucial importance for sensitive biological materials, the operational variables, including the strength of the field, which can be continuously manipulated within a very wide range, etc.

The lack of the commercially available instrumentation represents a limiting factor with regard to the widespreading of the focusing FFF methodology into current laboratory practice. However, this lack is only virtual, because all the particular components of the whole apparatus are absolutely identical as those for liquid chromatography, with the only exception being the separation channel.

A liquid chromatograph can be modular, which means comprised of individual parts commercially available, such as the pump, injector, detector, etc., with a column that can be changed for each specific application. The FFF apparatus can be assembled similarly with various channels which, in most cases, are easy to construct. This approach, rather than to be a limiting factor, can represent a challenge for creativity and invention.

The main activity of Cal Giddings in the domain of FFF was oriented toward polarization FFF methodology, in which the list of his and his collaborators' papers accounts for hundreds contributions published during exactly 30 years. But, he was remarkably present also in the field of focusing, hyperlayer, FFF and not only as a source of inspiration. I worked in his laboratory, under his expert leadership, during 1978-79 and, as a result, the dominating part of my subsequent research was specifically on FFF, which provided a great challenge on one hand, but a satisfaction in moments of a successful outcome.

ACKNOWLEDGMENT

This paper is dedicated to the memory of J. Calvin Giddings.

Precious contribution of my former and recent collaborators to the development of the focusing FFF methodology in the course of the past 15 years is gratefully acknowledged. Some of them are listed below as co-authors of the cited publications.

REFERENCES

1. G. Agricolae, **De Re Metallica**, Libri XII, QVI, Basileae, 1556.

2. J. Montgolfier, E. Montgolfier, **Description des Expériences Aérostatiques de MM. de Montgolfier, et de Celles Auxquelles Cette Découverte a Donné Lieu**, Cuchet, Paris, 1784.

3. M. Meselson, F. W. Stahl, J. Vinograd, Proc. Natl. Acad. Sci., U. S. A., **43**, 581 (1957).

4. H. Svensson, Acta Chem. Scand., **15**, 325 (1961).

5. J. C. Giddings, Sepn. Sci., **1**, 123 (1966).

6. J. Janča, Makromol. Chem., Rapid Commun., **3**, 887 (1982).

7. J. Janča, Trends Anal. Chem., **2**, 278 (1983).

8. J. C. Giddings, Sepn. Sci. Technol., **18**, 765 (1983).

9. J. Janča, J. Chmelik, Anal. Chem., **56**, 2481 (1984).

10. J. Janča, Trends Anal. Chem., **6**, 147 (1987).

11. J. Janča, **Field-Flow Fractionation: Analysis of Macromolecules and Particles**, Marcel Dekker, Inc., New York, 1988.

12. A. Kolin, in **Electrofocusing and Isotachophoresis**, B. J. Radola, D. Graesslin, eds., de Gruyter, Berlin, 1977.

13. J. Janča, Mikrochim. Acta, **112**, 197 (1994).

14. J. Janča, M. Špírková, Collect. Czech. Chem. Commun., **61**, 819 (1996).

15. J. Janča, R. Audebert, J. Appl. Polym. Sci., Appl. Polym. Symp., **52**, 63 (1993).

16. J. Janča, R. Audebert, Mikrochim. Acta, **111**, 163 (1993).

17. J. Chmelik, J. Janča, J. Liquid Chromatogr., **9**, 55 (1986).

18. J. Janča, D. Přibylová, unpublished results.

19. J. Janča, M. Janíček, V. Slavik, F. Stehlik, Czechoslovak Patent N° 230086, 2 June 1982 (PV 5061-82).

20. J. Janča, M. Janíček, D. Přibylová, M. Klesnil, Anal. Instrumentation, **15**, 149 (1986).

21. J. Janča, N. Nováková, J. Liquid Chromatogr., 10, 2869 (1987).

22. J. Janča, N. Nováková, J. Chromatogr., **452**, 549 (1988).

23. J. Janča, M. Špírková, J. Coll. Interface Sci., **184**, 000 (1996).

24. J. Chmelik, M. Deml, J. Janča, Anal. Chem., **61**, 912 (1989).

25. J. Janča, J. Chmelik, V. Jáhnová, N. Nováková, E. Urbánková, J. Appl. Polym. Sci., Appl. Polym. Symp., **45**, 39 (1990).

26. J. Chmelik, J. Chromatogr., **545**, 349 (1991).

27. W. Thormann, M. A. Firestone, M. L. Dietz, T. Cecconie, R. A. Mosher, J. Chromatogr., **461**, 95 (1989).

28. J. Chmelik, J. Chromatogr., **539**, 111 (1991).

29. J. Janča, V. Jáhnová, J. Liquid Chromatogr., **6**, 1559 (1983).

30. J. Chmelik, W. Thormann, J. Chromatogr., **600**, 297 (1992).

31. J. Chmelik, W. Thormann, J. Chromatogr., **600**, 305 (1992).

32. J. Chmelik, W. Thormann, J. Chromatogr., **632**, 229 (1993).

33. J. Janča, Makromol. Chem., Rapid Commun., **8**, 233 (1987).

34. E. Urbánková, J. Janča, J. Liquid Chromatogr., **13**, 1877 (1990).

35. J. C. Giddings, Sepn. Sci. Technol., **21**, 831 (1986).

36. G. Segré, A. Silberberg, Nature (London), **189**, 209 (1961).

37. E. H. Small, J. Colloid Interface Sci., **48**, 147 (1974).

38. K. D. Caldwell, Z. Q. Cheng, P. Hradecky, J. C. Giddings, Cell Biophys., **6**, 233 (1984).

39. K. G. Wahlund, A. Litzen, J. Chromatogr., **461**, 73 (1989).

40. K. Chen, K. G. Wahlund, J. C. Giddings, Anal. Chem., **60**, 362 (1988).

41. S. K. Ratanathanawongs, J. C. Giddings, J. Chromatogr., **467**, 341 (1989).

42. B. N. Barman, M. N. Myers, J. C. Giddings, Powder Technol., **59**, 53 (1989).

43. J. C. Giddings, S. Li, P. S. Williams, M. E. Schimpf, Makromol. Chem., Rapid Commun., **9**, 817 (1988).

44. J. Janča, M. Martin, Chromatographia, **34**, 125 (1992).

45. S. N. Semyonov, A. A. Kuznetsov, P. P. Zolotaryov, J. Chromatogr., **364**, 389 (1986).

46. J. C. Giddings, Sepn. Sci. Technol., **21**, 831 (1986).

Received December 19, 1996
Accepted May 1, 1997
Manuscript 4435

J. LIQ. CHROM. & REL. TECHNOL., 20(16 & 17), 2579–2597 (1997)

SEDIMENTATION FIELD-FLOW FRACTIONATION AT GRAVITATIONAL FIELD OF RED BLOOD CELLS: SYSTEMATIC STUDIES OF INJECTION CONDITIONS

Emmanuel Assidjo, Philippe J. P. Cardot*

Laboratoire de Chimie Analytique et de Bromatologie
Université de Limoges
Faculté de Pharmacie
2, rue du Dr Marcland
F-87025, Limoges Cedex, France

ABSTRACT

Field Flow Fractionation (FFF), which uses the gravitational field for retention, elution, and separation of cellular materials, appeared to obtain a constant success. Blood cells, as well as parasites, were separated and isolated using this very simple method. A need emerged, therefore, to evaluate its separation performance. Towards that objective, and because of numerous common features of FFF with chromatography, the injection conditions appeared to be critical. Therefore, we have analysed the effect of injected concentration, of injected volume, and of the specific injection procedure widely used in FFF the "stop flow time relaxation process."

In the light of numerous reports, red blood cells (RBC) appeared to be considered as a "model" for cell analysis in FFF, and were eluted according to a mechanism described as "Steric

Hyperlayer," retention properties of RBC were therefore analysed versus carrier flow rate intensities. Guidelines are given to elute RBC in gravitational FFF depending on the separation objectives i.e., analytical or semi preparative.

INTRODUCTION

Field Flow Fractionation is a family of dynamic separation methods, based on the elution of different sample constituents, in a ribbon-like channel, flowed by a carrier phase of various velocities.[1-3] Sample components are retained according to their sensitivity to a field applied in a direction perpendicular to the flow. Separations are induced and controlled by that field, and the flow.[4-6] Gravitational Field Flow Fractionation[7-10] belongs to the family of FFF sedimentation techniques,[11] the external field is simply the gravitational one.

One of the advantages of this technique in the elution of micron sized material is that the separation occurs in one phase (the carrier medium), which can be very simple. Because of the well established "Steric Hyperlayer" elution mode of micronic material in GFFF[12,13] one can expect that particle-separator interactions would be limited. Such a feature is particularly interesting in the case of biological materials, whose characteristics may be modified because of an interaction process.

For more than ten years, the use of FFF techniques in biological analysis has been in constant development. The feasibility of cell sorting with FFF was demonstrated, for the first time, in 1983, using the sedimentation (multigravitational) technique.[14,15] Flow FFF methods also were employed.[13,16,17]

In the early nineties, the simplest technique which uses a gravitational field regained interest because of its design and operating simplicity.[13,18] Retention and purification of different species of health and biological interest were obtained with this method: filariae,[19] trichomonas,[20] and Pneumocistis.[21] In the case of red blood cell analysis, normal and pathological material were analysed and sub population purifications were obtained.[20-24]

Because of the complex polydispersity of cellular material in terms of shape, of size, of density, it is obvious that it would be difficult to analyse retention data of RBC for the purpose of defining an "elution model." However, some empirical rules will emerge and will be of help for future developement, for separation enhancement, or optimization. Questions which

are studied in this report can be summarized follows: How do we inject the RBC into the FFF Channel? In what volume? At what concentration and flow rate?

MATERIALS AND METHODS

Human Red Blood Cells

Samples are drawn from the same healthy donor, prior to experiments, with the help of a Vacutainer® system (Vacutainer, Maylan, France) and mixed with a sodium salt of ethylene diamine tetraacetic acid (EDTA 1.5% w/w). Samples were stored at 0°C for a maximum duration of 24 hours. Extemporaneous dilutions were performed before FFF analysis by simple mixing of the sample with the carrier phase (v/v). Final concentrations were measured with a Coulter Counter TAII (Coulter Electronics LTD, Luton, UK). Flow system: A Gilson Model 302 (Gilson Medical Electronics, Inc., Middelton, WI, USA) HPLC pump connected to a pulse damper system allowed to obtain 0.1 to 5 mL/min flow rates. It was connected to the FFF separation device by means of a sample injection device.

The carrier phase used in this study is a classical buffer system pH=7.2, 0.15 Mol/L from BioMerieux (PBS 75511, BioMerieux Sa, Marcy l'Etoile, France) added with 0.1%(w/w) of bovine albumin (No A-4503, Sigma Chemical Company, St Louis, Mo, USA); the final carrier phase density was 1.002 g/mL, its viscosity 1.016 cp. Flow rate intensities were systematically controlled by weighing.

The injection device, a Rheodyne valve model 7125i (Rheodyne, Incorporated, Cotati, CA, USA), was used to flow the sample into the channel. Injected volume was set up using Upchurch Peek tubes of different lengths and internal diameters (from 0.508 mm id and 99 mm long for a 20μL loop to 1.016 mm id and 432 mm long for a 350 μL loop). This injection device was connected to the FFF channel inlet by means of a connecting tubing of known length and internal diameter (0.254 mm id, 20 cm long).

When stop-flow injection procedures were needed, the samples were injected into the channel inlet at low flow rate (0.3 mL/min) for a time corresponding to a volume slightly greater than the one corresponding to the injection volume measured by the connection tube.

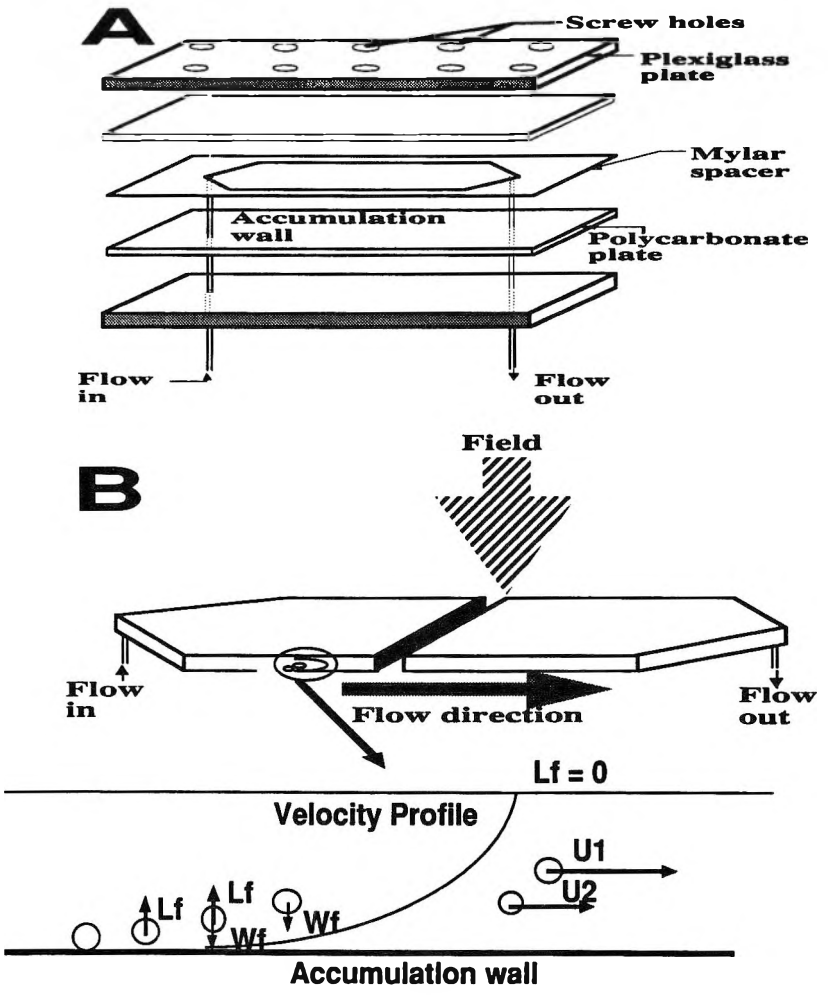

Figure 1. A: Design of the FFF channel, dimensions are: 49.5 ,2, 0.001 cm, inlet and oulet angle of 60°. B: Upper part channel geometry, field and flow directions. b lower part: schematic representation of the "hyperlayer" elution mechanism, Wf is the field-induced force acting on the particle, Lf the lifting force.

Ahead of the injection device, a switching valve model V.100L (Upchurch Scientific, Oak Harbour, WA, USA) was placed to divert the flow away from the channel. Systematic studies were performed by means of ink samples to visualise the sample entrance into the channel for the purpose of defining the experimental value of this volume.

Sedimentation Field Flow Fractionation Device

The gravitational FFF apparatus used in this report was set up in our laboratory; it as been modified from the one previously published by J. C. Giddings[1] to be compatible with biological conditions, and has been completely described by A. Bernard et al.[7] The paralellepipedic dimensions are 49.5 cm in length, 2 cm breadth, 0.01 cm thick; its volume was calculated at 0.99 mL. Including connection tubings and detection cell volume, the total void volume of the system was experimentally measured at 1.132 ±0.06 mL (n = 10) using 25 % (w/w) Dextran solutions (Dextran D-4626, Sigma Chemical Company) in the carrier phase. Planarity in length and breadth was set up and controlled over all experiments. A schematic representation of the system is shown in Figure 1A.

Detection device: A Waters Model 440 Photometer, set at 350 nm (Waters Corporation, Milford, MA, USA), operated in the turbidimetric mode, is connected to the outlet of the FFF channel by means of a Peek tube (0.254 mm id , 20 cm long). Data were recorded with an Atari ST 520 Computer (Atari Corp. , Sunnyvale, CA, USA) using a 14 bytes Keithley M1111 acquisition kit (Keithley Metrabyte Corporation, Taunton, MA, USA) at a 1Hz frequency.

Peak profile analysis: As the peak parameters of the gaussian-like fractogram, which signified the elution of RBC, will be analysed by the method described by B. A. Bidlingmeyer & F. V. Warren Jr.[25] For practicability, retention will be defined with the help of the peak summit elution time; as no statistical differences in the void volume measurements were found when plasma dilutions and Dextran solutions were compared, the characteristic sample plasma protein peak found on each fractogram was used as a probe for void volume measurement. The ratio, summit of the protein peak versus RBC signal summit is defined in this report as the RBC retention ratio. Peak dispersion parameters also will be calculated using analogous procedures, using peak width at different percentage (%) of the peak height, peak profile asymmetry, and equivalent plate height (HETP).

RESULTS AND DISCUSSION

Elution Mode of RBC in GFFF

Elution modes in FFF are now well-defined,[3,13,14,26,27] even in the case of biological material.[14] The separation process is based on the parallelepipedic geometry of a channel, which controls the interaction of particle velocity in the

carrier flow profile with an external field perpendicular to the great surfaces of the channel as schematized in Figure 1A. A pulse of mixed species is flowed into the ribbon-like channel, and species-external field interactions force the former toward one wall. As, usually, the carrier flow profile is parabolic in the channel thickness (laminar flow conditions), the species closer to the wall moves more slowly, being therefore, more "retained" compared to those not or less affected by the field. Therefore, band species are eluted at different speeds. It was established by K. Caldwell[14] and other research groups[13,16,19,20] that RBC and nucleated cells are eluted according to the so called "steric-hyperlayer" elution mode whose specificities are briefly exemplified in Figure 1B, upper part, and have been described by J. C. Giddings.[25] In the representation of Figure 1B, lower part, cells are shown scaled to the channel thickness. In such a model, the cells are focused by the external field (gravitational or multigravitational) into stream lines of the parabolic flow profile of the mobile phase. This focalisation process, whose kinetics and mechanism are, so far, not totally assessed, is one of the most important features in the analysis of cellular material by FFF techniques. The original position of the cell in the channel thickness (at the inlet), and the dynamics of the equilibrium process, as well as the cell characteristics, play a role in the cell travel along and across the channel. Because of the symmetry of the parabolic flow profile, it is of interest to place all the material under study in the accumulation half part of the channel as shown in Figure 1A; this is made possible by driving the cell into the channel directly on the accumulation wall, as set on our device. Moreover, it as been demonstrated that, during elution, even at high flow rates, particle-wall interactions could occur.[15,21] The channel wall, made of polycarbonate material (Lexan®), has been chosen[7] to minimize these interactions; such demonstration is made by simply flushing the channel after elution. Contrary to what has been observed in SdFFF with cellular material,[15] the flushing procedure did not remove any material from the channel, and fractions collected during this procedure were found to be free of any material, as shown on the elution volume dependent fractogram. The flushing procedure, made by simply flowing the channel at high flow rate (3 mL/min) was associated with a single step modification of the baseline intensity, probably due to the modification of the pressure drop in the detection cell as shown in Figure 2A; even at very low flow rates, no sorption of the samples were diagnosed by means of signal intensity and fraction collection.

Because of the linked elution characteristics of species with their position in the channel thickness, the use of retention ratio in FFF is rather practical. It is, therefore, relatively simple to plot fractograms using retention ratio units, as shown, for different flow velocities with the fractograms of Figure 2B. One can observe that such fractogram design showed, clearly, the focalisation process

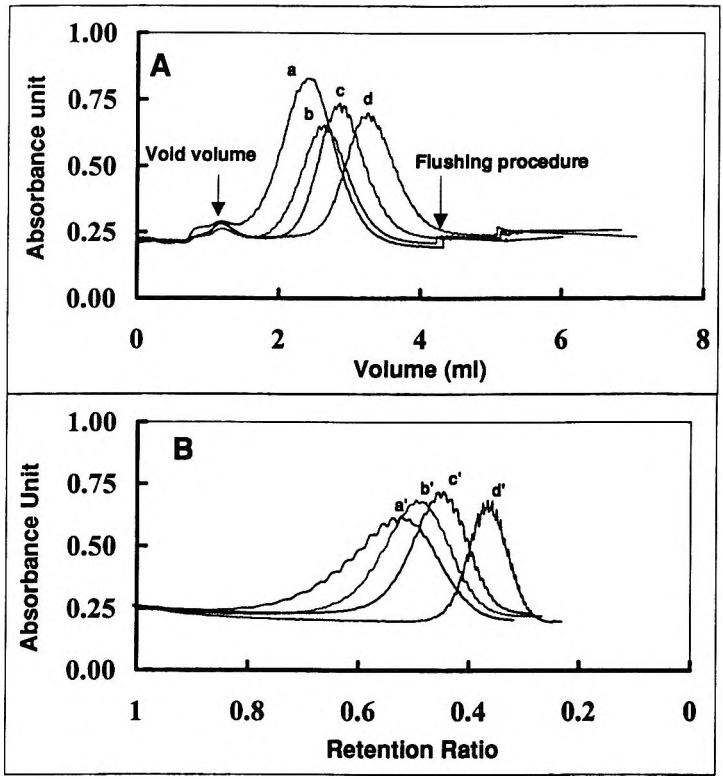

Figure 2. Fractograms of red blood cells in gravitational field flow fractionation, flow injection. 50 μL loop, dilution factor 300, flushing procedure :3ml/min. A: volume scaled signal (a = 0.33 cm/s, b = 0.28 cm/s, c = 0.23 cm/s,d = 0.17cm/s). B: retention ratio scaled signal (a' = 0.30 cm/s, b' = 0.25 cm/s, c' = 0.20 cm/s, d' = 0.13 cm/s).

obtained for micronic species. In particular, the fractogram obtained at 0.13 cm/s appeared much more retained and sharper than at higher average flow velocities. These retention ratio scaled fractograms demonstrated, clearly, the "focused" effect of lifting forces.

Sample Concentration Effect on RBC Peak Profiles

Total blood samples were diluted in a range from 4 (i.e 1 volume of blood added to 3 volumes of carrier phase) to 2000. The RBC injected concentration, thus, ranged from 1.2×10^6 to 2.5×10^3 cells/μL. The injection volume was

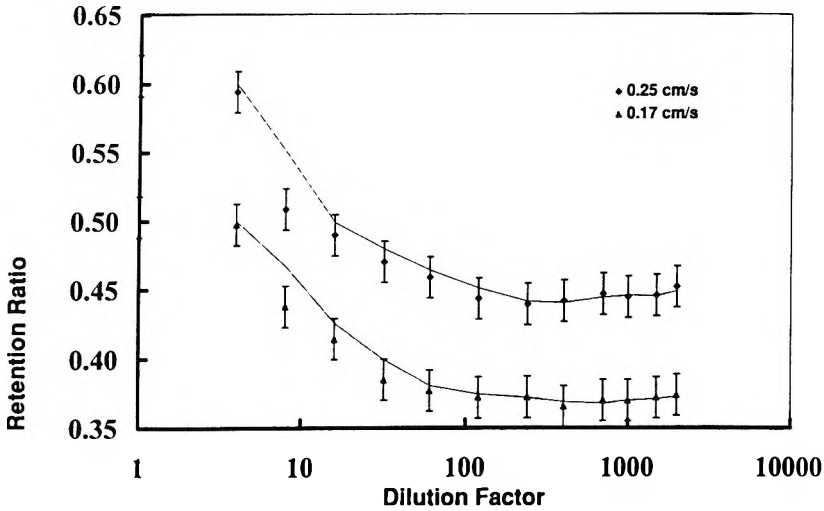

Figure 3. Effect of RBC dilution factor on retention ratio. Flow injection, 50 μL loop, dilution factor varying from 4 to 2000. Statistical data: n = 4, standard deviation = 1%.

chosen at 50μL and flow injections were performed. As the blood's main population is the RBC, these simple dilutions can be assumed to represent a rather pure RBC suspension. Elutions were obtained at two different linear velocities of the carrier phase: 0.17 and 0.25 cm/s. In Figure 3, retention ratio data at different concentrations and statistical estimation were plotted on a semi logarithmic scale, each experiment being performed four times.

Most of the described retention mechanism of micronic species in FFF assumes that, when the sample flows into the channel, the species undergo a field effect which leads to an equilibrium profile in the channel thickness. In the case of a Newtonian suspension, at a sufficient dilution (4% w/w ratio) this equilibrium can be shaped by a decreasing exponential profile. But, there is little information about the modification of the equilibrium profile in the case of concentrated suspensions.

It is observed that retention ratio decreased as dilution factor increased. This can be explained by some unmastered comportement of concentrated samples and/or by some specific features of living RBC suspensions. Rheological studies[28] have shown that a suspension of RBC will behave in a Newtonian manner when its concentration is lower than 10^5 cells/μL. Therefore, one can expect that the elution process is strongly modified, as the

sample band may behave differently at high concentration. It is obvious, in the light of data plotted in Figure 3 that, at high dilution, samples seemed to behave in an analogous way. However, chemometric methods will be of help to define the maximum analytical concentration of RBC.

The chemometric method employed in this report uses a linearity test (ANOVA), for the data. A linear model fitting test is performed over data and we determine the total variation due to the linear model and the variation due to the departure from this model. For that purpose, a total variability which is the sum of the residual variability, the linear model variability, and the variability due to a non linear model, is estimated. Fisher coefficients from the linear model and from the non linear one are calculated and compared, respectively. These Fisher coefficients enable to determine if the data fit a linear model or a non linear one. Such methodology was proposed by M. Feinberg.[29] That procedure is repeated using a mobile averaging technique of 5 successive data points.

For data plotted in Figure 3, it is observed that, at a constant flow rate, no modification of the retention ratio occurred when a dilution factor higher than 240 was used (the linearity test and regression gave a slope value of 0.0 ± 0.02). This dilution value can be considered, for this channel geometry, as the upper usuable one for analytical purposes. Retention ratios were systematically higher when a higher carrier phase velocity was employed, an effect characteristic of the "hyperlayer mechanism."

However, the retention ratio measurement technique, using the summit of the RBC peak profile, may be biased if this profile is strongly asymmetrical, which is observed experimentally in some cases. Therefore, using the same chemometric approach, we have analysed the asymmetry ratio, whose data are plotted in Figure 4. Again linearity test and moving average methods showed that asymmetry ratio was constant as long as the dilution factor is higher than 240, whatever the flow rate.

It is surprising that, in both cases (retention and asymmetry ratios) the "limit" high value was the same. Therefore, as the dilution factor increased, peak profile behaved more symmetrical and more retained; such a combined effect may have an impact on what is considered in chromatography as an "efficiency" measurement, the HETP, whose data are plotted in Figure 5. Again, the chemometric approach of these data showed two domains, whose boundary was a dilution factor of 240. These results showed that the peak efficiency was increased at low flow rate and, when Figures 3 and 5 are compared, such increase depends on the retention of the sample.

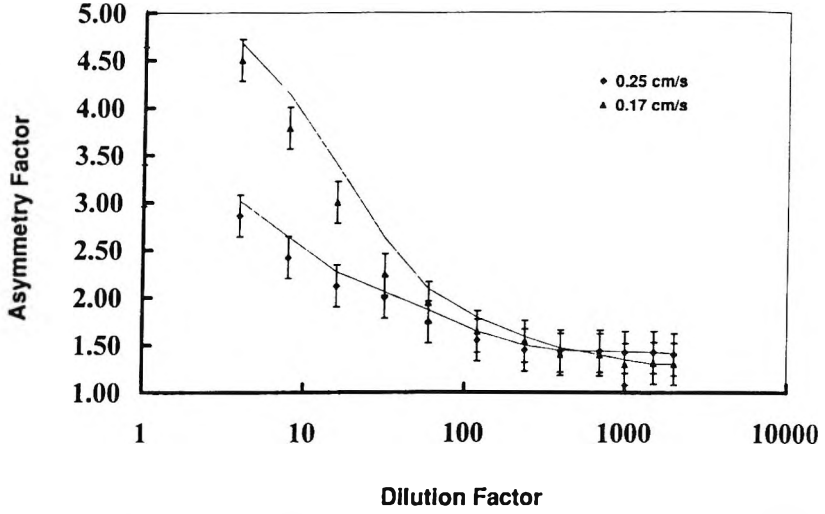

Figure 4. Effect of RBC dilution factor on asymmetry ratio; injection conditions identical to those of Figure 3. Standard deviation 2%.

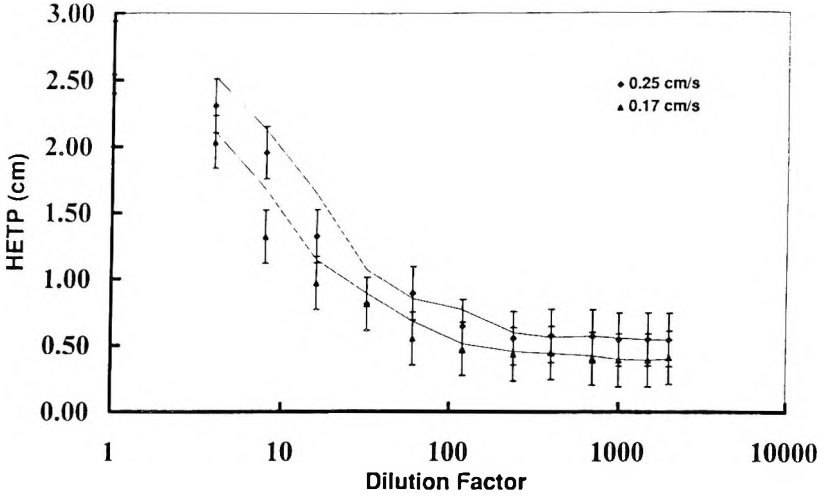

Figure 5. Effect of RBC dilution factor on HETP. Conditions identical to Figure 3, n = 4, standard deviation = 3%.

Because of the complex polydispersity of RBC samples, it is not obvious that the elution conditions of highest efficiency are those of highest separation power. However, HETP can be considered here as a probe for elution conditions comparison. Even if compared to chromatographic techniques, the HETP values are low (0.5 cm), one must have in mind that the species under study are much bigger than any molecule, meso or macromolecules. If we compare the ratio of the length of a theoretical plate (HETP) to the one of a cell (5μm), only 1000 queueing species can be found in a "plate;" this allowed to state that, even with a low plate number per column, such separation system is highly efficient.

Sample Volume Effect on the RBC Elution Characteristics

In the previous developement, the standard injection volume was 50μL, that is to say, 4.4% of the channel void volume. Because of the channel geometry, 4.4% of the channel length or surface is occupied by the injected volume. However, to avoid cell interactions, destruction, or viability decrease, it is necessary to use the greatest dilution of the cells.

Somehow, such procedure may lead to a larger injection volume, which may occupy a larger channel portion. As this injection volume increases, it becomes evident that the available and effective separation channel volume (length) will decrease. There is, therefore, a compromise to be found between dilution factor, injection volume and detection. For that purpose, a constant quantity of cells is injected into the channel at different concentrations, that is, with different injection volume, varying from 20 to 350 μL. The flow rate was chosen to obtain a rather low retention ratio.

As retention ratio values are obtained using the "protein peak method," modifications in the injection volume may modify retention factor calculations. The thicker is the channel, the more important is that effect. To take account of the channel length modification provoked by the injection volume, the protein peak elution volume was decreased by half of the injection volume to simulate the effect of a WISP injection; however, data obtained with both retention ratio methods were not significanlty different. Therefore, the most simple method was used whose results are shown in Figure 6A. Two domains can be found, up to 200μL the retention ratio is constant; this is confirmed again using the chemometric approach described above.[29] However, asymmetry description was also analysed; results are shown in Figure 6B. It is observed that asymmetry ratio was constant up to 200 μL injected into the channel, that is, a volume equivalent to 16% of the system total volume. When efficiency measurements were made, as shown in Figure 6C, major differences arose.

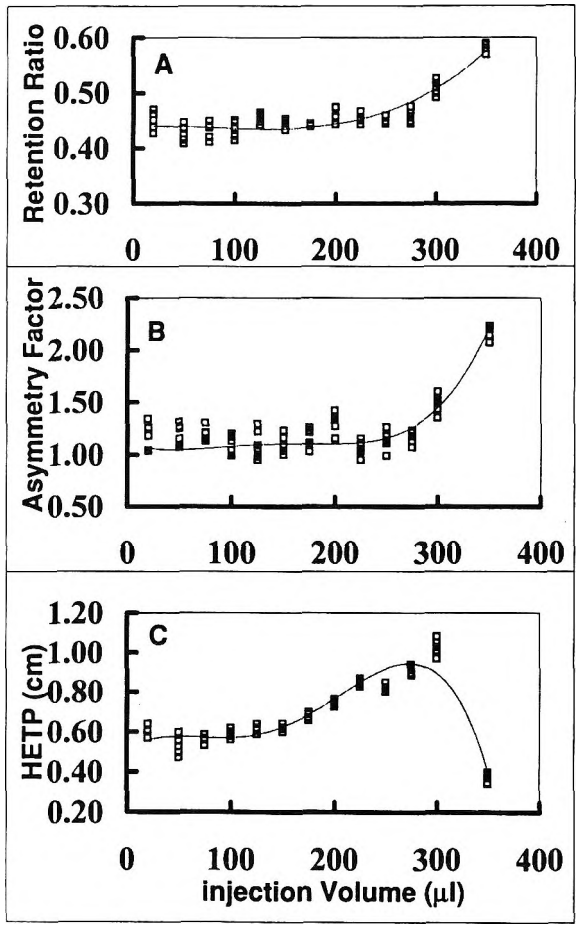

Figure 6. Injection volume effects on RBC fractogram characteristics. RBC dilution factor = 300. Flow linear velocity = 0.25 cm/s. Injection volume varying from 20 to 350 µL (20, 50, 75, 100, 125, 150, 175, 200, 225, 250,275, 300,350). n = 5, maximum standard deviation = 5%. A: Retention ratio, B: Asymmetry factor, C: HETP.

Constant HETP values were only obtained up to 100 µL of injected sample; at 300 µL, that is, at 25% of the void volume, a 100% efficiency loss was observed. Therefore, it can be concluded that, for this channel geometry, a maximum injection volume of 100 µL is possible, which is around 10% of the FFF void volume.

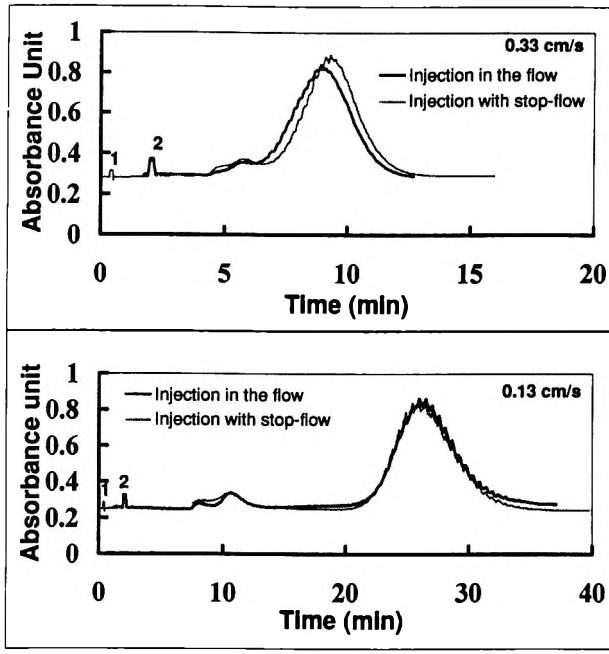

Figure 7. Effect of injection procedure on RBC fractograms. 50 µL loop, dilution factor 300. Stop flow time (when performed) = 2 min. 1: injection with stop flow, 2: injection into the flow. Upper: fractogram differences at high flow rate. Lower: fractogram differences at low flow rate.

This series of results showed clearly that, for a channel of 1 mL, up to 500,000 cells can be injected in a volume lower than 100 µL. As we know now how many cells in a given volume have to be injected in GFFF, the final step of this study is to analyse or define how to place this sample into the separation channel.

Flow and Stop Flow Injection Procedures

Since the early developemental stage of FFF techniques, a relatively original injection mode (compared to chromatography) was used and is now called: Stop Flow Injection or Primary Relaxation Process. If we consider particles or species injected into the channel without flow migration profile, the external field undergoes the distribution of the particles in the channel thickness. After a given time, the field-induced concentration effect, thwarted

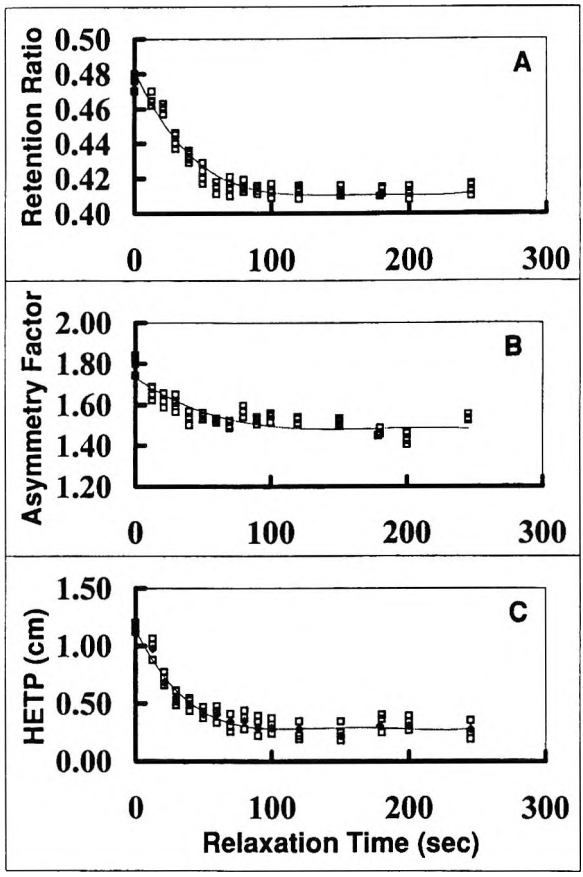

Figure 8. Effect of stop flow time on fractogram characteristics. RBC sample characteristics identical to Figure 7. Carrier phase linear velocity = 0.25 cm/s. Stop flow time varying from 0 to 300 s (0, 10, 20, 30, 40, 50, 60, 70, 85, 100, 120, 150, 180, 210, 250, 300). n = 4, maximum standard deviation = 4%.

by the particle diffusion effect, leads to an equilibrium state. It is obvious that, when particles are injected into the channel when the flow profile is established, a time is needed for the particles to reach this equilibrium state. The stop flow injection procedure, consisting of stopping the flow when all the sample is at the channel inlet for a time long enough where particles can reach this equilibrium state. At high flow rate, the retention factor is decreased when the stop flow procedure is used, as shown in Figure 7, upper part. At low flow rates, fractograms did not show any differences, as demonstrated by fractograms of Figure 7, lower part. Such differences are light because the set up of our device was designed to minimize them.

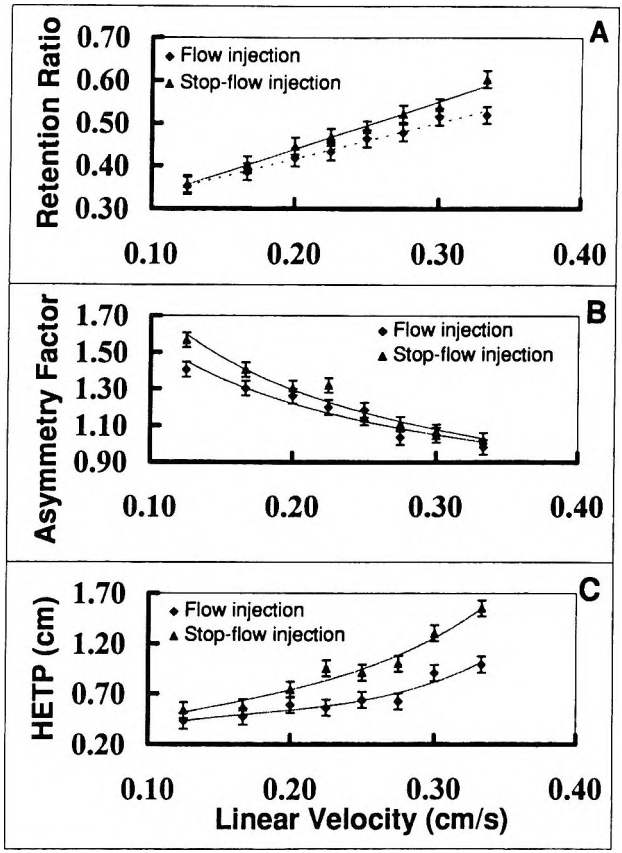

Figure 9. Flow rate and injection procedure effects on fractogram characteristics. RBC samples identical to Figure 7. Linear velocities varying from 0.13 to 0.25 cm/s (0.13, 0.17, 0.20, 0.23, 0.25, 0.28, 0.30, 0.33). A: Retention ratio, B: Asymmetry factor, C: HETP.

However, a closer investigation of peak characteristics allowed to describe the effect of both of these procedures. In some elution cases, even when the inlet tube is connected to the accumulation wall, retention, asymmetry factor, and HETP modifications are important, as shown in Figures 8 A, B, and C. In this study, injection volume and concentration of the samples are kept constant, and stop flow time will vary.

Strong modifications of the parameters under study are observed in the first minute; however, the chemometric approach using the three peak desciption parameters define a minimum stop flow time of 100 sec. There is

an empirical reference method to evaluate this relaxation time. This reference time is considered as the time required for a particle to fall through all the channel thickness (w), for example, with a spherical particle of diameter dp and density rp, falling under the effect of the gravity (981 cm/s^2) in a medium of viscosity h and density rm this time (sed_t) has been established for sedimentation FFF:[30]

$$sed\_t = 18\ h\ w / [\ dp^2(\ rp\text{-}rm)\ G]$$

If we consider the RBC as a sphere whose diameter and density are dp = 5 μm and rp = 1.051, respectively, a channel thickness of 100 μm, a liquid density of rm = 1.002, whose viscosity is 1.016 cp, a sed_t time is calculated at 137 sec. Therefore, this sed_t time is a probe for the "relaxation time" which slightly overestimated the relaxation time. However, if stop flow procedure and relaxation time can be of interest and estimated for monodisperse populations, in the case of highly polydisperse population like RBC, this estimation may be biased for RBC subpopulations. Flow injection of these latter materials may be of help to increase the selective elution of some species subpopulations according to their different sed_t times. As this time is a linear function of the channel thickness, at low flow rates, the channel length covered by the sample is low compared to the channel length.

If the flow increases, that covered length increases also. In the case of a flow injection, the displacement of the sample is a complex function of sed_t and of the "hyperlayer" equilibrium position. There is, therefore, a need to evaluate, experimentally, the balanced effects of "relaxation" and of flow rates.

Data are shown in Figures 9 A, B, and C. Whatever the injection procedure, the retention ratio increase with flow rate increase is characteristic of the presence of "lifting forces" which are at the origin of the "hyperlayer" elution mode of RBC. In all cases, systematic differences are found when the two injection procedures are compared. To point out that injection with "stop flow" procedure or not, generated higher differences at high flow rates and that, if flow rates are low, differences are reduced, driving to non statisitically significant differences.

It can be assumed then, that introducing the samples into the channel at low flow rates may simulate the stop flow procedure. This point is important in the case of biological samples, where species-species interactions will occur if the "local" concentration of the sample is too high or when species channel material interactions appear.

CONCLUSION

Of the specific features of gravitationnal field flow fractionation, in terms of simplicity in the separator design, in terms of simplicity of operation, the results presented in this report may be of practical use in most of the FFF techniques dealing with cellular species. Modifications, easily evaluated, can be set up if channel geometry is modified; however, extrapolation of these results with different wall materials are possible only if proofs are given of the absence of particles sticking at the channel accumulation wall surface. It appeared, in the light of these and, according to other previous work,[31] that it is practical to simply replace the HPLC column of a chromatographic system by an FFF separator to set up an FFF system. Both injection procedures are, therefore, possible, with some slight modifications. For biological elutions in FFF, instead of stop flow procedures, we recommend low-flow injections as already described in other studies.[15,31] When inlet tubing is positionned through the accumulation wall, it could be of interest to use connections of relatively large diameter to avoid complex hydrodynamic effects during injection.

REFERENCES

1. J. C. Giddings, M. N. Myers, Sepn. Sci. Tech., **13(8)**, 637-645 (1978),

2. K. D. Caldwell, Anal. Chem., **60**, 959A-971A (1988).

3. A. Litzen, Anal. Chem., **65**, 461-470 (1993).

4. J. C. Giddings, **Unified Separation Science**, Wiley, New York, 1991.

5. J. C. Giddings, J. Chem. Educ., **50**, 667-669 (1973).

6. S. Levin, Biomed. Chromatogr., **5**, 133-137 (1991).

7. A. Bernard, B. Paulet, V. Colin, Ph. Cardot, TRAC,**14(6)**, 266-273 (1992).

8. J. Plocek, P. Konecny, J. Chmelik, J. Chromatogr. B, **656**, 113-118 (1989).

9. E. Urbankova, A. Vacek, N. Novakova, F. Matulik, J. Chmelik, J. Chromatogr. B, **583**, 27 (1989).

10. P. Reschiglian, G. Torsi, Chromatographia, **40(7-8)**, 467-473 (1995).

11. J. C. Giddings, Anal. Chem., **67**, 592A-598A (1995).

12. J. C. Giddings, Sepn. Sci. Technol., **19**, 831-847 (1984).

13. J. Pazourek, J. Chmelik, Chromatographia, **35**, 591-596 (1993).

14. K. D. Caldwell, Z. Q. Cheng, P. Hradecky, J. C. Giddings, Cell Biophys., **6**, 233, 251 (1984).

15. S. Hoffstetter-Kuhn, T. Rosler, M. Ehrat, H. M. Widmer, Anal. Biochem., **206**, 300-308 (1992).

16. K. G. Wahlund, A. Litzen, J. Chromatogr., **461**, 73-87 (1989).

17. B. N. Barman, E. R. Ashwood, J. C. Giddings, Anal. Biochem., **212**, 35-42 (1993).

18. J. C. Giddings, Science, **260**, 1456-1465 (1993).

19. A. Merino, C. Bories, J. C. Gantier, P. J. P. Cardot, J. Chromatogr. B, **572**, 291-301 (1991).

20. A. Bernard, C. Bories, P. M. Loiseau, P. J. P. Cardot, J. Chromatogr. B, **664**, 444-448 (1995).

21. C. Bories, P. J. P. Cardot, V. Abramowski, C. Pous, A. Merino-Dugay, B. Baron, J. Chromatogr., **579**, 143-152 (1992).

22. P. J. P. Cardot, C. Elga, M. Guernet, D. Godet, J. P. Andreux, J. Chromatogr. B, **654**, 193-203 (1994).

23. P. J. P. Cardot, J. Gerota, M. Martin, J. Chromatogr., **568**, 73 (1991).

24. A. Merino-Dugay, P. J. P. Cardot, M. Czok, M. Guernet, A. P. Andreux, J. Chromatogr., **579**, 73 (1992).

25. B. A. Bidlingmeyer, F. V. Warren , Jr., Anal. Chem., **56**, 1583A (1984).

26. J. C. Giddings, Sepn. Sci. Tech., **18**, 765-773 (1983).

27. P. S. Williams, T. Koch, J. C. Giddings, Chem. Eng. Commun., **111**, 121-147 (1992).

28. R. S. Weinstein, in **The Red Blood Cell**, Vol 1, 2nd Ed., D. N. Surgenor ed., Academic Press, New York, 1974.

29. M. Feinberg, in **La Validation des Méthodes d'Analyse**, Masson, Paris 1996.

30. S. Lee, M. N. Myers, J. C. Giddings, Anal. Chem, **61**, 2439-2444 (1989).

31. V. Yue, R. Kowal, L. Neargarder, L. Bond, A. Muetterties, R. Parsons, Clin. Chem., **40(9)**, 1810-1814 (1994).

Received January 2, 1997
Accepted April 10, 1997
Manuscript 4443

J. LIQ. CHROM. & REL. TECHNOL., 20(16 & 17), 2599–2614 (1997)

CHARACTERIZATION OF INTRAVENOUS FAT EMULSION BY SEDIMENTATION FIELD-FLOW FRACTIONATION AND PHOTON CORRELATION SPECTROSCOPY

Young Hun Park, Won-Suk Kim, Dai Woon Lee

Department of Chemistry
Yonsei University
Seoul 120-749, Korea

ABSTRACT

Sedimentation field-flow fractionation (SdFFF) and photon correlation spectroscopy (PCS) were used to characterize fat emulsions. Mean diameters determined by SdFFF were in good agreement with those from PCS. Mean droplet sizes obtained from two SdFFF channels of different dimensions were also in good agreement, indicating no non-ideal phenomena such as solute-channel interaction occur during SdFFF fractionation. Flocculation of emulsion was affected by concentration of salt and the charge of cation. While freezing-thawing was one of the significant factors to the flocculation, storing emulsions at 60±5°C for 2- 3 days made no significant difference to the sample flocculation.

INTRODUCTION

Sedimentation field-flow fractionation (SdFFF) is capable of separating and characterizing colloidal and particulate materials.[1-4] Samples are separated

in a thin ribbon-like channel on the basis of their effective masses. The flow through the channel has a parabolic profile whose flow velocity approaches zero at both walls and reaches a maximum at the midpoint between the walls. When the centrifugal force is applied across the channel, particles are driven toward the bottom wall, and an equilibrium distribution is established between the external force and particles' diffusion.[5] Particles positioned close to the wall are displaced slowly because of the low flow velocity near the wall. Particles positioned further away from the wall are displaced more rapidly. Since the force exerted on sample particles are related to their effective masses, the equilibrium distance from the wall depends on the particles' mass or size.[6]

The relationship between the applied force and the particle mass in SdFFF is well understood. It allows accurate prediction of particle retention. It also allows calculation of particle size, length, density, and thickness of coated materials at the particle surface, etc.[7-13] In addition to the separation and characterization of particles, fractions can be collected and further analyzed using electron microscopy or light scattering.[14,15]

For particles subjected to normal mode of FFF, retention volume V_r is related to a retention parameter λ as[1,3]

$$\frac{V^0}{V_r} = 6\lambda\left[\coth(1/2\lambda) - 2\lambda\right] \tag{1}$$

where V^0 is the void volume of the channel. When λ is sufficiently small ($\lambda << 1$), eqn. (1) reduces to

$$\frac{V^0}{V_r} = 6\lambda \tag{2}$$

where λ is the ratio of particles' diffusion coefficient to the field-induced particle velocity. In SdFFF, λ is given by

$$\lambda = \frac{kT}{mG(\Delta\rho/\rho_s)w} \tag{3}$$

where k is the Boltzmann constant, T temperature, m particle mass, G centrifugal acceleration force, ρ_s particle density, and $\Delta\rho$ density different between carrier and sample. If particles are spherical, particle diameter d is expressed by[3]

$$d = \left(\frac{6kT}{\pi G \lambda \Delta \rho w}\right)^{1/3} \quad (4)$$

By combining eqn. (2) and (4), particle size can be determined from the measured elution volume of the particle. For samples having broad size distributions, particle size can be determined for each slice of their fractograms, and the size distributions can be obtained for the samples.

A commercial fat emulsion such as intralipid which have been emulsified in water with soybean oil is widely used for parenteral nutrition. The stability of the emulsion is limited to 18 months at about 4 °C. For rapid and efficient medication to patients, the intravenously fed patient required a number of nutrients such as amino-acid, electrolytes, carbohydrates, and trace elements as a total parenteral mixture. Such emulsion has some problems in its stability. The emulsion is rapidly flocculated by electrolytes and this makes it difficult to modify total parenteral nutrition. These flocculated emulsions can block the blood capillary and cause impaired circulation. It is, thus, important to determine the droplet size and size distribution of fat emulsions.[16-18]

SdFFF has been used for characterization of emulsion materials. A theoretical and experimental validation was provided for the measurement of the droplet size distribution of emulsion samples.[19] The size distributions of polydisperse emulsion samples were determined by using SdFFF and PCS.[20] Recently, SdFFF was established for emulsion characterization at various experimental conditions.[21,22]

Fat emulsions are polydisperse, and thus, it is difficult to measure their mean droplet sizes and size distributions accurately. SdFFF has merits for the characterization of fat emulsions. It provides good separating power and flexibility. Sample degradation is minimized owing to the open geometry of the channel. In this work, SdFFF was used, in combination with PCS, to measure the mean droplet sizes of fat emulsions. Narrow fractions were collected from SdFFF runs, and subjected to PCS measurements. Results obtained from SdFFF were compared with those from PCS. Stability of fat emulsions was examined against salt species, salt concentration, and temperature.

MATERIALS AND METHODS

Sedimentation FFF used in this study is the model S101 Colloid/Particle Fractionator from FFFractionation, LLC. (Salt Lake City, UT). The channel

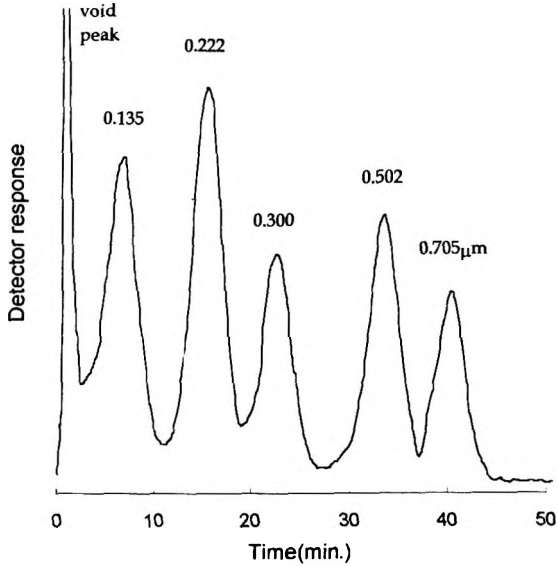

Figure 1. Fractogram of a five component-mixture of polystyrene latex beads obtained by a power programmed SdFFF. Experimental conditions are: initial field strength = 1950 rpm, final field strength = 75 rpm, pre-decay time = 6.0 min, t_a = - 48 min, and flow rate = 4.16 mL/min.

surface was a polished Hastelloy-C alloy. Two channels having different dimensions were used in this work. One ("channel-1") has the length of 89.1 cm, breadth of 1.0 cm, and thickness of 0.0127 cm. The void volume of the channel-1, measured as the elution volume of sodium nitrite minus the volumes between the injector and channel and between the channel and detector, was 1.19 mL.

Another channel ("channel-2") has the breadth of 2.0 cm and a thickness of 0.0254 cm and the same length. The void volume of the channel-2, measured by the same method used for the channel-1, was 4.30 mL. The radius of the rotor is 15.1 cm.

The intralipid 10% was obtained from the Green Cross Inc. (Seoul, Korea) and was injected into SdFFF without dilution. Injection volume was 1.0 to 3.0μL. Reported density of the sample is 0.917 g/cm^3. The carrier liquid was doubly distilled and deionized water containing 2.25% glycerol (Sigma, St. Louis, MO) and 0.02% sodium azide (Merck, Darmstadt, F. R. Germany) as a bactericide. Polystyrene latex standards were obtained from Duke Scientific

(Palo Alto, CA). The standards were diluted about 100 times with water containing 0.1% of FL-70 (Fisher Scientific, Pittsburgh, PA) and 0.02% of sodium azide.

Experiments were carried out using an SLC-100 pump (Samsung Electron Devices, Suwon, Korea), Durex metering pump cc-100-s-4 (Eldex Laboratories, Inc. Napa, CA), and a Linear UVIS 200 (Reno, NV) UV detector fixed at 254 nm of wavelength. Detector response was transferred to a IBM-compatible PC and processed using the Field-Flow Fractionation Data Analysis Software 2.0. A power programming[23] was used to avoid the steric transition and excess retention of fat emulsions. The programming parameter, p was set at 8, and the time constant t_a was set to be equal to - pt_1 to achieve constant fractionating power throughout the entire elution range.

Fractions of fat emulsions were collected from SdFFF runs and analyzed using photon correlation spectroscopy (PCS). Measurements were made at 25°C. The PCS system was 4700C from Malvern Instruments Ltd (Worcestershire UK). The light source of the PCS was He-Ne laser at 632.8 nm, and measurements were made at a 90 degree fixed angle.

RESULTS AND DISCUSSION

The performance of SdFFF system was tested using polystyrene latex standard particles. Figure 1 shows a separation of five standards in the diameter range of 0.135 to 0.705μm, obtained from the channel-2 (having 0.0254 cm thickness). The field strength was power-programmed with the initial field of 1950 rpm, final field of 75 rpm, pre-decay time (t_1) of 6 min, t_a of -48 min and flowrate of 4.16 mL/min. The carrier solution contained 0.1% (v/v) FL-70 and 0.02% sodium azide. Under these experimental conditions, five standard particles were separated within 50 min with a good resolution.

External field was varied for initial evaluation of the retention of fat emulsions. Figure 2a shows fractograms obtained using the channel-1 at three different initial field strengths, 380 G (1500rpm), 547 G (1800rpm), and 745 G (2100rpm). Field programming was employed to avoid steric transition. As previously explained, size distribution can be obtained from the SdFFF fractogram.

Figure 2b shows size distributions obtained for the fractograms shown in Figure 2a. Size distributions are broad with the high end reaching up to about 0.9 μm. No significant difference was found among size distributions obtained at different filed strengths. The mean droplet diameters were determined from

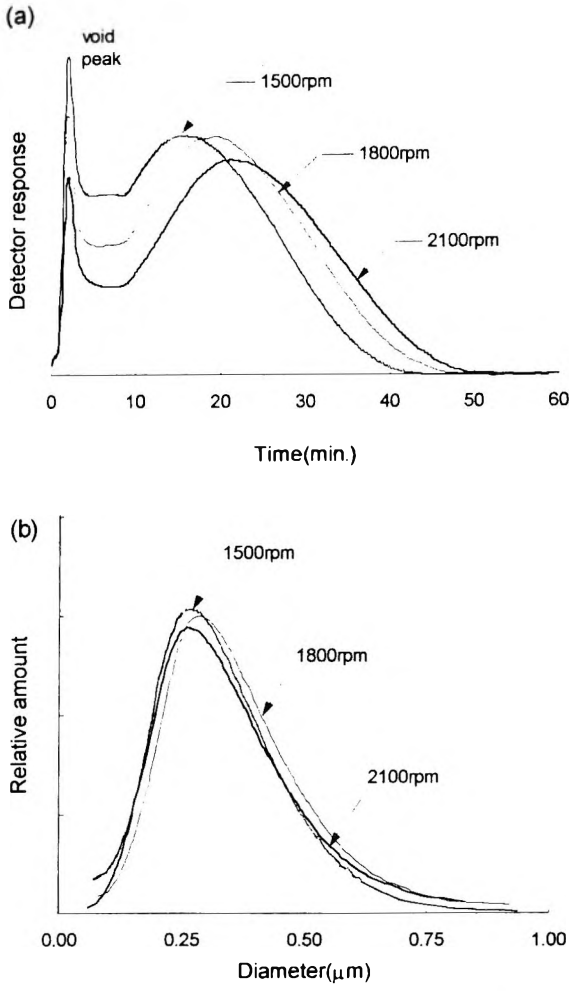

Figure 2. Fractograms (a) and size distributions (b) of fat emulsions obtained using the channel-1 (thickness of 0.0127 cm) at different initial field strengths, 380, 547, and 745 G. Experimental conditions are: pre-decay time = 8.0 min, t_a = - 64 min, and flow rate = 0.90 mL/min.

the first moment of the size distributions. Mean diameters obtained at three different field strengths were in good agreement with the relative different of less than ±5%. Measured mean diameters were 263 μm at 380 G, 280 μm at 547 G and 268 μm at 745 G.

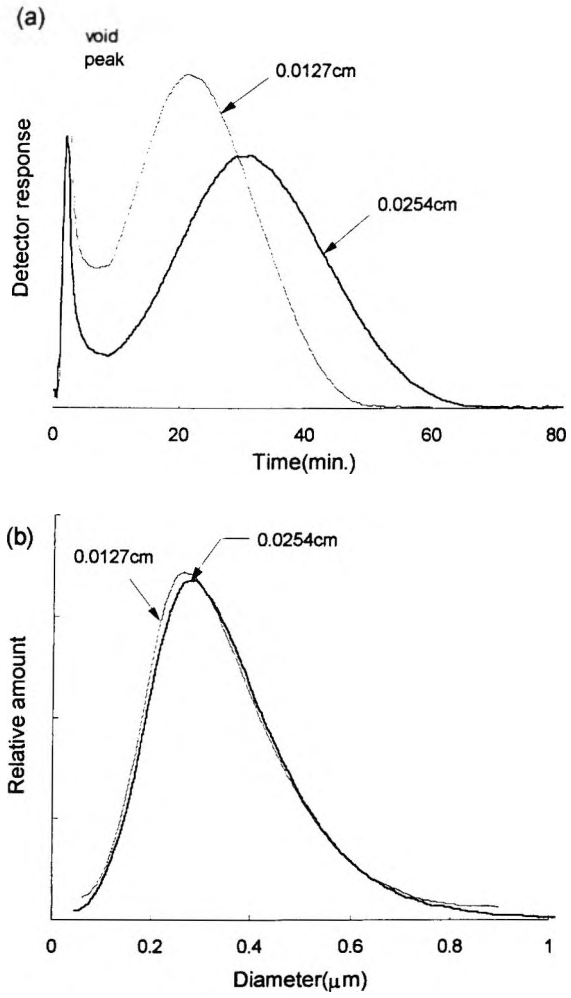

Figure 3. Fractograms (a) and size distributions(b) of fat emulsions obtained using channels of different thickness. Experimental conditions are: initial field strength = 745 G (2100rpm), final field strength = 1 G (75 rpm), stop-flow time = 12min, pre-decay time = 8.0 min, t_a = - 64 min for both channels. Flow rate = 0.90 mL/min for the channel-1 and 3.24 mL/min for the channel-2.

The validity of the size-based fractionation and of the resulting size distribution curves obtained from SdFFF can be verified in several ways. One is to compare the size distributions obtained under different experimental conditions, or to compare the size distributions obtained from different SdFFF systems. Another way is to collect fractions from SdFFF fractograms and to

examine them using other techniques such as electron microscopy or PCS.[24] Figure 3a shows elution profiles of the same sample obtained from two different channels: channel-1 has the thickness of 0.0127 cm and the channel-2 has the thickness of 0.0254 cm. The same field-programming parameters were used for two channels: initial field strength of 745 G (2100rpm), final field strength of 1 G (75rpm), pre-decay time of 8.0 min, t_a of - 64 min, and the stop-flow time of 12 min. Flow rate was set at 0.90 mL/min for the channel-1 and at 3.24 mL/min for the channel-2 to achieve the same linear flow velocity for both channels.

Figure 3b shows size distributions obtained from fractograms shown in Figure 3a. If there were non-ideal phenomena such as interaction between sample and the accumulation wall, or disruption of the sample distribution in the flow stream, or steric effect, then the size distributions obtained from two different channels will be different. The size distributions obtained from two different channels are similar with the mean droplet diameter of 0.27μm, suggesting no such non-ideal phenomena occurs. SdFFF is thus an useful tool for the determination of the size distribution of fat emulsions. It is noted that the thinner channel, channel-1 may not be useful for flocculated samples as steric inversion may occur during SdFFF run.

In order to confirm the accuracy of the mean diameter of fat emulsion measured by SdFFF, fractions were collected at 5 different positions of the fractograms and were analyzed using PCS. Each PCS measurement was repeated 20 times, and they showed good reproducibility with the relative error of less than ±4%. As shown in Figure 4, the mean diameters obtained from PCS are in good agreement with those obtained from SdFFF with relative difference of 4 - 11 %.

To study the effect of the salt concentration on the sample flocculation, various kinds of salts were added to the original sample and injected directly into the SdFFF without dilution. It is known that addition of electrolyte gradually reduces the energy barrier preventing aggregation until a point is reached where no barrier remains. The height of the energy barrier depends on the electrolyte concentration and counter-ion valence. The flocculation is dominated by the valence of the ion of the added electrolyte of charge opposite to that of the colloidal particles.[25,26] Elution profiles and size distributions of emulsions obtained at different concentrations of sodium chloride are shown in Figures 5a and 5b. At low salt concentrations, droplet size distributions do not change significantly from that of the original sample. When the concentration of sodium chloride is further increased, size distribution starts changing due to flocculation.

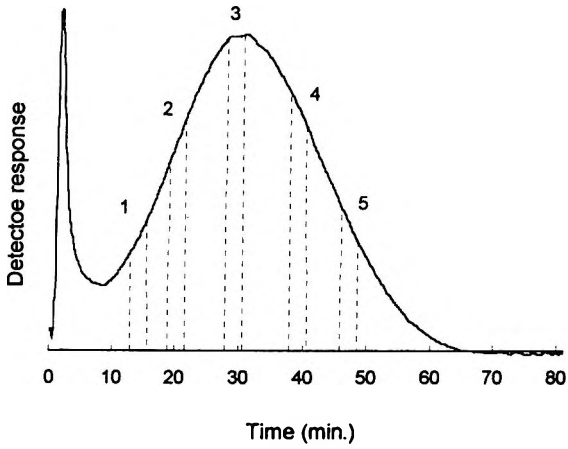

Fraction No.	PCS(nm)	SdFFF(nm)	rel difference(%)
1	164	156	-5.1
2	188	196	4.1
3	239	258	7.4
4	326	367	11.2
5	436	465	6.2

Figure 4. Fractogram and measured droplet size of fat emulsion obtained from the channel-2 (thickness of 0.0254 cm). Experimental conditions are: initial field strength = 745 G (2100rpm), final field strength = 1 G (75 rpm), pre-decay time = 8.0 min, t_a = - 64 min, stop-flow time = 12min, and flow rate = 3.24 mL/min.

In case of calcium and magnesium ions, as shown in Figures 6a and 6b, the change in the elution profile is more noticeable than in the case of sodium chloride, showing broadening of the profile and even a symptom of steric transition. The addition of magnesium ion made a slight change at the end of the elution profile compared to that of calcium ion. When the concentration of salt is further increased, the samples rapidly become creamy or oiled.

The cumulative mass distribution, Figure 6b, shows that droplets larger than 0.3 μm are produced by flocculation. It was impossible to determine accurate size distributions of flocculated samples due to the steric transition occurring at the later eluting region. It seems that divalent cations are more effective than monovalent cations for flocculation. These results indicate that both the type of electrolyte and electrolyte concentration are important factors to the flocculation of the fat emulsions during their storage.

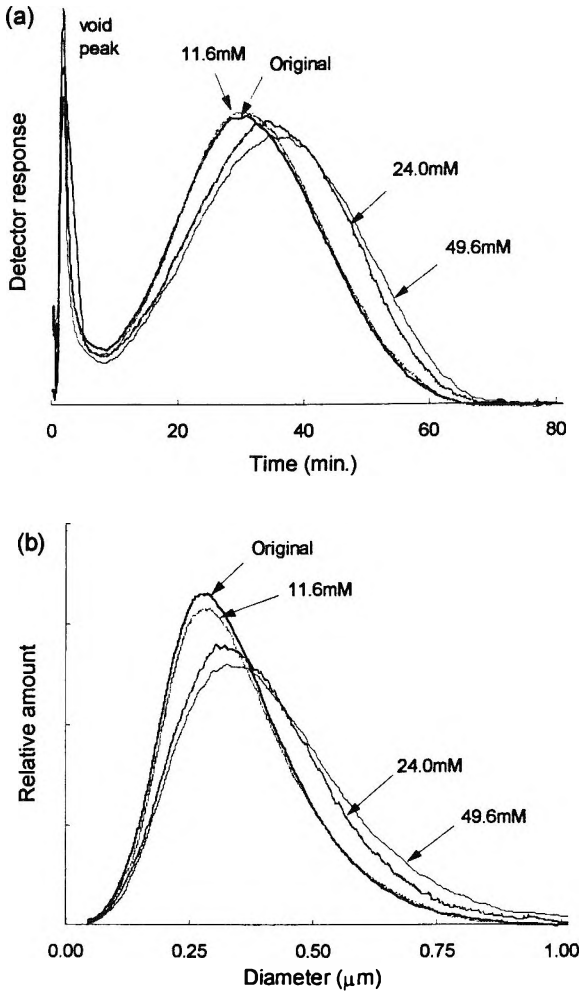

Figure 5. Fractograms (a) and droplet size distributions (b) of fat emulsion after the addition of sodium chloride. Experimental conditions are same as those of Fig. 4.

SdFFF is one of the methods that can be used to study critical concentration for flocculation. It is noted, however, that the samples (and also the salt) are diluted in the SdFFF channel, and this may affect the sample flocculation. Figure 7 shows fractogram of a sample flocculated by freezing. Freezing induces phase change, and causes sample flocculation. Eventually, emulsions become oiled.

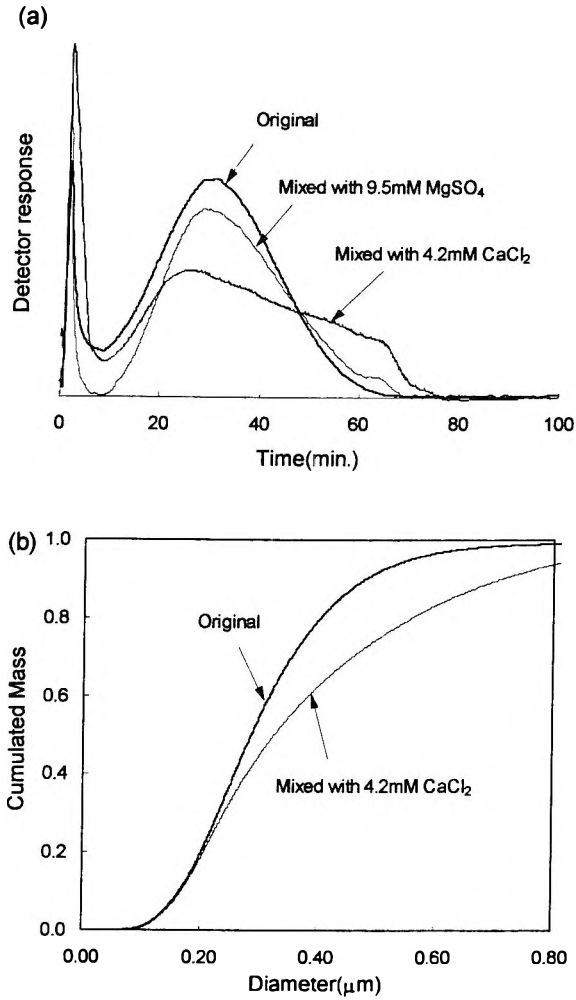

Figure 6. Fractograms (a) and cumulated mass distribution curves (b) of fat emulsion after the addition of magnesium sulfate and calcium chloride. Experimental conditions are same as those of Fig. 4.

To re-disperse the emulsion, the frozen sample was thawed and then homogenized at 10,000 rpm 3 times for 3 min each. The fractogram labeled "redispersion" is for the homogenized sample. It shows a slight change at the end of the fractogram. The size distribution, however, did not change. This indicates that, once intralipid is frozen (and thus flocculated), it can not be re-dispersed, even with the means such as shear-mixing homogenization. While

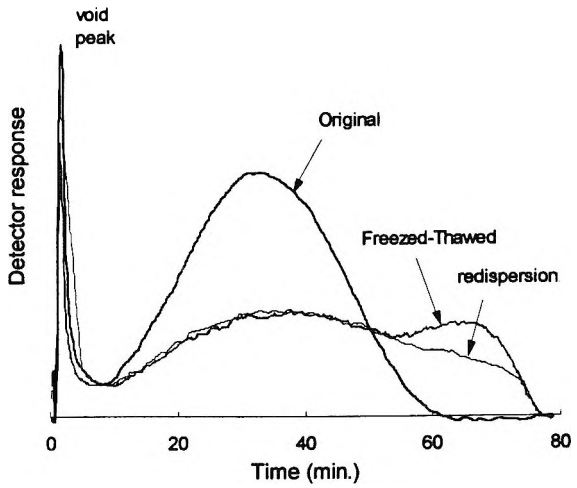

Figure 7. Fractograms of original and freezed-thawed fat emulsion. Experimental conditions are same as those of Fig. 4.

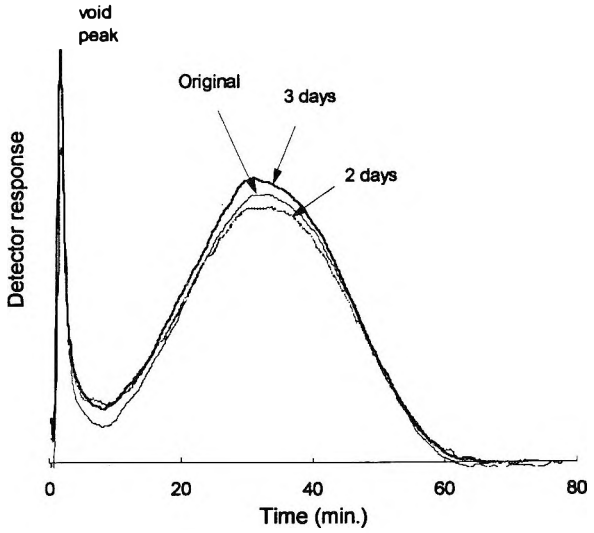

Figure 8. Fractograms of fat emulsion stored at 60±5 degrees. Experimental conditions are same as those of Fig. 4.

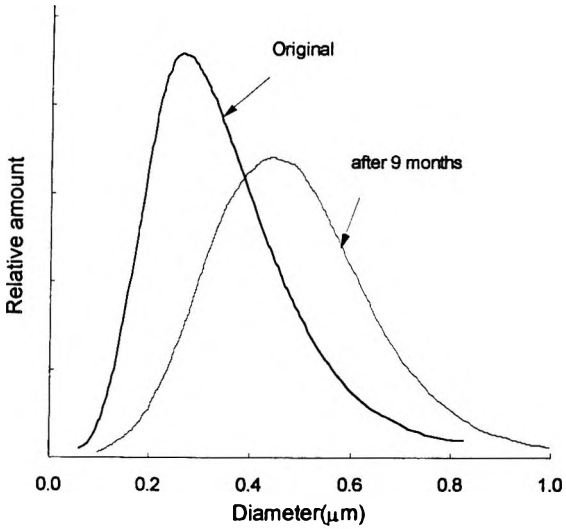

Figure 9. Size distribution curves of fat emulsion stored for 9 months at room temperature. Experimental conditions are same as those of Fig. 4, except the initial field strength = 1900 rpm.

storing the sample at below 0°C showed a significant difference in droplet size distribution, keeping them under high temperature did not make a significant change (see Figure 8). Samples were kept in an oven at 60±5 °C for 2 - 3 days. Increasing the temperature generally brings about changes in viscosity, interfacial tension, and adsorption at the interface. Also, potential energy and Brownian motion increase with temperature and double layer potentials change.[25] It was found that temperature, as a short term stress, was not a significant factor for emulsion stability. The stability of emulsion, however, decreased rapidly with increasing temperature, and it was impossible to obtain an SdFFF fractogram.

Aging effect was also studied. Generally, an emulsion stored at 4 - 8°C through the expired date changes droplet diameter less than about 5%. Figure 9 shows size distribution of a sample stored for 9 months at room temperature after the first sampling through a rubber septum. The mean droplet diameter increased by about 30% from that of the original sample. Small degree of temperature fluctuation during long term stress may have made the sample to be flocculated easier than when the sample is stored under 4°C.

In conclusion, SdFFF is a useful tool for determining the mean droplet diameter and the size distribution of fat emulsions. Good agreement was observed between mean diameters obtained from two different SdFFF channels. Mean diameters obtained from SdFFF and PCS were also in good agreement. SdFFF is applicable for characterization of flocculated fat emulsions, and for the determination of the critical flocculation concentration of the sample.

ACKNOWLEDGMENTS

This work was supported by the Korea Science and Engineering Foundation (KOSEF) through the Center for Molecular Catalysis at Seoul National University.

REFERENCES

1. J. C. Giddings, Science, **260**, 1456-1465 (1993).

2. K. D. Caldwell, Anal. Chem., **60**, 959A-971A (1988).

3. J. C. Giddings, G. Karaiskakis, K. D. Caldwell, M. N. Myers, J. Colloid Interface Sci., **92**, 66-80 (1983).

4. J. C. Giddings, K. D. Caldwell, "Field-Flow Fractionation," in **Physical Methods of Chemistry**, Vol. 3B, B. W. Rossiter, J. F. Hamilton, eds., John Wiley & Sons, New York, 1989, Chap. 8, pp. 867-938.

5. J. C. Giddings, F. J. F. Yang, M. N. Myers, Anal. Chem., **46**, 1917-1924 (1974).

6. M. Martin, P. S. Williams, "Theoretical Basis of Field-Flow Fractionation," in **Theoretical Advancement in Chromatography and Related Separation Techniques**, F. Dondi, G. Guiochon, eds., NATO ASI series C: Mathematical and Physical Science, Vol. 383, Kluwer, Dordrecht, 1992, pp. 513-580.

7. J. C. Giddings, M. H. Moon, Anal. Chem., **63**, 2869-2877 (1991).

8. Y. H. Park, M. H. Moon, D. W. Lee, Instrum. Sci. Technol., in press.

9. J. C. Giddings, M. H. Moon, P. S. Williams, M. N. Myers, Anal. Chem., 63, 1366-1372 (1991).

10. Y. Jiang, J. C. Giddings, R. Beckett, "Direct Measurement of Protein Adsorption on Latex Particles by Sedimentation Field-Flow Fractionation," in **Proteins at Interfaces II**, T. A. Horbett, J. L. Brash, eds., ACS Symp. series No. 602, ACS, Washington, DC, 1995, pp. 405-419.

11. R. Beckett, J. Ho, Y. Jiang, J. C. Giddings, Langmuir, 7, 2040-2047 (1991).

12. K. D. Caldwell, J. Li, J. T. Li, D. G. Dalgleish, J. Chromatogr., **604**, 63-71 (1992).

13. J. C. Giddings, G. Karaiskakis, K. D. Caldwell, Sepn. Sci. Technol., **16**, 607-618 (1981).

14. F.-S. Yang, K. D. Caldwell, J. C. Giddings, J. Colloid Interface Sci., **92**, 81-91 (1983).

15. K. D. Caldwell, H. K. Jones, J. C. Giddings, Colloids Surf., **18**, 123-131 (1986).

16. C. Washington, Int. J. Pharm., **66**, 1-21 (1990).

17. C. Washington, S. S. Davis, Int. J. Pharm., **39**, 33-37 (1987).

18. C. Washington, Int. J. Pharm., **64**, 67-73 (1990).

19. F. S . Yang, K. D. Caldwell, M. N. Myers, J. C. Giddings, J. Colloid Interface Sci., **93**, 115-125 (1983).

20. K. D. Caldwell, J. Li, J. Colloid Interface Sci., **132**, 256-268 (1989).

21. S. Levin, L. Stern, A.Ze'evi, M. Y. Levy, Anal. Chem., **66**, 368-377 (1994).

22. S. Levin, E. Klausner, Pharm. Res., **12**, 1218-1224 (1995).

23. P. S. Williams, J. C. Giddings, Anal. Chem., **59**, 2038-2044 (1987).

24. J. C. Giddings, M. N. Myers, M. H. Moon, B. N. Barman, "Particles Separation and Size Characterization by Sedimentation Field-Flow Fractionation," in **Particle Size Distribution II: Assessment and Characterization**, T. Provder, ed., ACS Symp. series No. 472, ACS, Washington, DC, 1991, pp. 198-216.

25. B. J. Carroll, "The Stability of Emulsion and Mechanism of Emulsion Breakdown," in **Surface and Colloid Science**, E. Matijevic, ed., Vol. 9, John Wiley & Sons, New York, 1976, pp. 1-67.

26. R. D. Vold, M. J. Vold, **Colloid and Interface Chemistry**, Addision-Wesley, Reading, 1983.

Received January 14, 1997
Accepted April 9, 1997
Manuscript 4438

J. LIQ. CHROM. & REL. TECHNOL., 20(16 & 17), 2615–2635 (1997)

EXPERIMENTAL ANALYSIS OF SECOND-ORDER EFFECTS ON GRAVITATIONAL FIELD-FLOW FRACTIONATION RETENTION OF SILICA PARTICLES

D. Melucci,† G. Gianni, G. Torsi, A. Zattoni, P. Reschiglian*

Department of Chemistry "*G. Ciamician*"
University of Bologna
Via Selmi 2
Bologna, Italy I-40126

ABSTRACT

One of the most attractive features of GrFFF is the possibility to perform particle size distribution analysis of supermicron particles dispersions by means of a very simple and inexpensive experimental apparatus, easily obtained by implementing a basic HPLC configuration. Optimization of the method requires the knowledge of the effects (second-order effects) capable of influencing sample retention and, thus, the accuracy of the scaling from the retention times axis to the particle size axis. In the framework of such an optimization, the role played by hydrodynamic effects in modulating retention is here first considered and the experimental verification of the empirical equations describing such effects is presented. The effects exerted on retention by changing different GrFFF systems is also studied by means of such an experimental approach.

INTRODUCTION

Gravitational field-flow fractionation (GrFFF) has been demonstrated to be able to characterize supermicron particles of either inorganic[1-6] or biological origin.[7-12] In particular, accurate particle size distribution analysis (PSD) by GrFFF of silica particles for HPLC column packing has been shown to be possible in a very simple, quick and inexpensive way.[4] PSD analysis requires the conversion of a fractogram, that is the signal *vs.* time response, into a size distribution curve, that is the mass frequency function *vs.* diameter curve. For a proper approach to GrFFF-based PSD optimization, however, it is required to focus on all factors which limit the direct application of the method.

First, the direct conversion from retention time to particle diameter values, which is required to obtain PSD profiles by GrFFF, is based on the assumption that fractionation is obtained in steric mode and that the relative steric correction factor γ is known or experimentally estimated. It has been reported, however, that in steric elution mode, that is, with γ values lower than two,[13] γ can be influenced by various effects such as the hydrodynamic effects and the mobile phase composition, both in GrFFF and sedimentation field-flow fractionation (SdFFF).[6,14-16] All these effects, here generally indicated as second-order effects, can, thus, significantly affect retention and even modify the elution mode in GrFFF. For instance, in a recent paper[6] it has been demonstrated that, with silica particles eluted by GrFFF, a reduction in ionic strength brings about a strong increase of the retention ratio and a significant reduction of the fractogram broadening in the case of spherical particles. Conversely, irregular particles do not show any significant change in peak retention parameters. Even the salt composition of the mobile phase has shown to significantly alter GrFFF retention. A reduction in retention was gradually attained by adding sodium chloride instead of sodium azide to the carrier solution. The effect of a retention modification ascribable to the presence of chloride ions suggests some kind of particle-wall interactions.

Second, quantitative PSD analysis requires the accurate control of the sample recovery:[17] second-order effects may play an important role also with respect to quantitative analysis. For instance, the role played by the mobile phase composition on retention and recovery was reported to be so critical to onset a hybrid elution mode which has been defined as Potential-Barrier FFF (PB-FFF).[18-20] The possibility to assess the presence of PB effects also in GrFFF has been recently described.[6,21]

In this paper a preliminary experimental approach to the evaluation of the second-order effects is presented. Among such effects, the extent of hydrodynamic forces, relative to the GrFFF systems here employed, has been

first studied. In particular, the semi-empirical model given by Williams *et al.*[14-16] has been applied. Such a model is based on the existence of two main hydrodynamic contributions to SdFFF retention in steric mode: the retardation effect and the lift forces contribution, the latter being separately considered as due to near-wall lift forces and inertial lift forces. Williams and coworkers proposed, and experimentally verified in SdFFF, some empirical equations which relate particles' elevation during steric elution to various experimental parameters. These are particles' size, density, and flow rate, density and viscosity of the mobile phase. By applying the model described it is possible to determine the predicted and the experimental particles' elevations as a function of the above experimental parameters.

The validation of Williams' model is fundamental for the calculation of particles' elevations. In fact, it is shown in MATERIALS AND METHODS that particles' elevation values are required for the accurate determination of particles' size (or density) when the experimental value of the steric correction factor (γ) is not known. In other words, if particles' elevation can be accurately predicted, the conversion from the retention time to particles' diameter can be performed in a GrFFF experiment with no need of previous knowledge of the γ value.

In this work, the agreement between measured and predicted particles' elevations is verified with respect to the elution of silica particles by GrFFF. It is also shown that second-order effects other than hydrodynamic forces can influence retention of such particles. The chemical composition of the channel walls and of the carrier fluid have shown effects on particles' elevation which are comparable to those given by hydrodynamic effects alone. The aim of such preliminary work is to single out the experimental conditions for which the extent of the above second-order effects can be predicted or controlled in the framework of an optimized method of absolute PSD analysis of silica particles by GrFFF.

MATERIALS AND METHODS

GrFFF Channel Systems

The GrFFF systems were built as described elsewhere:[4,6,22] two mirror polished plates were clamped together over a polymeric sheet (Mylar) a few tens of μm thick from which the channel volume had been removed.

Table 1

GrFFF Channel Systems

System	Length x Width (cm)	Walls	Ionic Modifier in the Mobile Phase	V_0 (cm^3)	w (cm)	C^a
1	50x2	glass, unmodified	NaN_3	1.92	0.0202	0.0797
2	50x2	glass, unmodified	NaN_3	2.01	0.0211	0.0932
3	50x2	glass, Cl-modified (2 weeks treatment)	NaCl	1.75	0.0184	0.0556
4	50x2	glass, Cl-modified (2 weeks treatment)	NaN_3	2.01	0.0211	0.0932
5	50x2	polycarbonate	NaN_3	1.81	0.0190	0.0632

[a] C evaluated by interpolation of data reported in literature (see Figure 2).

The effective void volume V_0 was experimentally determined by eluting an unretained spectroscopic standard: K_2CrO_4 in Na_2HPO_4 0.05 M. The system and the channel dead volumes were measured and the effective V_0 was then calculated. After channel assembling the effective channel thickness w must result very close in value to the spacer thickness which was accurately determined with a micrometer. Actual w is often somewhat thicker, particularly when sealant is used to prevent leaks between the spacer and the channel walls. Since channel thickness is really critical for the evaluation of the coefficient C (Eq. 6) and, hence, of particles' elevations, it was accurately calculated from the exact value of the channel void volume divided by the geometrical base surface of the channel. The channel systems used in the experiments are listed in Table 1.

Silica Samples

Samples were porous, spherical silica particles of 5 μm diameter for HPLC column packing (LiChrospher SI-60) (Merck, Darmstadt, Germany),

Table 2

Specifications of Used Silica Samples

Sample	Name	Surface type	Shape	Diameter [cm]	ρ_{dry} [g cm^{-3}]	V_P [cm^3 g^{-1}]	$\Delta\rho^a$ [g cm^{-3}]
1	LiChrospher SI 60	polar	spherical	$5.0\ 10^{-4}$	2.3	0.85	0.441
2	LiChrospher SI 60 RP18e	unpolar	spherical	$5.0\ 10^{-4}$	1.8	0.85	0.317

[a] $\Delta\rho$: see Eq. 9.

either non-derivatized or octadecil-sylanized. The first sample (Si-60) is polar, while the second (RP-18e) has a highly hydrophobic surface. Sample specifications are given in Table 2. Non-derivatized samples were dispersed at 0.5% (w/v) in Milli-Q water while RP18e samples were dispersed at the same concentration in TRITON X-100 5% (v/v). Injected amounts were always 100 μg.

GrFFF Experimental Conditions

Carrier flow was generated by a Model 2510 HPLC pump (Varian, Walnut Creek, CA). Flow rates spanned from 0.2 to 6.0 cm^3 min^{-1}.

Mobile phase was Milli-Q (Millipore, Bedford, Germany) water added with TRITON X-100 0.1 % v/v and with NaN_3 or NaCl $3.1\ 10^{-3}$ M. The carrier viscosity η was assumed to be 0.890 g cm^{-1} s^{-1} as reported in Ref. 16.

The detector was the Model 2550 UV-VIS flow-through spectrophotometer (Varian, Walnut Creek, CA) operating at 330 nm. Detector output was recorded on an X-Y chart strip integrator Model Mega 2 (Carlo Erba Strumentazione, Milan, Italy) and captured through a 12 bit I/O board Model Lab PC+ (National Instruments, Austin, TX) plugged into an AT-compatible 386-DX PC. Stop-flow injection procedure with 3 minutes of relaxation time was followed in all the experiments.

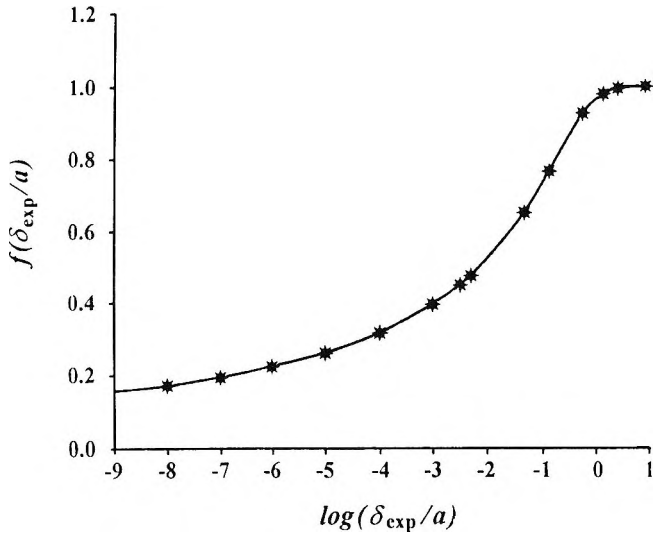

Figure 1. Interpolated retardation function $f(\delta_{exp}/a)$ from Ref. 14. (*): experimental data reported in Ref. 24.

Determination of Predicted Particles' Elevation Values

The basic equations for steric GrFFF retention are reported elsewhere [Ref. 23 and references therein]. For GrFFF in steric elution mode, the expression for retention is given by

$$R = 6\gamma \frac{a}{w} \qquad (1)$$

where R is the retention ratio, γ is the steric correction factor, a (cm) is the particles' radius and w (cm) is the channel thickness. The quantity γ can be experimentally determined by calibration, that is, by plotting R *vs.* a for various standard samples of different radius.

The steric correction factor is related to particles' mean elevation. The theoretical approach to the evaluation of particles' mean elevation in a SdFFF channel was given by P. S. Williams *et al.* through the analysis of the hydrodynamic effects able to influence retention, *i.e.* the retardation effect and the lift forces contribution.[14-16]

The first contribution is usually considered as given by a perturbation of the mobile phase stream by the presence of finite particles within the fluid. Retardation effects result in particles' velocities which are smaller than that of the surrounding fluid. This effect is expressed by the equation

$$f\left(\frac{\delta}{a}\right) = \frac{v_p}{v(x)} \tag{2}$$

where x (cm) is the distance of the center of the particles from the accumulation wall, $\delta = x - a$ (cm) is called the particles' elevation with respect to the accumulation wall, v_p (cm s^{-1}) is the velocity of the center of the particle, $v(x)$ (cm s^{-1}) is the velocity of the surrounding fluid, and $f(\delta/a)$ is the retardation function, which was evaluated by P. S. Williams *et al.*[14] by fitting numerical results previously given by A. J. Goldman *et al.*[24] The derived $f(\delta/a)$ function, in numerical form, was also employed in the present paper to calculate the experimental particles elevation values (δ_{exp}) through the expression reported below (Eq. 4). The retardation function profile is reported in Figure 1.

Williams and coworkers also reported that, with the parabolic profile of the mobile phase flow given by

$$v(x) = 6\langle v\rangle \frac{x}{w}\left(1 - \frac{x}{w}\right) \tag{3}$$

where $\langle v\rangle$ (cm s^{-1}) is the average flow velocity, by combining Eq. (1), Eq. (2) and Eq. (3), one gets the expression for the experimental retention ratio R_{exp} as a function of particles' elevation δ as

$$R_{exp} = 6f\left(\frac{\delta}{a}\right)\frac{x_{exp}}{w}\left(1 - \frac{x_{exp}}{w}\right) \tag{4}$$

The above expression makes it possible to calculate the experimental values of x (x_{exp}) and, hence, particles' mean elevation values (δ=x-a). It must be pointed out that Eq. (4) is strictly valid only if the R values correspond to the equilibrium values (R_{eq}), that is, when the steady-state distribution of the particles across the channel is rapidly obtained and maintained once elution starts. However, particles take a finite time for bringing themselves to the equilibrium distance (secondary relaxation) and, hence, the x value related to R_{exp} is a mean value. The direct consequence is that a correction should be applied to obtain R_{eq} from R_{exp} values. However, in a GrFFF system, if flow rates are not too high and particles of sufficiently high density are used, the

secondary relaxation time can be considered as negligible with respect to the retention time and correction for R_{exp} values can be avoided. Such limiting condition has been taken into account in the choice of the experimental conditions employed in this work, and, thus, δ_{exp} values have been directly calculated by means of eq. (4).

When particles' mean elevation values (δ_{exp}) are higher than zero, then these particles are lifted away from the accumulation wall and elute at higher velocity than that of the fluid lamina at a distance from the accumulation wall which corresponds to the particle radius (*i.e.*, particles eluting in physical contact to the accumulation wall). The presence of forces capable of lifting away particles from the accumulation wall during elution must be, thus, postulated. A quantitative approach to lift forces was given by P. S. Williams *et al.*[14-16] who described lift effects due to two additive lift forces: inertial lift forces (F_{in}) and near-wall lift forces (F_{nw}). The relative expressions were given as

$$F_{in} = 13.5\pi \frac{\langle v \rangle^2 a^4 \rho_{mp}}{w^2} 19.85\left(0.19 - \frac{x}{w}\right)\left(0.5 - \frac{x}{w}\right)$$

$$\left(0.81 - \frac{x}{w}\right)\left[1 + \frac{16}{25}\frac{x}{w}\left(1 - \frac{x}{w}\right)\right] \qquad (5)$$

$$F_{nw} = 6C \frac{a^3 \eta \langle v \rangle}{\delta w} \qquad (6)$$

where ρ_{mp} (g cm^{-3}) is the density, η (g cm^{-1} s^{-1}) is the viscosity of the mobile phase and C is an experimental coefficient which resulted strongly dependent on w.

In GrFFF, when the sample band approaches its steady-state distribution across the channel, particles' mean elevation predicted by lift forces theory can be determined by equating lift forces (F_L) to gravitational force (F_G), that is

$$F_G = F_L = F_{in} + F_{nw} \qquad (7)$$

$$F_G = \frac{4}{3}\pi a^3 \Delta \rho g \qquad (8)$$

where $\Delta\rho$ (g cm^{-3}) is the difference between particles' density and carrier's density and g is the earth gravity acceleration (cm s^{-2}). The exact value of $\Delta\rho$

can be calculated by the method proposed by J. C. Giddings *et al.*:[25]

$$\Delta\rho = \frac{\rho_{dry} - \rho_{mp}}{\rho_{dry} V_P + 1} \tag{9}$$

where ρ_{dry} (g cm^{-3}) is the density of bulk dry samples and V_P (cm^3 g^{-1}) is the sample porosity.

By comparing experimental particles' elevations (by Eq. 4) and predicted elevations computed through Eqs. 5, 6, 7, 8, it is possible to verify whether particles' elevations can be considered as only due to the lift forces described accordingly to Williams' model. A significant difference between experimental and predicted particles' elevation may suggest the presence of other forces which can act together with lift forces by either enhancing or reducing the extent of particles' lift.

Determination of the Experimental Coefficient for Near-Wall Lift Forces

As far as the evaluation of the coefficient C is concerned, Williams *et al.* determined its values for three different SdFFF systems.[14-16] Such an experimental determination of C was based on R measurements in a very large combination of particles' diameters and SdFFF systems with mobile phases of different viscosity. In this work, a sufficient number of channel systems and samples to follow the same systematic experimental approach for the determination of the coefficient C was not available.

An interpolation from data reported by Williams *et al.* was, thus, used. Such an interpolation method was thought to be reasonably acceptable for the following reasons: first, the reported measurements were based on SdFFF channels and the GrFFF systems are sedimentation systems in which the field is just Earth's gravity; second, the data were obtained through a very large number of measurements and hence can be considered representative and sufficiently accurate to be extended to other systems and, third, Williams and coworkers found that channel thickness w is the parameter that strongly influences C values.

Graphical results for the performed interpolation are shown in Figure 2. It must be pointed out that the plotted curve does not conform to any theoretical expression but it only corresponds to the best fitting polynomial for the reported data. The numerical values of interpolated C are reported in Table 1.

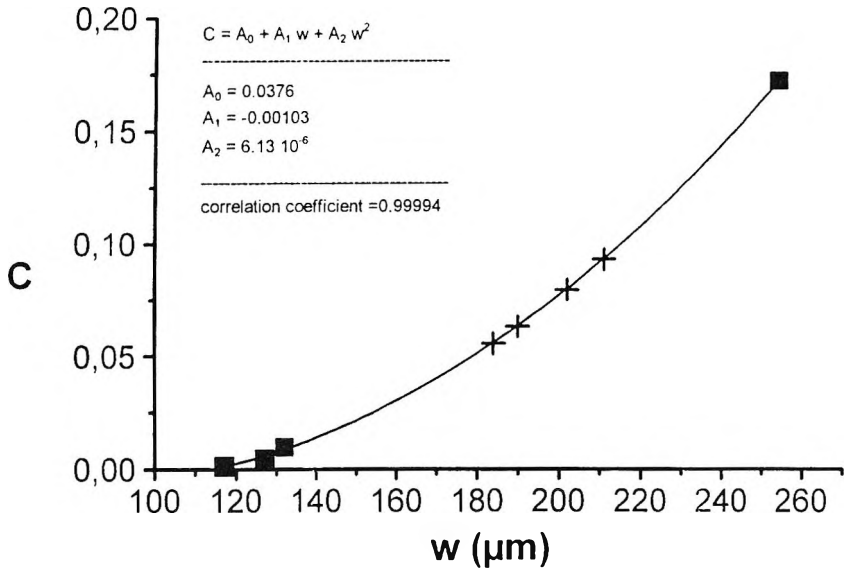

Figure 2. Interpolation of the C values relevant to the systems used. (■): experimental data; [14-16] (+): interpolated data.

RESULTS AND DISCUSSION

The main goal of this work was to check whether the model for hydrodynamic effects above described could be applied also in GrFFF. If experimental conditions for which Williams' approach holds true in GrFFF can be found, then it can be assumed that mean distances of particles from the accumulation wall (δ) during their elution in a GrFFF system can be predicted. In this case, then, the equation for retention (Eq. 4) can be used if it is known the retardation function $f(\delta/a)$ (Eq. 2).

Once verified, the applicability of Williams' model for the determination of particles' mean elevation, the experimental approach here presented through the comparison between experimental and predicted δ values, allows also to evaluate the presence of other second-order effects which can significantly act on retention. In this work, just some preliminary data obtained for two silica samples of a given diameter (5 μm) but different surface and density are presented. Further work on particles of different size and surface is currently on progress.

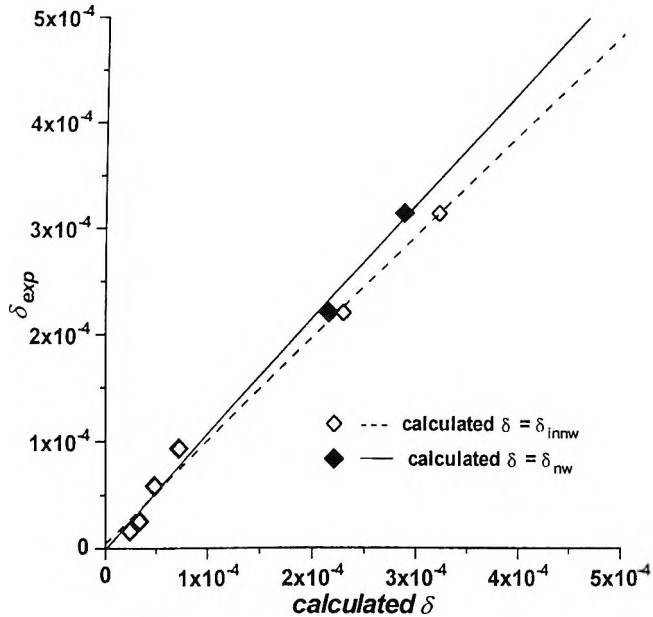

Figure 3. Comparison between experimental (δ_{exp}) and calculated elevations. *System 1, sample 1.* (dashed line): *calculated* δ values by Eqs. 5÷7; (solid line): *calculated* δ values by Eq. 6. See Table 3, rows 1, 2.

For each of the employed samples, different sets of retention measurements were performed for each channel system (Table 1) by varying the flow rate. The experimental approach here followed was always based on the comparison between predicted and experimental particles' elevation at various flow rate.

Experimental mean elevations (δ_{exp}) determined by Eq. 4 were reported against predicted mean elevations (*calculated* δ). These latter values were obtained for both samples by equating Eq. 8 to Eq. 7 and solving for δ the expression for lift forces in Eq. 5 and/or Eq. 6.

The prediction of δ values with changing channel systems and the analysis of the experimental deviations from Williams' model will be described below. All the discussed data are summarized in Table 3.

Table 3

Comparison Between Experimental and Calculated δ Values[a]

	System	Sample	Calc.δ	Intercept	Slope	Corr. Coeff.	Data Pts.	Range of Flow Rate ($cm^3\ min^{-1}$)
1	1	1	δ_{inrw}	$4\ 10^{-6}\pm2\ 10^{-5}$	1.0±0.1	0.9951	5	0.5÷6.0
2	1	1	δ_{rw}	$-9\ 10^{-7}\pm2\ 10^{-5}$	1.1±0.1	0.9954	5	0.5÷6.0
3	1	2	δ_{inrw}	$-5\ 10^{-6}\pm3\ 10^{-3}$	0.9±0.2	0.9952	5	0.5÷4.5
4	1	2	δ_{rw}	$-1\ 10^{-5}\pm4\ 10^{-5}$	1.0±0.2	0.9915	5	0.5÷4.5
5	2	1	δ_{rw}	$4\ 10^{-6}\pm1\ 10^{-5}$	0.93±0.09	0.9969	8	0.5÷6.0
6	2	2	δ_{rw}	$3\ 10^{-5}\pm2\ 10^{-5}$	1.1±0.1	0.9933	8	0.5÷6.0
7	3	1	δ_{rw}	$1\ 10^{-6}\pm5\ 10^{-5}$	3±1	0.9765	5	0.4÷1.8
8	3	2	δ_{rw}	$4\ 10^{-5}\pm5\ 10^{-5}$	2.9±0.8	0.9820	5	0.4÷1.8
9	4	1	δ_{rw}	$4\ 10^{-5}\pm5\ 10^{-5}$	1.6±0.3	0.9877	8	0.5÷4.0
10	4	2	δ_{rw}	$1\ 10^{-4}\pm1\ 10^{-4}$	1.4±0.4	0.9552	8	0.5÷4.0
11	5	1	δ_{rw}	$2\ 10^{-5}\pm2\ 10^{-5}$	0.5±0.1	0.9700	9	0.5÷6.0
12	5	2	δ_{rw}	$2\ 10^{-5}\pm2\ 10^{-5}$	0.5±0.1	0.9242	9	0.5÷6.0

[a] Regression analysis for the δ_{exp} *vs. calculated* δ. Confidence level: 95%.

Prediction of δ Values

The results for a GrFFF system with bare, unmodified floating glass walls and mobile phase containing Triton X-100 0.1% (v/v) and NaN_3 3.1 mM (*System 1*) are first considered with respect to *sample 1* (LiChrospher 5 μm). To predict particles' elevation (*calculated* δ) both the contributions due to inertial and near-wall lift forces (Eq. 5÷Eq. 7) have been first considered; in this case the calculated values of δ are indicated in Table 3 as δ_{inrw}. The comparison between experimental and predicted mean elevations is reported in Figure 3 (symbol ◊, dashed line) with the results of regression analysis reported in Table 3. One can first observe that retention ratio values increase with increasing flow rate. This is the first proof of hydrodynamic effects able to lift particles away from the accumulation wall: in fact, by Eq. 4, one calculates experimental particles' elevation values which increase with increasing flow rate. Linear regression analysis performed for experimental against predicted δ values is able to verify whether the applied model for the description of hydrodynamic effects on retention is valid. In our experiments, a straight line with null intercept and unit slope shows that such a model based on Eqs. 5÷9 is able to predict δ values for the given combination of *sample* and GrFFF *system*. From Figure 3, it is evident that there is no significant difference between experimental elevations (δ_{exp}) and the elevations predicted by taking into account both inertial and near-wall lift forces (δ_{inrw}) in Williams' model. Such

experimental finding is, to the authors' knowledge, the first experimental verification of Williams' model for lift forces in GrFFF. It is, therefore, demonstrated that δ values can be predicted in an optimized GrFFF system and, as a consequence, that accurate characterization of silica particles may be performed with no previous knowledge of the value of the steric correction factor. The use of GrFFF for size characterization without calibration is noteworthy for the low cost of this technique when compared to other FFF systems. Moreover, it is also possible to foresee that, if the model is followed, the experimental mean elevation values can be used also to determine particles' density through the use of Eq. 7 and Eq. 8.

From previous literature,[14] it has been deduced that, because of the low δ_{exp} values obtained in all the performed experiments, the contribution due to inertial lift forces could have been negligible and, therefore, the simple expression only for near-wall lift forces (Eq. 6) can be used to predict particles' mean elevation. That inertial lift forces could be actually neglected under the experimental conditions used with *system 1* and *sample 1*, it is demonstrated in Figure 3 where it is also reported the straight line obtained by plotting δ_{exp} values against the *calculated* δ values obtained by considering only near-wall lift forces (δ_{nw}) (symbol ◆, full line). It is found that a new straight line is obtained with intercept and slope values which are, still, not significantly different from zero and unity, respectively. Since in all data (Table 3) the experimental particles' elevation values were comparable in magnitude to those obtained for the case of *system 1* and *sample 1* above discussed, it was deduced that inertial lift forces could be considered negligible for all the experimental cases here discussed and, thus, Eq. 6 was always employed in determining predicted particles' elevation (δ_{nw}).

All the data up to now reported are referred to bare, polar silica particles. Similar results were obtained when the nature of particles' surface was changed to a highly hydrophobic one (RP18e). A set of experiments similar to those reported in Figure 3 was performed on *system 1* for LiChrospher RP18e (*sample 2*). The results are reported in Figure 4 and Table 3. It can be clearly observed that, also with this sample, the channel *system 1* behaved ideally with respect to predicted hydrodynamic effects. In Figure 4, the regression lines obtained by taking into account, for the prediction of particles' elevation, either inertial and near-wall lift forces (symbol O, dashed line) or near-wall lift forces alone (symbol ●, full line) are again compared. As in the cases discussed above (Figure 3), both straight lines in Figure 4 do not show significant differences in intercept and slope values which are, respectively, zero and one. The very similar retention behavior for highly hydrophilic and hydrophobic particles could be surprising. However, it can be explained by the fact that the

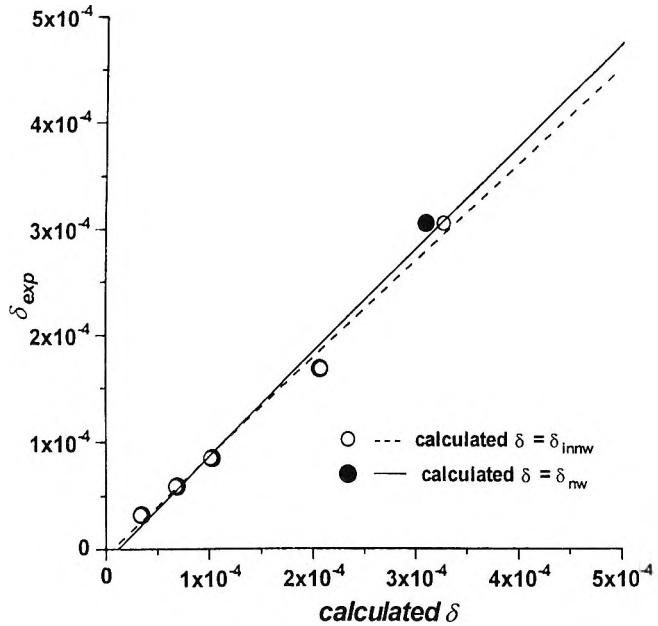

Figure 4. Comparison between experimental (δ_{exp}) and calculated elevations. *System 1*, *sample 2*. (dashed line): *calculated* δ values by Eqs. 5 ÷7; (solid line): *calculated* δ values by Eq. 6. See Table 3, rows 3, 4.

high concentration of surfactant (5%) used to disperse *sample 2* (LiChrospher RP18e) in the batch solution is able to drastically modify the surface polarity of the particles. It must be noted that, if the surface of RP18e particles were not modified by the adsorption of polar groups, they could not even be fractionated in a GrFFF channel.

In order to test whether the ideal behavior shown by a GrFFF system like that up to now discussed was reproducible, another GrFFF channel (*system 2*) made by other two bare, floating glass walls and another strip of Mylar of the same thickness as that used for *system 1* has been tested. The effective channel thickness w resulted slightly different from that of *system 1*, probably because of the effect of the somewhat different amount of silicone sealant used to prevent carrier leaks in the glass-made channels. *System 2* was assembled exactly in the same way as *system 1* and the same experimental procedures employed with *system 1* were repeated with *system 2* for both *sample 1* and *sample 2*. In both cases, regression analysis did not show any significant difference with respect to *system 1*. The results did not change, as it can be seen from the data relative

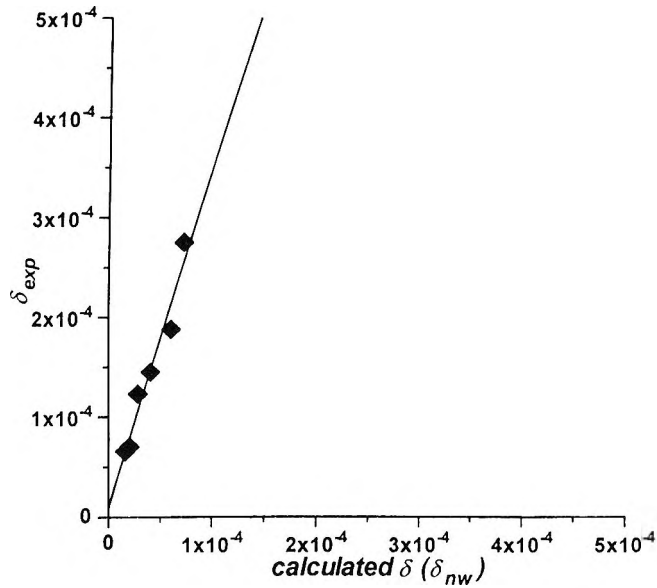

Figure 5. Comparison between experimental (δ_{exp}) and calculated elevations. *System 3, sample 1*. See Table 3, row 7.

to *system 2* in Table 3. Even though much more experimental work must be done for a systematic study of the second-order effects in GrFFF retention, from such preliminary results it can be observed that, under well-defined experimental conditions, the elution in a GrFFF channel can be described by using the model for hydrodynamic effects that was already verified for the elution of particles in Steric/SdFFF systems. These promising results can justify further efforts towards a wider applicability of GrFFF for the characterization of supermicron particles.

Deviations From Predicted δ Values

The possibility to predict particles' elevation of silica particles in a GrFFF channel by means of Williams' model for hydrodynamic forces in steric SdFFF would suggest that no second-order effects other than hydrodynamic ones exerted any influence on particles' elevation in the GrFFF experiments discussed above. However, it is known that particle-wall interaction, likely of electrostatic nature, can influence retention in steric FFF mode when particles

elute very close to the accumulation wall. At least in the case of *sample 1*, the effect of such particle-wall interactions could be offset in the channel systems discussed above by the similar nature and polarity of channel walls (glass) and particles' surface (silica).

In order to test whether modifications in the channel systems could change particles' retention from that one predicted by hydrodynamic effects alone, channel walls of different nature were employed. Since, in a previous work,[6] it was reported that the use of sodium chloride in the mobile phase can give adsorption of such an anion (Cl^-) on channel walls and modify GrFFF retention of silica particles, a set of retention measurements at different flow rates was performed in a channel in which NaCl in place of NaN_3 had been passed for two weeks before the experiments (*system 3*). The results for *sample 1* are reported in Figure 5 and Table 3. It must be observed that, in the case of *system 3*, although the range of the obtained δ_{exp} values was comparable to that obtained for *sample 1* with *systems 1* and *2*, here similar particles' retention values were obtained at slower flow rates. This is a first indication that other forces than hydrodynamic ones act on retention when chloride ions are present in the GrFFF system. In fact, a comparison between the data obtained for *sample 1* and *system 3* (Figure 5) and those for *sample 1* and *system 1* (Figure 3) indicates a large increase above unity of the slope value in the linear regression relative to the former case. Similar results were obtained with *sample 2*. Such an increase of the slopes indicates that experimental mean elevations steadily increase, at any flow rate, with respect to the calculated values. This effect must be ascribed to the presence of chloride ions on the accumulation wall, even though the mechanism of interaction has not, as yet, been fully understood. It is possible that adsorption of chloride ions on channel walls gives rise to repulsive effects with silica particles that are also negatively charged. Chloride ions, in fact, are known to display high chemical affinity for glass surfaces. Since silica particles have already shown to experience other type of interactions able to alter retention ratio values,[6] it is again demonstrated that mobile phase composition must be carefully chosen in the framework of an optimized approach to GrFFF. It is here shown that other effects, likely of electrostatic nature, can affect retention in GrFFF comparably to that exerted by hydrodynamic forces.

That repulsive effects can be partially due to a given amount of chloride ions permanently adsorbed on the accumulation wall can be deduced by analyzing the data obtained with *system 4* which is physically different from *system 3*, even if prepared and assembled in the same way. The main difference lies in the fact that while with *system 3* NaCl was also used as the ionic modifier of the mobile phase, with *system 4* after two weeks of treatment with NaCl in the mobile phase, the standard NaN_3-added mobile phase was

used for the retention experiments. From the comparison of the data obtained by these two systems (Table 3), it can be observed a repulsive effect also when chloride has been removed from the mobile phase. Such a repulsion is less intense than that observed with NaCl in the mobile phase (*system 3*), that is lower values of particles' elevation (lower slopes from the linear regressions) were obtained. It is possible that repulsive effects are determined by chloride ions adsorbed on glass walls. A desorption of chloride ions from channel walls when NaCl is no longer present in the carrier solution can explain the different behavior observed with *system 3* and *system 4*. In fact, some preliminary studies indicated that further changes in GrFFF retention ratio values of silica particles when NaCl was present in the mobile phase decrease with increasing the time of treatment with such a NaCl-added carrier solution.[6] In order to better explain the mechanism of the glass wall modification in presence of chloride ions, it would be interesting to study the kinetic of absorption of Cl^- on the glass walls. By this way, it could be possible to establish whether the system evolves towards a saturation state, with the final effect of giving constant and reproducible values of retention ratio.

Investigations on channel walls of different material than glass were also performed by using polycarbonate walls (*system 5*). Results for *sample 1* are reported in Figure 6 and in Table 3, while data for *sample 2* are reported only in Table 3. Both the two samples (polar and non polar surfaces, respectively) have shown identical behavior, *i.e.*, the slope values were comparable even though their values were lower than unit. Polycarbonate walls showed, therefore, an opposite effect to that observed with chloride ions on glass, since experimental elevation values lower than predicted were observed. It can be deduced that, with polycarbonate walls, some type of particle-wall interactions of attractive nature can play on retention, which are comparable in magnitude to those explained in terms of hydrodynamic forces alone.

It is important to focus on the significant differences observed between experimental and predicted values of δ by changing only the mobile phase or channel wall material, since it is a first indication of the existence of second-order effects other than hydrodynamic forces. These forces modulate retention to an extent comparable to the hydrodynamic forces alone, and their effect can be reflected in a change in the coefficient C values. In fact, although in all cases the values of the slopes can be influenced by the uncertainty associated with the coefficient C value, it is worth to note, for instance, that the behavior observed for one of the Cl-modified channels (*system 4*) with respect to the unmodified glass walls channel (*system 2*) can be only explained in terms of such electrostatic forces. *System 4* was indeed obtained directly from *system 2* by just passing the NaCl-added mobile phase. Consequently, no differences in

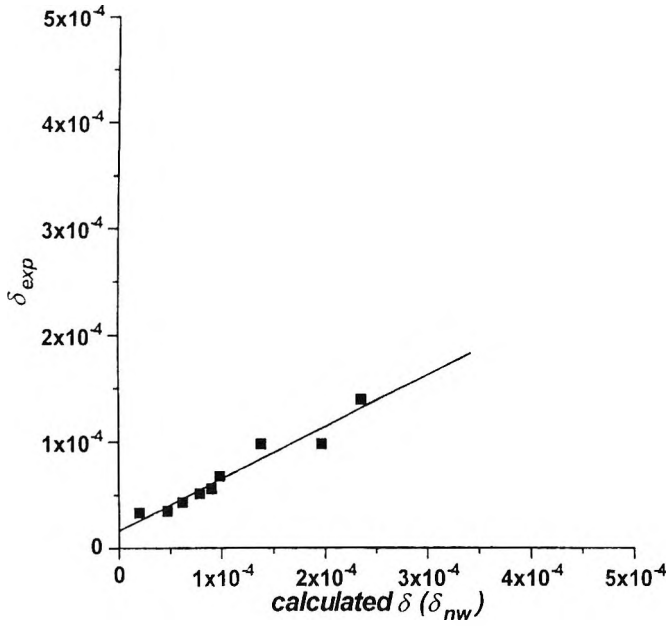

Figure 6. Comparison between experimental (δ_{exp}) and calculated elevations. *System 5*, *sample 1*. See Table 3, row 11.

the channel thickness and void volume values (see Table 1) can be ascribed in the measurements relatively to such channels. The value assumed for C for *system 4* can thus be thought of as being affected by the same level of uncertainty due to the channel thickness as it is the C value assumed for *system 2*.

As a consequence, it can be deduced that the different slope value obtained for channels of different walls composition, as *system 2* and *system 4*, can be due, at least partially, to electrostatic effects that are able to eventually affect the C coefficient value.

The method based on the validation of Williams' approach to hydrodynamic effects in steric FFF could thus be used as a tool for investigating and quantitatively evaluating the overall second-order effects acting on a GrFFF system.

CONCLUSIONS

A preliminary experimental study of the second order effects on GrFFF retention has demonstrated that, under well-defined experimental conditions for the elution of silica particles, a properly designed GrFFF system can follow the quantitative model reported in literature for hydrodynamic effects on SdFFF retention in steric mode.

It is also demonstrated that, for quite dense particulate matter used as injected sample and eluted at not too high flow rate, inertial lift forces can be negligible with respect to near-wall lift forces, thus simplifying retention prediction from lift forces equations.

By means of the experimental verification of the model for hydrodynamic effects, it has been also determined how other experimental variables as walls' surface nature and mobile phase composition can introduce significant changes on GrFFF retention. In particular, second-order effects induced by changing the GrFFF systems have been here demonstrated to be comparable, in magnitude, to hydrodynamic effects. Therefore, the approach here applied to validate lift forces equations in GrFFF has shown to be a promising tool also for the investigation of the nature of the overall second-order effects in the framework of a wider applicability of optimized GrFFF analysis.

ACKNOWLEDGMENTS

The authors wish to thank Dr. P. S. Williams, FFF Research Center, Salt Lake City, Utah, for having made available the numerical tools for the calculation of the experimental particles' elevation values.

Thanks also go to Prof. P. J. P. Cardot, Université de Limoges, France, for having granted two complete GrFFF systems and for the stimulating discussion.

REFERENCES

† Current address: Department of Chemistry, University of Ferrara, Via L. Borsari 46, Ferrara, Italy I-44100.

1. J. C. Giddings, M. N. Myers, K. D. Caldwell, J. W. Pav, J. Chromatogr., **185**, 261 (1979).

2. J. Pazourek, J. Chmelík, Chromatographia, **35**, 591 (1993).

3. J. Pazourek, E. Urbánkova, J. Chmelík, J. Chromatogr., **660**, 113 (1994).

4. P. Reschiglian, G. Torsi, Chromatographia, **40**, 467 (1995).

5. J. Pazourek, J. Chmelík, J. Chromatogr., **715**, 259 (1995).

6. P. Reschiglian, D. Melucci, G. Torsi, J. Chromatogr. A, **740**, 245 (1996).

7. Ph. J. P. Cardot, J. Gerota, M. Martin, J. Chromatogr., **568**, 93 (1991).

8. A. Merino-Dugay, Ph. J. P Cardot, M. Guernet, J. P. Andreux, J. Chromatogr., **568**, 73 (1992).

9. C. Bories, Ph. J. P. Cardot, V. Abramowski, C. Pons, A. Merino, C. Baron, J. Chromatogr., **579**, 141 (1992).

10. Ph. J. P. Cardot, C. Elgéa, M. Guernet, D. Godet, J. P. Andreux, J. Chromatogr. B, **654**, 193 (1994).

11. J. Plocek, P. Konecny, J. Chmelík, J. Chromatogr. B, **656**, 427 (1994).

12. A. Bernard, C. Bories, P. M. Loiseau, Ph. J. P. Cardot, J. Chromatogr. B, **664**, 444 (1995).

13. S. K. Ratanathanawongs, I. Lee, G. Giddings, in **Particle Size Distribution II: Assessment and Characterization**, T. Provder, ed., ACS Symposium Series 472, American Chemical Society, Washington, DC, 1992, Chapter 15.

14. P. S. Williams, T. Koch, J. C. Giddings, Chem. Eng. Commun., **111**, 121 (1992).

15. P. S. Williams, S. Lee, J. C. Giddings, Chem. Eng. Commun., **130**, 143 (1994).

16. P. S. Williams, M. H. Moon, Y. Xu, J. C. Giddings, Chem. Eng. Sci., **51**, 4477 (1996).

17. P. Reschiglian, D. Melucci, A. Zattoni, and G. Torsi, "A Quantitative Approach to Field-Flow Fractionation for the Characterization of Supermicron Particles," J. Microcol. Sepns., 1997, in press.

18. G. Karaiskakis, A. Koliadima, Chromatographia, **28**, 31 (1989).

19. A. Koliadima, G. Karaiskakis, J. Chromatogr., **517**, 345 (1990).

20. A. Koliadima, G. Karaiskakis, Chromatographia, **39**, 74 (1994).

21. A. Athanasopolou, G. Karaiskakis, Chromatographia, **40**, 734 (1995).

22. P. Reschiglian, D. Melucci, G. Torsi, Chromatographia, **44**, 172 (1997).

23. J. C. Giddings, Science, **260**, 1456 (1993).

24. A. J. Goldman, R. G. Cox, H. Brenner, Chem. Eng. Comm., **22**, 653 (1967b).

25. J. C. Giddings, M. H. Moon, Anal. Chem, **63**, 2869 (1991).

Received January 21, 1997
Accepted April 14, 1997
Manuscript 4446

J. LIQ. CHROM. & REL. TECHNOL., 20(16 & 17), 2637–2646 (1997)

INFLUENCE OF DENSITY OF ZEOLITE PARTICLES ON THEIR RETENTION IN GRAVITATIONAL FIELD-FLOW FRACTIONATION

E. Urbánková, J. Chmelík*

Institute of Analytical Chemistry
Academy of Sciences of the Czech Republic
Veveří 97
611 42 Brno, Czech Republic

ABSTRACT

Gravitational force is one of main forces necessary for separation of particles in gravitational field-flow fractionation. It is proportional to particle size and density. The influence of density on the elution behavior was studied using zeolites containing varying amounts of platinum. The other properties of the zeolite samples (e.g., size, shape, particle size distribution) were the same as those of the original zeolite sample without platinum. We proved that retention of particles was related to their densities. However, densities could not be calculated from elution data because we found that zeolites were eluted in a focusing elution mode. This mode was induced by hydrodynamic lift-forces and their nature has not been fully understood yet; this excludes exact calculation of density. The effects of sample preparation, amounts of sample injected, and flow rates of a carrier liquid are described.

INTRODUCTION

Gravitational field-flow fractionation (GFFF) is the experimentally simplest member of the family of field-flow fractionation (FFF) techniques. GFFF utilizes Earth's gravity as an external force field, which causes settlement of particles towards the channel bottom (accumulation wall).[1,2] However, there are also other forces acting on particles in the carrier liquid flow-hydrodynamic lift forces.[3,4] In contrast to the gravitation, they tend to drive particles away from the channel accumulation wall and focus them into narrow zones. The position of the zones in the flow velocity profile is determined by the particle size and density.

There are several other particle properties that may significantly influence retention of particles in GFFF, e.g., shape,[5,6] plasticity,[7] and surface charge.[8-10] GFFF has been used successfully for separation of glass beads,[1] chromatographic silica gel supports,[4,11-13] polystyrene (PS) latexes,[14] and blood cells.[5-7,15-17]

The density of particles was studied by several FFF techniques, e.g., sedimentation FFF (SFFF),[18-26] sedimentation-flotation focusing FFF (SFFFFF),[27,28] and GFFF.[3,6] Various samples were studied: PS latexes,[18-20,22-24,26,27] polyvinylchloride,[16,22] and polybutadiene latexes,[21,25] polyglycidylmethacrylate latexes,[27] and red blood cells.[6] For density measurements by SFFF, a method was developed in which density of polystyrene latex particles was determined by a series of runs using carrier liquids of different densities.[18] In SFFFFF, Percoll-based density gradients were used.[27]

Zeolites are a group of crystalline hydrated aluminasilicates of group I and II elements, such as sodium, potassium, magnesium, and calcium. Their structure is composed of an infinitely extending three-dimensional network of AlO_4 and SiO_4 linked through shared oxygen atoms.[29]

The paper describes behavior of various kinds of zeolites containing 0%, 3%, and 9% of platinum, respectively. The goal of this work was a description of the influence of particle density on the elution behavior of particles in GFFF. It is known that platinum is distributed inside zeolite particles, and it means that all samples used have the same average particle size and its distribution. This is an important advantage to previous studies dealing with the influence of particle density on retention in FFF, where particles made of different materials were used. Contrary to zeolites, those particles differed not only in density, but also in other properties (size, shape, etc.).

EXPERIMENTAL

Materials

All zeolite samples (a kind gift from Dr. Nováková) were prepared at the Institute of Physical Chemistry in Prague. Their average particle diameter was 1 μm. The samples were resuspended at the concentration of 2-10 mg/mL in redistilled water which was also used in all measurements as a carrier liquid. The samples were wetted either under vacuum or by sonication.

Methods

The experimental set up was described elsewhere.[4,6] The separation channel used in this work was cut in an 80 μm thick spacer, which was placed between two mirror-quality float glass plates. The channel had dimensions 20 mm x 360 mm, including the inlet and outlet triangles with a height of 30 mm (dead volume 0.53 mL). The pump was an HPP 4001 (Laboratory Instruments, Prague, Czech Republic). A spectrophotometric detector, Spectra 100 (Spectra-Physics), with a capillary cell (I.D. of 300 μm) was used at 254 nm.

Aliquotes (1 μL) of samples were injected with a syringe through a septum directly into the channel inlet. The injected sample was transported for 6 s at a flow rate of 200 μL/min. After 60 s without the carrier-liquid flow (for settlement of particles), the flow was switched on (the range of flow rates was 400-2000 μL/min), and the sample was eluted through the channel to the detector.

RESULTS AND DISCUSSION

Sample preparation is very important for porous particles in FFF. A suitable procedure should be able to remove contingent air cavities inside the particles. As a result, the particles are better wetted, and the apparent density of the particles is unified. In the case of porous silica gel particles, we found that sonication for several minutes was sufficient as a sample preparation procedure for samples in detergent solutions.[12] However, in the case of zeolites in pure water, sonication was inefficient, and peaks measured by GFFF were irregular and broad (data not shown). For this reason, zeolites were first wetted in water, under vacuum, and sonicated for 1 min just before injection.

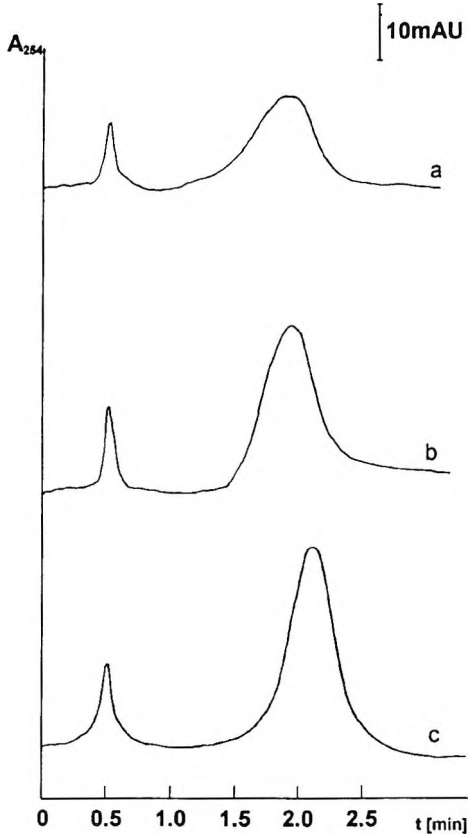

Figure 1. The fractogram of the zeolites with different contents of platinum (a - 0%, b - 3%, c - 9%). The experimental conditions: flow rate = 1000 μL/min, zeolite concentration = 5 mg/mL, injected volume = 1 μL.

Fractograms of all three kinds of zeolites used are shown in Figure 1, where one can see that elution times increase with increasing amounts of platinum in the zeolites. The observed retention ratios do not correspond to the steric elution model, where particles are rolling on the channel bottom.[1] Because the retention ratios are also dependent on the flow rate of the carrier liquid (see Figure 2), we can conclude that the elution mode is the focusing (hyperlayer) one.[30,31] Focusing of the particles above the channel bottom is caused by the influence of lift forces.[3,4,9] However, the nature of lift forces has not been fully understood yet and, therefore, we are not able to calculate the density of zeolites from their retention data.

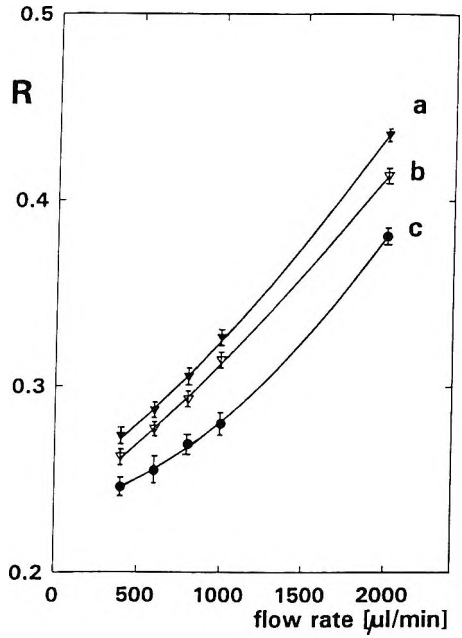

Figure 2. The dependence of the retention ratios of three zeolite samples with different platinum contents (a - 0%, b - 3%, c - 9%) on the flow rate. The experimental conditions: zeolite concentration = 5 mg/mL, injected volume = 1 µL.

Nevertheless, the influence of the particle density on retention of particles is evident. The samples used were prepared from the same original zeolite, which was identical with the sample without platinum. The particles of all three samples have identical sizes, particle size distributions, and shapes because platinum is located on the surface of the pores inside the zeolite particles and, therefore, it does not change the particle volume (V_0). From the shapes of fractograms of the different zeolites (see Figure 1), which are similarly broad, we can conclude that platinum does not block the pores. Blocked pores could not be completely wetted, and cavities containing air would cause appearance of broad peaks, as a result of a broad density distribution of samples with the same platinum content. This means that the samples differ only in density, which is based on the platinum content. This is the main advantage of zeolites with different platinum content to particles made of different materials used in previous studies.[3,4,27] Those particles differed also in size, shape, particle size distribution, etc. It is clear, from Figures 1 and 2, that zeolite samples without platinum are eluted first, which means that the position of their focused zones is the highest one above the

channel bottom. On the contrary, zeolite samples containing 9% of platinum are eluted as the last ones, which means that they are eluted near the channel bottom where are lower velocities of the carrier liquid. The exact density of the original zeolite sample is not known (the approximate value is 1.5 g/cm^3). However, we know exactly the amounts of platinum in particular samples. Thus, we can express their relative densities. The relative density is defined as a ratio of a particular zeolite sample density (ρ_p) to a density of the original zeolite without platinum (ρ_0). It is based on the identical particle volume (V_0) of all zeolites samples:

$$\rho_0 = \frac{m_0}{V_0} \tag{1}$$

$$\rho_p = \frac{m_p}{V_0} = \frac{m_0 + p_p m_0}{V_0} = \frac{m_0\left(1+p_p\right)}{V_0} \tag{2}$$

and, thus,

$$\frac{\rho_i}{\rho_0} = 1 + p_p \tag{3}$$

where m_0 is the mass of a zeolite particle containing no platinum, m_p is the mass of a zeolite particle containing platinum, p_p is the ratio of a platinum amount to the mass of a zeolite particle. The influence of relative densities on the retention ratio of zeolite samples at different flow rates is shown in Figure 3. This effect is more expressed at higher flow rates, which phenomenon is probably connected with the flow rate dependence of lift forces.

Recently, it was described that retention ratios in GFFF in the focusing elution mode are influenced by the number of injected particles.[13] Too large amounts of injected samples induce overloading effects, which cause an increase in the observed retention ratios with increasing amounts of injected silica gel particles. Similar results were observed, also, in the case of the zeolites used in this work (Figure 4). This observation complicates interpretation of the particle density from the elution data, because higher injected amounts of particles result in lower apparent densities than follows from the elution data obtained from the injection of lower amounts of particles. In order to obtain reasonable results, it is necessary to inject the same number of particles, as small as possible for a reasonable detection, in each experiment.

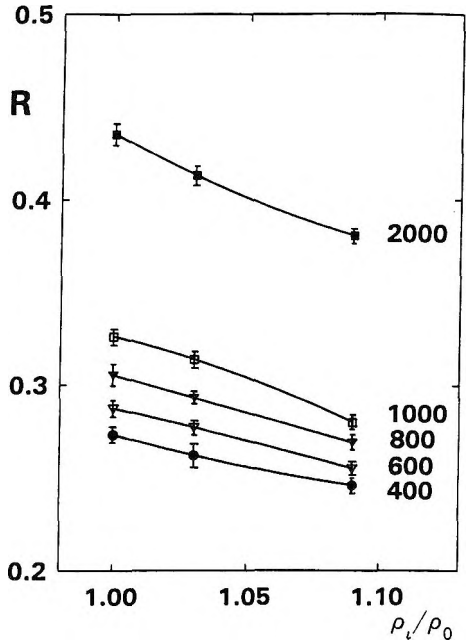

Figure 3. The dependence of the retention ratio on the relative densities of the zeolites at different flow rates ranging from 400 μL/min to 2000 μL/min. The experimental conditions: zeolite concentration = 5 mg/mL, injected volume = 1 μL.

Our results show that GFFF can be used for comparison of densities in the case of particles which differ only in their densities. Provided that certain conditions (e.g., sample preparation, injection of the same amounts of particles, application the same flow rate, and carrier liquid), are fulfilled, densities can be determined by using calibration curves.

In the case of particles with different shapes or sizes, other techniques have to be used, e.g., SFFFFF.

Although present knowledge of GFFF suggests that gravitational force and hydrodynamic lift forces are the most important forces affecting the samples, it is known that other forces (e.g., electrostatic and van der Waals forces) influence behavior of the particles.[8-10] Therefore, our future work will deal with an influence of these forces on the determination of the zeolite density by GFFF.

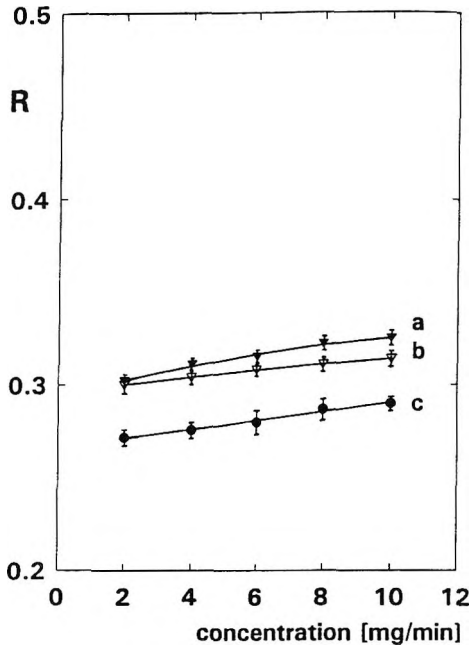

Figure 4. The dependence of the retention ratio on the amount of injected zeolite samples with different platinum content (a - 0%, b - 3%, c - 9%). The experimental conditions: flow rate: 1000 μL/min, injected volume = 1 μL.

ACKNOWLEDGMENT

This work was supported by Internal Grant No. 564 from the Institute of Analytical Chemistry, Academy of Sciences of the Czech Republic.

REFERENCES

1. J. C. Giddings, M. N. Myers, Sepn. Sci. Technol., **13,** 637-645 (1978).

2. J. C. Giddings, M. N. Myers, Anal. Chem., **54**, 2284-2289 (1982).

3. K. D. Caldwell, T. T. Nguyen, M. N. Myers, J. C. Giddings, Sepn. Sci. Technol., **14**, 935-946 (1979).

4. J. Pazourek, P. Filip, F. Matulík, J. Chmelík, Sepn. Sci. Technol., **28**, 1859-1873 (1993).

5. E. Urbánková, A. Vacek, N. Nováková, F. Matulík, J. Chmelík, J. Chromatogr., **583**, 27-34 (1992).

6. P. J. P. Cardot, C. Elgea, M. Guernet, D. Godet, J. P. Andreaux, J. Chromatogr. B, **654**, 193-203 (1994).

7. V. Yue, R. Kowal, L. Neargarder, L. Bond, A. Muetterties, R. Parsons, Clin. Chem., **40**, 1810-1815 (1994).

8. A. Athanasopoulou, G. Karaiskakis, Chromatographia, **40**, 734-746 (1995).

9. J. Pazourek, K.-G. Wahlund, J.Chmelík, J. Microcol. Sepn. **8**, 331-338 (1996).

10. P. Reschiglian, D. Melucci, G. Torsi, J. Chromatogr. A, **740**, 245-252 (1996).

11. J. C. Giddings, M. N. Myers, K. D. Caldwell, J. V. Pav, J. Chromatogr., **185**, 261-271 (1979).

12. J. Pazourek, E. Urbánková, J. Chmelík, J.Chromatogr. A, **660**, 113-118 (1994).

13. J. Pazourek, J. Chmelík, J. Chromatogr. A, **715**, 259-265 (1995).

14. J. Pazourek, J.Chmelík, Chromatographia, **35**, 591-596 (1993).

15. P. Cardot, J. Gerota, M. Martin, J.Chromatogr., **568**, 93-103 (1991).

16. N. Nováková, E. Urbánková, J. Chmelík, **New Approaches in Chromatography 91**, Intercongress, Budapest, 1992, p. 77.

17. E. Urbánková, A. Vacek, J. Chmelík, J. Chromatogr. B, **687**, 449-452 (1996).

18. J. C. Giddings, G. Karaiskakis, K. D. Caldwell, Sepn. Sci. Technol., **16**, 607-618 (1981).

19. J. J. Kirkland, W. W. Yau, Anal. Chem., **55**, 2165-2170 (1983).

20. K. D. Caldwell, H. K.Jones, J. C. Giddings, Colloids and Surfaces, **18**,123-131 (1986).

21. D. J. Nagy, Anal. Chem., **61**, 1934-1937 (1989).

22. J. C. Giddings, M. H. Moon, P. S. Williams, M. N. Myers, Anal. Chem., **63**, 1366-1372 (1991).

23. J. C. Giddings, M. H. Moon, Anal. Chem., **63**, 2869-2877 (1991).

24. J. C. Giddings, Analyst, **118**, 1487-1494 (1993).

25. M. Blanda, P. Reschiglian, F. Dondi, Polymer Int., **33**, 61-69 (1994).

26. J. C. Giddings, J. Ho, Langmuir, **11**, 2399-2404 (1995).

27. J. Chmelík, J. Janča, J. Liq. Chromatogr., **9**, 55-62 (1986).

28. J. Janča, J. Chmelik, V. Jahnová, N. Nováková, E. Urbánková, Chem. Anal., **36**, 657-666 (1991).

29. G. Perego, G. Bellussi, C. Corno, M. Taramasso, F. Buonomo, A. Esposito, "New Developments in Zeolite Science and Technology," in **Studies in Surface Science and Catalysis**, Z. Murakami, A. Iijima, J. Ward, eds., Elsevier, Amsterdam, 1986, vol.28, pp. 129-136.

30. J. C. Giddings, Sepn. Sci. Technol., **18**, 765-773 (1983).

31. J. Janča, J. Chmelík, Anal. Chem., **56**, 2481-2484 (1984).

Received January 27, 1997
Accepted April 14, 1997
Manuscript 4450

J. LIQ. CHROM. & REL. TECHNOL., 20(16 & 17), 2647–2667 (1997)

ESTIMATING THE EFFECT OF PARTICLE SURFACE COATINGS ON THE ADSORPTION OF ORTHOPHOSPHATE USING SEDIMENTATION FIELD-FLOW FRACTIONATION

Jason Van Berkel, Ronald Beckett*

CRC for Freshwater Ecology and Water Studies Centre
Department of Chemistry
Monash University
P. O. Box 197
Caulfield East, Vic. 3145, Australia

ABSTRACT

The adsorption behaviour of pollutants to natural colloids is affected by particle surface coatings such as hydrous iron oxides, manganese oxide and natural organic matter (NOM).

Sedimentation field-flow fractionation (SdFFF) was used to determine surface adsorption density distributions (SADD) for ^{33}P-labelled orthophosphate onto suspended colloidal samples from the Peel River (NSW, Australia). The surface adsorption density (SAD) is the amount of pollutant adsorbed per unit area of particle surface. For a homogeneous particle sample, the SAD is expected to be constant. The SAD for the Peel River sample increased significantly with particle size, which may be due to changes in particle shape, mineralogy, or the nature of the surface coatings.

Scanning electron microscopy (SEM) was used to determine particle shape by examining separated fractions. The SAD was shape corrected using recently developed theory.

Analysis of the sample suggested particle shape was fairly constant and, thus, did not influence the trends in the SAD significantly.

In light of the SEM analysis, it was more likely the nonconstant SAD was associated with a change in mineralogy or surface coating composition. The purpose of this work was to investigate the effect of these surface coatings on orthophosphate adsorption. The particle surface coatings were selectively removed from the colloidal particles by chemical treatment and the effects on orthophosphate adsorption were investigated. Removal of the iron oxyhydroxide coatings decreased the SAD slightly but removal of NOM coatings increased orthophosphate adsorption substantially.

INTRODUCTION

Many processes which determine the behaviour of pollutants in natural waters occur at the surfaces of colloidal particles. Consequently, the study of colloid-nutrient interactions is an important part of ongoing research into the causes of algal blooms. Iron and manganese hydroxy oxides and natural organic matter (NOM) can exist in nodules, concretions, cement between particles or simply as coatings on particle surfaces (See Fig. 1).

These oxides are excellent scavengers of trace metals (e.g. Zn^{2+}, Cu^{2+}) and nutrients (e.g. PO_4^{3-}).[1] Therefore, the adsorption of pollutants onto these surfaces is a major factor in determining their reactivity and fate (transport, deposition) in aquatic systems. The pollutants may then concentrate in the bottom sediments at certain locations such as reservoirs and estuaries with serious ecological and human health implications.[2]

This paper reports a study in which different extractants are used to remove either iron oxide or NOM surface coatings and the resultant effect on orthophosphate adsorption and particle chemical composition was determined. The widely applied extraction sequence of Tessier and coworkers[1] has been modified by various authors; a version by Kersten and Förstner[3] claims to differentiate between the easily and moderately reducible components of surface coatings. This procedure was used as a basis for this research. According to

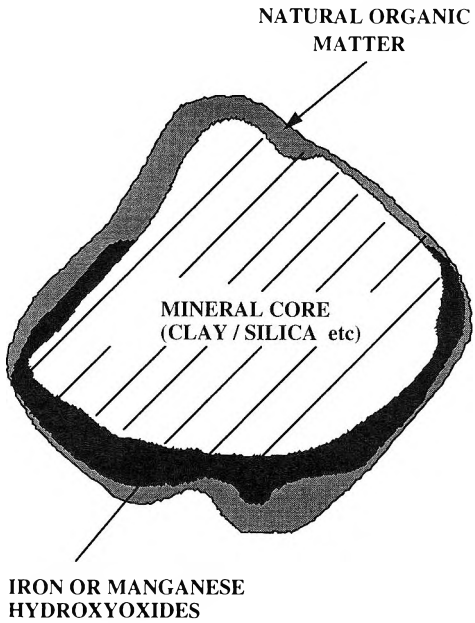

Figure 1. Schematic illustration of a natural suspended aquatic colloid, showing several types of surface coatings.

Kersten and Förstner,[3] 0.1 M oxalate extracts the moderately reducible surface coatings such as the amorphous Fe and Mn oxides. The effectiveness of oxalate arises from the low redox potential (-0.63V) and its ability to coordinate and form moderately stable metal complexes in weakly acidic solution, leading to the stripping of hydrous metal oxide layers.[4] However, it should be noted that these extraction methods are not absolutely selective for specific metal surface coatings and can also be influenced by the time of exposure and by the ratio of particulate matter to volume of extractants.[5]

Tessier et al.[1] evaluated the optimum extraction time for the removal of the Fe and Mn oxides. The results indicated the extraction was essentially complete after 6 hours. Longer times increased the possibility of attacking organic matter and residual solids within the crystalline structures.

In order for the organic matter to be successfully extracted, it must be oxidized to form carbon dioxide and water. This can be achieved with hydrogen peroxide. It is postulated that the organic matter competes with nutrients such as orthophosphate for adsorption sites. Once the organic matter

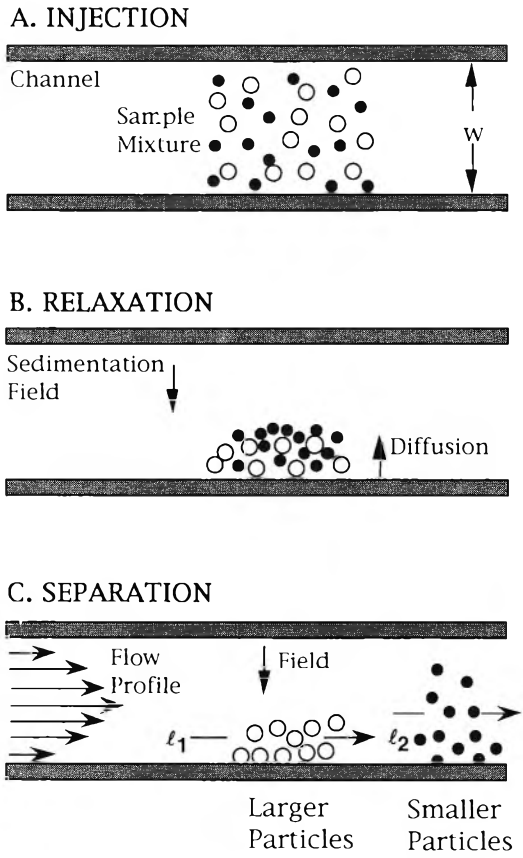

Figure 2. Cross-section of the SdFFF channel, showing different stages of an SdFFF analysis (a) injection, (b) relaxation, and (c) separation.

has been extracted, thus exposing the reactive hydrous Fe and Mn oxides surfaces, the amount of adsorption onto these surfaces is expected to increase. In previous publications, Beckett and coworkers have developed physical and chemical characterisation methods[6] based on sedimentation field-flow fractionation (SdFFF) for studying pollutant-colloid interactions.[2] SdFFF is a set of high resolution liquid chromatography-like elution methods used for separating and sizing colloidal particles.[7-10]

To perform a SdFFF separation, the sample is injected into the channel through a septum or injection valve (see Fig. 2a). An external centrifugal field is then applied at right angles to the ribbon-like channel which sits within a

centrifuge basket (see Fig 2b). This field forces the particles of different effective masses to accumulate at different average positions relative to the accumulation wall. This depends on how strongly the particles interact with the field and also their diffusivity.[11] This process is called relaxation and is usually achieved during a stop-flow period.

After the stop-flow period, the carrier liquid flow is turned on and the run begins. The carrier flow develops a parabolic profile within the channel with the highest flow rates in the centre of the channel and flow velocities approaching zero near the channel walls. The particles with a larger effective mass will have more compressed sample clouds (i.e., a smaller ℓ) and will be swept down the channel by the carrier flow at a lower average velocity than the smaller particles. Thus, the smallest particles will elute first (See Fig. 2c).

When an inductively coupled plasma-mass spectrometer (ICP-MS) is coupled to a SdFFF instrument, element-based size distributions and element molar ratio plots can be calculated.[7] This elemental data is valuable in interpreting mineralogy or surface coating changes across the size distribution.

The SdFFF approach is also amenable for studying pollutant-colloid binding.[2] Radiolabelled orthophosphate can be adsorbed onto the colloidal particles that can then be separated and sized with SdFFF. Fractions can be collected throughout the run and the radioactivity measured as a function of particle size. This adsorption data can also be used to determine a surface adsorption density distribution (SADD) plot. An SADD plot graphs the amount of pollutant adsorbed per unit area of particle surface as a function of particle size. For a homogeneous sample, the SADD plot should be constant across the entire size distribution. However, due to the complex nature of colloid particles (e.g., shape, mineralogy and surface coatings), a constant SADD plot is not always observed. It is the purpose of this paper to investigate the role of surface coatings on orthophosphate adsorption and their influence in generating nonconstant SADD plots.

THEORY

Sedimentation Field-Flow Fractionation

The sample is passed through a UV detector operating at 254 nm as it elutes from the channel. The retention ratio, R, and retention parameter λ for a constant field normal FFF run is obtained from the elution volume V_r and the channel void volume V^0 according to the general expression for normal mode

FFF separations:

$$R = \frac{V^0}{V_r} = 6\lambda\left(\coth\frac{1}{2\lambda} - 2\lambda\right) \quad (1)$$

where $\lambda = \ell/w$, with ℓ being the mean cloud thickness and w being the channel thickness. For constant field SdFFF runs, the equivalent spherical diameter, d can be calculated from λ provided the density difference between the particle and carrier liquid, $\Delta\rho$ is known.[7]

$$d = \sqrt[3]{\frac{6kT}{\pi\omega^2 rw\Delta\rho\lambda}} \quad (2)$$

where k is the Boltzmann constant, T the absolute temperature, ω the centrifuge speed (radians s^{-1}) and r the centrifuge radius.

A field decay program developed by Williams and Giddings[12] can be used for samples with broad size distributions. Initially, the centrifuge speed ω_0 is held constant for a lag period t_1, after which the field speed decays according to:

$$\omega = \omega_0\left(\frac{t_1 - t_\varepsilon}{t - t_a}\right)^4 \quad (3)$$

where t_a is a constant which along with t_1 controls the rate of field decay and t is the run time. This method can be used to prevent excessively long retention times for the larger particles, while still enabling the smallest particles to elute far enough from the void peak.

Fractograms

A fractogram is a plot of UV detector response versus elution time, where the UV signal is used as a surrogate for the mass concentration of particles in the eluent. Although the UV attenuation is affected to some extent, by the particle size according to the Mie theory, this has not been taken into account for this work. However, it has been observed that the UV based fractogram is often similar to the major element fractogram determined by the use of an inductively coupled plasma-mass spectrometer (ICP-MS) detector, which suggests that this Mie purturbation does not affect the particle size distribution substantially.[7]

Thus, the fractograms depict a plot of our estimate of the mass concentration of particles (dm^c/dV) measured by a UV detector, operating at 254 nm, versus elution time (t_r) or volume (V_r).[2] The y-axis is, therefore, shown in arbitrary units.

The mass concentration of an element E can be determined by using a sensitive analytical instrument such as an ICP-MS. After passing the sample through the UV detector, it is fed into the ICP-MS and an ion current I_E is generated, which is a measure of the mass concentration of elements eluting (i.e. dm^c_E/dV_r).

Mass Based Size Distribution

The particle size distribution represents the amount of material contained within different size ranges. It is a plot of dm^c/dd versus d, where m^c is the cumulative mass of sample eluted up to a given point and d the particle diameter at that point. The equivalent spherical diameter of a particle can be calculated by combining Equations 2 and 3. The run must be assumed to be made up of a large number of constant field increments stepping down from ω_0 as the field decays. The volume axis of the fractogram is divided into small volume increments of δV_r and the following expression is used:

$$\frac{dm^c{}_{(i)}}{dd_i} = \left\{\left(\frac{dm^c{}_{(i)}}{dV_{r(i)}}\right) \times \left(\frac{\delta V_{r(i)}}{\delta d_{(i)}}\right)\right\} \propto UV_{(i)} \times \frac{\delta V_{(i)}}{\delta d_{(i)}} \qquad (4)$$

where $dm^c{}_{(i)}/dV_{r(i)}$ is the value of the fractogram ordinate (assumed to be proportional to the UV detector response) at the midpoint of a given volume increment $\delta V_{r(i)}$, and $\delta d_{(i)}$ the diameter increment corresponding to the same increment in V_r. An element based size distribution can be calculated similarly using the ICP-MS data (I_E).

Surface Adsorption Density Distribution

The amount of pollutant adsorbed can be measured by collecting samples at various elution times and measuring the pollutant concentration. In suitable cases, this can be achieved using radiolabelled compounds and measuring the radioactivity in a scintillation counter. The amount of pollutant adsorbed per unit mass of particle at any point (i) along the elution time or volume axis is:

$$\frac{dm^{c}{}_{P(i)}}{dm^{c}{}_{(i)}} = \left\{ \left(\frac{dm^{c}{}_{P(i)}}{dV_{r(i)}} \right) / \left(\frac{dm^{c}{}_{(i)}}{dV_{r(i)}} \right) \right\} \propto \frac{DPM_{(i)}}{UV_{(i)}} \qquad (5)$$

where $DPM_{(i)}$ is the ß activity in disintegrations per minute per mL of eluent and $m^{c}{}_{P(i)}$ is the cumulative mass of the adsorbed pollutant P eluted up to elution volume $V_{r(i)}$. For spherical particles the particle area ($\delta A^{c}{}_{(i)}$) in an increment of elution volume ($\delta V_{r(i)}$) is given by $6\delta m^{c}{}_{(i)}/d_{(i)}\rho$. Thus, if constant spherical shape and density is assumed, a surface adsorption density distribution can be calculated utilizing equation 5. The expression for this sphere based surface adsorption density becomes:

$$\left(\frac{dm^{c}{}_{P(i)}}{dA^{c}{}_{(i)}} \right)_{sphere} = \left\{ \left(\frac{dm^{c}{}_{P(i)}}{dm^{c}{}_{(i)}} \right) \times \left(\frac{\delta m^{c}{}_{(i)}}{\delta A^{c}{}_{(i)}} \right) \right\} \propto \frac{DPM_{(i)}}{UV_{(i)}} \times d_{(i)} \qquad (6)$$

If there is a change in particle morphology to a more nonspherical shape, the amount of pollutant adsorbed per unit area would be underestimated. For example, a disc- or plate-like particle of the same mass as a spherical particle would have a larger surface area. A geometric expression has been developed for the ratio of surface areas of a coeluting disc (A_d) and sphere (A_s) in terms of the diameter ratio d_d/d_s where d_d is the equivalent circular cross-sectional diameter of the disc or rod and d_s is the diameter of a sphere with the same volume.[13] The expression is as follows:

$$\frac{A_d}{A_s} = \frac{1}{2}\left(\frac{d_d}{d_s} \right) + \frac{2}{3}\left(\frac{d_s}{d_d} \right) \qquad (7)$$

The specific surface area of a plate or rod is underestimated the more its shape deviates from a sphere. The SADD plot can be corrected by incorporating the above expression into Equation 6.

At each point i along the distribution, the true SAD for the nonspherical sample ($(dm^{c}{}_{P(i)}/dA^{c}{}_{(i)})_{sample}$) will be given by:

$$\left(\frac{dm^{c}{}_{P(i)}}{dA^{c}{}_{(i)}} \right)_{sample} = \left(\frac{dm^{c}{}_{P(i)}}{d\left(A^{c}{}_{(i)}\right)} \right)_{sphere} / \frac{1}{m}\sum_{j=1}^{m}\left(\frac{A_d}{A_s} \right)_{(j)} \qquad (8)$$

where A_d/A_s is the averaged ratio for the m particles examined by scanning electron microscopy (SEM) in the sample collected at point i along the fractogram. SEM is used to measure d_d and d_s is calculated from the SdFFF equations.[13]

Element Content of Particles

The amount of Fe per unit mass of particle ($dm^c_{Fe(i)}/dm^c_{(i)}$) at any point (i) along the elution time or volume axis can be calculated similarly to $dm^c_{P(i)}/dm^c_{(i)}$ (see Equation 5). The Fe concentration in the eluent $[Fe]_i$ can be measured by coupling an inductively coupled plasma-mass spectrometer (ICP-MS) to the SdFFF instrument. The expression is:

$$\frac{dm^c_{Fe(i)}}{dm^c_{(i)}} = \left(\frac{dm^c_{Fe(i)}}{dV_{r(i)}}\right) / \left(\frac{dm^c_{(i)}}{dV_{r(i)}}\right) \propto \frac{[Fe]_{(i)}}{UV_{(i)}} \qquad (9)$$

EXPERIMENTAL

Sample Collection

A sample containing suspended particulate matter was collected from the Peel River (New South Wales, Australia) just before it flowed into Chaffey Reservoir. The Peel River is a small urban stream which was dammed nearly 20 years ago to form Chaffey Reservoir. The latitude is about 31°20'S and the annual average inflow is 6.0×10^7 m^3. The sample was pumped through a continuous flow centrifuge to remove particles larger than 1 μm in size.[14] The filtrate (<1 μm) was then concentrated 100-fold using tangential flow filtration with 0.2 μm Millipore polysulphone membranes. The concentrate was refrigerated at 4°C and sonicated prior to separation by SdFFF.

Extraction Procedure

The above concentrated colloid sample was split into 3 equal subsamples of 0.5 mL volumes. 50 μL of 0.2 M ammonium oxalate (pH 3) was added to one subsample, 50 μL of 3% hydrogen peroxide was added to the second subsample, and the third subsample did not receive any extractants and was used as the control sample.

Each sample was stored at 4°C for 6 hours after which they were centrifuged to remove the supernatant and washed with 0.05% sodium dodecylsulphate (SDS). The samples were spun down in a centrifuge and washed with SDS two more times to remove all traces of the extractants and products from the reactions with the surface coatings.

Orthophosphate Adsorption

^{33}P labelled orthophosphate in dilute hydrochloric acid (370 MBq/mL) was obtained from the Australian Nuclear Science and Technology Organisation (ANSTO). The stock ^{33}P solution was diluted to 740 kBq/mL. At the time of injection into the sample concentrates the ^{33}P activity had decayed to 500 kBq/mL, as estimated from the decay rate law and length of storage. Ten mL of $^{33}PO_4^{3-}$ (500 kBq/mL) was injected onto 50 µL of the concentrated colloid samples and allowed to stand for 24 hours before separation by SdFFF.

Fractions were collected every 5 minutes as the particles eluted from the SdFFF. 0.5 mL of each collected fraction was added to 3.5 mL of scintillant (Ultima Gold), shaken and the ß activity measured for 10 minutes. The counts per minute (CPM) was recorded and, from this data, disintegrations per minute (DPM) per mL was computed.

Sedimentation Field Flow Fractionation

Apparatus

The SdFFF was similar to the basic systems described by Giddings and coworkers and available from FFFractionation LLC (Salt Lake City, Utah, USA), but modified as described in Van Berkel and Beckett.[12] The channel was made by clamping two concentric nickel-chromium rich alloy (Hastalloy) rings together with a 0.0254 cm mylar spacer, in which the channel shape had been cut out, sandwiched in between. There were two systems used. System 1 was used for the adsorption experiments and system 2 was coupled to an inductively coupled plasma-mass spectrometer (ICP-MS) to determine chemical composition of the particles. The channel length and breath for both systems was 89.1 cm long (inlet to outlet) and 2.15 cm respectively. The void volume was 4.91 mL and 2.5 mL for system 1 and 2, respectively. The channels were coiled to fit within a centrifuge basket. The radii of the channels were 15.1 cm and 15.5 cm for system 1 and system 2, respectively. O-rings were fitted at the axle ends to allow liquid to flow through the channel as the centrifuge rotates.

The centrifuge was powered by a DC motor (Baldor permanent magnet servomotor) and the speed controlled by in-house field-decay software. The carrier liquid was pumped through the channel by a Milton Roy ConstaMetricIII metering pump. The outlet stream was passed through an LDC Milton Roy SpectroMonitor variable wavelength detector operating at 254 nm. The samples were collected by an ISCO Retriever 500 fraction collector.

FFF Run Parameters

100 μL and 30 μL of sample concentrate was injected into systems 1 and 2, respectively, using a microsyringe. The samples were relaxed for 10 minutes at 1500 rpm under stop-flow conditions. For system 1, t_l was 5.6 minutes and t_a was -43 minutes. For system 2, t_l was 3.5 minutes and t_a was -28 minutes. The field was reduced using the power program to a minimum 20 rpm. The liquid carrier used for both systems was 0.05% w/v sodium dodecylsulphate (SDS) and 0.02% w/v sodium azide. The flow rates were 2 mL/min and 1 mL/min for system 1 and 2, respectively. Detector sensitivity was 0.02 a.u.f.s.

Scanning Electron Microscopy (SEM)

An Hitachi S-2300 model SEM was used to determine the shapes of the colloidal particles and to verify the accuracy of the SdFFF separations. The 10 mL fractions collected every 5 mins were filtered through either a 0.05 μm Nucleopore filter for sizes less than 0.1 μm or a 0.1 μm Nucleopore filter for sizes larger than 0.1 μm. The filters were cut (approximately 0.5 cm x 1 cm) and attached to an aluminium stub. For SEM analysis, the filters were coated with platinum.

Inductively Coupled Plasma-Mass Spectrometer Apparatus (ICP-MS)

The SdFFF was directly coupled to a VG Plasmaquad ICP-MS in order to obtain high resolution element distributions as a function of particle size. By using a t-piece after the UV detector and a peristaltic pump attached to the v-groove nebulizer of the ICP-MS, about half of the eluent from the SdFFF could flow into the ICP-MS, and the remainder could be collected with a fraction collector or go directly to waste. The internal standards present in the sodium dodecylsulphate (SDS) carrier were indium and cesium. These were used to make corrections for noise and drift. The ICP-MS run conditions were as follows: mass range 23.5 to 210.41 a.m.u.; number of scan sweeps 100 and the instrument operated in pulse-counting mode. Calibration was achieved using a

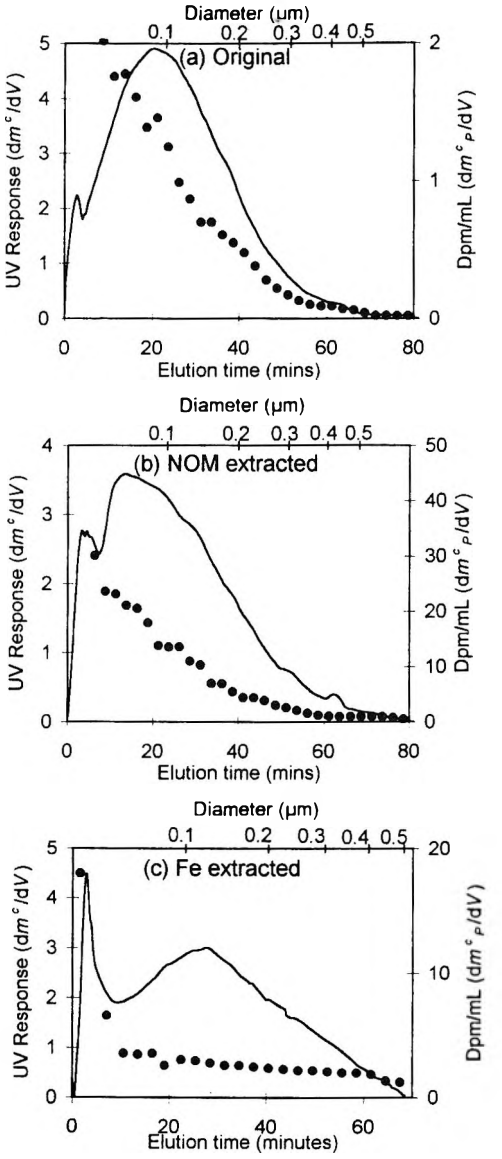

Figure 3. SdFFF fractograms (system 1) of Peel River colloids with adsorbed radiolabelled orthophosphate. The solid lines give the UV detector response (arbitrary units) and the points give the radioactivity (Dpm/mL) in the effluent. (a) original river sample, (b) natural organic matter extracted sample, and (c) hydrous iron oxide extracted sample.

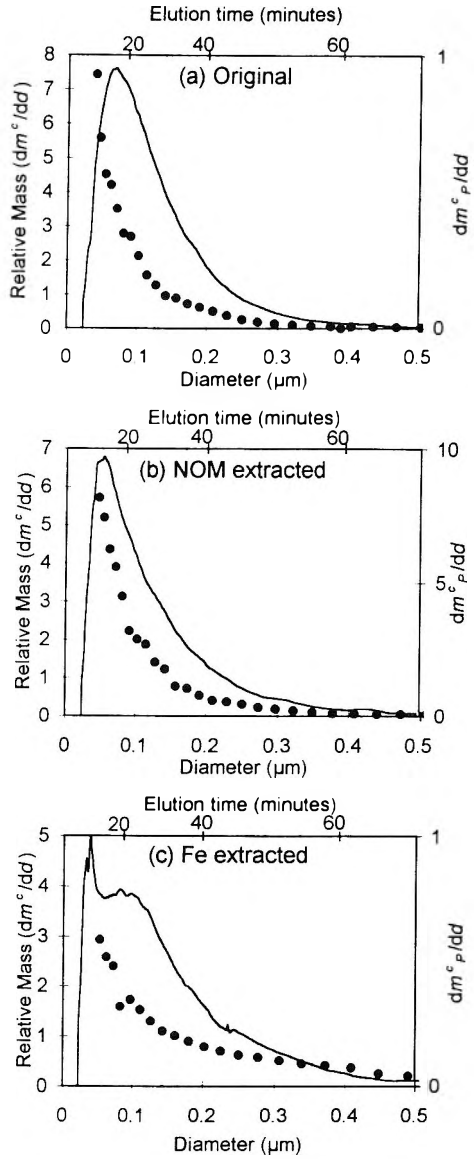

Figure 4. Particle mass based and adsorbate based size distributions. The solid lines give the relative mass of the particles and the points give the amount of orthophosphate adsorbed (both in arbitrary units). (a) original river sample, (b) natural organic matter extracted sample, and (c) hydrous iron oxide extracted sample.

standard solution containing 200 ppb Fe and other elements. This standard was diluted two-fold, four-fold and eight-fold with SDS/azide carrier and the solutions analysed by the ICP-MS prior to each run. An Excel, (Microsoft) macros program was used to perform element by element drift corrections and compute the element concentrations based on ion currents obtained for the above solution standards.

RESULTS AND DISCUSSION

Fractograms and Size Distributions

The raw UV detector and scintillation counter based fractograms, together with the computed particle size distribution for each sample, are shown in Figs. 3 and 4. All samples show a relatively narrow size distribution from 0.05-0.3 μm. The tail does extend to 0.5 μm but, since the signal is small from 0.3-0.5 μm, it is more difficult to analyse trends in this region (see Figs. 4a, b, and c). The size distributions for the NOM extracted sample did not change significantly from the original colloid sample (see Figs. 4a and b). The Fe oxide extracted sample showed a slight broadening of the particle size distribution (see Figs. 4a and c).

The $^{33}PO_4^{3-}$ adsorption experiments show that most orthophosphate is taken up by the smaller particles (see Figs. 4a, b and c). This is due to both the greater mass of material in the smaller size fractions and to the increase in the specific surface area of these particles as particle size decreases.

Analysis of Chemical Composition by SdFFF-ICP-MS

The new hyphenated technique of SdFFF-ICP-MS has excellent potential for determining any changes in particle mineralogy or surface coatings across the size distributions.[7] Fig. 5 shows the iron content of the particles as a function of particle diameter. For the original sample, the amount of iron per unit mass of particle (dm^c_{Fe}/dm^c) increases significantly with increasing particle size (see Fig. 5a). The Fe concentration increased by a factor of 2 over the size range 0.15 to 0.5 μm. The iron can be in either of the following forms: (a) within the solid mineral lattice core of the colloidal particles, or (b) as hydrous iron oxide coatings on the surface of the particles (see Fig. 1). After the extraction of the hydrous iron oxide surface coatings with ammonium oxalate,

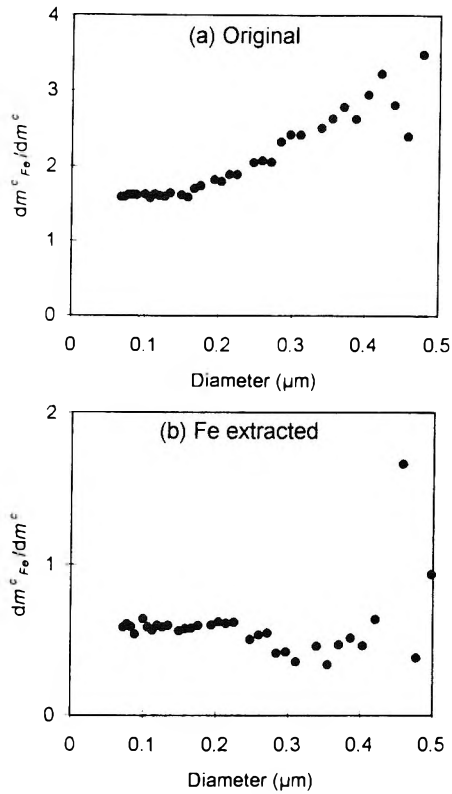

Figure 5. The concentration of Fe within the particles (dm^c_P/dA^c) in arbitrary units), plotted as a function of particle diameter. (a) original river sample and (b) hydrous iron oxide extracted sample.

the iron content plot was constant across the size distribution (see Fig. 5b). This suggests that the iron concentration within the mineral core of the particles is constant across the size distribution. This probably implies that the particle mineralogy remains unchanged.

The amount of iron found on the surfaces can be determined by the difference between the two samples. Figure 6 shows such a plot of the amount of iron associated with the particle coatings per unit area of particle surface. The trend is nonconstant, it increases substantially with increasing particle size (0.15-0.5 μm) indicating the iron surrounding the larger particles is more densely coated with hydrous iron oxides than the smaller particles.

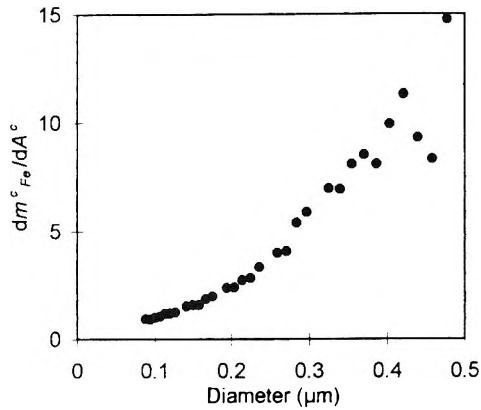

Figure 6. The calculated Fe surface coating density distribution plots (dm^c_P/dA^c versus diameter).

It should be noted that in this work the influence of particle size on the UV attenuation has been neglected and this could have some effect on the coating thickness distribution trend. However, as noted earlier, we believe this is likely to be a small effect since it was observed that the UV and Al based fractograms were very similar (data not included in this paper). In addition, if the UV signal increases with diameter, as may be expected in this size range ($d \approx \ell$), this would further increase the rate of increase of coating thickness with particle diameter.

Surface Adsorption Density Distributions

The surface adsorption density distribution (SADD) plots are shown in Fig. 7. The SADD plots are calculated from the UV and DPM shown on the fractograms in Figs. 3a, b, and c. The SADD plots for all samples were nonconstant. The plots showed an increase in SAD as particle size increased from 0.1 to 0.5 μm. This suggests the larger sized particles adsorbed more orthophosphate per unit area of particle surface than the smaller particles (see Fig 7a). This trend could be influenced by changes in particle shape, mineralogy or surface coatings. The particle shape corrected SAD (dm^c_P/dA^c_{sample}) is calculated using equation 8 as previously discussed. The closed circles represent the SAD values before particle shape correction (dm^c_P/dA^c_{sphere}) and the open circles represent the SAD values after particle shape correction (dm^c_P/dA^c_{sample}). It appears that changes in particle shape do

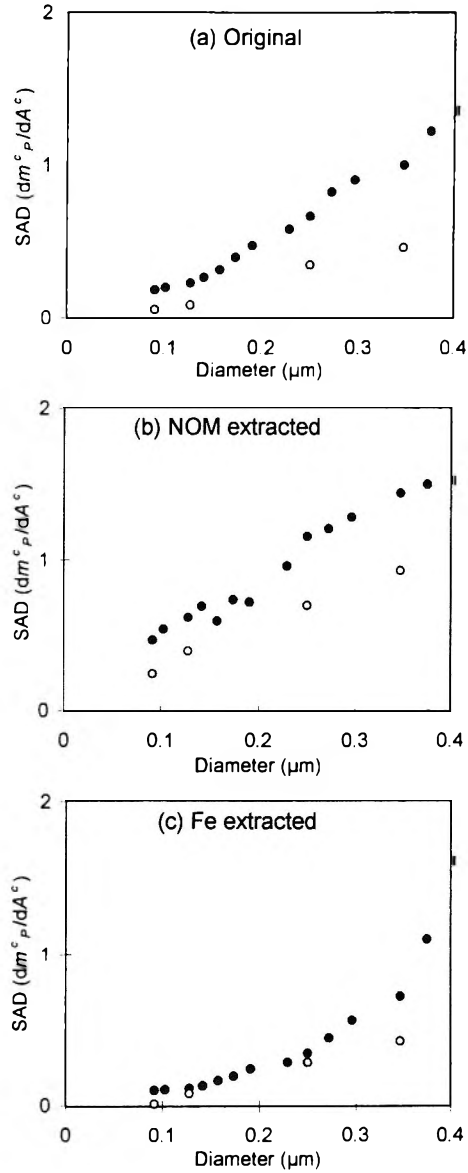

Figure 7. The effect of particle shape correction on the calculated orthophosphate surface adsorption density distribution (SADD) of a river colloid sample. The closed circles give the amount of orthophosphate adsorbed per unit area of particle surface (arbitrary units) assuming all particles are spherical and the open circles are corrected for changes in shape. (a) original river sample, (b) natural organic matter extracted sample, and (c) hydrous iron oxide extracted sample.

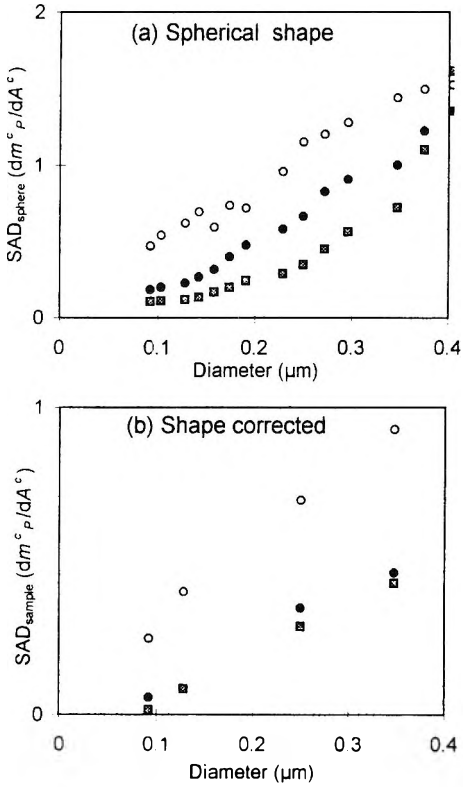

Figure 8. The effect of surface coating extraction on the orthophosphate surface adsorption density distribution (SADD) plots of a river colloid sample. (a) no shape correction and (b) after shape correction. The black circles refer to the original river sample, the open circles are for the natural organic matter extracted sample and the grey squares are for the hydrous iron oxide extracted sample.

not affect the trends in the SADD plots for these samples, even though there was a shift in the absolute values of the surface adsorption density in each case. The nonconstant SADD plot for the control sample is most likely associated with the increased surface coating density of iron around the larger colloidal particles as previously discussed (see Fig. 6).

Effect of Particle Surface Coatings on the SADD Plots

The SADD plot trends remained nonconstant for all samples even after surface coating extraction (see Figs. 7b and c, 8a and b).

The SAD for the Chaffey Dam sample after natural organic matter extraction increased about four-fold over the size range 0.1 to 0.5 μm. Thus, the presence of natural organic matter inhibits the adsorption of orthophosphate to the particles. The extraction of the organic matter apparently exposed the hydrous iron oxide surfaces underneath.

As previously discussed, since the larger particles contained more iron on their surface (see Fig. 6), this could explain the observed nonconstant SAD trend in this case (see Figs. 7b, 8a, and b).

Surprisingly, the attempted removal of the hydrous iron oxide coatings with sodium oxalate resulted only in a small decrease in the surface adsorption density and the shape corrected SADD plot retained its positive gradient (i.e., increasing SAD with increasing particle size).

Unfortunately, in these preliminary experiments we cannot discount the possibility that the extraction conditions did not remove all of the hydrous iron oxide coatings (see Figs 7c, 8a, and b). To investigate this possibility, further work needs to be conducted using more vigorous extraction procedures while carefully monitoring the extent of removal of the iron coatings.

CONCLUSION

The amount of orthophosphate adsorbed per unit area of particle surface as a function of particle size was found to be nonconstant for a Peel River suspended colloid sample. This observed nonconstant SAD trend is apparently associated with an increased surface coating density of hydrous iron oxides with increasing particle size.

The extraction of iron and natural organic matter did not change this observed nonconstant SAD trend. However, the amount of orthophosphate adsorbed per unit area of particle surface decreased slightly after iron surface coating extraction and increased substantially after organic matter surface coating extraction.

These preliminary experiments demonstrate a new methodology which combined previously developed SdFFF-ICP-MS and SdFFF-adsorption techniques to give new insights into the role of surface coatings on natural particles in biogeochemical processes in aquatic ecosystems. The methods introduced here should also be applicable to other industrial and biological samples.

ACKNOWLEDGMENTS

Jason van Berkel was supported by a CRCFE postgraduate scholarship. This research was supported by the CRCFE and the Australia Research Council. We also acknowledge the great contribution of Prof J. Calvin Giddings whose leadership and encouragement over the past 13 years have been invaluable in establishing this research program.

REFERENCES

1. A. Tessier, P. G. C Campbell, M. Bisson, Anal. Chem., **51**(7), 844-851 (1979).

2. R. Beckett, D. M Hotchin, B. T Hart, J. Chromatogr., **517**, 435-447 (1990).

3. M. Kersten, U. Förstner, Wat. Sci. Tech., **18**, 121-130 (1986).

4. W. F Pickering, CRC Crit. Rev. Anal. Chem., Nov: 233-266 (1981).

5. U. Förstner, **Contaminated Sediments: Lecture Notes on Environmental Aspects of Particle-Associated Chemicals in Aquatic Systems**, Springer-Verlag., New York, 1989.

6. R. Beckett, G. Nicholson, B. T Hart, M. Hansen, J. C Giddings, Water Res., **22**, 1535-1545 (1988).

7. D. M Murphy, J. R. Garbarino, H. E. Taylor, B. T. Hart, R. Beckett, J. Chromatogr., **642**, 459-467 (1993).

8. J. C. Giddings, Chem. Eng. News., **66**, 34-45 (1988).

9. R. Beckett, G. Nicholson, D. M. Hotchin, B. T. Hart, Hydrobiologia., **235/236**, 697-710 (1992).

10. R. Beckett, B. T. Hart, "Use of Field-Flow Fractionation Techniques to Characterize Aquatic Particles, Colloids and Macromolecules," in **Environmental Particles**, J. Buffle, Ed., Vol. 2, Lewis Publishers, Boca Raton, FL, 1993, pp. 165-205.

11. J. C. Giddings, Science., **260**, 1456-1465 (1993).

12. P. S. Williams, J. C. Giddings, Anal. Chem., **59**, 2038-2044 (1987).

13. J. Van Berkel, R. Beckett, J. Chromatogr., **733**, 105-117 (1996).

14. G. B. Douglas, R. Beckett, B. T. Hart, Hydrological Processes., **7**, 177-191 (1993).

Received February 2, 1997
Accepted April 16, 1997
Manuscript 4455

J. LIQ. CHROM. & REL. TECHNOL., 20(16 & 17), 2669–2685 (1997)

SURFACE PHENOMENA IN SEDIMENTATION FFF

S. N. Semenov

Institute of Biochemical Physics
Russian Academy of Science
117977 Moscow, Kosygin St. 4, Russia

ABSTRACT

The influence of the surface phenomena on the particle sedimentation in Sedimentation FFF is examined theoretically. It is shown that the tangential transport of surfactant in the particle surface layer, where the surfactant species are accumulated, causes the tangential concentration gradient of the surfactant, and the additional diffusiosmotic flow of the carrier liquid, which may decrease the particle sedimentation velocity. As numerical evaluations show, this change of sedimentation velocity may reach from ten to twenty percent for the particles being the typical objects of sedimentation FFF if surface potential well near the particle surface is deep (about 5-10 kT) and wide (about 10^{-6} cm) enough.

INTRODUCTION

Field-flow fractionation (FFF) presents the unique method, where quasi-equilibrium physicochemical parameters of the analyzed objects (particles, droplets or macromolecules) can be derived from the dynamic experiment, where these objects are driven by a liquid flow and certain transverse force (Ref. 1).

These quasi-equilibrium parameters are available in FFF experiments due to Boltzmannian transverse distribution of the analyzed objects in the FFF channel. Since these parameters are just quasi-equilibrium, but not thermodynamically equilibrium ones, they should be derived theoretically using kinetic approaches and methods of non-equilibrium thermodynamics. If the values of b and D are derived or measured, where b is the generalized mobility of a particle, a droplet or a macromolecule (the velocity in the unit gradient of the transverse potential), D is the particle diffusion coefficient, it is possible to obtain the transverse Peclet number

$$\mathrm{Pe} = \frac{\mathrm{bW}}{\mathrm{D}} \tag{1}$$

where W is the half of the potential drop across the FFF channel (we assume that the transverse particle velocity is constant over the FFF channel). Just the transverse Peclet number defines the retention of the FFF process Ret, and the width of the layer near a channel wall, where particles are accumulated. If transverse Peclet number is large enough, we can write (Ref. 1)

$$\mathrm{Ret} = \frac{\mathrm{Pe}}{3} \tag{2}$$

One can predict the parameter Pe, which defines the FFF behavior of the considered particles, by the procedure involving the measurement of the diffusion coefficient D or the derivation from Stokes expression (for the spherical particles,

$$\mathrm{D} = \frac{\mathrm{kT}}{6\pi\eta\mathrm{R}} \tag{3}$$

where η is the dynamic viscosity of a liquid, and R is the particle radius), by derivation the b value, and measurement or calculation of the transverse potential drop. The way considered above seems to be more complicated, but, in contrast to a more simple conventional way, it allows to take into account the contributions into the particle movement, which may be important. To demonstrate this, let us consider the sedimentation of particles, which is the basis of Sedimentation FFF. In this case, the common way to derive the transverse Peclet number Pe is the substitution of the gravity or sedimentation force acting on the particle

$$\mathrm{F} = \Delta\rho\upsilon\mathrm{G} \tag{4}$$

where $\Delta\rho$ is the density difference between the particle and the carrier liquid, υ is the particle volume and G is the acceleration of the centrifugal or gravity force, into the standard expression for the transverse Peclet number

$$\mathrm{Pe} = \frac{\mathrm{F} \cdot \mathrm{l}}{\mathrm{kT}} \tag{5}$$

where l is the half-width of the FFF channel. For the large particles, this way of consideration sometimes seems to be true. However, for the small particles being the objects of Sedimentation FFF (SdFFF), this approach may fail, since it does not take into account phenomena occurring in the surface layer of the particle. For example, in electrolytes, a so-called sedimentation electrostatic potential arises as a consequence of these surface phenomena (Ref. 2). This macroscopic sedimentation potential may change significantly the particle movement, and it is measurable even when the particles are so large as 0.6 mm diameter with the surface layer being about 0.1 micron thin.

Thus, to have the complete picture of the particle sedimentation, one should derive the particle mobility taking into account the phenomena near the particle surface.

The aim of this paper is to carry out the quantitative examination of the particle sedimentation using the hydrodynamic approach to surface phenomena, and to evaluate the effect of surface phenomena on the particle sedimentation.

HOW SURFACE PHENOMENA CAN AFFECT THE PARTICLE MOVEMENT

As the actual theory shows, the "surface-driven" movement may be caused by the flow of a carrier liquid in the surface layer, where the surfactant ions or (and) molecules are accumulated due to action of the surface potential. To simplify the further consideration, we will examine the surface accumulation of the single sort of surfactant species and neglect the effects due to electric fields generated by the concentration gradients in electrolytes. It should be possible, when the contribution of the electrostatic interactions to the value of the surface potential is small enough. The surfactant accumulation leads to the increase of the osmotic pressure in the surface layer. If the gradient of such an osmotic pressure arises, it causes a liquid flow in the surface layer. This "slipping" flow in a surface layer can cause either phoretic (surface-driven) movement of a particle or the osmotic flow of a liquid, when the particle together with its solid surface is fixed. Gradients of the osmotic pressure in the particle surface layer

may be due to the macroscopic gradients of surfactant concentration or temperature, which can be predetermined by the "boundary conditions" in the FFF channel. If the particle movement is due to the "body" force like to the centrifugal one, a gradient of the osmotic pressure also may arise in its movement. This may be caused by the transport of surfactant molecules or ions along the particle surface, which should be compensated by the exchange of these molecules or ions between the surface layer and the outer liquid. As a consequence, the longitudinal gradient of the concentration may arise, which leads to the osmotic pressure gradient, and, in turn, to the "slipping" of the liquid in the surface layer.

The above discussed mechanism may add the surface-driven movement to the "body-driven" sedimentation movement of the particle. This longitudinal concentration gradient in the surface layer, due to compensating surfactant fluxes is known as the main reason of so-called "concentration polarization" (Ref. 3) in electrophoresis, where these phenomena are shown to be the reason for the measurable changes in the electrophoretic properties of particles. Though in electrolytes, the main reason of a liquid slipping in the surface layer is the effect of electric force on the non-compensated electric charge in the diffusive electric double layer, a diffusio-osmotic slipping flow also arises there, which may contribute to the particle movement.

FLOW VELOCITY PROFILE IN THE SURFACE LAYER

The theory of the surface phenomena is based on the Navier-Stokes equations for the liquid in the surface layer (Ref. 4)

$$\eta \frac{\partial^2 u_z}{\partial y^2} = \frac{\partial p_o}{\partial z} + \frac{\partial p_{osm}}{\partial z} \qquad (7)$$

where $u_z(y)$ is the tangential flow velocity profile in the surface layer at the distance y from the particle surface, p_0 is the pressure excess due to sedimentation movement of particle and the corresponding hydrodynamic viscous stresses, p_{osm} is the osmotic pressure, and z is the longitudinal coordinate on the particle surface. For a spherical particle,

$$z = R \cdot \vartheta \qquad (8)$$

where ϑ is the angle between the direction of the vector $\vec{F}$ given by Expression 5 and the radius vector $\vec{r}$.

The condition of the transverse hydrostatic equilibrium in the surface layer leads to the equation[4]

$$\frac{\partial p_o}{\partial z} + \frac{\partial p_{osm}}{\partial z} + c(y,z)\frac{\partial \Phi}{\partial y} = 0 \qquad (9)$$

where $c(y, z)$ is the surfactant concentration in the surface layer. On the outer surface of the surface layer, the surfactant concentration is designated as

$$c_{0S}(y,z) \qquad (10)$$

which may differ from the surfactant concentration in a liquid far from the particle c_o due to concentration polarization. Usually, one assumes that the surfactant concentration distribution in the surface layer is the Boltzmannian one

$$c(y,z) = c_{os}(y,z)e^{-\frac{\Phi(y)}{kT}} \qquad (11)$$

which allows to solve Eqn. 9 and write its solution, the pressure distribution in the surface layer, as

$$p = p_o + kTc_{es}\left(e^{-\frac{\Phi}{kT}} - 1\right) \qquad (12)$$

Let us discuss the boundary conditions to Eqn. 7. The first one is obvious:

$$u_z = 0 \qquad \text{at} \quad y = 0 \qquad (13)$$

and expresses the absence of any liquid slipping on the particle surface.

The second boundary condition is more complicated and corresponds to the transformation of the flow profile in the surface layer into the flow profile known from the Stokes problem concerning the flow around a sphere at low Reynolds numbers.[2]

Such a transformation should occur outside the surface layer, but at distance $y << R$ from the particle surface. According to (Ref. 2), the external flow profile and the pressure excess can be written as

$$u_r^e = \left(\frac{a}{r} + \frac{b}{r^3} + U\right)\cos\vartheta \tag{14}$$

$$u_\vartheta^e = \left(-U - \frac{a}{2r} + \frac{b}{2r^3}\right)\sin\vartheta \tag{15}$$

$$p_o = \frac{A \cdot \cos\vartheta}{r^2} \tag{16}$$

where u_r^e and u_ϑ^e are the radial and tangential flow velocity; accordingly, U is the velocity of the particle movement to be determined, a, b and A are the constants of the boundary problem, which also should be determined using the "external" boundary conditions near the particle surface, but outside the surface layer. The second boundary condition to Eqn. 7 can be written as

$$\frac{\partial u_z}{\partial y}\Big| = \frac{\partial u_\vartheta^e}{\partial r}\Big|_{r=R} \tag{17}$$

Using Expression 15, the latter equation can be formulated as

$$\frac{\partial u_z}{\partial y}\Big|_{y=\infty} = \frac{\sin\vartheta}{2R}\left(\frac{a}{R} - \frac{3b}{R^3}\right) \tag{18}$$

Now, using boundary conditions given by Expressions 13 and 18, Expression 12 for the osmotic pressure, presenting the outer pressure in the surface layer as

$$p_o = \frac{A\sin\vartheta}{R^2},$$

and neglecting the terms containing the second power of y and the higher powers in this series, we have from Eqn. 7

$$u_z(y,z) \approx \frac{kT}{\eta}\frac{\partial c_{os}}{\partial z}\int_0^y dy \int_\infty^{y'} dy' \left[e^{-\frac{\Phi(y'')}{kT}} - 1\right] - \sin\vartheta\left(\frac{a}{R} - \frac{3b}{R^3}\right)\frac{y}{2R} \tag{19}$$

Outside the surface layer, where Expression 19 should transform into Expression 15, it can be written as

$$u_{\vartheta}^{e} = \frac{kT}{\eta \cdot R} \frac{\partial c_{os}(R,\vartheta)}{\partial \vartheta} \int_0^{\infty} dy \int_{\infty}^{y} dy' \left[e^{-\frac{\Phi(y')}{kT}} - 1 \right] - \sin\vartheta \left(\frac{a}{R} - \frac{3b}{R^3} \right) \frac{y}{2R} \tag{20}$$

which allows to write the boundary conditions to the external Stokes problem as

$$u_r^e(r = R) = 0 \tag{21}$$

$$u_{\vartheta}^{e}(r = R) = u_s \tag{22}$$

where

$$u_S = \frac{kT}{\eta \cdot R} \frac{\partial c_{os}(R,\vartheta)}{\partial \vartheta} \int_0^{\infty} dy \int_{\infty}^{y} dy' \left[e^{-\frac{\Phi(y')}{kT}} - 1 \right] \tag{23}$$

is the "slipping" flow velocity in the surface layer.

Expressions 21-23 allow us to determine the constants a and b from Expressions 14 and 15 (constant A is unimportant) and to define the force of the hydrodynamic friction acting on the particle, which moves with the velocity U[5]

$$F_{friction} = -4\pi\eta a \tag{24}$$

To derive the friction force, one should have the surfactant concentration distribution outside the surface layer.

CONCENTRATION POLARIZATION OF THE MOVING PARTICLE

As Expressions 22 and 23 show, the surface phenomena may effect the sedimentation of a particle only in the case when the tangential surfactant concentration gradient exists on the particle surface. To estimate this possibility, we should have the equation for the surfactant concentration.

If the sedimentation velocity is constant and slow enough (in FFF it is about 10^{-4} cm/s), we can write the stationary convection-diffusion equation for the surfactant concentration in the form

$$\text{div grad } c_{os} = 0 \tag{25}$$

and assume that the solution of Eqn. 25 may be written in "dipole" form[3]

$$c_{os} = \frac{M_c}{r^2}\cos\vartheta + c_o \tag{26}$$

where M_c is the concentration "dipole moment" of the particle, which will be defined below. Eqn. 25 is valid outside the surface layer, but the more general equation

$$\text{div}\,\vec{j} = 0 \tag{27}$$

for the stationary surfactant flux $\vec{j}$ should be valid anywhere.

If the surface layer, where the surfactant molecules or ions are accumulated, is thin enough, i.e., its width is significantly smaller than the particle radius, Eqn. 27 can be reformulated as[2]

$$\vec{j}_n = -\,\text{div}_s\,\vec{j}_s \tag{28}$$

where

$$\vec{j}_n = -D_s \frac{\partial c_{os}}{\partial r}\Big|_{r=R} \tag{29}$$

is the external surfactant flux on the particle surface, D_s is the diffusion coefficient of the surfactant, and

$$\vec{j}_s = \int_0^\infty \left[c_o u_z(y,z) - D_s \frac{\partial c_{os}}{\partial z}\Big|_{r=R} \right] \left[e^{-\frac{\Phi(y)}{kT}} - 1 \right] dy \tag{30}$$

is the total excess of the surfactant transport in the particle surface layer. Operator div_s in the thin surface layer can be written as

$$\mathrm{div}_s = \frac{\partial}{\partial z}.$$

Writing Eqn. 30, we assume that the tangential concentration gradient in the surface layer is too weak to cause the concentration changes comparable to c_o. Also, Expression 11 is taken into account. Using Expressions 19, 26, 29, and 30, Expression 28 can be written as

$$\frac{2M_c}{R^3} = \int_0^\infty \frac{c_o kT}{\eta D_s}\frac{M_c}{R^4}\left[e^{-\frac{\Phi(y)}{kT}} - 1\right]\int_0^y dy' \int_\infty^{y'} dy''\left[e^{-\frac{\Phi(y'')}{kT}} - 1\right]dy +$$

$$+\frac{c_o}{2D}\int_0^\infty \left(\frac{a}{R} - \frac{3b}{R^3}\right)\frac{y}{R}\left[e^{-\frac{\Phi(y)}{kT}} - 1\right]dy - \frac{M_c}{R^4}\int_0^\infty \left(e^{-\frac{\Phi(y)}{kT}} - 1\right)dy \tag{31}$$

Using Eqn. 31, we can obtain the concentration dipole moment M_c. However, to finish the derivations, a simplification is necessary. The most interesting situation is that, where the surface potential well is deep enough, because the concentration polarization should be the most significant due to the intensive transport of the surfactant highly accumulated in such a well. In this case, we can assume that

$$e^{-\frac{\Phi}{kT}} >> 1 \tag{32}$$

and present the surface potential (in kT units) as

$$\frac{\Phi}{kT} \approx -\varepsilon_o\left(1 - \frac{y}{h}\right) \tag{33}$$

where ε_o is the depth of the surface potential well, and h is the characteristic width of this well.

The physicochemical nature of these parameters will be discussed below. As the numerical evaluations show, the assumption given by Expression 32 is valid at

$$\varepsilon_o \geq 5. \tag{34}$$

Using the approximation given by Expression 33 and Expression 4 for the surfactant specie with radius d, we have from Expression 31

$$M_c = \frac{3\pi\eta\left(\frac{a}{R} - \frac{3b}{R^3}\right)c_o R^3 \cdot h \cdot d \cdot Re1}{kT \cdot \varepsilon_0\left(2 + Re1 + \frac{3\pi}{\varepsilon_0} c_o dhR \cdot Re1^2\right)} \tag{35}$$

where criterion *Rel* is introduced

$$Re1 = \frac{he^{\varepsilon_0}}{\varepsilon_0 R} \tag{36}$$

which characterizes the concentration polarization degree. Using Expressions 23, 24 and 35, we can express the slipping velocity as

$$u_s = \frac{3\pi c_0 dh^2 \cdot Re1^2\left(\frac{a}{R} - \frac{3b}{R^3}\right)}{\varepsilon_0^2\left[2 + Re1 + +3\pi c_0 d\frac{h}{\varepsilon_0} R \cdot Re1^2\right]} \tag{37}$$

As Expression 37 shows, the slipping velocity is small at $Re1 << 1$, and it reaches saturation at

$$Re1 >> \left(3\pi c_0 d\frac{h}{\varepsilon_0} R\right)^{-1} \tag{38}$$

This saturation value is

$$u_s^{max} = \left(\frac{a}{R} - \frac{3b}{R^3}\right)\frac{h}{\varepsilon_0 R} \tag{39}$$

The general expression for the slipping velocity can be written compactly as

$$u_s = \left(\frac{a}{R} - \frac{3b}{R^3}\right)\frac{h}{\varepsilon_0 R} f(\delta, \varphi, Re1) \tag{40}$$

where

$$\varphi = \tilde{n}_0 \frac{3\pi d^3}{4} \tag{41}$$

is the volume fraction of the surfactant, and

$$\delta = \frac{hR}{\varepsilon_0 d^2} \tag{42}$$

is the reduced parameter characterizing the relationship between the parameters of the surface potential well ($\frac{h}{\varepsilon_0}$), the particle (R) and the surfactant specie (d).

Here,

$$f(\delta, \varphi, Re1) = \frac{4\varphi \cdot \delta \cdot Re1^2}{2 + Re1 + 4\varphi \cdot \delta \cdot Re1^2} \tag{43}$$

is the function characterizing the concentration polarization in the sedimentation process. This function ranges from zero (at $Rel = 0$) to unity (at very large Rel values, where Expression 38 is valid). Using Expressions 40-42, and boundary conditions given by Expressions 21 and 22, we have for the constant a defining the particle sedimentation velocity

$$a = -\frac{3}{2} UR \frac{1 + \frac{h}{\varepsilon_o R} f}{1 + 2\frac{h}{\varepsilon_o R} f} \tag{44}$$

Taking into account the assumptions about the thin surface layer, the deep surface potential well, and Expression 42, the value of parameter $\frac{hf}{\varepsilon_o R}$ can not be larger than unity. The analysis of the Expressions 32 and 33 shows that the width of the layer, where surfactant species are accumulated, is about $\frac{h}{\varepsilon_0}$

Thus, considering the realistic potential wells with $h \le R$, we should evaluate the parameter $\frac{h}{\varepsilon_o R} f$ as $\frac{h}{\varepsilon_o R} f \le \frac{1}{\varepsilon_0}$.

For this reason, we can approximate 44 as

$$a \approx -\frac{3}{2} UR\left(1 - \frac{h}{\varepsilon_0 R} f\right) \tag{45}$$

Using Expressions 24 and 45, we can write the expression for the particle sedimentation velocity as

$$U = U_0\left(1 - \frac{h}{\varepsilon_0 R} f\right) \tag{46}$$

where

$$U_0 = \frac{F}{6\pi\eta R}$$

is the classic value of the sedimentation velocity. Since the maximum value of the parameter f is unity (see Expression 42), the maximum relative change of the particle sedimentation velocity at very large criterion Rel values (See Expression 38) is

$$\frac{U - U_o}{U_o} = -\frac{h}{\varepsilon_o R} \tag{47}$$

Let us note that the change of the particle velocity predicted by Expression 47 is not linked strictly to the sedimentation, but may be observed in any particle movement where the Stokes flow profile arises around the particle. For example, Expression 47 should be valid for the particle movement in Flow FFF.

To evaluate the possible changes in the particle movement due to surface phenomena, we should discuss the possible mechanisms of the surfactant accumulation within the surface potential well, the possible values of criterion *Rel* , and the possible values of the parameters φ and δ, which define the concentration dependencies of the surface effects in the sedimentation at the moderate values of criterion *Rel* and the conditions, where the saturation of the surface effects is reached.

DISCUSSION

Parameters of the Surface Potential Well

According to (Ref. 6), there are several main mechanisms to accumulate the ions or molecules near the surface:

a) dispersion or London - Van der Waals interaction with the potential

$$\Phi(y) = -A\frac{d^3}{y^3} \tag{48}$$

where A is Hamaker constant;

b) Coulomb electrostatic interaction in electrolytes with the potential

$$\Phi(y) = -q\zeta e^{-\frac{y}{\lambda}} \tag{49}$$

where q is the electric charge of the surfactant ion, ζ is the particle electrokinetic potential, and λ is the Debye length; and

c) the adsorption and structure forces, which have no analytical dependence of the surface potential on the distance, but have the parameters ε_o and h derived from the experimental data. These forces are due to structure changes in the surface layer and the correlation between different surfactant species.

Strictly, we can not examine the sedimentation in electrolytes due to the different nature of the slipping flow, which is discussed in introduction. But, in the cases, where electrical fields arising in the surface layer are too weak to contribute significantly to the liquid flow there, we can use Expressions 46 and 48 to analyze the surface phenomena in the particle sedimentation in electrolytes.

The results obtained should be valid, at least qualitatively. The data from (Ref. 6), concerning the surface potential well parameters ε_o and h, are collected in Table 1.

Table 1

Surface Potential Well Parameters

Surface Potential	Analytical Expressions for the $\Phi(y)$, ε_o and h			The Ranges of Values for Parameters ε_o and h	
	$\Phi(y)$	ε_o	h	ε_o	h
London - Van der Waals forces	$-A\frac{d^3}{y^3}$	$\frac{A}{kT}$	$\frac{d}{3}$	5 ÷ 50 *	$\approx 10^{-8}$ cm (low-molecular surfactant)
Coulomb electrostatic forces	$-q\xi e^{-\frac{y}{\lambda}}$	$\frac{q\xi}{kT}$	λ	0 ÷ 10	$10^{-7} \div 10^{-4}$ cm ** (aqueous electrolytes)
Adsorption forces	none	none	none	0 ÷ 10	$\approx 10^{-7}$ cm
Structural forces	none	none	none	0 ÷ 10	$\approx 10^{-5}$ cm

* The maximum values of Hamaker constant are characteristic for metals and some hydrocarbons. ** The maximum value of the Debye length is reached in the pure water, where only H^+ and OH^- ions exist.

According to (Ref. 2), the size of particle being the objects of FFF are ranged from 10^{-6} cm to 10^{-4} cm. Thus, Expression 46 predicts the observable contribution of surface phenomena to the particles sedimentation for all the types of the surface interactions excepting the Van der Waals interaction. This kind of interaction can not provide the significant width of the surface potential well, if low-molecular surfactants are used. However, for the metals having the extremely high values of Hamaker constants, the saturation of the surface effects should occur at relatively low surfactant concentrations. Also, the contribution of surface phenomena should be especially high if polymer surfactants are used, since, in such a situation, parameter *h* should have a value comparable to the thickness of the cloud consisting of random-flight fragments of the polymer chains, which can be very large in comparison with the *h* value from Table 1.

As Expression 47 shows, the significant contribution of the surface phenomena to the sedimentation needs moderate values of the parameter ε_o defining the depth of the surface potential well.

Table 2

Values of Criterion *Rel*

Depth of Surface Potential Well ε_o	Particle Radius R		
	10^{-6} cm	10^{-5} cm	10^{-4} cm
5	Rel = 30 (3)	Rel = 3 (0,3)	Rel = 0.3 (0,03)
7.5	Rel = 241 (24.1)	Rel = 24.1 (2.41)	Rel = 2.41 (0.24)
10	Rel = 2200 (220)	Rel = 220 (22)	Rel = 22 (2.2)

On the other hand, Expression 47 becomes valid at the values of criterion *Rel* large enough. Thus, we should estimate the possible values of criterion *Rel* to examine the role of the surface phenomena in the sedimentation.

The Values of Criterion *Rel*

As Table 1 shows, the typical values of parameter ε_o where the surface potential well is deep enough, are from about 5 to about 10. Moreover, the typical values of parameter h are ranged from about 10^{-7} cm to about 10^{-6} cm. The corresponding values of criterion *Rel* are collected in Table 2.

In Table 2, the upper *Rel* values present the case where $h \approx 10^{-6}$ cm, and the lower ones (in parentheses) are corresponding to $h \approx 10^{-7}$ cm. As data of Table 2 show, the most of the particles being the object of FFF should have an apparent degree of polarization at $\varepsilon_0 \geq 5$.

To finish these estimates, we should estimate the possible values of parameter δ and the volume fraction of surfactant φ. The latter one is estimated easily, because the molar concentration of surfactant usually is about $10^{-3} \div 10^{-2}$ m/L, i.e., the number of the surfactant species c_o is about $10^{18} \div 10^{19}$ per cubic centimeter. For the surfactant molecule radius $d = 3 \cdot 10^{-8}$ cm, using Expression 41, we have

$$\varphi \approx 10^{-4} \div 10^{-3} \qquad (50)$$

The values of parameter δ (Expression 42) at ε_o = 10 ranged from 10 (at h = 10^{-7} cm and R=10^{-6} cm) to 10^4 (at h=10^{-6} cm and R=10^{-4} cm). Thus, the condition of the saturation at the concentration polarization (Expression 38) may be fulfilled for the wide range of particles sizes if the surface potential well is deep enough. For example, using these evaluations, one can see that, at ε_o = 10 and h=10^{-6} cm, all the particles examined in Table 2 should be strongly polarized, and Expression 46 should describe adequately the contribution of the surface phenomena in the particle sedimentation. As Expression 47 shows for such particles, the relative decreasing of the sedimentation velocity due to concentration polarization should be about 0,1. For the smaller particles, where the saturation may be reached even at ε_0 = 5, this velocity change may reach up to 0,2. Such a change of the sedimentation velocity must be measurable in the real FFF conditions. Let us remember that, in experiments the standards often are used, which have size dispersion of about 2-3%, which gives the dispersion of about 4-6% of the peak maximum position.

The classical expression for the SdFFF retention gives the dependence of the retention on the particle radius as $\sim R^2$. The accounting of the surface phenomena gives more complicated dependence given by Expression 46 or 47, which should be not so steep. This difference can be useful in the determination of the role of surface phenomena in sedimentation. In electrolytes, where Debye length defines the width of the surface potential well and decreases with the concentration of the ionic surfactant as $c_o^{-\frac{1}{2}}$ (see, for example, Refs. 2 or 4), the increase of the sedimentation velocity with the surfactant concentration also may indicate the significant role of the surface phenomena. As Expression 43 and 46 show, at the moderate values of criterion *Rel*, the sedimentation velocity, that is, the retention of SdFFF, should depend on the surfactant concentration, besides the known concentration dependence of the liquid viscosity.

CONCLUSIONS

The most of the particles being the objects of SdFFF cause slipping flow within its surface layer, where surfactant species are accumulated, in the sedimentation. Due to this slipping flow, a concentration gradient of surfactant arises, which leads to additional diffusio-osmosis in the surface layer, which should compensate the convective surfactant transport. These surface

phenomena can decrease the particle sedimentation velocity up to ten - twenty percent if the surface potential well is deep enough (*5 - 10 kT*). Similar changes may occur also in Flow FFF, where this surface slipping of the carrier liquid in the particle surface layer should have the same nature and properties.

ACKNOWLEDGMENT

This work is supported by the Russian Foundation for Basic Research (Grant No. 95-03-08390a).

REFERENCES

1. M. Martin, P. S. Williams, "Theoretical Basis of Field-Flow Fractionation," in **Theoretical Advancement in Chromatography and Related Separation Techniques,** F. Dondi, G. Guiochon, eds., Kluwer Academic Publishers, The Netherlands, 1992, pp 513-580.

2. V. G. Levich, **Physicochemical Hydrodynamics**, State Publishing of Physical and Mathematical Literature, Moscow, 1959. [In Russian].

3. S. S. Dukhin, **Electric Conductivity and Electrokinetic Properties of Disperse Systems,** Naukova Dumka Publishing, Kiev, 1975 [In Russian]

4. J. L. Anderson, Anal. Rev. of Fluid Mech., **21**, 61-97 (1989).

5. L. D. Landau, E. M. Lifshits, **Mechanics of Continuous Media**, State Publishing of Technical and Theoretical Literature, Moscow, 1954. [In Russian].

6. B. V. Derjagin, **Theory of Stability of Colloids and Thin Layers**, Publishing Nauka, Moscow, 1986. [In Russian].

Received January 20, 1997
Accepted February 13, 1997
Manuscript 4349a

J. LIQ. CHROM. & REL. TECHNOL., 20(16 & 17), 2687–2702 (1997)

SURFACE PHENOMENA IN THERMAL FFF OF PARTICLES

S. N. Semenov

Institute of Biochemical Physics
Russian Academy of Science
117977, Moscow, Kosygin St. 4, Russia

ABSTRACT

The theory developed in this article presents the physico-chemical mechanism of particle thermophoresis in a liquid. It is shown, too, that polarization phenomena may play an important role in thermophoresis. The possible role of polarization as the reason of the features observed experimentally in the experiments on ThFFF of particles and macromolecules is discussed.

INTRODUCTION

One object of Prof. Giddings investigation for recent years was Thermal FFF of particles.[1-4] He also initiated my interest in this problem. As the result of our work, the paper[5] raised, where the principles of particle thermophoresis were explained using the general theory of the phoretic movement in liquids, which is presented in Ref. 6.

The main aim of our paper[5] was the explanation of metal particle thermophoresis, since it was the most obscure phenomenon observed by Prof. Giddings and Dr. Shiundu in their experiments. The possibility of thermophoresis for the metal particles was explained there. However, many details of the experimental data observed in Refs. 1-4 are still unexplained. This is the situation, which emphases the degree of originality and importance of these experiments. The unexplained features of particle thermophoresis can be formulated, roughly, as the following:

a) the particle thermophoretic mobilities depend on the particle size, while the theory developed in Ref. 5 does not predict such a dependence;

b) the particle thermophoretic mobilities increase as the salt concentration increases in the carrier liquid, while the theory developed in Ref. 5 does not predict such a dependence; and

c) different thermophoretic properties of the polymer particles and the polymer chains of the same chemical composition: in contrast to the particles, the thermophoretic mobilities of the polymer chains practically do not depend on the chain length and the salt concentration in the outer liquid.

The aim of this paper is to provide more a complete theory of thermophoresis in a liquid which may, at least qualitatively, explain the above-mentioned details observed in experiments.

There is a way to explain the above features of particle thermophoresis. It is the accounting of the surfactant concentration gradient along the particle surface, caused by its movement in thermophoresis. Due to the tangential transport of the surfactant ions or molecules in the particle surface layer, the exchange of surfactant should exist between this surface layer and the outer liquid to compensate the drain of the former and to maintain the stationary surfactant concentration.

This phenomenon, called *concentration polarization*, is known widely in the theory of particle electrophoresis.[8] Both electrophoresis and thermophoresis are related phenomena, which are surface-driven.[6-8] Since the concentration polarization plays an important role in electrophoresis, where it significantly changes the particle electrophoretic mobility, and where its degree depends on the particle size, we may hope that its role in thermophoresis also should be a significant one.

According to the current theory, the phoretic movement is due to the osmotic pressure gradient or the electrostatic force in the surface layer, where surfactant molecules or ions are accumulated. An electrostatic force acts on the non-compensated diffuse electric charge which exists in the double electric layers when the particle is suspended in an electrolyte. The osmotic pressure gradient may be due to both macroscopic temperature and surfactant concentration gradient. As a result, the "slipping" of the liquid in the surface layer arises, which leads either to particle phoresis or to the osmotic flow of the liquid, when the solid surface can not move. To derive the particle thermophoretic velocity we should solve four related mathematical problems:

a) derivation of the temperature distribution around the spherical particle in the outer constant temperature gradient;

b) derivation of the flow velocity profile in the surface layer;

c) derivation of the surfactant concentration distribution; and

d) derivation of the particle thermophoretic velocity.

To simplify the examination, we neglect the electric fields which may arise around the particle due to the concentration gradients of electrolyte, and examine the situation where the single type of the surfactant is accumulated in the surface layer with the concentration high enough.

TEMPERATURE GRADIENT AROUND THE PARTICLE

This problem is discussed widely in the literature,[5,9] and we present, here, only the statement of the problem and the main results.

One supposes that the temperature distributions inside and outside a particle (T_i and T_e, respectively) have the dipole form

$$T_i = \nabla T \cdot \mathbf{r} \cdot \cos\vartheta \tag{1}$$

$$T_e = T_0 + \nabla_i T \cdot \mathbf{r} \cdot \cos\vartheta + \frac{M_T}{r^2}\cos\vartheta \tag{2}$$

where T_0 is the temperature at the center of the particle, r is the distance from its center, ϑ is the angle between the vector $\vec{r}$ and the outer temperature

gradient $\nabla\vec{T}$, M_T is the temperature "dipole moment" of the particle, and $\nabla_i T$ is the internal temperature gradient in the particle, which should be determined.

On the particle surface, at $r = R$, we have the boundary conditions

$$T_i = T_e \tag{3}$$

$$\theta_i \frac{\partial T_i}{\partial r} = \theta_e \frac{\partial T_e}{\partial r} \tag{4}$$

where θ_i and θ_e are the thermal conductivities of the particle and the external liquid, respectively. Expressions 1-4 give the complete picture of the temperature distribution. In further calculations, we need only the outer temperature distribution

$$T_e = \nabla T \cdot R \cdot \cos\vartheta \left(\frac{r}{R} + \frac{n-1}{n+2} \frac{R^2}{r^2} \right) \tag{5}$$

where

$$n = \frac{\theta_i}{\theta_e}$$

is the ratio of the thermal conductivities.

In the thin surface layer, where a significant osmotic pressure arises, we will use the coordinate $y = r - R << R$. According to Expressionn 5, in this thin layer, the temperature gradient can be written as

$$\nabla_\vartheta T = \frac{1}{R} \frac{\partial T}{\partial \vartheta} = -\sin\vartheta \frac{3\nabla T}{2+n} \left(1 + n\frac{y}{R} \right) \tag{6}$$

Usually, the particles have thermal conductivities comparable to the liquids' (normal particles) or exceeding them significantly (metal particles).

FLOW VELOCITY PROFILE IN THE SURFACE LAYER AND THE PARTICLE THERMOPHORETIC VELOCITY

The flow velocity profile in the thin surface layer is defined by the Navier-Stokes equations in the form[6-8]

$$\eta \frac{\partial^2 u_z}{\partial z^2} = \frac{\partial p}{\partial z} \tag{7}$$

$$\frac{\partial p}{\partial y} = -c(y,z)\frac{\partial \Phi}{\partial y} \tag{8}$$

where η is the dynamic viscosity of a liquid, u_z is its tangential velocity, p is the pressure, $z = R \cdot \vartheta$ is the tangential surface coordinate, c is the concentration of the of surfactant molecules dissolved in the liquid, and Φ is the surface potential of this surfactant molecule.

Equation 8 expresses the condition of the hydrostatic equilibrium across the surface layer. Near the particle surface, a quasi-thermodynamic equilibrium is also established, and the surfactant concentration distribution is the Boltzmannian one[6,7]

$$c(y,z) = c_{os}(y,z)e^{-\frac{\Phi(y)}{kT(y,z)}} \tag{9}$$

where kT is thermal energy and c_{os} is the surfactant concentration at the distance y<<R from the particle surface, but, outside the surface layer. Equation 8, in combination with Expression 9, gives the excess pressure distribution in the surface layer

$$p = p_o + kTc_{os}\left(e^{-\frac{\Phi}{kT}} - 1\right) \tag{10}$$

where p_o is the "outer" pressure in the liquid far from the particle.

Substituting the pressure distribution given by Expression 10 into Eqn. 7, we have equation

$$\eta\frac{\partial^2 u_z}{\partial y^2} = kT\frac{\partial c_{os}(R,z)}{\partial z}\left(e^{-\frac{\Phi}{kT}}-1\right)+kc_o\frac{\partial T(y,z)}{\partial z}\left[e^{-\frac{\Phi}{kT}}\left(\frac{\Phi}{kT}+1\right)-1\right] \tag{11}$$

Writing Eqn. 11, we assume that the longitudinal concentration and temperature gradients are too small to cause the changes of temperature and concentration comparable to their mean values. We also neglect the second powers and the mathematical products of the gradients. These assumptions are used in the further derivations, too. The boundary conditions to Eqn. 10 can be written as[6]

$$u_z = 0 \qquad \text{at } y=0 \tag{12}$$

$$\frac{\partial u_z}{\partial y} = 0 \qquad \text{at } y=\infty$$

Using boundary conditions given by Expression 12, the flow profile in the particle surface layer can be written as

$$u_z(y,z) = \frac{kT}{\eta}\frac{\partial c_{os}(R,z)}{\partial z}\int_0^y dy'\int_\infty^{y'} dy''\left[e^{-\frac{\Phi(y'')}{kT}}-1\right]$$

$$-\sin\vartheta\frac{3kc_o\nabla T}{\eta(2+n)}\int_0^y dy'\int_\infty^{y'} dy''\left(1+n\frac{y''}{R}\right)\left\{e^{-\frac{\Phi(y'')}{kT}}\left[\frac{\Phi(y'')}{kT}+1\right]-1\right\} \tag{13}$$

where Expression 6 for the temperature gradient is used. The slipping velocity of the liquid in the whole surface layer can be written as

$$u_s = u_z(\infty,z) = -\frac{kT}{\eta}\frac{\partial c_{os}}{\partial z}\int_0^\infty ydy\left[e^{-\frac{\Phi(y)}{kT}}-1\right]+$$

$$+\frac{3kc_o\nabla T}{\eta(2+h)}\int ydy\left(1+n\frac{y}{R}\right)\left\{e^{-\frac{\Phi(y)}{kT}}\left[\frac{\Phi(y)}{kT}+1\right]-1\right\}\sin\vartheta \tag{14}$$

where integration by parts of Expression 13 is used. It is shown in Ref. 5 that the particle thermophoretic velocity u_T and the slipping velocity (Expression 14). which can be written in the form

$$u_s = u_{s0} \cdot \sin\vartheta$$

are interconnected by the relationship

$$u_T = u_{s0} \tag{15}$$

The structure of the slipping velocity and thermophoretic velocity contains two terms corresponding to thermophoresis and diffusiophoresis in the concentration gradient due to the particle movement in the temperature gradient. This secondary concentration gradient may significantly change the movement of the particle. To derive it, we should formulate the appropriate equations.

SURFACTANT CONCENTRATION DISTRIBUTION AROUND THE PARTICLE

If the thermophoretic movement of the particle is stationary and slow enough, the convection-diffusion equation for the surfactant concentration can be written in the form

$$\text{div grad } c_{os} = 0 \tag{16}$$

and its solution may be found as the "dipole" concentration distribution

$$c_{os}(r,\vartheta) = c_o + \frac{M_c}{r^2}\cos\vartheta \tag{17}$$

Expressions 16 and 17 are valid outside the particle surface layer. However, the equation expressing the stationary state of the surfactant concentration distribution in the stationary particle movement should be true, both in the particle surface layer and outside it. Such an equation can be written as

$$\text{div } \vec{j} = 0 \tag{18}$$

where

$$\vec{j} = \vec{u} \cdot c - D \cdot \text{grad}\, c \tag{19}$$

is the surfactant flux. Here, D is the diffusion coefficient of the surfactant molecules and $\vec{u}$ is their velocity. If the particle surface layer is thin enough (the question "how much is thin?" will be discussed later), we can formulate the boundary condition to Eqn. 16 using Eqn. 19. As shown in Refs. 6, 7, 8, this boundary condition can be formulated as

$$D\frac{\partial c_{os}}{\partial r}\Big|_{r=R} = \text{div}\vec{j}_s \tag{20}$$

where

$$\vec{j}_S = \int_0^\infty j_S dy \tag{21}$$

is the total excess transport of the surfactant in the surface layer and

$$j_S = \left(e^{-\frac{\Phi(y)}{kT}} - 1\right)\left[c_o u_z(y) - D\frac{\partial c_{os}}{\partial z} - \frac{Dc_o}{T}\frac{\partial T}{\partial z}\frac{\Phi(y)}{kT}\right] \tag{22}$$

is the longitudinal excess flux of the surfactant in the particle surface layer.

Further, we will discuss the most interesting situation for ThFFF, where the surface potential well is deep enough and we can assume that

$$e^{-\frac{\Phi}{kT}} >> 1 \tag{23}$$

In this situation, we also can approximate the real potential distribution by expression

$$\frac{\Phi}{kT} \approx -\varepsilon_o\left(1 - \frac{y}{h}\right) \tag{24}$$

where ε_o is he depth of the surface potential well in kT units and h is its characteristic width. This assumption (Expression 23) and approximation (Expression 24), together with Expressions 13, 17 and 20-22, allow us to write the equation defining the concentration "dipole moment" M_c

$$-\frac{2M_c}{R^3}=-\frac{c_o kT}{\eta D}\frac{M_c e^{2\varepsilon_o}}{R^4}\int_0^\infty e^{-\varepsilon_o\frac{y}{h}}dy\int_0^y dy'\int_\infty^{y'} dy'' e^{-\varepsilon_o\frac{y''}{h}}-$$

$$-\frac{3kc_o^2\nabla T e^{2\varepsilon_o}}{\eta(2+n)RD}\int_0^\infty e^{-\varepsilon_o\frac{y}{h}}dy\int_0^y dy'\int_\infty^{y'} dy'' e^{-\varepsilon_o\frac{y''}{h}}\left(1+n\frac{y''}{R}\right)\left[1-\varepsilon_o\left(1-\frac{y''}{h}\right)\right]+$$

$$+\frac{M_c e^{\varepsilon_o}}{R^4}\int_0^\infty e^{-\varepsilon_o\frac{y}{h}}dy-\frac{c_o}{T}\frac{3\nabla T e^{\varepsilon_o}}{(2+n)R}\int_0^\infty e^{-\varepsilon_o\frac{y}{h}}\left(1+n\frac{y}{R}\right)\varepsilon_o\left(1-\frac{y}{h}\right)dy \tag{25}$$

After much algebra, this equation allows us to derive the concentration "dipole moment' as

$$M_c=\frac{3c_o k\nabla T R^3}{(2+n)T}\mathrm{Rel}\frac{\varepsilon_o-1+\frac{nh}{\varepsilon_o R}(\varepsilon_0-2)+2\varphi\delta\cdot\mathrm{Rel}\left[2\varepsilon_o-5+\frac{nh}{\varepsilon_o R}(3\varepsilon_0-10)\right]}{2+\mathrm{Rel}+4\varphi\delta\cdot\mathrm{Rel}^2} \tag{26}$$

where the reduced parameters are introduced

$$\mathrm{Rel}=\frac{he^{\varepsilon_o}}{\varepsilon_o R} \tag{27}$$

is the criterion of the concentration polarization degree of the particle,

$$\varphi=c_o\frac{4\pi d^3}{3} \tag{28}$$

is the volume fraction of the surfactant molecules or ions having the radius d; and

$$\delta=\frac{h\cdot R}{d^2} \tag{29}$$

is the parameter characterizing the ratio of the main sizes considered in the problem. Deriving Expression 26, we also used the known Stokes expression for the diffusion coefficient:

$$D = \frac{kT}{6\pi\eta d} \tag{30}$$

Besides the above mentioned parameters, Expression 26 also contains the parameter

$$\frac{nh}{\varepsilon_o R} \tag{31}$$

which is small, when the particle/liquid ratio of the thermal conductivities is about 1, and it should be large for metal particles having high thermal conductivities. This parameter characterizes the role of the transverse temperature distribution in particle thermophoresis. We can consider these situations separately for the normal particles:

$$M_{cN} = \frac{3c_o \nabla T R^3}{T(2+n)} Re1 \frac{\varepsilon_o - 1 + 2\varphi\cdot\delta\cdot Re1(2\varepsilon_o - 5)}{2 + Re1 + 4\varphi\cdot\delta\cdot Re1^2} \tag{32}$$

and for the metal particles:

$$M_{cM} = 3c_o \frac{\nabla T}{T} R^3 \frac{h}{\varepsilon_o R} Re1 \frac{\varepsilon_o - 2 + 2\varphi\cdot\delta\cdot Re1(3\varepsilon_o - 10)}{2 + Re1 + 4\varphi\cdot\delta\cdot Re1^2} \tag{33}$$

DISCUSSION

Expressions 32 and 33 allow, after substitution into Expression 14, where Expression 17 is taken into account, to write the thermophoretic velocities for normal and metal particles

$$u_{TN} = \frac{3c_o k\nabla T}{\eta(2+n)} \frac{h^2 e^{\varepsilon_o}}{\varepsilon_o^2} \left\{ 3 - \varepsilon_o + \frac{Re1\left[\varepsilon_o - 1 + 2\varphi\cdot\delta\cdot(2\varepsilon_o - 5)Re1\right]}{2 + Re1 + 4\varphi\cdot\delta Re1^2} \right\} \tag{34}$$

$$u_{T\ddot{U}} = \frac{3c_o k\nabla T}{\eta}\frac{h^3 e^{\varepsilon_o}}{\varepsilon_o^3 R}\left\{2(4-\varepsilon_o)+\frac{Rel\left[\varepsilon_o - 2 + 2\varphi\cdot\delta\cdot Rel(3\varepsilon_o - 10)\right]}{2 + Rel + 4\varphi\cdot\delta\, Rel^2}\right\} \tag{35}$$

At small values of criterion *Rel*, the thermophoretic velocities of both normal and metal particles are negative, i.e., particles should be driven to the cold wall of the FFF channel.

We can determine, roughly, the regimes of the thermophoresis with the concentration polarization as:

a) non-polarization regime, where

$$Rel << 1;$$

b) first transition regime, where

$$Rel \cong 1;$$

c) regime with the moderately large values of criterion Rel, where

$$1 << Rel << (4\varphi\cdot\delta)^{-1},$$

in this regime, as shown in the exact analysis of the Expressions 25 and 26, the convective transport of surfactant in the particle surface layer can be neglected as compared to the diffusional transport;

d) second transition regime, where

$$Rel \approx (4\varphi\cdot\delta)^{-1},$$

in this regime, both the convective and diffusion transport of surfactant in the particle surface layer are important;

e) regime of very large Rel values, where

$$Rel >> (4\varphi\cdot\delta)^{-1},$$

in this regime, convective transport in the particle surface layer prevails.

Of course, the above classification is valid only at

$$4\varphi \cdot \delta << 1,$$

which condition seems to be true for the wide range of the experimental situations in FFF.[10]

The approximating expressions for the terms in the figure brackets of Expressions 34 and 35, which are designated as $f_N(\varepsilon_o, \delta, \varphi, Rel)$ and $f_M(\varepsilon_o, \delta, \varphi, Rel)$, correspondly, for the above mentioned regimes are represented in Table 1. The data represented in Table 1 show the transition from the negative thermophoresis at $Rel << 1$ (no polarization, particles are driven to the cold wall) to the positive one at $Rel \approx 1$ (moderate polarization, particles are driven to the hot wall). As criterion Rel increases, the isopolarization state may come on, where the particle thermophoretic velocity is equal to zero. For the normal particles, it occurs at

$$Rel_i = \frac{\varepsilon_o - 3}{\varepsilon_o - 2} \tag{36}$$

and for the metal ones, at

$$Rel_{iM} = \frac{4(4 - \varepsilon_o)}{\varepsilon_o - 6} \tag{37}$$

Taking into account the range of validity for the approximation by Expressions 23 and 24, based on the assumption concerning the deep surface potential well, we can define the range of ε_o values, where the isopolarization state is possible, for the metal particles, as

$$5 \le \varepsilon_o < 6 \tag{38}$$

This is the range which is narrow enough, and we can suppose that metal particles should have the isopolarization state rather rarely. However, taking into account the large values of parameter ε_o, which are characteristic for metals,[10] the metal particles should be strongly polarized and they should be driven to the cold channel wall. In the experiments on ThFFF, where particles of different sizes made of the same material were analyzed, one can observe different situations represented in Table 1, since there are different particles

Table 1

Approximate Expressions for the Terms in the Figure Brackets of Expressions 34 and 35

Regime	$f_N(\varepsilon_o, \delta, \varphi, \mathbf{Rel})$	$f_M(\varepsilon_o, \delta, \varphi, \mathbf{Rel})$
a) $\mathrm{Rel} << 1$;	$3 - \varepsilon_o$	$2(4 - \varepsilon_o)$
b) $\mathrm{Rel} \cong 1$	$3 - \varepsilon_o + \frac{(\varepsilon_o - 1)\mathrm{Re}}{2 + \mathrm{Rel}}$	$2(4 - \varepsilon_o) + \frac{(\varepsilon_o - 2)\mathrm{Rel}}{2 + \mathrm{Rel}}$
c) $1 << \mathrm{Rel} << (4\varphi \cdot \delta)^{-1}$	2	$6 - \varepsilon_o$
d) $\mathrm{Rel} \approx (4\varphi \cdot \delta)^{-1}$	See Exprn 34	See Exprn 35
e) $\mathrm{Rel} >> (4\varphi \cdot \delta)^{-1}$	$\frac{1}{2}$	$\frac{6 - \varepsilon_o}{2}$

having the same parameters of the surface potential wall ε_o and h should have different values of criterion Rel corresponding to the size. If Expression 35 is valid, the behavior of the both metal and normal particles in the various polarization regimes should be similar. The main difference between the normal and metal particles is the factor $\frac{h}{\varepsilon_o R}$ in the dependence of the thermophoretic velocity on the particle radius for the latter ones. As the particle size decreases, its thermophoretic velocity, which is negative at $\mathrm{Rel} << 1$ increases up to zero at Rel_i, then it increases further with the size decrease up to transition to regime c), reaches the maximum and decrease in respect to this maximum in regime e). For metal particles with $\varepsilon_o > 6$, the monotonous increase of the thermophoretic velocity modulus with the size decrease should be observed due to factor $\frac{h}{\varepsilon_o R}$. Due to high values of the Hamaker constant for metals, just this dependence should be the most common one.

Since the ThFFF experiments are carried out with polymer and silica particles, which can be considered as the normal ones, we examine the normal particles in detail, in an attempt to explain the experimental data. The possible ranges of values for the parameters $\varepsilon_0, h, \delta, \varphi, Rel$ are discussed in Ref. 10, where the possibility of all the above mentioned polarization regimes is shown.

The experimental data of [Ref.1] show a nonlinear, slow increase of the ThFFF retention with the particle diameter. For the particles being the objects of the experiments reported,[1-4] the retention can be written as

$$Ret = \frac{Pe}{3} \tag{39}$$

where Pe is the transverse Peclet number

$$Pe = \frac{b_T \Delta T}{D_p} \tag{40}$$

b_T is the particle thermophoretic mobility (thermophoretic velocity in the unit temperature gradient), ΔT is the temperature drop over the half-width of the channel, and D_p is the particle diffusion coefficient, which depends on the particle radius as Expression 30 shows. Thus, the dependencies observed in [Ref. 1] correspond to a slow decrease of the particle thermophoretic mobility modulus with the increase of its size.

As Table 1 shows, such a dependence corresponds to regimes b), or d), where the modulus of the particle thermophoretic mobility increases with the particle radius. In the first case, the particle must have the Rel values lower than Rel_i. In principle, regimes b) and d) can be differentiated, if one knows whether particles are driven to the cold wall or to the hot one. However, we had not found such information in [Refs. 1-4].

The effect of the salt addition observed in [Ref.1] also may provide certain arguments pro regime b). The salt addition decreases the Debye length, which depends on the ion concentration c_i as $c_i^{-\frac{1}{2}}$. In this way, the Rel values are decreasing too, and particles obtain higher thermophoretic velocity, either by transition into regime a) or into regime c), moving away from the isopolarization state. Also, the effect of the salt addition may be explained by the sharp increase in the surface potential due to ion's adsorption but, in this case, some new questions arise. In this number, one cannot explain why the

particles and macromolecules of the same material exhibit so different thermophoretic properties. An explanation can be found if we assume that the "particles"-monomers, which comprise the polymer chain, are strongly polarized. Using the data of Table 1, and above-mentioned dependence of the width of the surface potential well in electrolytes, i.e., the Debye length, on the ion's concentration

$$h \approx c_i^{-\frac{1}{2}}$$

and assuming that the salt added to solvent is the strong surfactant, i.e., $c_o \approx c_i$, one can see that the thermophoretic velocity of the strongly polarized particle both in regimes c) and e) should not depend on the electrolyte concentration. In this way, the macromolecules move in the temperature gradient as a set of small, strongly porarized particles, interconnected by the elastic forces. However, these strongly polarized particles should be driven to the hot channel wall, while the most of the macromolecules are driven to the cold one. Among many others, this feature of the macromolecule thermophoresis needs further explanation.

The hypothesis discussed in [Ref. 2], where the effect of the salt addition is explained by the decrease of the particle-wall repulsion layer, should not be valid, because this effect must be important for both the particles and macromolecules, which have the same Debye screening layer and should have the same repulsion interaction with the wall.

CONCLUSION

The theory developed shows the physico-chemical mechanism of particle thermophoresis in a liquid. It shows, too, that the polarization phenomena may play an important role in the thermophoresis. The polarization also may be the reason for the features observed experimentally in the ThFFF of particles and macromolecules.

ACKNOWLEDGMENT

This work is supported by Russian Foundation for Base Research (Grant No. 95-03-08390a).

REFERENCES

1. P. M. Shiundu, J. C. Giddings, J. Choromatogr. A, **715**, 117-126 (1995).

2. S. K. Ratanathanawongs, P. M. Shiundu, J. C. Giddings, Colloids and Surfaces, **105**, 243-250 (1995).

3. P. M. Siundu, E. E. Remsen, J. C. Giddings, J. Appl. Polymer Sci., **60**, 1695-1707 (1996).

4. P. M. Siundu, G. Liu, J. C. Giddings, Anal. Chem., **67**, 2705-2713 (1995).

5. S. N. Semenov, P. M. Siundu, J. C. Giddings, J. Colloid Interface Sci., **176**, 454-458 (1995).

6. J. L. Anderson, Anal. Rev. of Fluid Mech., **21**, 61-97 (1989).

7. S. S. Dukhin, **Electric Conductivity and Electrokinetic Properties of Disperse Systems**, Naukova Dumka Publ., Kiev, 1975. [In Russian]

8. V. G. Levich, **Physicochemical Hydrodynamics**, State Publishing of Physical and Mathematical Literature, Moscow, 1959. [In Russian]

9. L. D. Landau, E. M. Lifshits, **Mechanics of Continuous Media**, State Publishing of Technical and Theoretical Literature, Moscow, 1954. [In Russian]

10. S. N. Semenov, "Surface Phenomena in Sedimentation FFF," J. Liq. Chrom. & Rel. Technol., **20**, 2669-2685 (1997).

Received January 20, 1997
Accepted February 13, 1997
Manuscript 4349b

J. LIQ. CHROM. & REL. TECHNOL., 20(16 & 17), 2703–2722 (1997)

EFFECT OF CHANNEL ORIENTATION ON THERMAL DIFFUSION AND POLYMER RETENTION IN THERMAL FIELD-FLOW FRACTIONATION

Jun Xu, Chad A. Rue, Martin E. Schimpf*

Department of Chemistry
Boise State University
Boise, Idaho 83725

ABSTRACT

The ThFFF retention of polymers is enhanced in certain liquid mixtures. Previous studies of thermal diffusion in such mixtures indicate that the enhancement is due to an additional solubility-based force induced by a solvent gradient in the channel. The partitioning of solvent mixtures in a temperature gradient was shown to be correlated to solvent density, just as the thermal diffusion of polymers is correlated to polymer density.

This work examines the density effect more closely by looking at the effect of channel orientation on both polymer retention and the partitioning of liquids. A difference in the profiles of solvent partitioning with channel orientation indicates the presence of convection currents in an inverted ThFFF channel, yet polymer retention is independent of channel orientation in homogeneous solvents as well as solvent mixtures. The results indicate that the effect of density on polymer retention is rooted in thermal diffusion and not convection, but

that either the previously proposed mechanism of enhanced retention is incorrect or convection currents are confined to the channel edges, becoming significant only in the tapered regions of the channel. Finally, the effect of polymer concentration on retention is more pronounced in mixed carrier liquids.

INTRODUCTION

In field-flow fractionation (FFF), components are separated due to their differential interaction with an applied field.[1] That interaction can be defined by two opposing motions: 1) the movement of material in response to the applied field, and 2) the diffusion of material away from the concentration buildup arising from the field-induced motion. The analyte properties that govern the former motion depend on the nature of the applied field and, therefore, differ among FFF subtechniques. For example, sedimentation FFF separates materials according to their buoyant mass, while electrical FFF separates material according to their charge. Regarding the latter motion, diffusion is a factor in all FFF subtechniques. Therefore, in the application to macromolecules and submicron-sized particles, where diffusion is significant, all FFF subtechniques separate material according to size or molecular weight, in addition to the parameter(s) that govern(s) the field-induced motion.

In thermal FFF (ThFFF), the applied field is a temperature gradient. The movement of material in a temperature gradient, which is referred to as thermal diffusion, depends on the chemical composition of both the analyte and the carrier liquid.[2] As a result, composition has a direct influence on the ThFFF separation.[3-5] This is in contrast to size exclusion chromatography (SEC), where the role of polymer composition is a relatively minor one, affecting retention only by its influence on polymer conformation, which can influence diffusion and, therefore, retention. Although the separating power in ThFFF depends on the polymer-solvent couple, the separation of molecular weights above 100,000 g-mol^{-1} is generally more efficient in ThFFF compared to SEC.[6,7] On the other hand, ThFFF has a lower limit to the molecular weight range that can be separated. The lower limit varies with the polymer, but is generally a few thousand g-mol^{-1}. Molecular weights below 3000 g-mol^{-1} can been separated by ThFFF,[8] but the large temperature gradients necessary for such applications require the channel to be pressurized in order to raise the boiling point of the carrier liquid. Pressurization requires specialized equipment that is more costly and cumbersome. Thus, ThFFF cannot replace SEC as a general method for the analytical separation of polymers, rather the two techniques are complementary.

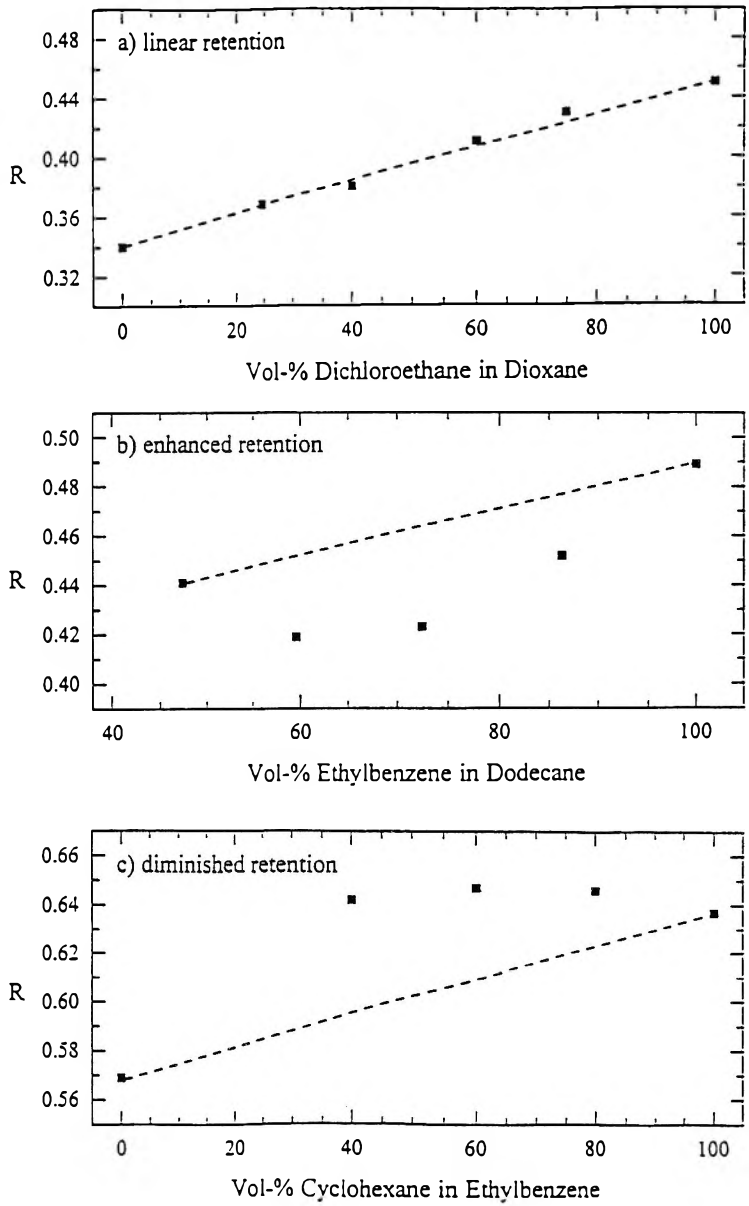

Figure 1. Plots of retention ratio R versus solvent composition in carrier-liquid mixtures, illustrating (a) linear dependence, (b) enhanced retention, and (c) diminished retention.

The lack of dependence of thermal diffusion on molecular weight in dissolved polymers[9] simplifies the characterization of molecular weight in such materials because the relationship between diffusion and molecular weight has been defined for many polymer-solvent systems. Even when such a relationship has not been defined, it can be established using size exclusion chromatography[10] or viscosity measurements.[11] Although a poor understanding of thermal diffusion has hindered full utilization of the compositional selectivity of ThFFF, recent improvements in that understanding have allowed for the development of methods to characterize the composition of certain copolymers.[12]

ThFFF typically employs a homogeneous carrier liquid. The first reported use of solvent mixtures involved mixtures of dimethylsulfoxide and water.[13] Later, Kirkland et al.[14] reported that certain mixtures can be used to raise polymer retention to levels not previously seen. In a systematic study by Sisson and Giddings,[15] the dependence of polymer retention on solvent composition in mixed carrier liquids was found to vary widely among different solvent mixtures. Figure 1 illustrates the three different types of relationships found between retention and solvent composition. In mixtures of dichloroethane (DCE) and dioxane, retention is a linear function of solvent composition. In mixtures of ethylbenzene (EB) and dodecane (DoD), the dependence of retention on solvent composition deviates from linearity toward lower R-values; this is subsequently referred to as enhanced retention, since lower R-values correspond to higher levels of retention. By contrast, the dependence of retention on solvent composition deviates from linearity toward lower levels of retention (higher R values) in mixtures of EB and cyclohexane (CYH); this behavior is subsequently referred to as diminished retention. Enhanced retention can be used to lower the molecular weight range to which ThFFF can be applied. Figure 2 illustrates the separation of five polystyrene standards, ranging in molecular weight from 2500 to 179,000 g-mol^{-1}, in a mixture containing 45 vol-% tetrahydrofuran (THF) in DoD. This fractogram represents the lowest molecular weight polymer ever resolved from the void peak without channel pressurization.

The enhanced retention of polymers in mixed carrier liquids appears to result from a synergistic effect that involves the thermal diffusion of both polymer and solvent. If the two components have different solvating powers for the polymer, retention is enhanced when the better solvent partitions in the same direction (to the cold wall) as the polymer. When the better solvent partitions to the hot wall, retention is diminished. Thermodynamic calculations confirm the significance of this solubility-based driving force, and the so-called partitioning effect was demonstrated in several carrier liquid mixtures,[16] including those represented in Figure 1. For example, in mixtures of EB and

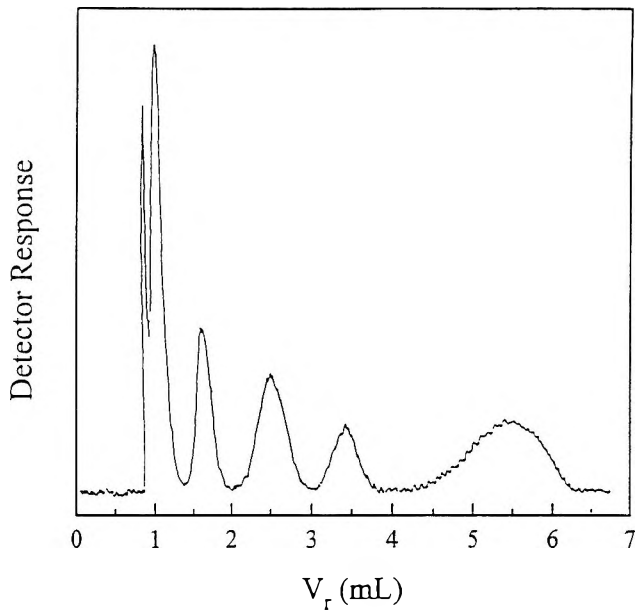

Figure 2. Separation of polystyrene components using a mixture of 45 vol-% THF in DoD as the carrier liquid. From left to right, the first peak is the void peak; successive peaks contain polystyrene standards of the following molecular weights, in thousands (k): 2.5k; 20k, 47k, 97k, and 179k. Reproduced with permission from Reference 16.

CYH, the better solvent (EB) partitions to the hot wall and retention is diminished, while in mixtures of EB and DoD, the better solvent (EB) partitions to the cold wall and retention is enhanced. In each of seven cases examined thus far, the dependence of polymer retention on solvent composition is consistent with the proposed mechanism.

The first series of liquid mixtures in which the partitioning effect was studied in detail involved DCE and CYH. The partitioning of an 81.8 vol-% mixture of DCE in CYH is illustrated in Figure 3. Plots like those in Figure 3 are obtained by exposing solvent mixtures to a temperature gradient as they flow through a specialized ThFFF channel. The channel contains a single inlet and two outlets, one at each (hot and cold) wall. The composition of the solvent layers at the hot and cold walls is sampled at the channel outlets. Thin layers at each wall are sampled by adjusting the back pressure at each outlet with needle valves, which allows the fraction of total flow eluting from each outlet (referred to as the split ratio) to be precisely controlled.

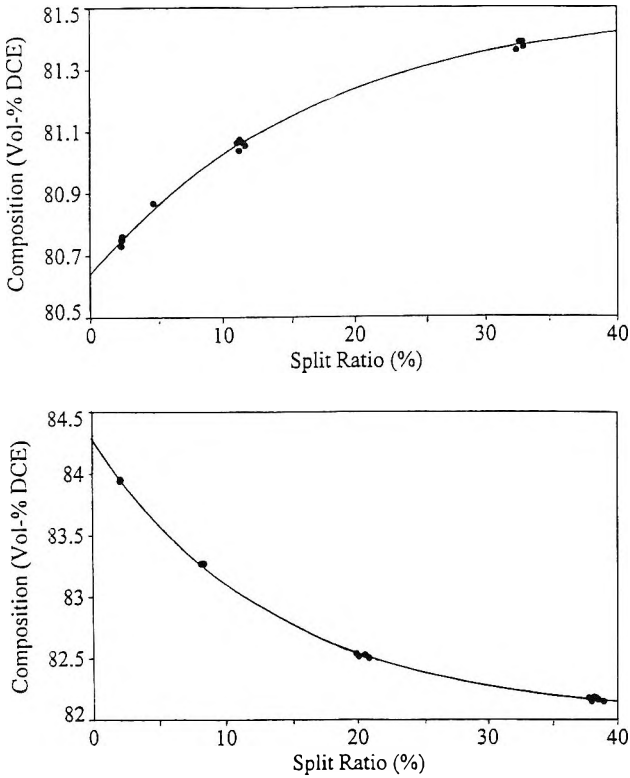

Figure 3. Measured concentration of DCE eluting from the outlets of a channel in the normal orientation (hot wall up) as a function of the split ratio in mixtures of 81.8 vol-% DCE in CYH. The solid lines represent a fit of the data to an exponential function: top, depletion (hot) wall; bottom, accumulation (cold) wall. Reproduced with permission from Reference 16.

The use of liquid mixtures to enhance polymer retention in ThFFF would benefit from a better understanding of thermal diffusion in liquids. In the work discussed above,[16] the partitioning of 12 solvents in 25 different binary combinations was measured. With the exception of CYH, the relative tendency of a solvent to partition to the cold wall follows the order of increasing density. An analysis of variance signifies the role of density at the 99% confidence level. Variance analysis also indicates that solvent partitioning is affected (99% confidence) by the solvent's activation energy for viscous flow, which is the coefficient in the exponential dependence of viscosity on temperature. Both correlations are consistent with previous studies of thermal diffusion in

polymers solutions,[10] where a significant fit was found in regressing the thermal diffusion coefficient (D_T) of the polymer to a function of the polymer density and the viscous activation energy of the solvent.

Since solvent partitioning is correlated to density, we must consider the existence of convective motions in the fluid. Convection is a macroscopic displacement caused by density gradients and is a process separate from thermal diffusion.

With homogeneous liquids, convection should be negligible in thin ThFFF channels, even though a small density gradient is induced by the temperature gradient. However, in mixed solvents, larger density gradients are possible due to solvent partitioning. Convective motions in mixed solvents may lead to instabilities in the concentration profiles established by thermal diffusion. Normally, the ThFFF channel is oriented with the cold wall down. In this case, when the denser liquid thermally diffuses to the cold wall, convective forces reinforce partitioning due to thermal diffusion.

However, if the denser liquid were to thermally diffuse up to the hot wall, convection could lead to remixing of the liquid components. In fact, we cannot rule out the possibility that convective instabilities completely counteract any partitioning due to thermal diffusion in the majority of cases where the denser liquid thermally diffuses to the hot wall. Therefore, the observed correlation between partitioning and density may be an artifact of convective motion in the channel.

The objective of the work reported here is to address the issue of convective motion while evaluating the role of density in thermal diffusion and polymer retention. Our approach is to measure both solvent partitioning and polymer retention in a ThFFF channel whose orientation has been reversed, so that the cold wall lies above the hot wall.

The results will be compared to those obtained with a channel oriented in the normal configuration. If thermal diffusion is governed by density at a fundamental level, then solvent partitioning and polymer retention will be unaffected by channel orientation in the absence of convective motion.

Even if convection is present, it may not affect polymer retention if it is confined to the edges of the channel. If, on the other hand, density plays a role that is separate from thermal diffusion, both solvent partitioning and polymer retention will be affected by channel orientation.

THEORY

Thermal Diffusion in Liquids and Polymer Solutions

The reader is referred to the literature for a detailed discussion of thermal diffusion in liquids.[17] In summary, attempts to present a unified, rigorous theory of thermal diffusion in condensed-state matter have been unsuccessful. As a result, the approach to defining thermal diffusion in liquids remains phenomenological. This approach states that the movement of material in a temperature gradient is governed by the balance of two opposing transport mechanisms. The thermal gradient along coordinate x causes transport toward one wall; as a concentration gradient is formed, mass diffusion serves as a counteracting transport mechanism. The balance of these two mechanisms yields the following concentration profile

$$c(x) = c_o \exp\left[\frac{D_T(dT/dx)}{D}x\right] \tag{1}$$

where D_T and D are the thermal and ordinary diffusion coefficients, respectively, dT/dx is the temperature gradient, and c_o is the concentration at the accumulation wall. Thus, a component's highest concentration is at the accumulation wall, decreasing exponentially away from the wall. The ratio D_T/D is referred to as the Soret coefficient. In binary mixtures, a similar equation is defined for each component, and the two equations are combined to yield the following extent of separation in an open cell

$$\frac{C_H(1-C_C)}{C_C(1-C_H)} = \exp\left[\frac{D_T\Delta T}{D}\right] \tag{2}$$

Here C_H and C_C are the concentrations of one of the components at the hot and cold walls, respectively, and ΔT is the temperature difference between the hot and cold walls. Thus, the extent of separation is governed by the Soret coefficient and ΔT. Values of the Soret coefficient for liquid mixtures have been measured in the range of 0.001 to 0.1 K^{-1}. For a mixture with an initial concentration ratio of 10:90 and a Soret coefficient of 0.01, the more dilute component will be enriched to 13:87 at the hot wall and diluted to 7:93 at the cold wall when the temperature difference is 50 K. Thermodynamic calculations, supported by empirical evidence, indicate that even this small difference in solvent composition affects the free energy of polymer solutions to a significant degree.[16]

Relaxation Time

In order to obtain precise values for the Soret coefficient, sufficient time must be allowed for the liquid to partition to its steady-state concentration profile under the influence of the temperature gradient. According to Von Halle,[18] the approach to steady state in a static thermal diffusion cell is exponential with a relaxation time approximated by

$$\tau = w^2/D\pi^2 \qquad (3)$$

where w is the thickness of the cell (or ThFFF channel). Assuming a diffusion coefficient of 10^{-5} cm^2/s, Eq. 3 predicts a relaxation time on the order of 10 s for the channel and conditions used in this work. At a flow rate of 0.6 mL/min, the solvent is in the channel for 225 s, yet in previous work with the normal orientation, partitioning continued to increase with residence times beyond 350 s. Unfortunately, we cannot keep the liquids in the channel for longer periods of time without losing satisfactory precision in our measure of solvent partitioning. Therefore, we did not attempt to obtain Soret coefficients in this work. However, by keeping the field strength and flow rate constant, while precisely controlling and measuring the outlet-split ratio, we are able to make qualitative comparisons required to evaluate the effect of channel orientation on thermal diffusion.

ThFFF Retention

In dilute polymer solutions, the opposing forces of thermal and ordinary diffusion result in a concentration profile that decreases exponentially away from the cold wall. The center of mass of the profile is defined by its distance ℓ from the cold wall. For mathematical convenience, ℓ is expressed in dimensionless form $\lambda = \ell /w$, which is related to the transport coefficients by

$$\lambda = \frac{D}{wD_T(dT/dx)} \approx \frac{D}{D_T\Delta T} \qquad (4)$$

Using the velocity profile of the carrier liquid, which is well defined in FFF because the flow is laminar, the volume V_r of carrier liquid required to flush a polymer component through the channel is related to λ as follows:

$$R = \frac{V^o}{V_r} = 6\lambda\left(\coth\frac{1}{2\lambda} - 2\lambda\right) \qquad (5)$$

Here V° is the void volume and R is termed the retention ratio. In the limit of high retention, the term in parentheses on the right side of Eq. 5 approaches one and Eqs. 4 and 5 can be combined to yield

$$R = \frac{1}{6\Delta T(D_T / D)} \tag{6}$$

Thus, a polymer's retention ratio varies directly with its Soret coefficient.

MATERIALS AND METHODS

The ThFFF instrument is similar to the FFFractionation Model T-100 (Salt Lake City, USA), except that temperature control is achieved using a proportional counter described previously.[16] The channel has a tip-to-tip length of 46 cm and a breadth of 2.0 cm. Two different channel thicknesses were used. For measuring the partitioning of solvent mixtures, we used a 254 μm-thick channel (void volume 2.25 mL) with a single inlet and two outlets. The flow rate through the channel was 0.60 mL/min. As described above, the composition of solvent layers were sampled at both channel outlets as the ratio of solvent out each wall was varied. The sampling port at each wall consisted of a t-union with a rubber septum, placed just upstream from the needle valves used to control the split ratio. The effluent was sampled by penetrating the septum with a microliter syringe. The collected effluent was injected directly into a gas chromatograph for analysis. This arrangement precluded selective evaporation of one component prior to analysis.

For measuring polymer retention, we used a 102 μm-thick channel with a resulting void volume of 0.90 mL. The flow rate of the carrier liquid was 0.20 mL/min and the concentration of the injected polymer solutions was 1.0 mg/mL. Sample detection was achieved with Polymer Laboratories (Amherst, MA) Model 950/14 evaporative mass detector. The polystyrene standards came from either Supelco Co. (Bellefonte, USA) or Pressure Chemical Co. (Pittsburgh, USA).

Samples were relaxed into their steady-state distributions at the accumulation wall using the stop-flow technique with a relaxation time of 1 min. In computing R from Eq. 5, V_r was calculated by subtracting the volume of the inlet and outlet tubing from the total volume of carrier liquid required to flush the sample from injector to detector. The void volume V° was equated to the retention volume of a polymer standard in the absence of an applied field.

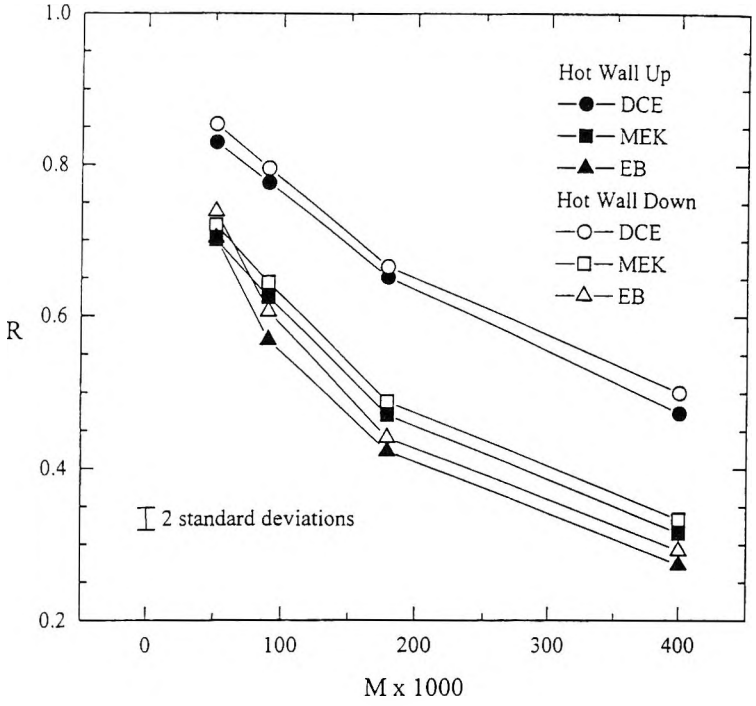

Figure 4. Plots of retention ratio R versus molecular weight M in homogeneous carrier liquids, illustrating the independence of retention on channel orientation.

RESULTS AND DISCUSSION

As we mentioned above, the retention of polymers in homogeneous solvents is highly correlated to polymer density. If thermal diffusion is governed by density in a fundamental way, i.e., there is not a separate density effect, then retention will not change with channel orientation. Figure 4 compares the retention of polystyrene standards ranging in molecular weight from 50,000 to 400,000 g-mol^{-1} in three different solvents. For each of the 12 polymer-solvent systems, the difference in retention with channel orientation is not greater than the empirically-defined uncertainty of the measurement, which lies in the range of 1-3%. However, if the entire data set is considered, there does appear to be a small effect, since R values are consistently higher in the inverted orientation. Still, the differences are very small (< 2%), and for all practical purposes they are negligible. We can conclude, therefore, that density is a significant predictor variable for the thermal diffusion of polymers in solution.

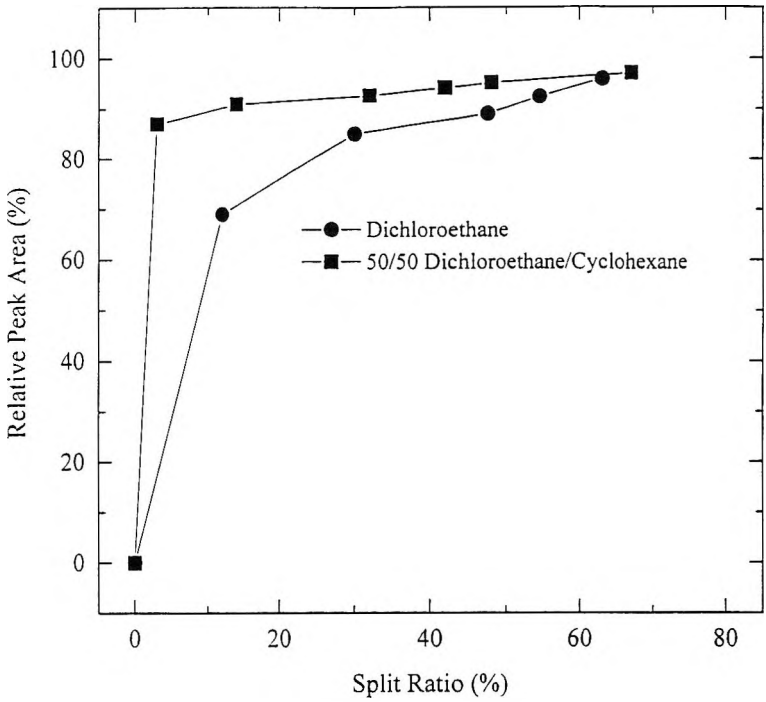

Figure 5. Plots of the relative amount of polymer eluting from the cold wall of an inverted channel as a function of the split ratio at that wall.

To confirm that the polymer does in fact move up to the cold wall in the inverted orientation, we split the outlet flow and quantified the amount of polymer eluting from the cold wall at several different split ratios. The results obtained in both a homogeneous carrier liquid (DCE) and a mixed carrier liquid (50/50 DCE/CYH) are illustrated in Figure 5. In a 50/50 (vol-%) mixture of DCE and CYH, 90% of the polymer is recovered by splitting only 15% of the carrier out the cold wall, indicating that the polymer is concentrated at that wall. In pure DCE, a larger split ratio is required to recover an equivalent amount of polymer because the mean layer thickness of the relaxed zone is greater, as indicated by a lower level of retention.

In the next series of experiments, we measured the partitioning of liquid mixtures after exposing them to a temperature gradient while they flowed through an inverted ThFFF channel. As we discuss above, measurements of the Soret coefficients are hindered by the dependence of solvent partitioning on flow rate. Accurate values of the Soret coefficients would require varying both

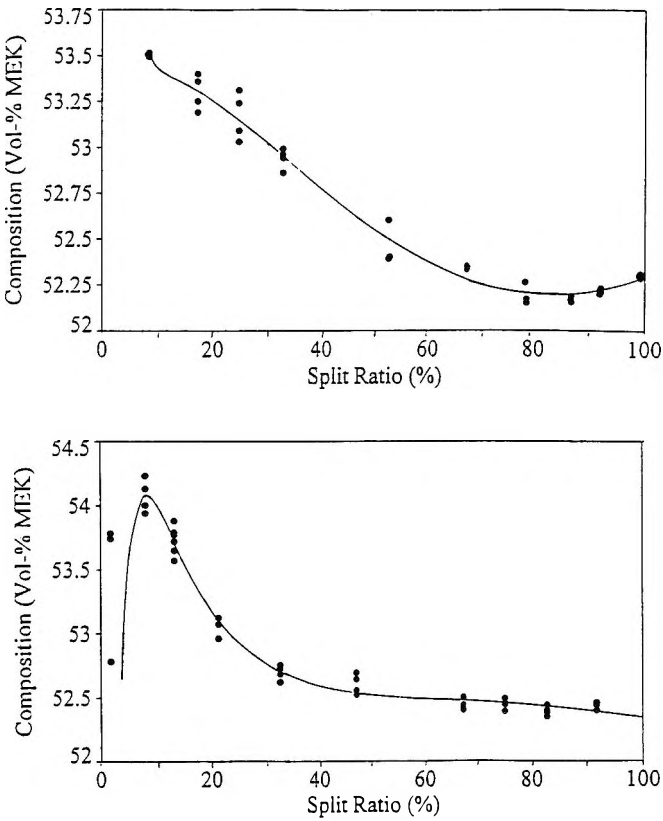

Figure 6. Measured concentration of MEK eluting from the outlets of an inverted channel as a function of the split ratio in mixtures of 52.4 vol-% MEK in CYH. The solid lines represent the best fit of the data using Tablecurve® software.

the split ratio and flow rate, so that multivariate regression methods could be used to obtain the solvent composition as both variables approach zero. Since the time required to produce such data would preclude the examination of several different liquids, while our primary objective is to compare partitioning in normal and inverted channel orientations, we opted to settle for qualitative information rather than take the time to measure precise values of the Soret coefficients.

Although the partitioning of several liquid mixtures was measured, we chose to focus on mixtures containing CYH because in the normal orientation this solvent proved to be an exception to the general trend of the denser solvent partitioning to the cold wall. Thus, CYH was enriched at the cold wall when

Table 1

Summary of the Partitioning of Binary Solvent Mixtures in an Inverted ThFFF Channel

		----- Hot Wall -----			----- Cold Wall -----		
Solvent Pair[a]	Component Enriched at Walls	Inlet Comp.[b,c]	Split Ratio[b] (%)	Wall Comp.[b,c]	Inlet Comp.[b,c]	Split Ratio[b] (%)	Wall Comp.[b,c]
DoD-CYH	DoD	50.9% DoD	2.4	53.5% DoD	50.4% DoD	2.5	51.1% DoD
EB-CYH	EB	50.0% EB	4.3	50.7% EB	49.8% EB	2.7	50.5% EB
BEN-CYH	BEN	51.0% BZ	3.1	51.3% BZ	51.1% BZ	2.9	51.6% BZ
MEK-CYH	MEK	49.4% MEK	1.4	51.1% MEK	48.9% MEK	2.7	50.8% MEK
CYH-THF	CYH	49.8% CYH	2.5	50.1% CYH	50.3% CYH	2.3	50.5% CYH
CYH-CCl_4	CYH	50.3% CYH	1.8	51.4% CYH	50.2% CYH	2.0	50.7% CYH
CYH-DCE	CYH	51.4% CYH	1.4	52.2% CYH	51.3% CYH	2.0	51.8% CYH
DoD-MEK	DoD	48.3% DoD	6.0	49.1% DoD	48.5% DoD	6.4	49.3% DoD
DoD-CCl_4	DoD	51.0% DoD	1.2	52.0% DoD	51.5% DoD	1.2	52.9% DoD
MEK-EtOH	MEK	48.8% MEK	2.0	50.3% MEK	48.8% MEK	2.0	49.8% MEK

[a] key: DCE, 1,2-dichloroethane; CYH, cyclohexane; EB, ethylbenzene; BZ, benzene; MEK, 2-butanone; THF, tetrahydrofuran; DoD, n-dodecane; EtOH, ethanol. [b] Standard error is 0.2%. [c] Compositions are in volume percent.

mixed with the denser liquids ethyl acetate, benzene (BZ), EB, and MEK.[16] Figure 6 contains plots of the outlet composition versus the split ratio at both walls for a mixture of 52.4 vol-% MEK in CYH using an inverted channel orientation. Unlike the results obtained with a normal channel orientation (see Figure 2), the partitioning profiles measured with an inverted orientation do not follow a simple exponential form. The solid lines in Figure 6 are the best-fit functions obtained from Tablecurve® (Jandell Scientific, San Rafael, CA, USA). The unusual profiles arise from the presence of convection currents in the channel. Convection currents plagued early studies of thermal diffusion in static cells and, in fact, play an integral role in the separation of polymers by the vertically-oriented Clusius-Duckel column.[19] However, for measuring Soret coefficients, convection is undesirable, and later studies of thermal diffusion indicated that convection currents could be avoided by the use of ultra-thin (<500 μm) cylindrical cells with high aspect ratios.

By sampling in the top-center of such cells, the potential existence of convective remixing near the edges was not a concern. However, in the ThFFF channel, convective remixing near the channel edges will be augmented in the tapered region of the channel near the exit ports. Although we did not measure the partitioning of MEK/CYH mixtures in detail with the normally oriented ThFFF channel, we did confirm that MEK is enriched at the hot wall and

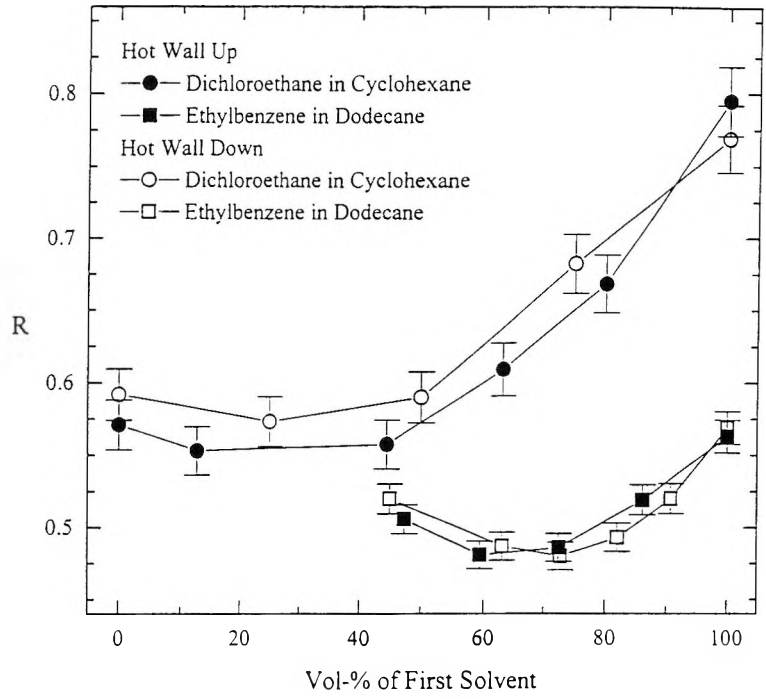

Figure 7. Retention ratio versus solvent composition in normal and inverted channel orientations, obtained with solvent mixtures that enhance retention. The polymer is 90,000 g-mol^{-1} polystyrene.

depleted at the cold wall. To determine whether the unusual behavior of MEK/CYH in an inverted channel is unique, we measured the partitioning of several other mixtures with the inverted orientation. The results are summarized in Table 1. The partitioning of each mixture represented in Table 1 was previously measured with the normal channel orientation. In each case, the solvent that is depleted from the cold wall in the normal orientation appears to be enriched at both walls in the inverted orientation.

If solvent partitioning in a ThFFF channel is truly different in the normal and inverted orientations, then the retention of polymers in mixed carrier liquids should be affected by channel orientation. This is not the case, however, as illustrated in Figure 7, which compares polystyrene retention as function of solvent composition in mixtures of DCE/CYH and EB/DoD using both channel orientations. In each mixture, the enhanced retention behavior is not affected by channel orientation. Thus, even though measurements indicate that the solvents partition differently depending on channel orientation, the

differences have little effect on polymer retention. Either polymer retention is unaffected by solvent partitioning, i.e., the partitioning effect is nonexistent, or convection currents are localized to the edges of the channel so that solvent partitioning in the bulk of the channel is unaffected by channel orientation. The latter explanation is supported by thermodynamic calculations, which indicate that even small amounts of solvent partitioning affect the free energy of the solution and, therefore, polymer retention should be affected as well. The dilemma may be solved by comparing solvent partitioning in different orientations with a static thermal diffusion cell. We are currently looking at sampling methods that will allow us to utilize a modified ThFFF channel for such measurements.

The effect of composition and channel orientation on retention in mixtures of MEK and CYH is illustrated in Figure 8. Also illustrated in Figure 8, is retention in mixtures of CYH and EB. In both cases, the better solvent partitions to the hot wall when the channel is oriented with the hot wall above the cold wall. Consistent with all solvent mixtures previously examined, retention is diminished in the CYH-EB system. In the CYH-MEK system, however, the dependence of retention on solvent composition takes a sigmoidal form. Of the 13 solvent mixtures that have been examined in this or previously published works,[15,16] CYH-MEK is the first mixture to exhibit such behavior.

Finally, we examine the effect of polymer concentration on retention. It is well known that polymer retention increases above that predicted by retention theory when the concentration of the injected polymer solution is above the critical concentration where chain entanglement occurs. In order to obtain consistent results, it is necessary to work with polymer solutions below the critical concentration. When analyzing a new sample, the concentration of the injected sample should be varied. If retention decreases with sample dilution, the sample should be further diluted until retention is no longer affected. The critical concentration increases with decreasing molecular weight, but for polystyrene, concentration effects are generally absent for molecular weights below 10^6 g-mol^{-1} when the injected concentration is below 3 mg/mL.

The proposed partitioning effect for enhanced retention of polymers in mixed solvents is based on the idea that solvent gradients act as a second force on the polymer due to differences in solvation energy. The solvation energy depends on the polymer concentration. Therefore, if the partitioning effect is valid, we can expect more pronounced concentration effects in mixed carrier liquids compared to homogeneous carriers. Figure 9 compares plots of retention versus polymer concentration in THF to similar plots in mixtures of THF and DoD. In both cases, the polymer is 90,000 g-mol^{-1} polystyrene and ΔT is 47 K. The concentration effect is clearly more pronounced in the mixed

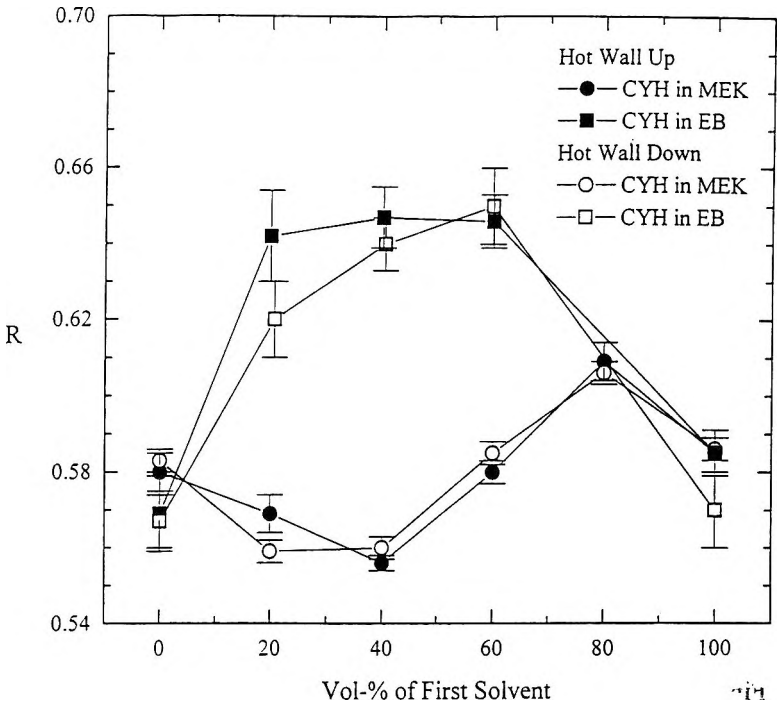

Figure 8. Retention ratio versus solvent composition in normal and inverted channel orientations, obtained with solvent mixtures in which the better solvent for the polymer partitions to the hot wall. The polymer is 90,000 g-mol^{-1} polystyrene.

solvent, with R decreasing by 10% between polymer concentrations of 1 and 10 mg/mL. In pure THF, retention decreases only 2.5% over the same concentration range. Furthermore, the concentration at which R-values level off is lower in the mixed solvent. These results further support the partitioning theory for enhanced polymer retention in mixed solvents. The results also indicate that concentration effects must be closely monitored in mixed solvents.

CONCLUSIONS

The purpose of this study was to determine whether channel orientation affects polymer retention while furthering our understanding of thermal diffusion. Regarding the latter purpose, our specific objective was to scrutinize the apparent role of density. As for the thermal diffusion of polymers, the fact

that polymer retention is not affected by channel orientation means that a separate density effect does not exist. The correlation of thermal diffusion to density must therefore be considered in the development of a working model for estimating D_T-values. Such a model is highly desirable because it will allow polymer retention to be predicted from fundamental physicochemical parameters of the polymer-solvent system.

Results from the measurement of solvent partitioning are less satisfying. In contrast to the study of thermal diffusion in polymers, it has become apparent that a ThFFF channel is not the ideal tool for measuring the Soret coefficients of liquids. Even qualitative information is difficult to obtain without ambiguity in an inverted channel, due to the presence of convection currents. However, the behavior of liquid mixtures is clearly different in channels with normal and inverted orientations. In the normal orientation, the denser solvent usually partitions to the cold wall, although cyclohexane mixtures are an exception. Furthermore, the solvent that is depleted from the cold wall in the normal orientation appears to partition to both walls when the channel is inverted. While this indicates the presence of convection currents, polymer retention is not affected by channel orientation. Taken together, these two results contradict the partitioning theory, which states that retention is enhanced or diminished in mixed solvents due to solubility-based forces that arise when solvents partition in a thermal gradient. However, we must consider that convection currents established in the inverted orientation are confined to the edges of the channel. Solvent partitioning in the bulk of the channel may not be affected by channel orientation, in which case the mechanism of thermal diffusion is similar in solvent mixtures and polymer solutions, and the partitioning theory remains a valid explanation for enhanced (or diminished) polymer retention in liquid mixtures.

It is worth noting that convection appears in the inverted channel with liquid mixtures regardless of which component partitions to the cold wall in the normal orientation. Thus, convection appears to be related to channel orientation rather than the relative densities of the two solvents in the mixture.

Although the retention of polymers can be enhanced by using solvent mixtures, retention is more sensitive to polymer concentration. The concentration effect can be expected to increase with molecular weight, and more study is required to establish the magnitude of this potential problem. In the meantime, users wishing to take advantage of the flexibility offered by mixed solvents must pay close attention to the concentration of injected samples. For molecular weight analysis, this means keeping concentrations small, and ensuring that retention levels remain constant when the concentration is varied.

ACKNOWLEDGMENT

This work is dedicated to the memory of the late J. Calvin Giddings, a good friend and excellent mentor. The work was funded by Grant CHE-9634195 from the National Science Foundation.

REFERENCES

1. J. C. Giddings, Science, **260**, 1456-1465 (1993).

2. M. E. Schimpf, Trends Polym. Sci., **4**, 114-121 (1996).

3. J. J. Gunderson, J. C. Giddings, Macromol., **19**, 2618-2621 (1986).

4. G. Liu, J. C. Giddings, Chromatographia, **34**, 483 (1992).

5. S. K. Ratanathanawongs, P. M. Shiundu, J. C. Giddings, Coll. Surf. A, **105**, 243-250 (1995).

6. J. J. Gunderson, J. C. Giddings, Anal. Chim. Acta, **189**, 1-15 (1986).

7. G. Stegeman, A. C. van Asten, J. C. Kraak, H. Poppe, R. Tijssen, Anal. Chem., **66**, 1147-1160 (1994).

8. J. C. Giddings, L. K. Smith, M. N. Myers, Anal. Chem., **47**, 2389-2394 (1975).

9. M. E. Schimpf, J. C. Giddings, Macromol., **20**, 1561 (1987).

10. M. E. Schimpf, J. C. Giddings, J. Polym. Sci., Polym. Phys. Ed., **27**, 1317 (1989).

11. J. J. Kirkland, W. Rementer, Anal. Chem., **64**, 904-913 (1992).

12. M. E. Schimpf, "Determination of Molecular Weight and Composition in Copolymers Using Thermal Field-Flow Fractionation Combined with Viscometry," in **Chromatographic Characterization of Polymers: Hyphenated and Multidimensional Techniques**, T. Provder, H. G. Barth, M. W. Urban, eds., American Chemical Society, Washington, D. C., 1995, Vol. 247, pp. 183-196.

13. M. N. Myers, K. D. Caldwell, Sepn. Sci., 9, 47-70 (1974).

14. J. J. Kirkland, L. S. Boone, W. W. yau, J. Chromatogr., **517**, 377-393 (1990).

15. R. M. Sisson, J. C. Giddings, Anal. Chem., **66**, 4043-4053 (1994).

16. C. A. Rue, M. E. Schimpf, Anal. Chem., **66**, 4054-4062 (1994).

17. J. E. Powers, in **Separation and Purification Methods**, E. S. Schoen, ed., Wiley-Interscience, New York, 1962, Vol. 1-98.

18. E. Von Halle, AEC Research and Development Report, K-1420 (1959).

19. P. Debye, A. M. Bueche, **High Polymer Physics**, Chemical Publishing Co., New York, 1948.

Received January 28, 1997
Accepted April 24, 1997
Manuscript 4452

J. LIQ. CHROM. & REL. TECHNOL., 20(16 & 17), 2723–2739 (1997)

EVALUATION OF A STANDARDLESS METHOD OF DETERMINATION OF MOLECULAR WEIGHT AND POLYDISPERSITY OF A POLYSTYRENE SAMPLE BY THERMAL FIELD-FLOW FRACTIONATION

Pierluigi Reschiglian,[1] Michel Martin,[2] Catia Contado,[3] Francesco Dondi[3]*

[1] Department of Chemistry "G. Ciamician"
University of Bologna
Via Selmi 2
40126 Bologna, Italy

[2] École Supérieure de Physique et Chimie Industrielles
Laboratoire de Physique et Mécanique des Milieux Hétérogènes
10 rue Vauquelin
75231 Paris Cedex 05, France

[3] Department of Chemistry
University of Ferrara
Via Borsari 46
44100 Ferrara, Italy

ABSTRACT

The possibility of an accurate determination of polymer molecular weight and polydispersity by thermal field-flow fractionation (ThFFF) retention measurements is here discussed with reference to the use of only physicochemical data of ordinary and thermal diffusivity, but without need of prior calibration of the ThFFF system.

Special emphasis is devoted to the check of linearity conditions of retention data determination, i.e., on the proper sample loading and thermal field strength to be chosen for unbiased polymer specifications determination. Different numerical methods of determining peak profile attributes (non - linear peak fitting procedures by Edgeworth-
Cramer series expansions, numerical integration, graphical determination) are compared. The approach is applied to a standard polystyrene sample, with ethylbenzene as polymer solvent and carrier liquid, as extensive physicochemical informations on this polymer-solvent system are available in the literature. In addition, it is shown that the combination of retention and plate height measurements provides an absolute and accurate method of determination of the thermal diffusion coefficient of the sample.

INTRODUCTION

The capability of the thermal field-flow fractionation (ThFFF) technique, which belongs to the family of field-flow fractionation (FFF) methods, for the determination of the molecular weight distribution (MWD) of a wide variety of organo-soluble polymers is generally recognized.[1] As compared to size-exclusion chromatography (SEC), ThFFF methods often exhibit higher separation selectivity for MWD determination.[2] For practical applications in the field of polymer characterization, the outstanding feature of ThFFF lies in the easy determination of polymer MWD from which average molecular weight (MW) and polymer polydispersity (μ) can be derived. Several methods have been suggested for these purposes. They are either based on calibration plots[3,4] or standardless methods through polymer/solvent constants.[5,6]

Giddings[7] critically considered the fundamentals of calibration and standardless method for MW determination in both SEC and ThFFF, emphasizing that ThFFF only needs physicochemical constants, but not "system" constants, such as the parameters of the calibration curve of the specific employed column, which are required in SEC. As noted by Giddings, "the calibration constants required in ThFFF are physicochemical constants describing ordinary and thermal diffusivities, which can be obtained from one thermal FFF system" or from other physicochemical measurements and "can thus be transferred to every thermal FFF system in the universe."[7] The significance of ThFFF for MW determination is thus enhanced and superior to

SEC. These appealing properties require careful experimental conditions be respected, e.g., that the experimental conditions under which the physicochemical data are employed be coherent with those under which they where originally derived.

In this paper, the standardless method of determining MW and polydispersity data, by using ordinary and thermal diffusivity data, is considered in reference to the proper check of the above mentioned experimental conditions — called here ideal conditions — which are, namely, the conditions of high dilution or the linearity conditions[8] and the control of the thermal field strength.

It is a necessary requirement that the ThFFF system behaves ideally for performing accurate ThFFF calibration-based measurements of complex samples of unknown physicochemical constants. Indeed, the standard retention equation in FFF[9] assumes especially that there are no interactions between sample molecules. This assumption is a necessary condition for a chromatographic process to be defined as linear.

It has been demonstrated that the Edgeworth-Cramér peak shape fitting methods[10,11] are able to check linearity conditions in stochastic processes with stationary and independent increments. These methods have been applied in chromatography,[11-13] sedimentation field-flow fractionation (SdFFF),[14] and, eventually, ThFFF.[8]

In the latter work, an experimental evaluation of nonlinearity effects on ThFFF retention was performed by means of a comparison made using different methods of estimating peak parameters (i.e., mean and standard deviation).

Necessary conditions for linearity (NCL) were verified by EC series fitting for the analysis of polystyrene (PS) standards in ethylbenzene (EB) and the results established practical rules for performing ThFFF measurements under conditions of linearity.

In the present work the reported experimental conditions for measurements under linear ThFFF elutions are chosen for the estimation of the accuracy of ThFFF for MW and μ evaluations without calibration. The polymer/solvent system (PS/EB) that was already used in the previous work has been chosen because of the extensive physicochemical characterization of this system in the literature. Correction for the departure from a parabolic flow profile due to the variation in viscosity with temperature[15] was also taken into account.

THEORY

Molecular Weight Determination

For most FFF systems for which the flow profile can be assumed to be parabolic, the retention ratio, R, is exactly related to the characteristic length of the analyte layer distribution, l, which, in the high retention limit, approximates, closely, the mean layer thickness of the migrating band, and to the channel thickness, *w*, as follows:

$$\lambda = \frac{l}{w} \tag{1}$$

$$R = 6\lambda\left[\coth(1/2\lambda) - 2\lambda\right] \tag{2}$$

Nonetheless, in ThFFF, the flow profile is distorted by the temperature gradient across the channel. Whatever the degree of retention, the retention ratio was then shown to be given as:

$$R = 6\lambda\nu\left(1 - R_p\right) + R_p \tag{3}$$

where the flow distortion parameter, ν, is a constant whose value is determined by the properties of the carrier, the cold wall temperature and the field strength.[15] R_p is here referred to as the standard retention ratio expressed by Eq. 2. By means of Eqs. 2 and 3, λ can be determined through numerical methods from experimental R data andν values.

For ThFFF, λ is given to a good approximation by:

$$\lambda = \frac{D}{D_T \Delta T} \tag{4}$$

where ΔT represents the temperature difference across the channel and D and D_T are the coefficients for ordinary and thermal diffusion, respectively.[16] The relationship between the ordinary diffusion coefficient, D, and the molecular weight, M, can be expressed by:[17]

$$D = \frac{A}{M^b} \tag{5}$$

where A and b are constants for the polymer/solvent system at a given temperature, and which have been previously reported for PS/EB.[5] As D_T does not show any significant dependence on M,[16] by substituting Eq. 5 into Eq. 4 and, with the experimental values of λ from experimental retention ratios R_p, one gets M as:[18]

$$M = \left(\frac{A}{\lambda D_T \Delta T} \right)^{1/b} \tag{6}$$

It should be noted that Eq. 3, like Eq. 2, is derived on the assumption of an exponential concentration distribution of the macromolecules along the temperature gradient. In fact, the dependencies of D and D_T on temperature leads to a distortion of the concentration profile from the exponential assumption. Similarly, the temperature dependence of the thermal conductivity of the carrier liquid modifies the effective temperature difference ΔT to be used in Eq. 4. Recently developed methods are available to take into account these effects.[19,20] Although they should improve the accuracy of the MW determinations, these effects are, in the present work, considered as of second-order, and are not taken into account.

Polydispersity Determination

In ThFFF, because of the rule of additivity of the variance, the total plate height H can be expressed as the sum of individual contributions arising from independent band broadening processes. For fractionation of narrowly disperse polymers in systems for which the instrumental contribution to band broadening can be assumed negligible, the main contribution is the nonequilibrium, H_n, term. For a polydisperse polymer there is an additional term due to the tendency of high MW species to move behind the lower MW sample components. The latter term is called polydispersity contribution, H_p. The experimentally observable plate height is thus:

$$H = H_p + H_n \tag{7}$$

The polydispersity contribution can be approximately expressed in terms of the mass-based selectivity, S_M, of the separation system as:[21]

$$H_p = L S_M^2 (\mu - 1) \tag{8}$$

where $\mu = \overline{M}_w / \overline{M}_n$ is the ratio of the weight average MW to number average MW.[22] The parameter S_M is the MW-based selectivity defined as:

$$S_M = \left|\frac{d\ln R}{d\ln M}\right| = \left|\frac{d\ln R}{d\ln \lambda} \cdot \frac{d\ln \lambda}{d\ln M}\right| \qquad (9)$$

In the above expression, the term $d\ln R / d\ln \lambda$, which depends on both λ and ν (see Eqs. 2 and 3) is nearly equal to 1 for highly retained samples. From Eqs. 4 and 5, it is seen that the term $d\ln \lambda / d\ln M$ is equal to -b since D_T is found to be independent of MW for most the homopolymers.[16] Since the nonequilibrium term H_n linearly depends upon the flow velocity, $<v>$, of the carrier, one gets:

$$H = H_p + C < v > \qquad (10)$$

For moderately polydispersed samples, μ can be obtained from the extrapolation at zero flow velocity of experimental total plate height H vs. linear flow velocity $<v>$ plots.[21] Furthermore, the ordinary diffusion coefficient D can be derived from the slope C as follows:

$$C = \chi w^2 / D \qquad (11)$$

provided that the dimensionless coefficient χ, which depends both on λ and ν,[23] is estimated with sufficient accuracy.

MATERIALS AND METHODS

Instrumentation

The ThFFF system used in this work was the model T100 ThFFF Polymer Fractionator (FFFractionation, LLC, Salt Lake City, UT, USA) already described in previous work.[8] The channel length, breadth and thickness were, respectively, 45.6 cm, 1.9 cm and 0.0139 cm.

The sample was a linear polystyrene standard obtained from Polymer Laboratories (Church Stretton, U.K.) with a nominal μ value of 1.04 and reported MW of 170,000. The carrier liquid and polymer solvent was extrapure ethylbenzene (EB03080, Fluka Chem., Buchs, Switzerland). The solutions of

Table 1

ThFFF-based Molecular Weight Determination of PS/EB Systems*

					EC			Integration			Graphic		
% w/v	T_c[2]	ΔT[2]	Flow[1]	ν	R	λ	MW	R	λ	MW	R	λ	MW
1	30	40	0.1	-0.135	0.356	0.0779	216,929	0.356	0.0779	217,181	0.348	0.0757	228,424
1	30	40	0.15	-0.135	0.386	0.0856	182,965	0.386	0.0856	183,069	0.376	0.0829	193,890
1	30	40	0.17	-0.135	0.363	0.0797	208,366	0.363	0.0797	208,244	0.356	0.0778	217,700
1	30	40	0.2	-0.135	0.377	0.0832	192,671	0.371	0.0818	198,639	0.374	0.0824	196,245
1	30	40	0.25	-0.135	0.370	0.0815	199,908	0.370	0.0815	200,140	0.363	0.0795	209,226
1	28	35	0.2	-0.122	0.420	0.0937	197,889	0.420	0.0937	197,784	0.416	0.0926	202,287
1	31	45	0.2	-0.148	0.345	0.0759	183,970	0.344	0.0758	184,195	0.340	0.0746	189,698
1	33	50	0.2	-0.160	0.317	0.0697	177,327	0.317	0.0696	177,789	0.314	0.0689	181,066
0.5	31	45	0.2	-0.148	0.361	0.0800	166,946	0.352	0.0778	175,916	0.352	0.0778	175,916
0.5	30	40	0.2	-0.135	0.394	0.0877	175,250	0.394	0.0877	174,959	0.382	0.0847	186,515
							MW=190,222±15,723			MW=191,792±14,655			MW=198,097±16,510

* PS sample MW=170,000; [1] Flow rate values are expressed in mL/min; [2] T_c and ΔT values are expressed in °C.

Table 2

Polydispersity, Molecular Weight, and Thermal Diffusion Coefficient Evaluation From Plate Height Measurements[a]

Flow[1]	Graphic H^2	Integration H^2	EC H^2
0.10	0.33	0.37	0.35
0.15	0.46	0.48	0.51
0.17	0.47	0.48	0.47
0.20	0.62	0.59	0.58
0.25	0.69	0.75	0.72
	H_p=0.0890±0.0491[2]	H_p=0.0996±0.0532[2]	H_p=0.111±0.059[2]
	μ=1.0089±0.0049	μ=1.0101±0.0054	μ=1.0112±0.0059
	r=0.982[3]	r=0.980[3]	r=0.974[3]
	D=2.800[4]	D=2.863[4]	D=3.008[4]
	D_T=0.879[5]	D_T=0.881[5]	D_T=0.922[5]
	MW=240,049[6]	MW=230,596[6]	MW=210,911[6]

[a] Sample 170,000 MW PS, 1% w/v sample load, ΔT =30°C, nominal μ=1.04;
[1] Flow values are expressed in mL/min; [2] H values are expressed in cm;
[3] r correlation coefficient; [4] *D* values determined by Eq. 11 and expressed in 10^7 cm^2s^{-1}; [5] D_T values computed by Eq. 14 and expressed in 10^7 $cm^2s^{-1}K^{-1}$;
[6] MW values obtained by Eq. 6 and Eq. 13.

polymer samples were injected by means of an injector with a 20μL loop (Rheodyne, model 7125) and relaxed as described in Ref. 8. A model 420 HPLC pump (Kontron Instruments S.p.A., Milan, Italy) was used to supply carrier flow. Peak detection was achieved with a model R410 Refractive Index Detector (Waters Associates, Milford, MA, USA). The void volume was determined, as described in Ref. 8, by injecting tetrahydrofuran 8441 for UV (J. T. Baker, Deventer, The Netherlands) as an unretained probe.

Computational

Data collection from the ThFFF system was driven by a software package from FFFractionation Inc. The routine also included a Savitzky-Golay smoothing procedure by which digitized raw fractograms were filtered. The EC series least-squares fitting routine described in Ref. 8 also included the

computation of first peak moments by integration. The retention and plate height data (R, H) reported in Table 1 and Table 2 for various experimental conditions. Plate height values H were calculated from peak variance according to the definition of plate height in chromatography and related techniques as:

$$H = L\left(\frac{\sigma}{t_r}\right)^2 \tag{12}$$

where L is the channel length, t_r the retention time and σ the peak standard deviation.

There are three methods for estimating these data: a) from the experimental fractograms; b) from the computation of the first and second moments of the digitized peaks; c) from the EC-series least-squares fit of the peaks, which, among others, provides t_r and σ as parameters. In Tables 1 and 2, methods a), b) and c) are, respectively, referred to as "graphic," "integration," and "EC." Note that, in methods b) and c), t_r corresponds to peak mean retention time. In method a), which is based on simple measurements from the paper record of the fractogram, t_r is taken as the elution time of the peak maximum and σ is determined from the measurement of the peak width at half-height, $b_{0.5}$, as $\sigma = 0.425\ b_{0.5}$.

Experimental void volume and retention volumes were both corrected for the external dead volume. Indeed, because of the relatively large value of the external dead volume, resulting corrections on retention volumes are not negligible for accurate MW and μ determinations without calibration.

RESULTS AND DISCUSSION

The onset of nonlinear conditions in ThFFF has been shown to be detectable by the EC procedure even at very modest concentrations.[8] Under nonlinear elution conditions, it has been therein reported that modest increases in sample polymer load result in shifts toward higher retention volumes as well as in some additional peak broadening. Therefore, molecular weight and polydispersity determinations, which are based on peak mean and standard deviation, can be significantly affected by concentration effects. EC series fitting experiments have proved highly accurate in monitoring any peak shape difference, even for almost Gaussian profiles, by defining some convenient nonlinearity markers. The accuracy of MW and μ determinations relies on the

accuracy with which retention and plate height, that is, peak mean retention time and standard deviation, can be determined. In common FFF practice, peak mean and standard deviation are measured either by a graphical approach or by integration. The EC method applied to FFF was shown to provide, not only accurate values of peak moments, but also practical rules to identify linear conditions for the elution of PS/EB systems by ThFFF.[8]

Concentration effects in thermal FFF arise from several origins. First, increasing the sample concentration, one increases the viscosity of the polymer solution in the vicinity of the accumulation wall, which tends to increase retention. Furthermore, this may lead to partial and temporary entanglement of polymeric chains, and again to increase retention as one expects two entangled chains to behave as a macromolecule of larger molar mass. On the other side, it is much likely that the gradient diffusion coefficient (which is the relevant diffusion coefficient in FFF) of polystyrene increases with increasing concentrations in ethylbenzene as it does in toluene.[24] This should result in a decreased retention (see Equation 4). The former effects are observed to be dominating the latter, in the case of polymer solutions, in contradiction with what is predicted for a hard sphere model[25] and observed for rigid particles.[26]

In this work EC fitting, graphical and integration methods are compared with respect to the level of accuracy in MW and μ determination. Specifically, the same PS sample and the same solvent (EB) that were previously used for the referred EC studies on linearity conditions are here employed. In Table 1 are reported the ThFFF-based determination for PS 170,000 MW in EB under different experimental settings for which linearity conditions for physicochemical measurements were considered as satisfyingly fulfilled.[8] The results of EC peak shape fitting, integration and graphical methods are compared. The MW values are calculated according to Eqs. 3 and 6 by taking peak means for the EC and integration methods, and peak maxima for the graphic method. The values of the A, b, and D_T constants were taken, respectively, as 2.613×10^{-4}, 0.552 and 0.95×10^{-7} (in CGS units with MW expressed in $gmol^{-1}$), as reported in the literature for PS/EB.[5] The ν parameter to be used in Eq. 3, accounting for the departure from a parabolic flow profile, was calculated using the procedure described in Ref. 15, which takes into account the viscosity and thermal conductivity dependencies with temperature.

It is noticeable, from Table 1, that all MW values obtained by the graphic method are larger than those obtained by the EC method, which, themselves, are generally close to those obtained by the integration method. This is due the fact that the peaks are somewhat fronting and that the peak mean times are slightly smaller than the peak maxima times as reflected by the slightly negative values of the peak skews as noted previously.[8] The first part of Table

1 reports data which were obtained in the same concentration and ΔT conditions, but at different flow rates. No systematic influence of the flow rate on retention, and, thus on MW, is apparent. The relative standard deviation of these MW values is similar for the three methods (between 6 and 7%) and appears, thus, to be some indication of the reproducibility of MW determination from ThFFF retention measurements, at least under the present experimental conditions.

This value is, however, smaller than the standard deviation of all data for PS 170,000 reported in Table 1, for which the mean molecular weight value is 14% higher than the nominal value. The difference between the overall standard deviation and that of the first part of Table 1 appears to arise from a rather distinct trend of evolution toward lower MW values on increasing ΔT. Indeed, the MW values obtained from the EC method at the flow rate of 0.2 mL/min and concentration of 1% w/v are: 197,890; 192,670; 183,970; and 177,330 for ΔT = 35°C; 40°C; 45°C; and 50°C, respectively. These data fit well the linear regression: MW = 247,783 - 1407 ΔT, with correlation coefficient r = 0.9957. In fact, this trend would be made more stronger if the data (λ = 0.06374, estimated MW=149,750) for ΔT = 60°C, which has been excluded from Table 1 because the EC series fitting pattern indicated a highly pronounced nonlinear behavior in that case, was added. Indeed, the intercept and negative slope of the regression would be both significantly increased (MW = 268,708 - 1921 ΔT) and the correlation coefficient worsened (r = 0.9815). This reinforces the warning of nonlinearity derived from the EC-series peak shape fitting analysis[8] and, again, indicates that data points for ΔT larger than 50°C are outliers.

Nevertheless, the systematic variation of the MW values obtained from Eqs. 3 and 6 with ΔT suggests that the influence of temperature on D and D_T, hence on the values of the constants A, b, and D_T involved in Eq. 6, should be taken into account, a topic far beyond the aims of the present treatment.

Although one cannot rule out that part of the differences between the nominal MW value and the experimentally determined data are due to inaccurate nominal specification, one may test whether the observed disagreement could be ascribed to systematic errors in retention parameter evaluation or to the effect of errors on instrumental and experimental variables. For this purpose, a plate height H vs. $\langle v \rangle$ study was performed, not only for polydispersity evaluations, but also for MW determinations. Indeed, according to Eqs. 5 and 11, M can be obtained from the diffusion coefficient derived from the slope of the plate height curve as:

$$M = \left(\frac{A\,C}{\chi\, w^2} \right)^{1/b} \qquad (13)$$

A comparison between the different methods employed for the determination of the peak parameters (t_r, σ), through which H can be evaluated, is reported in Table 2. Plate height values were measured for PS 170,000 at different flow rates and for the experimental conditions that were considered by EC fitting analysis as linear (1% w/v sample load, ΔT = 30°C field strength).[8] In Figure 1, the linear regressions of H vs. linear flow velocity $\langle v \rangle$ data are plotted. Data reported in Table 2 show MW values that are even larger than those determined through v-corrected λ values, which were discussed above and reported in Table 1.

The disagreement between MW data in Table 2 and the nominal value (170,000) is on the average 34% while the difference between MW data calculated from corrected retentions (see Table 1) was ca. 14%. Therefore, the difference between the two proposed methods of evaluation of MW is around 17% (but only 11% for the EC method). The discrepancy is not too dramatic if one notes that plate height measurements are generally less reproducible than retention measurement and, if one takes into account the effects that different experimental variables have on the accuracy, with which the slope of the H vs. $\langle v \rangle$ plot (by which D is derived) can be evaluated. In fact, if one supposes, for instance, an error of 3% on the measurement of the channel thickness, this indeterminacy translates into a possible error of 11% on MW through the slope of an H vs. $\langle v \rangle$ plot (see Eq. 13). Furthermore, the nonequilibrium coefficient C in Eq. 13 is highly sensitive to small variations of λ and, thus, of t_r.[23]

On the other hand, as the ratio of the thermal diffusion coefficient to the ordinary diffusion coefficient can be obtained from retention measurements and the latter from plate height determinations, this gives the possibility to determine the thermal diffusion coefficient only from ThFFF experiments. Indeed, from Eqs. 4 and 11, one gets:

$$D_T = \frac{\chi\, w^2}{\lambda\, C\, \Delta T} \qquad (14)$$

It is worth noting that thermal diffusion coefficient values D_T, determined through Eq. 14, are relatively close to the most recent published value[5] of 0.95×10^{-7} $cm^2 s^{-1} K^{-1}$ which was also employed for the MW values determined from the retention ratio values discussed above and reported in Table 1. The

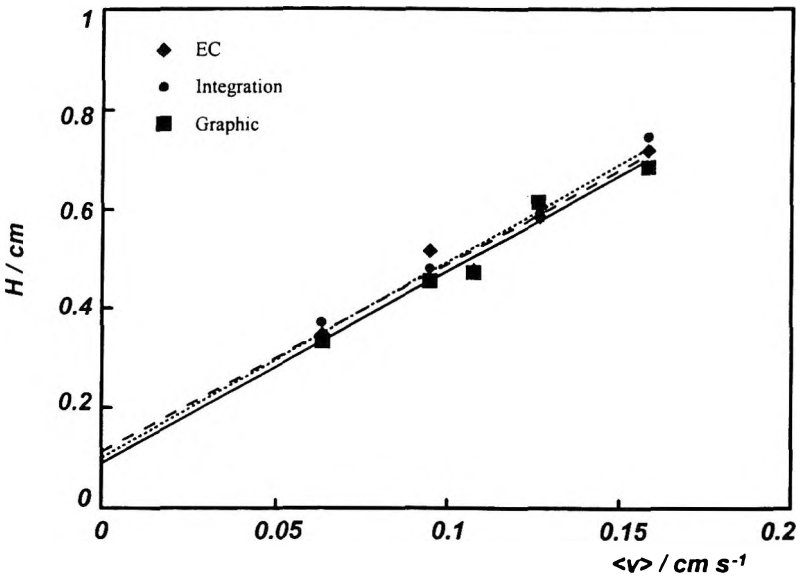

Figure 1. Polydispersity determination by linear regressions of H vs. linear flow velocity <v>; 170,000 MW PS sample. EC, Integration, Graphic corresponds to the different procedure of peak width determination (see text).

difference between the mean D_T for the three methods in Table 2 and this reference value is about 6% (it is only 3% for D_T obtained from the EC method). This finding does not contradict the previous observation of a large error on MW data from D values. Indeed, the effect of a channel thickness error on the accuracy for D_T is, for instance, smaller than the error reflected into a MW determination because of the different physical dependencies of M and D_T on the channel thickness as seen in Eqs. 13 and 14. Furthermore, the χ/λratio in Eq. 14 is less sensitive than χ in Eq. 13 to an error in t_r. Thermal diffusion coefficients have, thus far, never been determined by means of the method described here. The main advantage of the present approach lies in the fact that it does not require a separate, *à priori* knowledge of D. Altogether, this last finding enhances, *à posteriori*, the validity of the third-degree velocity profile approach for extracting physicochemical information on polymer by ThFFF.

Sample polydispersity was determined from plate height contribution H_p as expressed in Eq. 8; selectivity was derived according to Eq. 9 for the b value reported above for MW determinations and indicated in the literature for PS/EB

systems at the ΔT employed in these experiments.[5] The values of $d\ln R/d\ln\lambda$ in Eq. 9, corrected for the ν term accounting for the third-degree velocity profile, were computed according to the method reported in the literature (Eq. 41, Ref. 27). The resulting μ values are reported in Table 2 with their standard deviations. They appear to be much closer to unity than the nominal value.

This is not surprising. Indeed, it was already noted that very good agreement between the ThFFF-based and the nominal μ values of polymers of narrow polydispersity index, as those in Table 2, can hardly be reported since SEC, one of the most common methods thus far applied for giving nominal specifications of such polymer samples, is a technique of limited accuracy.[21] It, therefore, appears that ThFFF, by far, surpasses the possibilities of existing methods in this regard, and must be considered as a unique method of determination of polydispersity index values very close to one.

CONCLUSIONS

The molecular weight and polydispersity value of a polymer standard are evaluated, without previous calibration, from retention time parameters and polymer physicochemical constants under the necessary conditions for linearity previously determined in ThFFF by EC peak shape fitting analysis. Molecular weight determinations have been performed through retention parameters obtained by the EC method itself.

Results were compared tc molecular weight and polydispersity values obtained either by integration or graphical analysis. All the proposed methods have proved to be comparable within the commonly accepted experimental error; in fact, with respect to the EC method, no differences higher than 5% have been found using either the integration method or graphical analysis.

However, with respect to the conventional methods, EC peak shape fitting had also allowed for the detection of the best experimental set-up for ThFFF elution under conditions for linearity, which are known to be necessary for unbiased ThFFF measurements of polymer physicochemical properties.

Within such conditions, standardless and relatively accurate ThFFF-based determinations of MW and μ have proved to be possible for narrowly dispersed polymer standards, provided the values of the constants to be entered in the D vs. MW relationship for the given polymer/solvent system are available and that correction for the third-degree velocity profile is performed.

Once optimized conditions for unbiased measurements are found with standard systems, they can be eventually applied to the conventional calibration procedures commonly employed in ThFFF characterization of more complex polymer/solvent systems.

ACKNOWLEDGMENTS

The authors are grateful to Enichem S.p.A. for having made available the complete ThFFF apparatus for the data presented in this work and for having supported in part this work. Jamel Belgaied, presently with Institut National des Sciences Appliquées et de Technologie de Tunis (Tunisia) is acknowledged for performing the required ν calculations.

REFERENCES

1. H. G. Barth, R. B. Flippen, Anal. Chem., **67**, 257R-272R (1995).

2. J. C. Giddings, "Field-Flow Fractionation: an Alternative to Size Exclusion Chromatography," in **Size Exclusion Chromatography**, B. J. Hunt, S. R. Holding, eds., Blackie and Son, Glasgow, 1989, pp. 191-216.

3. J. J. Kirkland, W. W. Yau, Macromolecules, **18**, 2305-2311 (1985).

4. J. J. Kirkland, S. W. Rementer, W. W. Yau, Anal. Chem., **68**, 610-616 (1988).

5. M. E. Schimpf, J. C. Giddings, J. Polymer Sci., Polym. Phys. Ed., **27**, 1317-1332 (1989).

6. J. J. Kirkland, S. W. Rementer, Anal. Chem., **64**, 904-913 (1992).

7. J. C. Giddings, Anal.Chem., **66**, 2783-2787 (1994).

8. P. Reschiglian, M. Martin, C. Contado, F. Dondi, Int. J. Polym. Anal. & Charact., in press.

9. J. C. Giddings, **Unified Separation Science**, John Wiley & Sons, Inc., New York, 1991, Chapter 7.

10. F. Dondi, G. Blo, M. Remelli, P. Reschiglian, "Stochastic Theory of Chromatography. The Characteristic Function Method and the Approximation of Chromatographic Peak Shape," in **Theroretical Advancements in Chromatography and Related Separation Techniques**, F. Dondi, G. Guiochon, eds., NATO ASI Series, Kluwer Academic, Dordrecht, The Netherlands, 1992, pp. 173-210.

11. F. Dondi, A. Betti, G. Blo, C. Bighi, Anal. Chem., **53**, 496-504 (1981).

12. F. Dondi, F. Pulidori, J. Chromatogr., **284**, 293-301 (1984).

13. G. Blo, M. Remelli, F. Pedrielli, L. Balconi, F. Sigon, F. Dondi, J. Chromatogr., **556**, 249-262 (1991).

14. P. Reschiglian, G. Blo, F. Dondi, Anal. Chem., **63**, 120-130 (1991).

15. J. Belgaied, M. Hoyos, M. Martin, J. Chromatogr. A, **678**, 85-96 (1994).

16. J. C. Giddings, K. D. Caldwell, M. N. Myers, Macromolecules, **9**, 106-112 (1976).

17. M. E. Schimpf, J. C. Giddings, Macromolecules, **20**, 1561-1563 (1987).

18. M. Martin, R. Reynaud, Anal. Chem., **52**, 2293-2298 (1980).

19. A. C. van Asten, H. F. M. Boelens, W. Th. Kok, H. Poppe, P. S. Williams, J. C. Giddings, Sepn. Sci. Technol., **29**, 513-533 (1994).

20. M. Martin, C. Van Batten, M. Hoyos, Anal. Chem. submitted.

21. M. E. Schimpf, M. N. Myers, J. C. Giddings, J. Appl. Polym. Sci., **33**, 117-135 (1987).

22. F. W. Billmeyer Jr., **Textbook of Polymer Science**, 3rd ed., Wiley-Interscience, New York, 1984, Chapter I.

23. M. Martin, J. C. Giddings, J. Phys. Chem., **85**, 727-733 (1981).

24. B. Rauch, G. Meyerhoff, Z. Phys. Chem., **65**, 1-12 (1969).

25. M. Hoyos, M. Martin, Anal. Chem., **66**, 1718-1730 (1994).

26. M. Hansen, J. C. Giddings, R. Beckett, J. Colloid Interface Sci., **132**, 300-332 (1989).

27. J. C. Giddings, M. Martin, M. N. Myers, Sepn. Sci. Technol., **14**, 611-643 (1979).

Received January 22, 1997
Accepted April 16, 1997
Manuscript 4449

J. LIQ. CHROM. & REL. TECHNOL., 20(16 & 17), 2741–2756 (1997)

RETENTION BEHAVIOR OF COPOLYMERS IN THERMAL FIELD-FLOW FRACTIONATION AND GEL PERMEATION CHROMATOGRAPHY

Kyung-Ho Cho, Young Hun Park, Sun Joo Jeon,
Won-Suk Kim, Dai Woon Lee*

Department of Chemistry
Yonsei University
Seoul 120-749, Korea

ABSTRACT

Retention behavior of polystyrene copolymers having different structures and compositions was investigated for measuring thermal diffusion coefficient (D_T) using thermal field-flow fractionation (ThFFF). Samples were random poly(styrene-co-methylmethacrylate)s, poly(styrene-co-isoprene) block copolymers having molecular weights ranging from 10^4 to 10^5. It was found that the ThFFF retention of copolymers is related to the composition as well as the molecular size of copolymers. For random copolymers, D_T was a linear function of the monomer composition, and it was possible to determine the molecular weight of polymers by use of calibration curve of log(wt % $M[\eta]$) versus log(D/D_T). For block copolymers, D_T values of diblock copolymers were greater than those of triblock. It was found that the thermal diffusion varies with the copolymer structure as well as the composition.

INTRODUCTION

Various methods, including reversed phase chromatography (RPC), affinity chromatography, gel permeation chromatography (GPC), electrophoresis, and field-flow fractionation (FFF)[1] have been used to separate and characterize macromolecules.

Among those, FFF is a relatively new method. FFF is an elution method suited for high resolution separation of macromolecules[2,3] and various colloidal particles.[4,5] In FFF, differential retention (thus separation) is obtained by applying a perpendicular field across a thin ribbon-shaped flow channel within which the separation takes place.[6] The external field forces different components into the different stream laminae of the near parabolic flow, causes differential migration, which is followed by elution of the separated components into a detector.

As one of subtechniques of FFF, thermal field flow fractionation (ThFFF) is useful for analysis of various synthetic polymers.[7-9] ThFFF uses a temperature gradient established in a channel confined between two parallel plates, hot wall and cold wall, held at different temperatures. Under the temperature gradient, solute molecules are driven toward the channel wall by thermal diffusion process. Accumulation of solute is counteracted by ordinary diffusion of molecules and a steady-state layer is eventually established near the channel wall.

The distribution of molecules in the steady-state layer is of an exponential form. The layer thickness is expressed in a dimensionless form, $\lambda = \ell / w$, where ℓ is the effective thickness of the layer and w is the channel thickness. In FFF, retention ratio, R is defined as the channel void volume (V_0) divided by the observed retention volume (V_r) and is generally given by

$$R = \frac{V_0}{V_r} = 6\lambda\left[\coth\left(\frac{1}{2\lambda}\right) - 2\lambda\right] \qquad (1)$$

In ThFFF, eqn. (1) needs to be modified to account for the asymmetry of the channel flow caused by the temperature gradient and attendant viscosity change across the channel, which results in

$$R = \frac{1}{\sum_{i=1}^{5}\frac{h_i}{(i+1)}}\left\{\frac{1}{(1-e^{1/\lambda})}\left[\sum_{i=1}^{5} h_i \sum_{j=0}^{i-1}\frac{i!}{(i-j)!}\lambda^j\right] + \sum_{i=1}^{5} i!\, h_i \lambda^i\right\} \qquad (2)$$

Table 1

Characteristics of Polymers Used in This Study

Polymer		M_w	μ[a]	Weight %	Arrangement	Supplier
PS	1	28,600[b]	1.03	100	Linear	Shodex
	2	66,400[b]	1.03	100	"	
	3	156,000[b]	1.03	100	"	
	4	455,600[b]	1.04	100	"	
PI	1	252,000[b]	1.05	---	"	Polyscience, Inc.
	2	500,000[b]	1.10	---	"	
PMMA	1	27,000	$\leq$ 1.10	---	"	Polymer Labs,
	2	60,000	$\leq$ 1.10	---	"	Ltd.
	3	107,000	$\leq$ 1.10	---	"	
	4	185,000	$\leq$ 1.10	---	"	
	5	330,000	$\leq$ 1.10	---	"	
	6	590,000	$\leq$ 1.10	---	"	
	7	845,000	$\leq$ 1.10	---	"	
p(SI)	1	123,000[c]	1.04	26(35)	Linear, Diblock	Pohang Univ. of
	2	140,000[c]	1.07	49(60)	"	Sci. & Tech.
	3	228,000[c]	1.08	66(75)	"	
p(SIS)	1	79,000	1.03	31(41)	Linear, Triblock	Pohang Univ. of
	2	39,000[c]	1.03	50(60)	"	Sci. & Tech.
	3	78,000[c]	1.04	59(69)	"	
	4	52,000[c]	1.03	72(80)	"	
p(SM)	1	369,000[d]	1.9	29(30)[e]	Linear, Random	Pohang Univ. of
	2	116,000[d]	2.2	48(49)[e]	"	
	3	188,000[d]	3.0	49(50)[e]	"	
	4	108,000[d]	1.7	66(67)[e]	"	

[a] Polydispersity, $\mu = M_w/M_n$; [b] GPC results in THF; [c] Light scattering results; [d] GPC results in $CHCl_3$; [e] Measured by NMR.

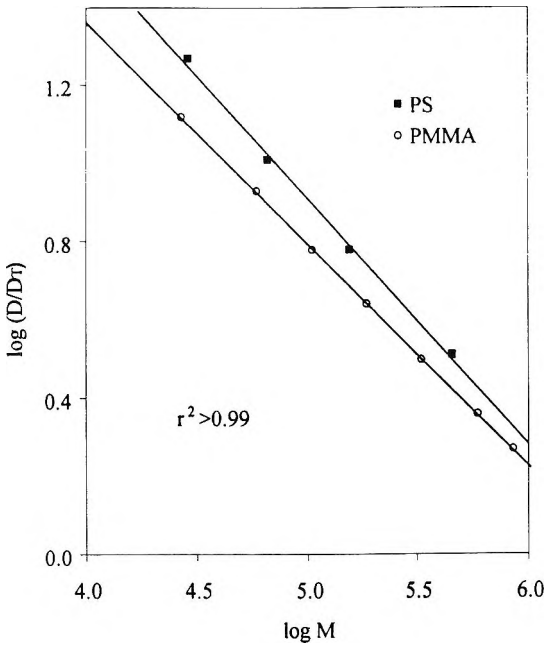

Figure 1. Plot of log (D/D_T) vs. log M for homopolymers.

where the hi's are composite constants(dependent on a_0-a_3, k, and dk/dT) reflecting the positional dependence of the viscosity and temperature gradient.[10] As those constants are different for different solvents, they must be obtained for the solvent used in the ThFFF experiment.

It is one of merits of FFF that retention is directly related to physicochemical parameters of solutes. In ThFFF, λ is given by

$$\lambda = \frac{D}{wD_T(dT/dx)} \cong \frac{D}{D_T \cdot \Delta T} \qquad (3)$$

where dT/dx is the temperature gradient across the channel, and D the diffusion coefficient and D_T the thermal diffusion coefficient for the given polymer-carrier combination. Thus the solute retention parameter λ depends on both D and D_T , and the ratio of the two coefficients is the determining factor for the solute retention. At infinite dilution, the diffusion coefficient D is related to the intrinsic viscosity,$[\eta]$ by[11]

Table 2

Molecular Weights and Intrinsic Viscosities of Copolymers

Polymer		M_w Reported[a]	M_w PS Std. Cal.[b]	Intrinsic Viscosity[c] (dL/g)
p(SI)	1	123,000	44,000	0.07
	2	140,000	96,000	0.16
	3	228,000	226,000	0.82
p(SIS)	1	79,000	54,500	0.47
	2	39,000	22,900	0.38
	3	78,000	78,800	0.33
	4	52,000	56,300	0.24
p(SM)	1	369,000	113,000	0.79
	2	116,000	198,000	0.39
	3	188,000	176,000	0.53
	4	108,000	111,000	0.40

[a] Same as Table 1; [b] Molecular Weight of copolymers measured by PS standard calibration; [c] Measured at 30°C.

$$D = \frac{RT}{6\pi\eta N}\left(\frac{10\pi N}{3M[\eta]}\right)^{1/3} \qquad (4)$$

where R is the gas constant, T temperature, η the carrier viscosity, M polymer molecular weight, and N Avogadro's number, and $[\eta]$ intrinsic viscosity. Eqn. (4) shows that D is a function of the product $M[\eta]$ which is a measure of the hydrodynamic volume of polymer. Once λ and D are determined, D_T can be obtained using eqn. (3). Unlike in ThFFF, separation in GPC is obtained based on the hydrodynamic volume (or D) alone.

As seen in eqns. (1) and (3), thermal diffusion coefficient D_T is an important parameter for the understanding of solute retention in ThFFF. Only a limited number of studies have been reported on the thermal diffusion phenomenon in ThFFF.[12-14]

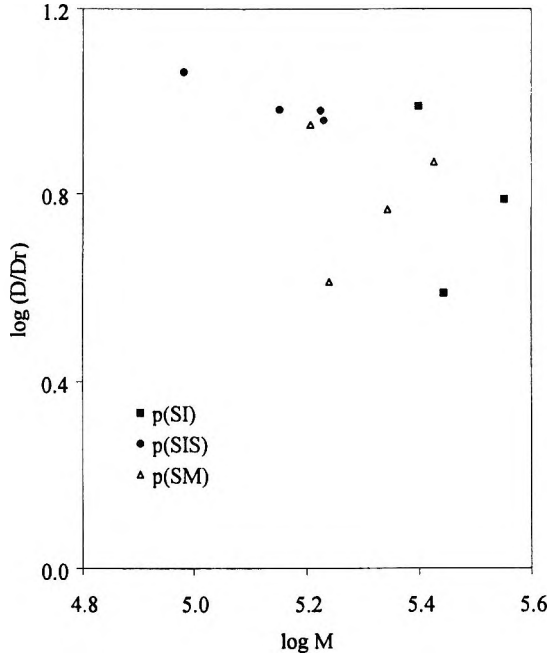

Figure 2. Plot of log (D/D_T) vs. log M for various copolymers.

In 1990, Schimpf et al.[15] used copolymers to study the effect of bonding arrangement and the shape of copolymer on the thermal diffusion coefficient. Jeon et al.[16] studied the variation of D_T with copolymer composition in ThFFF system. In this work, D_T of copolymers is studied using copolymers of various compositions and structures. ThFFF results are compared to those obtained from GPC.

MATERIALS AND METHODS

Thermal Field-Flow Fractionation (ThFFF)

ThFFF system used in this study is a model T100 polymer fractionator from FFFractionation, LLC (Salt Lake City, UT). The channel is 0.0127 cm thick, 1.9 cm wide, and the tip-to-tip length is 45.6 cm. The channel void volume (V_0) was measured to be 1.03 mL from injection of methanol.

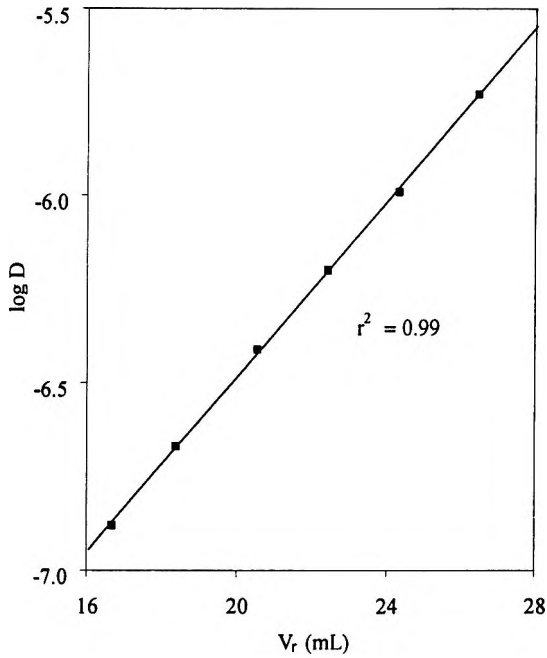

Figure 3. GPC Calibration curve of PS for determination of diffusion coefficient (D) of polymers.

A flow restrictor (Spectra-physics, San Jose, CA) was used to reduce the pulse from the pump. A model 6000A pump (Waters Associates, Milford, MA) was used for solvent delivery. An R401 Refractive Index detector (Waters Associates, Milford, MA) was used to monitor the sample elution and a Bromma 2210 recorder was used to display detector response.

Results were collected and processed using the data analysis software version 2.0 from FFFractionation, LLC. Flow rate was measured with a stopwatch and a buret.

Gel Permeation Chromatography (GPC)

Three μ-styragel GPC columns (7.8 x 300 mm, Waters Associates, Milford, MA) having pore sizes of 10^3, 10^4, and 10^5 Å were used.

Table 3

ThFFF Retention Data of Various Copolymers in THF

Polymer		PS (mol %)	V_r[a] (mL)	R	λ
p(SI)	1	26	1.34	0.77	0.25
	2	49	1.69	0.61	0.16
	3	66	2.34	0.44	0.10
p(SIS)	1	31	1.35	0.76	0.24
	2	50	1.34	0.77	0.25
	3	59	1.38	0.75	0.23
	4	72	1.26	0.82	0.29
p(SM)	1	29	1.94[b]	0.53	0.17
	2	48	1.39[b]	0.74	0.30
	3	49	2.30[b]	0.45	0.13
	4	66	1.18[b]	0.84	0.45

[a] Calculated from the peak maximum; [b] Calculated from the center of gravity of the peak.

Samples and Experimental Conditions

The cold wall temperature was kept at 30-32°C. The temperature difference, ΔT was varied from 20 to 60°C. Carrier solvent was tetrahydrofuran (THF, Burdick and Jackson, Muskegon, MI). Flow rate of carrier solvent was between 0.08 to 0.34 mL/min. Following the injection, carrier flow was stopped for 1min. for sample relaxation. Samples were random poly(styrene-co-methylmethacrylate) (p(SM)), diblock poly(styrene-co-isoprene) (p(SI)), and triblock poly(styrene-co-isoprene-co-styrene) (p(SIS)) copolymers ranging from 10^4 to 10^5 molecular weight. All their shapes are linear. NMR was used to determine the composition of p(SM) random copolymers. Polymer samples used in this study are summarized in Table 1. All samples were dissolved in THF and then filtered through a 0.45μm disposable syringe filter for the removal of impurities. The homopolymer samples were diluted to a concentration of 0.3% and the copolymer samples were diluted to a concentration of 0.5-1% prior to injection. Samples were introduced into the channel via sample injection valve fitted with a 20mL sample loop. In most cases, each run was repeated 3 or 4 times.

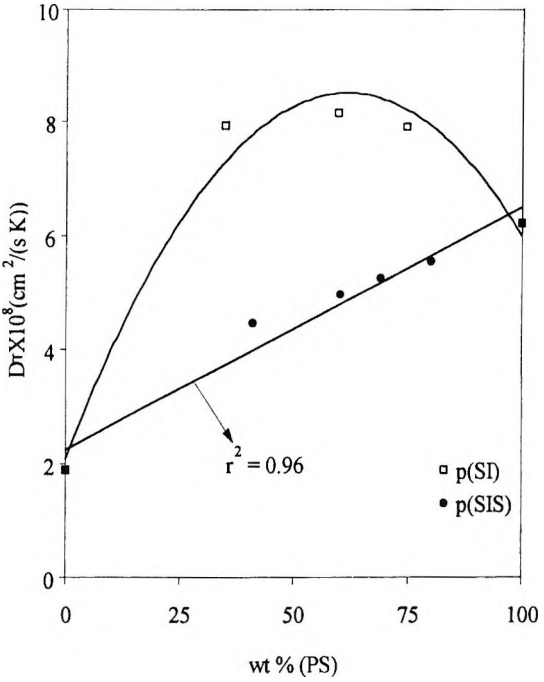

Figure 4. Dependence of D_T on the wt % of PS for p(SI) and p(SIS) block copolymers in THF.

RESULTS AND DISCUSSION

Measurement of MW

Table 2 shows measured molecular weights and intrinsic viscosities of samples. Molecular weights were determined by GPC using a calibration curve constructed with polystyrene (PS) standards.

Viscosities were measured at sample concentrations of 0.5-2.5 mg/mL by measuring the flow time of a certain volume of solution through a capillary of fixed length. Flow time is recorded in seconds as the time for the meniscus to pass between two designated marks in the viscometer. To establish similar condition as in ThFFF, viscosities were measured at 30°C which is the same as the cold wall temperature. Intrinsic viscosity was determined as the reduced specific viscosity extrapolated to c = 0.

Table 4

D and D_T Values of Homopolymers and Copolymers in THF

Polymer		D x 10^7 [a] (cm^2/s)	D/D_T	D_T x 10^8 ($cm^2/(s \cdot K)$)
PS	1	10.30	18.50	5.58
	2	6.35	10.30	6.19, 6.22[b]
	3	3.91	6.04	6.47
	4	2.13	3.21	6.63
PI	1	4.57	24.20	1.89
PMMA	1	16.10	13.20	12.2
	2	10.50	8.43	12.5
	3	7.50	6.06	12.4
	4	5.38	4.32	12.5, 12.4[c]
	5	3.63	3.13	11.6
	6	2.90	2.27	12.8
	7	2.43	1.86	13.1
p(SI)	1	7.76	9.77	7.94
	2	5.01	6.14	8.16
	3	3.09	3.90	7.92
p(SIS)	1	4.27	9.56	4.47
	2	4.79	9.64	4.97
	3	4.79	9.09	5.27
	4	6.46	11.60	5.57
p(SM)	1	3.98	4.11	9.68
	2	5.57	7.42	7.75
	3	4.27	5.83	7.32
	4	5.89	8.93	6.60

[a] Determined from plot of V_r vs. log D in GPC;
[b] Average [Standard deviation = 0.40 (0.18 except PS1)];
[c] Average [Standard deviation = 0.40].

Measured molecular weights of copolymers are different from reported values as they were determined using a PS calibration. Intrinsic viscosity increases with molecular weight for homopolymers, while it changes with the composition and molecular weight for copolymers. These values were used to investigate the hydrodynamic volumes of samples.

Retention in ThFFF

To examine the retention of copolymers of various chemical compositions (or structures), appropriate experimental conditions were chosen through preliminary experiments. The cold wall temperature, T_C, was kept constant in the range of 30-32°C as the retention varies with T_C. D_T and flow rate were in the range of 20 - 60 °C and 0.08 - 0.34 mL/min., respectively.

As explained earlier, solute retention depends on the ratio (D/D_T) in a given polymer-solvent system and a given D_T (see eqn.3). For PS and PMMA standards, retention time increases with the increase of molecular weight as shown in Fig. 1. This is expected, as D_T remains constant for homopolymers in a given solvent, and D decreases with increasing molecular weight (see eqn.4). Thus, for homopolymers, ThFFF separation is obtained based on the solute molecular weight.

Contrarily for copolymers, no linear relationship between molecular weight and retention was found (see Table 3 and Fig. 2). This result indicated that there is an additional factor (or factors) besides molecular weight affecting the retention of copolymers. This additional factor is related to chemical composition of copolymers. That is, change of chemical composition affects the D and D_T.

Since the retention of copolymer is influenced by two independent variables (composition and molecular weight), measurement of molecular weight of copolymer is not straightforward. A new calibration method accounting both composition and molecular weight effect is needed to measure molecular weights of copolymers.

Measurement of Thermal Diffusion Coefficient

From experimentally observed V_r, λ can be calculated using eqn. (2). D_T is then calculated using eqn.(3), provided D is known. D can be obtained by measuring intrinsic viscosity and molecular weight and then, by using eqn. (4)

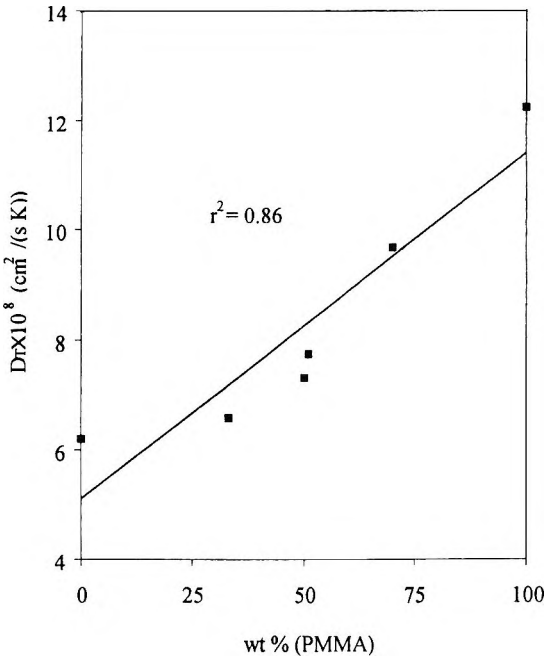

Figure 5. Dependence of D_T on the wt % of PMMA for p(SM) random copolymers in THF.

or by using a plot of retention volume (V_r) versus log D obtained from GPC data. In this study, we used the latter method with polystyrene standards. Fig. 3 illustrates the plot obtained from PS standards. Results are shown in Table 3. Values of D and D_T are shown in Table 4.

As previously reported,[11] D_T of homopolymer increases in the order of PI < PS < PMMA. Fig. 4 illustrates the dependence of D_T on the wt % of PS for p(SI) and p(SIS) block copolymers. It is shown that D_T changes with copolymer composition. In case of p(SI) block copolymers, D_T values are roughly the sum of D values of PS and PI constituents. A linearity exists for p(SIS) triblock copolymers, that is, D_T increases with the increase of wt % of PS. This linearity is similar to that of random copolymers.

This is illustrated in Fig. 4. The correlation coefficient (r^2) is 0.96. This result indicates that D_T of p(SIS) triblock copolymer is affected mostly polystyrene constituent. Fig. 5 shows a plot of D_T versus wt % of PMMA for p(SM) random copolymers. D_T increases with the increase of wt % of

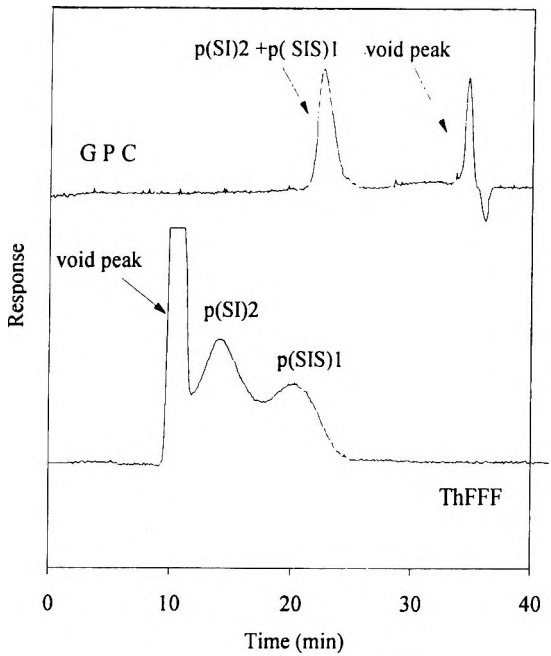

Figure 6. Comparison of separation efficiency of GPC and ThFFF for p(SI)2 and p(SIS)1 mixture.

methymethacrylate with the correlation coefficient (r^2) of 0.93. Results shown in Fig. 4 and 5 indicate D_T varies with structure of copolymer. These results suggests D_T of copolymer is affected, not only by the chemical composition, but also by the effect of structural change.

Comparison of Separation in ThFFF and GPC

Comparative studies on separation of homopolymers in ThFFF and GPC were previously reported,[8,17,18] but that of copolymers has not yet been reported. In this study, two techniques are compared for separation of copolymers.

Figure 6 shows results obtained for two copolymers; hydrodynamic size of p(SI)2 is 22,400 and that of p(SIS)1 is about 37,000. Retention in GPC depends only on the hydrodynamic size. The difference in hydrodynamic size between two copolymers is apparently too small for GPC to separate. ThFFF, however, provided good separation for the copolymers, probably due to the

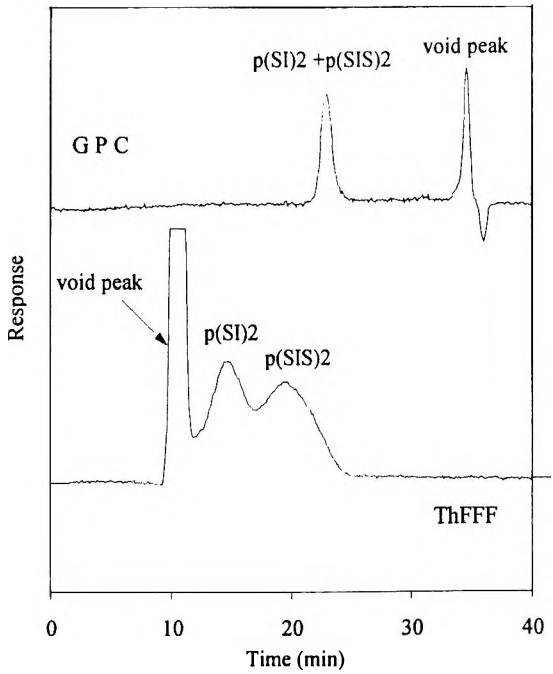

Figure 7. Comparison of separation efficiency of GPC and ThFFF for p(SI)2 and p(SIS)2 mixture.

difference in D_T. There are structural differences and 20% differences in styrene% between two copolymers. There are two factors causing the difference in D_T between two copolymers. First, the higher the composition of styrene is the larger then D_T. Second, D_T of triblock copolymer is higher than that of diblock copolymer.

Figure 7 shows results obtained for copolymers having similar chemical composition and hydrodynamic volume but different structures. Separation in this case is primarily due to the difference in D_T caused by the structural difference of copolymers.

In summary, separation mechanisms of GPC and ThFFF are different. In GPC, separation is based only on the hydrodynamic size of solute molecules. The hydrodynamic size of polymer is influenced by its composition and structure. Still, polymers having different compositions or structures may have similar hydrodynamic sizes, and they may not be separated by GPC. For ThFFF, separation is based on the thermal diffusion as well as the size. For

polymers (or copolymers) having similar hydrodynamic sizes, ThFFF may provide separations based on the difference in composition or structure and, thus, a tool for the analysis of such samples.

ACKNOWLEDGMENT

This work was supported by non directed research fund, Korea Research Foundation (No. 01-D-0583, 1994). The authors thank the Young-In Scientific Co., Ltd.

REFERENCES

1. J. C. Giddings, Sepn. Sci., **1**, 123-125 (1966).

2. J. C. Giddings, Science, **260**, 1456-1465 (1993).

3. J. C. Giddings, Anal. Chem., **67**, 592A-598A (1995).

4. J. C. Giddings, F. S. Yang, J. Colloid Interface Sci., **105**, 55-64 (1985).

5. B. N. Barman, J. C. Giddings, Anal. Chem., **67**, 3861-3865 (1995).

6. J. C. Giddings, Anal. Chem., **53**, 1170A-1175A (1981).

7. G. H. Thompson, M. N. Myers, J. C. Giddings, Anal. Chem., **41**, 1219-1222 (1969).

8. J. C. Giddings, Y. H. Yoon, M. N. Myers, Anal. Chem., **47**, 126-131 (1975).

9. G. Stegeman, A. C. Asten, J. C. Kraak, H. Poppe, R. Tijssen, Anal. Chem., **66**, 1147-1160 (1994).

10. J. J. Gunderson, K. D. Coldwell, J. C. Giddings, Sepn. Sci. Technol., **19**, 667-683 (1984).

11. J. J. Gunderson, J. C. Giddings, Macromolecules, **19**, 2618-2621 (1986).

12. M. E. Schimpf, J. C. Giddings, J. Polym. Sci., Part B: Polym. Phys., **27**, 1317 (1989).

13. M. E. Schimpf, J. C. Giddings, Macromolecules, **20**, 1561-1563 (1987).

14. S. L. Brimhall, M. N. Myers, K. D. Caldwell, J. Polym. Sci., Part B: Polym. Phys., **23**, 2443-2456 (1985).

15. M. E. Schimpf, J. C. Giddings, J. Polym. Sci., Part B: Polym. Phys., **28**, 2673-2680 (1990).

16. S. J. Jeon, D. W. Lee, J. Polym. Sci., Part B: Polym. Phys., **33**, 411-416 (1995).

17. S. Lee, "Gel-Content Determination of Polymers Using Thermal Field-Flow Fractionation," in **Chromatography of Polymers: Characterization by SEC and FFF**, T. Provder, ed., ACS Symp. Ser. No. 521, ACS, Washington, DC. 1993, pp. 77-88.

18. S. Lee, A. Molnar, Macromolecules, **28**, 6354 (1995).

Received January 14, 1997
Accepted April 8, 1997
Manuscript 4439

J. LIQ. CHROM. & REL. TECHNOL., 20(16 & 17), 2757–2775 (1997)

COLD WALL TEMPERATURE EFFECTS ON THERMAL FIELD-FLOW FRACTIONATION

Marcus N. Myers,* Wenjie Cao, Chien-I Chen,
Vijay Kumar,† J. Calvin Giddings‡

Field-Flow Fractionation Research Center
Department of Chemistry
University of Utah
Salt Lake City, UT 84112

ABSTRACT

Thermal field-flow fractionation is a powerful tool for separating and characterizing lipophilic polymers. The construction of calibration curves is required for converting retention data into molecular weight distributions because thermal diffusion of polymers in solution is not well understood. Retention behavior is determined by the physicochemical properties of the polymer and solvent and should be independent of and apply to any thermal field-flow apparatus. Among these properties is the effect of the cold wall temperature which has been studied in some detail and found to be very important in retention behavior. In addition, temperature effects on thermal diffusion have been measured.

INTRODUCTION

The ability of the various subtechniques of field-flow fractionation (FFF) to separate and characterize particles and macromolecules over a broad range is well established. The thermal field-flow fractionation (ThFFF) subtechnique has been primarily applied to lipophilic macromolecules up to 2 x 10^7 daltons, and also to particles in the submicron to micron range.

The physical parameters which operate in the other FFF subtechniques are well known, but the important parameter in ThFFF, thermal diffusion, is not well understood. Because of this, the use of ThFFF to characterize molecular weight distributions of polymeric samples requires the construction of a calibration curve obtained from well characterized standards of the polymer. Ideally, these standards are quite monodisperse, but the use of three or more well characterized broad standards has been shown to also provide good calibration curves.[1,2]

J. C. Giddings recently[3] suggested that calibration curves for one channel should be essentially transportable to all channels because the calibration curves depend on physicochemical properties of the polymer and solvent and not on the characteristics of the channel itself. If the proper parameters for a given polymer-solvent pair are measured in one channel, these parameters should hold in all channels. However, observed calibration curves by various workers in different laboratories, and even by the same person, have varied. Factors such as the cold wall temperature have not been carefully considered as contributing to the variation in calibration curves, although Brimhall et al.[4] examined temperature effects on the thermal diffusion coefficient, D_T.

Classical retention theory for FFF, considering an exponential concentration gradient across the channel and a parabolic velocity profile gives

$$R = \frac{V^0}{V_r} = 6\lambda\left(\coth\frac{1}{2\lambda} - 2\lambda\right) \qquad (1)$$

Figure 1 (right). Fractograms for a mixture of polystyrene standards in THF at different operating conditions in channel no. 21; a) the darker curve was obtained at ΔT = 50 K, with T_c = 290 K, while the second curve was at ΔT = 70 K, with T_c = 315 K; b) the ΔT values were the same as (a) but with T_c = 298 K in both fractograms; c) ΔT = 70 K for both fractograms, but T_c was 298 K for the darker curve and 315 K for the second curve.

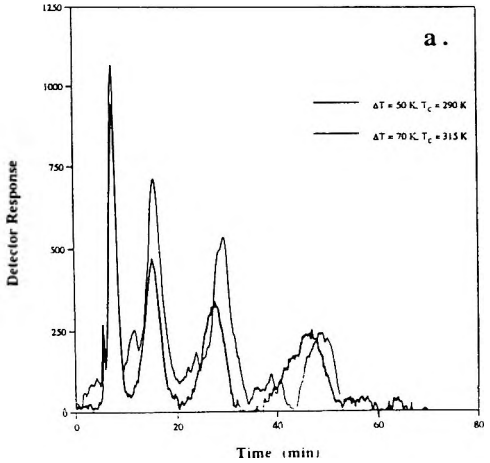
a.
ΔT = 50 K, T_c = 290 K
ΔT = 70 K, T_c = 315 K
Detector Response
Time (min)

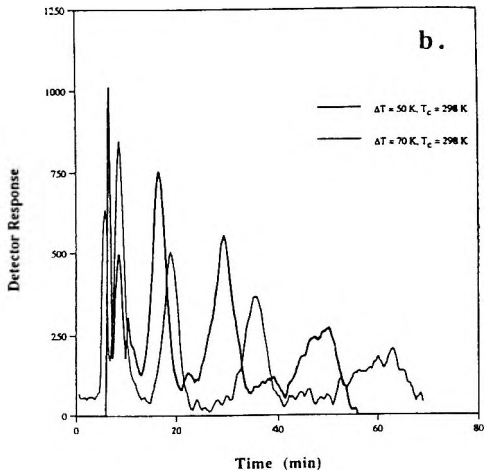
b.
ΔT = 50 K, T_c = 298 K
ΔT = 70 K, T_c = 298 K
Detector Response
Time (min)

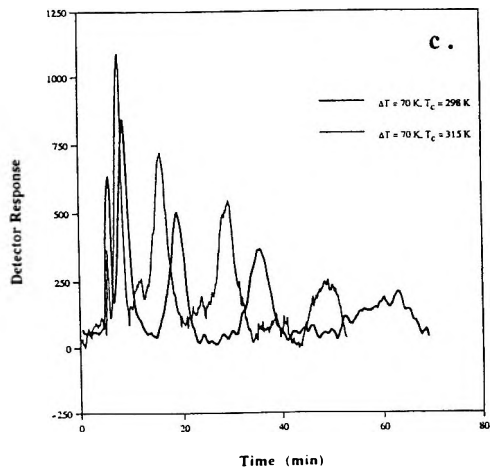
c.
ΔT = 70 K, T_c = 298 K
ΔT = 70 K, T_c = 315 K
Detector Response
Time (min)

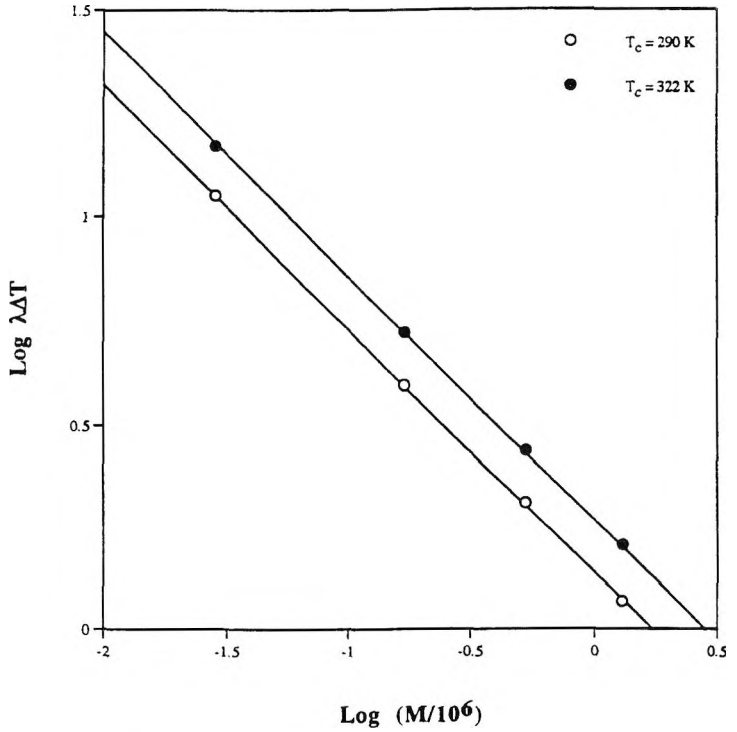

Figure 2. Calibration plots for polystyrene in THF showing the effect of T_c. Both plots were obtained at ΔT = 50 K, with the open circles at T_c = 298 K and the filled circles with T_c = 322 K.

where V^0 is the channel or void volume, V_r is the sample (or peak) retention volume, and λ (for ThFFF) is

$$\lambda = \frac{D}{D_T \frac{dT}{dx} w} \approx \frac{D}{D_T \Delta T} \qquad (2)$$

where D is the ordinary diffusion coefficient of the polymer in the carrier solvent, $\frac{dT}{dx}$ is the temperature gradient, w is the channel thickness and ΔT is the difference in temperature between the hot and cold walls of the channel. In ThFFF, the retention equation must be modified because of the variation of

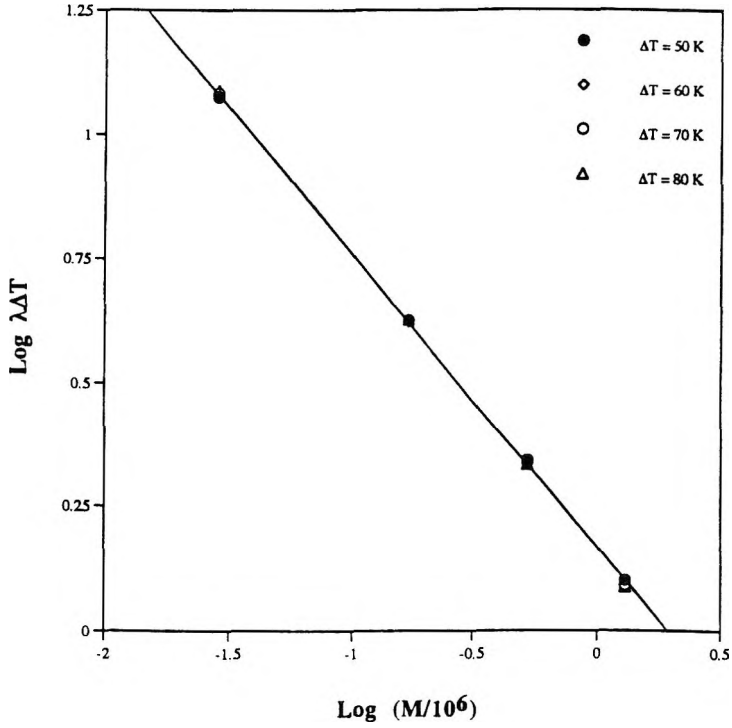

Figure 3. The effect of ΔT on the calibration plot for polystyrene in THF at T_C = 298, for ΔT values of 50, 60, 70 and 80 K.

viscosity of the solvent, η, and the thermal conductivity, κ, across the channel caused by the imposed temperature gradient

$$R = 6\lambda\left\{\nu + (1+6\lambda\nu)\left[\coth\frac{1}{2\lambda} - 2\lambda\right]\right\} \qquad (3)$$

where ν depends on the carrier, ΔT, and the cold wall temperature T_C.[5]

The ordinary diffusion coefficient, D, for polymers is often given as:

$$D = AM^{-b} \qquad (4)$$

where M is the molecular weight. Equation (2) is then rewritten as:

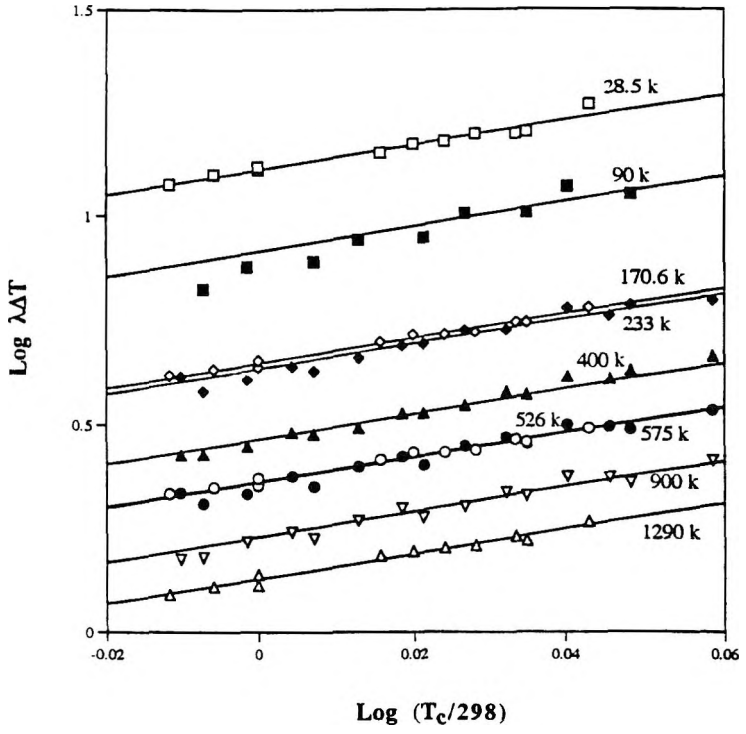

Figure 4. The effect of T_c on log $\lambda\Delta T$ for polystyrene in THF obtained from channels 15, 20, 21 and 22 with ΔT ranging from 30 to 70 K. Another sample series of five standards was also run which gave similar results but are not shown here. The slope of all the lines is 3.

$$\lambda\Delta T = \phi M^{-n} \tag{5}$$

where ϕ incorporates D_T and the nonmolecular weight-dependent portion of D, and n includes b and any molecular weight dependence of D_T. A calibration curve is obtained from:

$$\log \lambda\Delta T = \log \phi - n \log M \tag{6}$$

where the intercept gives log ϕ and the slope is n. In practice, to avoid extrapolation to M = 1, Eq (6) is modified to become:

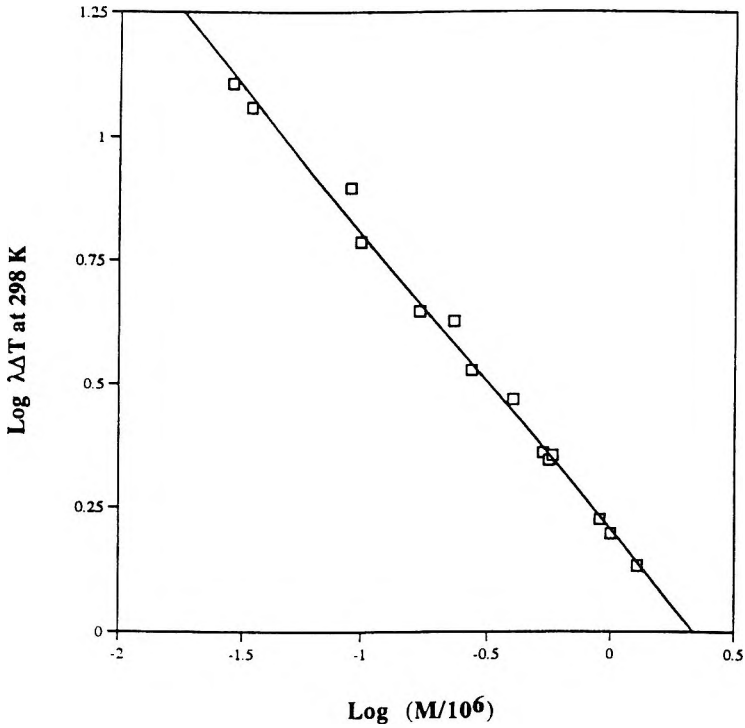

Figure 5. Values of log λΔT at 298 K obtained from Figure 4 and five additional standards give a calibration plot with a slope of -0.6.

$$\log \lambda \Delta T = \log \phi_6 - n \log \frac{M}{10^6} \qquad (7)$$

Changes in the velocity profile due to the temperature gradient across the channel are due primarily to changes in viscosity and to a lesser extent to the change in thermal conductivity (κ). Temperature corrections for η and κ are introduced in the ν term in Equation (3).

However, other changes due to temperature are also present in ThFFF. Ordinary diffusion, D, is given by the Stokes-Einstein equation:

$$D = \frac{kT}{6\pi\eta\gamma} \qquad (8)$$

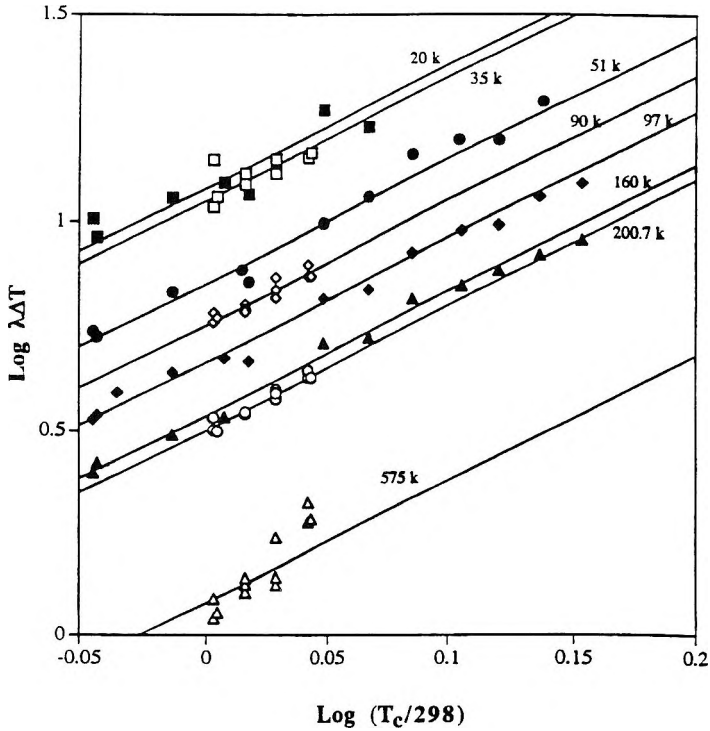

Figure 6. The effect of T_C on log $\lambda\Delta T$ for polystyrene in ethyl benzene from channels 5 (filled symbols) and 15 (open symbols) obtained 15 and 6+ years ago, respectively. The ΔT values varied from 40 K to 80 K. The slope of the lines is 3.

where k is Boltzman's constant, η is the viscosity of the solvent, and γ is the hydrodynamic radius of the molecule. Viscosity dependence on temperature can be expressed by[6]

$$\frac{1}{\eta} = a_0 + a_1 T + a_2 T^2 + a_3 T^3 \qquad (9)$$

As mentioned above, the thermal diffusion coefficient, D_T, has also been shown to be temperature-dependent[4] with very little, if any, dependence on molecular weight.[4,7] Since the cold wall is the accumulating wall for most polymers, the cold wall temperature, T_c, will be an important, even a determining, factor in retention behavior.

Table 1

Channel Characteristics

Channel No.	Effective Channel Length, cm	Channel Breadth, cm	Channel Thickness, μm	Temp. Meas. Ports (Hot + Cold Wall)	Bar Thickness, cm
5	45	1.8	254	10	2.5
15	42	2	76	12	2.5
20	23.5	2	127	22	3.75
21	30.3	1.5	127	32	3.75
22	32.5	2.0	127	44	3.75

One of the sources of variation in calibration curve parameters obtained by different operators with different channels is probably due in part to differences in T_c. Over several years, several workers in our labortory have obtained data on cold wall effects. We present these observations as a necessary preliminary step towards developing the "Universal Calibration Curve" suggested by Giddings.

EXPERIMENTAL

Several channels were used in this study. The channel dimensions and characteristics are given in Table 1. Channels 20, 21 and 22 were designed to flatten the temperature profile along the channel length with ports for measuring temperature less than 2 cm apart. These three channels gave the most reproducible and consistent results because the temperature along the channel length was very uniform. The data from the very old channel 5 were obtained 15 years ago.

A variation in temperature in channel 15 has been observed to be as much as 4-6°C along the channel length and a similar variation would be expected from channel 5 but was not measured. The T_C was taken as the average cold wall temperature. Channels 20, 21 and 22 used 127 μm I.D. tubing for the inlet and outlet to minimize dead volume. Various sizes of tubing were used for the other channels. The heat exchangers in channels 20, 21 and 22 were modified to allow operation at colder T_C.

Table 2

Polystyrene Standards Characteristics

Supplier	M_n	M_w	M_p	M_w/M_n
Polymer Standards Services				
	32,600	33,500	34,300	1.03
	245,000	257,000	273,000	1.05
	536,000	546,000	556,000	1.02
	880,000	944,000	1,000,000	1.07
Polymer Laboratories				
	27,833	28,422	28,500	1.03
	165,683	169,246	170,600	1.03
	513,242	532,152	526,000	1.04
	1,203,119	1,253,827	1,290,000	1.05
Supelco				
		35,000		≤1.06
		47,500		≤1.06
		233,000		≤1.06
		400,000		[2]1.06
Pressure Chemical Co.				
		90,000		≤1.06
		200,000		≤1.05
		575,000		≤1.06
		900,000		≤1.06

Spacers to define the channel were made from Mylar, polyimide or Teflon-coated polyimide. The solvent or carrier was reagent or spectrograde tetrahydrofuran (THF), or reagent grade ethyl benzene. The linear polystyrene standards came from several sources and are listed in Table 2.

Temperature control and data collection were accomplished with in-house software and XT, 286 or Pentium computers. The runs were also monitored with an Omniscribe strip chart recorder (Houston Instruments). Channel flow was provided with a Spectra-Physics Isochrome (San Jose, CA) or an SSI-2 (FFFractionation, Salt Lake City, UT) metering pump. The THF effluent was

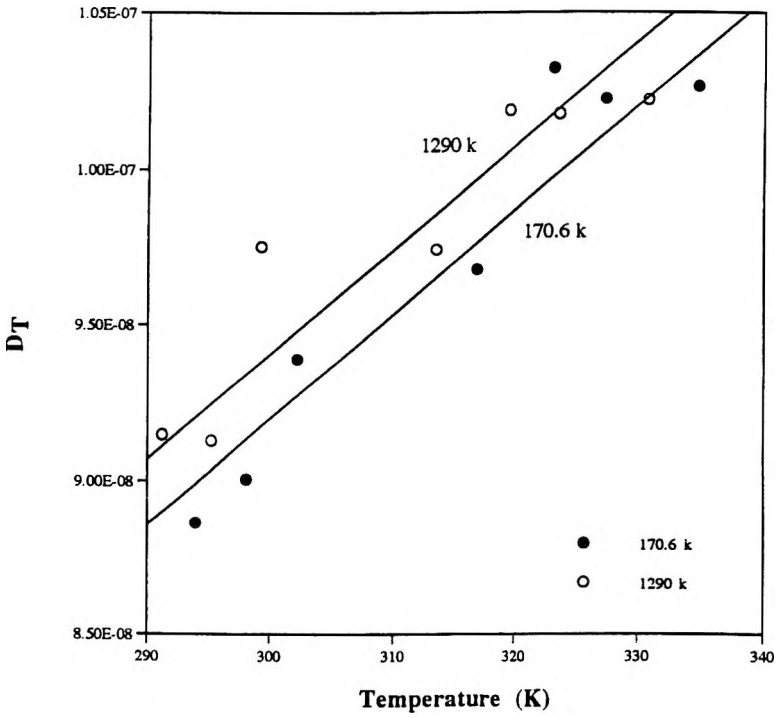

Figure 7. The dependence of D_T on temperature. The values of D_T were calculated at T_{cg} and show some molecular weight dependence. The lines were calculated from values of $\lambda\Delta T$ obtained from curve fitting the data shown in Figure 4.

monitored by an Applied Biosystems Model 757 (Ramsey, N.J.) or a Beckman Instruments Model 153 UV monitor. The ethyl benzene data utilized a Waters 401 Refractive Index detector (Milford, MA). Sample injections were made with a Rheodyne Model 7125 Sampling Valve (Cotati, CA), except for channel 22 which used an Alcott Model 718 autosampler (Norcross, GA).

The mass of sample injected varied from channel to channel. The injected masses in channels 5 and 15 were usually 10 μg or larger for each molecular weight standard in the sample mixture, while channel 20, 21 and 22 used 1 to 2 μg/each standard. Sample concentrations were ~1mg/mL of each standard for channels 5, 15, while channels 20, 21 and 22 used ~0.125 mg/mL.

Table 3

Coefficients for Estimating ν for THF

ΔT (K)	b_0 (x 10^1)	b_1 (x 10^3)	b_2 (x 10^6)	b_3 (x 10^8)
30	-4.235	1.551	-1.50	0.00
40	-5.3403	1.911	-1.805	0.00
50	-6.342	2.279	-2.145	0.00
70	-8.021	2.826	-2.581	0.00

Table 4

Coefficients for Estimating ν for Ethylbenzene

ΔT (K)	b_0	b_1 (x 10^3)	b_2 (x 10^6)	b_3 (x 10^8)
40	-2.255	16.49	-42.43	3.675
52	-1.580	7.660	-10.63	0.00
62	-1.386	6.622	-9.057	0.00
72	-1.280	6.158	-8.427	0.00
83	-1.081	5.141	-6.953	0.00

RESULTS AND DISCUSSION

The effect of T_C on retention is shown in Figure 1a, with two fractograms of polystyrene in THF with a large difference in both ΔT and T_C. The low ΔT (50 K) fractogram with low T_C (290 K) gave almost the same retention as the fractogram with a high ΔT (70 K) and T_C (322 K). At the same T_C, Figure 1b, the expected higher retention for the higher ΔT is obtained. The difference in retention caused by T_C at the same ΔT is illustrated in Figure 1c. The values of λ were calculated directly using Equation 3. The ν values were calculated using viscosity parameters given by Gunderson[6] and thermal conductivity parameters from Martin,[8] and can be very closely approximated over the temperature range studied from the empirical equation:

$$\nu = b_0 + b_1 T_c + b_2 T_c^2 + b_3 T_c^3 \qquad (10)$$

where values of the coefficients are given in Table 3 for THF and Table 4 for ethylbenzene.

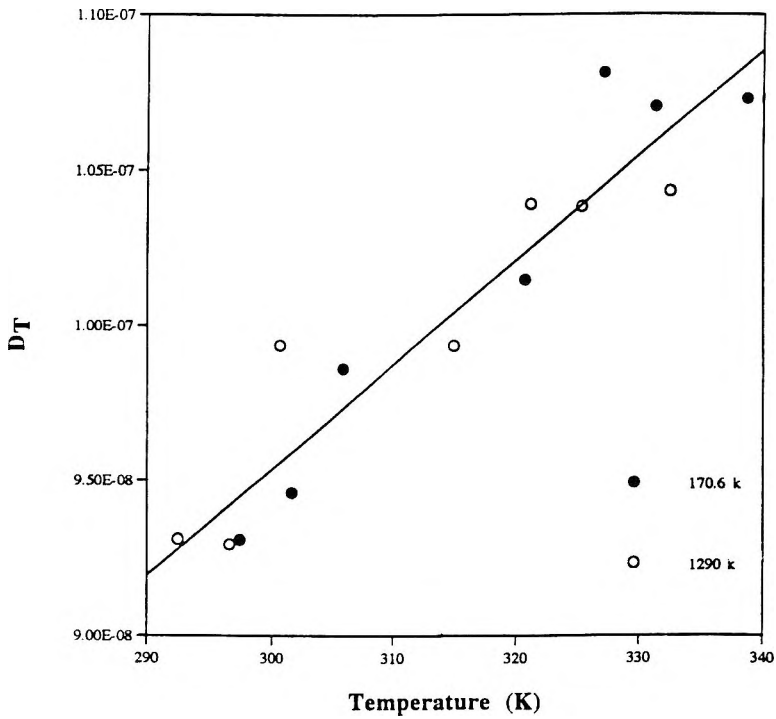

Figure 8. The dependence of D_T on temperature. The values of D_T were calculated at T(xeq) rather than T_{cg}. The lines were calculated from values of $\lambda\Delta T$ obtained from curve fitting the data in Figure 4.

The effect of T_c on the calibration plot is shown in Figure 2. The plots for different T_c values are linear and parallel. They have the same slope, *n*, but exhibit different values for $\log\phi_6$. When the same T_c is used with a range of ΔT values, the plots are essentially identical as illustrated in Figure 3. In the calibration function (Equation (7)), λ is multiplied by ΔT. As ΔT increases, λ decreases in value, with the product being very nearly constant, resulting in a calibration curve which is independent of ΔT.

Examining the effect of T_c on the values of $\lambda\Delta T$ by plotting $\log\lambda\Delta T$ versus $\log T_c/298$ (the division by 298 is in order to place the intercept within the data range) as shown in Figure 4, we obtain a series of plots for data from four channels, 15, 20, 21, and 22, for polystyrene in THF. Remarkably, the plots all exhibit a slope of 3.0 except for 90 k which were obtained on channel

15. The data shown were taken at several ΔT's ranging from 30 to 70 K but still fall on the same curve depending on molecular weight. The values of log $\lambda\Delta T$ obtained from the intercepts of the plots in Figure 4 are shown in Figure 5 as a calibration plot. The slope of this curve is -0.60. The data from channel 15 were obtained several years ago.

Data for polystyrene in ethyl benzene taken over 6 and 15 years ago on channels 15 and 5, respectively, are shown in Figure 6. Again, the value of the slopes is 3.0 for these data. The data for 575 k indicate a higher slope than the line shown with a slope of 3. These data were obtained using a refractive index detector which required larger sample amounts for detection than those used in the THF studies. The two channels are of a much older type where there may have been as much as 5° variation in temperature along the channel due to non-uniformity in the cartridge heaters, unlike channels 20, 21, and 22 which have a variation of only ± 0.5° over the channel length.

Using data for D at 297 K from the literature,[9] and using Equation (9) to calculate a value for η, the value for D at other temperatures may be estimated, assuming that γ has minimal changes over the temperature range being examined. With these values for D and the observed $\lambda\Delta T$ data, D_T can be determined using Equation (2). However, a problem exists for determining the temperature which should be used for calculating D and D_T. Using the classic approach, the temperature at the center of gravity, T_{cg}, would be used, where:

$$T_{cg} = \left\{ \frac{-1 + \left[1 + \lambda \frac{1}{\kappa} \frac{d\kappa}{dT} \Delta T \left(2 + \frac{1}{\kappa} \frac{d\kappa}{dT} \Delta T \right) \right]^{1/2}}{\frac{1}{\kappa} \frac{d\kappa}{dT}} \right\} \qquad (11)$$

When calculations of D and D_T are made at T_{cg} for polystyrene in THF, the results are shown in Figure 7 which indicate a slight molecular weight dependence of D_T. Martin, et al.[5] have suggested that T_{cg} is not the correct temperature to be used in ThFFF because the value of λ will not be constant across the channel due to the temperature gradient. Instead $T(x_{eq})$ should be used which is the temperature at the particular distance, s_{eq}, where the actual value of λ is the λ value calculated in the classical manner. The value of s_{eq} can be obtained from:

$$s_{eq} = 2\lambda - 2.2172(1+2v)\lambda^2 - 5.942(2-v)\lambda^3 . \qquad (12)$$

Assuming the temperature gradient across the channel is linear, $T(x_{eq})$ can then be determined. When these temperatures are used to calculate D and D_T, the D_T values fall on almost the same curve even with a molecular weight difference of a factor of nearly 10, as shown in Figure 8. The change in D_T is 0.35% per degree in the range shown.

Ethyl benzene values for D_T were not calculated because of the lack of good values for D.

A compilation of the cold wall data for polystyrene in THF from channels 15, 20, 21 and 22 is given in the Appendix.

ACKNOWLEDGMENT

This work was supported by Grant CHE-9322472 from the National Science Foundation.

APPENDIX

Summary of Cold Wall Data for Polystyrene in THF

Molecular Weight	ΔT	T_c (K)	R	λ
233000	30	291	0.565	0.137
		301	0.607	0.145
		311	0.651	0.162
		321	0.685	0.177
		331	0.715	0.192
		341	0.745	0.209
400000		291	0.43	0.089
		301	0.473	0.101
		311	0.514	0.112
		321	0.558	0.126
		331	0.587	0.135
		341	0.634	0.153
575000		291	0.36	0.072
		301	0.39	0.079
		311	0.428	0.088

(continued)

APPENDIX (continued)

Summary of Cold Wall Data for Polystyrene in THF

Molecular Weight	ΔT	T_C (K)	R	λ
		321	0.468	0.098
		331	0.49	0.104
		341	0.526	0.114
900000		291	0.265	0.05
		301	0.302	0.058
		311	0.338	0.066
		321	0.365	0.072
		331	0.39	0.078
		341	0.426	0.086
90000	40	293	0.649	0.167
		303	0.706	0.194
		313	0.75	0.221
		323	0.794	0.254
		333	0.823	0.281
233000		293	0.441	0.095
		303	0.485	0.106
		313	0.54	0.123
		323	0.588	0.139
		333	0.627	0.153
400000		293	0.332	0.067
		303	0.369	0.075
		313	0.405	0.084
		323	0.45	0.093
		333	0.49	0.106
575000		293	0.26	0.051
		303	0.288	0.056
		313	0.32	0.063
		323	0.354	0.071
		333	0.384	0.077
900000		293	0.202	0.038
		303	0.221	0.042
		313	0.247	0.047
		323	0.274	0.053
		333	0.298	0.057

APPENDIX (continued)

Summary of Cold Wall Data for Polystyrene in THF

Molecular Weight	ΔT	T_c (K)	R	λ
28500	50	290	0.745	0.237
		294	0.764	0.251
		298	0.772	0.257
		298	0.777	0.262
		309	0.802	0.283
		312	0.815	0.297
		315	0.82	0.301
		318	0.83	0.314
		322	0.832	0.314
		323	0.834	0.317
		329	0.869	0.37
90000		297	0.604	0.151
		307	0.663	0.175
		317	0.716	0.202
		327	0.766	0.234
170600		290	0.371	0.083
		294	0.386	0.086
		298	0.386	0.086
		298	0.398	0.09
		309	0.436	0.1
		312	0.451	0.104
		315	0.452	0.104
		318	0.457	0.105
		322	0.479	0.111
		323	0.479	0.111
		329	0.511	0.121
233000		297	0.382	0.081
		307	0.423	0.091
		317	0.481	0.106
		327	0.528	0.12
400000		297	0.279	0.056
		307	0.309	0.062
		317	0.343	0.07
		327	0.395	0.082
526000		290	0.206	0.043

(continued)

APPENDIX (continued)

Summary of Cold Wall Data for Polystyrene in THF

Molecular Weight	ΔT	T_c (K)	R	λ
		294	0.213	0.045
		298	0.216	0.045
		298	0.224	0.047
		309	0.249	0.052
		312	0.258	0.054
		315	0.26	0.054
		318	0.263	0.055
		322	0.278	0.058
		323	0.276	0.057
		329	0.296	0.062
575000		297	0.22	0.043
		307	0.255	0.05
		317	0.285	0.056
		327	0.319	0.063
900000		297	0.171	0.033
		307	0.192	0.037
		317	0.21	0.04
		327	0.244	0.047
1290000		290	0.121	0.025
		294	0.127	0.026
		298	0.128	0.026
		298	0.136	0.028
		309	0.152	0.031
		312	0.16	0.031
		315	0.159	0.032
		318	0.164	0.032
		322	0.17	0.034
		323	0.167	0.033
		329	0.184	0.037

REFERENCES

[†] Current address: TheraTech, 410 S. Chipeta Way, Salt Lake City, UT 84112.

[‡] Deceased: October 24, 1996.

1. M. Y. Nguyen, R. Beckett, Polym. Int., **30**, 337-343 (1993).

2. M. Nguyen, R. Beckett, Sepn. Sci. Technol., **31**, 291-317 (1996).

3. J. C. Giddings, Anal. Chem., **66**, 2783-2787 (1994).

4. S. L. Brimhall, M. N. Myers, K. D. Caldwell, J. C. Giddings, J. Polym. Sci., Polym. Phys. Ed., **23**, 2443-2456 (1985).

5. M. Martin, C. Van Batten, M. Hoyos, Anal. Chem., submitted.

6. J. J. Gunderson, K. D. Caldwell, J. C. Giddings, Sepn. Sci. Technol., **19**, 667-683 (1984).

7. M. E. Schimpf, J. C. Giddings, Macromolecules, **20**, 1561-1563 (1987).

8. J. E. Belgaied, M. Hoyos, M. Martin, J. Chromatogr. A, **678**, 85-96 (1994).

9. W. Mandema, H. Zeldenrust, Polymer, **18**, 835 (1977).

Received January 21, 1997
Accepted April 20, 1997
Manuscript 4445

J. LIQ. CHROM. & REL. TECHNOL., 20(16 & 17), 2777–2802 (1997)

SEPARATION OF LIPOPROTEINS FROM HUMAN PLASMA BY FLOW FIELD-FLOW FRACTIONATION

Ping Li,[1] Marcia Hansen,[1,*] J. Calvin Giddings[2,†]

[1] FFFractionation, LLC
4797 South West Ridge Blvd.
Salt Lake City, Utah 84118

[2] Field-Flow Fractionation Research Center
Department of Chemistry
University of Utah
Salt Lake City, Utah 84112

ABSTRACT

A flow field-flow fractionation (flow FFF) system was used in both isocratic and programmed-field procedures to rapidly analyze and characterize the HDL, LDL, and VLDL fractions of human blood plasma. In this paper, the general principles and theory of separation are briefly reviewed. The theoretically predicted retention values are shown to compare favorably with the experimental results. The sample recovery and system reproducibility were determined. The lipoprotein fractions were clearly separated into different peaks, although the peaks tended to be rather broad, predominantly due to the sample polydispersity and, to a smaller extent, due to systemic bandbroadening. Plasma samples were analyzed without sample pre-treatment and differences in lipoprotein profiles were observed for different individuals.

Not only could the HDL, LDL, and VLDL fractions be separated, but lipoprotein subspecies were also determined with the use of a programmed field. The hydrodynamic sizes and diffusion coefficients of plasma lipoproteins were deduced from their retention behavior based on FFF theory. The characterization of lipoprotein fractions, based on size or diffusion coefficient, provided additional information which may be useful for research or diagnostic purposes.

INTRODUCTION

Lipoproteins are complexes of lipids and proteins. These complexes have a heterogeneous distribution in density, size, protein composition, and charge. The outer surface of the lipoprotein particle is made up of polar groups of phospholipids, free cholesterol, and apolipoproteins. The interior of the particle includes neutral lipids, triglycerides, and cholesterol esters.[1]

Traditionally, plasma lipoproteins have been classified into high-density lipoproteins (HDL), low-density lipoproteins (LDL), and very low-density lipoproteins (VLDL) according to their ultracentrifugation rate of flotation in a solution of sodium bromide. The further classification into α-lipoproteins, β-lipoproteins, and pre-β-lipoproteins is based on electrophoretic mobility.[2] In general, LDL and VLDL are most strongly correlated with human coronary heart disease (CHD).[3,4] The HDL component, in contrast, has been linked to both prevention and regression of this disease.[5] Analysis of the total lipoprotein profile is useful for assessing the risk of atherosclerosis and for monitoring the treatment of lipid abnormalities. Therefore, lipoprotein profile measurements have become one of the most popular methods to assess lipoprotein abnormalities and CHD risk in clinical diagnosis.

Several technologies have been successfully used to separate lipoproteins and determine the lipoprotein profile in plasma, including ultracentrifugation, chemical precipitation, electrophoresis, and chromatography. Additional characterization can be done by proton nuclear magnetic resonance spectroscopy,[6] and near-IR spectroscopy.[7] The advantages and disadvantages of some of the methods have been discussed in recent years.[8-10] Of these methods, ultracentrifugation, precipitation, and the Friedewald procedure[11] are considered to be the basic methods for both specialized research laboratories and routine clinical laboratories. Ultracentrifugation is the reference research technique for studying lipoproteins and has many advantages for preparative scale isolation of lipoprotein fractions. However, there are drawbacks to this technique. The cost, sample volume, and amount of time required for

ultracentrifugation analysis prohibit routine application in clinical work.[12] Also, structural changes of the lipoprotein complex may be induced due to shearing and ionic-strength effects during the centrifugation.[13] Although the ultracentrifugation method has been improved in recent years by use of a microcentrifuge in combination with a precipitation method to reduce sample volume and the amount of time required, these improved procedures are still difficult to use routinely to check the size or density distribution of plasma lipoproteins in clinical work.[10,14]

To avoid ultracentrifugation altogether, enzymatic reactions and the Friedewald calculation are often used in many clinical laboratories. In this procedure, the total plasma cholesterol (TC) and triglyceride (TG) levels are determined by enzymatic reactions. The VLDL-cholesterol (VLDL-C) is estimated to be a fixed fraction of TG (VLDL-C = TG/5). HDL-C is determined by precipitating out LDL and VLDL from plasma using 50 k Dalton dextran sulfate and magnesium chloride. LDL-C is then calculated from the Friedewald formula: (LDL-C) = TC - (HDL-C) - 0.2TG.[11]

Although this procedure has been commonly used for clinical measurement, there are serious drawbacks. One important consideration is its inaccuracy and incompleteness because of the assumptions and indirect measurements. Large relative inaccuracies have been reported for TC measurements using enzymatic reactions.[15] The procedure also assumes that the triglyceride level is highly correlated with the VLDL-C level. To enhance this correlation, the procedure requires a plasma sample from fasting individuals, an inconvenience for many patients.[16] Additionally, poor reproducibility of the precipitation reaction has led to large errors, with coefficients of variation in the range of 5 to 38%.[15,17,18] Another disadvantage is that this procedure estimates only TC, TG, HDL-C, LDL-C, and VLDL-C. Information about subspecies of the lipoproteins, which may have important health implications, cannot be determined by these methods.

Field-flow fractionation (FFF) is a family of chromatographic-like techniques that are capable of the rapid and highly efficient separation of macromolecules and colloids.[19-21] Because an open flow channel and simple physical forces are used in this technique, FFF is a widely applicable separation method for macromaterials with great flexibility in sample type, carrier liquid or solvent, pH, ionic strength, and so on. Since FFF separation takes place in a single phase without the participation of second phases or surfaces, there is minimal possibility that biological materials will be altered or denatured by interaction with a surface. Because there is no channel packing material, there is little tendency for shear degradation of fragile high-molecular-weight species.

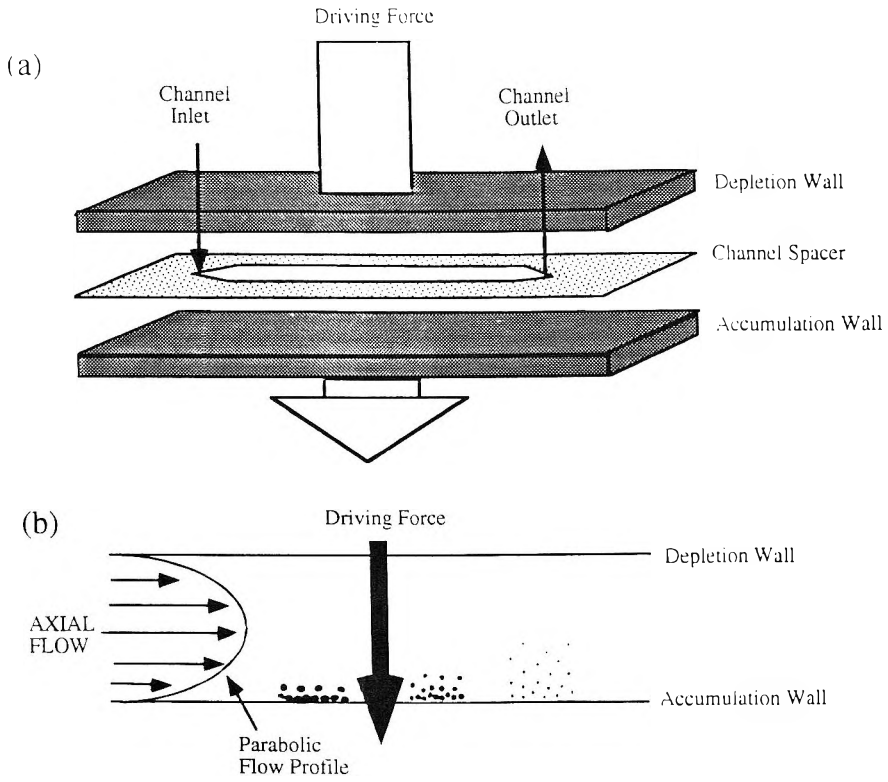

Figure 1. Schematic diagram of FFF channel (a) and separation process (b).

FFF has been successfully utilized for the separation of a variety of biological materials spanning a broad molecular weight and diameter range, including proteins,[20] protein aggregates,[21-24] protein-polymer conjugates,[25] DNA,[22,23,26] viruses,[23,27,28] bacteria,[21,29] and cells.[30] Preliminary results have also been shown for lipoproteins.[25] These results suggest that FFF should be examined at greater depth as a tool for the separation and characterization of lipoproteins.

The principles of FFF are shown in Figure 1. A stream of carrier liquid is introduced at one end of the channel and a small volume of sample is injected. The injected sample spreads out across the channel breadth and proceeds down the channel undergoing separation. The separation process originates in the

flow profile across the narrow dimension of the channel, which is parabolic in form. For parabolic flow, the flow velocity approaches zero at the walls (Figure 1b). An external driving force is applied on the contents of the channel in a direction perpendicular to the flow axis. The injected components are driven by the applied force toward one of the walls (the accumulation wall). They end up in different stream laminae near the accumulation wall, which causes the components to have different velocities and thus elute at different times.

Different driving forces lead to different FFF techniques, most notably sedimentation FFF, flow FFF, thermal FFF, and electrical FFF. In this work, flow FFF is used as the preferred method for characterizing human plasma lipoproteins. In flow FFF, a crossflow stream is applied as an external field.[19,21] The level of retention is determined by the flowrate of the crossflow stream and the sizes or diffusion coefficients of the components separated. The mechanism is as follows.

All species in the channel, large or small, are transported toward the accumulation wall at the same rate by the crossflow. They are driven away from the wall at different rates by diffusion. These opposing processes result in a steady-state exponential distribution of each component near the accumulation wall. The distributions have different thickness (as shown by component bands A, B, and C in Figure 1b) because of the unlike diffusion coefficients. Since smaller components have larger diffusion coefficients, they form thicker steady-state layers (for example, component band C in Figure 1b) and thus have a higher velocity in the parabolic flow stream. Consequently, smaller components are eluted first followed by larger ones (see theory section). The densities of lipoproteins vary from 1.063-1.210 g/mL for HDL, 1.019-1.063 g/mL for LDL, and <1.006 g/mL for VLDL. Their sizes are known to be inversely related to their densities; sizes vary from 5 nm up to 80 nm proceeding from HDL to VLDL.[31]

These large differences in size between the various lipoproteins result in differential retention and separation. The inverse correlation of size and density implies that the size-based separation of flow FFF also provides density fractionation. However, the subpopulations of lipoproteins may exhibit subtle variations in size and density that are meaningful but uncorrelated.

In the usual flow FFF procedure, small samples (a few tens of microliters) are injected into the flowstream entering the channel. Once the samples have entered the channel, the flow is stopped for a sufficient time (the stopflow time) to allow all sample components to reach the accumulation wall and become relaxed to their steady-state distributions. Flow is then resumed and the separation process begins. In this study, a modified flow FFF system was

utilized that employs hydrodynamic relaxation to avoid the flow disturbances and time delay of normal stopflow operation. The hydrodynamic relaxation was achieved using a special frit inlet channel.[32]

In flow FFF, the cross flowrate can be held constant or varied with time (programmed) during a run. Programmed operation has advantages for analysis, speed, and baseline enhancement, but the demands for flow control are more exacting.[33] The programming of a frit-inlet system has not previously been reported. In this study a programmed frit-inlet system was developed and used; a constant cross flowrate was also utilized for some experiments.

Using frit inlet flow FFF, the separation efficiency, recovery, and reproducibility of flow FFF were checked using proteins, purified lipoprotein fractions, and plasma samples. The hydrodynamic sizes and diffusion coefficients of the plasma lipoproteins were measured using flow FFF retention values and compared with literature values. Our goal is to achieve a direct and rapid measurement of lipoprotein fractions (especially LDL) that does not rely on the indirect techniques and assumptions of the usual clinical procedures.

THEORY

In flow FFF, the retention time is controlled by the crossflow. Since the geometry and flow profile of the channel are well defined, the retention times of the separated components can be theoretically predicted and can be related to the hydrodynamic diameters and diffusion coefficients of the components by mathematical expressions.[21] Below we give the limiting form of the equations valid for well-retained components.

The flow FFF retention time can be related to component diffusion coefficient D and to system operating parameters by[34]

$$t_R = \frac{w^2 \dot{V}_c}{6DV} \tag{1}$$

where w is channel thickness, $\dot{V}_C$ is the cross flowrate, and $\dot{V}$ is the channel flowrate. If D is replaced by the Stokes-Einstein equation,[35]

$$D = \frac{kT}{3\pi\eta d_h} \tag{2}$$

the retention time can also be related to the hydrodynamic diameter d_h

$$t_r = \frac{\pi \eta w^2 \dot{V}_c d_h}{2kT\dot{V}} \tag{3}$$

where η is the viscosity of the carrier, k is Boltzmann's constant, and T is temperature. When a programmed crossflow stream is applied in flow FFF, the retention time necessary to elute the sample through the entire particle size range can be greatly reduced. Using a linear programmed crossflow, the retention time t_r' can be approximated by[36]

$$t_r' = t_1 + t_p \left[1 - \exp\left(\frac{t_1}{t_p} - \frac{t_r}{tp} \right) \right] \tag{4}$$

where t_r is the retention time calculated using Equation (1) for the component at the initial crossflow, t_1 is the initial cross flowrate holding time, and t_p is the linear decay time of the cross flow rate.

Equations (1) and (3) show that the flow FFF retention time of a component is inversely proportional to the diffusion coefficient and directly proportional to the hydrodynamic diameter of the component.

EXPERIMENTAL

Equipment

The flow FFF system (Figure 2) consists of a channel whose breadth is 2.0 cm and length is 28.5 cm from tip to tip. A sheet of ultrafiltration membrane served as the accumulation wall in the channel, and the channel thickness is determined using the measured retention times of bovine serum albumin (BSA) and Equation (1). A 10 μL sample solution was injected using a septum injector placed near the inlet. Two Spectra-Physics Isochrom pumps (Spectra-Physics Inc., San Jose, CA, USA) were used to supply sample substream (flowrate $\dot{V}_s$) and frit inlet substream ($\dot{V}_f$) flows. A Kontron 410 HPLC pump (Kontron Electrolab, London, UK) was controlled by a microcomputer (designed and built in conjunction with the electronics shop at the Department of Chemistry, University of Utah) to supply either an isocratic or programmed crossflow substream ($\dot{V}_c$). A Shimadzu SPD-6A UV detector (Shimadzu

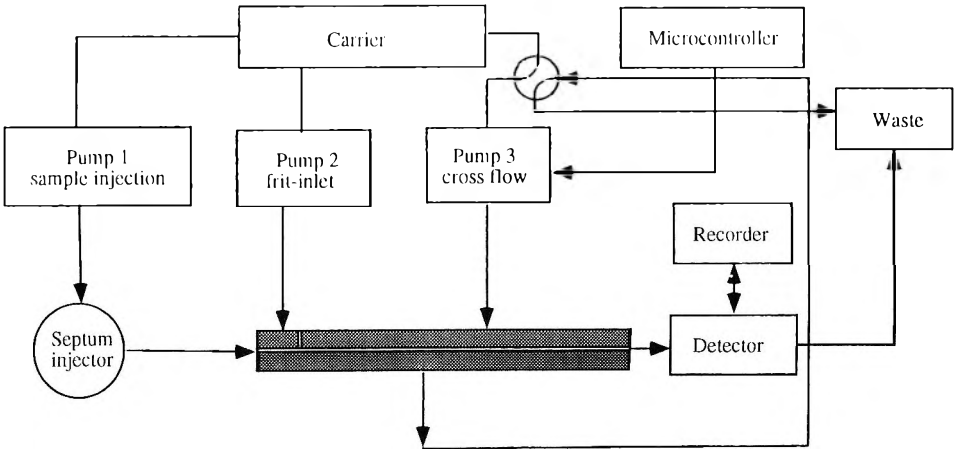

Figure 2. Schematic diagram of a frit-inlet flow FFF system.

Corporation, Kyoto, Japan) and a Linear UV-106 detector (Linear Instruments Corporation, Reno, Nevada, USA) along with a PC compatible computer were used to monitor and record the separation. The detector wavelength was set at 280 nm to monitor the separation. The experiments were carried out at room temperature (23 ± 1 °C).

Specimens

All protein samples were purchased from Sigma Chemical Company (St. Louis, MO). Doubly-distilled deionized water was used to prepare the carrier solutions. A phosphate buffer saline (PBS) solution (138 mM sodium chloride, 2.7 mM potassium chloride , and 10 mM phosphate buffer salts) at pH 7.4 was used as the carrier.

The plasma samples and the two batches, I and II, of purified lipoprotein fractions (HDL-I, LDL-I, and VLDL-I; HDL-II, LDL-II, and VLDL-II) were prepared by the following procedures. Plasma samples were obtained by collecting blood from different individuals after a 12 hour fast using an evacuated blood collection tube containing dry disodium EDTA (1mg/mL). The blood cells were spun out by centrifugation for about 30 minutes at 3000 rpm. The purified lipoprotein fractions were prepared by ultracentrifugation of the cell-free plasma. The plasma (density 1.006 g/mL) was ultracentrifuged at 40,000 rpm at 15°C for 24 hours. The VLDL components floated to the top in

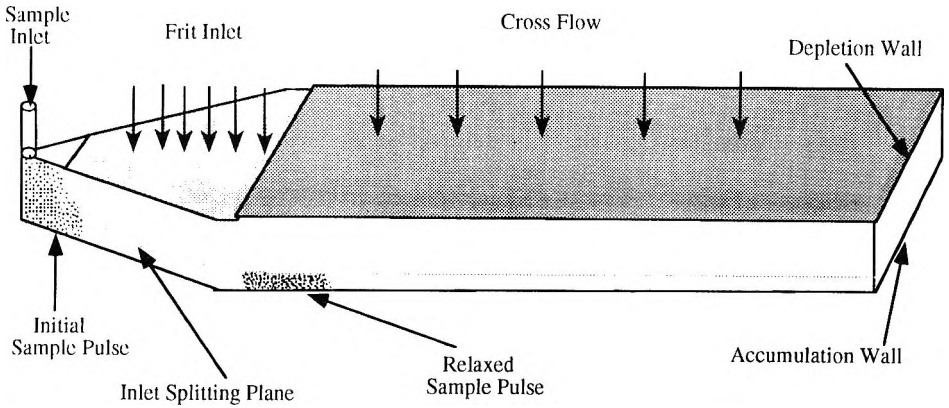

Figure 3. Illustration of hydrodynamic relaxation achieved in a frit-inlet flow FFF channel.

this step. The LDL and HDL components remained in the infranate. The centrifugal tube was sliced to separate the supernatant and infranatant fractions. The infranate density was adjusted to 1.063 g/mL with sodium bromide in order to float the LDL. Following this, the infranate was ultracentrifuged for another 24 hours. The HDL components were isolated from the infranate by spinning for 24 hours after further adjustment of the density from 1.063 to 1.210 g/mL.[37]

Procedures

Hydrodynamic relaxation

In typical FFF operation, a relaxation (or equilibration) step (known as the stopflow procedure) is carried out prior to separation.[19] As explained earlier, channel flow is halted during this step while the crossflow drives all components to the accumulation wall. This stopflow method has disadvantages that include increased analysis time, baseline instability, and increased probability of particle-membrane adhesion. A hydrodynamic relaxation technique using a frit inlet has been developed recently.[32] This procedure avoids the need for stopflow and thus minimizes the disadvantages listed above. The flow FFF system used in this work incorporates such a frit inlet system.

Frit-inlet hydrodynamic relaxation is a process in which sample material is rapidly driven close to its equilibrium position by the frit-inlet flow. The frit-inlet technique utilizes a special element of permeable wall material near the inlet of the channel through which a frit-inlet flowstream can be introduced into the channel. The sample enters the channel in a different substream that forms a thin lamina beneath the frit-inlet substream. The frit-inlet substream compresses the sample substream against the accumulation wall, thus achieving relaxation hydrodynamically (see Figure 3).

A flow FFF system can be modified for frit-inlet hydrodynamic relaxation simply by isolating a small element of the depletion wall to serve as the frit inlet as shown in Figure 3.[32] A substream of the flow is then fed into this isolated area, through the permeable wall, and into the channel. Typically, the frit inlet flow velocity is 20-50 times greater than the crossflow velocity. The channel flowrate $\dot{V}$ is then equal to the sum of the flowrates of the frit inlet substream ($\dot{V}_f$) and the sample substream ($\dot{V}_s$). The important advantage of this relaxation technique is its simplicity of operation and potential for automation.

Programmed crossflow

In this work, a linear programmed crossflow was supplied by a loop recycling system in which the crossflow outlet stream feeds the inlet crossflow pump (Figure 2). This system rigidly equalizes the flowrates of the crossflow inlet and outlet, thus assuring that the channel flowrate $\dot{V}$ can be kept constant or is free of gradients during the programmed operation. The dependence of the cross flowrate on time is illustrated in Figure 4. During time t_1 the cross flowrate is held constant prior to the initiation of linear programming. The cross flowrate reaches a final flowrate value in time t_p after the linear cross flowrate decay begins.

Cholesterol analysis

The cholesterol concentrations of the purified lipoprotein samples and of the fractions collected from the flow FFF system were measured enzymatically using a modified method of Allain[38] provided by Sigma Chemical Company. Samples were incubated with Sigma diagnostics cholesterol reagent (Cat. No. 352) for ten minutes at 25 °C. The light absorption for each incubated sample was determined at 500 nm. The cholesterol content was then calculated using a blank sample and a 200 mg/dL Sigma "cholesterol calibrator" (Cat. No. C0284).

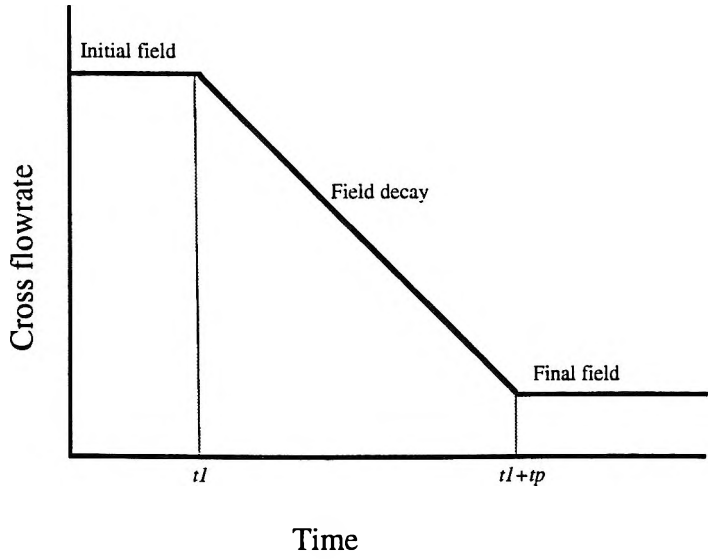

Figure 4. The profile of programmed field in the flow FFF channel.

Recovery determination

The system recovery for a component is defined as the amount of that component eluted from the channel outlet relative to the amount injected; the recovery is usually expressed as a percentage. Recoveries of various components were determined by measuring the amount of a specific component eluted and comparing this to the amount injected. For proteins, the initial sample was diluted into the same volume of carrier as the collected fraction and concentrations were determined using a UV-visible spectrophotometer at 280 nm. For lipoproteins, the initial sample and collected fractions were assayed for cholesterol concentration using the enzymatic method described above.

RESULTS AND DISCUSSION

HDL, LDL, and VLDL Separation and Size Distribution

Plasma lipoproteins are spherical lipid-protein particles with a heterogeneous density and size population. The average size of lipoprotein

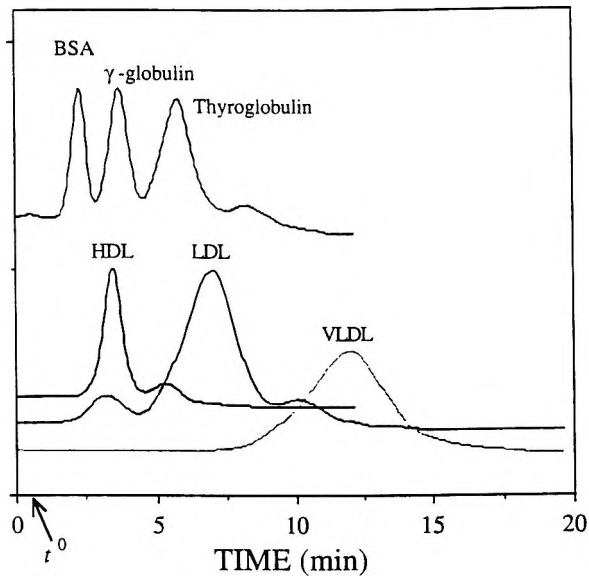

Figure 5. Flow FFF separation of proteins and lipoprotein fractions (HDL-I, LDL-I, and VLDL-I). Conditions are $\dot{V} = 2.2$ mL/min, $\dot{V}_c = 5.0$ mL/min, $\dot{V}_f / \dot{V}_s = 10$, UV 280 nm, $w = 153$ μm.

particles range from 5-12 nm for HDL, 20-30 nm for LDL, and 30-80 nm for VLDL fractions.[31] The significant difference in hydrodynamic sizes will cause differences in retention for the three lipoprotein fractions and, thus, their flow FFF elution sequence will be HDL, LDL and VLDL.

Individual lipoprotein fractions from the first batch of preparation (HDL-I, LDL-I, and VLDL-I) prepared as described in the Experimental Section, and three proteins, ranging from 7 to 17 nm in hydrodynamic diameter, were analyzed by a flow FFF system using an isocratic crossflow velocity to characterize their retention behavior. The elution times were also predicted according to Equation (1) or (3) based on diffusion coefficient or size of component and operation conditions, and the predicted results were compared with the experimental values. Figure 5 shows the retention characteristics of these components under channel and crossflow conditions of 2.2 and 5.0 mL/min, respectively. In the separation, the high concentrations of sodium bromide and other small molecular weight species in the purified lipoprotein fractions do not show any signal in the fractograms because they were eliminated by passing through the ultrafiltration membrane which was used as the accumulation wall in the channel. In Figure 5, LDL and VLDL fractions

Table 1

Molecular Weights, Diffusion Coefficients, Hydrodynamic Sizes, and Flow FFF Retention Times of Proteins and Lipoproteins

Sample	MW (k Dalton)	Diffusion Coefficient $D_{w,20}x10^{-7}$	Diffusion Coefficient $D_{PBS,23}x10^{-7}$	Size (nm)	t_r (min)† Cal.††	t_r (min)† FFF†††
BSA[1]	66	6.15	6.61	6.6	2.23	2.21±0.02
γ-globulin[1]	158	4.00	4.30	10.1	3.44	3.37±0.03
Thyroglobulin[1]	669	2.61	2.81	15.4	5.27	5.23±0.09
HDL[2]	150-300	8.12-3.36	8.73-3.61	5-12	1.7-4.1	3.29±0.04
LDL[2]	3000-5000	2.02-1.34	2.16-1.44	20-30	6.8-10.2	7.00±0.13
VLDL[2]	5000-80,000	1.34-0.50	1.44-0.54	30-80	10.2-27.3	12.0±0.33

† PBS pH 7.4, $\dot{V} = 2.2$, $\dot{V}_c = 5.0$ mL/min, w = 0.0153 cm, $V^0 = 0.81$ mL. †† Calculated from $D_{PBS,23}x10^{-7}$ using Equation (1). ††† At peak maximum, ± x.xx is the standard deviation, n = 5.

[1] H. A. Sober, ed., **CRC Handbook of Biochemistry**, 2nd ed., CRC Press, Cleveland, OH, 1970, pp. C3-C9. [2] Average value from **Biochemistry of Atherosclerosis**, A. M. Scanu, R. W. Wissler, G. S. Getz, eds., Marcel Dekker, Inc., New York, 1979, pp. 3-8, assuming that lipoproteins have the same size distributions in PBS buffer as in plasma. The average diffusion coefficients of lipoproteins were calculated from their average sizes using the Stokes-Einstein equation (Equation (2)).

showed partial peak overlap, which indicates that either these fractions are not purified by the ultracentrifugation procedure or that particles of similar size exist in different density fractions. However, the major components of each fraction were separated to a sufficient degree for analytical determination. Table 1 provides molecular weights, hydrodynamic sizes, diffusion coefficients, and retention times of the proteins and lipoproteins. The retention times were obtained from both theoretical prediction and flow FFF experiments. Because the experiment was done at 23 °C using a PBS buffer as carrier, the flow FFF retention times should be calculated using Equation (1) with the diffusion coefficients of proteins and lipoproteins in PBS buffer at 23 °C ($D_{PBS,23}$). The diffusion coefficient $D_{PBS,23}$ can be calculated from the diffusion coefficient of component in water at 20 °C ($D_{w,20}$) by the following equation that corrects for viscosity differences

$$D_{PBS,23} = D_{w,20} \frac{296}{293} \frac{\eta_{w,20}}{\eta_{PBS,23}} \qquad (5)$$

in which $\eta_{PBS,23}$ is the viscosity of PBS buffer at 23 °C and $\eta_{w,20}$ is the viscosity of water at 20 °C. Assuming that, $\eta_{w,20}/\eta_{PBS,20} = \eta_{w,23}/\eta_{PBS,23}$, thus $D_{PBS,23}$ can be calculated as

$$D_{PBS,23} = D_{w,20} \frac{296}{293} \frac{\mu_{w,20}}{\eta_{PBS,20}} \frac{\eta_{w,20}}{\eta_{w,23}} = 1.075 D_{w,20} \quad (6)$$

The retention results listed in Table 1 show that the flow FFF measured values are in very good agreement with the calculated values.

On the other hand, when unknown samples are analyzed using a flow FFF system, the diffusion coefficients or particle sizes of the eluted components can also be calculated from Equation (1) or (3) according to their retention times. Therefore, flow FFF fractograms do not simply provide general separation information as does chromatography. The diffusion coefficients or particle sizes can be deduced from retention times. Consequently, these results show that an isocratic crossflow field used in flow FFF is appropriate for the separation and size determination of the plasma HDL, LDL, and VLDL fractions, which demonstrates the potential of flow FFF for profiling lipoprotein contents.

System Recovery

As shown in Figure 3, a crossflow drives the sample to the accumulation wall of the channel. An ultrafiltration membrane acts as the accumulation wall to allow the flow across the wall while retaining sample components in the channel. Normally, the sample loss in flow FFF is contributed by sample adsorption on the membrane surface and sample loss across the membrane. Therefore, membrane properties such as polarity and pore size become two crucial factors affecting system separation efficiency and recovery. Since hydrophobic membranes have strong interactions with proteins, the hydrophilic membranes were chosen as the accumulation wall for the lipoprotein separation.

Several commercial ultrafiltration membranes have been used as the accumulation wall and their characteristics and sources are listed in Table 2. The study of FFF recovery (Table 3) indicated that hydrophilic membranes have less membrane adsorption with protein and lipoprotein probes. YM-type membranes as well as the PLGC membrane have negligible surface interactions with lipoproteins and are suitable for measuring lipoprotein profiles. Another important consideration is that the molecular weight cut-off of the membrane is a more significant factor for the system recovery for low molecular weight components; therefore, the pore size of the ultrafiltation membrane should be small enough to ensure that there is no sample loss across the accumulation

Table 2

Characteristics and Sources of Membranes

Materials	Membranes	MW/Size Cut-Off	Properties	Resources
Regenerated cellulose	YM-1	1,000	Hydrophilic	Amicon
"	YM-5	5,000	"	"
"	YM-10	10,000	"	"
"	YM-30	30,000	"	"
"	YM-100	100,000	"	"
Acrylic copolymer	XM-300	300,000	"	"
Regenerated cellulose	PLGC	10,000	"	Millipore
Polyethylene terephthalate	PETP(thick 12μm)	1μm	"	Cyclopore
"	PETP(thick 23 μm)	1μm	"	"
Polycarbonate	PC	1μm	"	"
Isotactic polypropylene	Celgard 2400	50 nm	Hydrophobic	Hoechst Celanese

Table 3

Flow FFF Recoveries

Membranes	Cytochrome C	BSA	γ-Globulin	Thyro-Globulin	HDL	LDL
YM-1	95	98	98	98	98	98
YM-5	85	96	95	97	99	98
YM-10	65	95	97	98	98	98
YM-30	5	95	96	97	98	98
YM-100	2	11	85	94	90	95
XM-300	2	5	18	87	40	95
PLGC	50	95	98	98	98	98
PETP(12μm)	2	3	5	6	2	5
PLGC(23μm)	2	4	5	5	2	5
PC	2	2	7	2	2	5
Celgard 2400		27	49			

wall. Since the molecular weight cut-off of an ultrafiltration membrane is affected by the flux (filtration flow per unit area), the real membrane cut-off in a flow FFF channel is related to the flowrate of crossflow and should be determined under the specific flow conditions employed. The results shown in Table 3 also indicate that YM membrane with nominal molecular weight cut-off 1000, 3000, 5000 and 10,000 shows good recoveries for all of the lipoprotein fractions.

The YM membrane with cut-off of 30k, 100k Dalton as well as XM membrane with cut-off 300k Dalton were determined as appropriate for large LDL and VLDL fractions.

For low MW species, the porosity or molecular weight cut-off of the membrane could lead to sample loss and low recoveries. In the case presented here and for other similar situations, the membrane cut-off feature can be applied to combine flow FFF and membrane separation to form the membrane-selective flow FFF.[39] The membrane-selective flow FFF can be used as a one-step purification and separation procedure to improve and simplify the lipoprotein analysis. The high concentration of sodium bromide in the ultracentrifuged lipoprotein fractions and the abundance of low molecular weight plasma proteins and albumin in a plasma sample can be removed easily by the flow FFF membrane with an appropriate MW cut-off. Without the bulk of these interfering small molecular weight components and proteins, the lipoprotein profile can be obtained directly from plasma samples. While the presence of these components does not affect flow FFF results, it does interfere with chromatographic and electrophoretic analyses.[40]

Reproducibility

The reproducibility of flow FFF determined diffusion coefficients and hydrodynamic size for lipoproteins was determined by (1) analyzing the same sample using different channel and crossflow conditions and calculating and comparing the flow FFF determined diffusion coefficients and hydrodynamic sizes, and (2) comparing the results of three different channels of the same dimensions.

Reproducibility over a range of flow conditions

Equations (1) and (3) show that the flow FFF retention times depend on the crossflow rate $\dot{V}_c$ and channel flow rate $\dot{V}$. But the magnitude of crossflow and channel flow also strongly affect resolution.[26] Figure 6 shows flow FFF fractograms of lipoprotein fractions (HDL-II, LDL-II, and VLDL-II) that resulted from using different $\dot{V}_c$ with a constant $\dot{V}$. Obviously, retention time and separation efficiency are increased by changing the driving force from 5.0 to 8.5 mL/min as shown by comparing Figures 6a and 6b. However, hydrodynamic sizes deduced from retention times show good agreement between the two different separation conditions. Average particle diameters were 8.0, 22, and 40 for the HDL, LDL, and VLDL components using the

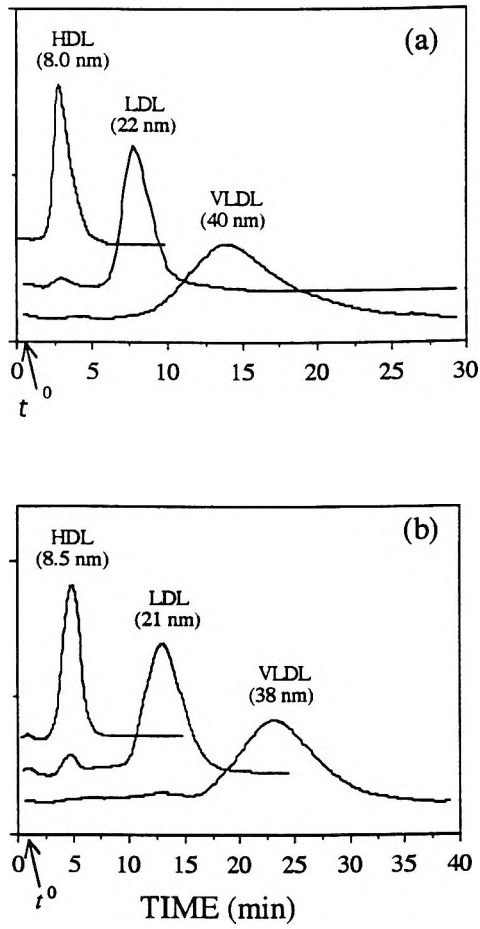

Figure 6. HDL-II, LDL-II, and VLDL-II fractions separation and size distribution using different crossflow field (a) $\dot{V}_c$ = 5.0 mL/min, (b) $\dot{V}_c$ = 8.5 mL/min. PBS pH 7.4, $\dot{V}$ =2.2 mL/min, $\dot{V}_f$ / $\dot{V}_s$ = 10, UV 280 nm, w = 158.

experimental conditions of Figure 6a versus 8.5, 21, and 38 nm for Figure 6b. The disadvantage of increased crossflow rate is also shown since the elution time of the last component, VLDL-II, increased from about 13 up to 23 minutes. The appropriate crossflow rate or channel flowrate would be chosen as the flowrate that adequately resolves the lipoprotein components within a reasonable elution time.

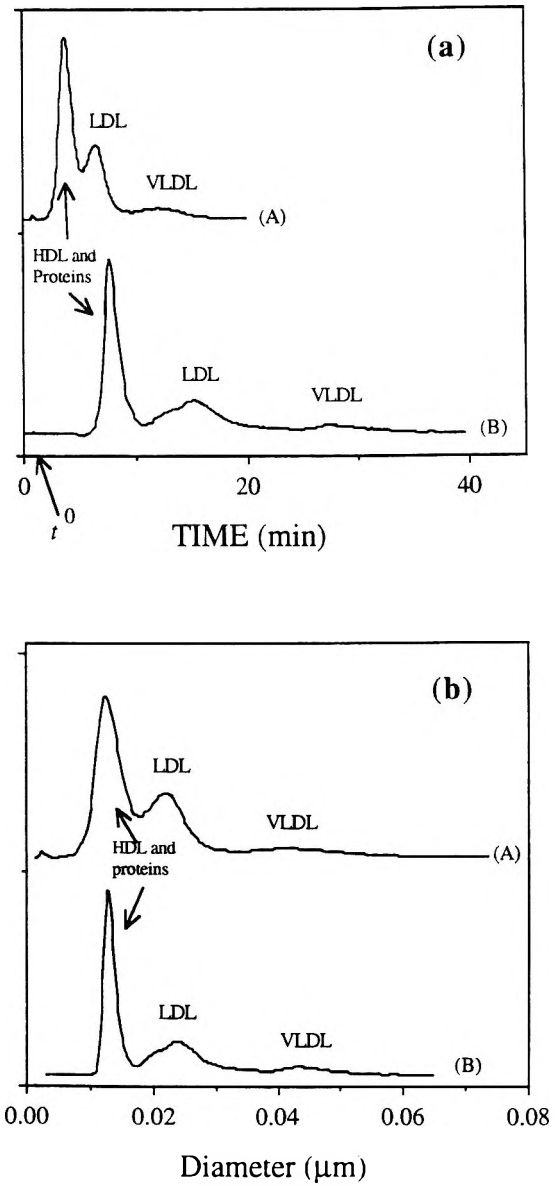

Figure 7. Flow FFF separation (a) and characterization (b) of human lipoproteins in plasma samples using different channel and crossflow conditions. Flow conditions are (A) $\dot{V}$ = 2.2 mL/min, $\dot{V}_c$ =5.0 mL/min, (B) $\dot{V}$ = 1.1 mL/min, $\dot{V}_c$ = 6.8 mL/min, $\dot{V}_f$ / $\dot{V}_s$ = 10, UV 280 nm, plasma sample No. 1.

The separation efficiency and reproducibility of lipoprotein analysis were checked using different flow conditions to analyze and characterize the lipoprotein fractions directly from blood plasma. Adjustments of the channel and crossflow rate values for different amounts of retention and resolution were made by increasing the ratio of $\dot{V}_c / \dot{V}$ from 2.3 to 6.2. A plasma sample of 10 µL was directly injected in the flow FFF channel without pretreatment. The lipoprotein profiles and size distributions are shown in Figure 7a and b, respectively. While the elution time and resolution are expected to differ due to the varying experimental conditions, the calculated sizes at peak maxima are found to be identical. The resolution was obviously improved when the ratio $\dot{V}_c / \dot{V}$ was increased to 6.2. The HDL and LDL fractions were baseline separated, and the LDL fraction was separated into a bimodal distribution. This result confirmed the good reproducibility of size determinations using a single channel at these different flow conditions.

Channel-to-channel reproducibility

The channel-to-channel reproducibility was measured using three channels to separate and characterize proteins and purified lipoprotein samples. The experimental results are compared in Table 4. Coefficients of variations between the channels were less than 4.5%. If the results were compared with the literature values in Table 1, good agreement was found.

It can be concluded that flow FFF has suitable reproducibility when using different operating conditions or different channels and can easily be used for determining diffusion coefficients or sizes of lipoprotein components.

Programming Field to Separate Lipoproteins and Their Subspecies

Because lipoproteins vary widely in size and diffusion coefficient, different conditions are needed to achieve complete separation between the various species and subspecies. HDL particles have the smallest molecular weight and largest diffusion coefficients of the lipoprotein fractions and so require a larger field than the LDL or VLDL particles. When a high isocratic field is used to characterize the lipoprotein profile, the HDL subspecies can be distinctly separated with high resolution. However, the high field conditions can be problematic for the LDL and especially the VLDL components. For example, using a cross flowrate of 9.0 mL/min, two main subclasses of HDL (HDL_3 and HDL_2) can be separated and a broad peak (indicating increased resolution of the size-based subspecies) results for the LDL components. However, the VLDL components will be difficult to detect and their retention

Table 4

Diffusion Coefficients and Hydrodynamic Sizes of Proteins and Lipoproteins Determination by Flow FFF[1]

Proteins	Diffusion Coeff. ($D_{PBS,23}x10^{-7}$) Channel I	Channel II	Channel III	----- Size ----- Channel I	Channel II	Channel III	CV%
BSA	6.65±0.06	6.67±0.04	6.65±0.07	6.5±0.06	6.4±0.04	6.5±0.07	0.2
γ-globulin	4.35±0.04	4.38±0.05	4.32±0.04	10.0±0.09	9.9±0.11	10.1±0.09	0.7
Thyro-globulin	2.60±0.06	2.71±0.05	2.72±0.03	16.7±0.38	16.0±0.30	15.9±0.18	2.5
HDL	4.65±0.08	4.84±0.07	4.85±0.04	9.3±0.16	9.0±0.13	8.9±0.07	3.8
LDL	1.95±0.04	2.10±0.03	1.94±0.04	22.2±0.53	20.6±0.29	22.4±0.46	4.5
VLDL	1.16±0.03	1.23±0.04	1.24±0.03	37.3±0.96	35.4±1.10	35.0±0.85	3.6

[1] With standard deviation and n = 5.

time will become unreasonably long. Additionally, under these experimental conditions, the VLDL components are forced to positions very close to the membrane and there is increased risk of adsorption onto the membrane. Therefore, the isocratic 9.0 mL/min crossflow field is useful for the subspecies separation of the HDL component only. A lower isocratic field is similarly useful for separating the subspecies of LDL and VLDL; however, the resolution of the smaller HDL components will suffer. In an attempt to achieve higher resolution without excessive analysis time or loss of resolution for the smaller components, programmed field conditions were used.

A linear field decay programming was used, that is, a constant but high initial field strength was applied for a predetermined period of time for the separation of HDL particles, after which the field strength was programmed downward to provide suitable conditions for the prompt elution of LDL and VLDL particles.

First of all, the crossflow pump was manipulated so that the initial flowrate was 9.0 mL/min. This crossflow field was then decreased by gradually slowing the cross flowrate to 1.0 mL/min with a constant channel flowrate of 2.0 mL/min. This procedure allowed for better resolution of the HDL components and was completed in 20 minutes using an initial t_1 = 1.7 minutes and then a decay time, t_p = 20.7 minutes (see Figure 4). In this case, the HDL_2 and HDL_3 components were separated, but better resolution of the LDL and VLDL was not achieved (Figure 8). This result illustrates that this programmed decay time is appropriate to the HDL subspecies, but a longer field

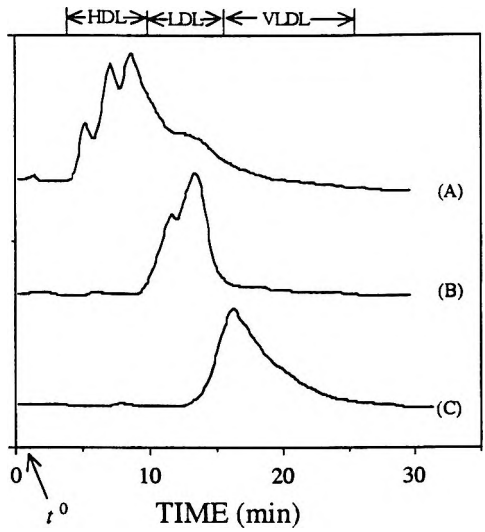

Figure 8. Flow FFF of human plasma lipoprotein fractions using a programmed field. (A) HDL-I, (B) LDL-I, and (C) VLDL-I fractions. Flow conditions are $\dot{V}$ = 2.0 mL/min, programmed $\dot{V}_c$ from 9.0 mL/min to 1.0 mL/min, t_1 = 1.7, t_p = 20.7 minute, $\dot{V}_f$ / $\dot{V}_s$ = 9, UV 280 nm, w = 174 μm.

decay time should be used to get better information regarding the LDL and VLDL subspecies. When the field decay time t_p is increased to 40 minutes, the LDL and VLDL fractions show longer retention times and broader size distributions. Figure 9 shows the separation of a mixture of the HDL-I, LDL-I, and VLDL-I standards and two blood plasma samples at these conditions. When the plasma fractograms (Figure 9 B and C) are compared with the corresponding lipoprotein fraction standards profile (Figure 9A), information regarding concentration and size distribution of lipoproteins is immediately available. Plasma 2 (Figure 9B) shows a large VLDL peak, which supplies information about the lipid abnormality of the individual.

It should be mentioned that overlap between LDL-I and VLDL-I fractions exists as shown in Figure 5 which is the result of isocratic field conditions; Figure 9a, which employed programmed field conditions, also showed this overlap. This is possibly due to overlapping size distribution which exists between the two density classed fractions since, even under varied field conditions, the aberration was noted. Since separation in normal mode flow FFF occurs according to the sample diffusion coefficient or hydrodynamic size, the overlap means that the same size particles exist in the different lipoprotein

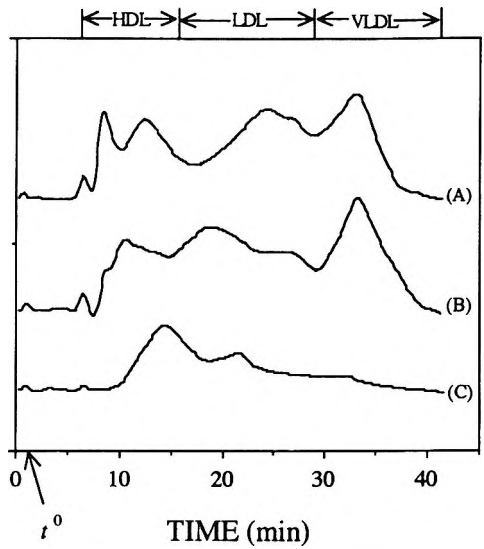

Figure 9. Lipoprotein fractions and human plasma lipoproteins separation by programmed flow FFF. (A) a mixture of HDL-I, LDL-I, and VLDL-I fractions, (B) human plasma No.2, (C) human plasma No.3. Conditions are same as Figure 8 except $t_1 = 8.3$, $t_p = 40$ minutes.

fractions. The reason for the overlap is not clear and a possible alternative reason is incomplete separation by the ultracentrifugation procedure. However, flow FFF is possibly the only convenient method capable to investigate this relationship between the density and hydrodynamic size. It should also be mentioned that the broad peaks and size distributions contain information regarding the lipoprotein subspecies, each of which has a distinct function for the development of coronary heart disease. Information about the subspecies in human plasma is important for both clinical and research work to assess the risk of atherosclerosis.

CONCLUSIONS

A frit-inlet hydrodynamic relaxation flow FFF system was successfully utilized for the separation and characterization of biological materials from small proteins to macromolecular lipoproteins. With improvements in instrumentation and techniques, flow FFF separations have become faster and more convenient. The separation of HDL, LDL, and VLDL fractions can be done in 10 to 20 minutes with only 10 μL of sample necessary. Plasma

lipoproteins can be separated directly from human plasma without sample pretreatment. The well developed FFF theory can be used to predict system operating conditions, and lipoprotein size distributions can be deduced from their retention times. The subspecies of the lipoprotein profile were determined when a programmed field was used. Distinctly different lipoprotein profiles were obtained for plasma samples from different individuals, providing a characteristic fingerprint for these important constituents and suggesting possible clinical and research applications.

ACKNOWLEDGMENTS

This work was supported by Public Health Service Grant GM10851-39 and by SBIR Grant R43HL50213 from the National Institutes of Health.

We would like to thank Dr. L. Wu of Cardiovascular Genetics Research Clinic, University of Utah, for the gift of various lipoprotein samples and the technical discussions on the lipoprotein purification and cholesterol analysis.

REFERENCES

† Deceased: October 24, 1996.

1. N. Rifai, Arch. Pathol. Lab. Med., **110**, 694-701 (1986).

2. F. T. Lindgren, L. C. Jensen, F. T. Hatch, in **Blood Lipids and Lipoproteins: Quantitation, Composition and Metabolism**, G. L. Nelson, ed., R. E. Publishing, Huntingdon, New York, 1979, pp. 181-274.

3. W. A. Bradley, S.-L. C. Hwang, J. B. Karlin, A. H. Y. Lin, S. C. Prasad, A. M. Gotto, Jr., S. H. Gianturco, J. Biol. Chem., **259**, 14728-14737 (1984).

4. T. Gordon, W. B. Kannel, W. P. Castelli, T. R. Dawber, Arch. Intern. Med., **141**,1128-1131 (1981).

5. G. R. Warnick, J. J. Albers, Clin. Chem., **24**, 900-904 (1978).

6. J. D. Otvos, E. J. Jeyarajah, D.W. Bennett, Clin. Chem., **37**, 377-386 (1991).

7. L. A. Cassis, R. A. Lodder, Anal. Chem., **65**,1247-1256 (1993).

8. G. R. Warnick, M. H. Dominiczak, Current Opinion in Lipidology, **1**,493-499 (1990).

9. G. Warwick, C. J. Packard, J. Shepherd, Current Opinion in Lipidology, **1**, 500-507 (1990).

10. N. Rifai, G. R. Warnick, J. R. McNamara, J. D. Belcher, G. F. Grinstead, I. D. Frantz, Jr. Clin. Chem., **38**, 150-160 (1992).

11. W. T. Friedewald, R. I. Levy, D. S. Fredrickson, Clin. Chem., **18**, 499-502 (1972).

12. B. H. Chung, J. P. Segrest, M. J. Ray, J. D. Brunzell, J. E. Hokanson, R. M. Krauss, Ken Beaudrie, J. T. Cone, Methods Enzymol., **128**, 181-209 (1986).

13. C. J. Fielding, P. E. Fielding, in **Biochemistry of Lipids and Membranes**, D. E. Vance, J. E. Vance, eds., The Benjamin/Cummings Publ. Co., Menlo Park, California, 1985, pp. 424-425.

14. L. L. Wu, G. R. Warnick, J. T. Wu, R. R. Williams, J. M. Lalouel, Clin. Chem., **35**, 1486-1491 (1989).

15. Laboratory Standardization Panel, "NCEP: A Report from the Laboratory Standardization Panel of the National Cholesterol Education Program," Clin. Chem., **34**, 193-201 (1988).

16. J. R. McNamara, J. S. Cohn, P. W. F. Wilson, E. J. Schaefer, Clin. Chem., **36**, 36-42 (1990).

17. S. M. Grundy, D. W. Goodman, B. M. Rifkind, J. I. Cleeman, Arch. Int. Med., **149**, 505-510 (1989).

18. G. R. Warnick, J. J. Albers, E. Teng-Leary, Clin. Chem., **26**, 169-170 (1980).

19. J. C. Giddings, ed., **Unified Separation Science**, John Wiley, New York, 1991.

20. M.-K. Liu, P. Li, J. C. Giddings, Protein Science, **2**, 1520-1531 (1993).

21. J. C. Giddings, Science, **260**, 1456-1465 (1993).

22. K.-G. Wahlund, A. Litzen, J. Chromatogr., **461**, 73-87 (1989).

23. A. Litzen, K.-G. Wahlund, J. Chromatogr. **476**, 413-421 (1989).

24. A. Litzen, K.-G. Wahlund, Anal. Biochem., **212**, 469-480 (1993).

25. J. C. Giddings, M. N. Benincasa, M-K. Liu, P. Li, J. Liq. Chromatogr., **15**, 1729-1747 (1992).

26. M.-K. Liu, J. C. Giddings, Macromolecules, **26**, 3576-3588 (1993).

27. J. C. Giddings, F. J. Yang, M. N. Myers, J. Virol., **21**, 131-138 (1977).

28. A. Litzen, K.-G. Wahlund, Anal. Chem., **63**, 1001-1007 (1991).

29. J. J. Kirkland, C. H. Dilks, Jr., S. W. Rementer, W. W. Yau, J. Chromatogr., **593**, 339-355 (1992).

30. B. N. Barman, E. R. Ashwood, J. C. Giddings, Anal. Biochem., **12**, 35-42 (1993).

31. W. Stoffel, C. Bode, in **Selective Plasma Component Removal**, A. A. Pineda, ed., Futural Publishing, New York, 1984, p. 2.

32. J. C. Giddings, Anal. Chem., **62**, 2306-2312 (1990).

33. S. K. Ratanathanawongs, J. C. Giddings, Anal. Chem., **64**, 6-15 (1992).

34. J. C. Giddings, F. J. Yang, M. N. Myers, Anal. Chem., **48**, 1126-1132 (1976).

35. C. Tanford, ed., **Physical Chemistry of Macromolecules**, John Wiley, New York, 1961.

36. P. S. Williams, J. C. Giddings, R. Beckett, J. Liq. Chromatogr., **10**, 1961-1998 (1987).

37. **Lipid and Lipoprotein Analysis, Manual for Laboratory Operations**, Lipid Research Clinics Program, Vol. 1, DHEW Publication No.(NIH)75-628, Washington, DC. U.S. Dept. of HEW, 1974.

38. C. A. Allain, L. S. Poon, C. S. G. Chan, W. Richmond, P. C. Fu, Clin. Chem., **20**, 470-475 (1974).

39. P. Li, J. C. Giddings, J. Pharm. Sci., **85**, 895-898 (1996).

40. Y. C. Ha, P. J. Barter, J. Chromatogr., **341**, 154-159 (1985).

Received January 8, 1997
Accepted April 24, 1997
Manuscript 4437

J. LIQ. CHROM & REL. TECHNOL., 20(16 & 17), 2803-2814 (1997)

STOPLESS SEPARATION OF PROTEINS BY FRIT-INLET ASYMMETRICAL FLOW FIELD-FLOW FRACTIONATION

Myeong Hee Moon,* Hansun Kwon, Ilyong Park

Department of Chemistry
Kangnung National University
Kangnung, 210-702, Korea

ABSTRACT

The frit inlet asymmetrical flow field-flow fractionation is applied to the separation of proteins by using a stopless flow injection procedure. By utilizing a small permeable frit near the injection point in an asymmetrical flow FFF channel, sample materials injected to the flow streams can be hydrodynamically relaxed by the compressing action of high speed frit flow and the focusing/relaxation procedure can be bypassed. The separation efficiency of the frit inlet asymmetrical flow FFF channel is demonstrated with few protein standards by examining the influence of the ratio of injection flow rate to frit flow rate on the band broadening during relaxation.

INTRODUCTION

Flow field-flow fractionation (FlFFF) has shown its capability in the separation and characterization of particulate materials and macromolecules such as proteins, DNA, water soluble polymers, and etc.[1-7] As one of a wide

variety of FFF subtechniques, flow FFF utilizes an external force to have sample components retained in a thin rectangular channel. The force type used in flow FFF is the secondary flow (crossflow) of carrier liquid moving across the channel while the channel flow (separation flow) drives sample materials toward the end of the channel.[1-3]

When the cross flow is applied to a flow FFF channel, sample materials are driven toward the bottom of the channel wall. Due to the diffusive extrusion of sample materials away from the wall, particles or macromolecules under the external field are differentially accumulated at finite distances from the channel wall according to their diffusion rates which are closely related to their Stokes diameters. When the separation flow is applied to the sample components located at their equilibrium, they will be migrated at different velocities due to the parabolic nature of laminar flow between the thin channel walls and this leads to a separation of each other.

In practice, the whole system operation of a conventional symmetrical flow FFF is carried out by two consecutive steps; the sample relaxation process which is essential in most forms of FFF and is generally executed by applying crossflow only while the channel flow is stopped for a certain period of time, and the separation process which is begun by resuming the channel flow after the relaxation is completed.[8] However, in a conventional asymmetrical flow FFF system there is only one permeable wall on the bottom of the channel.[9] Since there is no influx of crossflow to the asymmetrical channel, sample relaxation is achieved by the focusing/relaxation process in which two counter directed flows (one from the channel inlet and the other from channel outlet) are focused at or below the sample loading point.[9]

By the focusing procedure, sample components can be accumulated into their equilibrium states as a narrow initial band. After the focusing/relaxation, separation process begins by applying the separation flow via the channel inlet. Since the incoming flow divides into cross flow and outflow, linear flow velocity gradually decreases at the end of the channel. This effect is expected to keep the sample band from spreading during migration and it possibly leads to a concentration effect of sample components entering the detector. The asymmetrical flow FFF channel has been utilized to separate proteins and their aggregates, plasmids, water soluble polymers, etc., at a high speed.[9-13] However, focusing/relaxation process is somewhat inconvenient in the system operation and the conversion of flows during the relaxation causes a baseline shift in the detector signal. Therefore, it is desired to simplify the system operation if possible.

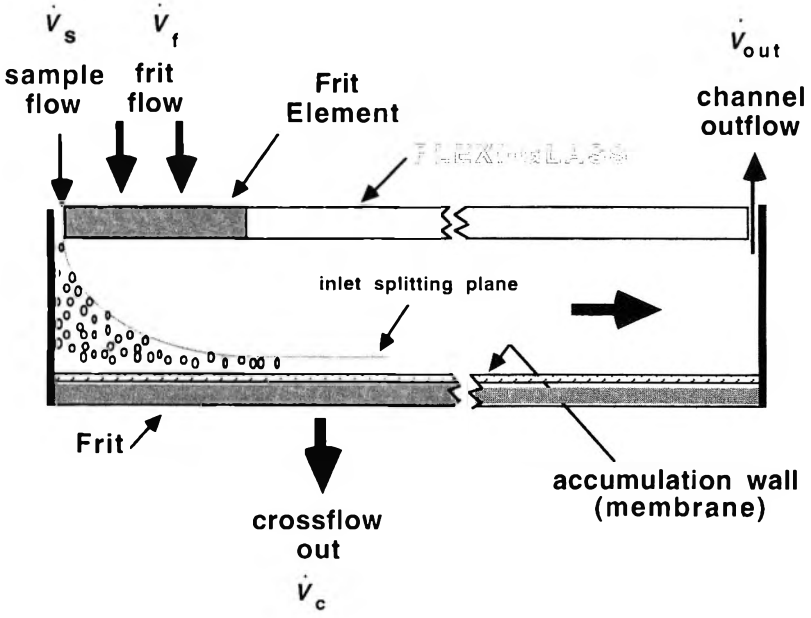

Figure 1. Schematic diagram of the side view of a frit inlet asymmetrical flow FFF (FIA-FlFFF) channel.

The present work utilizes a frit inlet relaxation technique to an asymmetrical flow FFF in order to simplify the relaxation procedure of asymmetrical flow FFF channel, and to facilitate the separation of macromolecules and particulate materials by stopless flow injection. The hydrodynamic relaxation technique has been applied to a conventional symmetrical flow FFF system earlier by using a frit inlet wall nearby the injection point.[7-8] In this work, a small frit element is implemented near the inlet of the plain wall of an asymmetrical channel. When sample materials are slowly introduced through the channel inlet of the so-called frit inlet asymmetrical flow FFF (FIA-FlFFF) channel, they are pushed toward the bottom of the channel wall by the incoming fast flow from the frit inlet wall. Thus, they can be hydrodynamically relaxed while they are continuously migrated down the channel. Relaxation pattern in FIA-FlFFF is expected to be similar to that observed in the frit inlet symmetrical system except that there is no crossflow into the channel. Figure 1 shows the side view of this channel, implemented with a small permeable frit wall at the inlet end of the upper channel wall. Once hydrodynamic relaxation is successfully achieved for the sample components entering the flow streams, they are expected to smoothly

migrate down the channel by being separated each other. With this channel design, a relaxation/focusing process can be bypassed and the system operation can be simplified by one-step injection without the stoppage of sample migration for relaxation. An initial evaluation of the channel was successful in the separation of polystyrene latex standards in both normal and steric/hyperlayer operating modes.[14] It is shown that the frit inlet asymmetrical channel is capable of separating latex particles without using the focusing process.

This paper, in memory of the late Professor J. Calvin Giddings, is written to demonstrate a possibility of separating proteins without the focusing/relaxation procedure, using a frit inlet asymmetrical flow FFF system. The importance of the ratio of injection flow to frit flow rate on the separation efficiency is discussed with the relaxational band broadening.

MATERIALS AND METHODS

The frit inlet asymmetrical flow FFF channel system is modified from a conventional flow FFF channel by substituting the top block with an in-house built lucite block which is implemented with a piece of frit for frit inlet. The channel has a tip-to-tip length of 27.2 cm and a frit inlet that is 3.1 cm long from the channel inlet. The channel space is made with a 254 μm thick Mylar sheet cut into a trapezoidal geometry having an initial breadth of 2.0 cm decreasing to 1.0 cm at the end of the channel. The inlet and outlet ends of the channel are treated as a triangle shape with 2.0 cm and 1.0 cm apart from the both ends, respectively.

Below the channel spacer, a membrane is used for the accumulation wall which enables the cross flow to pass through but keeps sample materials from penetration. The membrane material is YM-30, a regenerated cellulose, which has a molecular weight cutoff of 30,000 (Amicon Co., Beverly, MA, USA). Since the membrane is compressed by the channel spacer during the tightening of the channel blocks, the actual channel thickness is measured, by using the rapid breakthrough method, as 209 μm with the channel void volume of 1.05 mL.

The carrier solution used throughout the study was 0.1 M tris-HCl buffer solution (pH 7.8), prepared from water that is purified by reverse osmosis and deionized. For the delivery of the carrier solution to the channel inlet and frit inlet, two HPLC pumps are used: a Model 350 Soft Start Pump (Bio-Rad

Seoul, Korea). The eluted proteins were monitored by a model 720 UV detector (Young-In, Seoul, Korea) at a wavelength of 280 nm. The two oulet (channel and cross flow outlets) flow rates are controlled by a fine metering needle valve, Whitey SS-22RS2 (Crawford Fitting Co., Solon, OH, USA) located after the detector.

RESULTS AND DISCUSSION

Figure 2 shows the separation of three proteins: ovalbumin, γ-globulin, and thyroglobulin, by using frit inlet asymmetrical flow FFF under the different levels of hydrodynamic relaxation. The three runs are obtained at the same condition as outflow rate $\dot{V}_{out}$ of 0.41mL/min and crossflow rate ($\dot{V}_c$) of 5.78mL/min by controlling the ratio of sample flow rate ($\dot{V}_s$) to the frit flow rate ($\dot{V}_f$). When the ratio $\dot{V}_s / \dot{V}_f$ is set at 48/52 (2.91/3.10 mL/min in real flow rate) in run **a** of Figure 2, serious band broadening during the relaxation is observed for all proteins as broad and diffused peaks. This represents that hydrodynamic relaxation of proteins is not achieved at all with the current injection condition used in run **a**.

As $\dot{V}_s / \dot{V}_f$ is decreased to 8/92, it appears with individual peaks, but they are still broad. When the ratio is further decreased to 4/96 (0.24/5.90 mL/min), a better separation is obtained for the three protein samples with an almost baseline resolution. The small peak right after the peak of γ-globulin is presumed to be dimers of γ-globulin. Figure 2 demonstrates how the ratio of sample flow rate to frit flow rate is important in achieving a good relaxation by hydrodynamic means.

Figure 3 shows the separation of transferrin and apoferritin with the presumed aggregates obtained at the same run condition used in Figure 2 except that the ratio of sample flow rate to frit flow rate is slightly changed to 0.21/6.0 mL/min. Separation of these proteins is successfully achieved in frit inlet asymmetrical flow FFF with the clear identification of each component.

The small peaks right after each monomer peak are presumed to be from their dimers, and a flat peak shown at the very last in Figure 3 from trimers of apoferritin. The identification of the peak of presumed to be aggregates was not confirmed by other means. However, the relative increase in the retention time of the presumed dimer peak from that of the monomer is observed to be

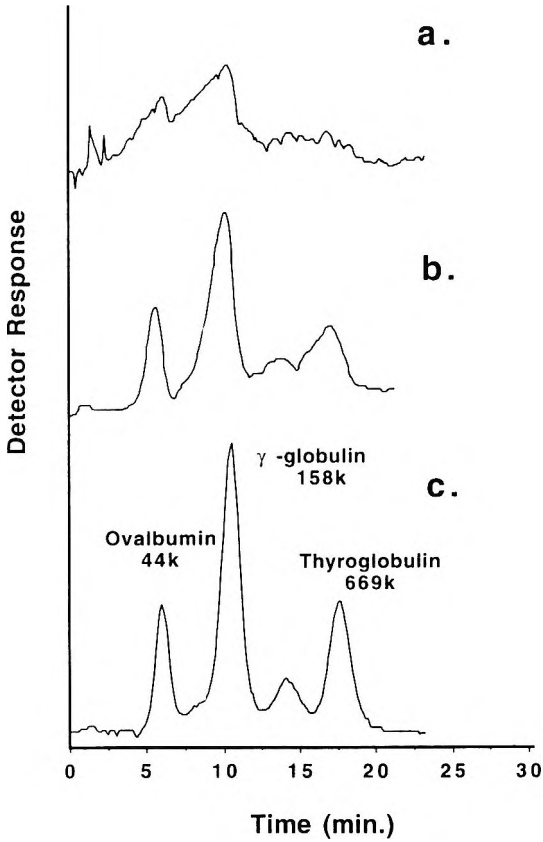

Figure 2. Elution profiles of proteins by varying the ratio of sample flow rate ($\dot{V}_s$) to frit flow rate ($\dot{V}_f$) by FIA-FlFFF: the ratios $\dot{V}_s$ / $\dot{V}_f$ are a) 48/52 (2.91/3.10 mL/min in real flow rates), b) 8/92 (0.80/5.40 mL/min.), and c) 4/96 (0.24/5.90mL/min.). Separation condition for all runs is fixed at $\dot{V}_{out}$ = 0.41 and $\dot{V}_c$ = 5.78 mL/min.

dimers, and a flat peak shown at the very last in Figure 3 from trimers of apoferritin. The identification of the peak of presumed to be aggregates was not confirmed by other means. However, the relative increase in the retention time of the presumed dimer peak from that of the monomer is observed to be about 1.35-1.40 which is very close to the reported value 1.40 reported earlier by a conventional asymmetrical flow FFF.[9] The presumed aggregates may be traced as follows.

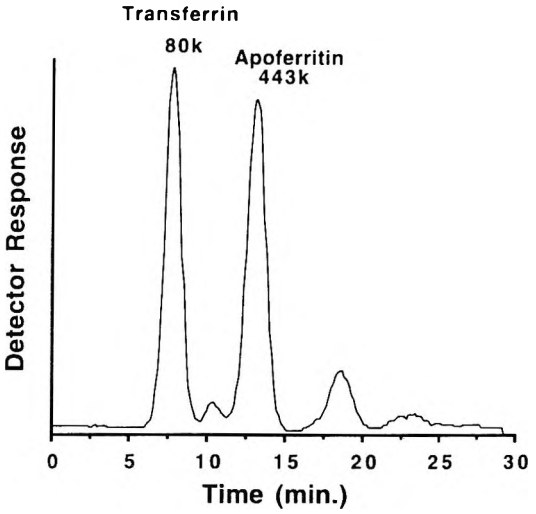

Figure 3. Separation of transferrin and apoferritin and their aggregates by FIA-FlFFF. Run condition is $\dot{V}_s / \dot{V}_f$ = 0.21/6.0 mL/min. and $\dot{V}_c / \dot{V}_{out}$ = 5.78/0.41 mL/min.

Figure 4 shows the correlation plot of log t_r vs. log M of protein monomers (marked as filled circles) shown in Figures 2 and 3, and the superimposed data points (marked as open triangles) of presumed aggregates. The correlation is done with the monomers only, and the straight line correlation is reasonably good with a slope of 0.37, which is slightly higher than the theoretical value of 0.33 in flow FFF,[7] but is somewhat lower than the molecular weight selectivity of 0.49 reported in a work done by conventional asymmetrical flow FFF.[9] The latter value was based on the calculation of exponent b in $D=AM^{-b}$ (D is diffusion coefficient of the protein, A is a constant, and M is the molecular weight of protein) from the ratio 1.40.[9] The retention time data of presumed aggregates appear to fit the correlation curve quite well. From these considerations, they could be assumed as the dimer peaks and a trimer peak. It is also demonstrated that the frit inlet asymmetrical flow FFF system behaves similarly to the conventional asymmetrical system in fractionating proteins and their aggregates.

In order to examine the influence of the flow rate ratio $\dot{V}_s / \dot{V}_f$ on the band broadening during the hydrodynamic relaxation in asymmetrical flow FFF, experimental plate heights are examined at various injection conditions. For a well retained peak provided with a complete relaxation, the relaxational

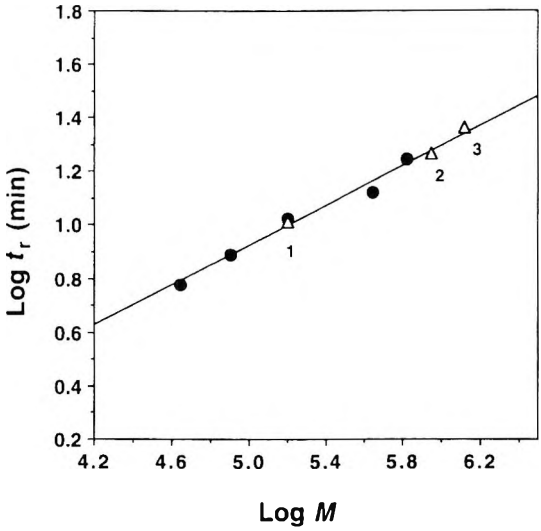

Figure 4. Plot showing correlation between retention time, t_r, and protein molecular weight, M for the monomers shown in Figure 2 and 3. The data points of presumed dimer and trimer peaks (marked as open triangles) are superimposed over the correlation plot. 1. Dimer of transferrin; 2 and 3 are the dimer and trimer of apoferritin, respectively.

contribution to total band broadening can be minimized. In case of using a hydrodynamic relaxation, incomplete relaxation in FIA-FlFFF leads to a substantial increase in the total band broadening of an eluted peak, as observed in Figure 2, which results in the increase of the observed plate height.

Figure 5 shows the plot of observed plate heights of apoferritin vs. the $\dot{V}_s / \dot{V}_f$ ratio. The data points marked as triangles show the plate height data obtained at $\dot{V}_{out}$ = 1.61 and $\dot{V}_c$ =7.45 mL/min, and the lower set (marked as open circles) obtained at $\dot{V}_{out}$ = 0.42 and $\dot{V}_c$ =5.81 mL/min. For the case of upper data set, observed plate height is minimized when the $\dot{V}_s / \dot{V}_f$ ratio decreases to about 3/97. It is shown that the band broadening gradually increases as the ratio increases. When the ratio decreases to a very low level (on the left side of the plot), an unexpected increase in band broadening is observed, due to the relatively slow introduction of sample materials to the sample inlet ($\dot{V}_s$ =0.10 and $\dot{V}_f$ = 8.96mL/min) compared to the fast frit flow.

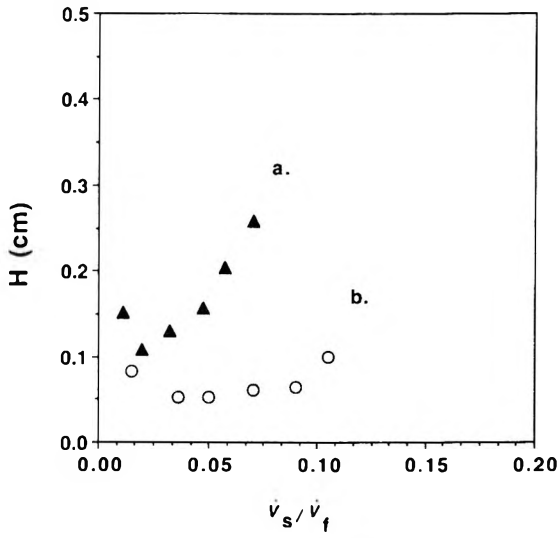

Figure 5. Plot of plate height, H, versus the $\dot{V}_s / \dot{V}_f$ ratio for apoferritin obtained at two different separation conditions; a) $\dot{V}_c / \dot{V}_{out}$ = 7.45/1.61 mL/min and b) $\dot{V}_c / \dot{V}_{out}$ = 5.81/0.42 mL/min.

Compared to the limited usage in optimum hydrodynamic relaxation at the upper set, a relatively strong field strength condition gives more flexibility in selecting the optimum ratio as illustrated in the lower data set. In this case, the outflow rate is decreased to 0.42 mL/min along with the reduction of crossflow rate to 5.81mL/min but $\dot{V}_c / \dot{V}_{out}$ ratio is increased to 13.8 from 4.63 for the upper run condition. In a conventional asymmetrical channel, an increase in the $\dot{V}_c / \dot{V}_{out}$ ratio leads to an improvement in separation efficiency. Thus, the increase in effective field strength in FIA-FlFFF appears to provide less chance of broadening of the initial sample band during hydrodynamic relaxation. The plate heights appear to be minimized in the region of $\dot{V}_s / \dot{V}_f$ from approxiamtely 4/96 up to 8/92 in extreme.

The maximum plate numbers obtained at $\dot{V}_s / \dot{V}_f$ = 4/96 is about 500. It is noted, in Figure 5, that the optimum $\dot{V}_s / \dot{V}_f$ to be used is not fixed and is dependent on experimental run conditions such as $\dot{V}_c / \dot{V}_{out}$ ratio.

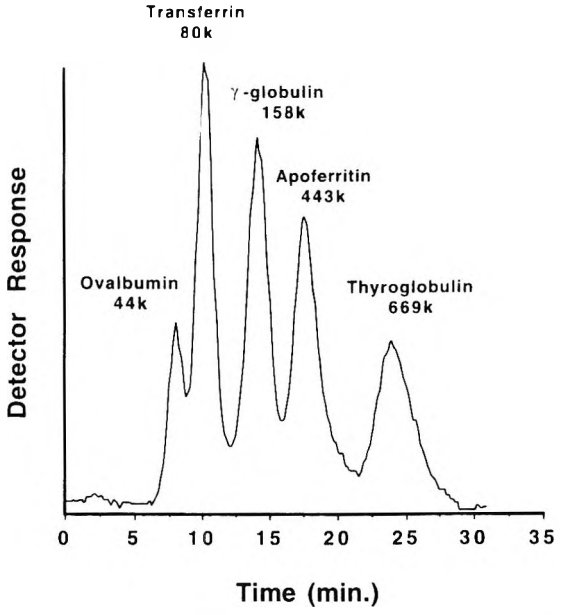

Figure 6. Separation of five proteins by AFI-FlFFF obtained at $\dot{V}_s = \dot{V}_{out} = 0.22$ mL/min. and $\dot{V}_f = \dot{V}_c = 5.80$ mL/min.

An extreme case of run condition is employed in Figure 6, as the outflow rate is adjusted to be the same as the sample flow rate so that all frit flow can be served as crossflow out. Figure 6 illustrates the separation of five proteins using FIA-FlFFF obtained at $\dot{V}_s = \dot{V}_{out} = 0.22$ and $\dot{V}_f = \dot{V}_c = 5.80$ mL/min. The resolution is reasonably acceptable to identify each protein but it takes about 30 minutes for the entire separation, which is somewhat slow. However, the enhancement of separation speed may be achieved if a thinner channel is properly used or the length of inlet frit is reduced. The latter modification leads to a reduction of area of frit inlet element and this may possibly increase the efficiency of hydrodynamic relaxation. In this report, it is demonstrated that FIA-FlFFF is capable of separating proteins and their aggregates by using a hydrodynamic relaxation technique. We note that a successful hydrodynamic relaxation requires a proper selection of $\dot{V}_s / \dot{V}_f$ which falls in the range of 3/97~6/94. This means that a relatively high frit flow rate must be used to efficiently suppress the sample stream toward the accumulation wall and to lead to their equilibrium hydrodynamically.

ACKNOWLEDGMENTS

This study was supported by KOSEF Fund 960501-7.

The authors are grateful to OromTech, Seoul, Korea for the kind donation of an HPLC pump and the data acquisition system.

REFERENCES

1. J. C. Giddings, Science, **260**, 1456-1465 (1993).

2. S. K. Ratanathanawongs, J. C. Giddings, in **Chromatography of Polymers: Characterization by SEC and FFF**, T. Provder, ed., ACS Symposium Ser. 521, ACS, Washington, D.C., 1993, pp. 13-29.

3. J. C. Giddings, S. K. Ratanathanawongs, M. H. Moon, KONA: Powder and Particle, **9**, 200-217 (1992).

4. S. Lee, P. Rao, M. H. Moon, J. C. Giddings, Anal. Chem., **68**, 1545-1549 (1996).

5. M. A. Benincasa, J. C. Giddings, Anal. Chem., **64**, 790-798 (1992).

6. M.-K. Liu, J. C. Giddings, Macromolecules, **26**, 3576-3588 (1993).

7. M.-K. Liu, P. Li, J. C. Giddings, Protein Sci., **2**, 1520-1531 (1993).

8. M.-K. Liu, P. S. Williams, M. N. Myers, J. C. Giddings, Anal. Chem., **63**, 2115-2122 (1991).

9. K.-G. Wahlund, A. Litzen, J. Chromatogr., **461**, 73-87 (1989).

10. A. Litzen, K.-G. Wahlund, Anal. Chem., **63**, 1001-1007 (1991).

11. A. Litzen, J. K. Walter, H. Krischollek, K.-G. Wahlund, Anal. Biochem., **212**, 469-480 (1993).

12. A. Litzen, Anal. Chem., **65**, 461-470 (1993).

13. B. Wittgren, K.-G. Wahlund, H. Derand, B. Wesslen, Macromolecules, **29**, 268-276 (1996).

14. M. H. Moon, H. Kwon, I, Park, Anal. Chem., **69**, 1436-1440 (1997).

Received January 16, 1997
Accepted April 18, 1997
Manuscript 4441

J. LIQ. CHROM. & REL. TECHNOL., 20(16 & 17), 2815–2833 (1997)

MONITORING THE BIOLOGICAL AND PHYSICAL REACTIVITY OF DEXTRAN CARBOHYDRATES IN SEAWATER INCUBATIONS USING FLOW FIELD-FLOW FRACTIONATION

S. Kim Ratanathanawongs Williams,[1] Richard G. Keil[2,*]

[1] Field-Flow Fractionation Research Center
Department of Chemistry
University of Utah
Salt Lake City, UT 84112, USA

[2] School of Oceanography
Box 357940
University of Washington
Seattle, WA 98195-7940, USA

ABSTRACT

In order to better understand the factors that modulate the size and reactivity of high molecular weight organic matter dissolved in seawater, fluorescently labeled dextrans were used as the model compounds whose molecular weight distributions were monitored by flow field-flow fractionation (flow FFF or FlFFF) during incubations in seawater matrices. Two fluorescein isothiocyanate (FITC) labeled dextrans (145k and 2M Da) were incubated in whole seawater (natural microbial population and natural dissolved organic matter (DOM) present), 0.02 μm filtered seawater (all microorganisms removed, but natural DOM

largely unaltered), and UV-oxidized seawater (no microorganisms or natural DOM present). Flow FFF fractograms of the two FITC-dextrans incubated in UV-oxidized seawater showed no changes, signifying that the dextrans did not undergo any alteration or aggregation. The dextrans incubated in filtered seawater with natural DOM present resulted in fractograms that are shifted to higher retention times, consistent with aggregation of the dextran and natural DOM.

In the whole seawater incubations, the complex changes in the fractograms over time indicated that the dextrans underwent both aggregation with natural DOM and degradation by heterotrophic microorganisms. The latter was confirmed by microscopic examination of the collected fractions after selectively staining the microorganisms with the fluorescent dye 4,6-diamidino-2-phenylindole (DAPI). The FITC dextrans were observed to be "attached" to the bacteria's outer cell membrane where they are subsequently hydrolyzed into small low molecular weight fragments by extracellular enzymes. Some of these degraded dextrans are assimilated by the bacteria and the rest (~70%) are released into the seawater. Approximately half of the released degraded dextrans are of high enough molecular weight to be retained by flow FFF at the conditions employed in these studies. The data presented in this paper illustrate that, when used as both a qualitative and semipreparative tool, flow FFF can provide information on the relationships between natural and model DOM and microorganisms that would be difficult or impossible to obtain using other methods.

INTRODUCTION

In seawater, dissolved organic matter is found at dilute concentrations that are typically less than one or two parts in a million, yet the large volume of the oceans hold a dissolved organic matter (DOM) pool that is of the same order of magnitude (0.60×10^{18} g carbon) as the atmospheric carbon dioxide pool (0.66×10^{18} g C) and the biomass contained within all terrestrial plants (0.95×10^{18} g C).[1] Due to the dilute nature of DOM in seawater and the fact that it is contained within an electrolyte-laden solution where the mass of salts outweigh organics by a factor of 35,000, exploring the dynamics of DOM has proven to be a challenging task. Adding further to the intrigue is the observation that most marine DOM is not readily available for biological consumption; the average "age" of DOM in the deep ocean (determined using ^{14}C) is ~6000

years,[2] long enough for DOM to cycle through the oceans several times prior to being degraded. Since the source of this dilute non-reactive DOM is ultimately the planktonic community at the ocean surface, links between the production, consumption, and preservation of DOM have been investigated for the past 70 years.[3]

The production and consumption of specific components of DOM (e.g. carbohydrates, proteins and lipids) by autotrophic and heterotrophic organisms are the primary forces that drive the oceanic DOM cycle. These processes can be monitored using labeled precursors and substrates.[4] For instance, the production and destruction rates of amino acids[5-7] and proteins[8,9] by organisms in seawater are now well established. However, physical and chemical (i.e., non-biological) processes may also affect the DOM cycle. Integrating studies of biological and physico-chemical influences on DOM have been difficult. Two central aspects of DOM cycling that have been especially difficult to study are the production of DOM intermediate in either size or bioavailability, and the abiotic (e.g. not biologically mediated) interactions of DOM with minerals or itself. These are important aspects of DOM cycling because they may provide insights about how DOM can become non-reactive, how it affects the light-scattering and radiative transferring properties of seawater (e.g. remote sensing),[10] and the role DOM may play in transferring carbon from the Earth's surface to the ocean's interior (where it would be out of contact with the atmosphere for hundreds to thousands of years). This last topic is currently receiving strong interest because the oceans are responding to the anthropogenic pumping of CO_2 into the atmosphere by increasing their carbon content (both inorganic and organic). One mechanism of transferring carbon from the ocean surface to depth is in the form of sinking particles formed by the aggregation of DOM to form particles of sufficient mass for sinking.[11,12]

Attempts to determine the molecular weight or size spectrum of DOM using size exclusion chromatography have generally been unsatisfactory[13] due to the high shear stresses that DOM is exposed to during separation and adsorption problems with the support matrix. Studies using ultrafiltration have generally limited separations to only a few broad size classes[14]. For example, Guo et al.[15] separated DOM into three fractions (<1000 Da, 1000-10,000 Da and >10,000 Da) and observed that 45% of the total organic carbon in the Gulf of Mexico was composed of DOM >1,000 Da in size. They and others[12,16] have observed that DOM exhibits spatial and temporal changes in quantity and molecular weight distribution. The causes of these changes (e.g., aggregation, degradation of specific components, sinking, etc.) could not be easily investigated because of the lack of a suitable technique capable of scanning the entire DOM pool and of isolating specific components. Amon and Benner[16] were able to determine that a carbohydrate-rich component of the >1000 Da

ultrafiltered DOM fraction was remineralized by bacteria more quickly than smaller material. However, isolation of, and discrimination between, the reactive and non-reactive DOM (>1000 Da) components remained elusive.

Field-flow fractionation (FFF) is a family of techniques that have not yet found routine application in marine systems. These separation techniques are similar in operation to chromatography. However, compounds are retained and separated in thin rectangular channels by interaction with an external field rather than an internal stationary phase. Separation occurs by differential retention of solute within a laminar flow stream bounded by thin parallel plates. With respect to traditional chromatographic techniques, advantages of applying an external force include elimination of adverse solute-stationary phase interactions and easily increased resolving power.[17] The theory behind flow FFF has been extensively presented elsewhere[17-23] and will not be discussed here.

MATERIALS AND METHODS

Flow FFF

The flowrate-programmable FFF system used in this work has previously been described in detail by Ratanathanawongs and Giddings.[24] A strong field (high cross flowrate) is applied during the initial portions of the run and decreased over time. Programming the field strength is analogous to programming solvent strength in HPLC. The advantage of programming over isocratic conditions is most apparent when dealing with broad particle size distributions; particles that elute at retention time extremes can be adequately and quickly resolved.[25,26] In our dextran experiments, the cross flowrate was held constant for 20 seconds at 2.4 mL/min and then decreased to 0.2 mL/min according to the power decay function.[26] The channel flowrate was held constant at 2.5 mL/min.

The flow FFF channel had dimensions of 0.011 cm thickness, 2.0 cm breadth and a tip-to-tip length of 27.2 cm. The membrane had a nominal cutoff of 10,000 Da and was composed of regenerated cellulose (YM-10; Amicon Corp., Beverly, Massachussetts). After flow FFF separation, the channel effluent was sent through a UV detector (Applied Biosciences, Foster City, California) and a fluorometer (St. John and Associates, Inc., Beltsville, Maryland). After detection, fractions were collected using an FC-80K Microfractionator (Gilson Medical Electronics, Middleton, Wisconsin).

Carrier Liquid

The carrier liquid for both the channel and crossflow was UV-oxidized seawater previously collected from 50 meters depth in central Puget Sound (see Experimental). The water was filtered through a nominal 0.7 μm glass fiber filter (GF/F, Gelman Scientific) to remove particulates and then UV oxidized for 6 hours. After oxidation, the water was placed in a sealed glass container for 1 week prior to experimental work in order to eliminate ozone and free radicals produced during UV oxidation. This procedure lowered the organic matter concentration of the water from 1.75 to ~0.15 mg/L organic carbon. Investigation by other researchers[27] indicated that much of this material is of very low molecular weight (<1,000 Da). Use of "organic-free" seawater allowed flow FFF studies of model compounds within a natural matrix. This is not a viable alternative for size exclusion chromatography, where mobile phases must be carefully controlled and high ionic strength solutions (>0.5M, such as seawater) cannot be used. For channel evaluation and standardization with polystyrene (PS) latex beads, surfactant- (FL-70; Fisher Scientific, Fair Lawn, New Jersey) containing seawater carrier fluid was used. For all the analyses involving dextran, no surfactant was added.

Model DOM

There are currently no acceptable analytical methods available to measure the low quantities of DOM found in natural systems after fractionation. The predominant technique, high temperature combustion to CO_2 followed by infrared detection,[28] is sensitive down to approximately 0.05 mg/L. A flow FFF separation of DOM would produce fractions that are at concentrations approximately equal to this or lower, making detection extremely difficult. For this reason, a model compound that mimics many of the characteristics of naturally occurring DOM was used. Dextran, a globular carbohydrate, was chosen because it is thought to be somewhat representative of the dissolved organic matter present in seawater,[27,29,30] of which >50% is complex carbohydrate. Additionally, these globular dextrans do not appreciably adsorb to regenerated cellulose membranes in seawater.[30,31] Benner et al.[27] have observed only low levels (<10%) of adsorption of natural DOM to regenerated cellulose membrane filters. The model DOMs used in the study were 145,000 and 2,000,000 Dalton globular dextrans (145k and 2M Da; Sigma Chemical Co., St. Louis, Missouri) that had been labeled along the chain with fluorescein isothiocyanate (FITC). A nonlabeled 9.4M Da dextran (Sigma Chemical Co., St. Louis, Missouri) and 20 nm, 54 nm, and 107 nm polystyrene latex standards (Duke Scientific, Palo Alto, California) were also used for evaluating and standardizing the channel.

EXPERIMENTAL

Seawater was collected from the south-west expansion of Useless Bay in central Puget Sound, Washington, USA. Seawater used as the carrier liquid was collected from a depth of 50 m using a pre-cleaned 30 L Go-Flo™ bottle approximately two weeks prior to sample collection. Seawater samples for the reactivity experiments were similarly collected from a depth of 10 m, but were then filtered through a 63 μm mesh screen to remove large organisms and particles. The primary population of organisms in the water were heterotrophic bacteria (~0.5 μm average size) and mixotrophic flagellates (~3-10 μm average size). The water was transfered to a clean 20 L polystyrene carboy, stored in the dark at *in situ* temperature (15°C) and immediately transported to the laboratory in Utah. All experimental work was started within 36 hours of sample collection.

Two 1 L cleaned polycarbonate bottles were filled with 63 μm filtered seawater (hereafter referred to as "whole" seawater because neither the heterotrophic microoganisms nor the DOM pools were disturbed), two bottles received 0.02 μm filtered water (all microorganisms removed, but DOM largely unaltered), and two bottles received UV-oxidized water (no microorganisms or DOM present). Three of the bottles (one each of the whole, filtered and oxidized water) received additions of the 2M Da fluorescently labeled dextran, and three bottles received additions of 145k Da fluorescently labeled dextran (Table 1). Additions were at a concentration of 0.01 mg/L, or approximately 1/175th the dissolved organic carbon of the water (as measured by a Shimadzu TOC5000 high-temperature catalytic oxidation analyzer). The bottles were then incubated in the dark at *in situ* temperature and subsamples were drawn after 0, 2, 4, 8, 12 and 23 h. Surfactants were not added to the carrier fluid of the flow FFF system during analysis of these samples so that artificially induced aggregation or disaggregation would not be an issue.

The experimental design allowed several possible fates for the added dextran. In the UV-oxidized seawater, all the organisms and >90% of the naturally occurring DOM was removed. Model DOM added to the UV-oxidized seawater could conceivably aggregate with itself, interact with dissolved metals and minerals in the water, or undergo no interactions. In the 0.02 μm filtered seawater, natural DOM was present but no microorganisms. This adds the potential that the model DOM could interact with the naturally occurring DOM to form abiotically produced aggregates. In the whole seawater, the two dominant organisms, mixotrophic flagellates (microorganisms that can act as either autotrophs or heterotrophs depending on conditions) and heterotrophic bacteria, were present at approximate densities of 10^4 cells/mL and 10^6 cells/mL, respectively. Flagellates are known predators

of heterotrophic bacteria, and have also been shown to consume DOM of very high molecular weight.[29] Heterotrophic bacteria are the primary consumers of DOM. Model DOM added to whole seawater could undergo any of the previous interactions, plus be consumed by either the bacteria or the flagellates. Because bacteria cannot assimilate large molecules across their cell membranes, they degrade macromolecules extracellularly and import the resulting smaller components into the cell. Often, extracellular enzymatic activity is membrane-associated, that is, the bacteria attach the substrate to their cell wall for degradation rather than releasing enzymes into the seawater.[33] It is an open question as to whether bacteria release a large portion of the hydrolyzed substrate into the water during hydrolysis and before uptake.[9] Degradation of the dextran by flagellates should be easily observed as fluroescence in the phagocysts of the flagellates.

Fluorescence Microscopy

In addition to measuring the molecular weight distribution via flow FFF, fractions of the column effluent were collected for microscopic analysis. Magnification used on the fluorescence microscope (X1001; Zeiss Inc., Hamburg) varied between 100-5000×. Fractions were analyzed for heterotrophic microorganism abundances after staining with 4,6-diamidino-2-phenyl indole (DAPI). DAPI and FITC fluoresce in different regions,[29] thereby facilitating discrimination between the dextran and the microorganisms. The percentage of fluorescence associated with the bacterial and flagellate size classes was measured by filtering material collected from the void peak through 1.0 and 0.2 μm filters and measuring changes in fluorescence (Table 2). Non-associated fluorescence was defined as the fluorescence in the 0.2 μm filtrate. Flagellate-associated fluorescence was defined as the total fluorescence minus the fluorescence in the 1 μm filtrate, and bacteria-associated fluorescence was defined as 1 μm filtrate fluorescence minus non-associated fluorescence. No attempt was made to correlate fluorescence of the fractions to the total fluorescence added to the incubations.

RESULTS AND DISCUSSION

An important aspect of this study was to identify suitable particle standards that can be used to evaluate flow FFF channel performance while using seawater as a carrier liquid. Initial experiments with polystyrene (PS) latex standards showed complete adsorption to the membrane wall (no elution). This problem was resolved by adding 0.1% (v/v) of FL-70 surfactant to the seawater carrier liquid. The resulting separation is shown in Figure 1a.

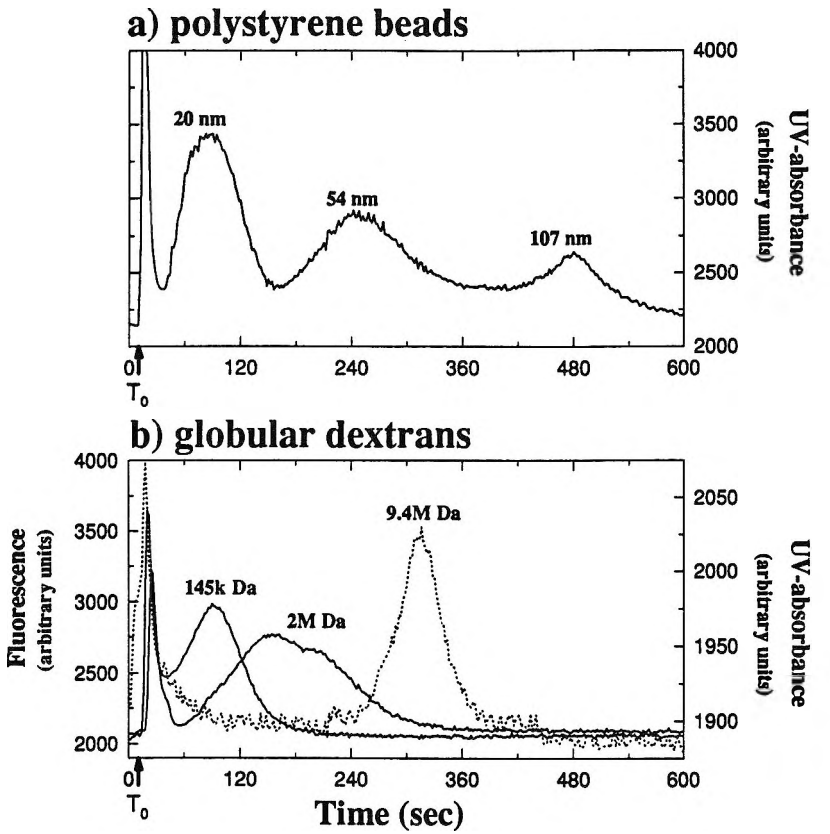

Figure 1. A) Separation of polystyrene latex standards in a flow FFF system using seawater as a carrier fluid with surfactant (FL-70) added at 0.1% (v/v). The channel and cross flowrates were 2.6 and 3.0 mL/min, respectively. B) Separation of dextran standards in a seawater carrier without added surfactant. The channel flowrate was held constant at 2.5 mL/min and the cross flowrate was programmed from 2.4 mL/min to 0.2 mL/min with a 20 s delay time using a power decay function with $p=2^{26}$.

Without surfactant, the high ionic strength of seawater collapses the electric double layer and thus promotes sorption of the PS beads to the regenerated cellulose membrane. The surfactant prevents adsorption through a steric stabilization mechanism.[34]

Retention times for the 20, 54, and 107 nm particles are 0, 9 and 17% longer than predicted by theory, reflecting the increasing effect of particle-membrane interactions with increasing proximity to the membrane.

Though the peaks are broader than usually observed in flow FFF runs using lower ionic strength carriers, the particles do not appear to be aggregating with each other.

In theory, since normal mode FFF retention is calculated from first principles,[17,18] it is possible to obtain size or molecular weight information directly from the retention times provided the flowrate, field strength, and channel void volume are known. However, in this case where particle-membrane interactions cause deviations from theoretical retentions, the PS standard run is only used to provide an approximate relationship between retention time and particle diameter and to provide a baseline run for qualitative comparisons with fractograms obtained at a later date.

It is important to note that, while the PS standards required addition of surfactant to the seawater carrier liquid, the presence of surfactant in these runs does not mitigate the use of measured retention times as size or molecular weight markers.

Fractograms of 145k, 2M and 9.4M Da dextrans are superimposed in Figure 1b. By programming the field strength, the separation times are kept below ten minutes. The order of elution of the dextran is as expected for normal mode operation of flow FFF, with the smaller (higher diffusion coefficient) components eluting first. Also, as expected for polydisperse globular dextrans, the three peaks are very broad (Figure 1b). Repeat injections of the standards throughout the experimental period illustrated that the elution profile was stable (data not shown). The amount of dextran recovered after a separation was calculated by ratioing the peak area of a normal run to that of a channel bypass run. The latter involves rerouting the flow path to directly connect the injector and the detector.

Assuming that the peak area resulting from the channel bypass run corresponded to 100% recovery of dextran, the recovery based on the peak area of the normal run was 85 ± 15%. The small interaction between the dextran and the regenerated cellulose membrane in the flow channel is similar to that reported by other groups.[27,30]

The generalized fate of the 145k and 2M Da dextrans under the three incubation schemes is outlined in Table 1. Dextran added to UV-oxidized seawater (no microorganisms or DOM present) showed no changes in fluorescene intensity or distribution (Figures 2a and 3a). This indicates that the dextran was not aggregating with itself during the experimental period and that the flow FFF system was stable and reproducible throughout this study. Slight differences in the spectra were attributed to the lack of an autoinjector or

Table 1

Experimental Matrices Used to Evaluate the Effects of Aggregation and Microbial Degradation of Fluorescent Dextrans in Seawater Incubations[a]

	Medium		
Dextran	**UV Oxidized sH_2O[b]**	**0.02 μm Filtered sH_2O[c]**	**Whole sH_2O[d]**
145k Da	aggregation: **no** degradation: **no**	aggregation: **yes** degradation: **no**	aggregation: **yes** degradation: **yes**
2M Da	aggregation: **no** degradation: **no**	aggregation: **yes** degradation: **no**	aggregation: **yes** degradation: **yes**

[a] sH_2O = seawater; [b] no DOM or microorganisms present; [c] DOM present but no microorganisms; [d] DOM and microorganisms present.

sample loop, and likely reflect our ability to repeatedly inject the same amount of sample. Although it is theoretically possible for the dextran to interact with metal ions and very fine mineral components of the seawater, these interactions are not measurable with the instrumentation used in this work.

Dextran added to the 0.02 μm filtered seawater (no microorganisms, but natural DOM largely intact) did not undergo significant change during the first twelve hours of incubation (Figures 2b and 3b). After 12 hours the distribution shifts and broadens toward higher molecular weights. Since the seawater was filtered, the shift to higher molecular weights may reflect interaction (aggregation) of the dextran with other organic matter or with other small colloidal materials present in the seawater. Such interaction has been hypothesized as a mechanism that might alter the lability of DOM in seawater,[35] and could ultimately lead to the formation of large organic aggregates (marine snow).[11]

Additions of dextran to whole seawater showed the most dynamic patterns (Figures 2c and 3c). For both the 145k and 2M Da dextrans, decreases in total fluorescence were observed over the 6-23 h period. The 145k Da dextran showed the greatest changes in molecular weight (Figure 2c). In the first 4 h, a shift to higher molecular weight (as indicated by longer retention times) was observed, but by 6 h the trend had reversed and the molecular weight of the dextran (or any dextran-DOM complex) appeared to be decreasing. By 23 h, the fluorescence intensity of the 145k Da dextran had decreased by half

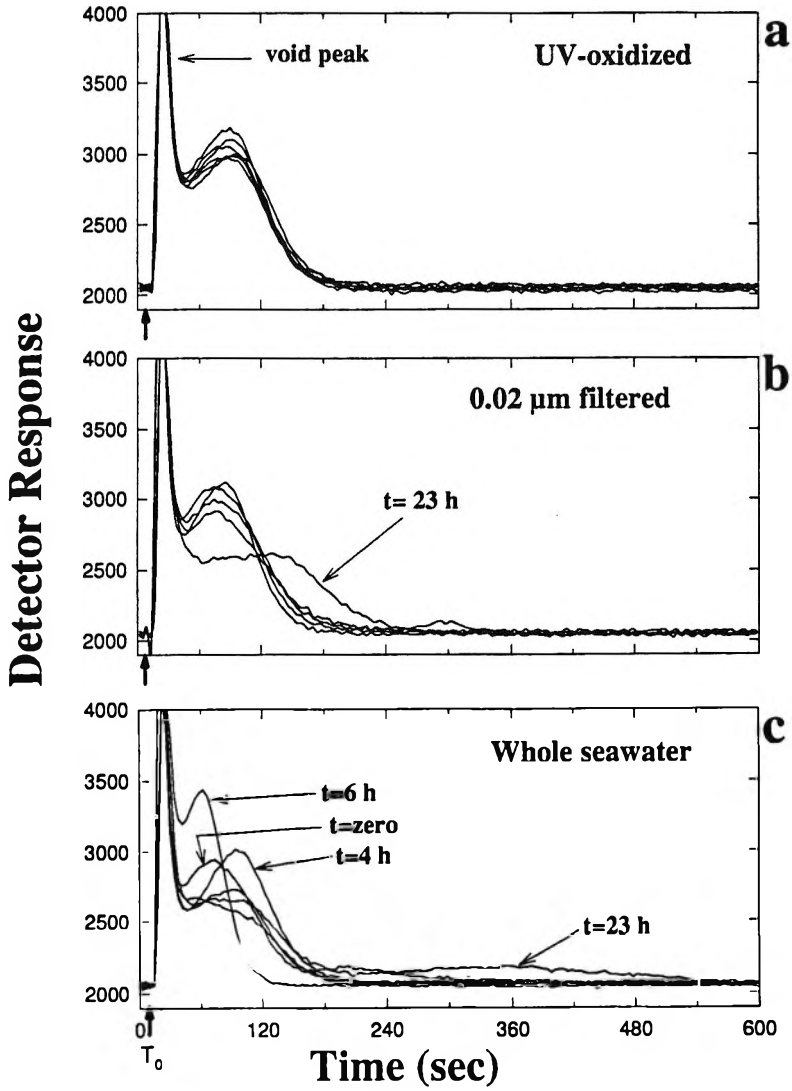

Figure 2. A) Incubation of 145k Da dextran in UV-oxidized seawater. B) Incubation in 0.02 µm filtered seawater. C) Incubation in whole seawater. FFF experimental conditions as described in Figure 1B.

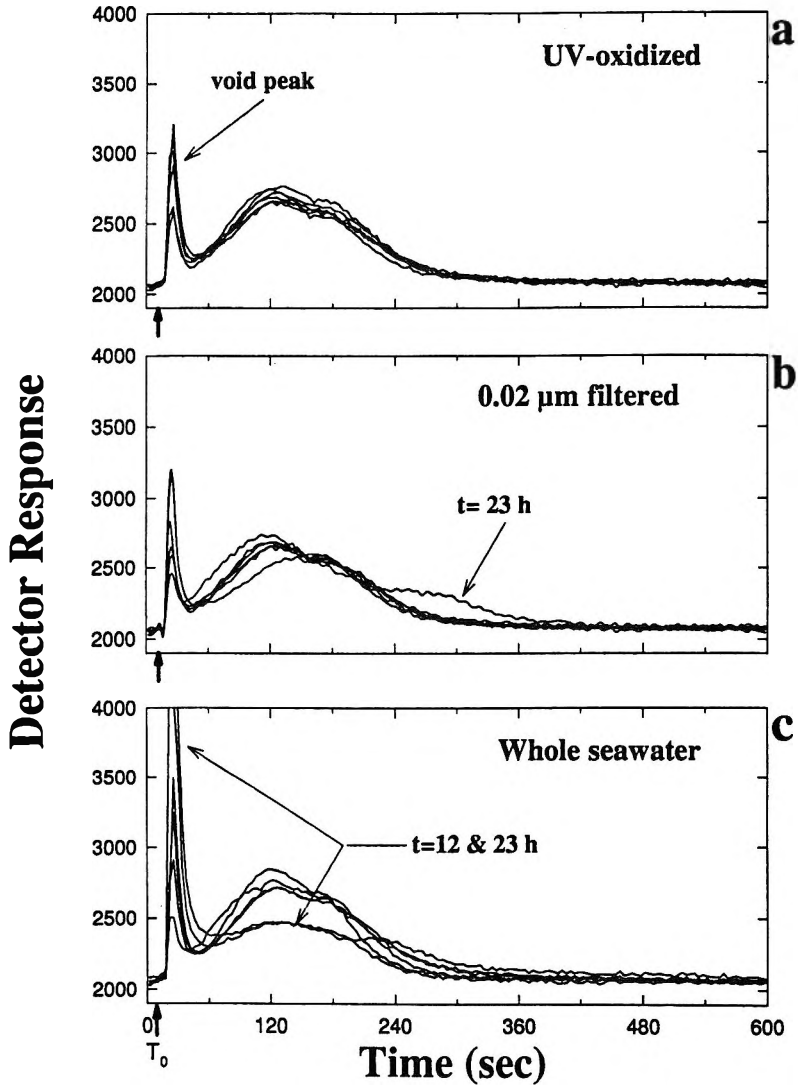

Figure 3. A) Incubation of 2M Da dextran in UV-oxidized seawater. B) Incubation in 0.02 µm filtered seawater. C) Incubation in whole seawater. FFF experimental conditions as described in Figure 1B.

compared to that at time-zero, and a broad peak was observed in the region of higher molecular weights (Figure 3c). This broad peak could be due to aggregation with DOM, such as the incorporation of the labeled dextran into high molecular weight carbohydrate mucus,[11] or to the release of high molecular weight digestive fragments during flagellate grazing.[36] The 2M Da dextran showed a consistent decrease in fluorescence intensity as a function of incubation time (Figure 3c). This decrease in the 2M Da dextran was accompanied by an increase in the fluorescence of the void peak (Figure 3c).

Thus far, the normal mode of flow FFF has been discussed and demonstrated. A second mode of operation, called steric FFF, becomes important when the particles being separated are large relative to their diffusion distance from the accumulation wall, or when the experimental conditions employed cause particles to reside directly on the membrane surface.[20,22] In these cases, larger particles will protrude further into the center of the channel (higher in the flow stream) than the smaller particles. Consequently, the larger particles will elute earlier than smaller particles, opposite to that of normal mode. The transition from normal to steric mode, or vice versa, occurs in the size range of ~0.2-3 μm,[20,37,38] and is determined by the field strength, channel dimensions, flowrate, carrier liquid viscosity and particle density.[20,37-39] FFF separation of samples that span this range is complicated because both normal and steric modes are in operation. For a polydisperse sample possessing a continuous range of particle sizes, coelution of particles of two different sizes will occur. A fractionation technique would be used to separate the particles into two size classes prior to FFF analysis. In the case of a polydisperse sample with two distinct populations it is possible to select experimental conditions that allow the two different populations to separate in the two different modes over two different time periods. In the situation studied here, the two populations are the smaller dextrans and the larger microorganisms. The operating conditions we employed caused bacteria and microflagellates to be rapidly swept through the column and eluted with the void peak (i.e., no retention) and the dextrans to be separated in the normal mode.

The sharp void peak at the beginning of each run contains both very large (bacteria and flagellates, etc.) and very small species. Consequently, changes in the fluorescent intensity of the void peak may reflect association of the dextran with bacteria, ingestion of dextran by flagellates, or degradation of the dextran to small FITC-labeled compounds of a mass between ~10,000 Da and ~5 nm (the channel membrane molecular weight cutoff and the approximate lower limit of separation, respectively). Two approaches were used to distinguish between these three possibilities. First, a portion of the void peak was examined microscopically after filtration and staining with DAPI (and using both blue and UV excitation).[30] At time-zero, we observed no association

of FITC fluorescence with either the bacteria or flagellates. After longer incubation times, FITC fluorescence was observed to be associated with both the bacterial and flagellate populations. The amount of FITC-fluorescence associated with both microorganisms was quantified as the proportion of cells with FITC fluorescence over the total number of cells in the sample. This is a rough measure of the percentage of the populations that assimilated the dextrans (Table 2; %cells). It should be noted that FITC fluorescence associated with flagellates could result either directly via ingestion of labeled dextran, or indirectly via ingestion of bacteria that had previously assimilated labeled dextran. Significant association of the FITC with microorganisms was only observed after 12 hours (Table 2). A higher proportion of the flagellate population (~16%) accumulated fluorescence when incubated with the 2M Da dextran than with the 145k Da dextran (<10%). The proportion of the bacterial population that assimilated fluorescence was also slightly higher when incubated with the larger dextran (Table 2).

A differential filtration method was used to determine the cause of increased fluorescence in the void peak over time. The percentage of fluorescence associated with bacteria and flagellates was measured by filtering material void peak material through 1.0 and 0.2 μm filters and measuring changes in fluorescence (Table 2). Initially, nearly all the fluorescence was in the <0.2 μm size class (i.e. not associated with bacteria or flagellates), but after 12 hours, nearly half the fluorescence signal was associated with either the bacterial or flagellate size classes. Heterotrophic flagellates also had measurable fluorescence associated with them as ingested particles, although at levels below that observed by Tranvik et al.[30] Similar to the result of direct observation, the association of 145k Da dextran with flagellates was much weaker than that of the 2M Da dextran (Table 2). In the 2M Da incubation, the percentage of non-associated fluorescence (fluorescence in the <0.2 μm filtrate) increased between 12 and 23 hours. This may be due to an increase in the degradation and release of small fluorescent materials relative to the rate of association or ingestion of the larger dextran. Taken as a whole, there was a good correlation between the change in the molecular weight and quantity of fluorescently labeled dextran in solution and the increase of bacterial- and flagellate-associated dextran in the void peak.

The incubations in the 0.2 μm filtered water illustrated significant interaction of the dextran with other organic matter in the same nominal molecular weight range (100K - 10M Da). This is one of the first pieces of direct evidence that dissolved organic matter may aggregate and form large conglomerates in seawater without the assistance of bubbling or shaking of the water, and on the same time scale as microbial degradation occurs. Whether these organic-organic interactions are also typical of natural organic matter

Table 2

FITC Fluorescence Associated With Bacteria or Flagellates During Whole Seawater Incubations of 145k Da and 2M Da Labeled Dextrans[a]

Time (h)	Flagellates % Fluor	Flagellates % Cells	Bacteria % Fluor	Bacteria %Cells	Non-Associated % Fluor
			145k Da Dextran		
0	1	0	1	0	97
2	2	0	8	<10	91
4	3	0	14	<10	81
8	3	0	28	<10	74
12	5	<10	44	24	49
23	5	<10	74	31	20
			2M Da Dextran		
0	1	0	2	0	101
2	2	0	6	<10	90
4	2	0	14	17	85
8	5	0	23	21	71
12	8	13	65	43	26
23	13	16	50	39	38

[a] Data are expressed as the percent of total fluorescence intensity (%Fluor) in the void peak (standard error of ±3%). Non-associated fluorescence is defined as the % of total fluorescence in the 0.2 μm filtrate. Heterotrophic flagellate-associated fluorescence is the total fluorescence minus the fluorescence in the 1 μm filtrate, and bacteria-associated fluorescence is the 1 μm filtrate fluorescence minus non-associated fluorescence. Microscopy-based data are also tabulated for the percent of total cells with associated FITC fluorescence (%cells).

remains to be investigated. The incubations with whole seawater illustrate that the dominant force acting upon the dextrans was degradation by heterotrophic microorganisms. The observation that the bacteria efficiently assimilate the extracellular breakdown products of the dextran (they cannot transport large molecules directly across their cell membranes) and that only small quantities of dextran of intermediate molecular weight accumulate in the medium is

consistent with observations made using radiolabeled proteins[9] and illustrates the efficiency of the bacterial degradation scheme. Finally, the assimilation of the dextran by heterotrophic flagellates is consistent with and extends the findings of Sherr[29] and Tranvik et al.[30]

This feasibility study illustrates that the processes acting upon dissolved organic substances in seawater can be fruitfully examined using flow FFF analysis coupled with other experimental and analytical techniques. Our results confirm previous studies of model DOM behavior in marine systems and for the first time include small relative changes in molecular weight that were not observable in earlier studies. Although this study leaves many unanswered questions about the factors that promote or limit changes in natural and model DOM, it is the first to show that these changes can be observed semi-quantitatively over a broad molecular weight range using natural seawater as a carrier fluid. Flow FFF analysis can potentially provide a great deal of information on the relationships between dissolved organic matter and microorganisms in seawater that would be difficult or impossible to obtain with other methods because seawater can be used as a carrier and because flow FFF can potentially fractionate both DOM and heterotrophic microorganisms in a single analysis.

ACKNOWLEDGMENTS

SKRW- During the ten years I worked with Professor J. Calvin Giddings, I enjoyed the freedom to make forays into new and exciting research areas. This paper, which represents the first flow FFF study ever conducted in the field of oceanography, is but one example. Without his support and encouragement, this work would not have been possible. I will always be grateful to Cal Giddings for encouraging me to develop and grow without bounds in the quest to satisfy my curiosity.

RGK- The work presented in this manuscript would not have been possible without the encouragement and indulgence that I received from Cal Giddings. His love of, and interest in, the environment was a strong force that permeated my every interaction with him. I recall the child-like curiosity and distinct sense of urging that Cal brought to all our discussions of this work and the work we conducted using SPLITT fractionation on environmental samples. Although I interacted with him only intermittently, his impact on my scientific direction has been profound. Thank you Cal.

This initial study was supported, in part, by an NSF grant to R.G. Keil (OCE9401081) and an NIH grant to J. C. Giddings (Public Health Service Grant GM10851-39). We thank J. C. Giddings, J. I. Hedges, E. Tsamakis, and S. Strom for helpful discussions. This is contribution number 2177 from the University of Washington, School of Oceanography.

REFERENCES

1. J. I. Hedges, R. G. Keil, Mar. Chem., 49, 81-115 (1995).

2. P.M. Williams and E.M. Druffel, Nature, 330, 246-248 (1987).

3. S. A. Waksman, C. L. Carey, J. Bacteriology, **29**, 545-561 (1935).

4. R. T. Wright, J. E. Hobbie, Ecol., 47, 447-468 (1965).

5. N. O. G. Jorgenson, Limnol. Oceanogr., **32**, 97-111 (1987).

6. J. Fuhrman, Mar. Ecol. Prog. Ser. **66**, 197-203 (1990).

7. R. G. Keil, E. A. Presley, D. L. Kirchman, Mar. Ecol. Prog. Ser. **73**, 1-10 (1991).

8. J. T. Hollibaugh, F. Azam, Limnol. Oceanogr., **28**, 1104-1116 (1983).

9. R. G. Keil, D.L. Kirchman, Limnol. Oceanogr., **38**, 1256-1270 (1993).

10. D. Risovic, Deep Sea Research, **40**, 1459-1473 (1993).

11. A. L. Alldredge, U. Passow, B. E. Logan, Deep Sea Research, **40**, 1131-1140 (1993).

12. M. L. Wells, E. D. Goldberg, Limnol. Oceanogr., **39**, 286-302 (1994).

13. R. Beckett, Z. Jue, J. C. Giddings, Environ. Sci. and Technol., **21**, 289-295 (1987).

14. B. E. Logan, Q. Jiang, J. Environ. Engin., **116**, 1046-1062 (1989).

15. L. Guo, C. H. Coleman, P. H. Santschi, Mar. Chem., **45**, 105-120 (1994).

16. R. M. W. Amon, R. Benner, Nature, **369**, 549-552 (1994).

17. J. C. Giddings, Science, **260**, 1456-1465 (1993).

18. J. C. Giddings, Anal. Chem., **67**, 592A-598A (1995).

19. S. K. Ratanathanawongs, J. C. Giddings, Chromatographia, **38**, 545-554 (1994).

20. K. D. Jensen, S. K. R. Williams, J. C. Giddings, Anal. Chem., **64**, 6-15 (1996).

21. M. A. Benincasa, J. C. Giddings, Anal. Chem., **64**, 790-798 (1992).

22. S. K. Ratanathanawongs, I. Lee, J. C. Giddings, "Separation and Characterization of 0.01 - 50 μm Particles Using Flow Field-Flow Fractionation," in **Particle Size Distribution II**, ACS Symposium Series 472, T. Provder, ed., American Chemical Society, Washington, DC, 1991, pp. 229-246.

23. S. K. Ratanathanawongs, J. C. Giddings, "Particle Size Analysis Using Flow Field Flow Fractionation," in **Chromatography of Polymers: Characterization by SEC and FFF**, ACS Symposium Series, No. 521, T. Provder, ed., American Chemical Society, Washington, D.C., 1993, pp. 13-29.

24. S. K. Ratanathanawongs, J. C. Giddings, Anal. Chem., **64**, 6-15 (1992).

25. J. C. Giddings, K. D. Caldwell, Anal. Chem., **56**, 2093-2099 (1984).

26. P. S. Williams, J. C. Giddings, J. Chromatography, **550**, 787-797 (1991).

27. R. Benner, J. D. Pakulski, M. McCarthy, J. I.Hedges, P. G.Hatcher, Science, **255**, 1561-1564 (1992).

28. J. I. Hedges, C. Lee, Mar. Chem., **41**, 1-249 (1993).

29. E. B. Sherr, Nature, **335**, 348-351 (1988).

30. L. J. Tranvik, E. B. Sherr, B. F. Sherr, Mar. Ecol. Prog. Ser., **92**, 301-309 (1993).

31. S. K. Ratanathanawongs, R. G. Keil, unpublished results.

32. J. D. Pakulski, R. Benner, Limnol. Oceanogr., **39**, 930-940 (1994).

33. A. L. Rosso, F. Azam, Mar. Ecol. Prog. Ser. **41**, 231-240 (1987).

34. D. H. Napper, **Polymeric Stabilization of Colloidal Dispersions**, Academic Press, Inc., New York, 1983.

35. R. G. Keil, D. L. Kirchman, Mar. Chem., **45**, 187-196 (1994).

36. T. Nagata, D. L. Kirchman, Mar. Ecol. Prog. Ser., **83**, 233-240 (1992).

37. Y. Jiang, Ph.D. Thesis, University of Utah, 1994.

38. M. H. Moon, J. C. Giddings, Anal. Chem., **64**, 3029-3037 (1992).

39. J. C. Giddings, Analyst, **118**, 1487-1494 (1993).

Received January 21, 1997
Accepted April 11, 1997
Manuscript 4447

J. LIQ. CHROM. & REL. TECHNOL., 20(16 & 17), 2835–2842 (1997)

EFFECTS OF SURFACTANTS ON WHEAT PROTEIN FRACTIONATION BY FLOW FIELD-FLOW FRACTIONATION†

S. G. Stevenson, K. R. Preston

Grain Research Laboratory
Canadian Grain Commission
1404-303 Main Street
Winnipeg, Canada, R3C 3G8

ABSTRACT

The effects of different nonionic (Brij 35, FL-70, Triton X-100, Tween 20 and Tween 80), cationic (CTAB) and anionic (SDS) surfactants in 0.05M acetic acid, at several concentrations, on flow field-flow fractograms of three wheat gluten fractions were assessed. Alcohol soluble gliadins, acetic acid soluble glutenins and sonicated acetic acid insoluble glutenin fractions all showed optimum resolution and reproducibility with FL-70, Brij 35 or Triton X-100. Fl-70 proved superior compared to the other two surfactants due to its lower tendency to foam, making buffer preparation much easier. Fractograms obtained in the presence of low concentration of other nonionic surfactants (Tween 20 and 80) and the cationic surfactant, CTAB, gave similar fractograms but resolution was inferior. At higher concentration, above the critical micelle limit, CTAB gave poor resolution and reproducibility.

Low concentrations of SDS caused protein precipitation. At a higher concentration of SDS, also above the critical micelle concentration, reproducibility was also a problem. However,

results indicated that SDS was able to release lower molecular weight proteins from the larger polymeric insoluble gluten fraction which remained bound with nonionic detergents.

INTRODUCTION

The proteins of wheat endosperm show a wide molecular weight range, ranging from less than 15,000 to values of 10 million daltons or more.[1,2] The lower molecular weight (<100,000 daltons) proteins consist of water soluble albumins, salt (0.5% NaCl) soluble globulins and alcohol (70% ethanol) soluble gliadins. The higher molecular weight insoluble glutenin proteins are polymeric in nature, consisting of mixtures of disulphide bonded high molecular weight (HMW) and low molecular weight (LMW) subunits. The size of these polymeric proteins is dependent on the subunit composition which is genetically determined.[3-6]

A strong positive relationship has been established between dough processing properties (dough strength) and baking quality, and the average molecular size of the gluten proteins (gliadin and glutenin).[7] The size distribution of the polymeric glutenin proteins, especially the larger polymers, plays a particularly important role in this relationship.[3,5,8-10]

Previous studies in our laboratory have shown that symmetrical flow field-flow fractionation (FFF) provides good resolution of wheat protein fractions.[11] Similar results have been obtained by Wahlund and co-workers using asymmetrical flow FFF.[12] Its use for studying the larger polymeric wheat proteins may be particularly advantageous since, unlike gel filtration, electrophoresis, and size-exclusion chromatography, resolution is not impeded by an exclusion limit.[13]

To optimize resolution in flow FFF, the channel manufacturer recommends addition of surfactant to condition the membrane. Although this conditioning process is not well understood, it is likely related to binding of surfactant to the membrane which reduces interactions between the membrane and the components being fractionated. Using gravitational FFF for fractionation of latex particles, Pazourek and Chmelík[14] demonstrated that the type and concentration of surfactant could strongly influence resolution. They attributed these differences to the effects of the surfactants on particle - particle, particle - eluent and particle - cell surface interactions. Although FL-70 has been the most widely used surfactant for flow FFF, other nonionic surfactants, such as Triton X-100, and charged surfactants, such as sodium dodecyl sulfate (SDS), have also been used.[12-13,15-16] At present, no information has been

published on the relative effects of these surfactants on wheat protein fractograms. In the present study, a number of nonionic, anionic and cationic surfactants in 0.05 M acetic acid (HAc) at different concentrations have been used to investigate their influence on the resolution of flow FFF fractograms obtained with the major wheat gluten protein fractions.

MATERIALS AND METHODS

Three wheat gluten protein fractions: gliadins (soluble in 70% ethanol); HAc soluble glutenins (soluble in 0.05M HAc), and sonicated HAc insoluble glutenins (insoluble in 0.05M HAc, but "soluble" following 30 sec. sonication) were extracted from defatted Katepwa red spring as previously described.[11] Flow FFF was run on a Model #F100 fractionator (FFFractionation Inc., Salt Lake City, UT) with nominal dimensions of: length-28.5 cm (tip to tip), breadth-2.0 cm and thickness-0.025 cm fitted with a YM-10 membrane. Protein fractions (approximately 1 μg protein in 20 μL in carrier fluid under examination) were injected into the channel, relaxed for 16 sec. and eluted at 2 mL/min with a cross flow of 5.0 mL/min using degassed 0.05 M acetic acid (HAc) containing surfactant as carrier fluid. A Shimadzu detector SPD-10AV, connected to the outlet of the FFF unit, was used to monitor the absorbance of the sample fractions at 210 nm. A formula for calculating Stokes diameters (d) based on retention time was derived in the same manner as previously described for the thin channel.[11] A calibration curve was obtained by plotting d against peak retention times (t_r) as recommended by the manufacturer (FFFractionation Inc.).

Proteins used for the calibration curve (values for MW in daltons, D in Ficks and d in nm, respectively, given in brackets) were cytochrome c (12,500, 13.0, 3.3), chymotrypsinogen A (25,000, 9.5, 4.5), hen egg albumin (45,000, 7.8, 5.5), bovine serum albumin (BSA)(67,000, 5.9, 7.3), aldolase (158,000, 4.6, 9.3), catalase (240,000, 4.1, 10.5) and ferritin (450,000, 3.6, 11.9). The linear curve, $d = 0.725+1.019\ t_r$ ($r = 0.93$), was then used to calculate corresponding values for wheat protein fractions based upon retention times. Cytochrome c (1/10 dilution of 0.001g/mL stock solution) and ferritin (1/2 dilution of 0.01mL/mL stock solution) were diluted with 0.05M HAc and run as markers at the beginning of each sample set. Three runs of samples and standards were done for each type and level of surfactant.

Surfactants were diluted in 0.05M acetic acid (HAc) to levels indicated in brackets to provide carrier fluids for this study: Surfactants included Brij 35 (0.002%, 0.001%; v/v), cetyl trimethylammonium bromide (CTAB) (0.36%, 0.002%, 0.001%, w/v), FL-70 (0.004%, 0.002%, 0.001%; v/v), SDS (0.17%,

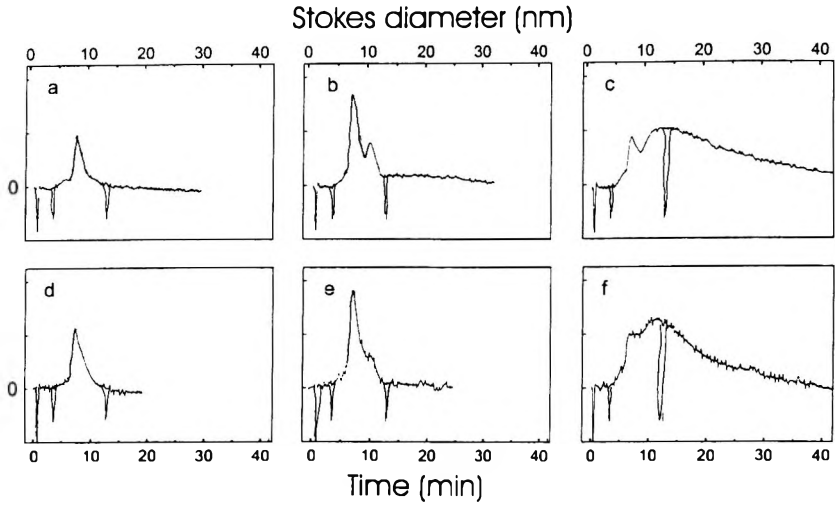

Figure 1. Representative fractograms for wheat protein fractions run in nonionic surfactants. a) gliadin, b) HAc soluble glutenin, c) HAc insoluble sonicated glutenin fractions in 0.002% FL-70, d) gliadin, e) HAc soluble glutenin, and f) HAc insoluble sonicated glutenin fractions in 0.002% Tween 80.

0.06%; w/v), Triton X-100 (0.002%,0.001%; v/v), Tween 20 (0.002%,0.001%; v/v) and Tween 80 (0.002%,0.001%; v/v). With the exception of FL-70, all the nonionic surfactants formed stable foams during buffer preparation which made mixing and vacuum filtering difficult. Three runs of samples and standards were also done using 0.05M HAc, without surfactant added, following the third run at 0.001% FL-70 in HAc.

RESULTS AND DISCUSSION

Fractograms are shown in Figure 1 for gliadin, HAc soluble glutenin, and HAc insoluble glutenin solubilized by sonication (HAc insoluble sonicated) fractions obtained with different surfactants. The location of the elution peak for cytochrome c (d=4.0) and ferritin (d =13.2) are indicated by bold lines for reference. Fractograms obtained for the three protein fractions, using 0.002% FL-70 (Fig. 1a,b and c), were very similar to those obtained for the same fractions in a previous study using the same concentration of surfactant under similar running conditions.[11] The gliadin fraction showed a single major peak with an estimated Stokes diameter (d) of 7.9nm while two peaks (d=7.2 and

10.5nm) were evident for the HAc soluble glutenin fraction. The HAc insoluble, sonicated glutenin fraction showed a peak at 6.8 min (d=7.6nm) and a broad peak with a maximum at approximately 12.2 min. (d=13.2nm).

Differences were not observed in fractograms for these protein fractions when the FL-70 concentration was reduced to 0.001% or increased to 0.004% (data not shown). Resolution was also not affected when FL-70 was replaced with the nonionic surfactants, Brij 35 and Triton X-100, at two different concentrations (0.001% or 0.002%; v/v). Fractograms for the nonionic surfactants, Tween 20 and Tween 80, were very similar to each other for both levels of surfactant (0.001% and 0.002%;v/v) tested and, in general, similar to those obtained with the other three nonionic surfactants, as shown in Figure 1d, 1e, and 1f. Peak resolution with Tween 20 and 80, however, was clearly inferior to that obtained with Brij 35, Triton X-100 or Fl-70, particularly for the two glutenin fractions.

Removal of FL-70 from treated channels by flushing and running fractions in 0.05M HAc resulted in fractograms equivalent to those obtained in the presence of FL-70 (data not shown). This procedure allows isolation of protein peaks with minimal levels of surfactant contamination. These results also suggest that surfactant interactions with the proteins were not required to optimize resolution. Sufficient FL-70 presumably remained bound to the membrane to ensure optimum conditioning.

At lower concentrations (0.001% and 0.002%; w/v), the cationic surfactant, CTAB, produced separations similar to those obtained with the nonionic surfactants Tween 20 and Tween 80 (Fig. 2a, b and c), but inferior to FL-70. Low concentrations of the anionic surfactant, SDS (0.001M), caused precipitation of the proteins. The negative charge on the SDS probably neutralizes the positively charged gluten proteins resulting in aggregation. Low concentration of salts show a similar effect.[17]

At higher concentrations, above their critical micelle concentration,[18] both CTAB and SDS have proven to be useful in promoting extractability of gluten protein, particularly the larger polymeric glutenin, due to their ability to decrease hydrophobic inter-protein interactions.[7,19] Poorly resolved, non-reproducible fractograms were obtained with CTAB, at a higher concentration of 0.36% (the concentration recommended by Meredith and Wren[19]). The buffer became viscous and maintenance of balanced channel and cross flows was very difficult. The interaction of CTAB micelles with the protein components may also have influenced resolution. SDS (0.05M in phosphate buffer) has been used by Wahlund and co-workers[12] to fractionate gluten proteins by asymmetrical flow FFF with good resolution. An SDS

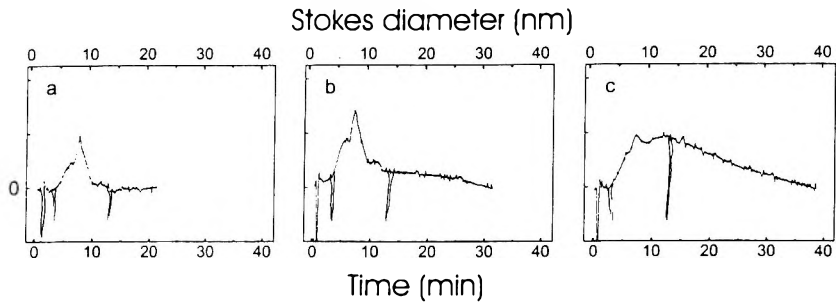

Figure 2. Representative fractograms for a) gliadin, b) HAc soluble glutenin, and c) HAc insoluble sonicated glutenin fractions run in cationic surfactant 0.002% CTAB.

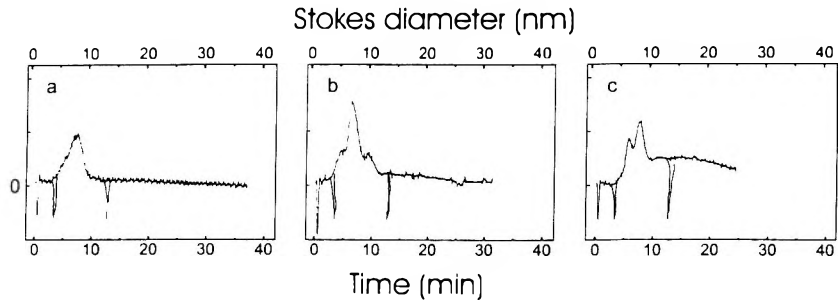

Figure 3. Representative fractograms for a) gliadin, b) HAc soluble glutenin, and c) HAc insoluble sonicated glutenin fractions run in anionic surfactant 0.17% SDS.

concentration of 0.17 % w/v was chosen to minimize buffer viscosity (reduce back pressure) while maintaining protein solubility. Some difficulty, however, was experienced with reproducibility of fractograms under these conditions. Lack of reproducibility may have been related to difficulties in balancing channel and cross flows due to the higher viscosity of the solution and to the tendency of proteins to absorb onto the membrane. It is possible that SDS is not as good a surfactant for membrane conditioning as some of the others used. Gliadin and soluble glutenin fractograms were generally similar to those obtained with nonionic surfactants, but resolution was inferior to that obtained with FL-70, Brij 35 and Triton X-100 (Fig. 3a and b). A second, earlier, peak at 5.6 min (d =6.4nm) was evident for the insoluble glutenin fraction. This peak was not present when nonionic surfactants were used. The amount of higher molecular size glutenin also was reduced (Fig. 3c). This result indicates

that SDS releases tightly bound lower molecular weight protein from the large polymeric glutenin. The presence of lower molecular weight proteins, tightly bound to high molecular weight polymeric glutenin, has also been demonstrated by gel filtration using chaotropic agents.[20]

In conclusion, this study demonstrates that optimum resolution and reproducibility of wheat protein flow FFF fractograms are obtained with nonionic surfactants. Of those studied, FL-70 is the best choice due to minimum viscosity and lack of foaming during buffer preparation. Different results may be obtained with base buffers other than dilute acetic acid. However, acetic and other dilute acids are preferable as solvents for wheat proteins since they provide good solubility and have minimal effects upon gluten structural and functional properties.[7,21]

REFERENCES

[1] Contribution No 750 of the Canadian Grain Commission, Grain Research Laboratory, 1404-303 Main St., Winnipeg, MB R3C 3G8.

1. P. R. Shewry, A. S. Tatham, J. Forde, M. Kreis, B. J. Miflin, J. Cereal Sci., **4**, 97-106 (1986).

2. Y. Pomeranz, "Composition and Functionality of Wheat Flour Components," in **Wheat Chemistry and Technology**, vol. II., Y. Pomeranz, ed., Am. Assoc. Cereal Chem., St. Paul, MN, 1988, pp. 219-343.

3. F. R. Huebner, J. S. Wall, Cereal Chem., **53**, 258-269 (1976).

4. P. I. Payne, K. G. Corfield, J. A. Blackman, Theor. Appl. Genet., **55**, 153-159 (1979).

5. J. M. Field, P. R. Shewry, B. J. Miflin, J. Sci. Food Agric., **34**, 370-377 (1983).

6. P. I. Payne, Ann. Rev. Plant Physiol., **38**, 141-153 (1987).

7. F. MacRitchie, Adv. Food Nutr. Res., **36**, 1-87 (1992).

8. J. A. Bietz, "High-Performance Liquid Chromatography of Cereal Proteins," in **Advances in Cereal Science and Technology**, vol. 8, Y. Pomeranz, ed., Am. Assoc. Cereal Chem., St. Paul, MN, 1986, pp. 105-170.

9. T. Dachkevitch, J.-C. Autran, Cereal Chem., **66**, 448-456 (1989).

10. R. B. Gupta, K. Khan, F. MacRitchie, J. Cereal Sci., **18**, 23-41 (1993).

11. S. G. Stevenson, K. R. Preston, J. Cereal Sci., **23**, 121-131 (1996).

12. K.-G. Wahlund, M. Gustavsson, F. MacRitchie, T. Nylander, L. Wannerberger, J. Cereal Sci., **23**, 113-119 (1996).

13. J. C. Giddings, F. J. Yang, M. N. Myers, Anal. Biochem., **81**, 395-407 (1977).

14. J. Pazourek, J. Chmelík, Chromatographia, **35**, 591-596 (1993).

15. C. B. Fuh, S. Levin, J. C. Giddings, Anal. Biochem., **208**, 80-87 (1993).

16. B. N. Barman, M. N. Myers, J. C. Giddings, Powder Technol., **59**, 53-63 (1989).

17. K. R. Preston, Cereal Chem., **61**, 76-83 (1984).

18. P. Mukerjee, K. J. Mysels, **Critical Micelle Concentrations of Aqueous Surfactant Systems**, Nat. Bur. Stand. (U.S.), Washington, D. C., 1971.

19. O. B. Meredith, J. J. Wren, Cereal Chem., **43**, 169-186 (1966).

20. U. J. S. Prasada Rao, S. N. Nigam, Cereal Chem., **65**, 373-374 (1988).

21. J. H. Skerritt, F. Bekes, D. Murray, Cereal Chem., **73**, 644-649 (1996).

Received January 21, 1997
Accepted April 15, 1997
Manuscript 4448

J. LIQ. CHROM. & REL. TECHNOL., 20(16 & 17), 2843–2856 (1997)

ELECTROSPRAY MASS SPECTROMETRY AS ONLINE DETECTOR FOR LOW MOLECULAR WEIGHT POLYMER SEPARATIONS WITH FLOW FIELD-FLOW FRACTIONATION

M. Hassellöv,*[1] G. Hulthe,*[1] B. Lyvén,*[1] G. Stenhagen[2]

[1] Dept. of Analytical and Marine Chemistry
Göteborg University
S-412 96 Göteborg, Sweden

[2]Dept. of Organic Chemistry
Chalmers University of Technology
S-412 96 Göteborg, Sweden

ABSTRACT

By coupling flow field-flow fractionation online to a high resolution mass spectrometer with electrospray ionisation, it was possible to separate low molecular weight polymers and to obtain mass chromatograms for specific polymers. Problems involved and their solutions in combining the mass spectrometer with field-flow fractionation are discussed. Separation efficiencies were tested for polystyrene sulphonates with different carrier solutions, and it was found that the ionic strength had to exceed about 20 mmol L^{-1} in order to achieve good separation. Salt clusters are formed in the electrospray interface at high ionic strengths, giving rise to a background in the mass spectra and it was found that the composition of the carrier solution and the tuning of the instrument were crucial to the signal to noise ratio. It was also found that, by adding a second electrolyte to the carrier solution, the extent of cluster formation was decreased.

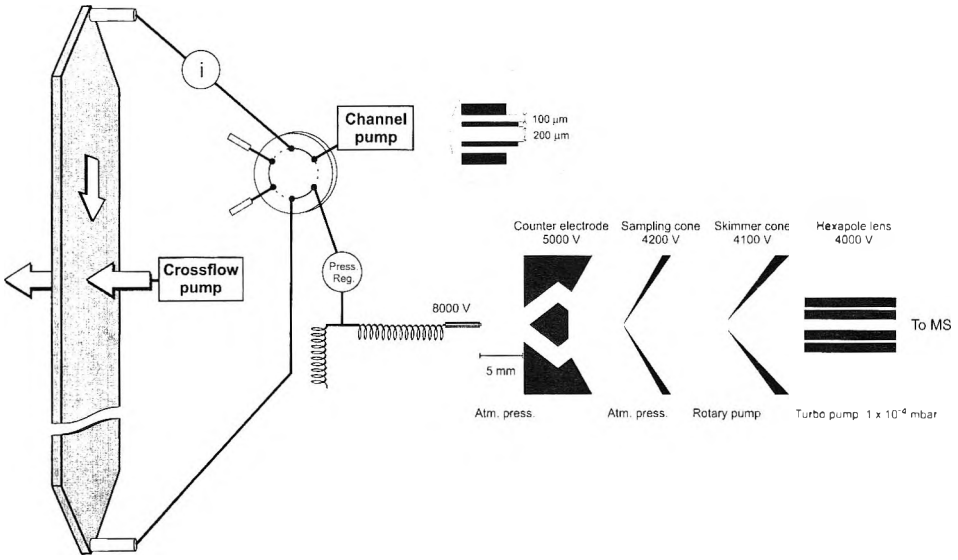

Figure 1. Experimental setup. Schematics of the FFFF channel, pumps, switching valve, flow splitting into 1/3 and the electrospray interface with counter electrode, sampling cone, skimmer cone and hexapole.

INTRODUCTION

Field-flow fractionation (FFF) has been shown to be suitable for the separation of polymers and for the determination of the size distribution of polymer systems.[1, 2, 3] Flow field-flow fractionation (FFFF) is the FFF technique with the widest dynamic range, from about 1000 Da, or a molecular diameter of 1nm, up to the steric inversion diameter of about 1 µm. The lower limit of FFFF is restricted by poor sample recovery due to loss of sample through the ultrafilter membrane.

Thermal FFF is suitable for high molecular weight polymer systems, especially hydrophobic systems in non-aqueous solutions, while FFFF is the more appropriate for low molecular weight hydrophilic polymers.

In general, FFF has minimal alteration to the sample, since it is a very gentle separation without any stationary phase that could cause interactions with the sample. The size distributions obtained consist of a polydispersity component of the sample plus a band broadening component and, since the field-flow fractionation techniques not have higher separation efficiencies than

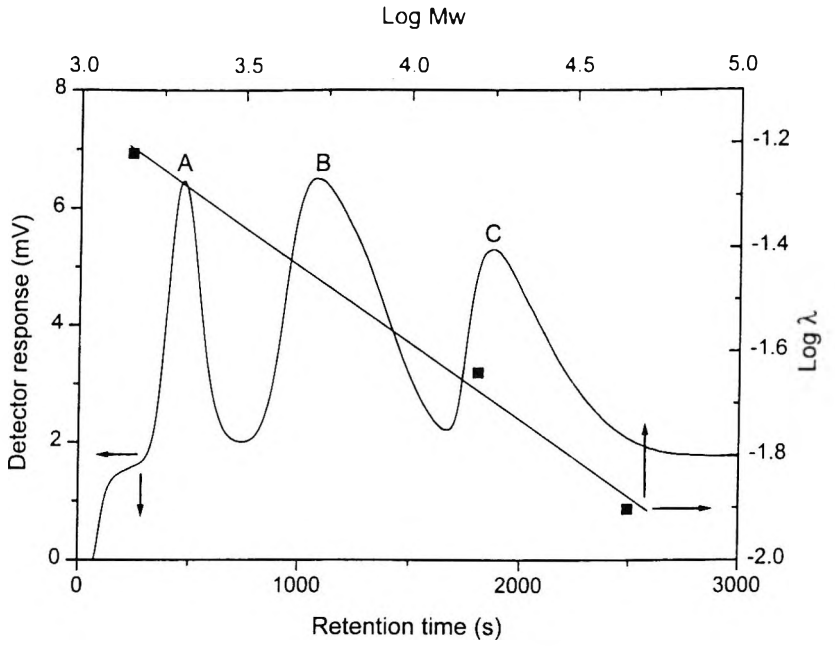

Figure 2. The figure shows a separation and the corresponding molecular weight calibration curve of three PSS standards with weight average molecular weight of 1430 (A), 16000 (B) and 46000 (C) Da. In the Mw calibration log λ is plotted versus log Mw where λ is calculated from $t_0/t_r = 6\lambda[\coth 1/2\lambda - 2\lambda]$. Carrier composition was tris 25 mmol L^{-1}, NaCl 20 mmol L^{-1} and HCl 12 mmol L^{-1}. Channel flow was 0.4 mL min^{-1}, crossflow 3.8 mL min^{-1}, injection loop 20 µL and concentration of sample was 150 mg L^{-1} of each; calculated number of plates, uncorrected for polydispersity, were 45, 31 and 131 for 1430, 16000 and 46000 Da respectively.

a few hundred theoretical plates, band broadening sometimes contributes significantly to the overall size distribution. The natural solution to this problem would be to take advantage of a more selective detector. When studying high molecular weight polymers, it has been shown that the multi angle laser light scattering detector (MALLS), combined with a concentration selective detector such as a refractive index detector, yields a mass selective detection system[4] which, consequently, gives information about polydispersity. However, the MALLS detector suffers from poor sensitivity for low molecular weight polymers, below about 10,000 Da.[5]

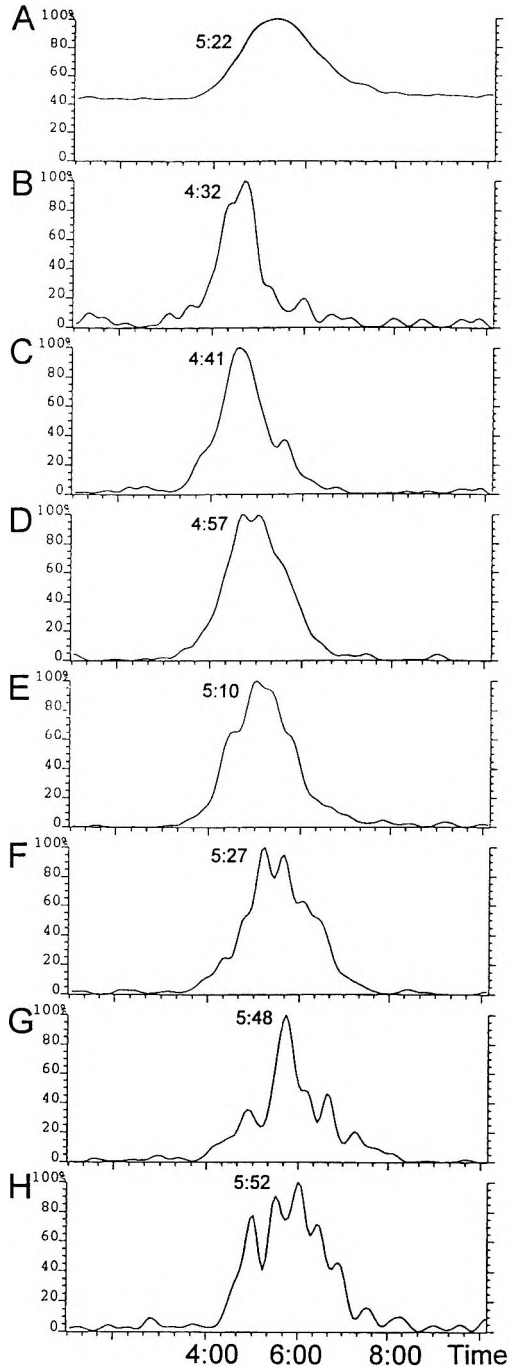
A
5:22
B
4:32
C
4:41
D
4:57
E
5:10
F
5:27
G
5:48
H
5:52
100%
80
60
40
20
0
4:00
6:00
8:00
Time

This was the reason to investigate the online combination of FFFF to a high resolution mass spectrometer with an electrospray (ES) interface, since the ES have proven to be suitable for low molecular weight polymers.[6, 7]

The basic principles of electrospray can be described as follows: small droplets from the exit of a capillary emerge in a dense electric field as an aerosol, assisted by the nebulizer gas, and evaporate in a warm counter-flow of nitrogen gas at atmospheric pressure, after which the analyte molecules are ionised either by exchange of protons (dissociation or protonation) or by adduction of charged groups, e.g. NH_4^+ or Na^+, added to the liquid phase.[8, 9]

MATERIALS AND METHODS

The electrospray experiments were carried out on a high resolution mass spectrometer (Zab-Spec, VG Analytical, Fisons instrument) equipped with the standard electrospray interface, including a hexapole placed before the acceleration path of the ions (Figure 1). The hexapole was scanned synchronously with the magnet which increases the transmission of ions considerably. The detector was the standard photomultiplier detector system.

The electric potentials in the ES interface, when run in the positive mode, were: spray needle +8000 V, counter electrode +5000 V, sampling cone +4200 V, skimmer cone +4100 V, hexapole and acceleration voltages +4000 V. Nitrogen was used as nebulizer gas purging out between the two capillaries and the bath gas, kept at 80°C entering in front of the counter electrode. The FFFF system was kept at ground potential and, therefore, a 2 m long and 0.12 ID mm PEEK capillary was inserted between the FFF channel and the needle. This sets the limit for maximum conductivity of the sample as corresponding to ~50-100 mmol L^{-1} of sodium chloride.

During these experiments, it was not necessary to clean the inlet system of the ES even though high salt contents were used. The separations were carried out in a commercially available FFFF system (F-1000, FFFractionation Inc.) equipped with modified polyethersulphone ultrafilter membrane, OMEGA,

---

Figure 3 (left). Ion chromatogram and every third polymer in a separation of PEG 1500. Flows and injection volume were as in Figure 2. Total sample concentration was 200 g L^{-1}. Ion intensities in B, C, D corresponds to 1+ and 2+ charged complexes, E to 1+, 2+ and 3+ complexes and F and G to 2+ and 3+ complexes. Picture A shows Total Ion Current, B is mass 1204, C is 1334, D is 1422, E is 1553, F is 1729, G is 1906 and H is 1994.

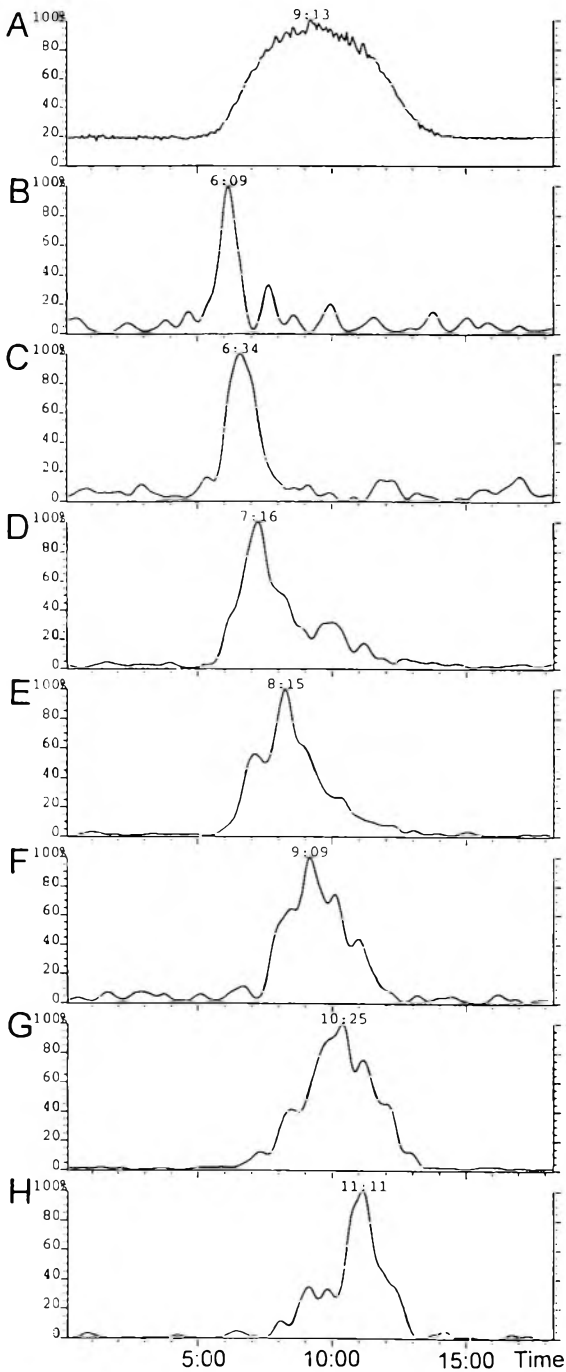
A
9:13
B
6:09
C
6:34
D
7:16
E
8:15
F
9:09
G
10:25
H
11:11
100%
80
60
40
20
0
5:00
10:00
15:00
Time

(Filtron) with a nominal molecular weight cutoff at 1000 Da. This membrane has shown superior performance compared to regenerated cellulose membranes used for low molecular weight polymers, with respect to sample recovery.[10] The channel was cut out of a mylar spacer and the channel dimensions are 28 cm long tip to tip, 2 cm wide and 0.225 mm thick. The channel flow and crossflow were delivered by two HPLC-pumps (P-880, Jasco); channel flow rate was 0.4 mL min^{-1} and the crossflow rate 3.8 mL min^{-1}.

The samples were loaded onto the channel through a Rheodyne sample injection valve (20 μL) and the sample plug was relaxed at the channel inlet by the crossflow in a conventional stop-flow procedure by switching the computer controlled 6-way Valco valve (Figure 1). In order to minimise the formation of crystals and accumulation of solvents in the ES inlet system, the liquid flow was kept at about 140 μL min^{-1} by splitting the channel flow 1/3 using a T-union (Valco) and two pieces of 0.12 ID mm PEEK tubing.

The test polymers in the FFFF-ESMS system have been polyethylene glycol (PEG) standards. In order to save analysis time on the ESMS, poly(styrene)sulphonate (PSS) standards were used for separation optimisation due to higher UV absorptivity than the PEG standards. During these optimisations the PSS was detected using a UV-detector (Jasco UV-975) at 254 nm.

All reagents used, were of analytical grade, except ammonia, which was of supra pure grade. The carrier solution is defined by the pH buffer and ionic strength selected. The buffers tested were acetic acid (Merck)/sodium hydroxide (EKA Nobel) (pH 4.7), tris(hydroxymethyl)aminomethane (tris) (Merck) / hydrochloric acid (Merck)(50:50, pH 7.9), boric acid (Riedel-de Haën) / sodium hydroxide (pH 8.5), and ammonium/ammonia (Merck) (pH 9.3).

To increase the ionic strength, sodium chloride (Merck) or sodium nitrate (Merck) were used. The water used was Milli-Q water (Millipore) or Milli-Q water redistilled with sulphuric acid and potassium peroxydisulphate present during the distillation.

Figure 4 (left). Ion chromatogram and every third polymer in a separation of PEG 2000, 3000 and 4000. Flows and injection volume as in Figure 2. Total sample concentration 20 g L^{-1}. Ion intensities in B and C corresponds to 3+ complexes, D to 3+ and 4+, E and F to 4+ and G and H to 5+. Picture A shows Total Ion Current, B is mass 1778, C is 2218, D is 2658, E is 3098, F is 3758, G is 4418 and H is 4858.

Table 1

Test Results Determining a Suitable Carrier Solution for Both the FFFF Separation and the ES Interface

Carrier Solutions	FFFF	ES-MS
2 mmol L^{-1} tris and 1 mmol L^{-1} HCl	Poor separation	Minor $TrisH(TrisHCl)_n^+$ cluster formation
10 mmol L^{-1} Tris and 5 mmol L^{-1} HCl	Reasonable separation	Dominated by $TrisH(TrisHCl)_n^+$ clusters
10 mM NaCl	Reasonable separation	Dominated by $Na(NaCl)_n^+$ clusters
20 mmol L^{-1} HAc and 10 mmol L^{-1} NaOH	Good separation	Dominated by $Na(NaAc)_n^+$ clusters
10 mmol L^{-1} NH_3 and 5 mmol L^{-1} HNO3	——	Dominated by $NH_4(NH_4NO_3)_n^+$ clusters
20 mmol L^{-1} $B(OH)_3$ and 6 mmol L^{-1} NaOH	Good separation	Dominated by $Na(NaB(OH)_4)_n^+$ clusters
25 mmol L^{-1} tris, 20 mmol L^{-1} NaCl and 12 mmol L^{-1} HCl	Good separation (Fig. 2)	Minor cluster formation.

Polyethylene glycol (PEG) standards (PEG 1000, PEG 1500, PEG 2000, PEG 3000 and PEG 4000, where the number corresponds to the weight average molecular weight)(Fluka), and poly(styrene)sulphonate standards with weight average molecular weight of 1430, 16000 and 46000 Da (American Polymer Standards Corporation and Polymer Standards Service) were used. The malto-oligosaccharide std. was polydisperse maltodextrine, PZ9 (Reppe, Sweden).

RESULTS AND DISCUSSION

Electrospray in positive mode has been applied to all polymers used. For PSS, normally a negatively charged polymer, ES in negative mode were also tested. A major problem with ESMS at high ionic strength is the formation of matrix ion clusters or adducts[11] which give rise to a background in the mass spectrometer and, thus, further complicate the mass spectra. This can, to some extent, be avoided by minimising the amount of salt introduced to the electrospray; normally the ionic strength is kept below 1 mmol L^{-1}.

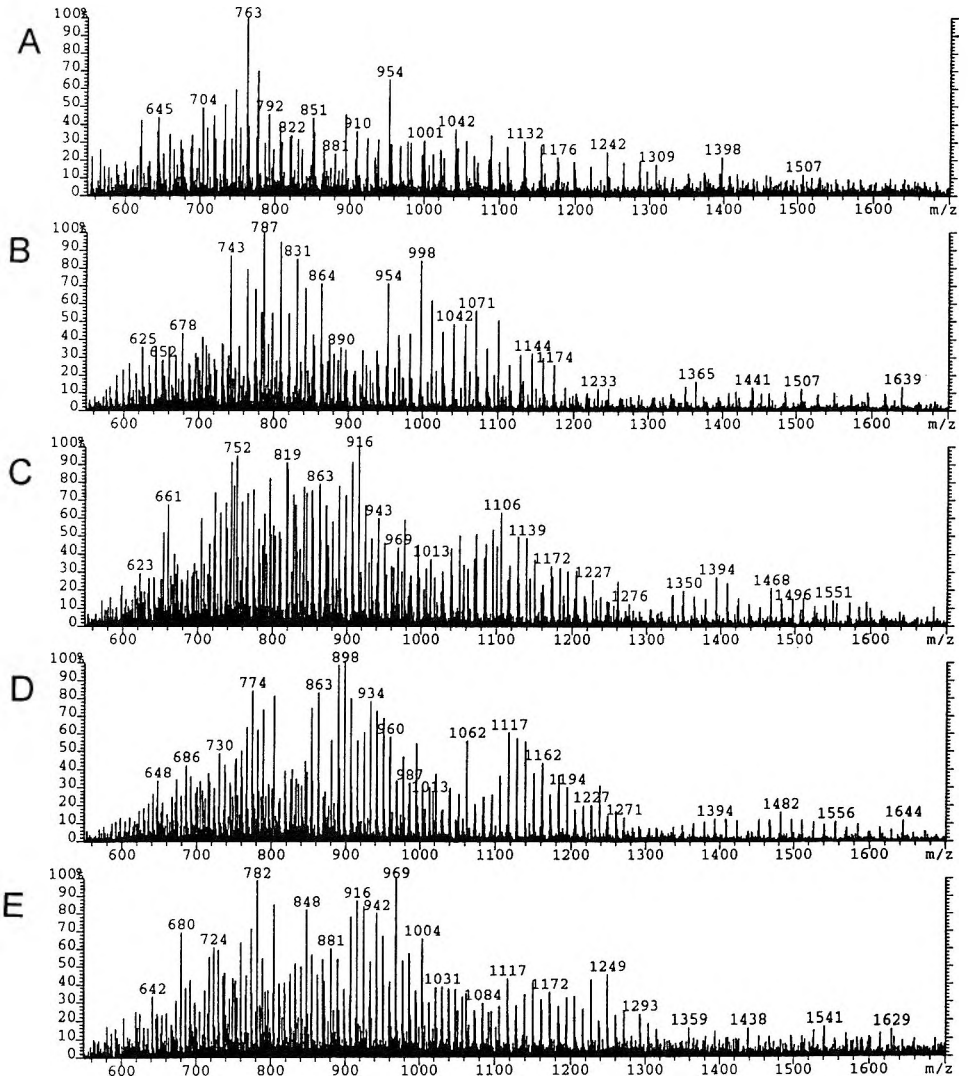

Figure 5. Mass spectra from selected parts of the separation in Figure 4. A corresponds to 5 min 55 s- 6 min 37 s. B to 7 min 27 s - 8 min 9 s, C to 8 min 59 s - 9 min 41 s, D to 10 min 31 s - 11 min 13 s and E to 12 min 3 s - 12 min 45 s.

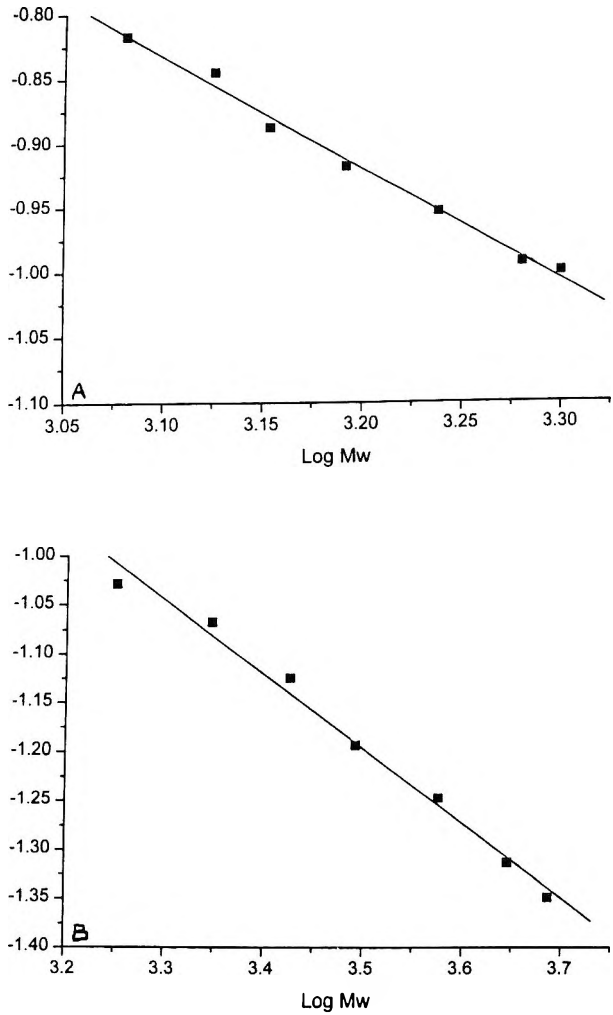

Figure 6. The plots show log λ versus log molecular weight, where λ is calculated as in Fig. 2. Figure 6A corresponds to the chromatogram in Figure 3 and Figure 6B corresponds to Figure 4.

Carrier liquids have been optimised to reconcile the demands of Flow FFF and ESMS with respect to ionic strength and ion composition. Effort was put into minimising the salt cluster background instead of just lowering the amount of salt present. It was found that cluster formation and, thus, the background,

were significantly reduced by tuning the skimmer cone voltage, to maximise the signal to noise ratio. It was also seen that the composition of the carrier liquid greatly influenced the formation of salt clusters.

Different buffering systems with pH from 4.7 to 9.3 were tested with respect to separation efficiency of PSS standards (Table 1). The pH did not have a significant effect on the separation efficiency, while ionic strength, on the other hand, has shown to be a very critical parameter. The apparent pH independence could be explained by the facts that both the PSS standards and the sulphonate groups on the OMEGA membrane have a constant negative charge in the pH range examined.

The separation of PSS standards collapsed when the ionic strength fell below a few millimoles per litre, and optimal separation is not achieved below approximately 20 mmol L^{-1}. An explanation for this behaviour can be that, for very low ionic strength, the negative charge on both the sample and the membrane exerts repulsive electrostatic forces which hinders the sample to come close enough to the accumulation wall but, when ionic strength increases, the electrostatic force is shielded and the sample clouds could establish at different distances from the wall. Another explanation for this ionic strength dependence could be conformational changes of the polymer for low ionic strength, which is stabilised in higher ionic strength.

Figure 2 shows a typical separation of PSS standards with corresponding molecular weight calibration data as logarithm of the retention parameter λ versus the logarithm of the molecular weight where λ is calculated from $t_0/t_r = 6\lambda[\coth 1/2\lambda - 2\lambda]$. Good FFFF separation was achieved with all of the higher ionic strength carrier solutions. On the other hand, ESMS worked well only for lower ionic strengths and for high ionic strength solution of tris, hydrochloric acid, and sodium chloride.

The latter mixture gave the lowest background, in combination with good separation efficiency. A probable explanation of this is that the lifetime of, e.g., a pure $Na(NaCl)_n^+$ cluster is long enough to travel through the MS (slightly less than 1 μs) while this is not the case for a mixed cluster. In order to further reduce the background, some hydrochloric acid was replaced with nitric acid and sulphuric acid in the above carrier solution, without any further improvement seen. The signal to noise ratio was studied by direct injection of PSS, PEG and malto-oligosaccharides dissolved in the different carriers. PSS gave low sensitivity both in negative and positive electrospray.

The malto-oligosaccharides were easily detected in ESMS[11,12] at the lower ionic strength, but turned out to exchange protons to sodium at sodium concentrations higher than 5mM. Because the intensities were shared by anumber of masses, the sensitivity decreases and the mass spectrum becomes complex. If the sodium concentration in the solution was decreased too much, clusters of tris started to become a problem. For this reason, the malto-oligosaccharides samples became difficult for FFFF-ESMS. PEG run on ESMS with tris/sodium chloride solution gave mainly sodium adducts with higher amounts of sodium attached to the larger PEG. The number of added sodium ions is highly dependent on the chain length, giving charges ranging from +1 to +6, and each molecule gave, normally, three peaks in the mass spectrum corresponding to three different charges (Figure 5).

When injecting PEG 1000 into the FFF channel, it was found that almost all of the sample passed through the membrane. The smallest PEG that could be separated and detected was around 1200 Da.

The membrane seems to have a somewhat higher molecular weight cutoff for PEG than for PSS for the same experimental setup. This could be due to the fact that PEG is neutral and does not experience the same electrostatic repulsion from the negative membrane as the negatively charged PSS.

Figure 3 shows the separation of PEG 1500, including seven of its components and the total ion current (TIC). The calculated number of theoretical plates, N, ranged between 60 and 215 with an average of 110. The FFFF peaks for different masses in the mass chromatogram are not baseline separated, but the centre points of the area for each mass are.

Figure 6A shows the logarithm of the retention parameter λ versus the logarithm of the molecular weight, which gives a linear fit ($r = 0.996$) showing good agreement between diffusion coefficient and molecular weight for the PEG chosen. It is, therefore, possible to obtain a calibration curve with a large number of points in just one run which could be useful in the study of the relationship between molecular weight and diffusion coefficient for different samples, in order to find relevant standards.

A separation of a mixture of PEG 2000, PEG 3000 and PEG 4000 is presented in Figure 4. In the mixture, all chain lengths from 40 to 115 (ca 1800-5100 Da) could be seen. There is no baseline separation of the chosen compounds but, when plotting the logarithm of the retention parameter λ versus the logarithm of the molecular weight, a linear fit with a good correlation ($r = 0.994$) is achieved (Figure 6B). Flow FFF simplifies the mass

spectra in terms of differently charged species (Figure 5). When comparing standards with samples of known molecular weight, it is possible to get a picture of three dimensional conformation or diffusion coefficients versus molecular weight. The calculated number of theoretical plates for the separation made with PEG 2000, PEG 3000 and PEG 4000 (Figure 4) ranged between 100 and 320 with an average of 176.

A comparison of the mass chromatograms on certain PEG components (Figure 3 and 4) with the TIC, which is the sum of all mass chromatograms, shows the benefit of the mass selective detection system. A comparative study as the slope of log retention ratio vs. log Mw for PSS and PEG (0.41 and 0.67 respectively) suggests a smaller effect of diffusion coefficient/molecular weight for PEG which likely is due to weaker van der Waal forces within the PSS than in the PEG or higher electrostatic repulsion within the polymer coils of PSS than for PEG.

To further reduce the background, which in this study, made the detection limits quite high, would be a major field of interest. As the sensitivity for many naturally uncharged compounds increases with sodium ion concentration, ESMS has the potential to be a sensitive detector if the carrier solution could be kept reasonably free from contaminants. A possible way to achieve this could be to recrystallise the buffer salts and purify the carrier solution by passage through a column, eg. C_{18}, before entering the channel.

CONCLUSIONS

We have presented a relatively simple method for using ES-MS as an online detector for flow FFF. Even though high electrolyte concentrations are used in the carrier solution, the ES system seems to be robust and can work for a longer time.

Because of the good correlation between log retention parameter and log molecular weight of the PEG components, the method can be useful for conformational or molecular weight distribution studies. To achieve better detection limits, more work with purifying the carrier solutions should be done.

REFERENCES

1. J. C. Giddings, M. Martin, M. N. Myers, J. Polym. Sci., Polym. Chem. Ed., **19**, 815 (1981).

2. S. L. Brimhall, M. N. Myers, K. D. Caldwell, J. C. Giddings, Sepn. Sci. Technol., **16**, 671 (1981).

3. J. C. Giddings, M. N. Myers, J. Janca, J. Chromatogr., **186**, 261 (1979).

4. H. Thielking, W.-M. Kulicke, Anal. Chem., **68**, 1169-1173 (1996).

5. P. J. Wyatt, Anal. Chim. Acta, **272**, 1-40 (1993).

6. J. E. Campana, T. Havard, A. Jarrell, Polym. Mater. Sci. Eng., Proc. ACS Div. Polym. Mater. Sci, **69**, 456-457 (1993).

7. W. J. Simonsick, Jr., L. Prokai, Polym. Mater. Sci. Eng., Proc. ACS Div. Polym. Mater. Sci. Eng., **69**, 412-413 (1993).

8. K. L. Duffin, J. Welpy, E. Huang, J. D. Henion, Anal. Chem., **64**, 1440 (1992).

9. W. M. A. Niessen, R. A. M. van der Hoeven, J. van der Greef, Org. Mass Spectrom., **27**, 341 (1992).

10. B. Lyvén, M. Hassellöv, C. Haraldsson, D. R. Turner, Anal. Chim. Acta, submitted, 1997.

11. G. Hulthe, G. Stenhagen, E. Fogelqvist, J. Chromatogr., accepted, 1997.

12. A. P. Tinke, R. A. M. van der Hoeven, W. M. A. Niessen, J. van der Greef, J.-P. Vincken, H. A. Schol, J. Chromatogr., **647**, 279-287 (1993).

Received January 2, 1997
Accepted April 8, 1997
Manuscript 4440

J. LIQ. CHROM. & REL. TECHNOL., 20(16 & 17), 2857–2872 (1997)

DEP-FFF: FIELD-FLOW FRACTIONATION USING NON-UNIFORM ELECTRIC FIELDS

Gerard H. Markx,[2]* Juliette Rousselet,[1] Ronald Pethig[1]

[1] Institute of Molecular and Biomolecular Electronics
University of Wales, Bangor
Dean Street, Bangor
Gwynedd LL57 1UT, United Kingdom

[2] Department of Chemical Engineering
UMIST
P.O. Box 88
Manchester M60 1QD, United Kingdom

ABSTRACT

Dielectrophoresis (DEP) – the movement of particles in non-uniform electric fields – can be used in combination with Field Flow Fractionation (FFF) to separate particles with differing dielectric properties. An introduction is given to the technique of DEP-FFF and its application to the separation of cells and other particles. The separation of yeast cells using the subtechniques of steric and hyperlayer DEP-FFF is demonstrated. It is shown that the hyperlayer-DEP-FFF techniques have a number of advantages, including an improved separation efficiency and reduced adhesion to chamber walls. The hyperlayer-DEP-FFF separation technique is also independent of particle size and allows the use of higher medium conductivities than for conventional DEP methods.

INTRODUCTION

Field-Flow Fractionation (FFF) is a family of techniques[1,2] in which a force field is applied perpendicular to the flow through a narrow chamber driving the particles towards the chamber wall. Through different factors such as diffusion, steric, hydrodynamic, and other effects the particles with different properties attain different positions away from the chamber wall, and separation of particles is achieved through the different velocities of the particles in the parabolic velocity profile in the chamber. The FFF techniques have various applications in the analysis and separation of industrial, environmental and biological samples, and can separate particles with diameters ranging from a nanometer to over 100 microns.

FFF separation techniques have been used in the separation of various biological materials. Viruses and various biopolymers were among the first to be separated.[3,4,5] The separation of human and animal cells, in particular blood cells, has been demonstrated.[6,7,8] Bacteria have been separated on the basis of mobility and cell size, shape, and density,[9] as have yeast cells grown under different conditions.[10]

Dielectrophoresis (DEP)[11,12] is the movement of particles in non-uniform electric fields. The DEP force is the result of the interaction between the dipole that is induced in the particle when an electric field is applied, and the non-uniformity of the electric field over the particle. The magnitude of the DEP force F_{dep} is given by the equation:

$$F_{dep} = 2\pi\varepsilon_0\varepsilon_m r^3 \, \mathrm{Re}\left(\frac{\sigma_p^* - \sigma_m^*}{\sigma_p^* + 2\sigma_m^*}\right)\nabla E^2(\mathrm{rms}) \qquad (1)$$

in which ε_0 is the permittivity of free space (8.854×10^{-12} F m^{-1}), ε_m the relative permittivity of the suspending medium, r the (equivalent) radius of the particle, σ_p^* and σ_m^* the complex conductivity of the particle and the medium, and ∇E defines the field non-uniformity. Re stand for "the real part of." The complex conductivity is defined as:

$$\sigma^* = \sigma + j\omega\varepsilon \qquad (2)$$

in which σ and ε are the permittivity of the particle or medium, $j = \sqrt{-1}$ and ω is the angular frequency of the applied electric field ($\omega = 2\pi f$).

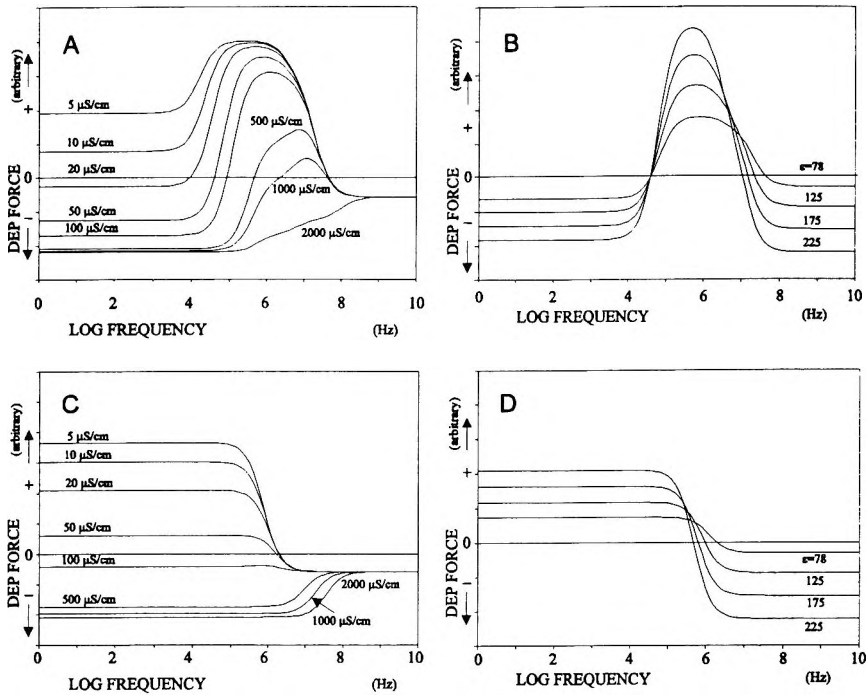

Figure 1. Effect of the medium conductivity and permittivity on the dielectrophoretic spectra of viable and non-viable yeast cells. The spectra were calculated using the multishell model.[20] For the calculation of the spectra of viable cells, the following parameters were used: relative permittivity of the cell interior, membrane and wall 50, 6 and 60, respectively; interior, membrane and wall conductivity 2000, 2.5×10^{-3} and 140 μS/cm, respectively; cell diameter 8 μm, wall thickness and membrane thickness 8 nm and 0.22 μm, respectively. The spectra of non-viable cells were calculated using the same parameters as for viable cells, but with an interior conductivity of 70 μS/cm and a membrane conductivity of 1.6 μS/cm. Figure 1a: viable cells, medium permittivity 78, varying medium conductivity. Figure 1b: viable cells, medium conductivity 30 μS/cm, varying medium permittivity. Figure 1c: non-viable cells, medium permittivity 78, varying medium conductivity. Figure 1d: non-viable cells, medium conductivity 30 μS/cm, varying permittivity.

Both positive DEP (movement towards high field strength regions) and negative DEP (movement away from high field strength regions) are possible, depending on the relative size of the complex conductivity of the particle compared to that of the medium. The phenomenon of dielectrophoresis can be

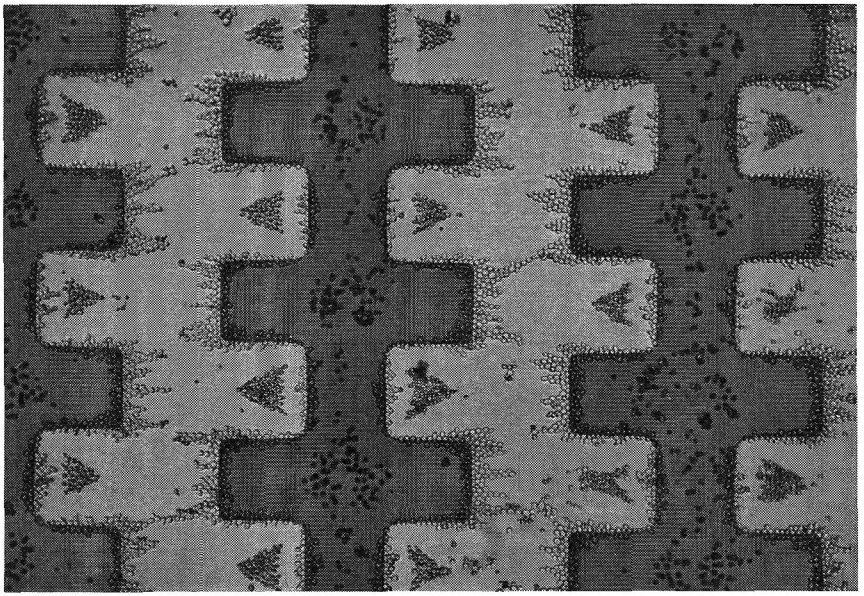

Figure 2. Dielectrophoretic separation of viable and non-viable yeast cells in a system of interdigitated castellated electrodes. The viable cells have accumulated at the electrode edges, whilst the non-viable cells have aggregated in triangular-shaped aggregations between the electrodes and diamond shaped aggregations on top of the electrodes.

observed with charged as well as uncharged particles and in both DC and AC electric fields. In the frequency range in which DEP is usually studied (1 Hz - 100 MHz), the effective complex medium conductivity σ_m^* is relatively constant, but the effective complex conductivity σ_p^* of many particles shows large changes as a function of the frequency of the applied electric field. By measuring the DEP force as a function of the frequency of the applied field, spectra can be obtained that are characteristic for the particle in question. Of particular interest are the frequency spectra of cells, since due to interfacial polarisation at the structures that form a cell (such as the cell wall, cell membrane, etc.) relatively large DEP forces are exerted on cells which are sensitive to small changes in the electrical properties of cellular structures and the suspending medium. As a consequence, efforts are being directed towards the utilisation of DEP forces in the separation of cells, and successful separations to date include the separation of normal and cancer cells,[13,14] stem cells from blood,[15] viable and non-viable cells,[16,17] and Gram-positive and

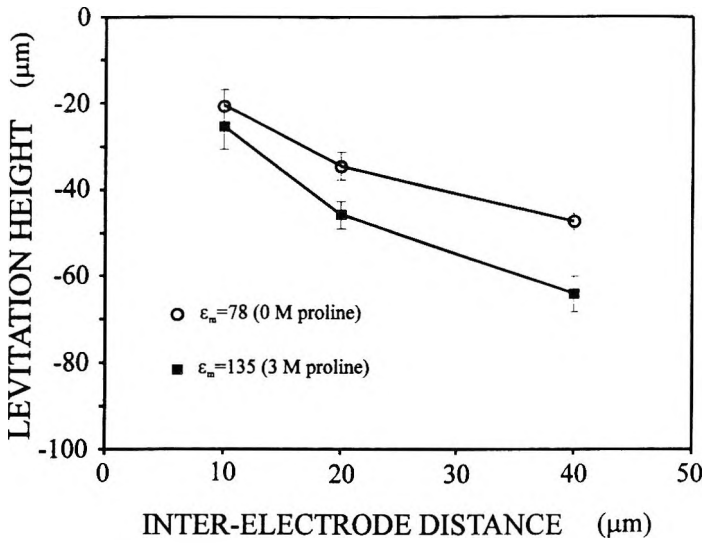

Figure 3. Effect of the relative permittivity ε_m of the suspending medium on the dielectrophoretic levitation height of non-viable yeast cells above interdigitated electrodes of varying spacing. The medium conductivity was 34 μS/cm and the applied voltage and frequency were 5 V pk-pk and 10 MHz, respectively.

Gram-negative bacteria.[18,19] Since the composition of the medium can be changed experimentally, this can be used to advantage in many separations. Figure 1a-d shows the DEP spectra of viable and non-viable yeast cells calculated for different medium conductivities and permittivities. The medium conductivity can easily be changed by the addition of salts, whilst the medium permittivity can be increased by the addition of zwitterions such as glycine or proline (or decreased by for example the addition of sugars).[21]

The combination of A.C. dielectrophoresis with field-flow fractionation techniques (DEP-FFF) is potentially a very gentle and selective method for the separation of cells and other particles. The already existing technique of electric FFF,[4] which can separate particles on the basis of their surface charge, makes use only of uniform DC electric fields, and is limited by electrode polarisation effects.

Although a large number of different designs has been used and proposed[11,12,22] to achieve the dielectrophoretic separation of particles, the most successful designs[12-17] to date make use of wide, long, narrow chambers similar

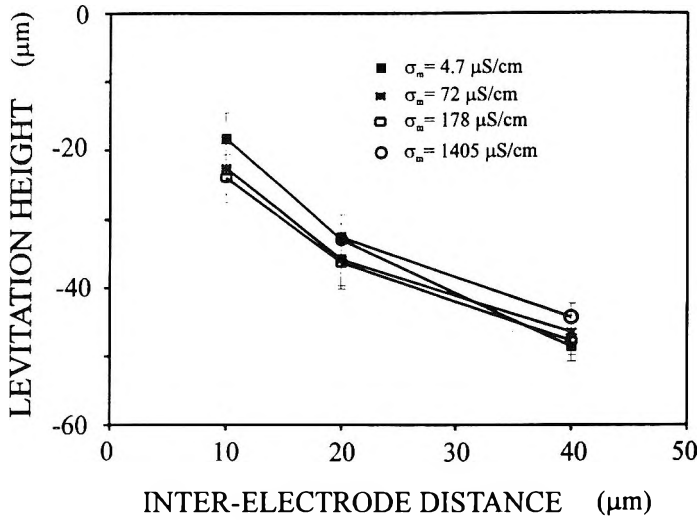

Figure 4. Effect of the medium conductivity σ_m on the dielectrophoretic levitation of non-viable yeast cells above interdigitated electrodes of varying spacing. The applied voltage and frequency were 5 V pk-pk and 10 MHz, respectively.

to FFF separation chambers, but containing large arrays of microelectrodes. The advantage of using microelectrodes rather than macroscopic electrodes is that relatively small voltages can be used to generate the high field gradients needed to observe dielectrophoresis. This not only simplifies the equipment needed to generate the electric fields, but also reduces side effects such as heating. The particles are held at the electrodes in the chamber by a DEP force that is dependent on the electrical properties of the particles and the surrounding medium, the frequency and magnitude of the electric field, and the design of the electrodes. An additional force over the surface of the electrodes, such as hydrodynamic forces, can remove any particles held by the electrodes.

DEP-FFF is an unconventional FFF technique in that the DEP force is inherently non-uniformly distributed over the chamber, not only in the plane of the electrodes/chamber wall, but also across the chamber above the electrodes.[23] Also, because the particles distort the electric field around them and in that way form local field non-uniformities, mutual attraction occurs between particles which can lead to what is called pearl-chain formation. As a consequence, interparticle interactions, involving both mutual attraction by DEP as well as electrostatic interactions between charged particles, can be considerable.[24]

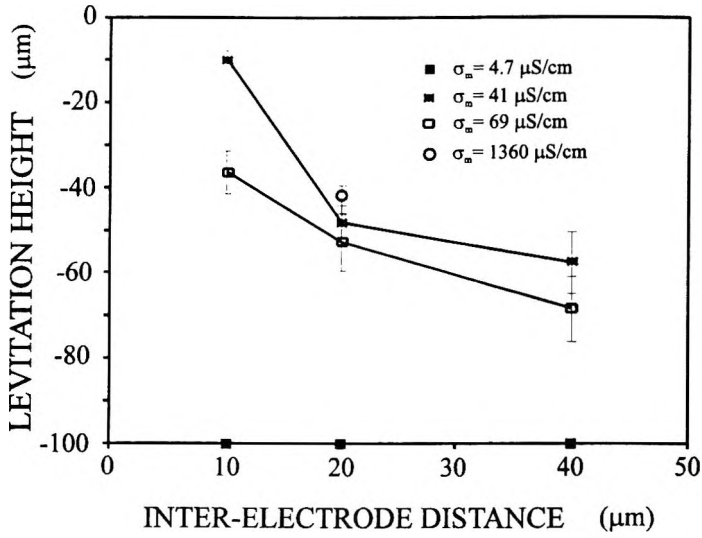

Figure 5. Effect of the medium conductivity σ_m on the dielectrophoretic levitation of viable yeast cells above interdigitated electrodes of varying spacing. The applied voltage and frequency were 5 V pk-pk and 20 kHz, respectively.

The main separation mechanisms in FFF are normal, steric, and hyperlayer modes.[1,2] In normal FFF, the earliest form of FFF, separation is achieved through back-diffusion of the particles away from the chamber wall against the driving force into different velocity regions. Washizu and co-workers[25] described the use of dielectrophoresis in combination with fluid flow through an open chamber with interdigitated sinusoidally corrugated electrodes to separate macromolecules such as proteins and DNA. Although it was not explicitly stated, this situation is very comparable to normal FFF.

Steric FFF is a separation principle that is generally seen in the separation of larger particles in which back-diffusion is negligible. In steric FFF, the driving force actually pushes the particle against the accumulation wall. Because of their size, larger particles protrude further into the channel and are caught in higher velocity streamlines.

Most dielectrophoretic separations of cells to date have used steric FFF. The cells are usually allowed to settle on the electrodes by gravity or attracted to the electrodes by positive DEP, and effectively immobilised in potential

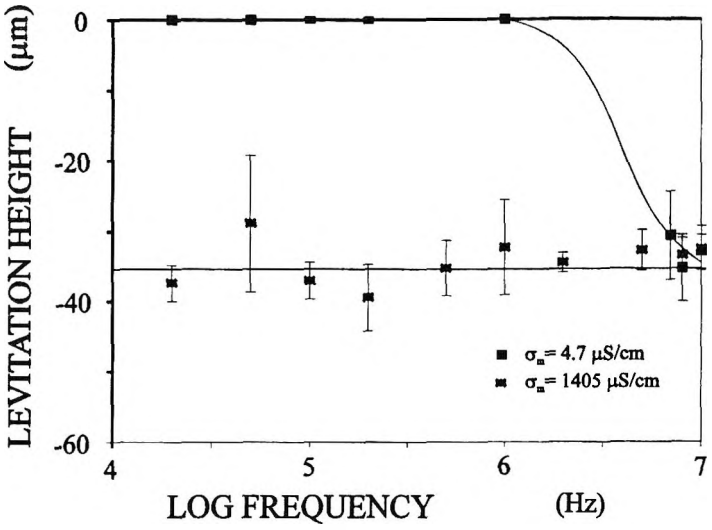

Figure 6. Effect of the medium conductivity and frequency on the dielectrophoretic levitation height of non-viable yeast cells above interdigitated electrodes with an electrode spacing and width of 20 μm.

energy minima[23] near the electrodes by primarily a combination of gravity and electric field forces. Fluid flow through the chamber is then used to apply additional hydrodynamic forces to the particles, and remove those particles that are held less strongly at the electrodes.

In most DEP separations, only positive DEP is used, or a combination of positive and negative DEP.[11-19] The particles are still held at the same plane as the electrodes, resulting in hydrodynamic forces being exerted on the particles similar to steric FFF. In a recent development,[26] negative DEP forces have been used to levitate particles above the electrodes. The DEP force on particles has already been given by Equation (1), whilst the gravitational force F_g on a particle with density ρ_p in a medium of density ρ_m is given by:

$$F_g = \frac{4}{3}\pi r^3(\rho_p - \rho_m)g \qquad (3)$$

in which g is the gravitational constant.

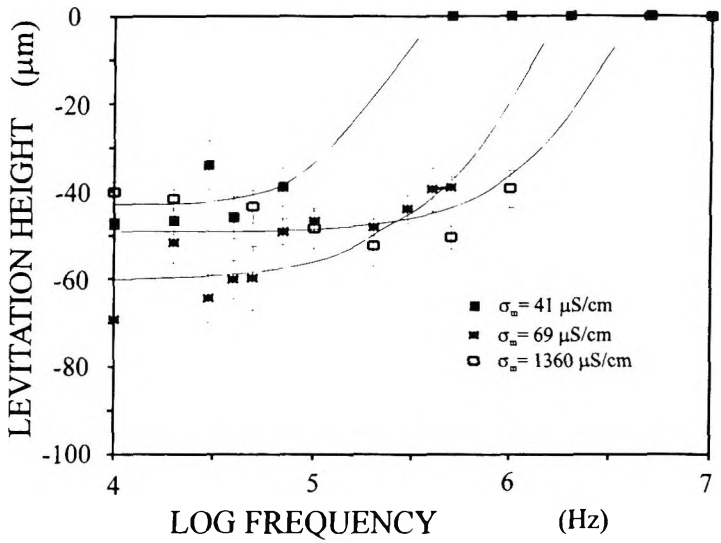

Figure 7. Effect of the medium conductivity and frequency on the dielectrophoretic levitation height of viable yeast cells above interdigitated electrodes with an electrode spacing and width of 20 μm.

Since the DEP force and gravitational force have a similar dependence on the volume of the particle, particles with the same electrical properties and density but with different sizes are levitated to approximately the same height above the electrodes.[26] Negative DEP could thus be used to levitate particles above the chamber wall into different velocity streamlines of the flowing liquid in a similar way as hyperlayer-FFF. In this paper, we will compare the use of steric DEP-FFF and hyperlayer-DEP-FFF in the separation of viable and non-viable yeast cells using media of different conductivities and permittivities.

MATERIALS AND METHODS

Yeast Cells

The yeast used was baker's yeast (*Saccharomyces cerevisiae*) strain R12. The yeast was grown overnight at 30 °C in a medium containing 0.5 % yeast extract, 0.5 % bacterial peptone and 5 % sucrose. Part of the yeast culture was rendered non-viable by heating to 90 °C for 20 minutes. The yeast cells were washed 4 times in deionised water and resuspended in deionised water, dilute

NaCl solutions (to change the conductivity) or concentrated proline solutions (to raise the permittivity). Conductivity measurements were made using an HP4192A impedance analyser using a cell with a cell constant of 1.573 cm^{-1}.

DEP Chambers

For the steric-DEP-FFF experiments, a dielectrophoretic separation chamber was used as described previously.[17,19] The chamber had a length of 30 cm, a width of 2 cm, a height of 200 μm, and contained electrodes of the interdigitated castellated type with a characteristic size of 70 μm.

The electrodes were made by photolithography from gold on a thin layer of chromium and had a thickness of approximately 0.3 μm. Liquid was pumped through the chamber using a Gilson Minipuls 3 pump. For the levitation experiments, interdigitated electrodes (without castellations) with a width and inter-electrode spacing of 10, 20 and 40 μm were used. An AC voltage of 5V pk-pk was applied to the electrodes at a frequency between 10 kHz and 10 MHz using a HP33120A frequency generator. The levitation height was estimated by focusing on either the electrodes or on the particles, and reading off the grading on the calibrated focus adjustment of the microscope (Nikon Labophot-2).

For hyperlayer-DEP-FFF experiments, a chamber was used as described for the steric FFF experiments, but with a length of 12.5 cm and containing electrodes of the interdigitated kind (without castellations) with a width of 40 μm and an interelectrode spacing of 60 μm. The electrodes were observed under a microscope and the speed at which particles travelled over the electrodes was measured at different flow rates and voltages.

RESULTS AND DISCUSSION

Steric-DEP-FFF

Referring to Figure 1a-d, one can expect that at modest conductivity values viable cells (with intact membranes) will show positive dielectrophoresis at a frequency of approximately 5 MHz, whilst non-viable cells show negative dielectrophoresis at this frequency. When a mixture of viable and non-viable cells is placed in a chamber containing interdigitated castellated electrodes, one can see (figure 2), as has been shown previously,[16] that the viable cells accumulate at the high field gradient regions near the edges of the electrodes,

whilst non-viable cells accumulate at the low field gradient regions between and on top of the electrodes (in "triangular" and "diamond"-shaped aggregations, respectively). Since the non-viable cells are held in relatively shallow potential energy wells by a combination of gravitational and DEP forces, these cells can easily be removed from the electrodes (and hence from the viable cells) by fluid flow through the chamber – provided the positive DEP force holding the viable cells is strong enough.

Hyperlayer-DEP-FFF

The use of a combined hyperlayer-DEP-FFF technique would have a number of advantages over steric-DEP-FFF, including overcoming the need for positive DEP, the use of high suspending medium conductivities, making better use of the parabolic velocity profile in the chamber, and the reduction of cell entrapment in the pearl chains formed by DEP.

As a model system, to demonstrate the hyperlayer-DEP-FFF technique, we chose the separation of viable and non-viable yeast cells. To establish the conditions for the separation of cells, the effect of the permittivity and conductivity of the medium, the size of the electrodes, and the frequency of the applied field were investigated.

Figures 3-5 show the effect of the medium permittivity and conductivity on the levitation of viable and non-viable yeast cells above interdigitated electrodes of different electrode spacings. The width of the electrodes was the same as the distance between the electrodes. The results correspond well with the predictions in Figs. 1a-d that the effect of the medium conductivity on the levitation height of non-viable cells at 10 MHz is small, whilst an increase of the medium permittivity increases the levitation height.

The influence of the medium conductivity on the levitation height of viable cells at 20 kHz involves many contributing factors, including the fact that, at this frequency, the conductivity of the cell wall, which is affected by the suspending medium conductivity,[27] plays an important role in the determination of the effective particle conductivity of the cell. The data also show that an increase in the electrode size increases the levitation height. As shown elsewhere,[26] this is a consequence of using a periodic electrode array and can be further understood by the fact that the electric field and the factor ∇E^2 of Equation (1) extend further above the electrodes with increasing interelectrode distance. From these and other data (Rousselet *et al.*, in preparation) it can be concluded that the optimum interelectrode distance is in the region of 40-100 μm.

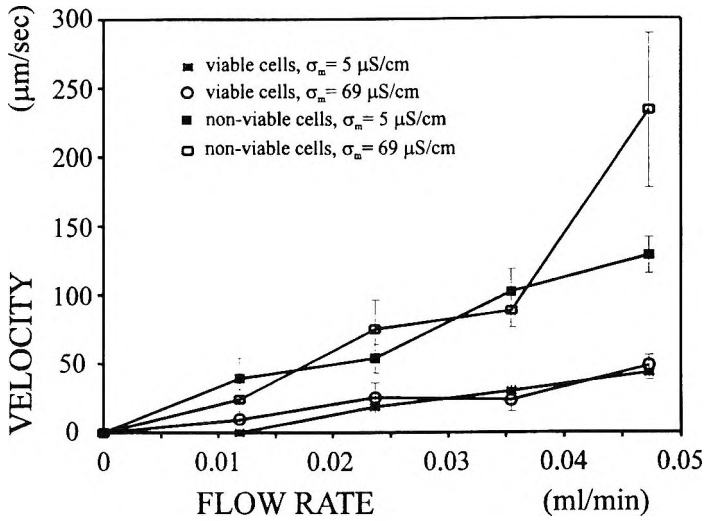

Figure 8. Separation of viable and non-viable yeast cells using hyperlayer-DEP-FFF. The velocity at which non-viable yeast cells (which are levitated high above the electrodes) travel through the chamber is considerably higher than that of viable yeast cells. The applied voltage and frequency were 5 V pk-pk and 5 MHz, respectively.

Figures 6 and 7 show the effect of the frequency of the applied electric field on the levitation height of viable and non-viable yeast cells above the electrodes at different medium conductivity values. The experimental data closely resemble those obtained (Figure 1a-d) from the modelling of the cells, taking into account electrode polarisation effects.[26] Some of the differences observed may be explained by the fact that any changes in the cell wall conductivity have been ignored in the modelling whilst it has been shown before[27] that, because the cell wall of yeast cells acts as an ion exchanger, the dielectric properties of yeast varies with medium conductivity. The data show that, if one is to achieve the most efficient separation of viable and non viable cells, it is best to use a frequency of 2-10 MHz. This conclusion is relatively independent of the medium conductivity.

To achieve the separation of viable and non-viable yeast cells using hyperlayer DEP-FFF the speed was measured at which viable and non-viable cells travelled at different flow rates through a chamber containing interdigitated electrodes. Two different conductivities (5 and 68 μS/cm) and applied voltages (5 and 10 V pk-pk) were used, whilst the applied frequency in

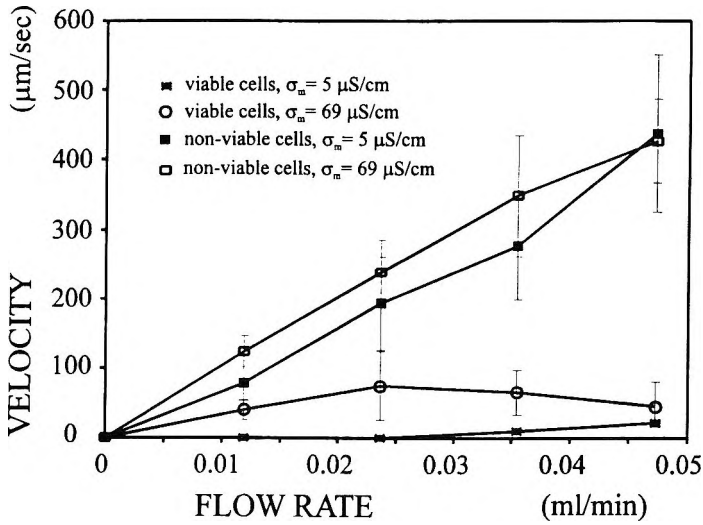

Figure 9. As in Figure 8, but with an applied voltage of 10 V pk-pk.

each case was 5 MHz. The results are shown in Figures 8 and 9. As expected, since the non-viable cells are levitated high above the electrodes, and the viable cells are attracted to the electrodes, the velocity at which non-viable yeast cells travel through the chamber is considerably higher than that of viable yeast cells. Especially at low conductivities and high voltages, the positive DEP force on viable cells was so strong that a considerable number of viable cells remained attracted to the electrodes. For an efficient separation experiment in which positive DEP occurs, it may be necessary to use a pulsed electric field to allow cells to become detached from the electrodes. The cell "mixing" effect that occurs between pulses will also improve the separation. During the levitation experiments, it was observed that near the crossover points from positive to negative DEP the cells could be observed to redistribute themselves over a range of heights near the electrodes. This indicates that it would be relatively straightforward to separate the cells into further fractions. Further work will be aimed at achieving this as well as the separation of other cell types.

CONCLUSIONS

The separation of particles with differing dielectric properties using normal-DEP-FFF, steric-DEP-FFF and hyperlayer DEP-FFF has been

discussed. To demonstrate steric-DEP-FFF and hyperlayer-DEP-FFF the separation of viable and non-viable yeast cells was chosen. The effects of the frequency of the applied field and conductivity and permittivity of the medium was investigated. The separation of viable and non-viable yeast cells is best achieved at a frequency of 2-10 MHz, and for moderate conductivities is relatively independent of the conductivity of the surrounding medium. The hyperlayer-DEP-FFF technique, which was here described for the first time, has a number of advantages over the steric-DEP-FFF technique that is normally used. The hyperlayer-DEP-FFF technique makes better use of the parabolic velocity profile of the fluid flowing through the chamber by pushing the particles to different heights in the chamber, whilst in steric-DEP-FFF the particles stay in the layer near the chamber wall. The levitation height of the particles is independent of particle size, and only dependent on their dielectric properties and density. Also, hyperlayer-DEP-FFF can be performed at high conductivities, adhesion of the particles to the chamber wall is largely reduced as contact with the walls is minimal, and trapping of cells in pearl chains is largely reduced.

ACKNOWLEDGMENTS

This work has been supported by the BBSRC under the ROPA scheme (grant PAC 02711), and by grants from the French Foreign Office and the British Council. We thank J. Tame for micro-electrode fabrication, and Dr. W. M. Arnold for practical advice and useful discussions.

REFERENCES

1. J. C. Giddings, Science, **260**, 1456-1465 (1993).

2. S. K. Ratanathawongs, J. C. Giddings, Anal. Chem., **64**, 6-15 (1992).

3. J. C. Giddings, F. J. Yang, M. N. Myers, J. Virol., **21**, 131-138 (1977).

4. K. D. Caldwell, L. F. Kesner, M. N. Myers, J. C. Giddings, Science, **176**, 296-298 (1972).

5. L. E. Schallinger, W. W. Yau, J. J. Kirkland, Science, **225**, 434-437 (1984).

6. B. N. Barman, E. R. Ashwood, J. C. Giddings, Anal. Biochem., **212**, 34-42. (1993).

7. J. C. Bigelow, Y. Nabeshima, K. Kataoka, J. C. Giddings "Separation of Cells and Measurement of Surface Adhesion Forces," in **Cell Separation Science and Technology** D. S. Kompola, P. Todd, eds., ACS Symp. Series 464, ACS, Washington D. C., 1991, pp. 146-158.

8. J. C. Bigelow, J. C. Giddings, Y. Nabeshima, T. Tsuruta, K. Kataoka, T. Okano, N. Yui, Y. Sakurai, J. Immunol. Methods, **117**, 289-293 (1989).

9. R. V. Sharma, R. T. Edwards, R. Beckett, Appl. Env. Microb., **59**, 1864-1875 (1993).

10. S. Hoffstetter-Kuhn, T. Rösler, M. Ehrat, H. M. Widner, Anal. Biochem., **206**, 300-308 (1992).

11. H. A. Pohl, **Dielectrophoresis**, Cambridge University Press, Cambridge, 1978.

12. R. Pethig, "Application of AC Electric Fields to the Manipulation and Characterisation of Cells," in **Automation in Biotechnology**, I. Karube, ed., Elsevier, Amsterdam, 1991, pp. 159-185.

13. F. F. Becker, X. B. Wang, Y. Huang, R. Pethig, J. Vykoukal, P. R. C. Gascoyne, Proc. Natl. Acad. Sci. USA., **92**, 860-864 (1995) .

14. P. R. C. Gascoyne, Y. Huang, R. Pethig, J. Vykoukal, F. F. Becker, Meas. Sci. Technol., **3**, 439-445 (1992).

15. M. S. Talary, K. I. Mills, T. Hoy, A. K. Burnett, R. Pethig, Med. Biol. Eng. Comp., **33**, 235-237 (1995).

16. G. H. Markx, M. S. Talary, R. Pethig, J. Biotechnol., **32**, 29-37 (1994).

17. G. H. Markx, R. Pethig, Biotechnol. Bioeng., **45**, 337-343 (1995).

18. G. H. Markx, Y. Huang, X. F. Zhou, R. Pethig, Microbiology, **140**, 585-591 (1994).

19. G. H. Markx, P. A. Dyda, R. Pethig, J. Biotechnol., **51**, 175-180 (1996).

20. Y. Huang, R. Hölzel, R. Pethig, X. B. Wang, Phys. Med. Biol., **37**, 1499-1517 (1992).

21. W. M. Arnold, A. G. Gessner, U. Zimmermann, Biochim. Biophys. Acta, **1157**, 32-44 (1993).

22. J. M. Davis, J. C. Giddings, Sepn. Sci. Technol., **21**, 969-989 (1986).

23. X. B. Wang, Y. Huang, J. P. H. Burt, G. H. Markx, R. Pethig, J. Phys. D: Appl. Phys., **26**, 1278-1285 (1993).

24. M. E. Hansen, J. C. Giddings, R. Beckett, J. Coll. Interf. Sci., **132**, 300-312 (1989).

25. M. Washizu, S. Suzuki, T. Nishizaka, T. Shinohara, 1992 IEEE Ind. Appl. Soc. Ann. Meeting, 1446-1452 (1992).

26. J. Rousselet, G. H. Markx, R. Pethig, Coll. Surf. A: Phys. Chem. Asp. submitted for publication (1997).

27. G. H. Markx, X. F. Zhou, R. Pethig "Dielectrophoretic Manipulation of Micro-organisms in Microelectrode Arrays," in **Electrostatics '95**, S. Cunningham, ed., IOP Conf. Series No 143, IOP, London, 1995, pp 145-148.

Received January 2, 1997
Accepted April 18, 1997
Manuscript 4444

J. LIQ. CHROM. & REL. TECHNOL., 20(16 & 17), 2873–2886 (1997)

FIELD-FLOW FRACTIONATION WITH ASYMMETRICAL ELECTROOSMOTIC FLOW. II. CHARGED PARTICLES

V. P. Andreev,* Y. V. Stepanov

Institute for Analytical Instrumentation
Russian Academy of Sciences
26 pr. Rigsky
St. Petersburg 198103, Russia

ABSTRACT

The study of field-flow fractionation (FFF) with asymmetrical electroosmotically driven flow is extended to the case of charged sample particles. In this case, field-flow fractionation is combined with capillary zone electrophoresis in the same flat FFF channel.

Retention, dispersion, and resolution for sedimentation and gravitational FFF of charged particles with asymmetrical electroosmotic flow are studied by mathematical modeling.

INTRODUCTION

The new variant of field-flow fractionation was proposed[1] and studied.[2] It was suggested to use the electroosmotically driven flow instead of the Poiseuille flow. Electoroosmotic flow of conducting fluid (buffer) is generated by applying an electric field along the channel with charged (having the nonzero zeta-potentials) walls.

The usual electroosmotic flow can't be used for FFF, because its profile is too close to uniform. In order to realize the FFF type of separation, one neads to have nonuniformity of the longitudinal flow. So, it was proposed to realize the asymmetrical electroosmotic flow by making the channel walls of different materials or by chemically modifying them in order to have the different (nonequal) values of the zeta-potentials of the walls. As was shown, in[1,2] different kinds of asymmetrical electroosmotic flow profiles in FFF channels can be generated. Some of these profiles were shown to be very promising as far as high efficiency and resolution are concerned.

Yet, in Refs. 1 and 2, only the case of the uncharged sample particles was studied. In this paper, we extend the study to the case of the charged sample particles. In this case the particles are not only moving with the longitudinal flow (here asymmetrical electroosmotic flow) but are also forced by the longitudinal electric field to move along the channel electrophoretically. The case is similar to the usual capillary zone electrophoresis (CZE) where the total velocity of the particle is the sum of the electroosmotic velocity of the flow and the electrophoretic velocity of the particle.

The difference from the CZE case is that, in our situation, electroosmotic flow is nonuniform and that we also have some kind of transversal field (as usually in FFF). So, the two processes and two types of separation are combined here: FFF and CZE.

A great variety of variants of FFF and CZE combination could be imagined,[3] depending on the various factors such as: the ratio of the zeta-potentials of the channel walls, the sign and the value of the ratio of the electrophoretic and electroosmotic velocities, the type of the transversal field, and so on.

In this paper, we will restrict ourselves to the case, where the charges of the particles have the same sign as the zeta-potentials of the walls, so that the particles are electrostatically subtracted by the walls. It also means that the particles are moving electrophoretically in the direction opposite to the electroosmotic flow of the fluid. This case is easier for theoretical studies and experimental realization because the problem of particle sorption on the walls is reduced.

Retention, efficiency and resolution for FFF with asymmetrical electroosmotic flow of charged particles are studied in this paper for the cases of different functional dependences of particle charge versus particle radius. Very high values of resolution are predicted for some cases.

THEORY

The analytical solution for the electroosmotic flow profile V(Y) in the flat FFF channel with the arbitrary (nonequal) values of the zeta-potentials of the walls was derived in Ref. 2:

$$V(Y) = A[(\zeta_R - 1)\frac{\sinh kY}{\sinh k} + (\zeta_R + 1)\frac{\cosh kY}{\cosh k}$$

$$+ (1 - \zeta_R)Y - (1 + \zeta_R)] \qquad (1)$$

where

$$A = \frac{\zeta_2 \varepsilon\varepsilon_0 E_Z}{2\eta}, \quad k = æw / 2, \quad \zeta_R = \zeta_1 / \zeta_2,$$

$\varepsilon, \varepsilon_0$ - dielectric constant of the buffer and permitivity of the free space, η - viscosity of the buffer, E_z - external longitudinal electric field, ζ_1 - the zeta-potential of the accumulating wall, ζ_2 - the zeta-potential of the opposite wall, w - the thickness of the FFF channel, Y = 1-2y/w - dimensionless transversal coordinate (0<y<w), $æ^{-1} = \left(\frac{2ne^2}{\varepsilon\varepsilon_0 k_B T}\right)^{-\frac{1}{2}}$ - Debye length, n - number of ions per init volume of the buffer, e - proton charge, k_B - Boltzman constant, T - temperature. For large values of k, the first two terms in the square brackets are substantially non-zero only in the immeadiate vicinity of the walls (in the Debye layer distance) while everywhere else the electroosmotic flow profile is dominated by the last two terms in the square brackets. Even for the very diluted buffer with concentration $C_0=10^{-5}$M the Debye length is equal to $æ^{-1} = 0.1 \mu m$, and so, for usual FFF channels, the values of k are rather high (k>5000).

When the charged sample particle is placed in the FFF channel with such asymmetric electroosmotic flow, it is moving with the electroosmotic flow with velocity V(Y) and is moving electrophoretically relatively to the flow, so that longitudinal velocity of the charged particle is equal to

$$V_p(Y) = V(Y) + \mu_{ep} E_Z \qquad (2)$$

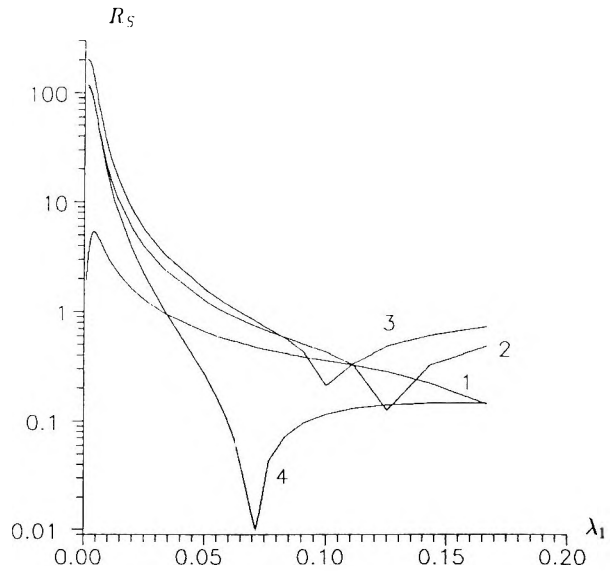

Figure 1. FFF with linear electroosmotic flow ($\zeta_R = 0$). Resolution of charged particles.

$r_1 / r_2 = 1.2 \Rightarrow \lambda_1 / \lambda_2 = 0.58$

$k = 10000$, $|V_{ep_1}| = 0.5|A|$, $V_{ep} \uparrow\downarrow V_{osm}$, $L = 0.5m$

$1 - \mu_1 / \mu_2 = 1$ $\quad z \sim r$

$2 - \mu_1 / \mu_2 = 1.2$ $\quad z \sim r^2$

$3 - \mu_1 / \mu_2 = 1.44$ $\quad z \sim r^3$

$4 - \mu_1 / \mu_2 = 0.832$ $\quad z = const$

μ_{ep} - electrophoretic mobility of the particle, that is considered here to be independent of coordinate (this assumption is usually used in CZE when the transversal temperature gradients are not too high).

In addition to these two types of motion, there is, as usually, in FFF, the movement of the particles in the transversal direction. Particles are forced by the external transversal field of some kind to drift towards the accumulating wall with velocity - u, and take part in the Brownian motion, characterized by the diffusivity - D.

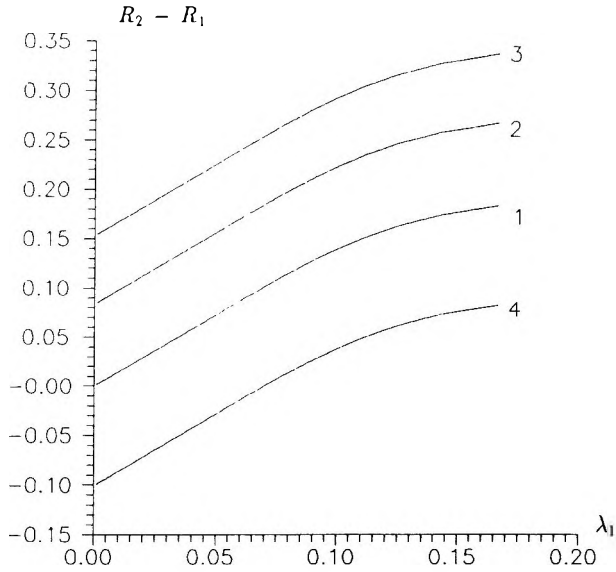

Figure 2. FFF with linear electroosmotic flow ($\zeta_R = 0$). Retention difference R_2 - R_1. Conditions the same as in Figure 1.

We will consider the relaxation processes to be completed and exponential transversal distribution of the particles to be established. So we use the usual FFF equations[4] to calculate mean zone velocity $\bar{U}$, retention R, and height equivalent to theoretical plate, H:

$$\bar{U} = \int_{-1}^{1} V_p(Y) \exp(Y / 2\lambda)\, dY \Big/ \int_{-1}^{1} \exp(Y / 2\lambda)\, dY = V_{FFF} + V_{ep} \tag{3}$$

where

$$V_{FFF} = [4\lambda \sinh(1 / 2\lambda)]^{-1} \left[\int_{-1}^{1} V(Y) \exp(Y / 2\lambda)\, dY \right],$$

$$V_{ep} = \mu_{ep} E_Z,$$

$\lambda = uw / D$ - the basic FFF parameter, characterizing the transversal distribution of the particles.

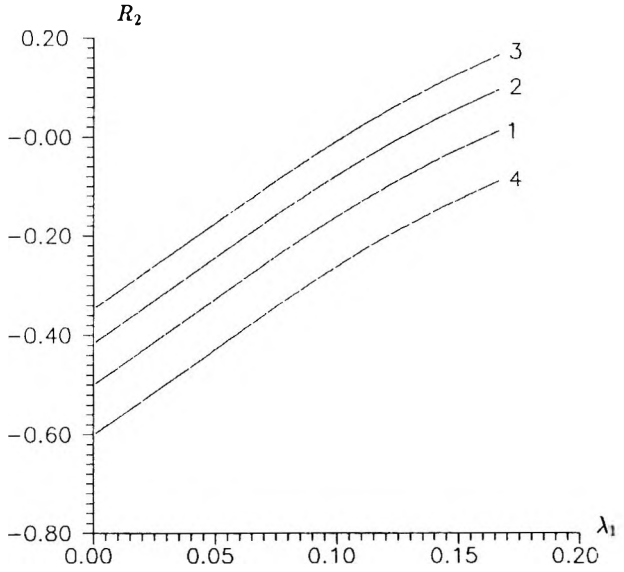

Figure 3. FFF with linear electroosmotic flow ($\zeta_R = 0$). Retention for the second sort of particles. Conditions the same as in Figure 1.

$$R = \bar{U} / < V > \tag{4}$$

where $< V >= \frac{1}{2}\int_{-1}^{1} V(Y)\,dY$ - mean flow velocity, for the case when V(Y) is given by equation (1) $< V >$:

$$< V >= -A(1+\zeta_R)(1-\frac{1}{k}tanhk) \tag{5}$$

Height equivalent to theoretical plate is determined by two terms: molecular diffusion and Taylor dispersion terms

$$H = 2D / \bar{U} + \chi \frac{w^2 < V >}{D} \tag{6}$$

Coefficient χ is characterizing the role of Taylor dispersion and can be calculated for the case of arbitrary flow profile according to Refs. 5,6:

$$\chi = D_U / (2 < V >^2 R) \tag{7}$$

where

$$D_U = \int_{-1}^{1} B^2(Y) \exp(-Y / 2\lambda)\, dY / (4\lambda \sinh(1 / 2\lambda))$$

and finally

$$B(Y) = \int_{-1}^{Y} (\bar{U} - V(Y'))\exp(Y' / 2\lambda)\, dY'$$

We also studied resolution and described it in the usual chromatographic way:

$$R_S = \frac{(\bar{U}_1 - \bar{U}_2)L}{2(\sigma_1 + \sigma_2)\bar{v}_2} \tag{8}$$

where $\bar{U}_1, \bar{U}_2$ are the mean zone velocities for the particles of two different sorts and $\sigma_1 = \sqrt{H_1 L}, \sigma_2 = \sqrt{H_2 L}, H_1, H_2$ - are the peak widths and HETP's for these two sorts of particles correspondingly, L - length of the FFF channel.

It is generally accepted in the theory of FFF to study R, χ and H dependences versus λ. In our case, we have also another parameter characterizing the particles and the separation process - electrophoretic mobility μ_{ep}. So, we need to make some assumptions about the possible correlations between lambdas and electrophoretic mobilities. Let us consider the cases of Gravitational FFF and Sedimentation FFF. As it is well known for these types of FFF, λ is inversely proportional to the cube of particle radius. Let us consider the case when we are analyzing the sample that is the mixture of particles of various sizes but equal density. Electrophoretic mobility of the particle can be written as:

$$\mu_{ep} = z / 6\pi\eta r \tag{9}$$

where z - effective electric charge of the particle, r - radius of the particle.

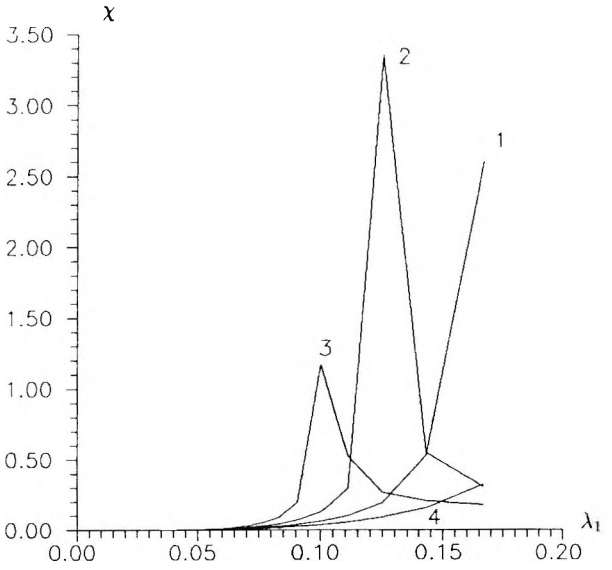

Figure 4. FFF with linear electroosmotic flow ($\zeta_R = 0$). χ - coefficient for the second sort of particles. Conditions the same as in Figure 1.

Different situations may take place. Charge of the particles can be proportional to radius; then electrophoretic mobilities are independent of radius. This is the case of DNA fragments, for example. In this case there will be no CZE type of separation and all resolution will be only due to FFF mechanism.

Another situation takes place if charges are sorbed by the surface of the particle. Then, electrical charge is proportional to r^2 and electrophoretic mobility is proportional to r. Charge of the particle can also be proportional to the volume of the particle or r^3; then, electrophoretic mobilities are proportional to r^2. It is also possible that all of the particles have equal charges, (for example, different macromolecules that have the same charged group); then their electrophoretic mobilities will be inversely proportional to r. The results for these four cases are presented in the following section.

RESULTS AND DISCUSSION

Figures 1-4 present the results for the case of linear electroosmotic flow with $\zeta_R = 0$ (the zeta-potential of the accumulating wall is equal to zero). As

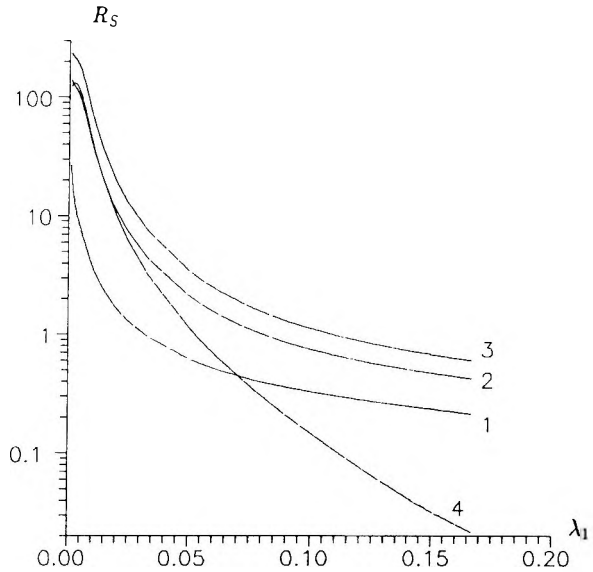

Figure 5. FFF with trapezoidal electroosmotic flow ($\zeta_R = 0.5$). Resolution of charged particles. Conditions the same as in Figure 1.

was previously mentioned, we considered only the case of the particles moving electrophoretically in the direction opposite to the direction of the electroosmotic flow. The resolution of two sorts of particles with different by 20% radii is presented in Figure 1. Other functions are presented in Figures 2-4 to explain some anomalies in the dependence of resolution versus λ. Electrophoretic velocity of the first sort of particles was taken equal to 1/4 of the maximum of V(Y) ($|V_{ep_1}| = 0.5\,|A|$).

Curve 1 is for the case of equal electrophoretic mobilities of the particles; curve 2 for the case where the ratio of electrophoretic mobilities is proportional to the ratio of radii; curve 3 for the ratio of mobilities proportional to the square of the ratio of radii; and curve 4 for mobilities inversely proportional to radii.

The same designation of the curves was used throughout the paper. Through the entire paper, parameter λ for the first sort the particles - λ_1 was taken as the independent variable.

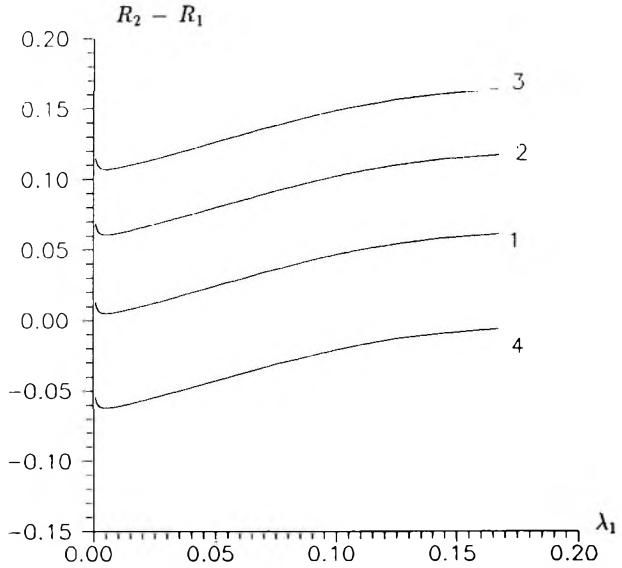

Figure 6. FFF with trapezoidal electroosmotic flow ($\zeta_R = 0.5$). Retention difference R_2 - R_1. Conditions the same as in Figure 1.

Parameter λ_2 for the second sort of particles was calculated as $\lambda_2 = \lambda_1 \left(\frac{r_1}{r_2}\right)^3$ (this is right for Sedimentation FFF and Gravitational FFF).

As can be seen from Figure 1, resolution is especially high for very small values of λ for cases 2, 3, and 4. There are some points in this figure that need to be explained. First, one is the decrease of resolution with the decrease of λ_1 for the curve 1. In this case, the difference in electrophoretic velocities of the particles is equal to zero and, when λ_1 is decreased, the difference of the mean zone velocities $\bar{U}_1 - \bar{U}_2$, or the difference in retentions R_2 - R_1 is also lineary decreasing with λ_1. But, the dispersion for very small λ is significantly influenced not only by Taylor dispersion, but also by molecular diffusion part of H, so that σ_1, σ_2 are decreasing more slowly than lineary with λ_1, and this leads to the decrease of resolution, R_S, for very small values of λ_1. For the rest of the curves, there is the non-zero difference in the electrophoretic mobilities of the two sorts of the particles, so that retention

differences R_2 - R_1 are not going to zero with λ_1 for these cases. Peak widths σ_1 and σ_2 are decreasing with λ_1, and so, the resolution is growing. The dependences of retention difference R_2 - R_1 versus λ_1 are presented in Figure 2. Note that, for cases 2 and 3, selectivity due to FFF mechanism and CZE mechanism are acting in the same direction, that is, differences in FFF velocities $(V_{FFF_2} - V_{FFF_1})$ and electrophoretic velocities $(V_{ep_2} - V_{ep_1})$ of the particles have the same sign. While, for the fourth case, the signs of these differences are opposite and there is the point where retention difference and resolution turn to zero. Two other minimums at curve 2 and curve 3 must be explained. They can be understood from the Figure 3 that presents retention of the second sort of particles R_2. Curves 2 and 3 for R_2 cross the zero line just at the points where resolution, R_S, for the same cases 2 and 3 has minimum. This is quite understandable, because the fact that retention is crossing zero means that, for this sort of particles, both signs of velocity are equally probable. The particles, characterized by these values of λ can move with equal probabilities in one direction with electroosmotic flow and in the opposite direction electrophoretically. This means zero mean zone velocity and extremely high variance due to Taylor dispersion mechanism. The extremely high level of Taylor dispersion at these special points is presented in Figure 4, where $\chi_2(\lambda_1)$ dependences are shown. The fact that dependences of R_2 and χ_2 are presented versus parameter λ_1 may seem unusual, but it only means that λ_2 was calculated as $\lambda_2 = \lambda_1 \left(\frac{r_1}{r_2}\right)^3$, and the presentation of $R_2(\lambda_1)$ and $\chi_2(\lambda_1)$ is more convinient for the explanation of $R_S(\lambda_1)$ dependences then $R_2(\lambda_2)$, $\chi_2(\lambda_2)$.

Figures 5-7 present the same functions for the same cases as Figures 1-3, but for the different flow profile. Here, the zeta-potential of accumulating wall is equal to half the zeta-potential of the upper wall $(\zeta_R = 0.5)$. So, the electroosmotic flow velocity is changing from $V_{osm} \approx |A|$ at Y=1-k to $V_{osm} \approx 2|A|$ at Y= -1+k (going to zero only in the immeadiate vicinity of the walls). Figure 5 presents the resolution of the two sorts of particles with radii differing by 20%. For very small values of λ resolution is high for all functional dependences of $\mu_{ep}(r)$ studied in the paper; for larger values of λ resolution for cases 1, 2, 3 stays rather high while, for the case 4, it decreases significantly. As can be seen from Figure 6, it is due to the closeness to zero of retention difference (R_2 - R_1) curve for the values of $\lambda_1 \approx 0.2$.

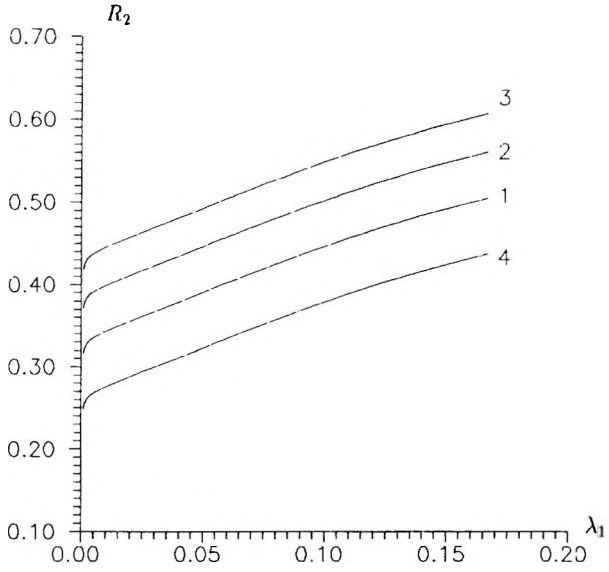

Figure 7. FFF with trapezoidal electroosmotic flow ($\zeta_R = 0.5$). Retention for the second sort of particles. Conditions the same as in Figure 1.

Curve 1 (Figure 5) presenting the resolution of the particles with equal electrophoretic mobilities, is significantly higher in the case of the non-zero zeta-potential of the accumulating wall than in the case $\zeta_R = 0$ represented by curve 1 in Figure 6. The reason is that the mean zone velocity in the case $\zeta_R = 0.5$ is not going to zero, and so, the molecular diffusion part of HETP is not high. The curves presented in Figures 6 and 7 have a high value of curvature in the regions of very small λ. The reason for this is the presence, in the case $\zeta_R = 0.5$, of the Debye layer in the vicinity of the accumulating wall, where electroosmotic velocity is very rapidly changing from $V_{osm} \approx |A|$ to $V_{osm} = 0$. When λ is commensurable with $k^{-1} = 10^{-4}$, the nonuniformity of the flow velocity in this layer starts influencing retention.

The important difference between Figure 1 and Figure 5 is that, for the case of the trapezoidal electroosmotic flow ($\zeta_R = 0.5$) resolution versus λ dependences are much more monotonous than in the case of linear electroosmotic flow ($\zeta_R = 0$). Monotonous $R(\lambda)$ and $R_S(\lambda)$ dependences are,

naturally, more desirable for experimental realization and interpretation of experimental results, so situations when $V_{FFF} \approx -V_{ep}$ must be generally avoided.

On the other hand, in a well known paper,[7] it was predicted that the maximum resolution could be realized in CZE when electroosmotic velocities of the particles were approximetely equal and counterdirected with the electroosmotic velocity of the fluid. In this case, the extremely high resolution was predicted to be realized though, due to the very long time of analysis. This situation was not yet experimentally realized, probably because both electroosmotic and electrophoretic velocities are proportional to the external field strength and can't be changed independently during the experiment. In the case of FFF of charged particles with asymmetric electroosmotic flow V_{ep} is determined by the external field strength E_Z, while V_{FFF} is determined by E_Z and λ, so these velocities can be changed independently during the experiment and the balance $V_{FFF} = -V_{ep}$ can be established and the prediction of Ref. 7 can be experimentaly tested.

ACKNOWLEDGMENTS

The authors are grateful to Prof. M. Martin and Dr. J. Chmelik for interesting and productive discussions.

REFERENCES

1. V. P. Andreev, M. E. Miller, J. C. Giddings, Paper 23 presented at the 5th Int. Symp. on FFF, Park City, Utah, USA, July 10-12, 1995.

2. V. P. Andreev, Y. V. Stepanov, J. C. Giddings. J. Microcol. Sepns., 1997, submitted for special J. C. Giddings issue.

3. V. P. Andreev, Y. V. Stepanov, Paper 10 presented at the 6th Int. Symp. on FFF, Ferrara, Italy, September 9-11, 1996.

4. J. C. Giddings, J. Chem.Phys., **49**, 81 (1968).

5. H. Brenner, L. J. Gajdos, J. Colloid Interface Sci., **58**, 312 (1977).

6. M. Martin, J. C. Giddings, J. Phys. Chem., **85**, 727 (1981).

7. J. M. Jorgenson, K. Lukacs, Anal. Chem., **53**, 1298 (1981).

Received January 27, 1997
Accepted April 14, 1997
Manuscript 4451

J. LIQ. CHROM. & REL. TECHNOL., 20(16 & 17), 2887–2905 (1997)

CYLINDRICAL SPLITT AND QUADRUPOLE MAGNETIC FIELD IN APPLICATION TO CONTINUOUS-FLOW MAGNETIC CELL SORTING

M. Zborowski,[1] P. S. Williams,[2] L. Sun,[3]
L. R. Moore,[1] J. J. Chalmers[3]

[1] Department of Biomedical Engineering
The Cleveland Clinic Foundation
9500 Euclid Avenue
Cleveland, OH 44195-5254, USA

[2] Field-Flow Fractionation Research Center
University of Utah
Salt Lake City, UT 84102, USA

[3] Department of Chemical Engineering
The Ohio State University
Columbus, OH 43210-1080, USA

ABSTRACT

The quadrupole magnetic field has been used for quadrupole mass spectroscopy and for industrial and mining dry separations. We propose to use it for rapid, continuous-flow cell sorting in biomedical and biotechnological applications. We set out to investigate the performance of such a sorter using the theoretical methods of split-flow thin channel separation (SPLITT). Comparison of theoretical results and preliminary experimental

data, using a model system of human peripheral lymphocytes labeled with immunomagnetic colloid, led us to the identification of the most important parameters of the system.

INTRODUCTION

Magnetic cell separation has become an important part of research related to cell surface chemistry and cell function.[1,2] It relies on the development of antibodies against cell surface markers, and suitable magnetic labels.[3] It has been successfully applied, also, to bone marrow transplantation therapy and stem cell transplantation.[4,5] The current, state-of-the art, commercial magnetic cell separators operate on the basis of a batch process.[1,3] The advantage of the batch process is relative simplicity of the separator design and its use. The disadvantages of such a process are limitations in the separator performance, such as unequal treatment of enriched and depleted fractions, and limited sorting capacity.[6]

Small (molecular or colloidal) magnetic label and a well-defined and simple magnetic field geometry are prerequisites for continuous-flow cell sorting. The advantages of using submicrometer, colloidal magnetic particles for cell separation have been recently recognized.[6] High purity and high recovery separation of the positive cell fraction have been achieved using such colloidal labels and high-gradient magnetic separation (HGMS).[1,6] The small size, and small magnetization, of the microbead require higher fields and gradients than the particulate label. However, the small size of the beads offers better control over cell motion in the aqueous solution than is possible with the use of large, particulate bead.

We identified the quadrupole magnetic field as a field of particular simplicity and, therefore, promising for a continuous-flow cell separation.[7] In designing the quadrupole field separator with its characteristic annular flow of separands and carrier medium, and the presence of flow split cylinders at the inlet and outlet ports, we noted analogies with the SPLITT technique.[8-11] These observations lead us to the conclusion that the further development of magnetic cell sorting could be accelerated by combining existing theoretical and experimental methods of SPLITT with the theory of the quadrupole magnetic field. The aim of this study is the preliminary investigation of analogies between the processes of quadrupole magnet sorting and SPLITT. In particular, we set out to predict the resolution, purity, recovery, and throughput of the sorted fractions using the mathematical formalism developed for SPLITT separation, and compare these with the preliminary experimental data.

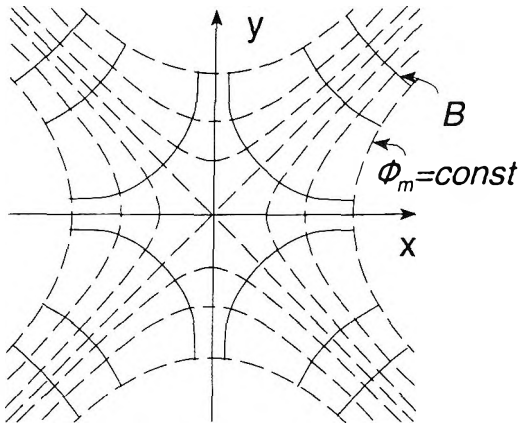

Figure 1. Equipotential, ϕ_m = const., and field, B, lines of the quadrupole field.

MATERIALS AND METHODS

Theory

The collective effect of the external magnetic field, $\boldsymbol{H}$, on the colloidal magnetic labels bound to the cell surface leads to the linear relationship between cell magnetic moment, μ, and $\boldsymbol{H}$, $\mu = V\chi\boldsymbol{H}$. In a diamagnetic medium (such as water) $\boldsymbol{B} = \mu_0\boldsymbol{H}$ [T], where $\boldsymbol{H}$ [A/m] is magnetic field strength.[12] The magnetostatic force, $\boldsymbol{F}_m$, acting on the labeled cell, is given by the expression (in SI system of units):

$$F_m = (\mu \cdot \nabla)B = V\chi(H \cdot \nabla)B = 1/2\frac{V_{cell}\,\Delta\chi}{\mu_0}\nabla B^2 \qquad (1)$$

where χ - the volumetric magnetic susceptibility [dimensionless], $\Delta\chi$ - the difference between the volume-averaged magnetic susceptibility of the cell and that of the medium, V_{cell} - cell volume [m^3], and $\mu_0 = 4 \times 10^{-7}$ [Tm/A]. Note that the magnetostatic force acting on a freely suspended dipole follows the lines of the steepest increase of B^2. In homogenous media, such as aqueous solutions of electrolytes, the value of B^2 is directly proportional to the magnetic field energy density. The properties of the small magnetic particles in the external magnetostatic field are such that one is justified in using the scalar potential field, ϕ_m, to describe their motion, where $\boldsymbol{H} = -\nabla\phi_m$.

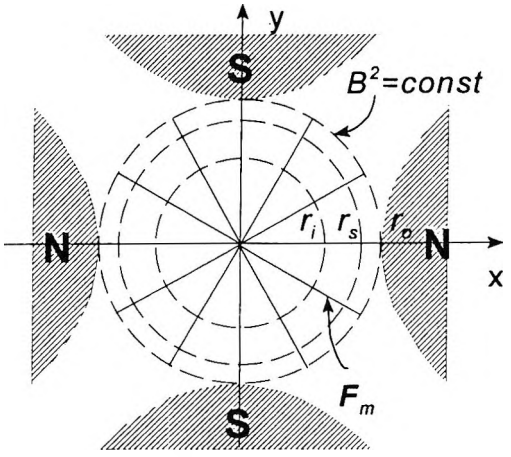

Figure 2. Constant field energy density, B^2 = const., and force, F_m, lines acting on a freely-suspended magnetic dipoles in the quadrupole field. The magnetic particles migrate radially between r_i - inner cylinder radius, through r_s - split cylinder radius, towards r_o - outer cylinder radius.

The quadrupole field is defined by the linear dependence of $\boldsymbol{B}$ on the radial coordinate.[7] The equipotential, ϕ_m = const., and field, B, lines of the quadrupole field are shown in Fig. 1. The magnetic force acting on the magnetic dipole in the quadrupole field is obtained from the definition of the quadrupole field, and from the relation in Eq. 1:

$$B = B_0 r' \qquad (2)$$

$$F_m = \frac{V_{cell}\,\Delta\chi}{\mu_0}\frac{B_0^2}{r_0} r', \quad \phi \in [0,2\pi]$$

where (r, ϕ) are cylindrical coordinates, r_0 is the aperture radius at the pole tips, $\boldsymbol{r}' = \boldsymbol{r}/r_0$, and B_0 is the magnetic field at the pole tip, $B_0 = B(\mathbf{r})$, Fig. 2.

The order of magnitude of F_m can be calculated using the following parameters, characteristic of a practical system: B_0 = 0.5 T, $r_0 = 5{+}10^{-3}$ m, V_{cell} = 4/3π(5 μm)^3 = 524 μm^3 = $5{+}10^{-16}$ m^3, $\Delta\chi$= 100 10^{-6} (in SI system of units). Assuming r' = 1, O[F_m] = 10^{-12} N, which is well within the resolving power of SPLITT.[13]

Geometrical Similarity Between Quadrupole Field Separator and SPLITT

The radial migration of magnetically-labeled cells in the quadrupole field, along the force lines defined by Eq. 2, dictates the separator geometry. The preferred geometry is that of a thin annulus pressed against the pole tips of the quadrupole magnet, with the cylindrical flow splitters inserted at inlet and outlet ends of the annulus. The cell mixture is injected into the portion of the flow contained between the split cylinder and the inside cylinder, as shown in Fig. 2, which also represents the plan view (cross-section) of the separator. The separation is achieved by the differential radial migration of cells – the magnetically-labeled cells migrate in the outward direction, Eq. 2, while the unlabeled cells remain in the vicinity of the inside cylinder wall. Given sufficient time (or length of the separation channel), the magnetic cells are sufficiently displaced towards the outer cylindrical wall of the annulus so that they can be collected between the outlet flow splitter and the outer cylindrical wall, Fig. 3. The unlabeled cells follow the flow streamlines and are collected between the inside cylindrical wall and the flow splitter.

The elevation view of the quadrupole field separator, Fig. 3, reveals characteristic features of a SPLITT separator, i.e., split flows at the inlet and outlet portions of the channel, labeled a', b', and a, b, respectively, and the thin flow channel exposed to the separation force (magnetic) normal to the general direction of flow.[8-11] It may be noted that the magnetic force is independent of angular coordinate, and is directly proportional to radial coordinate, Eq.2.

The important distinguishing feature of the quadrupole field separator is its axial symmetry, unlike any of the SPLITT channels described to date, which are all rectangular. Retention by field-flow fractionation in annular channels has been described before.[14] This formal analogy between the quadrupole field separator and SPLITT is the basis of mathematical analysis of the separator performance presented below.

Cell Trajectory Within the Quadrupole Field SPLITT System

Radial position of splitting cylinders

The splitting cylinders are equivalent to the splitting planes of conventional SPLITT systems. The inlet splitting cylinder (ISC) lies between the streamlines originating at the two different inlets, and the outlet splitting cylinder (OSC) lies between the streamlines exiting the different outlets, Fig. 3.

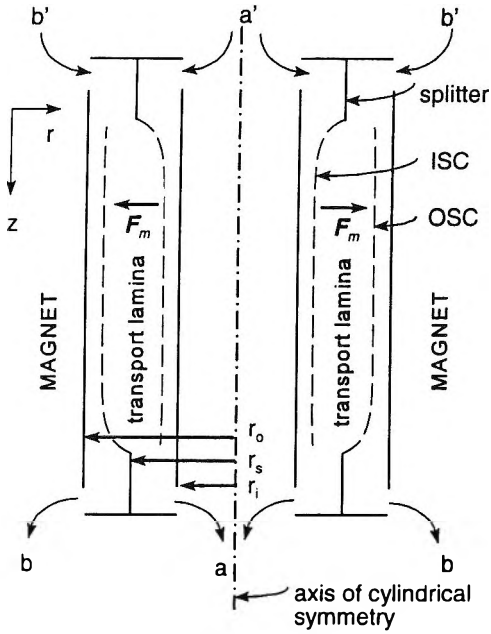

Figure 3. Elevation view of the cylindrical SPLITT quadrupole magnetic field sorter. ISC - inlet splitting cylinder, OSC - outlet splitting cylinder. Cell sample is fed through port *a'*, carrier medium is pumped through port *b'*, sorted fractions are collected at ports *a* and *b*.

The velocity profile within the annulus[15] is given by the equation

$$v(r') = \frac{2 < v >}{A_1}(1 - r'^2 - A_2 \ln r') \qquad (3)$$

where $r' = r/r_0$, $r'_i < r' \leq 1$, r'_i corresponds to the radius of the inner cylinder, $A_2 = (1-r'^2_i)/\ln r'_i$, $A_1 = 1 + r'^2_i + A_2$,and $<v>$ is the mean fluid velocity. The total volumetric flowrate $\dot{V}$ is given by

$$\dot{V} = \pi r_0^2 (1 - r_i'^2) < v > \qquad (4)$$

while the volumetric flowrate $\dot{V}_a$ between the inner wall and some radial position r_a is given by

$$\dot{V}_a = \int_{r_i}^{r_a} 2\pi r v(r) dr = \frac{4\pi r_0^2 < v >}{A_1} \int_{r'_i}^{r'_a} r'(1 - r'^2 - A_2 \ln r') dr' \quad (5)$$

Hence

$$\frac{\dot{V}_a}{\dot{V}} = \frac{2r'^2_a - r'^4_a - 2A_1 r'^2_a \ln r'_a + A_1 r'^2_a - r'^4_i - A_1 r'^2_i}{(1 - r'^2_i)(1 + r'^2_i + A_1)} \quad (6)$$

Cell trajectory within the system

Radial velocity at position r' is given by

$$u(r') = \frac{F_m}{6\pi\eta R} = \frac{2R^2 \Delta\chi}{9\eta\mu_0} \frac{B_0^2}{r_0} r' \quad (7)$$

where η is the fluid viscosity and R is cell radius. We can write $u(r')$ as $r_0 dr'/dt$, and $v(r')$ as dz/dt, and it follows that $dz = (r_0 v(r')/u(r'))dr'$. Hence,

$$\int_0^L dz = \int_{r'_1}^{r'_2} \frac{2 < v > r_0}{A_1} (1 - r'^2 - A_2 \ln r') \frac{9\eta\mu_0}{2R^2 \Delta\chi} \frac{r_0}{B_0^2} \frac{dr'}{r'} \quad (8)$$

where r'_1 and r'_2 correspond to the initial and final radial positions of a cell passing through the system. On integrating and rearranging, we obtain the result

$$\Delta\chi = \frac{9\dot{V}\eta\mu_0}{\pi A_1 L R^2 B_0^2 (1 - r'^2_i)} \left[\ln r' - \frac{r'^2}{2} - \frac{A_2}{2} (\ln r')^2 \right]_{r'_1}^{r'_2} \quad (9)$$

which we can write as $\Delta\chi = K_s \dot{V} I(r'_1, r'_2)$ in which K_s depends on fixed system parameters and dimensions and is given by

$$K_s = \frac{9\eta\mu_0}{\pi A_1 L R^2 B_0^2 (1 - r'^2_i)} \quad (10)$$

and

$$I(r'_1, r'_2) = \left[\ln r' - \frac{r'^2}{2} - \frac{A_2}{2}(\ln r')^2 \right]_{r'_1}^{r'_2} \qquad (11)$$

Let F_b denote the ratio of the number of the magnetically-labeled cells exiting the outlet port b to that entering the inlet port a'. It follows that if r'_{ISC} and r'_{OSC} represent the radial positions of the inlet and outlet splitting cylinders, respectively, then

$$F_b = 0 \quad \text{if} \quad \Delta\chi \leq K_s \dot{V} I(r'_{ISC}, r'_{OSC}) \qquad (12a,b)$$
$$F_b = 1 \quad \text{if} \quad \Delta\chi > K_s \dot{V} I(r'_i, r'_{OSC})$$

If we assume that a cell is damaged and/or does not exit the system if it contacts the outer wall, then we also have

$$F_b = 1 \quad \text{if} \quad \Delta\chi < K_s \dot{V} I(r'_{ISC}, 1) \qquad (13a,b)$$
$$F_b = 0 \quad \text{if} \quad \Delta\chi \geq K_s \dot{V} I(r'_i, 1)$$

It is possible for $F_b = 1$ only if conditions (12b) and (13a) are fulfilled. Then suppose we require $F_b = 1$ for some range of $\Delta\chi$ from $\Delta\chi_{low}$ to $\Delta\chi_{high}$; it is apparent that flow conditions must be set up such that

$$\Delta\chi_{low} = K_s \dot{V} I(r'_i, r'_{osc}) \quad \text{and} \quad \Delta\chi_{high} = K_s \dot{V} I(r'_{isc}, 1) \qquad (14)$$

for which we require that $I(r'_{ISC}, 1) > I(r'_i, r'_{OSC})$ and $r'_{ISC} < r'_{OSC}$.

Setup of flow regime

For the present system $r'_i = 0.5$. Consider $r'_{ISC} = 0.6$ and $r'_{OSC} = 0.75$, and suppose we require $\Delta\chi_{low}$ and $\Delta\chi_{high}$ to bracket $\Delta\chi$ of $150 \cdot 10^{-6}$, so that

$$\frac{\Delta\chi_{low} + \Delta\chi_{high}}{2} = 150 \cdot 10^{-6} \qquad (15)$$

From equations (14) we see that

$$K_s \dot{V} = \frac{\Delta\chi_{low}}{I(0.5,0.75)} = \frac{\Delta\chi_{high}}{I(0.6,1.0)} \quad (16)$$

For the present system parameters and dimensions these equations may be solved to obtain $\Delta\chi_{low} = 122 \cdot 10^{-6}$, $\Delta\chi_{high} = 178 \cdot 10^{-6}$, and $\dot{V} = 3.782$ mL/min. For the assumed r'_{ISC} and r'_{OSC} we obtain the required sample feed flowrate $\dot{V}(a') = 0.323$ mL/min, outlet flow rate adjacent to the inner wall $\dot{V}(a) = 1.710$ mL/min, and outlet flow rate adjacent to the outer wall $\dot{V}(b) = 2.072$ mL/min.

We may also calculate that $F_b = 0$ for $\Delta\chi \leq 91 \cdot 10^{-6}$ and for $\Delta\chi \geq 209 \cdot 10^{-6}$, the latter corresponding to cells that contact the outer wall before exiting the system.

EXPERIMENTAL

The test cell model system consisted of human peripheral lymphocytes, collected from healthy volunteer donors in accordance with the CCF Institutional Review Board guidelines. The mononuclear cell fraction, rich in lymphocytes (90-95%), with an admixture of monocytes (5-10%) and occasional contamination of erythrocytes, was obtained by centrifugation on a Ficoll cushion. The cells were handled using routine laboratory procedures.[16]

Lymphocytes were targeted using monoclonal antibodies (mAb) against T cytotoxic cells (bearing CD8 surface marker). The cells were labeled using a sandwich of primary antibody-fluorescein (FITC) conjugate, and secondary antibody-magnetic label (MACS) conjugate (MACS microbeads, Miltenyi Biotec, Auburn, CA). The presence of the iron dextran particle on the cell conferred on it the magnetic susceptibility $\Delta\chi$. The indirect magnetic label method was selected for its versatility and the magnetic susceptibility amplification. The use of fluorescein-conjugate sensitized the magnetically-labeled cells to UV light and made them visible to FACS analysis. The small label did not interfere with the FACS analysis, and the FACS analysis could be performed directly on the sorted cell fractions, to measure the sorter performance. A typical cell fluorescence histogram by FACS analysis is shown in Fig. 6(a) (by FACScan Analyzer, Becton-Dickinson, San Jose, CA). Each test sample was accompanied by negative controls for non-specific labeling by primary and secondary antibodies, and a positive control using a primary, but not secondary, antibody (not shown).

Table 1

Summary of CD8 Lymphocyte Sorting in Quadrupole Magnetic Field

#	Purity %[a]			Recovery %[b]						Total Cell No.	Cell Sorting Cap.
	a'	*a*	*b*	F_a	F_b	Total	$\dot{V}$[c] (mL/min)	$\frac{\dot{V}(a')}{\dot{V}}$	$\frac{\dot{V}(b')}{\dot{V}}$	x10^6	cell/s
1	27	21	54	60	11	71	3.1	0.45	0.55	6.5	12,000
2	20	16	48	49	37	86	3.1	0.41	0.59	10.1	10,000
3	25	21	52	54	27	81	3.1	0.45	0.55	12.5	12,000
4	16	9	24	26	38	64	3.1	0.1	0.88	3.4	4,800
5	22	11	31	41	30	71	3.1	0.1	0.88	7.6	6,000

[a] Purity: percent CD8 cell fraction; [b] Recovery: ratio of absolute CD8 cell count in the sorted fraction to that in feed; [c] $\dot{V} = \dot{V}(a') + \dot{V}(b') = \dot{V}(a) + \dot{V}(b)$ total flow rate.

The quadrupole field was generated by permanent magnets (28 MGOe cobalt-iron-boron magnets from Dexter Magnetics, Toledo, OH). Maximum field, $B_0 = 0.5$ T, gradient, $\partial B/\partial r = 0.1$ T/mm. Magnet aperture was 9.53 mm, length 64.5 mm. The inner cylinder diameter was $2r_i = 4.76$ mm, split cylinder inner diameter was $2r_s = 6.44$ mm, thickness 0.35 mm. The flow rate was controlled by syringe pumps (Harvard Apparatus, Natick, MA) connected by 0.8 mm i.d. Teflon® tubing to ports *a'*, *b'*, and *b* (port *a* was left open to atmosphere to equilibrate the pressure). The volumetric flow rates were varied as indicated in Table 1. The following parameters were calculated to describe the quadrupole field sorter performance: (1) purity - percent CD8 fluorescent cell subpopulation in each fraction (as measured by flow cytometry); (2) recovery or retrieval factor, F_b - ratio of absolute CD8 cell count in the sorted fraction to that in feed; (3) sorting capacity: total number of cells sorted in a given time interval.

RESULTS

Trajectory simulations were performed for ten initial cell positions set equidistant between the inner wall, r_i, and the inlet splitting cylinder, r_{ISC}, Fig. 4. The cells migrated radially, across the annular transport lamina defined by the radii r_{ISC} and r_{OSC}. The following extreme cases are illustrated in Figs. 4(a),

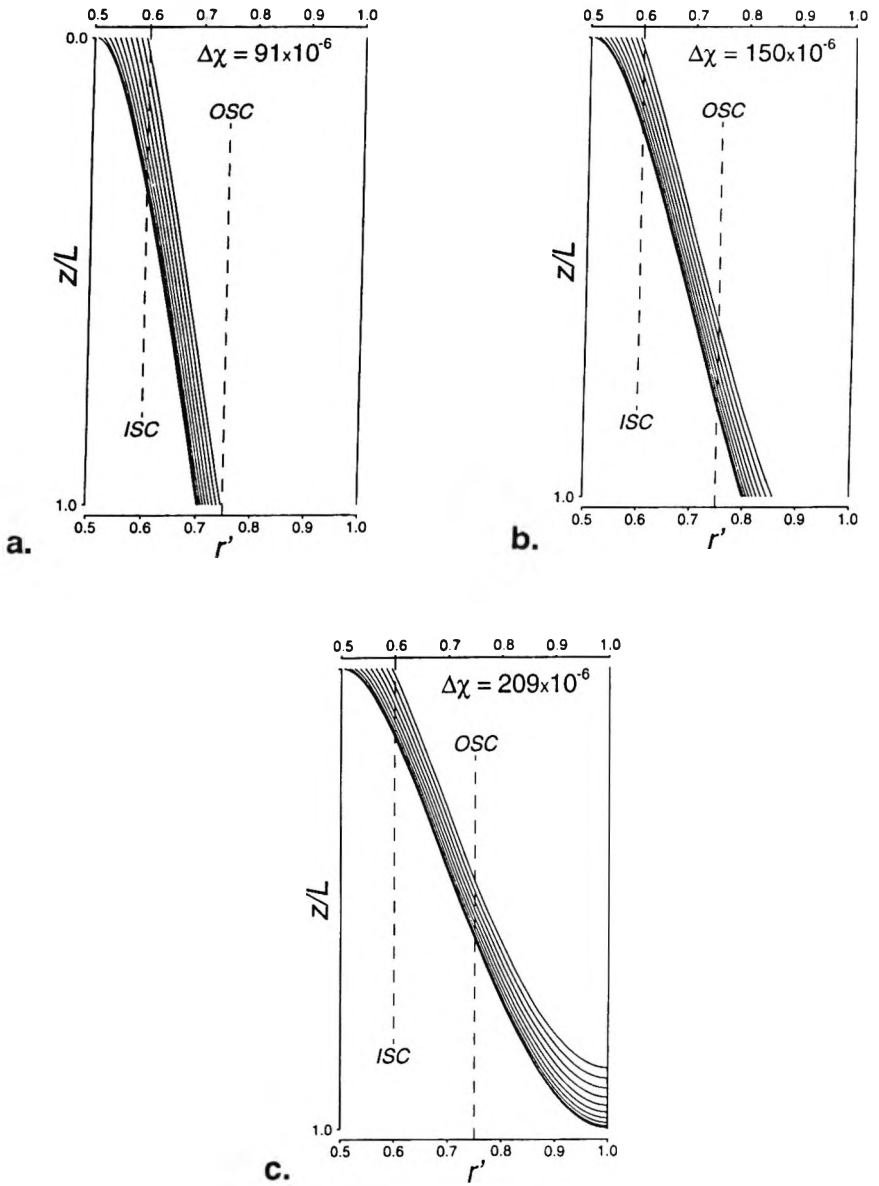

Figure 4. Examples of magnetically-labeled cell trajectories in the cylindrical SPLITT channel. The net average cell magnetic susceptibilities, $\Delta\chi$, are indicated; $r' = r/r_o$.

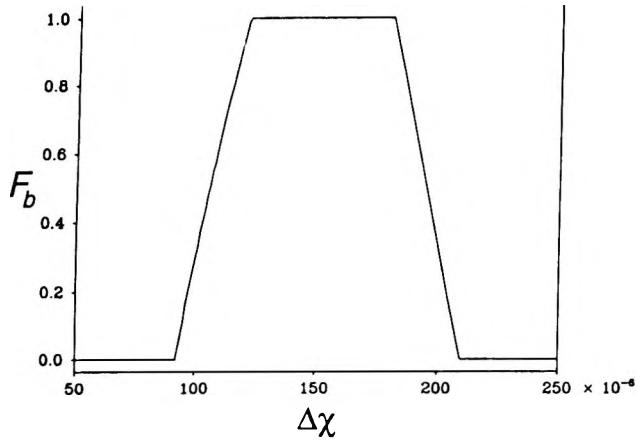

Figure 5. Fractional recovery, F_b, of the magnetically-labeled cells at the port *b*, as a function of net average cell magnetic susceptibility, $\Delta\chi$.

(b), and (c): depending on the value of the net cell magnetic susceptibility, $\Delta\chi$, either none of the magnetically-labeled (positive) cells traversed the transport lamina during the residence time in the magnetic field and, therefore, were re-collected at the *a*-port ($F_b = 0$, see Fig. 4(a)); or all of the positive cells crossed the transport lamina, without hitting the outer wall, and were collected in the *b*-port ($F_b = 1$, Fig. 4(b)); or all of the positive cells hit the outer wall and therefore were lost to the separation ($F_b = 0$, Fig. 4(c)).

The results of trajectory simulations are summarized in Fig. 5. One must bear in mind that the numerical values shown in Figs. 4 and 5 depend on the selected flowrates $\dot{V}$, $\dot{V}(a')$, $\dot{V}(b)$, and that the results shown in these figures were selected for the purpose of illustrating the characteristic features of the separator, rather than presenting any particular result. One may interpret the results shown in Fig. 5 considering two different cell model systems: 1) consisting of a group of different sets of cells, $i = 1, \ldots N$, each characterized by a discrete value of cell magnetic susceptibility, $\Delta\chi_i$; and 2) consisting of a single set of cells characterized by a continuous distribution of $\Delta\chi$ among cells in the set. The prediction of cell separation results differs depending on which cell model system one uses to approximate the actual situation. According to model number one, one may hope to obtain a complete recovery of all positive cells in the *b*-port (and thus a complete separation) if one matches the cell set $\Delta\chi_i$ with the range of $\Delta\chi$ for which $F_b = 1$ in the separator (such as $91 \quad 10^{-6} \leq \Delta\chi < 209 \quad 10^{-6}$; see Fig. 5). In short, model one predicts a possibility of an all-or-

nothing outcome of the separation. According to model number two, one may never hope to obtain a complete separation of positive from negative cells because there will be always positive cells in the sample such that $\Delta\chi < 91{+}10^{-6}$ or $\Delta\chi \geq 209{+}10^{-6}$, Fig. 5. The actual value of the fractional cell recovery in the *b*-port will depend on how many cells fall outside of the range between the low and high value of $\Delta\chi$, or, in other words, on the dispersion of the $\Delta\chi$ distribution in the cell sample.

The preliminary experiments establishing the feasibility of the cell separation method were performed using human lymphocytes tagged with immunofluorescent label and magnetic colloid, Fig. 6. In five experiments, the cell sample of 16% to 27% CD8 cell purity was fed into the *a'*-port, the cell medium was fed into the *b'*-port, and the sorted fractions were collected at *a*- and *b*-ports; see Fig. 3. The changes in cell sample fluorescence histograms following magnetic sorting indicated an increase of CD8 cell purity in the *b*-port, and therefore enrichment of positive (fluorescent) cells, up to 54% of CD8 cell purity. The recovery of the enriched cells, F_b, was rather low, 11% to 38%, and had a tendency to increase with the decreasing purity of the enriched cell fraction, Table 1. This indicates contamination of the positive fraction by negative cells due to less-than-optimal flow conditions inside the channel. The fact that the total CD8 cell recovery was less than 100% indicated cell loss due to magnetic deposition on the outside cylinder wall (and possibly elsewhere in the flow system). This, and the contamination of negative cells by positive cells in the *a*-port, Table 1, indicated a substantial dispersion of the cell $\Delta\chi$ value and, therefore, supported the validity of the model two discussed above.

DISCUSSION

In this study, we present tentative results of continuous-flow magnetic cell sorting using the quadrupole field separator, and preliminary sorter evaluation based on analogy with the SPLITT process. The properties of the electric and magnetic quadrupole fields are well understood in applications to ionic and molecular beams.[7] The magnetic quadrupole field has been evaluated for high throughput dry separation of pulverized coal to separate the ash and pyritic fractions (weakly paramagnetic) from maceral fractions (diamagnetic).[17,18] The quadrupole magnetic field has been used to increase the efficiency of batch-type magnetic cell separation.[19] We propose that the true advantages of using the quadrupole field in cell separation are in its use for continuous-flow separation. Unlike the current high-gradient magnetic separation (HGMS) columns, the open gradient quadrupole field offers advantages of the unhindered cell flow through the high field, B, and gradient, ∇B, area, and, thus, a precise control of

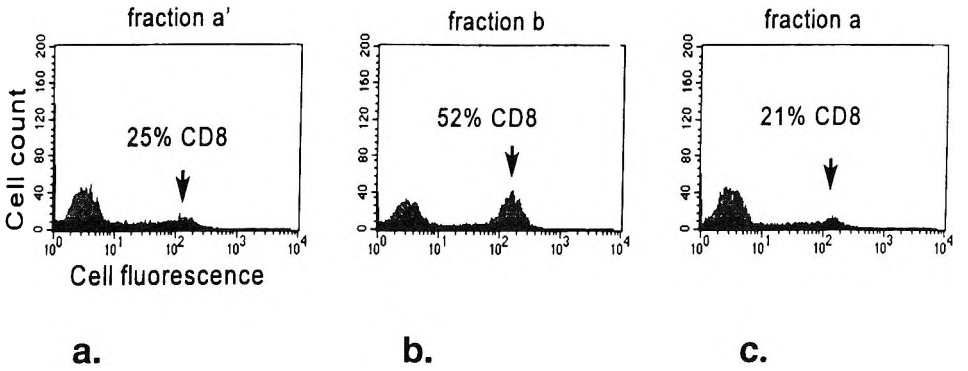

Figure 6. Experimental results of sorting of cytotoxic T cell (CD8 cells) from a mixture of human peripheral blood mononuclear cells. Note increase in purity of the magnetically-labeled CD8 cells in the *b* fraction, and a decrease of such cells in the *a* fraction. The much smaller decrease in purity in *a* fraction as compared to the increase in purity in *b* fraction is the result of a rather low recovery of these cells at the *b* - port (Table 1).

the cell trajectory. The magnetic energy gradient of the open-gradient field, ∇B^2, determining the magnetic force acting on the magnetic particle, is not limited by the magnetic properties of the components, as is the case with the high-gradient magnetic matrices, but only by the magnetomotive potential of the source. Fields of 1.6 Tesla (T), and gradients of 50 T/m were achieved in a volume of 4,000 mL in a superconducting quadrupole magnet used for the coal cleaning.[18]

Significantly, the highest separation resolution (of materials differing only slightly in the magnetic susceptibility) has been achieved in dynamic (particle stream) rather than static (batch) devices.[20] Part of the reason for this is that in the dynamic system the particles are exposed not only to the magnetic force but also to other forces (such as buoyancy and hydrodynamic drag) which contribute to the differentiation of the particles. This observation led us to a hypothesis that, in analogy to the industrial magnetic sorting in a stream, the sensitivity and specificity of the magnetic cell sorting could be increased if applied in combination with the flow, bringing it into the realm of field-flow fractionation. Deflection of the magnetically-tagged cells in a flowing stream, and separation of magnetic from non-magnetic cell fraction in a flow rather than on solid walls, requires precise information about the magnetic field geometry and flow effects on separation. Such information was provided by applying SPLITT methods to the analysis of the sorting process in the quadrupole field.

The results of this study represent work in progress and, therefore, are only a preliminary indication of the capabilities of the quadrupole field to continuous-flow cell sorting. The analysis of the system using a SPLITT analogy indicates the importance of cell susceptibility, $\Delta\chi$, distribution in the cell sample as a sorting parameter.

At the time of this study, no information about the cell $\Delta\chi$ distribution was available to us, and the experimental parameters were chosen by trial and error. This has resulted in sub-optimal selection of flow parameters, and a subsequent significant loss of high $\Delta\chi$ and low $\Delta\chi$ cell fractions, presumably due to deposition on the outer wall, and due to significant mixing with the unlabeled cells, respectively. The analogy with the SPLITT process, and the information of $\Delta\chi$ distribution for a given cell system, should provide sufficient information for selection of the best flow parameters in the future.

The current work is directed toward further study of the quadrupole cell sorting system using SPLITT formalism.

ACKNOWLEDGMENTS

This work is supported by grants NCI R01 CA62349 (M.Z.) and Whitaker Foundation (J. J. C.).

SYMBOLS AND OPERATOR DEFINITIONS

The magnitude of electromagnetic quantities were given in SI system of units (Système Internationale d'Unités).

Symbols

a, b	related to inner and outer annulus of separator outlet, respectively, (Fig. 3)
a', b'	related to inner and outer annulus of separator inlet, respectively, (Fig.3)
A	ampere, unit of electric current
A_1, A_2	constants defined below Eq. 3
$\boldsymbol{B}$	magnetic induction (magnetic flux density). In aqueous media, $\boldsymbol{B} = \mu_0\boldsymbol{H}$
B_0	magnitude of the magnetic field at the pole tips

F_a, F_b fractional recovery rates in inner and outer outlet annuli, respectively, (below Eq. 11)

$\boldsymbol{H}$ magnetic field strength

I function defined by Eq. 11

ISC Inner Splitting Cylinder, Fig.3

K_s function defined by Eq.10

m meter, unit of length

OSC Outer Splitting Cylinder, Fig.3

r_0 quadrupole magnet aperture radius; radial position of the pole tips

r_i inner cylinder radius

r_s split cylinder radius

r_{ISC}, r_{OSC} ISC and OSC radii, respectively

$r' = r/r_0$ dimensionless radial position

$\boldsymbol{r} = [x, y]$ radial coordinate

T tesla, *SI* unit of magnetic induction; corresponds to 10^4 Gauss in *em cgs* units

u radial flow linear velocity

v axial flow linear velocity

$\langle v \rangle$ spatial average of v

V volume

$\dot{V} = \dot{V}(a') + \dot{V}(b') = \dot{V}(a) + \dot{V}(b)$ total volumetric flowrate

$\dot{V}(a') = \dot{V}_a$, $\dot{V}(b') = \dot{V}_b$ volumetric flow rates at inner and outer inlet annuli, respectively

$\dot{V}(a) = \dot{V}_a$, $\dot{V}(b) = \dot{V}_b$ volumetric flow rates at inner and outer outlet annuli, respectively

z axial coordinate

$\mu_0 = 4 \cdot 10^{-7}$ Tm/A magnetic permeability of free space (a constant)

μ magnetic dipole moment. For a sphere of a homogenous, magnetically-polarizable medium, $\mu = V\chi\boldsymbol{H}$

ϕ angular coordinate

ϕ_m magnetic scalar potential; $\boldsymbol{H} = -\nabla\phi_m$

χ magnetic susceptibility, for homogenous media defined by the relationship between μ/V and $\boldsymbol{H}$ above

$\Delta\chi = \chi_{cell} - \chi_{medium}$ magnetic susceptibility of the cell relative to that of the medium

Vector and Operator Notation[12]

Vectors are indicated as such by the use of bold face ($\boldsymbol{A}$), their magnitude by the Roman letters (A). The Cartesian coordinates are denoted x, y, z, their

direction by unit vectors i, j, k

Scalar Product

$$A \cdot B = A_x B_x + A_y B_y + A_z B_z$$

Del or Nabla Operator

$$\nabla \equiv i\frac{\partial}{\partial x} + j\frac{\partial}{\partial y} + k\frac{\partial}{\partial z}$$

Gradient

$$\nabla \phi_m \equiv i\frac{\partial \phi_m}{\partial x} + j\frac{\partial \phi_m}{\partial y} + k\frac{\partial \phi_m}{\partial z}$$

Differentiation with respect to vector H

$$(H \cdot \nabla)A = i(H_x\frac{\partial A_x}{\partial x} + H_y\frac{\partial A_x}{\partial y} + H_z\frac{\partial A_x}{\partial z})$$

$$+ j(H_x\frac{\partial A_y}{\partial x} + H_y\frac{\partial A_y}{\partial y} + H_z\frac{\partial A_y}{\partial z})$$

$$+ k(H_x\frac{\partial A_z}{\partial x} + H_y\frac{\partial A_z}{\partial y} + H_z\frac{\partial A_z}{\partial z})$$

REFERENCES

1. A. Radbruch, B. Mechtold, A. Thiel, S. Miltenyi, E. Pflüger, Methods in Cell Biology, **42**, 387-403 (1994).

2. T. E. Thomas, P. M. Lansdorp, "Selective Separation of Cells Using Magnetic Colloids," in **Proceedings of the Fourth International Symposium on Bone Marrow Purging and Processing**, A. P. Gee, S. Gross, D. A. Worthington-White, eds., Wiley-Liss, New York, 1994, pp.65-77.

3. J. Ugelstad, P. Stenstad, L. Kilaas, W. S. Prestvik, R. Herje, A. Berge, E. Hornes, Blood Purif., **11**, 347-369 (1993).

4. A. P. Gee, Immunomethods, **5**, 232-242 (1994).

5. S. Roath, T. E. Thomas, J. H. P. Watson, P. M. Lansdorp, R. J. S. Smith, A, J. Richards, "Specific Capture of Targeted Hematopoietic Cells by High Gradient Magnetic Separation by the Use of Ordered Wire Array Filters and Tetrameric Antibody Complexes Linked to a Dextran Iron Particle," in **Proceedings of the Fourth International Symposium on Bone Marrow Purging and Processing**, A. P. Gee, S. Gross, D. A. Worthington-White, eds., Wiley-Liss, New York, 1994, pp.155-163.

6. J. T. Kemshead, "The Immunomagnetic Manipulation of Bone Marrow," in **Bone Marrow Processing and Purging. A Practical Guide**, A. P. Gee, ed., CRC Press, Boca Raton, 1991, pp. 293-305.

7. P. H. Dawson, **Quadrupole Mass Spectrometry and Its Applications**, Elsevier Scientific Publishing Company, New York, 1976.

8. J. C. Giddings, Sepn. Sci. Technol., **23**, 931-943 (1988).

9. S. Levin, J. C. Giddings, J. Chem. Tech. Biotechnol, **50**, 43-56 (1991).

10. P. S. Williams. Sepn. Sci. Technol., **29**, 11-45 (1994).

11. C. B. Fuh, E. M. Trujillo, J. C. Giddings, Sepn. Sci. Technol., **30**, 3861-3876 (1995).

12. R. Becker, **Electromagnetic Fields and Interactions**, Dover Publications Inc., New York, 1982, p.112.

13. J. C. Giddings, Science, **260**, 1456-1465 (1993).

14. J. M. Davis. J. C. Giddings, J. Phys. Chem., **89**, 3398-3405 (1985).

15. R. B. Bird, W. E. Stewart, E. N. Lightfoot, **Transport Phenomena**, John Wiley & Sons, New York, 1960, p.53.

16. G. G. B. Klaus, **Lymphocytes. A Practical Approach**, IRL Press, Oxford, 1987.

17. R. D. Doctor, C. B. Panchal, C. E. Swietlik, "Recent Advances in Separation Techniques - III," AIChE Symposium Series, **82**, 154-168 (1986).

18. R. D. Doctor, C. D. Livengood, Proceedings of the Intersociety Energy Conversion Engineering Conference, **Session 25.2**, 160-165 (1990).

19. P. A. Liberti, B. P. Feeley, "Analytical- and Process-Scale Cell Separation with Bioreceptor Ferrofluids and High Gradient Magnetic Separation," in **Cell Separation Science and Technology**, D. S. Compala, P. Todd, eds., ACS Symposium Series, Vol. 464, Washington, 1991, pp.268-288.

20. D. Lewis, T. D. Wellington, IEEE Transactions in Magnetics, MAG-12, 480-485 (1976).

Received January 17, 1997
Accepted April 10, 1997
Manuscript 4442

J. LIQ. CHROM. & REL. TECHNOL., 20(16 & 17), 2907-2929 (1997)

FEASIBILITY STUDIES ON PHOTOPHORETIC EFFECTS IN FIELD-FLOW FRACTIONATION OF PARTICLES

V. L. Kononenko,[1] J. K. Shimkus,[1,*] J. C. Giddings,[2] M. N. Myers[2]

[1] Institute of Biochemical Physics
Russian Academy of Sciences
117977 Moscow, Kosygin Street 4, Russia

[2] FFF Research Center
The University of Utah
Salt Lake City, Utah 84112, USA

ABSTRACT

Various mechanisms of particles photophoresis, both of direct and indirect type, are considered theoretically. The analytical expressions are obtained for photophoretic and photo-thermophoretic mobilities of particles, and their dependence on particle size, optical, and physicochemical properties is analyzed. The motion of latex spheres, glass beads, and carbon black particles of 3-22 μm diameter, in water, under the action of focused Ar^+-ion laser beam, was studied experimentally at λ=514.5 nm and power 0.1-0.8 W, using two arrangements. In the first one, the particles' motion was observed through the microscope. The positive photophoresis (away from the light source) was registered for all kinds of particles. Photophoretic velocities of particles were evaluated in connection with their size, optical properties, and laser power density.

In another arrangement, the laser power was focused at the entrance glass window of a round metallic capillary, along its axis, in the direction of suspension flow inside the capillary. The elution curves for polydisperse carbon black particles were registered in the gravity-sedimentation FFF mode with the laser power switched on and off. Typical curves possessed a strong initial maximum, attributed to the fraction of smaller particles, and a substantially lower secondary maximum related to large particles. The action of light changed the shape of the first maximum and shifted to a smaller time the second one. Both experimental and theoretical results show the possibility to generate, under FFF conditions, the photophoretic velocities of particles in the range 1-100 mm/sec, depending on the light intensity, which are sufficient to accomplish their separation relative to size, optical, and surface charge properties.

INTRODUCTION

The use of photophoresis, i.e., the motion of particles and molecules under the action of light, offers, potentially, many advantageous separation possibilities due to a great variety of particular mechanisms of light interaction with these objects.[1] However, the practical realization of Photophoretic FFF requires, apart from the solution of very specific technical problems, a more detailed investigation of the nature and manifestation conditions of various photophoretic mechanisms, as well as their connection to the size, optical, and relevant physicochemical properties of particles.

MECHANISMS OF DIRECT PHOTOPHORESIS

There are two principal mechanisms of direct photophoresis. The first one, usually referred to as the *light pressure*, is associated with the momentum transfer from electromagnetic field to particles and molecules irradiated due to the scattering and absorption of light. The second one, named the *gradient force*, manifests itself in spatially inhomogeneous fields only, and has the same nature as the forces acting on electric or magnetic dipoles in static inhomogeneous electric or magnetic fields.

The calculations of both light pressure and gradient force are based on the solution of the light scattering problem for a particle of given shape and optical parameters. The latter are described by the complex refractive index of the particle material, relative to that of surrounding medium at the wavelength λ of

light: $m(\lambda)=n_r(\lambda)-i\cdot\kappa(\lambda)$, n_r being the relative refraction index, κ being the index of absorption. In general, the final results can be obtained only numerically. However, the analytical results exist in some limiting cases, namely, for Rayleigh scattering, Rayleigh-Gans scattering, and for the case of very large particles.[2-6] Following the treatment reported in Ref. 6, let us consider a spherical particle of radius a placed in a wide, slightly divergent light beam with effective radius $w_0 >> a$ and angular divergence $|\Delta\theta| << 1$, $|\Delta\theta| \geq a/w_0$.

A particle is characterized by the size parameter $\rho=2\pi a/\lambda$. (There is a large diversity of notations used for the size parameter: x in Refs. 2, 4, 5, α in Refs. 3, 11, ρ in Refs. 6-8, 14, and q in Ref. 15. We adopt ρ here, keeping x for the coordinate notation in the optical problem).

It is assumed that relative complex dielectric permittivity $\varepsilon=\varepsilon'-i\cdot\varepsilon''$ and relative magnetic permeability $\mu=\mu'-i\cdot\mu''$ of particle material (related to the permittivity ε_m and permeability μ_m of surrounding medium) satisfy the Rayleigh-Gans conditions $|\varepsilon-1|<<1$, $2\rho|\varepsilon-1| <<1$, $|\mu-1|<<1$, $2\rho|\mu-1| <<1$. (Note, that $\varepsilon'=n_r^2-\kappa^2$ and $\varepsilon''=2\, n_r\kappa$).

Then, the direct photophoretic force F_{ph} can be written as a sum of the radiation-pressure force and the gradient force:[6]

$$\begin{aligned} \vec{F}_{ph} &= \vec{F}_{pr} + \vec{F}_{\nabla} \ , \\ \vec{F}_{pr} &= \varepsilon_m \frac{\pi a^2}{c} Q_{pr}(\rho)\cdot \vec{J}_0 \ , \\ \vec{F}_{\nabla} &= \varepsilon_m \frac{2\pi a^3}{c}\left(\frac{\varepsilon'-1}{\varepsilon'+2}+\frac{\mu'-1}{\mu'+2}\right)\cdot\nabla\vec{J}_0 \ . \end{aligned} \qquad (1)$$

Here, J_0 is the incident light irradiance, measured in units of energy per unit time per unit area, c is the light velocity. The factor Q_{pr} in Equation 1 is the dimensionless efficiency factor of radiation pressure, $Q_{pr}= Q_{ext}-\langle\cos\theta\rangle Q_{sca}$, and $Q_{ext}= Q_{sca}+ Q_{abs}$. Here Q_{ext}, Q_{sca} and Q_{abs} are the efficiency factors of the extinction, scattering, and absorption of light, $\langle\cos\theta\rangle$ is the cosine of the scattering angle θ weighted by the scattering diagram of a particle.[2-4]

It is convenient to introduce the transport efficiency factor $Q_{tr}=(1-\langle\cos\theta\rangle)Q_{sca}$, which describes the contribution to the light pressure from the light scattering only. In the case considered, these factors can be shown to be:

$$
\begin{aligned}
&Q_{pr}(\rho) = Q_{tr}(\rho) + Q_{abs}(\rho) \ , \\
&Q_{tr}(\rho) = \frac{9}{4}\left(\left|\frac{\varepsilon-1}{\varepsilon+2}\right|^2 + \left|\frac{\mu-1}{\mu+2}\right|^2\right)\cdot I_1(\rho) \\
&+\frac{9}{2}\mathrm{Re}\left\{\left(\frac{\varepsilon-1}{\varepsilon+2}\right)\cdot\left(\frac{\mu-1}{\mu+2}\right)^*\right\}\cdot I_2(\rho) \ , \\
&Q_{abs}(\rho) = 4\rho\cdot\left|\mathrm{Im}\left\{\frac{\varepsilon-1}{\varepsilon+2}\right\} + \mathrm{Im}\left\{\frac{\mu-1}{\mu+2}\right\}\right| \ .
\end{aligned}
\tag{2}
$$

Here $I_1(\rho)$ and $I_2(\rho)$ are given by:[6]

$$
\begin{aligned}
&I_1(\rho) = -3 + \frac{\sin 4\rho}{\rho} - \frac{3\left(1-\cos 4\rho\right)}{4\rho^2} + \frac{9\left(1-\cos 4\rho - 8\rho^2\right)}{32\rho^4} + \\
&\quad + \frac{9\left(4\rho - \sin 4\rho\right)}{8\rho^3} + \left(2 - \frac{1}{\rho^2}\right)\cdot I_0(\rho) \ , \\
&I_2(\rho) = -4 + \frac{1-\cos 4\rho}{\rho^2} + \left(2 - \frac{1}{\rho^2}\right)\cdot I_0(\rho) \ , \\
&I_0(\rho) = 2\int_0^{2\rho}\frac{\sin^2 z}{z}dz = C + \ln 4\rho - \mathrm{Ci}(4\rho) \ .
\end{aligned}
\tag{3}
$$

where C=0.5772 is the Euler's constant, $Ci(z)$ is the cosine integral.[2]

The analysis of Equations (1)-(3) shows that, depending on the geometrical and optical parameters of a particle and on the light beam parameters, each term in the expression (1) for F_{ph} can be the dominating one. Correspondingly, the dependence of photophoretic force on particle size parameter and optical properties is quite different in these cases. We shall illustrate this by considering a particular, but rather common situation when μ=1 and $\varepsilon'' << |\varepsilon - 1|$. Taking $\Delta\theta > 0$ for divergent beam, $\Delta\theta < 0$ for convergent beam, considering the transverse and the longitudinal gradients of beam irradiance to be $\nabla_{\perp}(J_0) \approx J_0 / w_0$, $\nabla_{\parallel}(J_0) \approx -\Delta\theta \cdot J_0 / w_0$, and regarding $(\varepsilon'+2) \approx 3$ because of $|\varepsilon - 1| << 1$, we obtain Eq. 4 from (1)-(3).

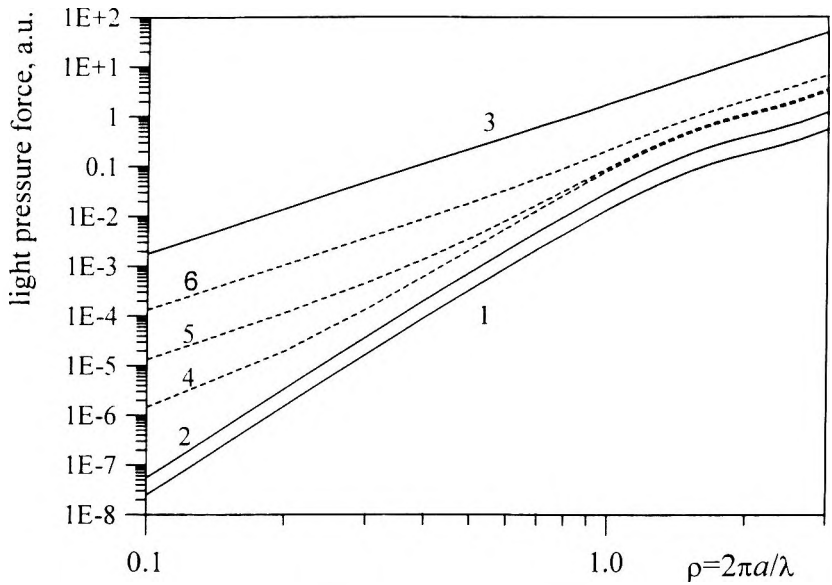

Figure 1. Size dependence of the light pressure force, calculated for particles of various materials according to equation (4). 1 - glass (ε'=2.28, $\varepsilon''\approx$0 at λ_0=589 nm), 2 - latex (ε'=2.53, $\varepsilon''\approx$0 at λ_0=589 nm), 3 - carbon black (ε'=2.4, ε''=2.38 at λ_0=489 nm), 4-6 - model substances with ε'=1.7 and ε''=0.001 (4), 0.01 (5), 0.1 (6).

$$F_{ph\parallel} \equiv F_{pr} + F_{\nabla\parallel} \approx \varepsilon_m \frac{\lambda^2\rho^2}{4\pi c}\cdot\left[\frac{1}{4}(\varepsilon'-1)^2\cdot I_1(\rho)+\frac{4}{3}\varepsilon''\cdot\rho\right]$$
$$\cdot J_0 - \Delta\theta\cdot F_{\nabla\perp} \ , \qquad (4)$$
$$F_{ph\perp} \equiv F_{\nabla\perp} \approx \varepsilon_m \frac{\lambda^3\rho^3}{12\pi^2 c w_0}\cdot(\varepsilon'-1)\cdot J_0 \ .$$

Fig. 1 shows the size dependence of the light pressure calculated for particles with different optical parameters according to relationships (4). For small particles (ρ<<1) Equation (3) gives $I_1(\rho)\approx(32/27)\cdot\rho^4$ while, for large particles (ρ>>1) $I_1(\rho)\approx2[\ln(4\rho)+C]$-3. Depending on the relationship between the magnitudes of (ε'-1) and ε'', the non-absorbing, "low absorbing," and "highly absorbing" particles can be distinguished conventionally. For non-absorbing particles with ε''=0 Equation (4) gives $F_{pr} \propto (\varepsilon'-1)^2\cdot\rho^6\cdot J_0$ practically up to $\rho\sim1$ (Fig. 1, curves 1, 2). For "low absorbing" particles with $\varepsilon''<<(\varepsilon'-1)^2$ it follows from (4) that $F_{pr} \propto \varepsilon''\cdot\rho^3\cdot J_0$ at ρ<<1, with the change to $F_{pr} \propto (\varepsilon'-1)^2\cdot\rho^6\cdot J_0$ at higher ρ, and possible return to the initial dependence at very large

ρ, if the inequality $2\rho|\varepsilon-1| < 1$ still holds at such ρ (Fig. 1, curves 4,5). The transverse gradient force $F_{\nabla\perp}$ may exceed the radiation pressure for all $\rho<1$ if the beam radius is as small as $w_0<\lambda/|\varepsilon'-1|$, while for the longitudinal gradient force $F_{\nabla\|}$ that requires $w_0<\lambda\cdot\Delta\theta/|\varepsilon'-1|$. The direction of gradient force is determined by the sign of $(\varepsilon'-1)$: the particles with $\varepsilon'>1$ are pulled into the maximum of the radial distribution of field intensity, while the particles with $\varepsilon'<1$ are pushed either out of the beam, or into the minimum of the field intensity. For the "highly absorbing" particles, classified by condition $(\varepsilon'-1)^2<<\varepsilon''<<|\varepsilon'-1|$, the radiation pressure is due to the light absorption mainly, and $F_{pr} \propto \varepsilon''\cdot\rho^3\cdot J_0$. Here $F_{\nabla\perp}>F_{pr}$ if the beam radius $w_0<\lambda|\varepsilon'-1|/4\pi\varepsilon''$, and $F_{\nabla\|}>F_{pr}$ if $w_0<\lambda\cdot\Delta\theta\ |\varepsilon'-1|/4\pi\varepsilon''$.

The analysis of the direct photophoretic force for Rayleigh-Gans scattering conditions, described by Equations (1)-(4), is expedient for a general insight into the dependence of this force on the particles parameters varied in a broad range. In practice, however, the validity of this approximation is restricted usually by the region of rather small ρ values. For example, in the case of latex particles in water ($n_r=1.59/1.333$ at $\lambda=589$ nm) we have $2\rho|m-1|\approx 0.39\rho$ and, in the case of glass beads ($n_r=1.51/1.333$ at $\lambda=589$ nm), we get $2\rho|m-1|\approx 0.27\rho$. Thus, the range of the quantitative validity of (1)-(4) in these cases is restricted by $\rho<2$-3.

If particle parameters $m(\lambda)$ and ρ fall outside validity limits of analytical approximations considered above, it is necessary to perform the numerical calculations of $Q_{pr}(\rho)$ entering (1) using the exact Mie theory of light scattering by a sphere. Some relevant examples of such calculations can be found in Refs. 2-5, 7, 8. The most detailed and extensive are the results of Ref. 5, where $Q_{pr}(\rho)$ was calculated for the following set of parameters: 1) $n_r=1.20$, 1.33, 1.50 with $\kappa/(n_r-1)=0$, 0.01, 0.1, 1.0, 10, and ρ in the range $0.5\le\rho\le 30$; 2) $n_r=1.33$, $\kappa=0$, $50\le\rho\le 51$ and $100\le\rho\le 102$ with the fine resolution $\Delta\rho=0.01$; 3) $\rho>>1$, $2\rho|m-1|>>1$, $\kappa/(n_r-1)=0.0001$, 0.001, ..., 1.0, 10.

The results of Refs. 2, 3, 5, 7, and 8 can be summarized as follows. For $n_r<1.2$ and $\kappa/(n_r-1)<0.1$ the plot of $Q_{pr}(\rho)$ in the region $0<\rho<30$ is similar to the plot of $l_1(\rho)$ defined by (3), and its behavior agree with the Equations (2)-(4): $Q_{pr}(\rho) \propto \rho^{\alpha}$, $1<\alpha<4$ (depending on κ value) for $\rho<<1$, $Q_{pr}(\rho) \propto \ln(\rho)$ for $\rho>1$, and $Q_{pr}(\rho)\approx$const for $\rho>20$. With the increase of either n_r or κ, the curve $Q_{pr}(\rho)$ appears to be scaled as a whole to higher values. With the further increase of n_r over ≈ 1.2 and/or $\kappa/(n_r-1)$ over ≈ 1 the dependence $Q_{pr}(\rho)$ at low ρ remains a power law with an increasing amplitude factor, and $Q_{pr}(\rho)$ at large ρ remains a constant, but a maximum starts to develop in the region $1<\rho<10$. The exact position and the amplitude of this maximum depend both on n_r[2,8] and κ[5] values.

For non-absorbing spheres (κ=0) the limiting ($n_r \to \infty$) position of this maximum is ρ_m=1.12, and the maximum value is $Q_{pr}(\rho_m)$=2.57 [Ref. 2, Sec. 10.62]. For intermediate n_r=1.33-1.8, the position of the maximum obeys an approximate relation $\rho_m \approx 2.5/(n_r-1)$, and the maximum value of Q_{pr} depends rather strongly on the refraction index: $Q_{pr}(\rho_m) \approx 3 \cdot (n_r-1)^{1.362}$ [See Ref. 8]. For absorbing spheres, the development of the maximum in $Q_{pr}(\rho)$ with the increase of κ has a similar qualitative picture, and its limiting position for large κ is approximately the same as for non-absorbing spheres.[5] The asymptotic value of $Q_{pr}(\rho)$ for $\rho >> 1$ and $2\rho|m-1| >> 1$ varies within Q_{pr}=0.956-1.01, depending on n_r=1.20-1.75 and $\kappa/(n_r-1)=10^{-4}$-10 [See Ref. 5]. Hence, for such "very large" particles (practically, for a>2 μm at λ~0.5 μm) the light pressure force is described by (1) with $Q_{pr} \approx 1$.

In the case of "geometrically large" particles ($\rho >> 1$ or a> ~10 μm for visible range of light) the direct photophoretic force can be calculated also using the geometrical optics approach of reflected and refracted rays, which exert an appropriate light pressure on the particle surface at the refraction points. The total acting force is obtained by integration of this pressure over the particle surface.[9,10] In the framework of this approach, there is no computational difference between the radiation-pressure component and the gradient component of photophoretic force. This approach appears to be most useful for practical design of Photophoretic FFF systems for large particles separation using highly convergent light beams.

INDIRECT PHOTOPHORETIC MECHANISMS

Indirect photophoretic mechanisms involve, as the primary action of light, a nonuniform heating of particles and/or a surrounding fluid. This heating results in thermophoretic motion of particles due to tangential gradients of interfacial energy arising near the particle surface. Such mechanism of motion can be termed photothermophoresis, to distinguish it from the direct photophoretic mechanisms. Because for real particles neither n_r=1, nor κ=0, the light pressure should always accompany the photothermophoretic force. However, the relative magnitudes and signs of these two contributions to the total phoretic velocity of a particle depend essentially on the optical properties and phase state of particles and surrounding medium. Light pressure always induces the positive photophoresis – away from the light source.

On the contrary, photothermophoresis of solid particles in gaseous ambient may be either positive or negative, depending on the particles parameters and gas pressure.[11] Photothermophoresis of strongly absorbing

liquid drops in another immiscible transparent liquid, according to experiments,[12] is negative, and its magnitude exceeds substantially the contribution from the light pressure.

In regard to photothermophoresis problem, it is natural to consider two mutually complementary extremes: first, a light-absorbing particle surrounded by transparent liquid; second, a transparent particle placed in a channel flow of light-absorbing fluid. Here we shall consider the first extreme only, which can be referred to as the *internal problem*. The other case – the *external problem* – will be considered elsewhere. The solution of photothermophoresis problem includes three rather independent stages: the calculation of the optical field inside and outside the particle; determination of the temperature field resulting from the light absorption; the calculation of the thermophoretic mobility of a particle in this field on the basis of appropriate physicochemical models for the particle, surrounding medium and their interfacial region.

Optical Problem

The aim of the optical problem is the calculation of the distribution of absorption centers. This distribution is characterized by the source function $B(x,z) = E_i^2(x,z) / E_0^2$, where $E_i(x,z)$ is the electric field strength inside the particle, E_0 is the incident plane wave amplitude, x is the radial distance from particle main diameter parallel to the light propagation direction, z is the distance along the main diameter measured from the center of a particle (Fig. 2). Depending on the particle size parameter ρ, there are three domains where both the internal field patterns and their calculation procedures are essentially different. If $\rho<<1$ (Rayleigh scattering), the internal field can be considered as a plane wave, exponentially decaying along the main diameter due to absorption. For intermediate $\rho\sim1$-10, the particle behaves like a spherical cavity, and the internal field distribution is a complicated system of minima and maxima.[13,14] Here $B(x,z)$ strongly depends on particular combination of particle size and optical constants, and can be found only using the rigorous Mie theory.[13,14] In the third domain, $\rho>>10$, a particle behaves like a tiny spherical lens which focuses the incident radiation. The focusing process begins inside the particle, and (for $n_r<2$) is completed in the surrounding medium at some distance from the rear pole of a particle. Here $B(x,z)$ can be successfully calculated using the geometrical optics approach, and the general relationship can be established between the particle parameters and the field distribution. This specific situation, termed the *lens mechanism* of photothermophoresis, will be considered in detail below.

Consider the incident plane wave as a collection of finite pencils of rays parallel to the z-axis, h being the distance of the pencil axis from the z-axis. Each pencil becomes a convergent (for $n_r>1$) or divergent (for $n_r<1$) bundle of rays after the refraction at the particle surface (Fig. 2). Tracing the rays' path inside the particle according to the geometrical optics laws, and taking into account the conservation along the bundle axis of the product of the light intensity and the bundle cross-section,[15-17] we obtain:

a) central bundle, h=0:

$$B(z)=\frac{\left[1-R(h)\right]\exp\left[-2\frac{\kappa\rho}{n_0}(z+1)\right]}{\left[1-\frac{n_r-1}{n_r}(z+1)\right]^2}, \qquad z=\frac{\ell}{n_r}-1, \quad n<2 \qquad (5)$$

b) noncentral bundles, $0<h\le 1$:

$$B(x,z)=\frac{h\left[1-R(h)\right]\exp\left[-2\frac{\kappa\rho}{n_0 n_r}\left(\ell-1+\sqrt{1-h^2}\right)\right]}{x(\ell,h)\sqrt{\left(\frac{\partial x}{\partial h}(h,\ell)\right)^2+\left(\frac{\partial z}{\partial h}(h,\ell)\right)^2}},$$

$$x(\ell,h)=h-\left(\ell-1+\sqrt{1-h^2}\right)\frac{\sin(\alpha-\beta)}{n_r}, \qquad (6)$$

$$z(\ell,h)=-\sqrt{1-h^2}+\left(\ell-1+\sqrt{1-h^2}\right)\frac{\cos(\alpha-\beta)}{n_r},$$

$$\alpha=\arcsin(h), \quad \beta=\arcsin\left(\frac{h}{n_r}\right), \qquad \ell\ge 1-\sqrt{1-h^2}, \quad n_r<\sqrt{2}.$$

Here l is the optical path measured from the plane z=-1, i.e., the product of the geometrical distance along the bundle axis and an appropriate refraction index, $R(h)$ is the Fresnel reflection coefficient,[15] $n_0=\sqrt{\varepsilon_m}$. The coordinates and the distances in (5), (6), and below are dimensionless quantities measured in units of particle radius a. So, the point (0,-1) corresponds to the front (illuminated) pole of the particle, and the point (0,1) is the rear pole. The relations (5) and (6) are valid until the focal points lie outside the particle, that is for $n_r<2$ for paraxial rays, and $n_r<\sqrt{2}$ for outer rays with h=1. They neglect the light reflection inside the particle, for visible range $R<<1$ usually.

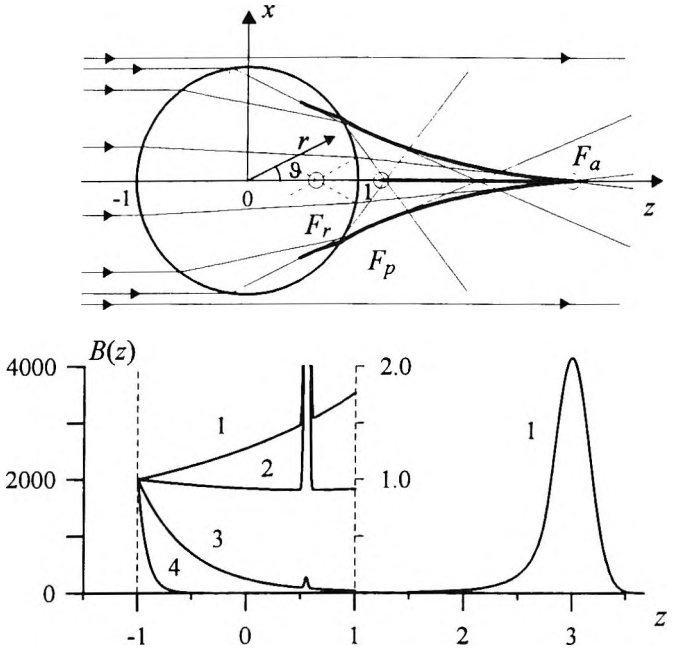

Figure 2. Geometrical optics picture of light focusing by a particle (top) and heat sources distribution $B(z)$ along the main optical axis (bottom). Thickened curves are the caustics lines. F_a, F_p and F_r are the focal points for paraxial rays, extremely outer rays, and reflected inside the particle rays. Calculations are done for n_r=1.2, but picture is qualitatively valid for $1 < n_r < \sqrt{2}$. $B(z)$ curves are calculated for $\kappa\rho$=0.06 (1), 0.23 (2), 1.22 (3), 6.1 (4). Note, that the scales differ by 2000 times inside and outside the particle.

Fig. 2 shows the geometrical optics view of light focusing by a particle, and the distribution of the heat sources along the main optical axis for various values of absorption. Numerical calculations of $B(x,z)$ used for solution of the thermal problem were based on (5), (6) with the inclusion of the first internal reflection of rays. The intensity of the field near the focal points and caustic curves was evaluated using the formulae from Refs. 15-17.

The comparison with the results based on exact Mie theory[14] showed, that the geometrical optics approach gives good quantitative results starting from $\rho > 10^2 \div 10^3$ (depending on specific values of n_r and κ), while the qualitative agreement keeps down to $\rho \sim 10$.

Thermal Problem

The temperature distribution $T(r,\theta)$ is defined by the stationary heat-transfer equation with the heat sources proportional to the source function $B(r,\theta)$:[13,14]

$$\nabla^2 T(r,\theta) = -\frac{4\pi n_r \kappa}{\lambda_0 k_i} I_0 B(r,\theta) \tag{7}$$

where k_i is the thermal conductivity of the particle. Due to the axial symmetry of the problem the polar coordinates are used, the polar angle θ being measured from the rear pole (Fig. 2). It is expedient to introduce the characteristic temperature T_0 of particle's heating due to the light absorption and to use the dimensionless temperature $\tau(r,\theta)=T(r,\theta)/T_0$. Then, the thermal problem can be written as:

$$\begin{aligned}
&\nabla^2 \tau_i(r,\theta) = -B(r,\theta), && |\vec{r}| \le 1 \\
&\nabla^2 \tau_e(r,\theta) = 0, && |\vec{r}| > 1 \\
&\tau_i = \tau_e, \quad k_i \vec{\nabla} \tau_i = k_e \vec{\nabla} \tau_e, && |\vec{r}| = 1 \\
&\tau_e = \tau_\infty, && |\vec{r}| = R_0 \\
&T_0 = 2\kappa\rho \frac{n_r a}{n_0 k_i} I_0, \qquad \rho = \frac{2\pi a n_0}{\lambda_0}.
\end{aligned} \tag{8}$$

Here, indexes i and *e* refer to the particle and to surrounding medium, k_e is the thermal conductivity of the medium, $T_0 \cdot \tau_\infty$ is the ambient temperature far from the particle, $R_0 >> 1$ is a characteristic outer boundary of the temperature field induced. In our calculations we took $R_0=100$.

As Equations 5 and 6 show, the source function $B(r,\theta)$ depends on two parameters of the particle, n_r and $\kappa\rho$. Hence, the solution $\tau(r,\theta)$ of (8) depends on three parameters: n_r, $\kappa\rho$, and (k_i/k_e), the latter having rather small influence in practically important range of values. Thus, the use of dimensionless temperature in units T_0 enables to obtain a general-type solution, which can be used both for general analysis of photothermophoresis phenomenon and for numerical evaluation of particular cases.

The main interest presents the temperature distribution over the particle surface. As Fig. 3 shows, three essentially different distribution types may exist depending on the combination of the size and optical constants of a particle,

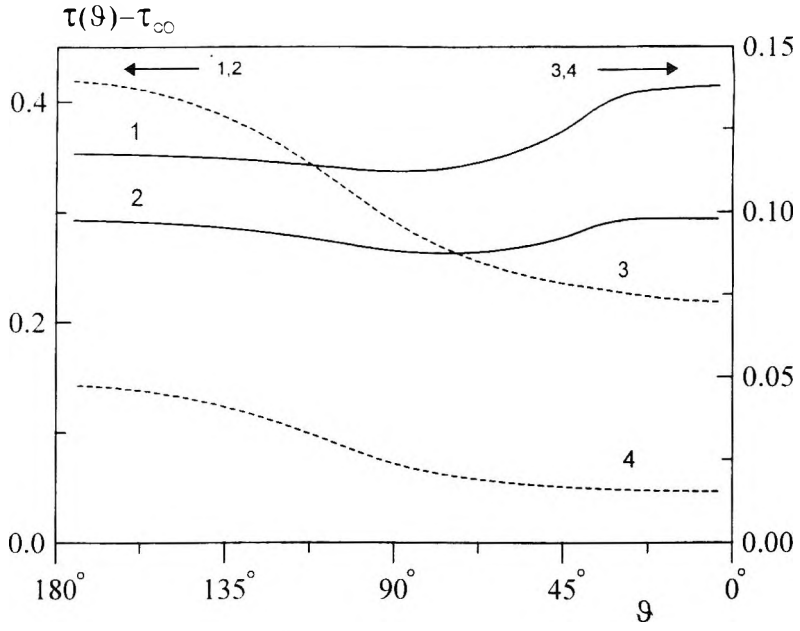

Figure 3. Surface temperature distributions calculated for a light-absorbing particle. $k_i=k_e$; $n_r=1.2$, $\kappa\rho=0.06$ (1), 0.23 (2), 1.22 (3), 6.1 (4).

mainly, on the $\kappa\rho$ value. They correspond to the three main types of *B(z)* curves shown at Fig. 2. If $\kappa\rho<<1$, the rear pole domain of a particle is heated preferentially due to the light focusing (see curve 1 for *B(z)* in Fig. 2 and curve 1 in Fig. 3). With the increase of $\kappa\rho$, the attenuation of light due to the absorption in the particle material becomes significant enough to compensate the focusing effect (curve 2 for *B(z)* at Fig. 2). So, for some intermediate $\kappa\rho=0.13$-0.34 (depending on the $n_r=1.1$-1.4) the poles temperatures became equal, while the temperature minimum with the depth of 6-8% develops near the equatorial strip $\theta\sim90^0$ (curve 2 in Fig. 3). For high absorption values ($\kappa\rho>0.5$-1), the attenuation of light prevails over the focusing, so the front pole has the highest temperature value, which decreases monotonously along the surface to the rear pole (curves 3, 4). Fig. 4 shows the dependencies of poles temperatures on the "optical density" $\kappa\rho$ of a particle. They were calculated in the general form using (8), and then were specified by multiplication by T_0 to a particle of diameter $2a=50$ μm and to some particular value $I_0=10^7$ W/m^2 of laser power density. This value corresponds to 1 W of Ar^+-ion laser radiation focused into the spot of $\sim2\cdot10^{-4}$ m diameter. These plots can be easily scaled to any other values of I_0 and a using the formula (8) for T_0.

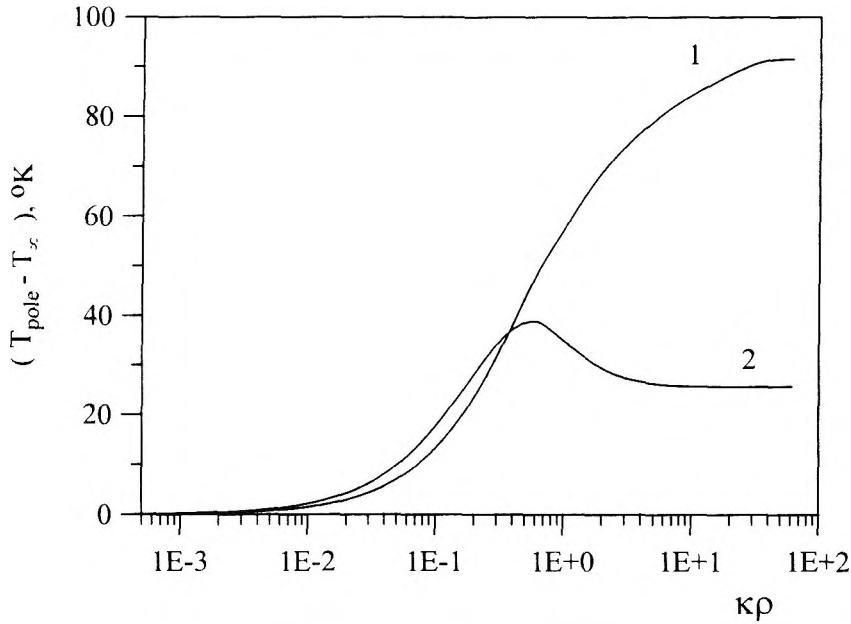

Figure 4. Temperature of the front (1) and the rear (2) poles of light-absorbing particle as a function of the absorption parameter $\kappa\rho$, calculated for $I_0=10^7$ W/m^2, λ=514 nm, $a=5\cdot10^{-5}$ m (ρ=406), $k_i=k_e$=1 W/m/^{0}K, and n_r=1.4.

Photothermophoretic Mobility

With the known temperature distribution, the problem reduces to the calculation of particle thermophoretic mobility for the given temperature field. We consider a solid particle in electrolyte solution, using the approach suggested initially in Ref. 18 and further developed in Refs. 19-21.

According to this approach, phoretic motion of a particle arises due to the flow generated within the thin interfacial region near its surface by the interaction between the ion (molecular) solute and some external (electrical, thermal etc.) applied field. A specific distinctive feature of photothermophoresis is that this "external" temperature field arises from the particle's heating by light. Because characteristic width of interfacial layer is usually small compared with the particle size, this layer can be considered as locally flat. So, the flow velocity profile is defined by two-dimensional Stokes equations:[18-20]

$$\frac{\eta}{a}\frac{\partial^2 u}{\partial \xi^2}-\frac{\partial p}{\partial \zeta}=0\,,\quad \frac{\partial p}{\partial \xi}+C_m(\xi)\frac{\partial \Phi}{\partial \xi}=0$$
$$u\big|_{\xi=0}=0\,,\quad \left.\frac{\partial u}{\partial \xi}\right|_{\xi\to\infty}=0\,,\quad p\big|_{\xi\to\infty}=p_0\,. \tag{9}$$

Here ξ is the normal and ζ is the tangential dimensionless coordinates at some point (r,θ) at the particle surface, $\Phi(\xi)$ is the interaction potential of solute ions with the surface, $C_m(\xi)$ is the ions concentration distribution near the surface, η is the fluid viscosity, $u(\xi)$ is the fluid velocity field near the surface, $p(\xi,\zeta)$ is the pressure field. The directions of ζ-axis and z-axis coincide for $\theta=90^0$. The ions concentration near the surface obeys the Boltzmann distribution law: $C_m(\xi)=C_{m0}\cdot\exp[-\Phi(\xi)/k_BT]$, where C_{m0} is the bulk ions concentration, k_BT is the thermal energy. The use of this expression for $C_m(\xi)$ in the second Equation 9 gives, after the direct integration, the pressure field in the interfacial layer $p(\xi,\zeta)$. Due to the gradient of the surface temperature, this pressure has the tangential gradient which induces the fluid flow along the particle surface. The flow velocity is obtained from the second of Equations 9 after substitution of $p(\xi,\zeta)$ and integration by parts with the use of the boundary conditions (Eq. 9). Taking into account that in dimensionless form $\xi=r-1$ and $d\zeta=-d\theta$, we get for $u(\xi,\theta)$ and for the slip velocity $u^S=u(\xi\to\infty)$ at the outer boundary of interfacial layer:

$$u(\xi,\theta)=C_{m0}k_BT_0a\left\{\int_\xi^\infty \frac{\partial\tau(1+\xi,\theta)}{\partial\theta}W(\xi,\theta)d\xi+\int_0^\xi \xi\frac{\partial\tau(1+\xi,\theta)}{\partial\theta}W(\xi,\theta)d\xi\right\},$$
$$u^S=C_{m0}k_BT_0a\int_0^\infty \xi\frac{\partial\tau(1+\xi,\theta)}{\partial\theta}W(\xi,\theta)d\xi\,,$$
$$W(\xi,\theta)=\frac{1}{\eta}\left\{\exp\left[-\frac{\Phi(\xi,\theta)}{k_BT_0\tau(1+\xi,\theta)}\right]\cdot\left[1+\frac{\Phi(\xi,\theta)}{k_BT_0\tau(1+\xi,\theta)}\right]-1\right\}. \tag{10}$$

The local temperature $T_0\cdot\tau(r,\theta)$ in (10) is the solution of the thermal problem (Eq. 8). The use of (10) and the general hydrodynamic result[20]

$$\vec{u}_{ph}=-\frac{1}{S}\oiint_S \vec{u}^S dS \tag{11}$$

enables to determine the resulting particle velocity $\vec{u}_{ph}$. The integration in (11) is done over the outer boundary of the interfacial layer, i.e., practically over the particle surface.

To keep the connection with the usual thermophoresis, it is convenient to define the magnitude of photothermophoretic mobility b_{phth} of a particle from the relation $u_{ph}=b_{phth}\cdot(T_0/a)$. Here T_0/a is the characteristic temperature gradient of the problem, which is proportional to the incident light intensity I_0 (see (8)). The sign of b_{phth} is taken, usually, as positive when the directions of $\vec{u}_{ph}$ and $\vec{I}_0$ coincide. Taking into account the axial symmetry of the problem and the relations $u_x^s = u^s\cdot\cos\theta$, $u_y^s = u^s\cdot\sin\theta$, we get from (10), (11):

$$b_{phth} = -\frac{k_B C_{m0} a^2}{2}\int_0^{\pi}\int_0^{\infty}\xi\frac{\partial\tau(1+\xi,\theta)}{\partial\theta}W(\xi,\theta)\sin^2\theta\,d\xi\,d\theta \qquad (12)$$

The formula (12) can be further simplified considering that, in practice, $\tau-\tau_\infty<<\tau_\infty$, and variations of the temperature with ξ and θ near the particle surface are mutually independent:

$$\tau(1+\xi,\theta)\approx\tau_\infty + f_1(\xi)\cdot f_2(\theta) \qquad (13)$$

As the numerical calculations showed, in the range $1<1+\xi<1.2$ the relationship (13) holds true with the accuracy better then 1% for all θ. Note that, for a particle in a constant external temperature gradient $\vec{\nabla}T$ the relationship (13) is the exact result: $T = T_0 + \nabla T\cdot r\cdot\cos\theta$. From (12) and (13) we obtain finally:

$$u_{ph} = b_{phth}\cdot\frac{T_0}{a}, \qquad b_{phth} = b_{th}\cdot g_{an}(n_r,\kappa\rho), \qquad \frac{T_0}{a} = 2\kappa\rho\frac{n_r I_0}{n_0 k_i},$$

$$b_{th} = \frac{2k_B C_{m0} a^2}{2+\frac{k_i}{k_e}}\int_0^{\infty}\xi W(\xi,\theta)f_1(\xi)d\xi,$$

$$g_{an}(n_r,\kappa\rho) = -\frac{1}{4}\left(2+\frac{k_i}{k_e}\right)\int_0^{\pi}\frac{d\tau(1,\theta)}{d\theta}\sin^2\theta\,d\theta. \qquad (14)$$

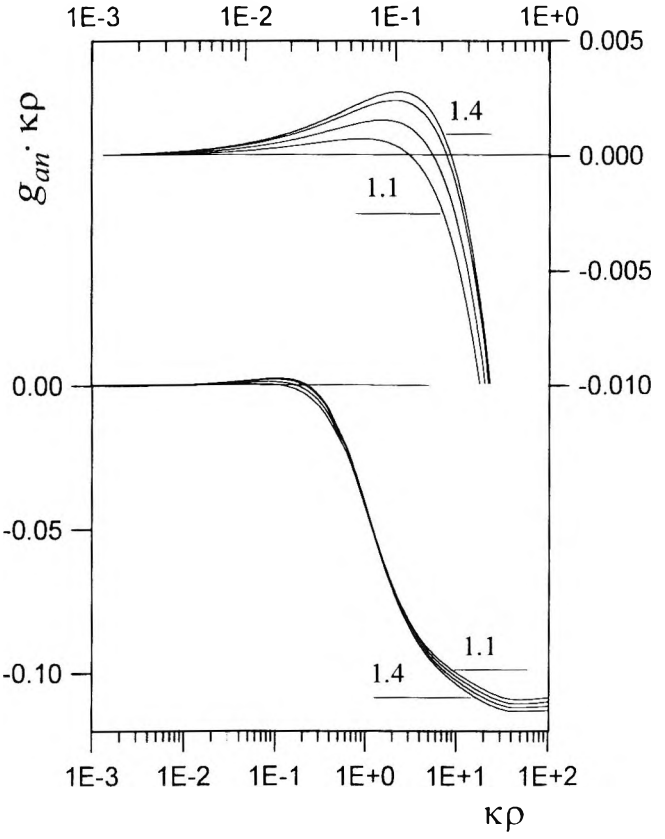

Figure 5. Dependence of the optical heating factor $g_{an}(n_r, \rho)\cdot\kappa\rho$ of photothermophoretic velocity of a particle on its size and optical constants. Curves are calculated for increasing values of n_r=1.1, 1.2, 1.3, 1.4, and for $k_i=k_e$. It is supposed that ρ>10.

According to (14), the photothermophoretic mobility of a particle is a product of its ordinary thermophoretic mobility and the factor $g_{an}(n_r,\kappa\rho)$. The latter is actually the surface average of the dimensionless gradient of the surface temperature of a particle. For $\kappa\rho<<1$, when the focusing process governs the internal distribution of light intensity, $[d\tau(1,0)/d\theta]<0$ (see Fig. 3), hence, $g_{an}(n_r, \kappa\rho)>0$. For $\kappa\rho>1$, when the main governing factor is the light absorption, $[d\tau(1,0)/d\theta]>0$ and $g_{an}(n_r, \kappa\rho)<0$. Fig. 5 shows the plots of the product $\kappa\rho\cdot g_{an}(n_r, \kappa\rho)$, which determines the dependence of photothermophoretic velocity of a particle on its optical constants and size.

The thermophoretic mobility of solid particle in electrolyte solution was considered.[21] For the model of electrostatic attractive potential at the particle surface, the result has the form:

$$b_{th} \approx -\frac{2k_B C_{m0}\delta^2(W_0-3)\exp(W_0)}{\eta\left(2+\frac{k_i}{k_e}\right)W_0^2}; \qquad \delta^2 \approx \frac{\varepsilon_0\varepsilon_m k_B T}{2C_{m0}(Ze)^2} \quad (15)$$

Here W_0 is the depth of potential well in units of thermal energy k_BT, δ is the width of the double electric layer near the particle surface, Ze is the charge of ions in electrolyte, ε_m is the relative dielectric constant of the liquid, ε_0 is the absolute permittivity. Formula (15) was derived for W_0 exceeding ~5, so for solid particles in electrolytes $b_{th}<0$. Hence, we obtain that photothermophoretic mobility of such particles is negative for $\kappa\rho<<1$, goes through the zero in the range $\kappa\rho\sim0.1\div0.3$, then stays positive and monotonically increases for $\kappa\rho>0.5$, with the saturation at very high $\kappa\rho$ values ~40.

Consider the relative magnitudes of the contributions from the light pressure and photothermophoresis to the total velocity of a particle. Using (1), (14), (15), we obtain:

$$\frac{u_{ph}}{u_{pr}} = -48\pi c k_B \frac{\kappa\rho\cdot g_{an}(n_r,\kappa\rho)}{\rho\cdot Q_{pr}(n_r,\kappa\rho)}\cdot\frac{n_r C_{m0}\delta^2(W_0-3)}{\lambda_0 k_i\left(2+\frac{k_i}{k_e}\right)W_0^2}\exp(W_0) \quad (16)$$

For typical values $W_0=5$, $n_r=1.2$ at $\lambda_0=500$ nm, and $k_i\approx k_e=1$ W/m/^{0}K that gives $(u_{ph}/u_{pr})= -1.13(\kappa\rho\cdot g_{an}/\rho Q_{pr})T(^0K)$. Using the plot of $\kappa\rho\cdot g_{an}$ from Fig. 5 and $Q_{pr}\approx0.35$,[5,7,8] the estimate for a particle with $2a=5\cdot10^{-5}$ m ($\rho=418$) at $\kappa\approx0.1$ and $T\approx300$ K is $(u_{ph}/u_{pr})\approx0.5$. Hence, for large absorbing particles, the photothermophoretic velocity component can be quite comparable with the light pressure component.

EXPERIMENTAL

The observations of particles photophoresis were made in two experimental arrangements. First, the motion of solid particles under the action of green light ($\lambda=514.5$ nm) from the Coherent INNOVA'300 Ar^+-ion laser was observed using the microscope. The laser beam was focused by a lens with the focal distance 10 cm at the opening of a glass capillary with a

Table 1

Characteristic Photophoretic Velocities of Various Particles*

Type and Diameter of Particles	Mean Velocity, μm/sec	Maximum Velocity Observed, μm/sec
latex red, 3 μm	7.4±2.3	10.3
latex white, 20.5 μm	13.5±1.7	15.7
latex red, 20.1 μm	24.3±2.5	26.3
glass, 22.1 μm	34.5±3.9	38.5

*Measured at P=0.36 W ($J_0 \approx 7.2 \cdot 10^7$ W/m^2).

Table 2

Characteristic Values of Photophoretic Velocities Measured for Glass Beads of 22.1μm Diameter at Various Magnitudes of Laser Power

Incident Light Irradiance, W/m^2	Mean Velocity, μm/sec	Maximum Velocity Observed, μm/sec
$7.2 \cdot 10^7$	34.5±3.9	38.5
$9.0 \cdot 10^7$	53.6	53.6
$10.7 \cdot 10^7$	64.4±35.6	130.4

rectangular cross-section, placed horizontally at the microscope stage along the beam direction. The capillary of ~300 μm height, ~5 mm breadth and 4 cm length was filled with a suspension of particles in distilled water. Particles velocity was evaluated using the eyepieces' graticules and the stop clock. The particles investigated were monodisperse white and red latex spheres, glass microspheres, and carbon black particles taken from polydisperse mixture subjected to sonication. The laser power P varied from 0.1 to 0.8 W. The diameter of focused laser beam was evaluated from the light-scattering trace visible in the suspension to be ~80 μm. That gave a relation $J_0 \approx 2 \cdot 10^8 \cdot P(W)$ W/m^2 for the mean incident light irradiance.

The results of direct velocity measurements are given in Tables 1,2. The positive photophoresis was observed for all particles. Within the measurements' uncertainty, their photophoretic velocity depended linearly on

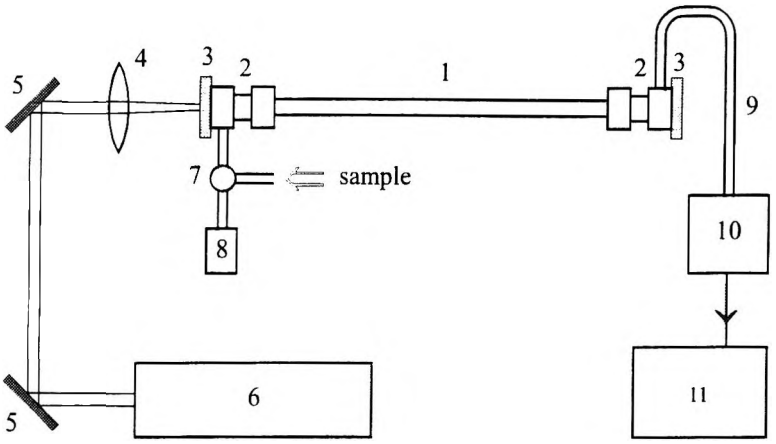

Figure 6. Experimental arrangement used for registration of particles photophoresis in a flow: 1 -metallic capillary; 2 - standard metallic gasket with a specially machined and polished face; 3 - optical window (glass plate) glued to the gasket; 4 - lens; 5 - mirror; 6 - Ar^+-ion laser; 7 - injection valve; 8 - syringe pump; 9 - output tubing; 10 - UV-detector; 11 -chart recorder.

the incident light irradiance. For carbon black particles of ~12 μm diameter and for latex particles of 9.87 μm diameter, the best-fit lines were $y=4.77x+0.51$ (carbon black) and $y=1.08x-0.24$ (latex) in the range $0<x<7$, where y is u_{ph} in μm/sec, x is J_0 in 10^7 W/m^2.

In the second arrangement, shown at Fig. 6, the observations were made of the redistribution of polydisperse carbon black particles in a flow under the action of laser light. The laser beam was focused at the entrance window of a round channel in the direction of suspension flow. To prevent the light escape from the channel due to the refraction, the channel was made of a metallic capillary. It had 0.765 mm inner diameter and 168 mm length. The elution curves of polydisperse carbon black particles injected into a flow of distilled water were registered using a UV detector in the gravity-sedimentation FFF conditions with the laser power switched on and off. The flow velocity at the channel axis was estimated to be 1.2 mm/sec. Typical elution curves are shown in Fig. 7. They had a strong initial maximum which we believe to correspond to the small particles fractions, and a considerably lower secondary maximum which can be attributed to larger particles. (No special measurements with the calibrated particles were carried out to determine exactly the operation mode of the channel system used).

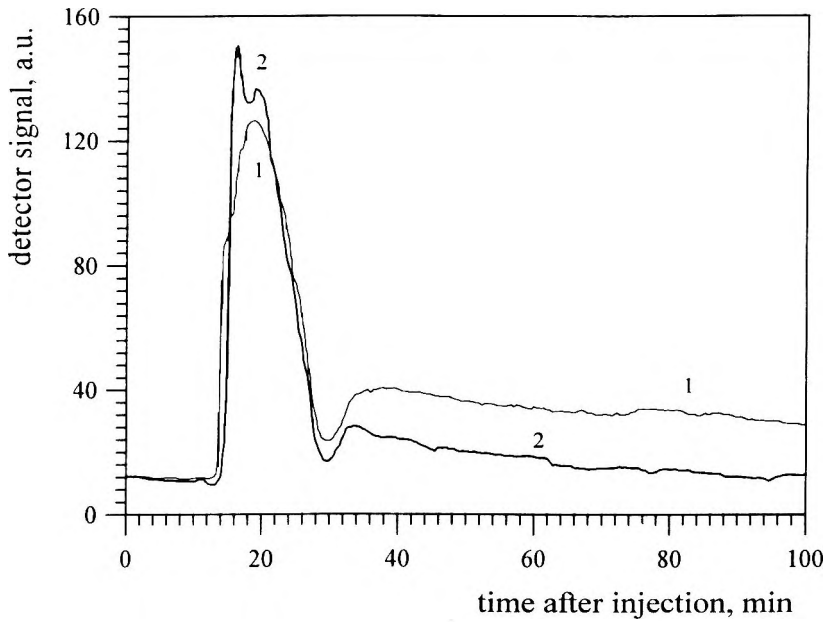

Figure 7. Elution curves obtained for injected samples of polydisperse carbon black particles using the flow system shown at Fig. 6: (1) - with no light; (2) - under the action of the focused laser light of 0.65 W power at λ=514.5 nm.

As Fig. 7 shows, the laser light action manifested itself as a change in the shape (splitting) of the initial maximum, and as a 4-5 minutes (~11%) shift of the secondary maximum towards the smaller times. The latter shift evidences the acceleration of particles along the flow under the light action.

DISCUSSION

Both the direct observations and the shape changes of the elution curves evidence the positive photophoresis of large solid particles in a fluid, namely, the motion in the direction of light propagation. The microscopic observation showed no visible indications, such as gaseous bubbles or convection flows, of appreciable heating of particles or surrounding water, even in the case of carbon black particles, provided the suspension was dilute enough. The estimates of the temperature rise due to the light absorption also give negligibly small values both for water and for latex or glass particles. Thus, the primary mechanism of the motion observed seems to be the light pressure, at least for

latex particles and glass beads. However, the contribution from the photothermophoretic mechanisms can be large enough in the case of highly absorbing carbon black particles. Let us estimate photophoretic velocities of particles under the observation conditions using the theoretical results of preceding sections. In water, the latex particles have $m_{rel}=1.191$ at $\lambda_0=589$ nm, and carbon black particles have $m_{rel}=1.27-i\cdot0.52$ at $\lambda_0=489$ nm. The particles investigated had very large values of size parameter, ranging from $\rho=24.45$ for $2a=3$ mm up to $\rho=180.2$ for $2a=22.1$ μm. According to Mie theory,[2,5,8] for such ρ values the efficiency factor $Q_{pr}(\rho)\approx$const, the estimates being $Q_{pr}\approx 0.25$ for latex and glass particles, and $Q_{pr}\approx1.1$ for carbon black particles. From the formula (1) we obtain $u_{ph}\approx7\cdot10^{-7}\cdot J_0(W/m^2)$ μm/sec for latex particles and $u_{ph}\approx3\cdot10^{-6}\cdot J_0(W/m^2)$ μm/sec for carbon black particles of size $2a\approx10$ mm in water. For carbon black particles, the formula (16) gives also $(u_{ph}/u_{pr})\approx0.4$ at T=300 °K. These estimates agree with slopes ratio $u_{carb}/u_{lat}=4.4$ of the best-fit lines for the measured light intensity dependencies of photophoretic velocities of latex and carbon black particles. The absolute values of the measured velocities are systematically lower than the estimated values, but this seems to be a result of overestimation of the incident laser power in the process of microscopic observation. It should be noted also that, for the same laser power the magnitudes of particles, velocities registered under the microscopic observations will be substantially higher then those observed in the channel measurements, because of light divergence in the channel.

Both the experimental observations and the theoretical estimates of the light-induced velocities of particles show, that velocities in the range 10-100 μm/sec (depending on the particles material and light intensity) can be easily obtained under FFF conditions using the focused laser radiation. These values can even be comparable with some flow velocities used in FFF, as evidences the change of the elution curves of Fig. 7 registered in the longitudinal field-flow geometry. In practical schemes of Photophoretic FFF, the incident light irradiance will be considerably lower because in the transverse field-flow geometry it is rather difficult to produce such a high irradiance value along the whole surface of a channel wall. So, the photophoretic velocities expected for the practical schemes will be essentially lower then those reported in this work. However, the transverse velocities of particles required for their longitudinal separation are also very small compared with the flow velocity. That gives a reason to expect, that the practical transverse-geometry Photophoretic FFF schemes can be implemented. The most promising is the use of highly convergent light beams enabling the light-trapping of particles[9,10] due to the gradient force, and the use of photophoretic forces in combination with some counter-balancing force, such as the gravity force.

ACKNOWLEDGMENTS

This work was supported, in part, by the RFBR grant #95-03-08390-a.

REFERENCES

1. J. C. Giddings, Chem. Eng. News, **66**, 34-45 (1988).

2. H. C. van de Hulst, **Light Scattering by Small Particles**, Wiley, New York, 1957.

3. M. Kerker, **The Scattering of Light and Other Electromagnetic Radiation**, Academic Press, New York, 1969.

4. C. F. Bohren, D. R. Huffman, **Absorption and Scattering of Light by Small Particles**, Interscience, New York, 1983.

5. W. M. Irvine, J. Opt. Soc. Am., **55**, 16-21 (1965).

6. A. V. Kats, Izvestija VUZov. Radiofizika, **18**, 566-576 (1975). [in Russian].

7. K. S. Shifrin, I. L. Zelmanovich, Optika i Spectroscopija, **17**, 113-118 (1964). [English Translation: Optics and Spectroscopy (USSR), **17**, 57 (1964)].

8. K. S. Shifrin, Optika i Spectroscopija, **18**, 690-697 (1965). [English Translation: Optics and Spectroscopy (USSR), **18**, 1345 (1965)].

9. G. Roosen, Canad. J. Phys., **57**, 1260-1279 (1979).

10. A. Ashkin, Biophysical J., **61**, 569-582 (1992).

11. M. Kerker, D. D. Cooke, J. Opt. Soc. Am., **72**, 1267-1272 (1982).

12. A. T. Sukhodol'skii, Bull. Acad. Sci., USSR, Physical Series, **50**, 51-57 (1986). Translated and published by Allerton Press, New York.

13. P. W. Dusel, M. Kerker, D. D. Cooke, J. Opt. Soc. Am., **61**, 55-59 (1979).

14. A. P. Prishivalko, **Optical and Thermal Fields Inside Light-Scattering Particles**, Nauka i Tekhnika Publ., Minsk, 1983. [in Russian].

15. M. Born, E. Wolf, **Principles of Optics**, Pergamon Press, Oxford, London, Edinburgh, New York, Paris, Frankfurt, 1964.

16. S. Solimeno, B. Crosignani, P. DiPorto, **Guiding, Diffraction, and Confinement of Optical Radiation**, Academic Press, Orlando, etc, 1986.

17. Yu. A. Kravtsov, Yu. I. Orlov, **Geometrical Optics of Nonhomogeneous Media**, Nauka Publ., 1980. [in Russian].

18. B. V. Derjaguin, G. P. Sidorenkov, E. A. Zubaschenko, E. P. Kiseleva, Kolloid. Zh., **9**, 335-341 (1947). [in Russian].

19. V. G. Levich, **Physicochemical Hydrodynamics**, Prentice-Hall, Englewood Cliffs, New Jersey, 1962.

20. J. L. Anderson, Ann. Rev. Fluid Mech., **21**, 61-99 (1989).

21. J. C. Giddings, P. M. Shiundu, S. N. Semenov, J. Colloid Interfacial Sci., **176**, 454-458 (1995).

Received February 4, 1997
Accepted April 17, 1997
Manuscript 4454

J. LIQ. CHROM. & REL. TECHNOL., 20(16 & 17), 2931–2932 (1997)

AWARD ANNOUNCEMENT

SPECIAL AWARD

will be presented to

PROFESSOR EDWARD S. YEUNG

at the

Frederick Conference on Capillary Electrophoresis

October 20 - 22, 1997
at
Hood College
Frederick, Maryland

The Frederick Conference on Capillary Electrophoresis Award will be presented to Professor E. S. Yeung for his outstanding contributions to capillary electrophoresis. A special session will be held in his honor on Tuesday, October 21, 1997, when a plaque will be presented to him.

Additional information about the award and the conference may be obtained from Ms. Margaret Fanning, Tel: (301) 846-5865; FAX: (301) 846-5866.

EDUCATION ANNOUNCEMENT

BASIC PRINCIPLES OF HPLC AND HPLC SYSTEM TROUBLESHOOTING

A Two-Day In-House Training Course

The course, which is offered for presentation at corporate laboratories, is aimed at chemists, engineers and technicians who use, or plan to use, high performance liquid chromatography in their work. The training covers HPLC fundamentals and method development, as well as systematic diagnosis and solution of HPLC hardware module and system problems.

The following topics are covered in depth:

- Introduction to HPLC Theory
- Modes of HPLC Separation
- Developing and Controlling Resolution
- Mobile Phase Selection and Optimization
- Ion-Pairing Principles
- Gradient Elution Techniques
- Calibration and Quantitation
- Logical HPLC System Troubleshooting

The instructor, Dr. Jack Cazes, is founder and Editor-in-Chief of the Journal of Liquid Chromatography & Related Technologies, Editor of Instrumentation Science & Technology, and Series Editor of the Chromatographic Science Book Series. He has been intimately involved with liquid chromatography for more than 35 years; he pioneered the development of modern HPLC technology. Dr. Cazes was Professor-in-Charge of the ACS Short Course and the ACS Audio Course on GPC, and has taught at Rutgers University. He is currently Visiting Scholar at Florida Atlantic University.

Details may be obtained from Dr. Jack Cazes, P. O. Box 970210, Coconut Creek, FL 33097. Tel.: (954) 570-9446; E-Mail: cazes@worldnet.att.net.

J. LIQ. CHROM. & REL. TECHNOL., 20(16 & 17), 2933-2940 (1997)

LIQUID CHROMATOGRAPHY CALENDAR

1997

OCTOBER 5 - 8: Conference on Formulations & Drug Delivery, La Jolla, California, sponsored by the ACS Div. of Biochem. Technol. Contact: ACS Meetings, 1155 16th St, NW, Washington, DC 20036. Tel: (202) 872-6286; FAX: (202) 872- 6013; Email: miscmtgs@acs.org.

OCTOBER 6 - 10: Validation d'une Procedure d'Analyse, Qulification de l'Appareillage; Application a la Chromatographie Liquide, Montpellier, France. (Training course given in French) Contact: Prof. H. Fabre, Tel: (33) 04 67 54 45 20; FAX: (33) 04 67 52 89 15; Email: hfabre@pharma.univ-montpl.fr

OCTOBER 19 - 22: 49th ACS Southeast Regional Meeting, Roanoke, Virginia. Contact: J. Graybeal, Chem Dept, Virginia Tech, Blacksburg, VA 24061, USA. Tel: (703) 231-8222; Email: reglmtgs@acs.org.

OCTOBER 21 - 23: Sensors Expo: Conference on Exposition of Sensors, Detroit, Michigan. Contact: Expocon Mgmt. Assoc., 3363 Reef Rd, P. O. Box 915, Fairfield, CT 06430-0915, USA. Tel: (203) 256-4700; Email: sensors@expo.com.

OCTOBER 21 - 23: Biotechnica Hannover '97: Int'l. Trade Fair for Biotechnology, Hannover, Germany. Contact: D. Hyland, Hannover Fairs USA, Inc., 103 Carnegie Center, Princeton, NJ 08540, USA.

OCTOBER 21 - 24: 152nd Fall Technical Meeting & Rubber Expo'97, Cleveland, Ohio, sponsored by ACS Div. of Rubber Chem. Contact: ACS Meetings, 1155 16th St, NW, Washington, DC 20036. Tel: (202) 872-6286.

OCTOBER 21 - 25: 33rd ACS Western Regional Meeting, Irvine, California. Contact: L. Stemler, 8340 Luxor St, Downey, CA 90241, USA. Tel: (310) 869-9838; Email: reglmtgs@acs.org.

OCTOBER 25 - 30: 24th Annual Conference of the Federation of Analytical Chemistry & Spectroscopy Societies (FACSS), Providence, Rhode Island. Contact: ACS Div. of Anal. Chem., Tel: (301) 846-4797; FAX: (301) 694-6860.

OCTOBER 26 - 29: ISPPP'97 – 17th International Symposium on the Separation of Proteins, Peptides, and Polynucleotides, Boubletree Hotel, Washington, DC. Contact: Janet Cunningham, Barr Enterprises, P. O. Box 279, Walkersville, MD 21793, USA. FAX: (301) 898-5596.

OCTOBER 26 - 29: 8th Symposium on Handling of Environmental & Biological Samples in Chromatography and the 26th Scientific Meeting of the Group of Chromatography and Related Techniques of the Spanish Royal Society of Chemistry, Almeria, Spain. Contact: M. Frei-Hausler, IAEAC Secretariat, Postfach 46, CH-4123 Allschwill 2, Switzerland. FAX: 41-61-4820805.

OCTOBER 29 - NOVEMBER 1: 32nd ACS Midwest Regional Meeting, Lake of the Ozarks, Osage Beach, Missouri. Contact: C. Heitsch, Chem Dept, Univ of Missouri-Rolla, Rolla, MO 65401, USA. Tel: (314) 341-4536; FAX: (314) 341-6033.

NOVEMBER 2 - 6: AAPS Annual Meeting & Expo, Boston, Mass. Contact: AAPS, 1650 King Street, Alexandria, VA 22314-2747, USA. Tel: (703) 548-3000.

NOVEMBER 2 - 6: 11th International Forum on Electrolysis in the Chemical Industry, Clearwater Beach, Florida. Contact: P. Klyczynski, Electrosysthesis Co., 72 Ward Rd., Lancaster, NY 14086, USA.

NOVEMBER 6 - 8: 2nd North American Research Conference on Emulsion Polymers/Polymer Colloids, Hilton Head Is., SC. Contact: A. V. Patsis, SUNY New Paltz, Inst. of Mater. Sci., New Paltz, NY 12561, USA.

NOVEMBER 7 - 8: 6th Conference on Current Trends in Computational Chemistry, Jackson, Miss. Contact: J. Leszcynski, Jackson State Univ., Chem. Dept., 1400 J. R. Lynch St., Jackson, MS 39217, USA. Tel: 601) 973-3482; Email: jersy@iris5.jusms.edu.

NOVEMBER 11 - 15: 5th Chemical Congress of North America, Cancun, Mexico. Contact: ACS Meetings, 1155 16th St, NW, Washington, DC 20036-4899, USA. Tel: (202) 872-6286; FAX: (202) 872-6128.

NOVEMBER 16 - 21: AIChE Annual Meeting, Westin Bonaventure/Omni Los Angeles, Los Angeles, California. Contact: AIChE, 345 East 47th St., New York, NY 10017, USA. Tel: 1-800-242-4363.

NOVEMBER 16 - 21: Eastern Analytical Symposium, Garden State Convention Center, Somerset, New Jersey. Contact: S. Good, EAS, P. O. Box 633, Montchanin, DE 19710-0635, USA. Tel: (302) 738-6218.

NOVEMBER 20 - 21: New Horizons in Chemistry Symposium, Los Angeles. Contact: J. May, Tel: (213) 740-5962; Email: jessy@methyl.usc.edu.

1998

FEBRUARY 28 - MARCH 1: 28th Annual Spring Prog. in Polymers: Degradation & Stabilization of Polymers, Hilton Head Is., South Carolina. Contact: A. V. Patsis, SUNY New Paltz, Inst. of Mater. Sci., New Paltz, NY 12561. Email: ims@mhv.net.

MARCH 1 - 6: PittCon '98, New Orleans, Louisiana. Contact: PittCon '98, Suite 332, 300 Penn Center Blvd., Pittsburgh, PA 15235-5503, USA. Tel: (800) 825-3221; FAX: (412) 825-3224.

MARCH 8 - 12: AIChE Spring National Meeting, Sheraton, New Orleans. Contact: AIChE, 345 East 47th St., New York, NY 10017, USA.

MARCH 15 - 18: 14th Rocky Mountain Regional Meeting, Tucson, Arizona. Contact: R. Pott, Univ of Arizona, Tucson, AZ 85721.

MARCH 23 - 25: 5th Meeting on Supercritical Fluids: Materials and Natural Products Processing, Nice, France. Contact: F. Brionne, Secretariat, ISASF, E.N.S.I.C., 1 rue Grandville, B.P. 451, F-54001 Nancy Cedex, France. Email: brionne@ensic.u-nancy.fr.

MARCH 29 - APRIL 2: 215th ACS National Meeting, Dallas, Texas. Contact: ACS Meetings, 1155 16th Street, NW, Washington, DC 20036, USA.

MAY 3 - 8: HPLC'98 – 22nd International Symposium on High Performance Liquid Phase Separations and Related Techniques, Regal Waterfront Hotel, St. Louis, Missouri. Contact: Janet Cunningham, Barr Enterprises, P. O. Box 279, Walkersville, MD 21793, USA.

MAY 20 - 22: 32nd Middle Atlantic ACS Regional Meeting, Wilmington, Delaware. Contact: G. Trainor, DuPont Merck, P. O. Box 80353, Wilmington, DE 19880-0353. Email: reglmtgs@acs.org.

MAY 26 - 29: VIIIth International Symposium on Luminescence Spectrometry in Biomedical and Environmental Analysis: Detection Techniques and Applications in Chromatography and Capillary Electrophoresis, Las Palmas de Gran Canaria (Canary Islands), Spain. Contact: Dr. Jose Juan Dantana Rodriguez, University of Las Palmas of G. C., Chem. Dept., Faculty of Marine Sci., 35017 Las Palmas de G. C., Spain. Tel: 34 (9) 28 45.29.15 / 45.29.00; FAX: 34 (9) 28 45. 29.22; Email: josejuan.santana@quimica.ulpgc.es.

MAY 27 - 29: 30th Central Regional ACS Meeting, Ann Arbor, Michigan. Contact: D. W. Ewing, J. Carroll Univ., Chem. Dept., Cleveland, OH 44118. Tel: (216) 397-4241. Email: ewing@jevaxa.jeu.edu.

JUNE 1 - 3: 31st Great Lakes Regional ACS Meeting, Milwaukee, Wisconsin. Contact: A. Hill, Univ. of Wisc., Chem. Dept., Milwaukee, WI 53201, USA. Tel: (414) 229-4256; Email: reglmtgs@acs.org.

JUNE 2 - 5: Third International Symposium on Hormone and Veterinary Drug Residue Anbalysis, Congres Centre Oud Sint-Jan, Bruges, Belgium. Contact: C. Van Peteghem, Dept. of Food Analysis, University of Ghent, Harelbekestraat 72, B-9000 Ghent, Belgium. Tel: (32) 9/264.81.34.

JUNE 10 - 12: 53rd ACS Northwest Regional Meeting, Columbia Basin College, Pasco, Washington. Contact: K. Grant, Math/Science Div, Columbia Basin College, 2600 N 20th Ave, Pasco, WA 99301, USA.

JUNE 13 - 19: 26th ACS National Medical Chemistry Symposium, Virginia Commonwealth Univ/Omni Richmond Hotel, Richmond, Virginia. Contact: D. J. Abraham, Virginia Commonwealth Univ, Dept of Med Chem, P. O. Box 581, Richmond, VA 23298, USA. Tel: (804) 828-8483.

JULY 12 - 16: SFC/SFE'98: 8th International Symposium & Exhibit on Supercritical Fluid Chromatography, St. Louis, Missouri. Contact: Janet Cunningham, Barr Enterprises, P. O. Box 279, Walkersville, MD 21793, USA.

AUGUST 23 - 28: 216th ACS National Meeting, Boston, Massachusetts. Contact: ACS, 1155 16th Street, NW, Washington, DC 20036, USA.

AUGUST 31 - SEPTEMBER 3: AIChE Conference on Safety in Ammonia Plants & Related Facilities, Charleston Place, Charleston, South Carolina. Contact: AIChE, 345 East 47th St., New York, NY 10017, USA. Tel: 1-800-242-4363.

SEPTEMBER 7 - 11: 15th International Symposium on Medicinal Chemistry, Edinburgh, Scotland. Contact: M. Campbell, Bath University School of Chemistry, Claverton Down, Bath, BA2 7AY, UK. Tel: (44) 1225 826565; FAX: (44) 1225 826231; Email: chsmmc@bath.ac.uk.

SEPTEMBER 13 - 18: 22nd International Symposium on Chromatography, ISC'98, Rome, Italy. Contact: F. Dondi, Chem. Dept., Universita di Ferrara, Via L. Borsari, 46, I-44100 Ferrara, Italy. Tel: 39 (532) 291154; FAX: 39 (532) 240707; Email: mo5@dns.Unife.it.

SEPTEMBER 24 - 26: XIVth Conference on Analytical Chemistry, sponsored by the Romanian Society of Analytical Chemistry (S.C.A.R.), Piatra Neamt, Romania. Contact: Dr. G. L. Radu, S.C.A.R., Faculty of Chemistry, University of Bucharest, 13 Blvd. Reepublicii, 70346 Bucharest - III, Romania.

NOVEMBER 4 - 7: 50th ACS Southwest Regional Meeting, Res. Triangle Pk, North Carolina. Contact: B. Switzer, Chem Dept, N Carolina State University, Box 8204, Raleigh, NC 27695-8204. USA. Email: switzer@chemdept.chem.ncsu.edu.

NOVEMBER 15 - 20: AIChE Annual Meeting, Fontainbleu/Eden Roc, Miami Beach, Florida. Contact: AIChE, 345 East 47th St., New York, NY 10017, USA.

1999

MARCH 7 - 12: PittCon '99, Orlando, Florida. Contact: PittCon '99, Suite 332, 300 Penn Center Blvd., Pittsburgh, PA 15235-5503, USA.

MARCH 21 - 25: 217th ACS National Meeting, Anaheim, Calif. Contact: ACS Meetings, 1155 16th Street, NW, Washington, DC 20036-4899, USA.

AUGUST 22 - 26: 218th ACS National Meeting, New Orleans, Louisiana. Contact: ACS Meetings, 1155 16th Street, NW, Washington, DC 20036-4899, USA. Tel: (202) 872-4396; FAX: (202) 872-6128; Email: natlmtgs@acs.org.

OCTOBER 8 - 13: 51st ACS Southeast Regional Meeting, Knoxville, Tennessee. Contact: C. Feigerle, Chem Dept, University of Tennessee, Knoxville, TN 37996, USA. Tel: (615) 974-2129; Email: reglmtgs@acs.org.

2000

MARCH 5 - 10: PittCon 2000, Chicago, Illinois. Contact: PittCon 2000, Suite 332, 300 Penn Center Blvd., Pittsburgh, PA 15235-5503, USA.

MARCH 26 - 31: 219th ACS National Meeting, Las Vegas, Nevada. Contact: ACS Meetings, 1155 16th Street, NW, Washington, DC 20036. Email: natlmtgs@acs.org.

JUNE 25 - 30: HPLC'2000 – 24th International Symposium on High Performance Liquid Phase Separations, Seattle, Washington. Contact: Barr Enterprises, P.O.B. 279, Walkersville, MD 21793, USA.

AUGUST 20 - 25: 220th ACS National Meeting, Washington, DC. Contact: ACS Meetings, 1155 16th Street, NW, Washington, DC 20036-4899, USA. Email: natlmtgs@acs.org.

DECEMBER 14 - 19: 2000 Int'l Chemical Congress of the Pacific Basin Societies, Honolulu, Hawaii. Contact: ACS Meetings, 1155 16th St., NW, Washington, DC 20036, USA. Tel: (202) 872-4396; FAX: (202) 872-6128; Email: pacific@acs.org.

2001

APRIL 1 - 6: 221st ACS National Meeting, San Francisco, Calif. Contact: ACS Meetings, 1155 16th Street, NW, Washington, DC 20036. Email: natlmtgs@acs.org.

AUGUST 25 - 31: 222nd ACS National Meeting, Chicago, Illinois. Contact: ACS Meetings, 1155 16th Street, NW, Washington, DC 20036-4899, USA. Email: natlmtgs@acs.org.

2002

APRIL 7 - 12: 223rd ACS National Meeting, Orlando, Florida. Contact: ACS Meetings, 1155 16th Street, NW, Washington, DC 20036-4899, USA. Email: natlmtgs@acs.org.

SEPTEMBER 8 - 13: 224th ACS National Meeting, Boston, Mass. Contact: ACS Meetings, 1155 16th Street, NW, Washington, DC 20036-4899, USA. Email: natlmtgs@acs.org.

2003

MARCH 23 - 28: 225th ACS National Meeting, New Orleans, Louisiana. Contact: ACS Meetings, 1155 16th Street, NW, Washington, DC 20036-4899, USA. Email: natlmtgs@acs.org.

SEPTEMBER 7 - 12: 226th ACS National Meeting, New York City. Contact: ACS Meetings, 1155 16th Street, NW, Washington, DC 20036-4899, USA. Tel: (202) 872-4396; FAX: (202) 872-6128; Email: natlmtgs@acs.org.

2004

MARCH 28 - APRIL 2: 227th ACS National Meeting, Anaheim, California. Contact: ACS Meetings, 1155 16th Street, NW, Washington, DC.

AUGUST 22 - 27: 228th ACS National Meeting, Philadelphia, Pennsylvania. Contact: ACS Meetings, 1155 16th Street, NW, Washington, DC 20036-4899, USA. Tel: (202) 872-4396; FAX: (202) 872-6128.

2005

MARCH 13 - 18: 229th ACS National Meeting, San Diego, California. Contact: ACS Meetings, 1155 16th Street, NW, Washington, DC 20036-4899, USA. Tel: (202) 872-4396; FAX: (202) 872-6128; Email: natlmtgs@acs.org.

AUGUST 28 - SEPTEMBER 2: 230th ACS National Meeting, Washington, DC. Contact: ACS Meetings, 1155 16th Street, NW, Washington, DC 20036-4899, USA. Tel: (202) 872-4396; FAX: (202) 872-6128; Email: natlmtgs@acs.org.

2006

MARCH 26 - 31: 231st ACS National Meeting, Atlanta, GA. Contact: ACS Meetings, 1155 16th Street, NW, Washington, DC 20036-4899, USA. Tel: (202) 872-4396; FAX: (202) 872-6128; Email: natlmtgs@acs.org.

SEPTEMBER 10 - 15: 232nd ACS National Meeting, San Francisco, California. Contact: ACS Meetings, 1155 16th Street, NW, Washington, DC 20036-4899, USA. Tel: (202) 872-4396; FAX: (202) 872-6128; Email: natlmtgs@acs.org.

2007

MARCH 25 - 30: 233rd ACS National Meeting, Chicago, Illinois. Contact: ACS Meetings, 1155 16th Street, NW, Washington, DC 20036-4899, USA. Tel: (202) 872-4396; FAX: (202) 872-6128; Email: natlmtgs@acs.org.

AUGUST 19 - 24: 234th ACS National Meeting, Boston, Massachusetts. Contact: ACS Meetings, 1155 16th Street, NW, Washington, DC 20036-4899, USA. Tel: (202) 872-4396; FAX: (202) 872-6128; Email: natlmtgs @acs.org.

The Journal of Liquid Chromatography & Related Technologies will publish, at no charge, announcements of interest to scientists in every issue of the journal. To be listed in the Liquid Chromatography Calendar, we will need to know:

a) Name of the meeting or symposium,
b) Sponsoring organization,
c) When and where it will be held, and
d) Whom to contact for additional details.

Incomplete information will not be published. You are invited to send announcements to **Dr. Jack Cazes, Editor, Journal of Liquid Chromatography & Related Technologies, P. O. Box 970210, Coconut Creek, FL 33097, USA.**

INSTRUCTIONS TO AUTHORS

The ***Journal of Liquid Chromatography & Related Technologies*** is published in the English language for the rapid communication of research results in liquid chromatography and its related sciences and technologies.

Directions for Submission

One complete original manuscript and two (2) clear copies, all with figures, must be submitted for peer review. After all required revisions have been completed, and the final manuscript has been accepted, the author will be asked to provide, if possible, a 3½" or 5¼" PC-Compatible computer diskette containing the complete manuscript. Microsoft Word, Word for Windows, WordPerfect, WordPerfect for Windows and ASCII are preferred formats. Text, tables, and figure captions, should be saved in a single file on the diskette; tables and figure captions should be placed at the end of the text. Label the diskette with the corresponding author's last name, the title of the manuscript and our file number assigned to the manuscript.

Submission of a manuscript on diskette, in a suitable format, will significantly expedite its publication.

Manuscripts and computer diskettes should be mailed to the Editor:

Dr. Jack Cazes
Journal of Liquid Chromatography & Related Technologies
P. O. Box 970210
Coconut Creek, FL 33097

Reprints

Due to the short production time for papers in this journal, it is essential to order reprints immediately upon receiving notification of acceptance of the manuscript. A reprint order form will be sent to the author with the letter of acceptance for the manuscript. Reprints are available in quantities of 100 and multiples thereof. Twenty (20) free reprints will be included with orders of 100 or more reprints.

Format of the Manuscript

NOTE: Failure to adhere to the following guidelines will delay publication.

1. The preferred dimensions of the printed area of a page are
   6" (15.2 cm) width by 8.5" (21.6 cm) height.
   Use Times New Roman 12 point font, if possible.

The general organization of the manuscript should be:

Title
Author(s)' names and full addresses
Abstract
Text Discussion
References

2. **Title & Authors**: The entire title should be in bold-face capital letters and centered within the width of the printed area, located 2 inches (5.1 cm) from the top of the page. This should be followed by 2 lines of space, then by the names and addresses of the authors, also centered, in the following manner:

A SEMI-AUTOMATIC TECHNIQUE FOR THE SEPARATION AND DETERMINATION OF BARIUM AND STRONTIUM IN WATER BY ION EXCHANGE CHROMATOGRAPHY

F. D. Pierce, H. R. Brown

Utah Biomedical Test Laboratory
520 Wakara Way
Salt Lake City, Utah 84108

3. **Abstract**: The heading **ABSTRACT** should be typed boldface, capitalized and centered, 2 lines below the address(es). This should be followed by a *single-spaced*, concise abstract. Allow 2 lines of space below the abstract before beginning the text of the manuscript.

4. **Text Discussion**: Whenever possible, the text discussion should be divided into major sections such as

INTRODUCTION
EXPERIMENTAL
RESULTS
DISCUSSION
ACKNOWLEDGMENTS

These **major headings** should be separated from the text by two lines of space above and one line of space below. Each major heading should be typed boldface, in capital letters, centered.

Secondary headings, if any, should be in boldface, placed flush with the left margin, and have the first letter of main words capitalized. Leave two lines of space above and one line of space below secondary headings.

5. The **first line of each paragraph** within the body of the text should be indented a third of an inch.

6. **Acknowledgments**, sources of research funds and address changes for authors should be listed in a separate section at the end of the manuscript, immediately preceding the references.

7. **References** should be numbered consecutively and placed in a separate section at the end of the manuscript. They should be typed single-spaced, with one line space between each reference.

Each reference should contain names of all authors (with initials of their first and middle names); do not use *et al.* for a list of authors. Abbreviations of journal titles will follow the American Chemical Society's Chemical Abstracts List of Periodicals. The word **REFERENCES**, in boldface type, should be capitalized and centered above the reference list.

Following are acceptable reference formats:

Journal:

1. D. K. Morgan, N. D. Danielson, J. E. Katon, Anal. Lett., 18, 1979-1998 (1985).

Book:

1. L. R. Snyder, J. J. Kirkland, **Introduction to Modern Liquid Chromatography**, John Wiley & Sons, Inc., New York, 1979.

Chapter in a Book:

1. C. T. Mant, R. S. Hodges, "HPLC of Peptides," in **HPLC of Biological Macromolecules**, K. M. Gooding, F. E. Regnier, eds., Marcel Dekker, Inc., New York, 1990, pp. 301-332.

8. Each page of manuscript should be numbered lightly, with a light blue pencil, at the bottom of the page.

9. Only standard symbols and nomenclature, approved by the International Union of Pure and Applied Chemistry (IUPAC) should be used. **Hand-drawn characters are not acceptable.**

10. Material that cannot be typed, such as Greek symbols, script letters and structural formulae, should be drawn carefully with dark black India ink. Do not use any other color ink.

Additional Typing Instructions

1. The manuscript must be prepared on **good quality white bond paper**, measuring approximately 8½ x 11 inches (21.6 cm x 27.9 cm). International paper, size A4, is also acceptable. The typing area of the first page, including the title and authors, should be 6" (15.2 cm) wide by 8.5" (21.6 cm) height.

2. All text, except the abstract, should be **typed 1½ or double-spaced**.

3. It is essential to use **dark black** typewriter or printer ribbon so **that clean, clear, solid characters** are produced. Characters produced with a dot/matrix printer are not acceptable, even if they are "near letter quality" or "letter quality." Erasure marks, smudges, hand-drawn corrections and creases are not acceptable.

4. **Tables** should be typed separate from the text, at the end of thye manuscript. **A table may not be longer than one page**. If a table is larger than one page, it should be divided into more than one table. The word **Table** (followed by an Arabic number) should precede the table and should be centered above the table. The title of the table should have the first letters of all main words in capitals. Table titles should be typed single line spaced, across the full width of the table.

5. **Figures** (drawings, graphs, etc.) should be printed or professionally drawn with black India ink on separate sheets of white paper, and should be placed at the end of the text. They should not be inserted into the body of the text. They should not be reduced to a small size. Preferred size for figures is from 5 inches x 7 inches (12.7 cm x 17.8 cm) to 8½ inches by 11 inches (21.6 cm x 27.9 cm). Photographs should be professionally prepared, black and white, *glossy* prints. All labels and legends in figures should be large enough to remain legible when figures are reduced to fit the journal's pages. They should not be hand-drawn.

Captions for figures should be typed, single-spaced, on a separate sheet of white paper, along the full width of the type page, and should be preceded with the word **Figure** and an Arabic numeral. Figure numbers, name of senior author and an arrow indicating "top" should be written in light blue pencil on the back of each figure. Indicate the approximate placement for each figure in the text with a note written with a light blue pencil in the margin of the manuscript page.

6. The reference list should be typed single-spaced. A single line space should be inserted after each reference. The format for references should be as given above.

Manuscripts which require correction of English usage will be returned to the author for major revision.

Improve your laboratory skills with the ***new edition*** *of the...*

Handbook of Thin-Layer Chromatography

Contains **timesaving** features such as an extensive glossary of **key** terms *and* a **useful** directory of manufacturers/suppliers of TLC instruments and products!

Second Edition, Revised and Expanded

(Chromatographic Science Series/71)

edited by
JOSEPH SHERMA and
BERNARD FRIED
Lafayette College, Easton, Pennsylvania

March, 1996
1128 pages, illustrated
$225.00

Written by over **40** internationally acclaimed authorities on thin-layer chromatography (TLC), this comprehensive ***Second Edition*** presents the **latest** techniques, instrumentation, and applications of overpressurized, rotational, and high-performance quantitative TLC.

Provides in-depth discussions of theory and optimization that facilitate a thorough understanding of experimental procedures!

Offering a **systematic** approach to TLC, the ***Handbook of Thin-Layer Chromatography, Second Edition*** covers

- introductory information
- sample preparation
- layers and mobile phases
- chromatographic techniques
- detection
- quantification
- applications to many sample types

Marcel Dekker, Inc.
270 Madison Avenue
New York, NY 10016
(212) 696-9000

Hutgasse 4, Postfach 812
CH-4001 Basel, Switzerland
Tel. 061-261-8482

Praise for the First Edition...

"...The wealth of practical detail can potentially save many hours of laboratory experimentation. The purchase price is easily covered by just one hour of saved labour."
—Chromatographia

"...overall this book should serve for many years as *the* source of information on TLC."
—Analytica Chimica Acta

"...one of the best practical books in the field."
—International Journal of Environmental and Analytical Chemistry

"...contains a wealth of expertise from the practitioner point of view and provides many practical tips on the application of thin-layer chromatography to anyone using this analytical technique."
—Journal of Labelled Compounds and Radiopharmaceuticals

"...extremely useful for those who wish to discover how a TLC separation has been performed."
—Talanta

The ***Second Edition*** contains **new**, practical information on

- the detection, identification, and documentation of chromatogram zones
- optical quantitation
- flame ionization detection
- automation and robotics
- nucleic acid derivatives

Furnishing more than **3150** up-to-date literature citations and over **800** drawings, photographs, tables, and equations, the ***Handbook of Thin-Layer Chromatography, Second Edition*** is an essential reference for analytical chemists, chromatographers, biochemists, biologists, laboratory technicians, medical technologists, biotechnologists, forensic and environmental scientists, veterinary toxicologists, pharmaceutical analysts, and graduate school students in these disciplines.

Contents

continued on back

Handbook of Thin-Layer Chromatography

Second Edition, Revised and Expanded

Contents *(continued)*

ISBN: 0—8247—9454—0

This book is printed on acid-free paper.

Also in the ***Chromatographic Science Series...***

Thin-Layer Chromatography

Techniques and Applications

Third Edition, Revised and Expanded

BERNARD FRIED and **JOSEPH SHERMA**/ 464 pages, illustrated / $185.00

"...an excellent reference book...gives an almost encyclopedic review of all aspects of TLC that should be appreciated by beginners and experts alike." —***Inform***

"...an honest effort has been made to revise and update the material in the earlier edition....succeeds admirably in providing an introductory text in TLC....extensively and well illustrated." —***Analyst***

"...offers an up-to-date survey of TLC techniques in the 1990s." —***Journal of Chromatography***

"...presents up-to-date developments in modern instrumental TLC, along with the conventional techniques of planar chromatography." —***Journal of Liquid Chromatography***

Contents

ISBN: 0—8247—9171—1

Achieve accurate and precise quantitative analysis with...

Generously illustrated with 160 richly detailed diagrams that clarify the construction of the detectors, facilitating understanding of their performance and function!

Chromatographic Detectors

Design, Function, and Operation

(Chromatographic Science Series/73)

RAYMOND P. W. SCOTT
Georgetown University, Washington, D.C., and Birbeck College, University of London, United Kingdom

July, 1996 / 536 pages, illustrated / $150.00

Written by a seasoned chromatographer with more than 40 years' experience in the field, this reference comprehensively covers the design, construction, and operation of gas chromatography (GC), liquid chromatography (LC), and thin-layer chromatography (TLC) detectors—*all in one convenient, up-to-date source.*

Emphasizing the essential use of common specifications to describe all detectors, allowing easy comparison of their attributes, this practical guide

- discusses the properties of chromatography detectors and the best way to measure their efficacy
- reviews factors that impair the column resolution *before* solutes reach the detector
- describes and explains the relatives merits of the more popular detectors, including the most recent commercially available models as well as lesser-known devices
- explores the exclusive number of TLC detectors available, including automatic scanning devices
- surveys those chromatograph/spectrometer tandem systems that have been satisfactorily developed and details their interfacing, function, and areas of application
- and more!

Chromatographic Detectors serves as an important on-the-job tool for chromatographers; analytical, physical, pharmaceutical, oil, petroleum, clinical, forensic, environmental, and synthetic chemists and biochemists; biotechnologists; and upper-level undergraduate, graduate, and continuing-education students in these disciplines.

Contents

ISBN: 0—8247—9779—5

This book is printed on acid-free paper.

Marcel Dekker, Inc. 270 Madison Avenue, New York, NY 10016 • (212) 696-9000
Hutgasse 4, Postfach 812, CH-4001 Basel, Switzerland • Tel. 061-261-8482

Analyze bulk and formulated drug products with the ***new edition*** *of...*

Chromatographic Analysis of Pharmaceuticals

SECOND EDITION

(Chromatographic Science Series/74)

edited by **JOHN A. ADAMOVICS**
Cytogen Corporation, Princeton, New Jersey

October, 1996 / 544 pages, illustrated / $165.00

Praise for the first edition...

"There is no doubt that this book should have wide appeal to all those involved in pharmaceutical analysis. Over 1300 drugs and related substances are considered....**a veritable mine of information.**"—*Analyst*

"...an **excellent** reference for those who are involved in the chromatographic analysis of pharmaceutical compounds and their formulation."
—*Journal of Pharmaceutical Sciences*

"...**recommended** as a primary source of information for drug analysis in different drug forms."
—*Journal of Chromatography*

"...a **valuable** reference source for practicing chromatographers in the pharmaceutical industry."
—*Microchemical Journal*

"...provides a **comprehensive** overview of the chromatographic methods of analysis for pharmaceuticals."
—*Analytical Chemistry*

"...has a place as a **quick reference tool** and as a general introduction to chromatography in pharmaceutics."
—*LC-GC*

"...contains **a wealth of information** on the main chromatographic techniques and numerous examples on the application of these methods in the drug industry."
—*Journal of Labelled Compounds and Radiopharmaceuticals*

Updated and revised throughout, the ***Second Edition*** of ***Chromatographic Analysis of Pharmaceuticals*** explores the chromatographic methods used for the measurement of drugs, impurities, and excipients in pharmaceutical preparations—such as tablets, ointments, and injectables.

Contains a 148-page table listing the chromatographic data of over 1300 drugs and related substances—including sample matrix analyzed, sample handling procedures, column packings, mobile phase, mode of detection, and more!

Maintaining the features that made the first edition so popular, ***Chromatographic Analysis of Pharmaceuticals, Second Edition*** now offers

- *new chapters* on capillary electrophoresis and supercritical fluid chromatography
- *up-to-the-minute* information on proteinaceous pharmaceuticals
- *new coverage* of chromatographic methods from the Chinese Pharmacopoeia
- *updated data* from *US Pharmacopoeia 23* and from the British and European Pharmacopoeias
- the *latest methods* developed by Instrument and column manufacturers
- over 2100 key literature citations, including *recent references* from the chromatographic literature up to 1996

Written in a clear, easy-to-read style, ***Chromatographic Analysis of Pharmaceuticals, Second Edition*** serves as a timesaving resource for analytical, bioanalytical, pharmaceutical, organic, clinical, physical, quality control, and process chemists and biochemists; chromatographers; pharmaceutical scientists; and professional seminars and graduate-level courses in these disciplines.

Contents

ISBN: 0—8247—9776—0

This book is printed on acid-free paper.

Marcel Dekker, Inc.

270 Madison Avenue, New York, NY 10016 • (212) 696-9000
Hutgasse 4, Postfach 812, CH-4001 Basel, Switzerland • Tel 061-261-8482

Establish efficient strategies for the practical application of liquid chromatography in the field of oligomer characterization with...

LIQUID CHROMATOGRAPHY OF OLIGOMERS

(Chromatographic Science Series/72)

CONSTANTIN V. UGLEA
Institute of Biological Research, Ministry of Research and Technology, Iasi, Romania, and the Medical and Pharmaceutical University, Iasi, Romania

June, 1996 / 360 pages, illustrated / $150.00

This **state-of-the-art** reference details the principles and mechanisms of, and the equipment and optimal working conditions for, the liquid-chromatographic separation of well-defined oligomeric species and fractions with narrow molecular weight distribution.

Provides a complete description of the applications and possible performance of liquid chromatography in the field of oligomer separation!

Liquid Chromatography of Oligomers

- elucidates theoretical concepts such as the mechanism of retention and the thermodynamic explanation of oligomer separation
- discusses the definition and history of chromatography
- covers both simple and complex forms of chromatographic instrumentation
- delineates procedures used for the fractionation of oligomeric mixtures
- lists the main producers of chromatographic devices
- describes the chemical nonhomogeneity of polymers and oligomers
- presents the nomenclature of oligomers
- examines gel-permeation chromatography
- and more!

Containing over **1475** citations to key literature sources, ***Liquid Chromatography of Oligomers*** is an ideal reference for analytical chemists, biochemists, chromatographers, laboratory technicians, and upper-level undergraduate and graduate students in these disciplines.

Contents

ISBN: 0—8247—9720—5

This book is printed on acid-free paper.

Marcel Dekker, Inc.

270 Madison Avenue
New York, NY 10016
(212) 696-9000

Hutgasse 4, Postfach 812
CH-4001 Basel, Switzerland
Tel. 061-261-8482